

*Discriminating Interceptor
Technology Program
(DITP) Support*

February 1999

Prepared by:

*Schafer Corporation
1901 N. Ft. Myer Drive
Suite 800
Arlington, VA 22209
703/558-7900*

DISTRIBUTION STATEMENT A
Approved for Public Release
Distribution Unlimited

19990409 080

DMIC QUALITY INSPECTED 2

**Task Report – Naval Research Laboratory
Contract N00014-97-D-2014/001**

Discriminating Interceptor Technology Program (DITP) Support

This documents Schafer Corporation's support to the Discriminating Interceptor Technology Program (DITP). Schafer provides support to three activities in DITP, the Ballistic Missile Defense Organization, the Naval Space and Warfare Systems Command and the Naval Research Laboratory.

DITP is a result of BMDO's need for advanced technologies to enhance and enable current and future interceptor seeker systems. The charter of the Technical Operations (TO) Deputate is to "support research on more advanced ballistic missile defense technologies to improve performance of components of both TMD and NMD systems, and provide advanced capabilities such as Boost Phase Intercept (BPI)." In light of this charter, TO conducted an FY93 survey of technologies needed for advanced and future BMD systems. The survey, based on Operational Requirements Documents (ORDs), the System Threat Analysis Report (STAR), and the Architecture Integration Study (AIS), identified several core technology needs. Midcourse discriminating interceptor seekers, BPI sensors, and cruise missile acquisition sensors were recognized as requiring component improvements. The fusion of data from dissimilar sensors on a single platform, was viewed as an area in which modest investment could significantly enhance existing seeker performance and produce high payoffs.

Based on an exhaustive advanced sensor technology review during FY94, weighing technology deficiencies against existing research efforts, several advanced component technologies were selected for development. These technologies included: passive simultaneous multi-color infrared (IR) sensors, long-range laser radars (LADAR), and multispectral discrimination algorithms.

This led to a technology development program, the Advanced Sensor Technology Program (ASTP) which was initiated to investigate advanced technologies in the areas of IR focal plane arrays (FPAs), LADAR technologies and multi-sensor tracking and discrimination algorithms. DITP seeks to capitalize on ASTP's advancements and focus selected technologies to answer the advanced interceptor issues developed in the DITP Technology Program Goals Document (TPGD). Target data from these advanced sensors will be synergistically fused to demonstrate enhanced target acquisition, selection, and hit-to-kill aimpoint performance for the multispectral domain.

The aim then of DITP is to choose a technology from each of the potential technologies for the two color passive sensor, the Laser Radar and the Fusion Processor and Algorithms and integrate them to do a series of ground and flight demonstrations. These will demonstrate advanced detection and discrimination technology to be used against the advanced threats described in the TPGD. In accordance with the guidance of the Director, BMDO, the TO Deputate has involved the three US military services in DITP to take advantage of expertise and advancements in seeker technology. Motivations for this partnership include the need to decrease technology development time and build upon existing research programs.

The DITP system is thus being developed under the direction of four government entities. The Naval Research Laboratory (NRL) serves as the Test Bed Integrator and is responsible for integrating and testing the DITP technologies to demonstrate system level objectives. This culminates in a flight demonstration which is also NRL's responsibility.

DITP includes Executive Agents (EA) identified by the BMDO TOS to provide government furnished equipment (GFE) as well as technical expertise to support the successful completion of the overall program goals. BMDO/TOS, NRL, EA, and contract support representatives will be called upon to participate in the overall program management. The EAs will develop the following advanced seeker technology subsystems:

- Passive Sensor Subsystem (PSS), Air Force Research Laboratory/VSSS (Kirtland) (AFRL/VSSS (Kirtland));
- Laser Radar Subsystem (LADAR), U. S. Army Space and Missile Defense Command/TC/SR (Huntsville) (USASMDC/TC/SR (Huntsville));
- Fusion Processor and Algorithms Subsystem (FP&A), Air Force Research Laboratory/IFSB (Rome) (AFRL/IFSB (Rome)).

SPAWAR heads the development of the angle-angle-range three dimensional imaging radar being developed under DITP. BMDO who provides management and technical direction provides analytical support to each of the EAs. As such technical work for both serves the dual purpose of developing analytic and technical capability and using the analytic tools to simulate system performance and thus demonstrate utility for DITP and the individual technologies. In terms of this technical support most of Schafer's activity is in support of the laser radar development and the development of discrimination algorithms required to perform the experiments and demonstrations.

During this phase of the NRL contract important advances were made in developing the DITP design and in preparing concepts for the flight test. The most significant of these are reviewed here:

1) **White PCN targets:** AMOR test data at 532 nm were received from SSDC on 8/10 for two objects covered with white PCN: "S3_RV" and "S3_LREP." An initial guess at fitting the data indicated that the objects were long cones with 22% and 88% diffuse reflectivity, respectively. Later, the exact dimensions and surface construction of these objects were specified by TDC: S3_RV was loose WPCN with perforations and aluminized mylar backing, and S3_LREP was tightly fitting WPCN with no perforations. A refit to the data with the exact conical dimensions yielded a good data fit assuming 21% diffuse + 2.2% retro-reflective and 86% diffuse + 7% retro-reflective, respectively. The diffuse reflectivities are much higher than that assumed in the IET target specification (8%).

1. **EOO / Fibertek ladar tests:** Short test-range speckle statistics simulation and Gaussian mode radiometry were investigated in order to implement the short-range ladar tests. Following conversations with Frank Hanson and the EOO staff, simulating the correct speckle by pinhole selection and placement was determined. The Gaussian mode radiometry for the test was analyzed. Data were received from EOO/Fibertek resulting from their opal glass diffuser plate with annular-mask and circular -mask experiments. By fitting a negative-binomial with arbitrary N_s , M , good M values (agreeing with theory) were obtained for fitting the histogram data.

The receiving optics design and pinhole filter layout for the EOO/Fibertek full scale styrofoam cone test was reviewed. After some initial confusion about lens orientation and the deviation away from the AMOR and Hanson optical layouts, agreement with the Zeemax raytrace results by EOO were reached.

A precision fit of the Intevac detector (IPD) output pulse height distribution was made to Max Planck Institute data supplied by Intevac. Following discussions with Intevac staff, a revised model was also constructed. This model PHD is used in fitting any ladar measurement data to theory when the Intevac IVPD is used.

Shot-noise stochastic process theory calculations were implemented to refine the ladar signal processing theory. This treatment takes into account the impulse response of the electronics and the detector and, in particular, pulse "pile up" effects as the photon / photo-

electron arrival rate increases and impulse-responses superimpose. The theory was then applied to the EOO/Fibertek simulated far-field cone data and the opal glass with mask data. Much better fits to the theoretical cone "M" values were obtained, about 10% lower than actually measured for the 10 range-bins. The opal glass diffuser plate with mask data, however, still produced higher "M" values than expected. An IRIS-Active Systems speckle paper was prepared describing this work.

3) **Laser super-Gaussian mode:** Fibertek pointed out that the output of the laser amplifier is about 1 cm in diameter and is a super-Gaussian of order 4 to 6. As the super-Gaussian mode propagates through space, it will decompose into the TEM₀₀ (Gaussian) mode plus higher order Laguerre-Gauss modes, as these are the solutions to the wave equation in free space. This will change the far field irradiance distribution. A "Hankel-transform radial E-field propagator" code was rewritten in order to examine the propagation of the DITP laser super-Gaussian mode output. The Gaussian mode options in optical design codes do not handle super-Gaussians. It was found that, for a super-Gaussian of order 5, if the mode were expanded to a 6 mm $1/e^2$ radius beam-waist near the telescope exit aperture, then a 52 μ r $1/e^2$ irradiance diameter near-Gaussian resulted in the far field. (DITP spec.) If the super-Gaussian were expanded in size closer to the 25 cm diameter aperture and also diverged, then central irradiance maxima or minima will result along with radial lobes. A memo was written on 9/21 summarizing these analyses.

4) **IRIS Publications:** At the Missile Defense, Sensors, Environments, and Algorithms conference January 26- 28, Schafer staff presented two papers on the DITP ladar and signal processing: "DITP 0.5 μ m Ladar Target speckle Statistics and Their Impact on Discrimination" and "Three-Dimensional Template Correlations for Direct Detection Laser-Radar Target Recognition." Copies of the papers are attached below.

5) **DITP Algorithms:** Schafer corrected several misconceptions which were built into the "optimization" approach which was planned for FPSim. A global optimization scheme had been concocted which failed to reflect the three stage engagement which the active sensor in DITP carries out. By carefully analyzing the timeline needed for effective use of the ladar Schafer had already determined an efficient path for ladar utilization. In this path acquisition of all available objects is first executed, then intensity modulation measurements on all objects whose length and shape make them credible as RV's are made, and finally angle-angle-range-intensity imagery is gathered on those two or three objects most likely to be the RV. This resolved imagery is processed by the moment-of-inertia algorithm. At long ranges, it is

advisable to do complete acquisition including reduction of the range rate error to 40 cm/s because at that range that is all that really can be done with the ladar. There are not enough photoelectrons per pulse to make efficient use of any other type of measurement.

A detailed tutorial was given by Schafer on this three stage engagement and the three different types of measurement involved, one for each stage.

The dangers of trying to somehow capture the essence of what is really a very simple and effective sensor resource management scheme through parameters like "priority" and "urgency" were underlined. What has to happen is no more complicated than using artillery, machine gun fire, rifles, side arms, and bayonets sequentially against an advancing force. A "global optimizer" is poorly positioned to make smart use of some of the most attractive sensor fusion available to DITP, such as using the passive sensor to accurately cue the ladar as to when a precessing object is at maximum cross section, and minimum cross section, in gathering intensity modulation measurements. A deterministic scheduler embodying a deep understanding of the nature of the measurements being made and the motivation for them was emphatically recommended by Schafer as being far more appropriate to this task than a "global optimizer" taking pride in its lack of engineering judgement as to what to do when.

Schafer also pointed out shortcomings in the multiple target tracking algorithm development which was described at the analysts meeting. Much of the state of the art in multiple target tracking, especially multiple hypothesis tracking (MHT) and the observation to track assignment approach taken by MHT was apparently being reinvented with difficulty. Schafer indicated that precursor programs which eventually became DITP had explored these issues in depth.

The thirteen attached reports appendices A - M document the progress made under this phase of the DITP development.

The Navy Center for Space Technology at the Naval Research Laboratory was selected to serve as the Test Bed Integrator (TBI) for DITP. As such Schafer provided support to the three critical areas of TBI activity; System Engineering, the Test and Demonstration Working Group (TDWG) and the Optics, Pointing and Stabilization Working Group (OPS WG).

The System Engineering activity centered around developing the DITP System Specification. The specification serves as a compendium of the requirements for the DITP

system which would allow it to complete its proposed experiments and demonstrations. The input comes from the entire TBI/EA DITP team and must be filtered for consistency and realizability. Schafer's role has been to develop the specification consistent with these inputs. Appendix N is the latest version of the document at the end of the present period of performance and served as our input to NRL.

The TDWG activity was to participate in the development of the DITP Test Program and then support its execution. As such we attended several TDWG working meetings. We helped prepare the Systems Requirements Design Review presentation for the TDWG and was assigned the lead for developing the DITP System Test Plan. Again this plan has inputs from the entire DITP Team. Appendix O is the present draft input to NRL. Two presentations of note which Schafer presented at the most recent TDWG provided in Appendices P and Q. Appendix P is a presentation on the capabilities of the Innovative Science and Technology Experimentation Facility (ISTEF). This facility would provide a test site for field testing of the sensors and processors to verify both functionality and performance. Appendix Q provides analyses to show the laser radar performance using different target geometries, orientations, coning, reflectivities, etc. This is important because the level of target tolerancing and performance on these parameters can affect the cost of a successful flight demonstration.

The OPS WG activity centered on developing the requirements for the optical system for performing all the DITP functions. Appendix R is the Requirements Summary and Analysis which documents this activity. These requirements will have to be modified as any of the sensor requirements change. Also included is the Preliminary Report on the optical system dichronic beamsplitter (Appendix S) and a discussion on the issues related to the laser radar concept of operations (Appendix T).

Appendix A

HANKEL-TRANSFORM PROPAGATION OF THE DITP SUPER-GAUSSIAN LASER MODE

Douglas G. Youmans (Rev. 11/2/98)

At a meeting at Fibertek on August 26, Ralph Burnham / Fibertek stated that the output of the DITP laser amplifier and the doubler-crystal would be a super-Gaussian of order 4 to 6 and about 7 mm in diameter. Using the Hankel-transform propagator, we show that if the super-Gaussian mode were 9 mm in $1/e^2$ -irradiance-waist-radius near the telescope exit aperture, then a near Gaussian irradiance with $52 \mu\text{r } 1/e^2$ diameter would result, meeting the DITP specifications. Also, the super-Gaussian may be expanded and defocused to fill the exit aperture and also meet the $52 \mu\text{r } 1/e^2$ irradiance diameter requirement. In this case the far-field and near-field irradiance can have significant maxima and minima as a function of radius. Propagation from the laser amplifier/doubler to the exit aperture primary mirror is TBD pending element spacing information.

1.0 Review of TEM₀₀ (Gaussian) Mode Propagation

To propagate Gaussian or TEM₀₀ modes, we may follow the treatment of Siegman¹⁻³. The beam waist radius, ω_1^0 , denoted by superscript "o", is generally the best starting point. The mode radius at the next mirror or lens, ω_2 , is given by¹

$$\omega_2(z) = \left(\omega_1^{o^2} + \left(\frac{\lambda}{\pi \omega_1^o} \right)^2 z^2 \right)^{1/2} \quad (1)$$

where z = waist to element distance. The phase-front radius of curvature at z is¹

$$R_2(z) = z + \left(\frac{\pi \omega_1^{o^2}}{\lambda} \right)^2 z^{-1} \quad (2)$$

After reflecting off the mirror or passing through the lens, the radius of curvature is²

$$R_3 = \left(\frac{1}{R_2} - \frac{1}{f} \right)^{-1} \quad (3)$$

and also

$$\omega_3 = \omega_2 \quad (4)$$

where "f" is the focal length, and, for a flat mirror, $f = \text{infinity}$.

The distance to the next (virtual) beam waist is given by³

$$z_3 = \frac{R_3}{1 + (\lambda R_3 / \pi \omega_3^2)^2} \quad (5)$$

and the beam waist at this location would be given by³

$$\omega_3'' = \omega_3 \left(1 + (\pi \omega_3^2 / \lambda R_3)^2 \right)^{-1/2} \quad (6)$$

The mode is then propagated to the next optical element or "z" value by

$$z_3' = z_{\text{element}} + z_3 \quad (7)$$

and the mode radius and curvature are again given by equations (1) and (2), with a new waist radius, ω_3^0 , and propagation distance, z_3' . The mode is propagated down any optical train by cycling through equations

(1) through (7). The sign convention assumed here is that the light propagates from left to right and negative "R" and negative "z" indicate a converging mode. Equations (1) through (7) allow easy propagation of a laser mode down the optical train and out the telescope exit aperture provided there is no clipping or obscuration.

We note that Gaussian modes do not obey geometrical optics. For example, the standard thin lens formula,

$$\frac{1}{s} + \frac{1}{s'} = \frac{1}{f}$$

where s and s' are the object and image distances, respectively, becomes

$$\frac{1}{s + z_R^2 / (s - f)} + \frac{1}{s'} = \frac{1}{f}$$

where $z_R = \pi(\omega^0)^2 / \lambda$ is the Rayleigh range.

When the Gaussian mode becomes clipped, centrally obscured, or aberrated it is no longer Gaussian, and the equations (1) to (7) do not exactly apply. The Hankel-transform propagator may be used to determine the propagating E-field in these situations, as discussed below.

2.0 The Hankel Transform Propagator for Azimuthally Symmetric E-fields

If the mode is a super-Gaussian, then we may use the fast Hankel transform propagator^{4,5} for propagating cylindrically symmetric E-fields⁶. The "fast" Hankel transform utilizes FFT's in the computation instead of solving eigenvalue-integral-equations iteratively, and it is therefore much faster and can handle any cylindrically symmetric optic, gain, loss, or conjugation elements.

The Fresnel-Kirchoff integral in cylindrical co-ordinates from (r_1 at $z=0$) to (r_2 at $z=L$) is given by

$$E_{2\lambda}(r_2) = \frac{j^{\lambda+1}}{L} k \exp(-jk r_2^2 / 2L) \int_0^a E_{1\lambda}(r_1) J_\lambda\left(\frac{k r_1 r_2}{L}\right) \exp(-jk r_1^2 / 2L) r_1 dr_1 \quad (8)$$

where " 2λ " is the number of azimuthal nulls and is zero here. Defining

$$\psi_{2\lambda}(r_2) = r_2 E_{2\lambda}(r_2) \left(\frac{j^{\lambda+1}}{L}\right) \exp(jk r_2^2 / 2L), \quad (9)$$

we then get

$$\psi_{2\lambda}(r_2) = \frac{k}{L} \int_0^a E_{1\lambda}(r_1) J_\lambda\left(\frac{k r_1 r_2}{L}\right) \exp(-jk r_1^2 / 2L) r_1 r_2 dr_1. \quad (10)$$

The Gardner transform,

$$r_1 = \rho_1 \exp(\alpha x) \quad r_2 = \rho_2 \exp(\alpha y), \quad (11)$$

is applied resulting in

$$\begin{aligned} \psi_{2\lambda}[\rho_2 \exp(\alpha y)] &= \frac{k}{L} \int_{-\infty}^{\infty} E_{1\lambda}[\rho_1 \exp(\alpha x)] J_\lambda\left(\frac{k \rho_1 \rho_2 \exp[\alpha(x+y)]}{L}\right) \times \\ &\quad \exp\left(\frac{-jk [\rho_1 \exp(\alpha x)]^2}{2L}\right) \rho_1^2 \rho_2 \exp[\alpha(x+y)] \alpha \exp(\alpha x) dx. \end{aligned} \quad (12)$$

For numerical analysis we let

$$r_1 = \rho_1 \exp(\alpha n), \quad r_2 = \rho_2 \exp(\alpha m). \quad (13)$$

Defining

$$f_\lambda(n) = [\rho_1 \exp(\alpha n)] E_{1\lambda}[\rho_1 \exp(\alpha n)] \exp\left(\frac{-jk[\rho_1 \exp(\alpha n)]^2}{2L}\right) \quad (14)$$

and

$$g_\lambda(n+m) = \frac{\alpha k \rho_1 \rho_2 \exp[\alpha(n+m)]}{L} J_\lambda\left(\frac{k \rho_1 \rho_2 \exp[\alpha(n+m)]}{L}\right) \quad (15)$$

the Fresnel-Kirchoff integral then becomes

$$\psi_{2\lambda}(m) = \sum_{n=0}^{N-1} f_\lambda(n) g_\lambda(n+m) = f_\lambda(n) \otimes g_\lambda^*(n+m) \quad (16)$$

Which can be solved using Fourier transforms (FT) as

$$\psi_{2\lambda}(n) = FT[FT(f_\lambda(n)) IFT(g_\lambda(n))] \quad (17)$$

and finally

$$E_{2\lambda}(r_2) = (j^{\lambda-1}) \psi_{2\lambda}(r_2) \exp(-jk r_2^2 / 2L) / r_2. \quad (18)$$

We note that the same sign conventions as for the Gaussian mode propagation algorithms are assumed.

2.1 Super-Gaussian Sizing at the Exit Aperture (normal ladar technique)

The most common definition of a super-Gaussian with circular symmetry is

$$I(r) = \frac{2 P_{\text{laser}}}{\pi \omega^2} \exp(-2((x^2 + y^2) / \omega^2)^{S_g}) \quad (19)$$

If we select $S_g = 5$ and place the mode at the exit aperture, we can adjust the $1/e^2$ -irradiance radius, ω , to

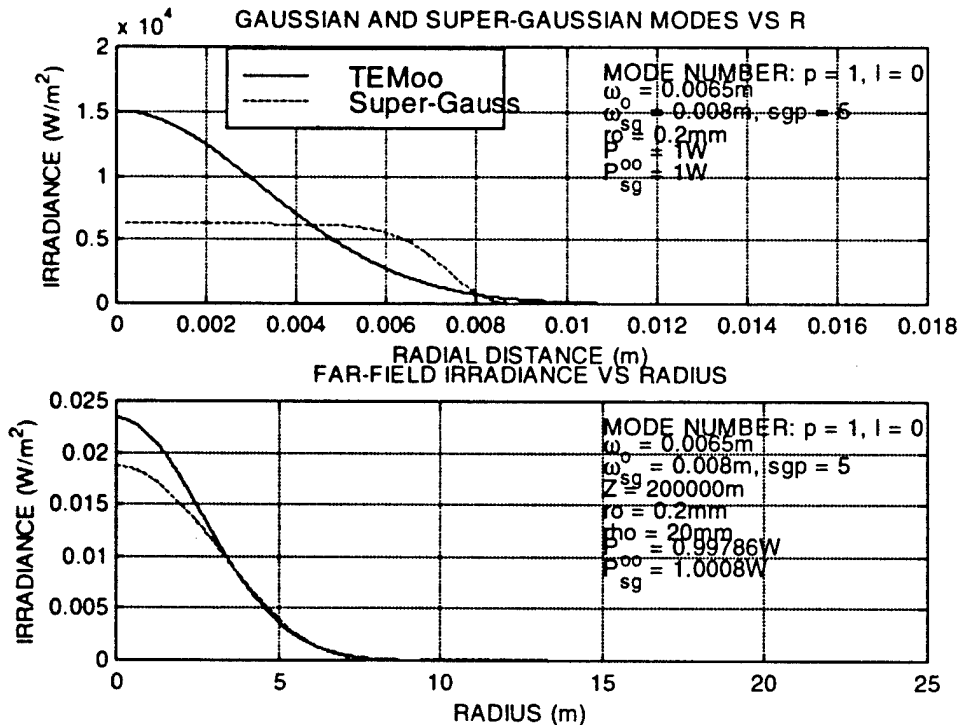


Figure 1A. Super-Gaussian beam waist radius = 8 mm.

produce a desired near-field or far-field irradiance distribution. The actual beam waist, ω° , might be somewhat behind the primary (virtual), or somewhat in front of the primary with negligible effect at distance.

In Figures 1A, 1B, and 1C are the exit aperture and 200 km range irradiance distributions at for a 8 mm, 9 mm, and 10 mm super-Gaussian transmitted mode.

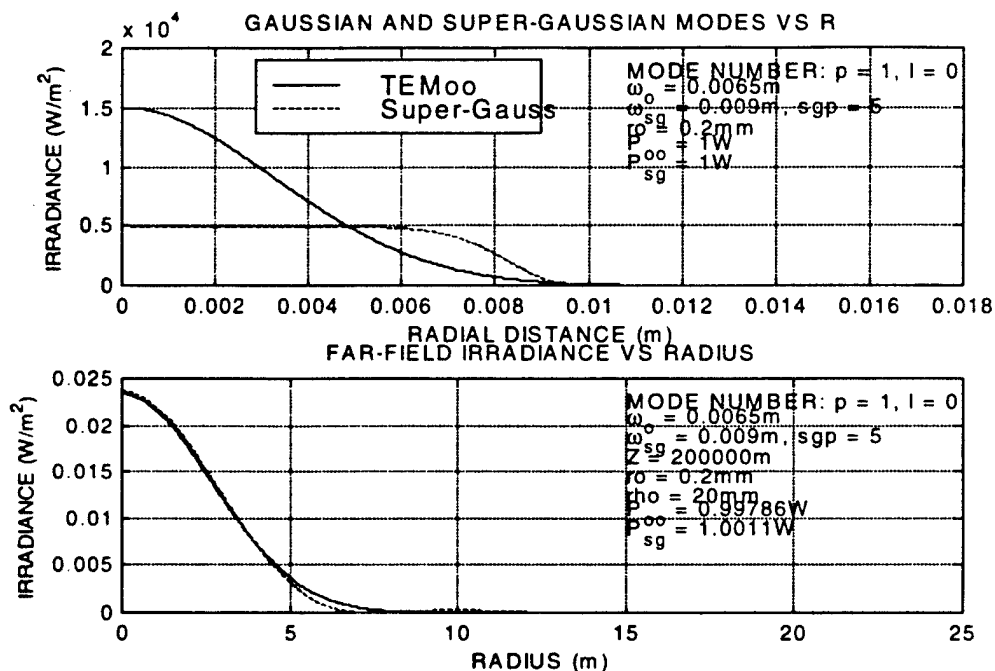


Figure 1B. Super-Gaussian beam waist radius = 9 mm.

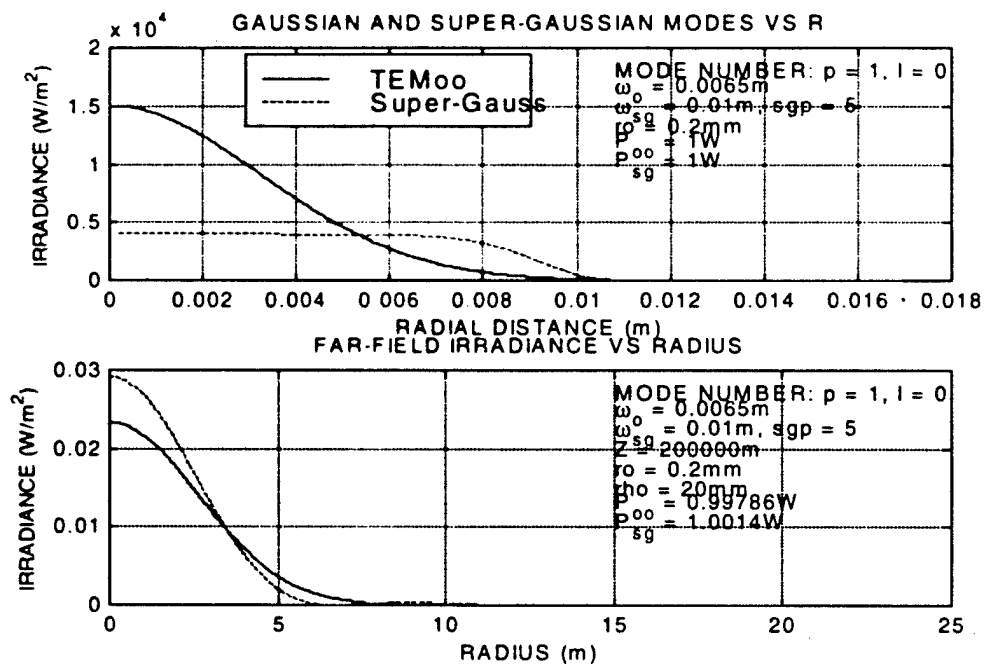


Figure 1C. Super-Gaussian beam waist radius = 10 mm.

We see that by setting the super-Gaussian waist radius at 9 mm, it produces very nearly the same Gaussian distribution as a TEM₀₀ mode having a 6.5 mm waist radius: $(4/\pi) \lambda / (2\omega^0) = 52 \mu\text{r}$ per the DITP spec.

2.2 Filling the Exit Aperture and Diverging the Laser Mode

The super-Gaussian mode $1/e^2$ irradiance radius was expanded out to 7 cm, 10 cm, and 12.5 cm at the telescope exit aperture. The down-range irradiance was calculated at distances of 10 km to 800 km with some phase-front curvature added to increase divergence. A 10 cm radius with a phase-front curvature of around 3500 m appeared to give the most uniform (flat) down-range irradiance with approximately 52 μr full-angle. Some representative plots are included below. Exact super-Gaussian expansion and divergence can be selected in view of over all systems performance.

2.3 Amplifier/Doubler to Exit Aperture Propagation

TBD pending approximate lens focal lengths and lens separation values.

REFERENCES

1. Siegman, A., *An Introduction to Lasers and Masers*, McGraw-Hill Book Co., 1971, p. 308.
2. Siegman, p. 312.
3. Siegman, p. 310.
4. Siegman, A., "Quasi fast Hankel transform," *Opt. Lett.* 1, 1977, p. 13.
5. Murphy, W., Bernabe, "Numerical procedures for solving nonsymmetric eigenvalue problems associated with optical resonators," *Appl. Opt.* Vol. 17, No. 15, 1 Aug. 1978, p. 2358.
6. Gaskill, J., *Linear Systems, Fourier Transforms, and Optics*, John Wiley, 1978, p. 317.
7. Fink, D., "Coherent Detection Signal-to-Noise," *Appl. Opt.*, Vol. 14, No. 3, Mar 1975.

The **local oscillator E-field** is assumed to be 5% of the 150 mW reference sample from the master-oscillator and having a beam waist (i.e., nearly collimated) radius of 5 mm at the lens in front of the detector. The Gaussian local-oscillator mode is then propagated, using the Gaussian mode equations, onto the detector surface. The mixing efficiency and the CNR are then determined following the "overlap" integral treatment of Fink⁷. The mixing efficiency is defined as

$$\gamma = \frac{\left| \int_{A_{det}} E_s E_{LO}^* ds \right|^2}{\int_{A_{det}} |E_s|^2 ds \int_{A_{det}} |E_{LO}|^2 ds}$$

where E_s is the backscattered deterministic "signal" E-field and the integrals are over the detector area, A_{det} . The CNR is then

$$CNR = \frac{\gamma \eta_{QE} P_s}{h\nu(50 \times 10^6 \text{ Hz})}$$

since the IF bandwidth of each SAW is 50 MHz. Since this is a perfect sinewave backscattered, we also have the full time-bandwidth product enhancement of $50 \times 10^6 \times 100 \times 10^{-6} = 5,000$. The Narcissus filter can remove 80dB of this return. In **Figure 5** the backscattered irradiance and LO irradiance are plotted from the center of the detector. For the 5 mm mode radius case, a mixing efficiency of only .0143 is calculated. This is well below the 0.83 peak value⁷ for mixing an Airy disk with a Gaussian LO. However, even with this low mixing efficiency, a CNR = +77.49dB results, and subtracting 80dB for the filter, and multiplying by 5,000, we are left with a residual CNR of 2,803. Likewise for the 4.35 mm mode radius case, we are left with a residual CNR of 450 as shown in **Figure 6**. Consequently, a redesigned annular alignment including a wedged surface at 9.115 mm and reduced power reflectivity is being implemented.

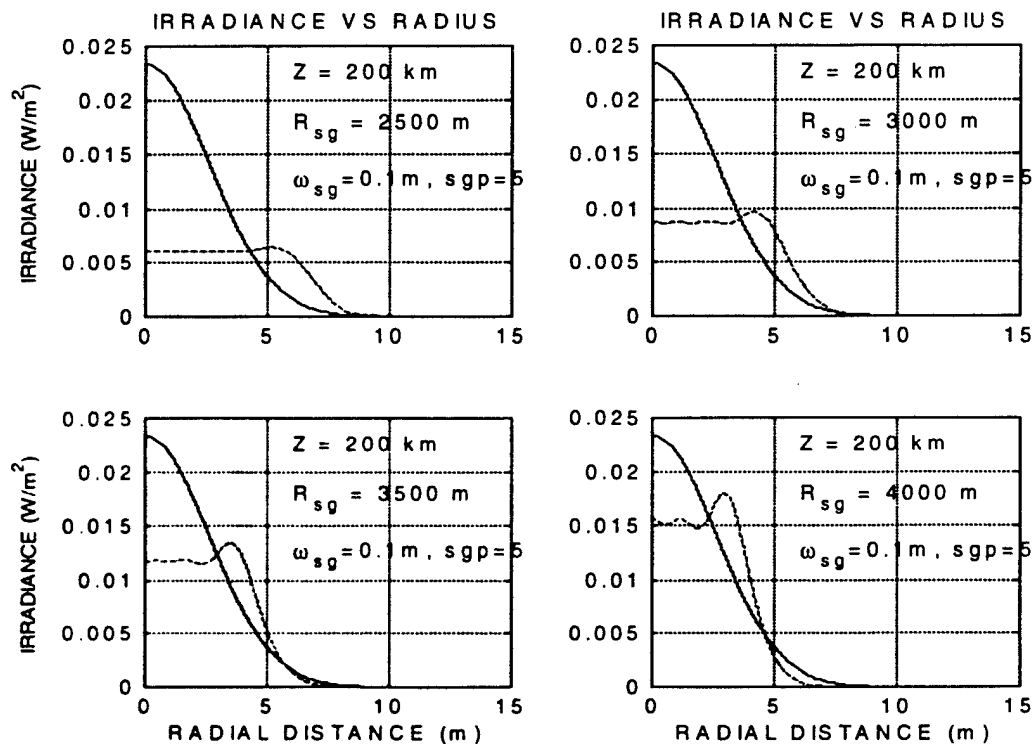


Figure 10. Irradiance (W/m^2) at 200 km range versus phase-front curvatures of 2500, 3000, 3500, and 4000 m. Solid line is reference Gaussian mode.

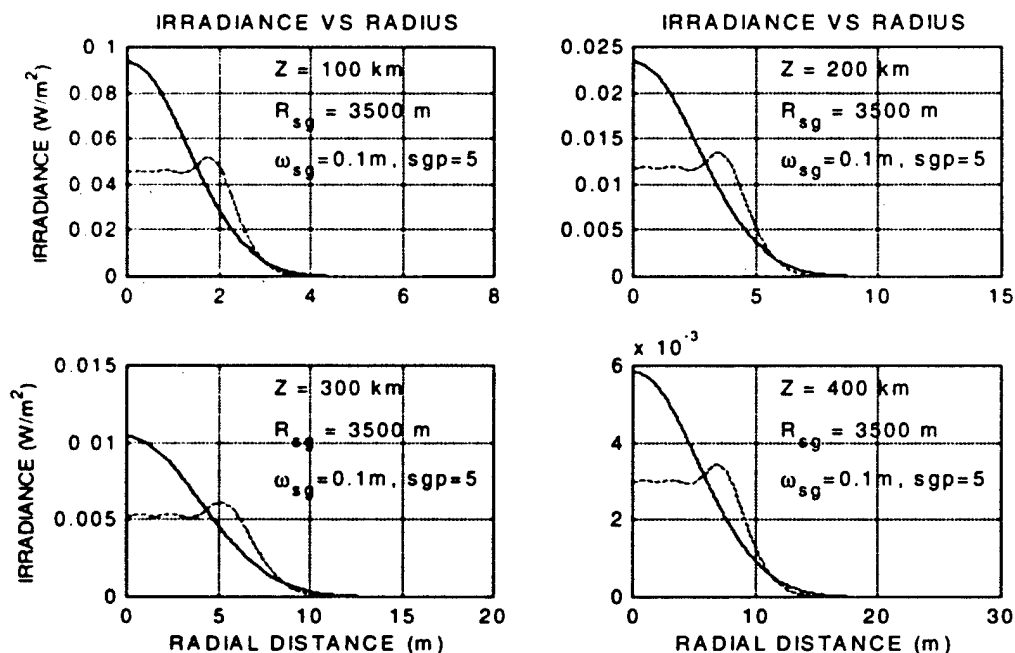


Figure 11. Irradiance (W/m^2) vs radial distance at ranges of 100 km to 400 km with a constant phase front curvature of 3500 m. Solid line is reference Gaussian mode.

Appendix B

White PCN AMOR Data Fit

Douglas Youmans (9/1/98 DITPwpc2.doc)

The AMOR facility recently made measurements on two white PCN covered targets. The target S3_RV was covered with loosely fitting white PCN with perforations and aluminized mylar backing. The target S3_LREP was covered with tightly fitting white PCN having no perforations. The exterior shape of both targets was a cone 2.52 m long and 0.84 m base diameter. A rounded edge at the cone base with a radius of 0.08 m was also noted.

1.0 Cone Cross-section

For a cone of length "h" and base diameter "2a", the total cone **diffuse** scattering-function in (m^2/sr) is given by

$$\sigma_d(\theta) = \frac{\rho_d h^2}{2\pi} \frac{\sin(\alpha)}{\cos^2(\alpha)} I_{cn}(\theta) \quad (1)$$

where

$$I_{cn} = \begin{cases} \frac{\pi E}{D\sqrt{1-\Gamma^2} + E\cos^{-1}(-\Gamma)} & \theta \leq \alpha \\ 0 & \alpha < \theta \leq (\pi - \alpha) \\ 0 & (\pi - \alpha) < \theta \end{cases} \quad (2)$$

and

$$\Gamma = \tan(\alpha)\cot(\theta) \quad (3)$$

$$D = 3\sin(\alpha)\cos(\alpha)\sin(\theta)\cos(\theta) \quad (4)$$

$$E = \cos^2(\alpha)\sin^2(\theta) + 2\sin^2(\alpha)\cos^2(\theta) \quad (5)$$

where α is the cone half-angle. Note that at $\theta = 0^\circ$, this reduces to:

$$\sigma_d(0) = \rho_d \frac{(\pi a^2) \sin(\alpha)}{\pi} \quad (\text{m}^2 / \text{sr}) \quad (6)$$

and at broadside becomes about 4 times larger.

The **retro-reflective** component (m^2 / sr) is given by

$$\sigma_r(\theta) = \frac{\rho_r a}{2\pi} (h \sin(\theta) \sin(\gamma) + a \gamma \cos(\theta)) \quad (7)$$

where

$$\gamma(\theta) = \begin{cases} E & \theta \leq \alpha \\ \cos^{-1}(-\tan(\alpha)\cot(\theta)) & \alpha < \theta \leq (\pi - \alpha) \\ 0 & (\pi - \alpha) < \theta \end{cases} \quad (8)$$

The **glint** scattering-function (m^2 / sr) is

$$\sigma_g(\theta) = \frac{\rho_g h^2}{4\pi} \frac{\tan(\theta)}{\cos(\alpha)} \exp\left(-c|\theta - (\pi/2 - \alpha)|^b\right) \quad (9)$$

where the c and b parameters must be determined experimentally. Equation (9) is a TDC analytical fit to the specular surface component data. (This is not found in reference 1.)

2.0 AMOR Data Fit

By correctly choosing the five reflection coefficients above, we may fit the WPCN target data set. The upper line in the plots is the sum of the diffuse and retroreflective components.

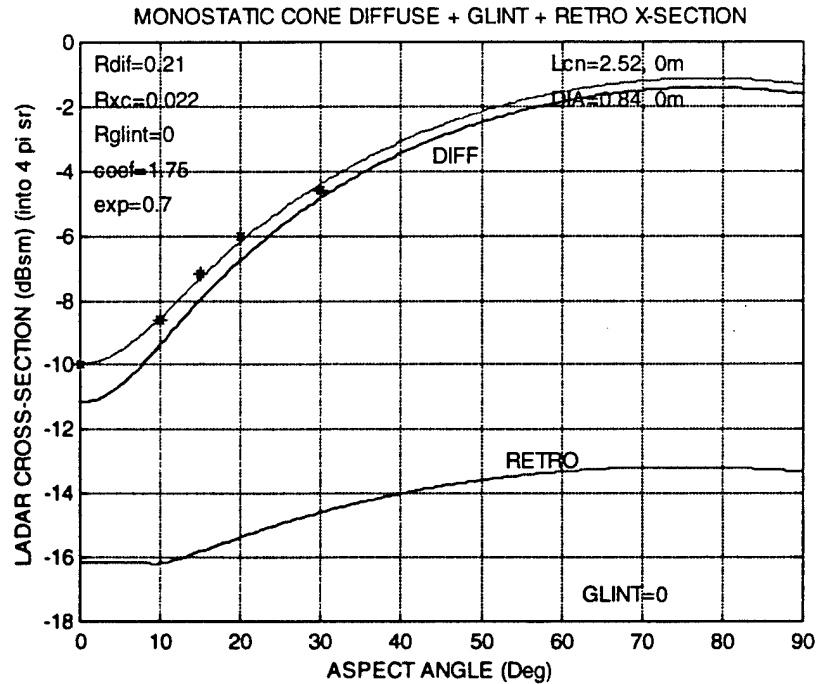


Figure 1. Data fit to S3-RV: 21% diffuse, 2.2% retroreflective, and 0% glint reflection coefficients.

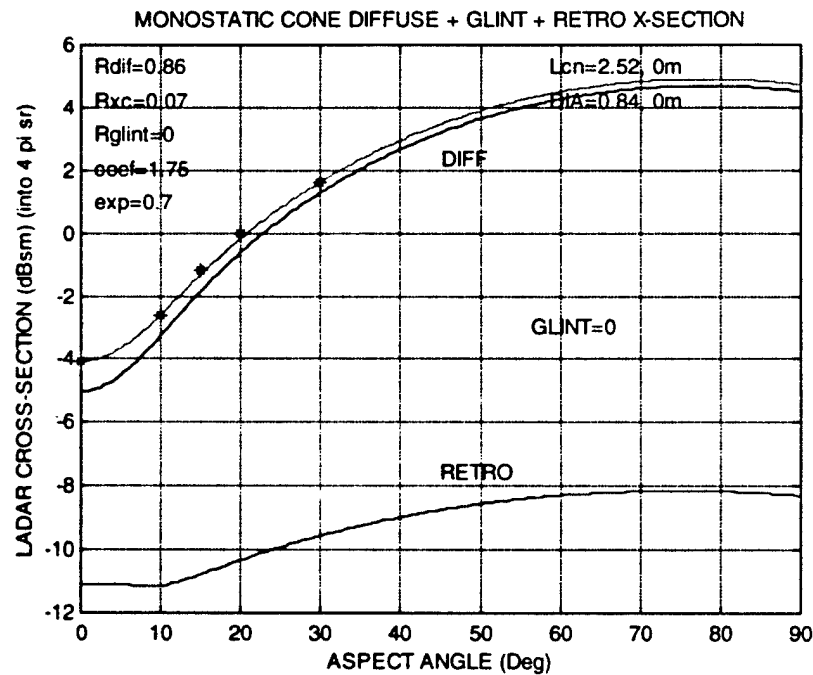


Figure 2. Data fit to S3-LREP: 86% diffuse, 7% rectroreflective, 0% glint reflection coefficient.

We note that in both targets a small retroreflective component must be added to bring up the 0° aspect point to fit the AMOR data. Data near broadside might require a glint component term.

REFERENCES

1. *Laser Cross Section Handbook*, Mission Research Corp., WRDC-TR-889-9010.

Appendix C

EOO Test Range Radiometry with $\pm 5\%$ Irradiance Uniformity
Douglas Youmans (DITPtrad.doc)

It is possible to put hard numbers on things like "fill factor efficiency of 0.58" since Fibertek has provided us a nearly perfect TEM₀₀ mode. A cone at 30° is 1.43 m across. The average fluence (or irradiance) over this diameter is:

$$2\pi \int_0^{0.715} \frac{2E_{\text{total}}}{\pi\omega^2} \exp(-2r^2 / \omega^2) dr / \pi 0.715^2 = E_{\text{total}} (1 - e^{-2(0.715)^2 / \omega^2}) / \pi 0.715^2 = 0.1205 E_{\text{total}} / \text{m}^2 = 0.90 \frac{2E_{\text{total}}}{\pi 2.18^2}$$

assuming $\omega = 2.18$ m from equation (2) below. Therefore, 0.90 multiplies equation (5) below:

The DITP 0.5 μm laser mode is a nearly perfect TEM₀₀ mode, and the fluence is given by

$$E(r; z) = \frac{2 E_{\text{total}}}{\pi \omega^2(z)} \exp(-2 r^2 / \omega^2(z)) \quad (\text{J} / \text{m}^2) \quad (1)$$

If the mode were expanded out such that the irradiance or fluence were 90% of the peak value at a radius of 50 cm from the optical axis ($\pm 5\%$ uniformity) for example, we would have

$$0.9 \frac{2 E_{\text{total}}}{\pi \omega^2(z)} = \frac{2 E_{\text{total}}}{\pi \omega^2(z)} \exp(-2 (0.5^2) / \omega^2(z)) \quad (\text{J} / \text{m}^2) \quad (2)$$

and $\omega(z) = 2.18$ m.

The test cone has a total (all cross-range + all down-range pixels) cross-section in m^2/sr of

$$\sigma_d(0) = \rho_d \frac{(\pi a^2) \sin(\alpha)}{\pi} \approx 0.05 \quad (\text{m}^2 / \text{sr}) \quad (3)$$

at zero degrees aspect and about 4 times larger at broadside assuming $\rho_d = 0.8$ for styrofoam. At broadside the cone tip or base would extend beyond the 0.9 irradiance radius (50 cm) thereby reducing signal strength.

The collecting solid angle for the 100 km simulation is

$$\Omega = \frac{\pi}{4} \alpha_{\text{FA}}^2 = \frac{\pi}{4} \left(\frac{0.25}{100,000} \right)^2 = 4.9 \times 10^{-12} \quad (\text{sr}), \quad (4)$$

Assuming 0.8 optical transmission both ways and an 0.5 transmission filter, we have

$$\frac{2 E_{\text{total}}}{\pi 2.18^2} (0.05) \Omega (0.8^2) 0.5 \quad \text{collected Joules} \quad (5)$$

or about 26.4 photons / mJ at 0° and about 106 photons / mJ broadside.

Appendix D

A short test-range simulation of the operational DITP geometries relies primarily on the fact that even at short distances, the angular speckle size can be given by λ / D_{eff} , where D_{eff} is a target geometry dependent effective diameter. From Lyle Shirley's report¹ we find: "Near the scatterer the speckles are small in both directions, but not smaller than the wavelength λ . Note that the rule of thumb for the average speckle size, d_{\perp} , applies **well into the near field**, as the transverse speckle size appears to increase linearly with distance from the scattering object." Data to this effect are presented on page 380 of reference one.

1.0 Speckle Size (Transverse Dimension)

Consider a cylinder of diameter D and length $L = 2m$ rotating about the axis of symmetry and having an aspect angle of θ . Following the above arguments, the average transverse speckle size back at the transmitter/receiver at a distance R is

$$\langle d_{\text{speckle1}} \rangle = \frac{\lambda R}{D_{\text{eff}}}, \quad \langle d_{\text{speckle2}} \rangle = \frac{\lambda R}{L_{\text{eff}} \sin(\theta)} \quad (1)$$

where the subscript *effective* takes into account the pixel-range-bin target segmentation geometry effects for short laser pulses (producing a larger D_{eff} w. smaller speckles) as well as the target reflectivity/illumination distribution effects (producing a smaller D_{eff}) for a rough target.

1.1 Comparison with the complex coherence factor speckle size

The complex coherence factor^{2,3,4} or spatial coherence function is the inverse Fourier transform of the irradiance distribution backscattered from the target:

$$\mu_E(\Delta x, \Delta y) = \frac{\iint |E(\xi, \eta)|^2 \exp\left(\frac{j2\pi}{\lambda z} (\xi \Delta x + \eta \Delta y)\right) d\xi d\eta}{\iint |E(\xi, \eta)|^2 d\xi d\eta} \quad (2)$$

The integral of this function

$$A_c = \iint |\mu_E(\Delta x, \Delta y)|^2 d\Delta x d\Delta y \quad (3)$$

is a good estimate of the speckle size at the receiver aperture. For a flat diffuse disk of diameter D , equations (2) and (3) can be evaluated as

$$A_c = \frac{4\lambda^2 z^2}{\pi D^2} = \frac{\pi}{4} \left(\frac{\lambda z}{D} \right)^2 \times \frac{16}{\pi^2} \quad (4)$$

thus, A_c is $16/\pi^2$ or 1.62 times larger than that area given by equation (1) or 1.27 larger in transverse size. Which expression is more accurate is TBD.

2.0 Target Rotation Effects (Axis = Perpendicular to the LOS)

The speckle velocity perpendicular to the target axis of rotation (at an aspect angle of θ) is given by

$$V_{\text{speckle1}} = 2\omega R \sin(\theta), \quad (5)$$

and, therefore, the transit time over an aperture smaller than d_{speckle} is approximately

$$\tau_{\text{transit}} = \frac{\langle d_{\text{speckle}} \rangle}{V_{\text{speckle}}} = \frac{\lambda}{2 D_{\text{eff}} \omega \sin(\theta)} \left(= \frac{1}{\Delta f_{\text{total}}} \right), \quad (3)$$

making use of equation (2).

Nicholas George⁵ has calculated the average irradiance backscattered from an unresolved rotating cylinder, approximately side on, and found that the number of traversed speckles (due to rotation) required for an uncorrelated irradiance measurement is given by

$$N = (8 D / \lambda)^{1/2} \quad (4)$$

Therefore, the required target angular rotation for speckle decorrelation is

$$\theta_{\text{decorr}} = (8 D / \lambda)^{1/2} (\lambda / D) = (8 \lambda / D)^{1/2} = 2 \text{ mr} \quad (5)$$

assuming a 1 m diameter object. Assuming a mean cone diameter of 0.5 m, this would become 2.8 mr and N would equal 894 speckles. Equation (4) has also been experimentally validated by Shirley¹.

2.0 Speckle Cell Length (z-axis Dimension)

For CW illumination, the length of a speckle in the z-axis dimension, at $z = R$, is^{1,6}

$$d_{\parallel} = 4 \lambda^2 R^2 / D^2 \quad (6)$$

For a pulsed ladar, the length of the laser pulse is $c \tau$. When one-half of the scattering points on the target surface have been replaced by new scattering points, a new speckle pattern is generated. Therefore,

$$d_{\parallel} = c \tau / 2 \quad (7)$$

for the pulsed case. This decorrelation distance has been measured at the AMOR facility.

3.0 Laser Wavelength Change for Speckle Decorrelation

George⁵ has also calculated the required laser frequency change to obtain a new speckle pattern from an unresolved, stationary rough sphere. He evaluates the correlation function

$$R_c = \langle E_r(v_1, \phi_1 = 0, t_1) E_r^*(v_2, \phi_1 = 0, t_1) \rangle \quad (8)$$

where ϕ is the receiver bistatic angle w.r.t. the transmitter, $E(v_1)$ is held constant, and v_2 is varied. The integral is a function of the target mean surface slope, the target surface-correlation-length, and the rms surface roughness, given that $\lambda \leq \sigma$. For surface-correlation-lengths divided by rms roughness-length values of 0.63, 1, and 2, an uncorrelated speckle pattern results for:

$$D_{\text{sphere}} \times (2\pi \delta v / c) \text{ equal to } 10 \text{ to } 30.$$

For a one m diameter sphere, this corresponds to

$$\delta v = 10 \text{ to } 30 \times \frac{c}{2\pi D_{\text{sphere}}} = 477 \text{ MHz to } 1,431 \text{ MHz} \quad (9)$$

in frequency change or 0.4 to 1.2 pm in wavelength change. With the smaller diameters of the tilted cone, the required frequency shifts will be larger, thus, it is not clear that a new speckle realization will be produced with each new laser pulse.

Shirley¹ has also shown that a laser frequency change while the E-field propagates down the target's surface will result in a new speckle pattern. If the round trip time delay multiplied by the laser frequency change rate or *chirp* results in a 2π phase shift, Shirley has shown that a new speckle pattern is formed. This effect is the basis for his report, using CW illumination of a target. The required frequency change for a generating a new speckle pattern is

$$\Delta\nu \geq \frac{c}{2 \Delta R_{\text{target}}} = 750 \text{ MHz if } \Delta R_{\text{target}} \text{ is } 20 \text{ cm} \quad (10)$$

The maximum range extent allowed per voxel is 20 cm, thus, if there were a 750 MHz change or greater within the 1.3 ns laser pulse, those voxels subtending maximum target range extent would incur speckle averaging—M would go from 1x to 2x the nominal M value for that voxel.

Shirley's results are specific to quasi-CW ladar where the length of the laser pulse is much much larger than the depth of the target and the laser is deliberately wavelength tuned to generate new speckle patterns with the tuning period. For short pulse ladar operation, Monte Carlo E-field simulations of spinning cone target returns indicate that some speckle smoothing results when a frequency chirp of 400 MHz (or more) occurs during the 1.3 ns pulse. That is to say, the nulls in the received intensity do not go precisely to zero, as they do for a fully developed speckle pattern, due to the chirp. Target spin produced Doppler spread is only about 4 MHz, thus, its contribution is negligible. The increase in the M parameter due to intra-pulse laser chirp needs to be further quantified.

4.0 Target Transverse Translation for Speckle Decorrelation

The target scattering points are all rigidly fixed to the target body. As the body is translated, the speckle pattern is translated. For simplicity we neglect the incident wavefront curvature. A curved wavefront would also add rotational effects. From equation (4) we would need approximately $(8D/\lambda)^{1/2} \approx 894$ speckles to go past the receiving aperture before an uncorrelated portion of the speckle pattern were generated. Therefore, we require a translation of

$$(8D/\lambda)^{1/2} (\lambda/D) \times 8 \text{ m} = 2.2 \text{ cm} \quad (11)$$

for an 8 m target range. This equation is based on the assumption that the target surface points are basically the same given the small rotation angle of equation (5). Therefore, this is approximately equivalent to moving $(8D/\lambda)^{1/2}$ speckles sideways.

5.0 Target Rotation (Axis = Parallel to the LOS)

Assume the cone is at a small aspect angle and rotating parallel to the LOS. Following the arguments of the previous section, if the cone were displaced, say 25 cm from the optical axis 8 m away, than an uncorrelated irradiance measurement would be obtained with a rotation angle

$$25 \text{ cm} \phi = (8D/\lambda)^{1/2} (8 \text{ m} \times \lambda/D) \quad \text{or} \quad \phi = 4 \text{ mr} \quad (12)$$

This implies that precisely on axis the same irradiance measurement would always be made given a perfect laser.

6.0 Proposed Optical Layout

Frank Hanson has proposed an optical layout as shown in Figure 1 (shown here using a 2 mr full-angle for clarity). A weak second lens ($f = 4 \text{ m}$) allows a large pinhole to be used as the FOV control stop, minimizing the diffraction effects from the pinhole and, therefore, not corrupting the simulated FOV. Following the AMOR design approach, the simulated angular-aperture-pinhole size may be set according to the true receiving aperture size and the simulated target range:

$$\begin{aligned} 0.25 \text{ m} / 200 \text{ km} &= 1.25 \text{ } \mu\text{r} \\ 0.25 \text{ m} / 100 \text{ km} &= 2.5 \text{ } \mu\text{r} \\ 0.25 \text{ m} / 50 \text{ km} &= 5 \text{ } \mu\text{r} \end{aligned}$$

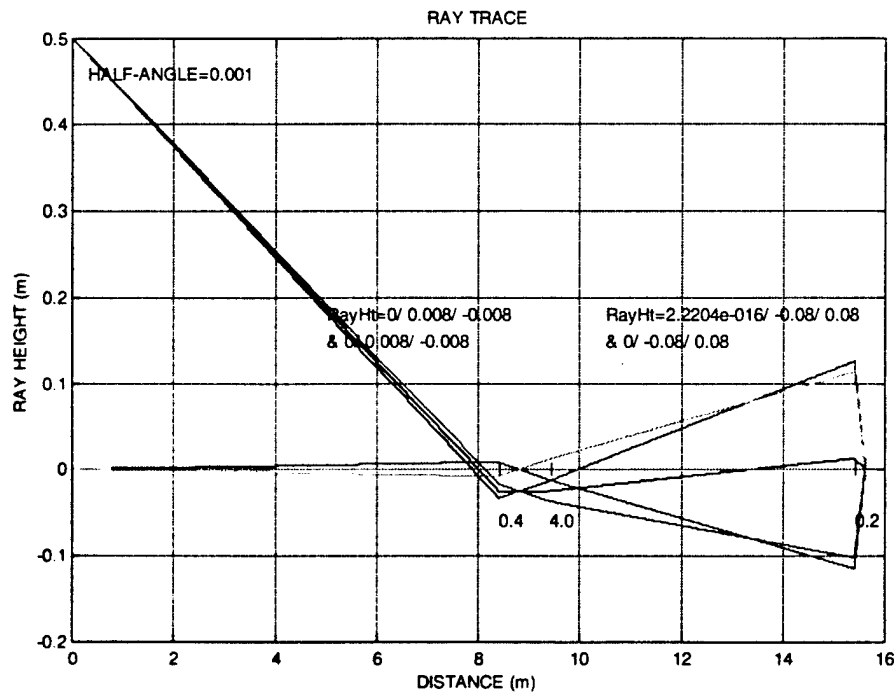


Figure 1. Proposed optical layout (F.H.).

To simulate a 100 km range we need a $2.5 \mu\text{m}$ full angle FOV. From Figure 1, there is an effective field stop 0.4 m in front of L1 ($z = 8 \text{ m}$) which is 0.4/4.0 times as large as the pinhole field stop. Thus, a $8 \text{ m} \times 2.5 \mu\text{m} \times 10 = 200 \mu\text{m}$ diameter pinhole is required for 100 km simulation. If a stronger 2 m focal length lens were used, then a $100 \mu\text{m}$ pinhole would be required. The $\cos^2(\theta)$ distribution from the target surface elements should have a small effect since Figure 1 is expanded 20:1 in the radial direction.

7.0 Radiometry

The DITP $0.5 \mu\text{m}$ laser mode is a nearly perfect TEM_{00} mode, and the fluence is given by

$$E(r; z) = \frac{2 E_{\text{total}}}{\pi \omega^2(z)} \exp\left(-2 r^2 / \omega^2(z)\right) \quad (\text{J} / \text{m}^2) \quad (13)$$

If the mode is expanded out to a 1 m $1/e^2$ radius, the fluence at the center would be $2E_{\text{total}}/\pi$. The cone has a total (all cross-range + all down-range pixels) cross-section in m^2/sr of

$$\sigma_d(0) = \rho_d \frac{(\pi a^2) \sin(\alpha)}{\pi} \approx 0.05 \quad (\text{m}^2 / \text{sr}) \quad (14)$$

at zero degrees aspect and about 4 times larger at broadside. The collected solid angle for the 100 km simulation is

$$\Omega = \frac{\pi}{4} \alpha_{\text{FA}}^2 = 4.9 \times 10^{-12} \quad (\text{sr}), \quad (15)$$

Assuming 0.8 transmission both ways we have, therefore, about 250 photons / mJ at 0° and 1000 photons / mJ broadside.

References

1. Shirley, L., et al, "Advanced Techniques for Target Discrimination Using Laser Speckle," MIT Lincoln Laboratory Journal, Fall 1992, Vol. 5, No. 3.
2. Goodman, J., "Some Effects of Target-Induced Scintillation on Optical Radar Performance," Proc. IEEE, Vol. 53, No. 11, Nov. 1965.
3. Goodman, J., "Comparative Performance of Optical-Radar Detection Techniques," IEEE Trans. AES, Vol. AES-2, No. 5, Sept. 1966.
4. Goodman, J., *Laser Speckle and Related Phenomena*, J.C. Dainty Ed., Springer-Verlag, 1975, Second Edition, 1984.
5. George, N., "Speckle from rough, moving objects," J. Opt. Soc. Am., Vol. 66, No. 11, Nov. 1976.
6. Halford, C., et al, "Experimental investigation of the longitudinal characteristics of laser speckle," Opt. Engr., Dec. Vol. 26, No.12, 1987.

Appendix E

DITP Laser Radar Cross-Section History
Douglas Youmans, George Hart (12/11/98)

In the TPGD documents of 9/96, 2/98, and their earlier drafts, the laser radar cross-sections were listed as 0.015 m^2 @ 532 nm, 0.012 m^2 @ $1.06 \mu\text{m}$, and 0.003 m^2 at $10.6 \mu\text{m}$. In 11/95 and many times thereafter I discussed these values with George Dezenberg, Goeff Benedict-Hall, Rich Marino, Bill Keicher, and others.

1) The target cross-sectional areas are defined to be into $\pi \text{ sr}$ in order to differentiate and separate the **ladar** cross-sections from **radar** cross-sections which are defined to be into $4\pi \text{ sr}$. (Ladar cross-sections in the literature may be found scattering into $1, \pi, 2\pi$, or $4\pi \text{ sr}$, and confusion may be eliminated by using m^2/sr values.)

2) These area values were obtained from averaging approximately 5 AMOR target data sets with 5 analytical target models. The target's aspect angles were all at about 5° . What analytical models and which AMOR data sets were averaged are unknown at this point.

3) Just prior to the IET downselect it was requested that 30° aspect target cross-sections be provided in order to be more realistic. Looking at the two larger targets of the 403 and 405 threats, it was seen that they are practically cones 2 m long and 1 m in diameter. Assuming a diffuse reflectivity coefficient of 8% for this nominal cone target at 5° aspect, we find excellent agreement with the $0.015/\pi \text{ m}^2/\text{sr}$ (or 0.015 m^2 into $\pi \text{ sr}$) specification. This nominal 8% diffuse cone target was then rotated to 30° aspect angle to obtain a $0.0125 \text{ m}^2/\text{sr}$ value.

4) At the July 1998 DITP review, Steve Kosovac presented some AMOR data at 532 nm with white PCN covered targets. I asked to receive a copy of these data as my AMOR files covered only 1.06 and $10.6 \mu\text{m}$ data. Using the 2.52 m long, 0.84 m dia. conical target shape, the white PCN surfaces exhibited 21% diffuse and 2.2% retroreflective diffuse components for "S3-RV" and 86% diffuse and 7% retroreflective diffuse components for "S3-LREP." "S3-RV" had perforated loose WPCN and "S3-LREP" had unperforated taught WPCN covering. The data went only from 0° to 30° due to the size of the target. Official acceptance of this material on a test target or a threat target surface is TBD at this point, to my knowledge. There is obviously a large difference between the WPCN targets and the average targets assumed prior to the TPGD releases.

Appendix F

Comparison of Analytical and Computed Principle Moments of Hemispherical Shells

Doulas G. Youmans, Frank Hanson

The principle moments of a hemispherical shell of radius "a" can be analytically evaluated by

$$A = \int_0^{2\pi} \int_0^{\pi/2} a^2 \sin(\theta) d\theta d\phi = 2\pi a^2 \quad (1)$$

$$\langle z \rangle = \frac{1}{A} \int_0^{2\pi} \int_0^{\pi/2} (a \cos(\theta)) a^2 \sin(\theta) d\theta d\phi = \frac{1}{2} a \quad (2)$$

$$\langle z^2 \rangle = \frac{1}{A} \int_0^{2\pi} \int_0^{\pi/2} (a \cos(\theta))^2 a^2 \sin(\theta) d\theta d\phi = \frac{1}{3} a^2 \quad (3)$$

$$\langle x \rangle = \langle y \rangle = 0 \quad (4)$$

$$\langle x^2 \rangle = \langle y^2 \rangle = \frac{1}{A} \int_0^{2\pi} \int_0^{\pi/2} (a \sin(\theta) \cos(\phi))^2 a^2 \sin(\theta) d\theta d\phi = \frac{1}{3} a^2 \quad (5)$$

$$M_{xx} = \langle x^2 \rangle + \langle y^2 \rangle = \frac{2}{3} a^2 = 0.1617 \text{ m}^2 @ 50\text{cm} \quad (6)$$

$$M_{yy} = M_{zz} = \langle x^2 \rangle + \langle y^2 \rangle - \langle z \rangle^2 = \frac{5}{12} a^2 = 0.10417 \text{ m}^2 @ 50\text{cm} \quad (7)$$

When a two dimensional matrix of z values is formed (in the computer), the dx by dy area elements are projections of the hemisphere on to the x,y plane. Consequently, equations (1) to (5) must be evaluated with another cos(θ) inside the integral.

$$A = \pi a^2 \quad (8)$$

$$\langle z \rangle = \frac{2}{3} a \quad (9)$$

$$\langle z^2 \rangle = \frac{1}{2} a^2 \quad (10)$$

$$\langle x^2 \rangle = \langle y^2 \rangle = \frac{1}{4} a^2 \quad (11)$$

$$M_{xx} = \langle x^2 \rangle + \langle y^2 \rangle = \frac{1}{2} a^2 = 0.125 \text{ m}^2 @ 50\text{cm} \quad (12)$$

$$M_{yy} = M_{zz} = \langle x^2 \rangle + \langle y^2 \rangle - \langle z \rangle^2 = \left(\frac{3}{4} - \frac{4}{9} \right) a^2 = 0.07639 \text{ m}^2 @ 50\text{cm} \quad (13)$$

The computer code moment-of-inertia tensor eigenvalues are 0.1232, 0.0754, and 0.0751 m², for z, x, and y moments, respectively. Using the **unweighted** tensor and multiple z values (hence, not a shell) per x,y pixel (9x9x3 pixels on target), 0.1211, 0.0748, and 0.0748 m² eigenvalues are obtained.

The analytical principle moments incorporating **signal weighting** would include a cos(θ)² weighting, resulting in

$$A = \frac{2\pi}{3} a^2 \quad (14)$$

$$\langle z \rangle = \frac{3}{4}a \quad (15)$$

$$\langle z^2 \rangle = \frac{3}{5}a^2 \quad (16)$$

$$\langle x^2 \rangle = \langle y^2 \rangle = \frac{3}{15}a^2 \quad (17)$$

$$M_{zz} = \langle x^2 \rangle + \langle y^2 \rangle = \frac{9}{20}a^2 = 0.1125 \text{ m}^2 @ 50\text{cm} \quad (18)$$

$$M_{xx} = M_{yy} = \langle x^2 \rangle + \langle z^2 \rangle - \langle z \rangle^2 = \frac{21}{80}a^2 = 0.0656 \text{ m}^2 @ 50\text{cm} \quad (19)$$

Likewise, formation of an x,y,z matrix would, following the above arguments, would require a $\cos(\theta)$ weighting to include the projection on to the x,y plane

$$A = \frac{\pi}{2}a^2 \quad (20)$$

$$\langle z \rangle = \frac{4}{5}a \quad (21)$$

$$\langle z^2 \rangle = \frac{2}{3}a^2 \quad (22)$$

$$\langle x^2 \rangle = \langle y^2 \rangle = \frac{1}{6}a^2 \quad (23)$$

$$M_{zz} = \langle x^2 \rangle + \langle y^2 \rangle = \frac{1}{3}a^2 = 0.0833 \text{ m}^2 @ 50\text{cm} \quad (24)$$

$$M_{xx} = M_{yy} = \langle x^2 \rangle + \langle z^2 \rangle - \langle z \rangle^2 = \left(\frac{1}{6} + \frac{2}{3} - \frac{16}{25} \right) a^2 = 0.0483 \text{ m}^2 @ 50\text{cm} \quad (25)$$

Using the **weighted** moment-of-inertia tensor, the computer code (9x9x3 pixels on the sphere, multiple z values per x,y) eigenvalues are 0.0903, 0.0577, 0.0574 m^2 , respectively which is in reasonable agreement.

Appendix G

Potential Features for DITP Ladar ATR/I Signal Processing

SPWG Action Item 6/4/98

Douglas G. Youmans (DITPfeat.doc 2/3/99)

Traditionally, "features" are combined in a feature weighting metric:

$$F_{\text{object}} = \sum_i w_i f_i \geq T_{\text{object}}$$

where the weighting, w_i , and threshold, T_{obj} , must be optimally set. For a particular object, say a bi-cone at 15° aspect angle and 10° pitch, the weighted sum of the features for that bi-cone object would exceed the threshold, and an "identification" (ATI) would be made. (A "detection" (ATD) would indicate something was there, and "recognition" (ATR) would say that it is a bi-cone not a cylinder.) Alternatively, a set of feature values may be displayed in a multi-dimensional feature space for target discrimination. Some potential features, algorithms, and signal processing techniques are listed here with **current leading features in *italics***:

Low-Computational Features:

- 1) *Total signal count (total LRCS) vs time*
- 2) *Peak signal count (peak LRCS) vs time*
- 3) *Target length (first z-plane to last z-plane) vs time*
- 4) *Range resolved signal counts vs time*

1) ALPHAtch, Inc. Tensor

For those pixels exceeding a threshold (> 0 counts for DITP) and using the first z return per (x,y) pixel and no image intensity weighting, define the co-ordinates:

$$\bar{x} = \frac{1}{N} \sum_{i=1}^N x_i, \quad \bar{y} = \frac{1}{N} \sum_{i=1}^N y_i, \quad \bar{z} = \frac{1}{N} \sum_{i=1}^N z_i, \quad (1)$$

$$\delta x_i = x_i - \bar{x}, \quad \delta y_i = y_i - \bar{y}, \quad \delta z_i = z_i - \bar{z}, \quad (2)$$

ALPHAtch then formed the tensor:

$$D = \begin{bmatrix} \sum_i \delta x_i^2 & \sum_i \delta x_i \delta y_i & \sum_i \delta x_i \delta z_i \\ \sum_i \delta x_i \delta y_i & \sum_i \delta y_i^2 & \sum_i \delta y_i \delta z_i \\ \sum_i \delta x_i \delta z_i & \sum_i \delta y_i \delta z_i & \sum_i \delta z_i^2 \end{bmatrix} \quad (3)$$

The three eigenvalues were then computed and the ratio of d_{max} to d_{min} or d_{max} to d_{mid} was taken as the feature. The mean, median, or maximum (last) z value per (x,y) pixel may be also be used or any combinations thereof.

1A) Signal Weighted ALPHAtch Tensor

The Alphatech tensor in 1) may be weighted by N_i for each element as in 2A) below.

2) Moment of Inertia Tensor

A different tensor from classical mechanics of shell structures (single z values and $N_i = 1$) has been likewise used (G. Hart)

$$I = \begin{bmatrix} \sum_i \delta y_i^2 + \delta z_i^2 & -\sum_i \delta x_i \delta y_i & -\sum_i \delta x_i \delta z_i \\ -\sum_i \delta x_i \delta y_i & \sum_i \delta x_i^2 + \delta z_i^2 & -\sum_i \delta y_i \delta z_i \\ -\sum_i \delta x_i \delta z_i & -\sum_i \delta y_i \delta z_i & \sum_i \delta x_i^2 + \delta y_i^2 \end{bmatrix} \quad (4)$$

The eigenvalues $I_{1,2,3}$ are computed, and the ratio or the difference ratio $(I_{\max}-I_{\min})/(I_{\text{mid}}-I_{\min})$ is taken. For a hemispherical shell, $I_z > I_x = I_y$.

2A) with Signal Weighted Tensor (Note, 2A) Is Current Leading Feature)

The moment of inertia tensor corresponding to a shell structure (equation (4)) may be weighted by the signal strength, N_i , corresponding to the classical mechanics definition of the moment of inertia:

$$I_w = \begin{bmatrix} \sum_i N_i (\delta y_i^2 + \delta z_i^2) & -\sum_i N_i \delta x_i \delta y_i & -\sum_i N_i \delta x_i \delta z_i \\ -\sum_i N_i \delta x_i \delta y_i & \sum_i N_i (\delta x_i^2 + \delta z_i^2) & -\sum_i N_i \delta y_i \delta z_i \\ -\sum_i N_i \delta x_i \delta z_i & -\sum_i N_i \delta y_i \delta z_i & \sum_i N_i (\delta x_i^2 + \delta y_i^2) \end{bmatrix} \quad (5)$$

Likewise, the eigenvalues for a weighted hemispherical shell are $I_z > I_x = I_y$. The eigenvectors can be used to estimate the cone pitch and yaw angles.

1B) and 2B) Signal Weighted δx , δy , δz

The signal weighted δx_i , δy_i , and δz_i may also be used. A signal weighted mean of

$$\bar{x} = \sum_i N_i x_i / \sum_i N_i \quad (6)$$

and a centroid difference of

$$\delta x_i = N_i x_i / \sum_i N_i - \bar{x} \quad (7)$$

where N_i are the photo-electron counts at pixel 'i' may be used for signal weighting in the unweighted tensor (4). The signal count weighted δz values alone may alternatively be used with the unweighted δx and δy .

The eigenvectors can be used to estimate the cone pitch and yaw angles.

1C) and 2C) Signal Weighted Tensor and Signal Weighted δx , δy , δz

Both the signal weighted tensor (5) and signal weighted δx , δy , and δz , (6) and (7), may be used together in creating the tensor. The eigenvectors can be used to estimate the cone pitch and yaw angles.

3) Variance (The following may be extended from 2D to 3D, or the mean, max, min, median or weighted z values may be used for each i,j.)

$$f = \sum_i \sum_j (i - j)^2 I_{ij} \quad (8)$$

4) Entropy

$$f = -\sum_i \sum_j I_{ij} \log(I_{ij}) \quad (9)$$

5) Angular Second Moment

$$f = \sum_i \sum_j I_{ij}^2 \quad (10)$$

6) Contrast (N gray levels)

$$f = \sum_{n=0}^{N-1} n^2 \sum_i \sum_j I_{ij}^2 \quad (11)$$

7) Correlation

$$f = \sum_i \sum_j (i j I_{ij} - \mu_x \mu_y) / \sigma_x \sigma_y \quad (12)$$

8) Inverse Difference Moment

$$f = \sum_i \sum_j \frac{1}{1 + (i - j)^2} I_{ij} \quad (13)$$

9) Similar Parameters as 3) to 8) for x only, y only, x + y, and x - y

10) Classical Template Matching (Modified for 3D), Correlation over x, y, & z Simultaneously

- 1) Invert a reference image through origin -- x, y, and z location values
 - 2) Take 3DFFT
 - 3) Store in computer
 - 4) Take 3DFFT of each noisy ladar image
 - 5) Multiply by reference images for that range
 - 6) Take Inverse 3DFFT
 - 7) Select max correlation peak or max sum (energy)
- Note that this is independent of image location (pointing jitter, range fluctuations)

11) Template Matching w. Phase-only Filters (PoF)

- 1) Filter = $\exp(j \text{ angle}(3\text{DFFT}(\text{reference-image})))$, same steps as 10)
- 2) Gives sharper correlation peak

12) Binary Phase-only Filter (BPoF)

- 1) The phase-only filter of 11) is made binary by $H(f_x, f_y) = +1, \cos(\phi) \geq 0$; -1 otherwise
- 2) Follow steps from 10)

13) Symmetric (Normalized) Phase-only Matched Filter (SPoF)

- 1) Filter = $\exp(j \text{ angle}(3\text{DFFT}(\text{reference-image}))) / \text{magnitude}(3\text{DFFT}(\text{input-image}))$
- 2) Same steps as 10)

14) Quad-phase-only Filter (QPoF)

- 1) Let $F_{ref} = 3\text{DFFT}(\text{reference-image})$
- 2) Then, $F_{qpof} = \text{sgn}(\text{Real}(F_{ref})) + i \text{sgn}(-\text{Imag}(F_{ref}))$
- 3) Works better when the reference object has both even and odd components

15) Joint Transform Correlator (JTC)

- 1) Add noisy ladar 3D image to reference image
- 2) Take 3DFFT
- 3) Take magnitude squared

- 4) Take inverse 3DFFT
- 5) Select correlation peak or max sum (energy)

16) Binary Joint Transform Correlator (BJTC)

- 1) Add noisy ladar 3D image to reference image
- 2) Take 3DFFT
- 3) Take magnitude squared
- 4) Select threshold value and $PSD = 1 > \text{threshold}, = -1 < \text{threshold}$
- 5) Take inverse 3DFFT
- 6) Select correlation peak or max sum (energy)

17) Joint Transform Correlation with Phase-encoded Reference

- 1) Reference image is multiplied by an inverse 3DFFT {pseudo-random phasors}
- 2) Take 3DFFT of sum
- 3) Take magnitude squared and multiply by pseudo-random phase mask from 1)
- 4) Take inverse 3DFFT
- 5) Select correlation peak or max sum (energy)

18) Inverse Filter (Optimum for Zero Signal-Independent Additive Gaussian Noise)

- 1) Invert reference image through origin -- x, y, and z location values
- 2) Take 3DFFT and compute inverse 3D-matrix
- 3) Store in computer
- 4) Take 3DFFT of each noisy ladar image
- 5) Multiply by stored filter for that range
- 6) Take Inverse 3DFFT
- 7) Select max correlation peak or max sum (energy)

19) Fourier Descriptor Differencing

- 1) The reference images' x and y components are combined to form a complex number, $x + jy$, for each z slice
- 2) A 1D FFT is taken in each z plane
- 3) Translation independence is obtained by ignoring the DC component at the origin for each z
- 4) The magnitude of each Fourier component is taken to eliminate rotation effects
- 5) Size effects are eliminated by dividing the magnitudes by that of element (1) at each z level
- 6) The Fourier descriptors are compared to the same from each ladar measurement via steps 1) to 5), in a least squares difference sense, as the ladar data are taken

20) Analytical Feature Filter Construction

- 1) Simple analytical (vs numerical) filters may be constructed corresponding to target features that are expected, i.e. a cone pointed tip.
- 2) Spatial-frequency domain filters following 10) through 18) may then be applied.

21) X, Y, Z Axis Summations

- 1) Sum the 3D input image along the x, y, and z axes: This produces 40×10 , 40×10 , and 10×10 2D matrices or 900 elements total. Allows easy data visualization.
- 2) Feature algorithms number 3) through 19) may then be applied to the 2D combined matrix.

22) X, Y Centroids vs Z

1) The x and y centroid are computed for each z slice. These may be projected onto the $x-z$ and $y-z$ planes for estimation of elevation and azimuth.

23) Co-Occurrence Statistics

- 1) Pixel values are ranked smallest to largest.
- 2) The image is scanned in one or more directions to determine the frequency which with these pixel values follows another.

24) The Reference Image Set may be Combined using the Following Filters from the Literature:

- 1) Equal correlation peak filter (ECP)
- 2) Hybrid composite filter (HC)
- 3) Minimum average correlation energy filter (MACE)
- 4) Maximum average correlation height filter (MACH)
- 5) Minimum noise and correlation energy filter (MINACE)

25) Joint Time Frequency Transforms may be Applicable

- 1) Wigner
- 2) Choi-Williams
- 3) Rihaczek
- 4) Choquet
- 5) Born-Jordan
- 6) Margenau-Hill

26) Analytic Signal Utilization Effects are Unknown

Negative frequency components are set to zero using complex signals. This forms an "analytic" signal which can improve signal processing performance. In 3 dimensions it is not clear what a negative frequency component is. A 3D Hilbert transform may be used to investigate this concept.

27) Reference Image Correlation

- 1) Create suite of reference images vs range for all x , y , z as well as θ and ϕ at each range, $z = R$.
- 2) Given target range, multiply noisy radar image by reference set, element by element
- 3) Sum over x , y , and z
- 4) Maximum correlation peak or max sum (energy) is the ID

Appendix H

Focused-Mode Short-Range DITP Ladar Testing

Douglas Youmans (DITPfcsm.doc 8/24/98)

In the short-range (≈ 17 m) focused laser-mode tests, the laser spot is focused to a small Gaussian spot on a rough surface to create large speckles back at the small receiving aperture. This results in small M values simulating those observed in the real situation.

1.0 M-parameter Determination

The complex coherence factor^{1,2,3} or spatial coherence function is the inverse Fourier transform of the irradiance distribution backscattered from the target:

$$\mu_E(\Delta x, \Delta y) = \frac{\iint |E(\xi, \eta)|^2 \exp\left(\frac{j2\pi}{\lambda z}(\xi \Delta x + \eta \Delta y)\right) d\xi d\eta}{\iint |E(\xi, \eta)|^2 d\xi d\eta} \quad (1)$$

The integral of this function

$$A_c = \iint |\mu_E(\Delta x, \Delta y)|^2 d\Delta x d\Delta y \quad (2)$$

is a good estimate of the speckle size at the receiver aperture. Analytically, Δx and Δy are $x_1 - x_2$ and $y_1 - y_2$ and numerically they are multiples of $(\lambda z / N \delta x)$ with $\delta x = \delta y$ being the grid spacing across the source region and N the grid size.

For a small Gaussian spot on a large target (resolved target), equations (1) and (2) can be evaluated as

$$A_c = \lambda^2 z^2 / (\pi \omega^2(R)) \quad (3)$$

Thus, an approximate solution for M is given by A_m / A_c .

A more exact determination of M is obtained by using the autocorrelation of the receiving aperture, R_{A_m} . Multiplying equation (1) squared and then summing over $\Delta x, \Delta y$ we have:

$$\frac{1}{M} = \frac{1}{A_m^2} \iint R_{A_m}(\Delta x, \Delta y) |\mu_E(\Delta x, \Delta y)|^2 d\Delta x d\Delta y \quad (4)$$

Equation (4) has been solved by MacKerrow⁴ assuming a circular receiving aperture

$$M = \frac{\pi}{16} \left[\int_0^1 dy \left(y \cos^{-1}(y) - y^2 \sqrt{1-y^2} \right) \exp\left(\frac{-4A_{rec}}{A_c} y^2\right) \right]^{-1} \quad (5)$$

but this would also require numerical integration.

Some results using equation (4) are

$\omega(17 \text{ m}) = 1.0 \text{ mm } 1/e^2 \text{ irradiance radius, } z = 17 \text{ m}$	
<u>Circular receiver radius</u>	<u>M value</u>
20 mm	50.6
10 mm	13.4
5 mm	3.8
3 mm	2.1
2 mm	1.4
1 mm	1.1

If we select a 2 mm receiving aperture pupil radius and a 2 mm $1/e^2$ mode radius on target, a black absorber central obscuration at the target surface will produce increased M values, and a black clipping radius would reduce M:

$\omega(17\text{ m}) = 2.0\text{ mm } 1/e^2\text{ irradiance radius, } z = 17\text{ m}$

<u>Circular receiver radius</u>	<u>Rclip</u>	<u>Robscuration</u>	<u>M value</u>
2 mm	0.5 mm	0 mm	1.10
2 mm	1.0 mm	0	1.42
2 mm	2.0 mm	0	2.33
2 mm	2.0 mm	1.8 mm	4.35
2 mm	4.0 mm	0	2.84
2 mm	4.0 mm	0.6 mm	3.32
2 mm	4.0 mm	1.2 mm	4.53
2 mm	4.0 mm	1.8 mm	5.61
2 mm	4.0 mm	2.4 mm	6.79
2 mm	4.0 mm	3.0 mm	7.93
2 mm	4.0 mm	3.6 mm	8.84
2 mm	20 mm	0	2.84
2 mm	inf	0.5 mm	3.19
2 mm	inf	1.0 mm	4.12
2 mm	inf	2.0 mm	6.00
2 mm	inf	3.0 mm	8.13

$\omega(17\text{ m}) = 4.0\text{ mm } 1/e^2\text{ irradiance radius, } z = 17\text{ m}$

<u>Circular receiver radius</u>	<u>Rclip</u>	<u>Robscuration</u>	<u>M value</u>
2 mm	0.4 mm	0.0 mm	1.06
2 mm	0.8 mm	0.4 mm	1.35
2 mm	1.2 mm	0.8 mm	2.34
2 mm	1.6 mm	1.2 mm	3.35
2 mm	2.0 mm	1.6 mm	4.38
2 mm	2.4 mm	2.0 mm	5.32
2 mm	2.8 mm	2.4 mm	6.38
2 mm	3.2 mm	2.8 mm	7.35
2 mm	3.6 mm	3.2 mm	8.33
2 mm	4.0 mm	3.6 mm	9.37

The M values would be multiplied by two for detection of both polarizations.

2.0 Radiometry

The laser pulse energy is reflected into π sr off the near normal rough target, and, assuming 0.8 transmission each way, the collected light would be

$$\rho_d \frac{0.8 E_{\text{laser}}}{\pi} \frac{A_{\text{rec}}}{(17\text{ m})^2} 0.8 = 1.9 \times 10^7 \text{ photons / mJ} \quad (14)$$

per laser pulse, assuming the 2 mm radius pupil and 80% diffuse reflectivity with no source obscuration.

3.0 Speckle Realizations

In this test whenever one-half the target surface scatter points are replaced, we have a new speckle realization. At intermediate source-point changes, the speckle pattern will presumably alternate between minima and maxima at a fixed receiver pupil location.

References

1. Goodman, J., "Some Effects of Target-Induced Scintillation on Optical Radar Performance," Proc. IEEE, Vol. 53, No. 11, Nov. 1965.
2. Goodman, J., "Comparative Performance of Optical-Radar Detection Techniques," IEEE Trans. AES, Vol. AES-2, No. 5, Sept. 1966.
3. Goodman, J., *Laser Speckle and Related Phenomena*, J.C. Dainty Ed., Springer-Verlag, 1975, Second Edition, 1984.
4. MacKerrow, E., M. Schmitt, "Measurements of integrated speckle statistics of CO₂ lidar returns from a moving, non-uniform, hard target," Appl. Opt. Vol. 35, No. 27, 20 Sept. 1997.
5. Youmans, D., G. Hart, "Numerical evaluation of the M parameter for direct detection ladar," SPIE Proc. Vol. 3380, April 1998.

Appendix I

DITP 0.5 μ M IMAGING LADAR TARGET SPECKLE STATISTICS AND THEIR IMPACT ON DISCRIMINATION

George A. Hart, Douglas G. Youmans, Michelle A. Thomas
Schafer Corporation
321 Billerica Road, Chelmsford, MA 01824

ABSTRACT

The direct detection 3D imaging laser radar developed by BMDO under the DITP effort and currently being integrated for a demonstration test flight in FY2001 has the capability of significantly improving the P_k of an interceptor by providing substantially enhanced discrimination. This is especially true for threats of high interest where closely spaced objects defeat the capability of passive sensors to discriminate based on intensity modulation due to coning. The DITP 3D ladar can easily resolve such CSO's, it also has an inherent advantage in that the same amount of coning will result in 3 times as much modulation as the passive sensor would observe. The 3D ladar can also observe the actual object orientation once it is angularly resolved. This can cut through confusion the passive sensor could experience where different combinations of aspect and coning angle can yield the same modulation amplitude.

The ability of the 3D ladar to deliver such benefits hinges on the accuracy of its intensity measurements. This paper will present analysis backed by experiments, which indicates that while speckle is a potential problem, the intensity fluctuations it introduces can be mitigated by multi-pulse averaging. Sufficient engagement timeline exists for such an approach when proper trades between pulse energy, rep rate, and beam profile are made. Such trades will be presented in detail, as will the proper method for estimating the extent of speckle expected for an overall target, individual range bin, or single angle-angle pixel within a range bin.

1.0 INTRODUCTION

The BMDO Discriminating Interceptor Technology Program (DITP) is developing sensor systems to provide enhanced seeker and guidance capability against postulated advanced NMD/TMD threats^(1,4). These systems include multicolor infrared imaging detectors, laser radars, tracking and discrimination software, and a fusion processor. The laser radar is required to provide high-resolution imagery and track data for discrimination of threat objects from decoys and debris. During the past several years both coherent and direct-detection laser radar designs and hardware concepts have been evaluated for use in DITP. Recently the direct-detection solid-state laser radar was selected by BMDO/DITP for integration as a space-qualified 5-kg package as part of a demonstration flight in FY2001 which will also include a DITP advanced passive sensor system and fusion processor. Although the direct-detection system does not provide direct Doppler measurement, the other advantages of the direct-detection system, including compactness, processing simplicity, and experimentally demonstrated robust discrimination performance against representative targets, provide BMDO with a near-term laser radar for such space-based demonstrations.

The BMDO DITP scenario envisions a ground-based interceptor launched at an approaching threat cloud. The threat cloud may consist of one or more RV targets and as many as 10 or 20 lightweight decoys and randomly shaped deployment debris objects. The decoys closely resemble the RVs in shape and exterior surface properties, but are perhaps 1-5% of the RV mass. Since the static optical properties of the two target sets are quite similar, the laser radar is used to measure differences in dynamics of decoy vs. RV.

2.0 INTENSITY MODULATION

One of the most important differences in dynamics between RV's and decoys is the coning angle (precession angle). When used as weapons of terror against an extended urban area there is no need for precision targeting of RV's and measures such as spin stabilization are not necessary. But any attempt to destroy U.S. retaliatory strike capability requires precisely targeted counterforce weapons whose attitude upon reentry must be carefully controlled. For precise targeting, RV's are deployed with as small a coning (or precession) angle as possible, where deflection by the atmosphere on reentry is minimized by orienting the RV so that its body symmetry axis is co-aligned with the velocity vector it will follow on the downward sweep part of its trajectory. The large mass of the RV, careful balancing of that mass, and precision deployment by the post boost vehicle (PBV) results in a spin stabilized motion

with relatively low coning. Coning angles of 2-4 degrees are typical. This is a representative value not derived from any specific threat document.

Heavy and light decoys on the other hand simply do not have the mass required to achieve and sustain such small coning angles. Even with concerted efforts towards careful balancing and deployment, medium weight "precision" decoys end up with coning angles around 8 degrees. Light replicas exhibit coning angles of approximately 12 degrees. Conical lightweight balloons will have even greater coning angles.

A direct detection laser radar, such as that to be used in the DITP FY2001 demo flight, can exploit this difference in dynamical behavior as a discriminant, because such coning produces a sinusoidal variation in the signal returned to a laser radar as the RV completes one coning cycle with a period from a few seconds to a few tens of seconds. By revisiting the RV anywhere from 5 to 10 times during its coning cycle, the direct detection radar can determine the extent of fluctuation or modulation during that cycle. Knowledge of that modulation depth or amplitude can be translated into a determination of the coning angle.

It should be strongly emphasized that over most of its discrimination engagement timeline the laser radar is collecting this intensity modulation data. Depending on the reflectivity of the target, useful modulation measurements can begin to be made at ranges from 400 to 450 km. Up until ranges less than 200 km the aperture sizes which an interceptor aperture can accommodate (of the order of 25 cm) do not make available the necessary angular resolution for full 3D imaging. Therefore other features for measuring precession and orientation are simply not accessible for the majority of the engagement fly-in. In several scenarios it is desirable to reach a final target selection decision by approximately 150 km to allow sufficient time to reach the target given realistic interceptor divert capabilities. At a nominal NMD closing velocity of 10 km/s, 20-25 seconds will be spent making intensity modulation measurements, while typically 5, or at the most 10, seconds will be involved in full 3D imaging. This underscores the importance of the reliability of intensity modulation as a discriminant and the impact of speckle statistics and other considerations on that reliability. Before turning to an examination of error sources which must be considered in making intensity modulation measurements, it is useful to have a thorough understanding of the source of the modulation, its expected magnitude, and the special advantages an active rather than passive sensor has in observing such modulation.

From the point of view, literally, of an oncoming LADAR equipped interceptor, coning motion produces a cyclical variation of the net aspect angle between the line of sight to the threat object and that object's body symmetry axis. For example for a cone with a mean aspect angle of 30 degrees and an 8 degree coning angle the effective aspect angle will swing from 38 degrees down to 22 degrees and back up to 38 degrees over the time of one coning (precession) cycle.

This change in aspect angle is very apparent to the laser radar because it produces a corresponding and substantial change in the laser radar cross section. For a cone this cross-section has a minimum at a head on orientation. It has its maximum at 90 degrees. (Actually its maximum will be at 90 degrees minus the cone half angle. At this point one side of the cone will be exactly perpendicular to the LADAR line of sight. This "glint" line will be returned to in a subsequent discussion of moment-of-inertia algorithm^(5,6) (M-O-I) determination of the threat object orientation). In going from 0 degrees to 90 degrees the cross section is given by an S shaped curve like the sine function. As shown in Figure 1 for aspect angles between 10 and 60 degrees this curve is very linear⁷. It is this linear dependence of cross section on aspect angle which produces the intensity modulation discrimination feature.

As is depicted in Figure 1, for a mean aspect angle of 30 degrees and a coning angle of 8 degrees there will be a 60 percent increase or modulation of the returning laser radar signal as the instantaneous aspect varies from 22 degrees to 38 degrees. This behavior was confirmed in experimental measurements made at the AMOR test facility in December 1997⁸. The degree of modulation is independent of the target reflectivity on radar output power, but the signal to noise ratio depends on these two quantities together with the speckle statistics which form the core of this analysis. Before turning to those critically important photon statistics, it is instructive to note that for the same target behavior (30 degree mean aspect angle, 8 degree coning angle) only 18 percent modulation in the target's emissivity area product occurs. Where the "signal" of interest is in fact intensity modulation, the radar thus has a factor of three advantage over the passive sensor. The radar also benefits from the advantages of active illumination whereas the passive sensor must contend with cold targets which can challenge the sensitivity and noise characteristics of passive arrays and their associated optics. It can also be seen that the aspect angle region where modulation is useful only extends from 15 to 50 degrees for the passive sensor.

But far more important in this comparison of radar and passive sensor capability to reliably measure intensity modulation is the problem of closely spaced objects (CSO's). For targets which are well separated and warm enough to provide adequate passive sensor signal-to-noise, the passive sensor could autonomously determine the intensity modulation. But passive sensor pixels are typically of the order of 50 μ m and the blur spot for 10 micron

radiation with a typical interceptor aperture of 25 cm is $100\text{ }\mu\text{r}$. Objects within 50-100 μr cross range at 400 km (20-40 meters) are CSO's, and the summed signals from their individual coning behavior can present an impossible puzzle for the passive sensor to untangle. Many threats of high interest are heavily populated with such CSO pairs.

But with a wavelength $1/20^{\text{th}}$ of 10 micron radiation the active sensor at 532 nm using the same a 25 cm aperture has an individual pixel blur spot diameter of $5.2\text{ }\mu\text{r}$ corresponding to 2 meters at 400 km for each pixel in its 10×10 array. The 20 cm range resolution of the ladar can further assist in isolating one object from another in conducting these critically important intensity modulation measurements. Beyond the strongly enhanced confidence in target designation which the ladar can provide, with concomitant significant reductions in needed interceptor launches per kill (at least a factor of 3), the essential benefit the ladar introduces is the ability to perform discrimination in CSO circumstances where the passive sensor simply cannot.

There is an additional source of potential confusion which can defeat intensity modulation based discrimination by the passive sensor alone even in the absence of closely spaced objects. As is depicted in Figure 2 there are various combinations of coning angle and aspect angle which can produce the same percent modulation. For example a 4 degree coning angle at a mean aspect angle of 15 degrees will produce 37 percent modulation. But this same 37 percent figure could arise from 8 degree coning at a mean aspect angle of 6 degrees or 8 degree coning at a mean aspect angle of 41 degrees. This degeneracy can only be clarified by directly observing the aspect angle of the target. The direct detection 3D imaging ladar can do this once it is able to angularly resolve the target. This becomes possible at 200 km or less range to the target when the receiver electronically zooms its intensified photo diode detector to shift to $2.6\text{ }\mu\text{r}$ Rayleigh pixels. By applying the Moment-of-Inertia algorithm the apparent "azimuth" and "elevation" of the target can be determined to a one sigma one axis uncertainty of approximately 2 degrees. This was also demonstrated in the December 1997 AMOR field tests of the direct detection system⁶. Once so angularly resolved it is possible to observe the coning motion in stop motion snapshot fashion throughout whole precession cycles in this way. But engagement timeline considerations make this impossible to accomplish.

What can be done, however, is to quickly establish which of the three "degenerate" cases in the example being considered is actually responsible for the observed modulation. An effective strategy would be to make such an orientation angle measurement at the time when the modulation would be expected to be halfway between its peak and minimum values, at the "zero crossings." This is easy to predict from the angularly unresolved measurements of modulation made between 450 and 200 km which provide a time history from which the amplitude, period, and phase of modulation can be determined. At the moment of "zero crossing" modulation, the net aspect angle resulting from the coning angle adding to the mean aspect angle would be momentarily equal to the mean aspect angle, or 8, 15 or 41 degrees for the three cases under consideration. These values would be easily distinguishable. There are two zero crossing observation opportunities per coning cycle which eases the issue of scheduling measurements. As further confirmation measurements could be made at the time of minimum modulation where the net aspect angle is the mean aspect angle minus the coning angle or $6-8 = -2$, $15-4 = 11$, $41-8 = 33$ for the three possible degenerate cases in this example. Again, these are easily distinguishable. A similar approach could be taken at the time of maximum modulation.

It should be emphasized that in most cases there will not be a need to use 3D imaging extraction of orientation angles to break degeneracies arising from intensity modulation measurements. As illustrated in Figure 2, 8 degree coning will most often produce 50 to 80 percent modulation which is easily separable from the maximum of less than 40 percent modulation seen for 4 degree coning at any aspect angle. But if because of variation in deployment and a resulting spread in decoy aspect angles a handful of objects display modulation resembling that from an RV, the ladar can distinguish decoys from the RV once the objects become angularly resolved. In addition because of the aforementioned purpose of spin stabilization and careful deployment for precise targeting, the orientation of the RV with respect to its velocity vector at any point in its trajectory may be well known on an a priori basis. The orientation angle measurement capabilities of the 3D imaging direct detection laser can thus provide further confidence enhancing confirmation, thereby increasing the net system P_k per interceptor launched.

As an aside, it should be noted in Figure 2 that no modulation is seen for a head-on encounter even if the target is coning. While coning will change the orientation, the net aspect angle remains the same. For lethality reasons an encounter other than head-on is preferable. As a practical matter actual scenarios of interest produce aspect angles between 20 and 40 degrees.

A more important consideration arising from Figure 2 is also directly related to the probability of a successful kill per interceptor launched. At a mean aspect angle of 30 degrees the modulation intensity is 25 percent for 4 degrees coning and 60 percent for 8 degrees coning. If each measured as 25 ± 7 and 60 ± 7 where the ± 7 denotes the standard deviation values, the difference in means divided by the root sum squared standard deviations would be $(60-25)/\text{sqrt}(49 + 49) \equiv 35/10 = 3.5$. This would be the so-called K factor for discrimination between

these two classes, and is a measure of the confidence of separability. It increases with the "distance" between the distinguishable features and decreases as measurement uncertainty blurs that distinction.

Uncertainty in the overall estimate of modulation intensity arises from the uncertainty in individual measurements the laser radar makes at successive points during the precession cycle. As mentioned above the lidar has an observation period of approximately 20 seconds in which to gather intensity measurements from which modulation parameters (amplitude, period, and phase) are extracted. The precession period can vary between 5 and 30 seconds depending on the threat, so anywhere from 4 full coning cycles down to 2/3 of one cycle will occur during this 20 second window. As the sinusoidal variation of the signal is observed the lidar must accumulate enough samples to accurately determine the sine wave's amplitude and period.

At least 4 or 5 measurements should be made during the precession period, and each measurement should be accurate enough in terms of determining intensity so that the error bars on the individual measurements do not seriously degrade the quality of the sine wave fit to the data.

For a 10 second period this would translate into one measurement every 2 seconds. It will take of the order of 20 laser pulses to obtain an individual measurement of sufficient quality as will be discussed below. At a 100 Hz rate this will allow for 5 measurements per second. As a result 10 targets can be addressed with 5 measurements every 10 seconds.

The question of optimal allocation strategies for the available laser pulses will be addressed in a subsequent section, but two points regarding implementation warrant noting here. The first is that the requirement for 4 or 5 measurement points in each pixel applies for the most challenging case where no a priori knowledge is available concerning the period or the phase of the modulation. For those targets where confusion due to the presence of another CSO is not an issue, cueing by the passive sensor can be a very valuable form of sensor fusion in instructing the lidar exactly when to make its measurements on a given object to achieve maximum benefit. As previously discussed the active sensor will often have a factor of three greater modulation to work with, thereby enhancing discrimination potential. The passive sensor could indicate to the active sensor the times when the modulation would hit its maximum and its minimum, so that only two measurements per precession cycle would be necessary. The passive sensor in non CSO cases can do a sufficiently accurate job of determining period and phase, which are not the primary quantities of interest to discrimination. The lidar can then confirm and refine the passive sensor's estimate of the modulation amplitude.

Returning to the example of targets with a 10 second coning period, if only 2 measurements per precession period were required (one every 5 seconds), with each taking 20 laser pulses, or 1/5 second, 25 targets could be addressed. More likely some hybrid approach would be employed, where this fused cueing would be used when the passive sensor had a high confidence estimate of a non-CSO object's period and phase, while the more measurement intense 4 to 5 lidar samples per period would be directed at those objects which were CSO's or otherwise confusing to the passive sensor. As a result anywhere from 10 to 25 objects could be addressed depending on the possible extent of cueing of the lidar by the passive sensor.

This approach becomes important if the target coning period can be as short as 5 seconds, for here one measurement per second would be needed without cueing, and one every 2.5 seconds with cueing. From 5 to 12 objects could be treated depending on the fraction of objects which could be cued. This number of objects addressed might be increased by as much as a factor of 2 because data on more than two periods is probably not necessary, and this would mean then an individual object need not be interrogated for the full 20 seconds flight time between 400 and 200 km range. A 10 second observation window per object would be sufficient.

The second point regarding implementation worthy of note here is that the current 100 Hz, 250 mJ per pulse operating parameters of the lidar are most likely not yet fully optimized. Originally for the direct detection lidar option, DITP had envisioned 50 Hz, 500 mJ operation, but analysis of the impact of speckle statistics on measurement quality, as is discussed subsequently, made it clear that as long as initial acquisition range were not penalized severely, it was beneficial to trade joules per pulse for repetition rate. That trade perhaps should be pushed further, or a pulse energy/rep rate agile mode of operation developed which can adjust this trade during fly-in. The 25 watt average power of the lidar is also not an inflexible figure which cannot be adjusted upwards. Weight, power and volume efficiencies were gained in going to fewer joules per pulse which could open the path to a higher rep rate at the same joules per pulse in subsequent lidar designs.

There are several potential sources of error for each measurement of intensity during a precession cycle. There is shot noise including speckle, intensity variation due to the target being in a different section of the outgoing Gaussian laser beam from one measurement to the next, and power variation in the laser itself.

Laser power variation has been measured to be no more than 1 to 2 percent over much longer periods than an interceptor engagement would involve. As an additional safeguard against this unexpectedly becoming a non-negligible error source, it is planned to measure outgoing laser power on a shot to shot basis to detect any problems and, if necessary, serve as a normalizing factor.

If a Gaussian laser profile is used, it is necessary to position the object whose reflected intensity is being measured at the center of the beam. Each time the target is reacquired it must be pulled to center. The outgoing laser beam has a $1/e^2$ diameter of 52 μ r spanning 20 meters at 400 km. Some number of shots, currently assumed as 3, will be required to effect this centering. There is a presumption in this that the ladar detector and outgoing laser beam are perfectly aligned. After the stresses of launch this may not be the case, and at present DITP is carrying a worst case uncorrected boresight offset of up to 7.5 μ r for these two components. This could only exact a penalty of 15% as compared to being at true beam center, and would be replicated revisit to revisit, thereby not serving to corrupt the intensity measurements. However jitter about this position could compromise intensity measurements, if the jitter magnitude and time characteristics were such that it served to introduce undesirable intensity variation. This has been the subject of thorough analysis and for jitter value of 1 sigma 1 axis of 5 μ r or less is negligible. An alternate approach, which will be subsequently discussed, would be to erect a top hat rather than a Gaussian in the far field. This avoids the three shot overhead required for centering and removes the concern with jitter. However it imposes a factor of three penalty in terms of intensity reduction. Detailed trades are still underway to establish which is the more promising path. At present the Gaussian approach still has the upper hand. Primarily because it is preferable to make fewer high quality measurements during a precession cycle (using ~20 laser pulses each) rather than more low quality measurements (with 1-4 laser pulses each). If the latter approach were preferable, then the 3 pulse centering overhead would be unacceptably burdensome. For 20 pulse measurements this is not the case.

What drives the need to use 20 laser pulses rather than 1 for a usable measurement of intensity is the large shot to shot variation, 30-70 percent in relative intensity, which is inherently involved in photon emission which is a random process. In the limit of very low photon counts, of the order of 1 per detection period, the variation is primarily described by Poisson statistics where the variance is given by $\sigma^2 = N$, and the standard deviation is given by $\sigma = (N)^{1/2}$ where N is the mean number of photons, or photoelectrons after conversion by a detector. For $N = 1$, which is representative of the total target return at ~450 km range, the standard deviation is equal to the mean so that the relative accuracy of a single laser pulse measurement would be $\sigma/N = 1$ or 100 percent relative error. In addition to this inherent shot noise, which would characterize emission or reflection from any source, ladar intensity measurements may be corrupted by target surface produced "laser speckle". Here reflections from various regions of the surface produce small zones of coherence which can interact with other such subareas in "mutual coherence". In this way these subareas can either constructively or destructively reinforce to produce outgoing irregularly shaped regions, rays, or beamlets of either greater or lesser intensity producing a mottled or "speckled" appearance of the target as viewed at a distant aperture. The number of such light and dark pairs, or speckle cells, is given by M , the mean number of speckle cells in the aperture. Involving self-interaction of the reflected light, speckle is an inherently non-linear process and the variance associated with its effect is given by $\sigma^2 = N^2/M$.

M includes speckle cells from both polarizations when the illuminating laser includes both, or when the target depolarizes an incoming beam upon reflecting it. In support of the DITP program an exact computational method was developed to calculate the mean number of speckle cells appearing in the aperture¹. The often used approximate formula for this quantity is

$$M = 1 + (A_s A_r) / (\lambda^2 R^2) \quad (1)$$

where A_s is the area of the source region, A_r is the area of the receiver aperture, λ is the wavelength, and R is the range to the target.

The central topic of this paper is the effect of laser speckle on the accuracy of intensity measurements made to determine the intensity modulation due to coning as a critical discriminant. At the long target ranges of interest to DITP, the small target source regions, particularly per voxel (range-bin per angle-angle pixel, or per 3D pixel), result in large speckle sizes back at the ladar receiver. M per voxel is typically 2-4 for both polarizations. This can produce strong fluctuation in the signal per voxel depending on the intensity of the light captured by the detector from the small source regions.

However for very small source areas, and especially for non-contiguous areas of any size (e.g., an annulus) the approximation of Equation 1 can underestimate the true M value given by a rigorous wave optics treatment. Such an underestimation could have a negative impact on assessments of potential system performance because it would suggest greater intensity uncertainty than is actually present. This in turn would indicate more laser pulses

were needed to ensure discrimination feature accuracy thereby stretching out the time required to characterize each threat object. Timeline effectiveness is critically important to the DITP mission.

The M values characterizing the DITP engagement for targets of interest will be described in detail, as will the mean number of photoelectrons per voxel. This latter quantity is important because for typical DITP M values per voxel ($M=2-4$, dual polarization) if $N_s < 1$, Poisson behavior dominates, and speckle becomes a secondary perturbation. Once N_s /voxel approaches 4-10, speckle effects become of prime importance.

If the photon statistics are non-Poisson (negative binomial), careful attention must be given to the precise fashion in which expected intensity fluctuations from different voxels are added together to yield the total intensity fluctuations for a given range bin, or total intensity fluctuations for the entire target. Negative binomial distributions do not simply sum the way the normal and Poisson distributions do in producing a cumulative distribution from contributing components. This becomes important in deriving a total target return in the angularly unresolved case from the photons in each range bin as they are added together. Here, as previously discussed, the modulation of the total return is a valuable means of determining target coning angle, but only if this modulation is not masked by photon statistics noise. In the angularly resolved case the contributions must be summed over both angle-angle pixels and range in deriving a total photon return whose statistics must not be so noisy as to obscure reliable modulation information. Similarly the summation over angle-angle pixels in a given range bin needs to produce a total for that range bin which can be used to reliably determine the range-sliced intensity profile of the object in questions.

Under DITP sponsorship an exact technique has been developed for calculating the number of speckle cells returned to a receiver aperture from a target illuminated by a lidar. This number of speckle cells, the M value, has a direct impact on the shot to shot fluctuation in the intensity returned to each 3D pixel (voxel), each range bin, and from the target as a whole in a 3D imaging lidar. As previously discussed, when N_s is the number of photons (or equivalently photoelectrons after photon conversion by the detector) the standard deviation of the intensity taking into account Poisson shot noise and speckle effects is given by

$$\sigma = (N_s + N_s^2/M)^{1/2} \quad (2)$$

For many situations of interest to DITP the reflecting area of the target will not have a simple rectangular or circular disk shape. Those are the only cases previously treated in detail in the literature where the assumption of uniform illumination was usually made^(10,12). The BMDO DITP funded effort has completely generalized the computational method for M , fully and rigorously treating the mutual coherence effects responsible for speckle. These effects are diffraction-like in their dependence on the shape of the reflecting surface, and especially so if that shape has any open or non-reflecting areas. Annular regions produce M values far larger than would be expected on the basis of their area alone.

Beyond developing a previously unavailable method for obtaining critically important M values, this study also has established how such M values for separate range bins of a target can be summed to yield the M value for the target cross section as a whole. Moving in the opposite direction, how such an M value for the target area appearing in a given range bin should be apportioned over the multiple detector angle-angle pixels which may view that area was determined. Neither the summing nor apportioning methods were previously available. Consequently the methodology developed here represents a significant advance not only to the DITP solid state lidar direct detection approach but also to all similar 3D imaging applications where speckle is an important consideration.

The M -value summing method developed by Youmans can be used for three types of summing: summing angle-angle pixels within a given range bin; summing contributions from different range bins; or summing intensities in a given 3D-pixel (voxel) captured over several laser pulses or "shots."

For the M value summing technique to be strictly applicable the terms which are combined must be from regions which are uncorrelated in terms of speckle lobes. For 2D pixels this is satisfied when the individual pixel centers are separated by at least $2.44 \lambda/D$. More accurate results are obtained when the pixel separation is $4.88 \lambda/D$. For Rayleigh pixels of $1.22 \lambda/D$ separation adjacent pixels are highly correlated in many cases with respect to the speckle lobes which are viewed, especially when the mean number of speckle lobes per pixel, denoted by M , is $M \leq 10$.

As a consequence the initial simple summation procedure suggested by Youmans where pixels are summed together to yield a net negative binomial distribution whose effective M value is given by

$$M_{\text{eff}} = \sum_i M_i \quad (3)$$

such an approach to summing over the pixels in a given range bin can produce an erroneously high value of M_{eff} if the speckle cells in adjacent pixels are correlated. The same can be true for summing M values over adjacent range bins if the coherence time τ_c is such that $c\tau_c/2$ is greater than the range bin depth.

There is another potential problem in the simple M value summation even when the pixel speckle cells are uncorrelated. That arises from the fact that the "floor" on M is 1, indicating that M is never expressed as a fraction of a speckle cell or lobe. But in summing to an M_{eff} this "floor" will potentially make the total M value several times greater than it should be.

In the pixel summing case where speckle cell correlation or the M value floor of 1 can be a problem, the approach which should be taken is to evaluate the M value for the entire area within a range bin. This is the true M_{eff} . As has been discussed above and is treated in depth in another paper, this M_{eff} calculation must carefully take into account diffraction effects not considered by the commonly used approximation for M given in Equation 1. Once the M_{eff} value has been properly computed it should be apportioned to the individual pixels contributing to it.

Here another assumption implicit in Youmans' initial memo on M value summation emerges as important. His memo assumed that each source area was emitting or illuminated with the same intensity per square meter. In many situations of interest this will not be the case. The M_{eff} should be apportioned on the basis of the fraction of the total intensity emanating from each pixel. If this fractional apportionment would produce an M value less than one, the previously discussed floor of one should be applied.

The way to apportion the M_{bin} for the entire illuminated area in a given range bin to the individual pixel viewing that area is

$$M_{pixel} = \max\left(\frac{N_{pixel} M_{bin}}{N_{bin}}, 1\right) \quad (4)$$

where M_{pixel} is the speckle M value for an individual pixel, N_{pixel} is the intensity in that particular angle-angle pixel and N_{bin} is the total intensity in a given range bin. This is a single polarization result and should be multiplied by two to account for two polarizations.

The method for accumulating the total M_{target} for multiple range bins where the coherence length is not greater than the range bin depth is to weight the contribution of each range bin by the total intensity in that bin compared to the bin with the greatest intensity

$$M_{target} = \sum_{bins} \frac{N_{bin} M_{bin}}{N_{max\ bin}} \quad (5)$$

where M_{target} is the net M value for the target taken as a whole, N_{bin} is the intensity in a given range bin, M_{bin} is the speckle cell number for that bin, and $N_{max\ bin}$ is the intensity of the bin with the greatest reflected illumination. Equation 5 will be used repeatedly in a subsequent discussion of representative target M values at different ranges and aspect angles.

One of the instances where the most simple version of the Youmans' M value summation method, Equation 3, can be used is for the case of a total target, individual range bin, or single 3D pixel (voxel) where multiple shots are accumulated to reduce the uncertainty in measured intensity. This issue of intensity accuracy expressed as σ_{N_i}/N_i arises due to the requirements of various discrimination algorithms. Intensity modulation as an indication of precession angle requires about ten percent intensity accuracy (relative, not absolute) while the moment-of-inertia algorithm as a source of shape and orientation information is more forgiving. It requires about forty percent relative accuracy. Youmans' formulae

$$N_{s-eff} = \sum_i N_{s_i} \quad (6)$$

$$M_{eff} = \sum_i M_i \quad (7)$$

apply directly to this shot summation case for a total target, individual range bin, or single voxel. There are some algebraic manipulations which can be applied to the resulting expression for standard deviation which are extraordinarily useful in system effectiveness assessment and timeline determination.

For a single shot

$$\sigma_{1\text{-speckle}} = (N_s + N_s^2 / M)^{1/2} \quad (8)$$

For n multiple shots

$$N_{s\text{-eff}} = \sum_i N_{s_i} = nN_s \quad (9)$$

$$M_{\text{eff}} = \sum_i M_i = nM \quad (10)$$

so that

$$\sigma_{\text{eff-speckle}} = (nN_s + n^2 N_s^2 / nM)^{1/2} \quad (11)$$

$$= n^{1/2} (N_s + N_s^2 / M)^{1/2} \quad (12)$$

$$= n^{1/2} \sigma_{1\text{-speckle}} \quad (13)$$

where $\sigma_{1\text{-speckle}}$ is the standard deviation for a single shot.

The quantity of most interest is

$$\frac{\sigma_{\text{eff}}}{N_{s\text{-eff}}} = \frac{n^{1/2} \sigma_{1\text{-speckle}}}{nN_s} = \frac{1}{n^{1/2}} \frac{\sigma_{1\text{-speckle}}}{N_s} \quad (14)$$

This is precisely the $(1/n^{1/2})$ reduction in relative error from multiple shots dependency seen in the case of Poisson statistics where

$$\sigma_{1\text{-Poisson}} = (N_s)^{1/2} \quad (15)$$

where 1-Poisson denotes a single shot for a Poisson case and N_s is the single shot intensity, and

$$\frac{\sigma_{1\text{-Poisson}}}{N_s} = \frac{1}{(N_s)^{1/2}} \quad (16)$$

Multiple shots in the Poisson case produce

$$\begin{aligned} N_{s\text{-eff}} &= nN_s \\ \frac{\sigma_{\text{eff-Poisson}}}{N_{s\text{-eff}}} &= \frac{1}{(nN_s)^{1/2}} = \frac{1}{n^{1/2}} \frac{\sigma_{1\text{-Poisson}}}{N_s} \end{aligned} \quad (17)$$

This similarity of dependency is shown in Figure 3.

There is a "penalty factor" to be applied in going from the Poisson to the speckle case in terms of more shots being required. This "penalty factor", pf, can be computed exactly.

To make the relative accuracy of the speckle case after n shots equal that of the Poisson after one shot set

$$\frac{\sigma_{1\text{-Poisson}}}{N_s} = \frac{\sigma_{n\text{-speckle}}}{nN_s} \quad (18)$$

$$\frac{(N_s)^{1/2}}{(N_s)} = \frac{(nN_s + (nN_s)^2 / nM)^{1/2}}{nN_s} \quad (19)$$

$$(N_s)^{1/2} = \frac{n^{1/2} (N_s + N_s^2 / M)^{1/2}}{n} \quad (20)$$

$$n = (1 + N_s / M) = \text{ppf} \quad (21)$$

Here n is the number of shots required, and represents the multiplicative "photoelectron penalty factor" ppf introduced by considering speckle. It represents how many times more total photoelectrons are required due to speckle compared to those for a pure Poisson case to achieve the same level of relative accuracy. For $N_s=4$ and $M=2$ ppf = $1+2=3 = n$. So three shots in the speckle case will be necessary.

$$\frac{\sigma_{1-\text{Poisson}}}{N_s} = \frac{(N_s)^{1/2}}{N_s} = \frac{2}{4} = .5 \quad (22)$$

$$\frac{\sigma_{3-\text{speckle}}}{3N_s} = \frac{(nN_s + (nN_s)^2 / nM)^{1/2}}{nN_s} = \frac{(12 + 144/6)^{1/2}}{12} = \frac{6}{12} = .5 \quad (23)$$

For $N_s = 2$ and $M = 2$ ppf = $1+1 = 2 = n$

$$\frac{\sigma_{1-\text{Poisson}}}{N_s} = \frac{(2)^{1/2}}{2} = \frac{1}{(2)^{1/2}} \quad (24)$$

$$\frac{\sigma_{n-\text{speckle}}}{nN_s} = \frac{(4 + 16/4)^{1/2}}{4} = \frac{1}{(2)^{1/2}} \quad (25)$$

For $N_s = 1$ and $M = 2$ ppf = $1 + .5 = 1.5$. For a numerical example to make sense compare the case where m Poisson shots are accumulated and $1.5 m$ is an integer as for $m = 2$ and $1.5 m = 3$.

$$\frac{\sigma_{2-\text{Poisson}}}{2} = \frac{(2)^{1/2}}{2} = \frac{1}{(2)^{1/2}} \quad (26)$$

$$\frac{\sigma_{3-\text{speckle}}}{3} = \frac{(3 + 9/6)^{1/2}}{3} = \frac{((6+3)/2)^{1/2}}{3} = \frac{1}{(2)^{1/2}} \quad (27)$$

For $N_s = .5$ and $M = 2$ ppf = $1 + .25 = 1.25$. Compare $m=4$ Poisson shots ($N_s = .5$ per shot) with $n=5$ speckle shots ($N_s = .5$ per shot).

$$\frac{\sigma_{4-\text{Poisson}}}{2} = \frac{\sqrt{2}}{2} = .707 \quad (28)$$

$$\frac{\sigma_{5-\text{speckle}}}{2.5} = \frac{(2.5 + 6.25/10)^{1/2}}{2.5} = .707 \quad (29)$$

It can thus be seen that this "penalty factor" approach is applicable to N_s values greater than, less than or equal to one.

In arriving at the equation ppf = $(1 + N_s/M)$ it was assumed that $N_{\text{Poisson}} = N_{\text{speckle}} = N_s$, the mean number of photoelectrons per shot. To more transparently handle the general case where N_{Poisson} is not equal to N_{speckle} another expression can be derived. This is useful because the Poisson case is so easily handled when N_{Poisson} is set equal to one. Then for example it is immediately apparent that for ten percent relative accuracy one hundred shots are needed, and for one percent accuracy ten thousand shots are required. It is desirable to be able to immediately translate such shot counts into a speckle case for $M = 2$ (the nominal DITP value per voxel) with $N_{\text{speckle}} = 0.6, 1.2, 3.8$, etc. mean photoelectron counts per measurement.

A given fractional relative error P (e.g., 0.10 for 10 percent) can be achieved for the Poisson case by averaging over multiple shots so as to accumulate m photoelectrons. The relative error for that total is given by

$$\frac{\sigma_{m-\text{Poisson}}}{m} = \frac{m^{1/2}}{m} = \frac{1}{m^{1/2}} = P \quad (30)$$

The total required Poisson photoelectrons m is thus equal to the well known result $1/P^2$. Applying the penalty factor, ppf = $(1 + N_s/M)$, gives the total number of photoelectrons required in the speckle case

$$PE_{tot} = pf / p^2 = (1 + N_s / M) / P^2 \quad (31)$$

The number of shots n in the speckle case to produce P fractional relative error is thus given by

$$n = PE_{tot} / N_s = (1/N_s + 1/M) / P^2 \quad (32)$$

$$n = (1/P^2) (1/N_s + 1/M) \quad (33)$$

If speckle were negligible, $M = \infty$, this would reduce to

$$n = (1/P^2) / N_s \quad (34)$$

and would describe the Poisson case with N_s photoelectrons per shot. The additive $1/M$ term in Equation (33) causes the need for additional shots. If $M = \infty$ there is no penalty for going to larger photoelectrons per shot N_s . But as M approaches 1 the $1/M$ term can come to dominate the $(1/N_s + 1/M)$ factor unless N_s is comparably small. From a system point of view it would be energetically wasteful to have a large N_s per pulse and yet have the $1/M$ term call for as many pulses as if N_s were small. To keep the speckle "penalty" in check from the point of view of the number of shots required for an intensity measurement of given accuracy, it is advisable to keep $1/N_s$ four or more times greater than $1/M$, or $N_s/M \leq .25$. This analysis in terms of shots required relates back to the "photoelectron penalty factor" of Equation 21 $(1 + N_s/M)$. Operationally it means that a ladar may be far more efficient operating at a higher rep rate and lower energy per pulse. To turn that assertion into useful engineering guidance requires accurate estimates of the M values for the total target, individual range bins and single voxels together with the expected return from the target based on geometry and reflectivity.

Applying $n = (1/P^2) (1/N_s + 1/M)$ to a DITP issue of high interest will illustrate the utility of this expression. Consider a situation where ten percent relative accuracy of the intensity estimates is required for four different N_s values 0.5, 1, 2 and 4. The $N_s=1$ Poisson case would necessitate 100 shots. Here $M=2$ is assumed.

Table 1

$\bar{N}_s (M=2)$	0.5	1	2	4	8	16	32	64
$(1/N_s + 1/M)$	2.5	1.5	1	0.75	0.625	0.5625	0.53125	0.515625
Shots	250	150	100	75	62.5	56.25	53.125	51.5625
Energy Required = shots x N_s	125	150	200	300	500	900	1700	3300

For the Poisson case where $M = \infty$ this table would become

Table 2

$\bar{N}_s (M=\infty)$	0.5	1	2	4	8	16	32	64
$(1/N_s)$	2	1	0.5	0.25	0.125	0.0625	0.03125	0.015625
Shots	200	100	50	25	12.5	6.25	3.125	1.5625
Energy Required = shots x N_s	100	100	100	100	100	100	100	100

demonstrating the well known Poisson result that photoelectrons are photoelectrons no matter how many arrive per voxel per measurement.

An important point apparent from Table 1 is that from a system design perspective it would be optimal to be able to adaptively adjust the ladar transmitter joules per pulse and pulse rate so that the mean number of photoelectrons per voxel per measurement was kept around one once the target is angularly resolved. This is where the knee in the net energy per intensity measurement requirement curve occurs. There is some additional benefit in going down to a mean value of 0.5, but only a slight advantage, and it introduces detector signal to noise problems.

Examining some examples of M values calculated for individual range bins and M value summing over those range bins to get a total target M value is probably the best way to get a firm grasp on the potential performance of the system and the system operating parameter trades under investigation.

The graph at the top of Figure 3 shows the M value per range bin for the case of a 2 x 1m cone at 200 km and 0 degree aspect angle calculated both using the standard approximation and the exact technique developed under DITP and validated by data taken in September-November 1998¹³. The graph at the top of Figure 4 is for the same conditions with 30 degree aspect angle. Figure 3 clearly illustrates the substantial difference between the standard approximation for M and the true M for the head-on cone. Although a head-on engagement is unlikely, and undesirable, a mean aspect angle of 15 degrees and a coning angle of 12 degrees will sweep through this near zero region during the coning cycle. The returning amplitude will be a minimum here, and is accordingly important in estimating total modulation and the implications of the exact M calculation method will provide significant positive system benefit.

As the graph at the top of Figure 4 indicates, at an aspect angle of 30 degrees where the reflective area in each range bin much less resembles an annulus and is much more like a solid contiguous area, the standard approximation is far more valid. Here the diffraction effects leading to the M value, enhancement seen for the head-on annuli play a much smaller role except in range bins eight and nine. Even here the effect is less than would be expected from the "annular" shape of the area because most of the intensity is concentrated around the "centerline". As discussed before the M value is an intensity weighted phenomenon.

For the purposes of discrimination using range template matching (range profiling) or intensity modulation as a means of determining precession angle and frequency, both the exact M value calculation technique and intensity weighted method for summing M values become of critical importance.

In terms of intensity modulation it is the photoelectron sum over all range bins which must be accumulated. For the head on cone case the M values of the ten annuli are added together with a weighting factor. As previously discussed that weighting factor is the intensity in a given range bin normalized to the range bin with the greatest intensity.

In the table at the bottom of Figure 3 for the head-on cone case at 200 km the computation flow is captured for calculating shots required for range template matching as well as intensity modulation. The photoelectrons per range bin are given along with the resulting weighting factor shown in column three. In this case range bin 10 had the greatest intensity and its photoelectron count becomes the normalizing divisor. The M values which would have been computed from the standard or Yura approximation are given in column four. The M values calculated exactly are given in the sixth column. It cannot be stressed greatly enough how significantly this impacts the DITP system timeline. For the range bins which most significantly contribute to range template matching and intensity modulation there is a factor of three to four enhancement of M.

The net M value for the target taken as a whole to be used in determining the uncertainty in the intensity measurement from the total cross section is arrived at by multiplying the weighting factor in column three by the exact M's in column six. These sum to a net M of 21.67. This net M is then multiplied by 2 to take into account two polarizations returned by the target. The fifth column shows the corresponding number from the standard approximation which is a factor of three smaller.

To calculate how many of these shots (each returning 20.11 photoelectrons) are required to match the 10 percent accuracy of 100 Poisson photoelectrons the expression

$$n = (1/P^2)(1/N_{s-eff})(1 + N_{s-eff}/M_{eff}) = (1/P^2)(1/N_{s-eff})pf \quad (35)$$

is used where n is the "penalty factor" due to speckle, N_{s-eff} is the photoelectrons summed over all range bins (20.11) and M_{eff} is the weighted sum of M over range bins (43.34). Here, as shown in the table at the bottom of Figure 3, $(1/N_{s-eff})pf=0.073$. So 7.3 DITP shots would be needed to produce the 10 percent accuracy which would result from capturing 100 Poisson photons. If seven shots are used

$$\frac{\sigma}{N_s} = \frac{[(7 \times 20.11) + (7 \times 20.11)^2 / (7 \times 43.34)]^{1/2}}{(7 \times 20.11)} = 0.102 \quad (36)$$

To get five percent accuracy $4 \times 7.3 = 29$ shots would be needed.

Using similar information in the table at the bottom of Figure 4 for the 200 km 30 degree aspect angle cone case, the number of shots required for 10% and 5% intensity modulation accuracy can be determined. That would be 8 and 32 respectively.

Turning to range template matching, the tables at the bottom of Figures 3 and 4 determine the shots needed for usable data.

The second graphs in Figures 3 and 4 show the photoelectrons per range bin for the 0 degree and 30 degree aspect angle cases at 200 km. If the intensity is held to 10 percent uncertainty (standard deviation) in the range bin with greatest intensity it can be seen that a usable profile results. This ten percent standard deviation is shown on the photoelectrons per range bin curves. Also shown as separate curves are the resulting standard deviations from one shot and multiple shots, where the multiple shots are whatever number is required to produce ten percent relative accuracy in the range bin with the greatest intensity. In each instance the "penalty factor" for the most intense range bin was used to determine the number of shots required. For example in the case of the head-on cone at 200 km range bin 10 is involved. Here $N_i = 3.82$ and $M = 5.95$ (times 2 for two polarizations) so $(1/N_{i,eff})pf = 0.346$ and 35 shots are required.

Had the standard Yura approximation for M been used, M would have been 3.30 not 11.90 and the shot requirement would have ballooned to 56, a 60 percent increase. Analysis of the impact of speckle on the number of laser pulses needed to obtain sufficiently accurate intensity measurements during a precession cycle to use the degree of intensity modulation as a discriminant, as has just been discussed, is central to the evaluation of system effectiveness. It also is essential to determining the most suitable strategies for ladar usage. Here the question of accuracy as a function of range becomes paramount.

Table 3 extends the previous analysis of the 30 degree aspect angle, 8 percent target reflectivity, 200 km case to the entire spectrum of ranges of interest, roughly 400 down to 100 km. The ranges in Table 3 were chosen to

Table 3 Impact Of M Values On Timeline 30 Degree Aspect 8% Reflectivity

Range (km)	365	300	260	210	180	150	120
N_i (photoelectrons)	4	9	16	36	64	144	324
$\sigma = \sqrt{N_i}$ Poisson	2	3	4	6	8	12	18
σ/N_i	.50	.33	.25	.17	.13	.08	.06
Shots for $\sigma/N_i = 10\%$	25	11	6	3	2	1	1
M_{Yura}	11	12	14	16	20	24	30
$\sigma = \sqrt{N_i + N_i^2/M}$	2.33	3.97	5.86	10.82	16.40	31.75	61.83
σ/N_i	.58	.44	.37	.30	.26	.22	.19
Shots for $\sigma/N_i = 10\%$	34	19	13	9	7	5	4

Table 4 Impact Of M Values On Timeline 16 Degree Aspect 8% Reflectivity

Range (km)	365	300	260	210	180	150	120
N_i (photoelectrons)	8	18	32	72	128	288	648
$\sigma = \sqrt{N_i}$ Poisson	2.82	4.24		8.49		16.9	25.46
σ/N_i	.35	.24	.18	.12	.09	.06	.04
Shots for $\sigma/N_i = 10\%$	13	6	3	1	1	1	1
M_{Yura}	11	12	14	16	20	24	30
$\sigma = \sqrt{N_i + N_i^2/M}$	3.72	6.71	10.25	19.90	30.78	61.12	121.02
σ/N_i	.46	.37	.32	.28	.24	.21	.19
Shots for $\sigma/N_i = 10\%$	22	14	10	8	6	5	4

Table 5 Impact Of M Values On Timeline 0 Degree Aspect 8% Reflectivity

Range (km)	365	300	260	210	180	150	120
N_s (photoelectrons)	1.6	3.5	6.3	14.7	27.2	56.4	137.5
$\sigma = \sqrt{N_s}$ Poisson	1.26	1.87	2.51	3.83	5.21	7.50	11.73
σ/N_s	.79	.53	.40	.26	.19	.13	.08
Shots for $\sigma/N_s = 10\%$	63	29	16	7	4	2	1
M_{exact} Speckle	19	26	32	42	54	64	80
$\sigma = \sqrt{N_s + N_s^2/M}$	1.32	1.99	2.75	4.45	6.40	10.30	19.33
σ/N_s	.82	.57	.44	.30	.24	.18	.14
Shots for $\sigma/N_s = 10\%$	68	32	19	9	6	3	2
M_{approx} Speckle	11	12	14	15	17	20	25
$\sigma = \sqrt{N_s + N_s^2/M}$	1.35	2.13	3.02	5.40	8.41	14.68	29.90
σ/N_s	.85	.61	.48	.37	.31	.26	.22
Shots for $\sigma/N_s = 10\%$	72	37	23	13	10	7	5

Table 6 Impact Of M Values On Timeline 0 Degree Aspect 16% Reflectivity

Range (km)	365	300	260	210	180	150	120
N_s (photoelectrons)	3.2	7.0	12.6	29.4	54.4	112.8	275.0
$\sigma = \sqrt{N_s}$ Poisson	1.79	2.65	3.55	5.42	7.37	10.60	16.59
σ/N_s	.56	.38	.28	.18	.13	.09	.06
Shots for $\sigma/N_s = 10\%$	31	15	8	3	2	1	1
M_{exact} Speckle	19	26	32	42	54	64	80
$\sigma = \sqrt{N_s + N_s^2/M}$	1.93	2.98	4.19	7.07	10.45	17.65	34.93
σ/N_s	.60	.43	.33	.24	.19	.16	.13
Shots for $\sigma/N_s = 10\%$	36	18	11	6	4	3	2
M_{approx} Speckle	11	12	14	15	17	20	25
$\sigma = \sqrt{N_s + N_s^2/M}$	2.03	3.33	4.89	9.32	15.12	27.37	57.45
σ/N_s	.64	.48	.39	.32	.28	.24	.21
Shots for $\sigma/N_s = 10\%$	40	23	15	10	8	6	4

match points where the number of photoelectrons were the squares of integers to facilitate use of the table. The table indicates the standard deviation and relative error which would hold if Poisson statistics were applicable were $\sigma/N_s = (1/N_s)^{1/2}$. The corresponding standard deviations and relative errors are also shown when speckle is considered. Here 36 percent more up to 4 or 5 times more shots would be required as the range decreases from 365 to 120 km. This reflects the point underlined earlier that the "photoelectron penalty factor" associated with speckle is $(1 + N_s/M)$. At 365 km M is 3 times greater than N_s and the impact of speckle is perceptible but not overwhelming. At 150 km N_s is 6 times as large as M and the impact of speckle is great reflecting its non-linear dependence on intensity.

As this would suggest, as the target reflectivity is doubled along with the number of photoelectrons at each range, the energy efficiency price exacted by speckle becomes more acute. As shown in Table 4 at 365 km N_s is 72 percent of M so 72 percent more radar pulses are required than would be the case in the absence of speckle, 22 vs. 13. So although as expected the greater returning signal reduces the number of pulses required, the energy efficiency has dropped. This could be regained by a rep rate agile device which could drop the pulse energy and increase the firing rate, keeping the net power draw constant.

For the head-on cone case the effects of speckle are more muted because the number of photoelectrons drops by a factor of 2.5 while the M values increase by about a similar factor, decreasing the N/M ratio by a factor of six as is seen in Table 5. For ranges of 200 km and above there is little difference between the speckle and Poisson calculations of the number of shots required for 10 percent relative error. Below 200 km N becomes comparable to M and 50 to 100 percent more spots would be required.

The speckle situation would have been markedly worse at ranges less than 250 km if the M values from the standard approximation were used. This is apparent in the bottom section of Table 5. As previously discussed, experiments in September-November 1998¹¹ validated the exact approach for calculating the speckle mutual coherence function as a way of determining M .

As the reflectivity at 0 degrees aspect is increased from 8 percent to 16 percent in Table 6, the impact of speckle becomes pronounced (a 50% increase in the number of shots required) by 250 rather than 200 km. It's at this point that $N/M = 0.5$.

There are many scenario factors (target reflectivity), and system trades (laser power, rep rate, Gaussian vs. top hat beam, number of laser shots per intensity measurement, etc.), which must be considered in overall performance assessment. It is useful to assume different levels of intensity at 400 km, invoke R^4 intensity scaling, select a typical aspect angle in computing M (e.g. 30 degrees), and compute the Poisson and speckle standard deviations and relative errors. This is what is done in Figure 5 for intensity values of 2, 4 and 8 photoelectrons at 400 km. As a point of reference an 8 percent reflective, 2×1 meter cone, at the center of a $52 \mu\text{m}$ $1/e^2$ diameter Gaussian 250 millijoule beam for a 25 cm aperture, 40 percent quantum efficiency, 80 percent transmission efficiency and 64 percent reception efficiency will return 2.8 photoelectrons.

Of particular interest are the N and M curves, and the ranges where N first becomes equal to and then exceeds M . As previously mentioned, under active analysis is the question of whether fewer pulses per intensity measurement and more measurements rather than vice versa is optimal. The ability to do that would hinge on whether a flat top could be erected at range so that there was not a severe penalty for shots required to center the target in a Gaussian, if only a few "measurement" pulses were then to be launched. The feasibility of constructing such a flat top has been questioned. Such flatness usually comes at the expense of broadening the beam to such an extent that there is a severe intensity penalty. If the flat top radius is reduced, unacceptable "ringing" patterns could corrupt intensity modulation measurements. The width of the flat top is determined by the radius of curvature of the outgoing phase front. As is shown in Figure 6 for a beam radius at the primary aperture of 10 centimeters and a super-Gaussian parameter of 5, a phase front radius of curvature of 3500 m produces an acceptable compromise between beam width at range and flatness. Figure 7 illustrates that this beam profile extends from 100 to 400 km range.

With the relative accuracy curves of Figure 5 in hand, key implementation questions can be addressed, such as how many laser pulses should be used per intensity measurement. There are two possible approaches, either choose a fixed number of pulses and let the relative error decrease with range, or select a fixed relative error and let the number of pulses decrease with range. In either case it is useful to gauge approximately how many pulses will be required to produce useful measurements. In trying to fit a sinusoid to a series of measurements, if the measurements are of too poor quality, no matter how many there are, the fitting algorithm can be defeated altogether. The standard deviation of the individual measurements should not be more than roughly half of the modulation amplitude. As an example, for an intensity of 2 at 400 km the relative error at 300 km is 50 percent. Averaging 25 shots would push that down to 10% which would be appropriate for a 4 degree coning angle whose modulation depth is 25 percent. At 200 km the same 25 shots would decrease the expected relative error from 30 percent to 6 percent, while at 400 km the 75 percent relative error would have been reduced to 15 percent.

As previously discussed 25 shots per measurement may not fit within the engagement timeline and still permit sufficient measurements per precession cycle. Trades involving 4, 9, 16 and 25 shots per measurement does not lend itself to Fourier techniques for extracting reliable estimates of amplitude and period. Variations on the Nelder-Mead simplex algorithm are especially effective in extracting modulation parameters from measurements.

3.0 SUMMARY

The direct detection 3D imaging laser radar developed by BMDO DITP and currently being integrated for a demonstration test flight in FY2001 has the capability of significantly improving the P_x of an interceptor by providing substantially enhanced discrimination. This is especially true for threats of high interest where closely spaced objects defeat the capability of passive sensors to discriminate based on intensity modulation due to coning.

The DITP 3D ladar not only has no problem in resolving such CSO's, it also has an inherent advantage in that the same amount of coning will result in 3 times as much modulation as the passive sensor would observe. Beyond that the 3D ladar can observe the actual variation in orientation once the targets are angularly resolved. This can cut through confusion the passive sensor could experience since different combinations of aspect and coning angle can yield the same modulation amplitude.

The ability of the 3D ladar to deliver such benefits hinged on the accuracy of its intensity measurements. Analysis backed by experiments indicates that while speckle is a potential problem, the intensity uncertainty it introduces can be mitigated by multi-pulse averaging. Sufficient engagement timeline exists for such an approach when proper-trades between pulse energy, rep rate, and beam profile are made. As evidenced by the ongoing demo flight integration effort this technology has advanced significantly beyond the laboratory demonstration stage. The integration effort surfaced many of the implementation issues, which in turn required a thorough understanding of speckle photon statistics.

4.0 ACKNOWLEDGEMENTS

This work was partially sponsored under BMDO/NRL contract N00014-97-D-2014 supporting the Discriminating Interceptor Technology Program. The authors would like to thank Dr. Frank Hanson, executing agent; LCDR James Buckley, program manager; and Dr. Walter Dyer, technical advisor, for their support and guidance. The authors would also like to thank Guy Beaghtler of Fibertek, Inc., and Dr. Daniel Leslie of ThermoTrex, Inc. for useful technical discussions concerning the DITP ladar system and photon statistics.

5.0 REFERENCES

1. Dyer, W., "Missile Seeker Technology at the Ballistic Missile Defense Organization," Proc. AIAA Missile Sciences Conf., Dec. 1996.
2. Burnham, R., et al., "Short Pulse 3D Imaging Ladar for Advanced Target Discrimination," Proc. IRIS Active Systems, Vol. 1, 1997.
3. Leslie, D., et al., "Direct Detection Laser Radar Angle/Angle/Range-Imaging Target Identification Capabilities," Proc. IRIS Active Systems, Vol. 1, 1997.
4. Dyer, W., "Review of the Ballistic Missile Defense Organization's Advanced Sensor and Seeker Technology Programs," Proc. IRIS Active Systems, Vol., 1997.
5. Hart, G., et al., "Solid-state Laser Radar for DITP - New Discrimination Algorithms and Test Results with AMOR Targets," Proc. IRIS Active Systems Conf. March 1998.
6. Hart, G., et al., "New Discrimination Algorithms and Test Results Using a Solid-state 3D Imaging Laser Radar," Proc. 7th AIAA/BMDO Technology Readiness Conf., Aug. 1998.
7. MacFarland, A., et al., *Laser Cross Section Handbook*, Mission Research Corp., WRDC-TR-89-9010, June 1990.
8. Youmans, D., Hart, G., "Numerical evaluation of the "M" parameter for direct detection ladar," SPIE Proc. Vol. 3380, April 1998.
9. Yura, H., "Ladar detection statistics in the presence of pointing errors," Appl. Opt., Vol. 33, No. 20, Sept. 1994.
10. Goodman, J., "Some Effects of Target-Induced Scintillation on Optical Radar Performance," Proc. IEEE, Vol. 53, No. 11, Nov. 1965.
11. Goodman, J., "Comparative Performance of Optical-Radar Detection Techniques," IEEE Trans. AES, Vol. AES-2, No. 5, Sept. 1966.
12. Goodman, J., *Laser Speckle and Related Phenomena*, J.C. Dainty Ed., Springer-Verlag, 1975, Second Edition, 1984.
13. Driscoll, T., et al., "Comparison of Theory and Experiments in the Effects of Speckle on NMD/TMD Target Recognition with Direct-Detection LADAR," Proc. IRIS Active Systems, Feb. 1999.

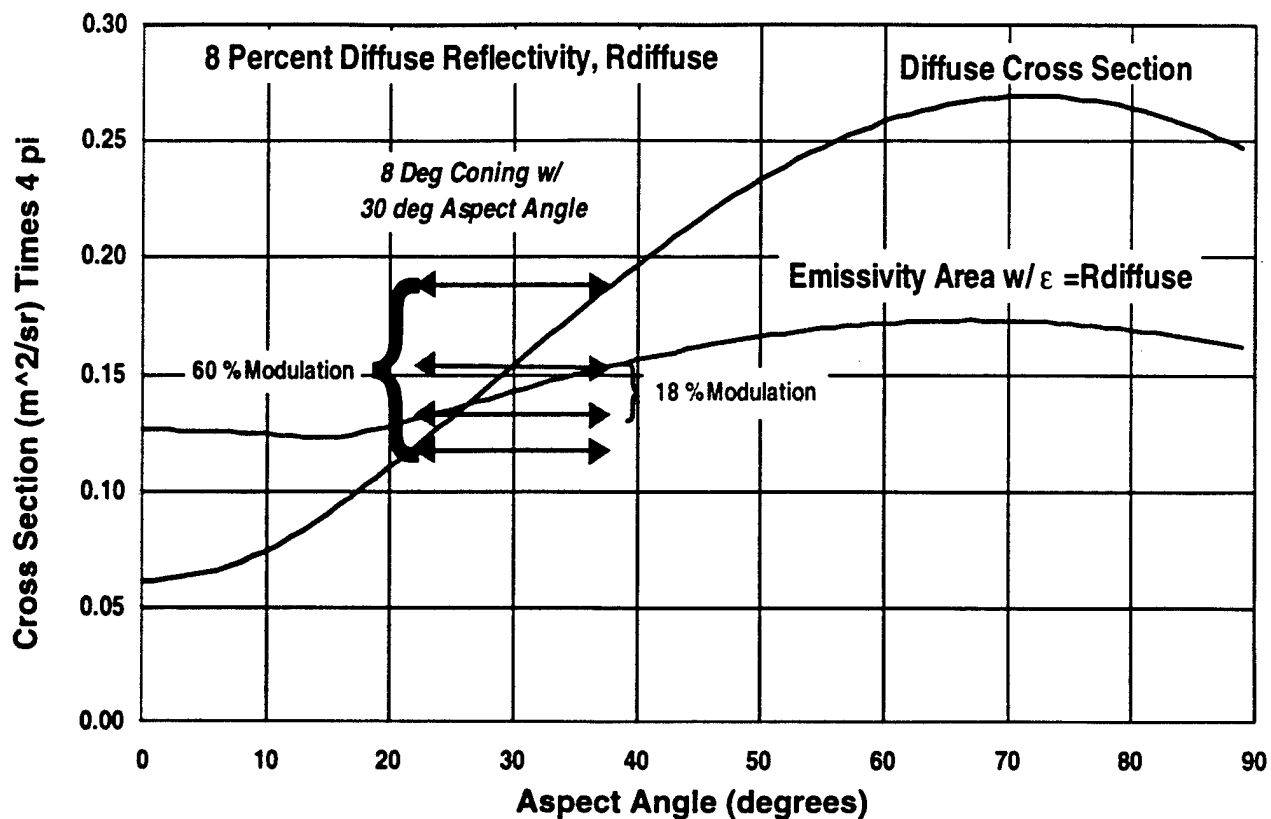


Figure 1. Cone (2m x 1m) LADAR Total Cross Section vs Aspect Angle

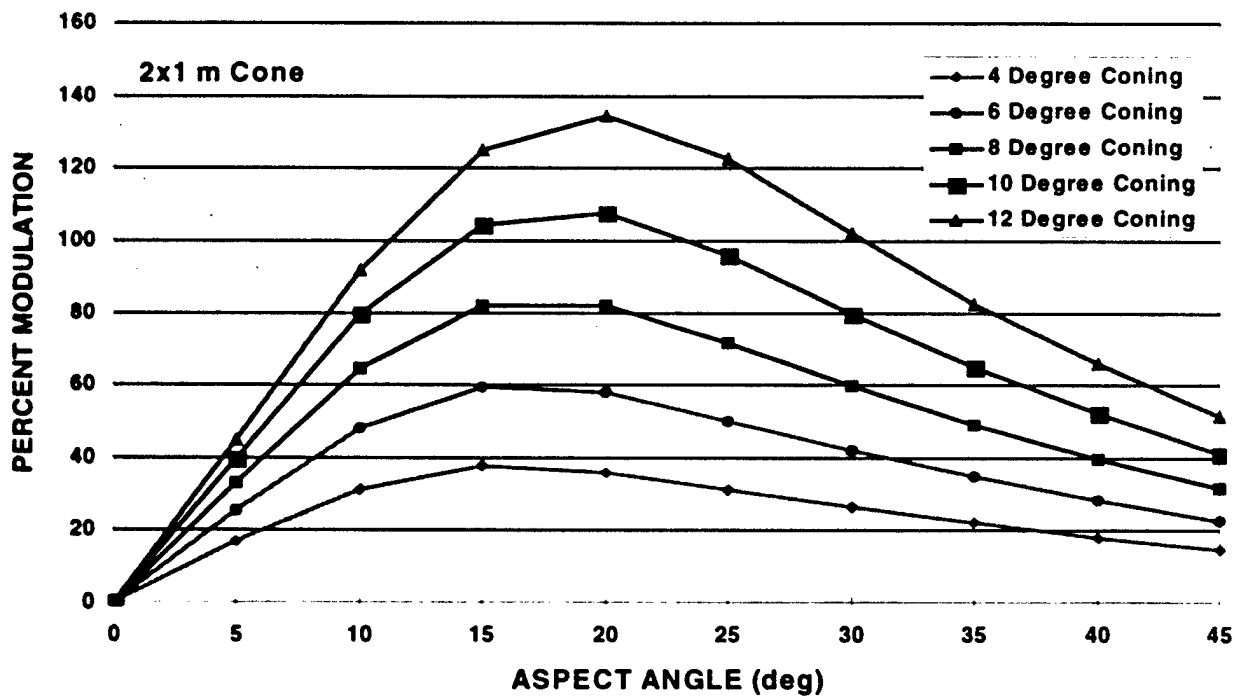


Figure 2. Intensity Modulation vs Aspect & Coning Angle

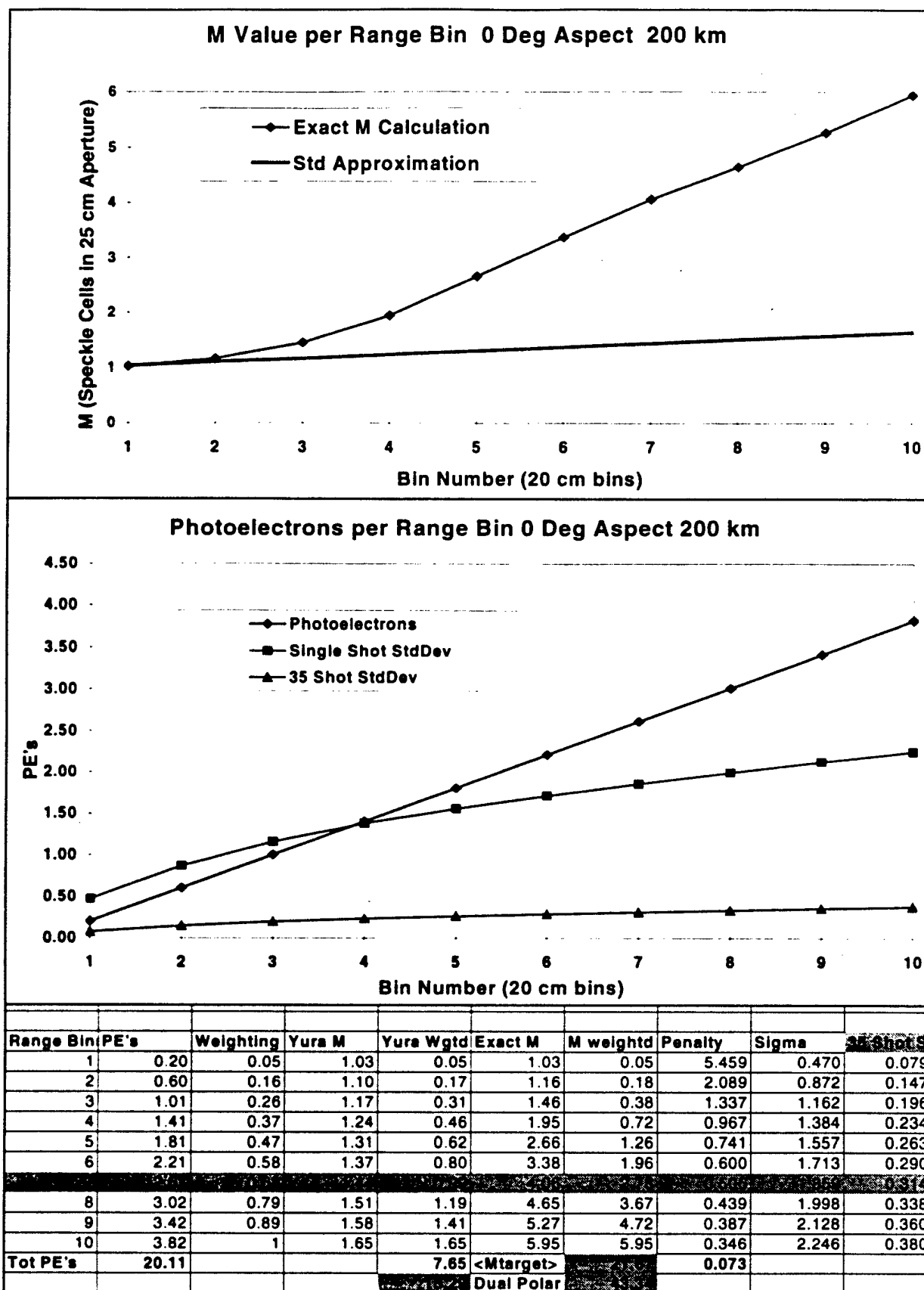


Figure 3. Speckle Analysis for 200 km Range 0 degree Aspect Angle

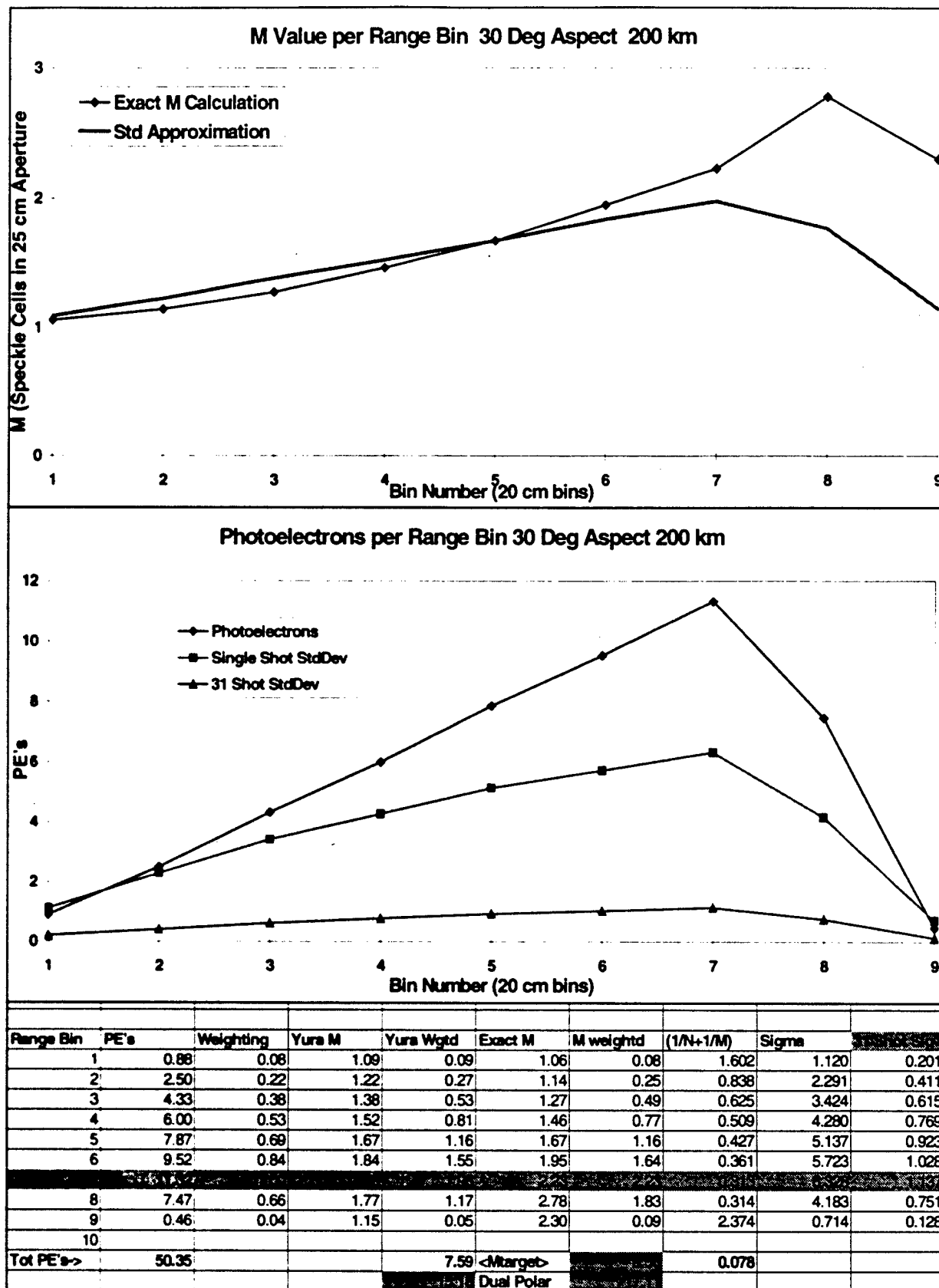


Figure 4. Speckle Analysis for 200 km Range 30 degree Aspect Angle

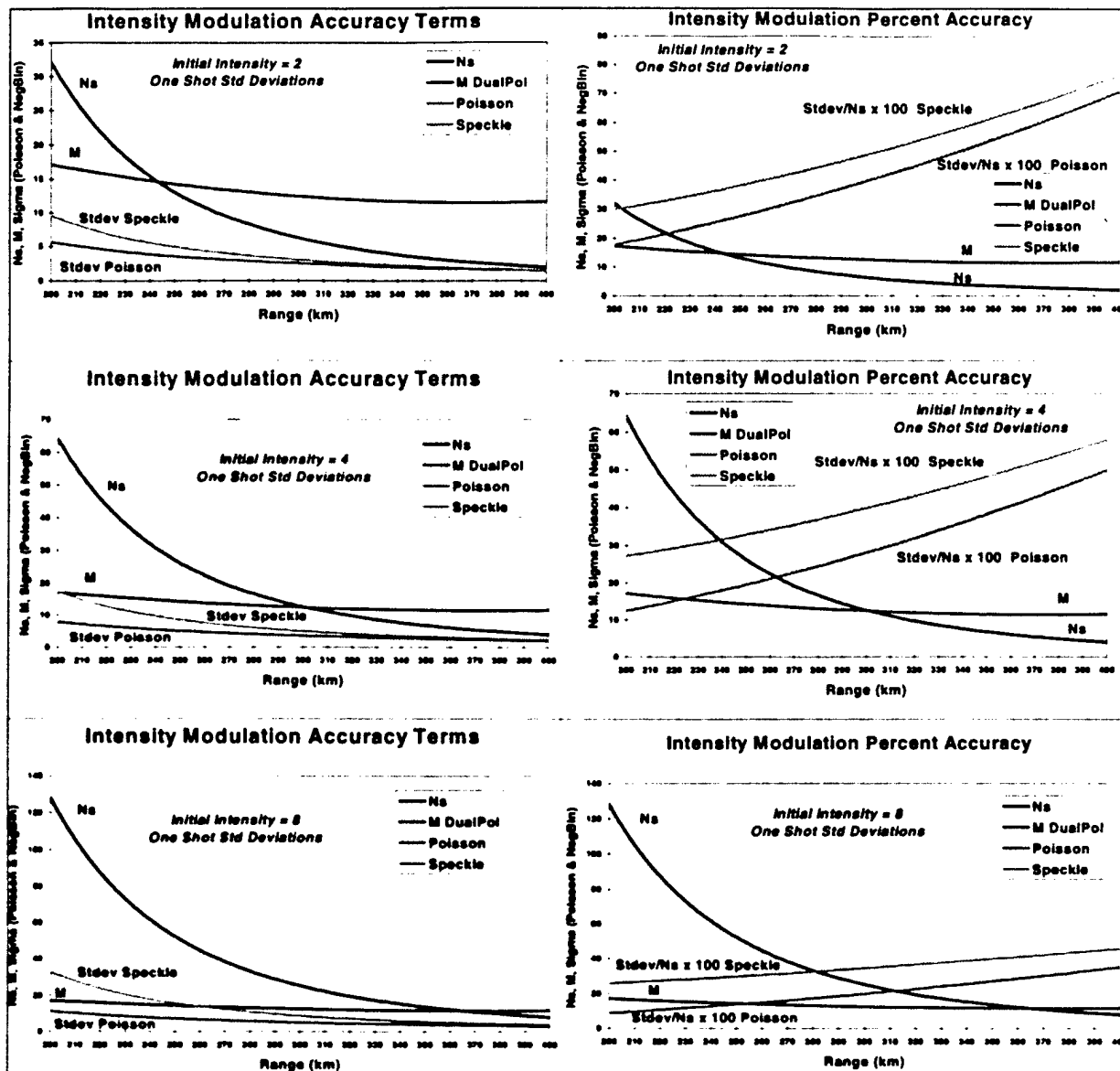


Figure 5 Speckle vs Range and Initial Intensity.

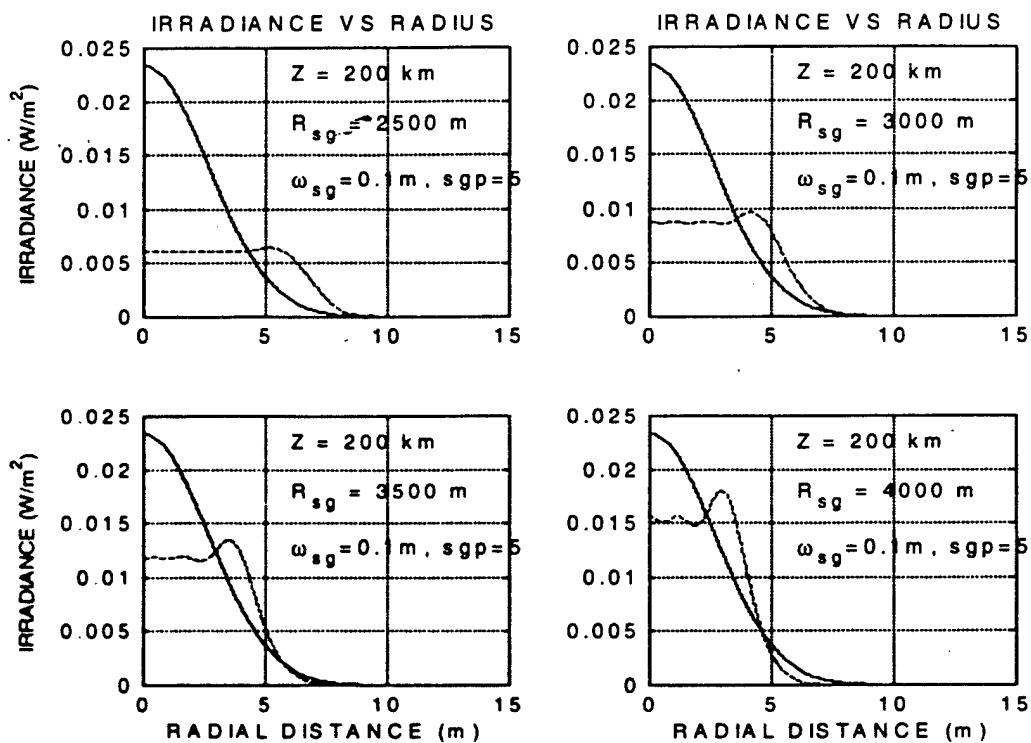


Figure 6. Irradiance (W/m^2) at 200 km range versus phase-front curvatures of 2500, 3000, 3500, and 4000 m. Solid line is reference Gaussian mode.

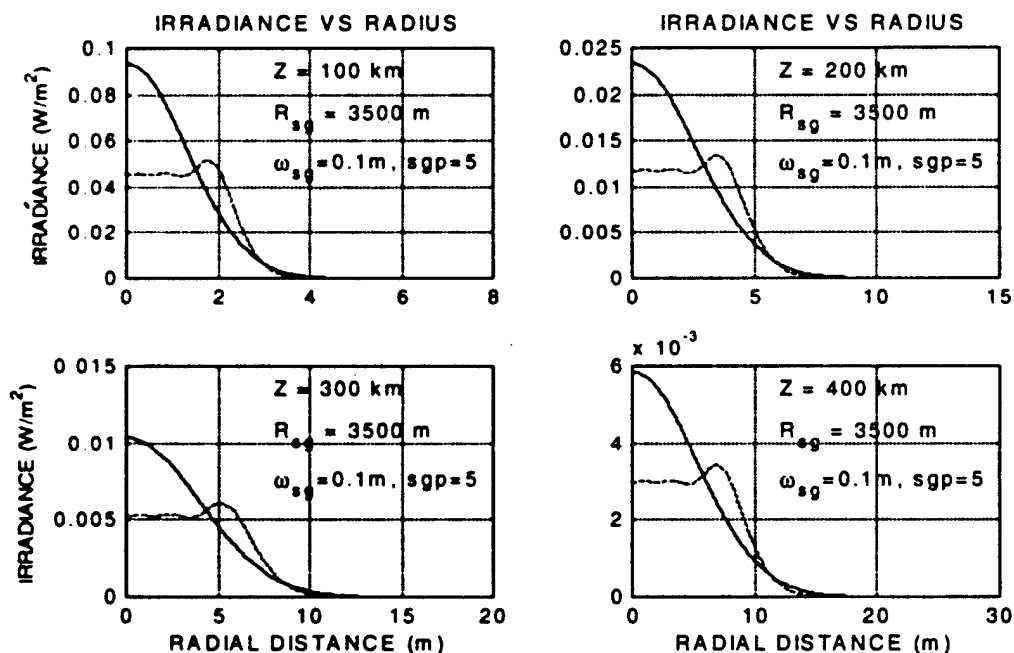


Figure 7. Irradiance (W/m^2) vs. radial distance at ranges of 100 km to 400 km with a constant phase front curvature of 3500 m. Solid line is reference Gaussian mode.

Appendix J

THREE-DIMENSIONAL TEMPLATE CORRELATIONS FOR DIRECT-DETECTION LASER-RADAR TARGET RECOGNITION

Douglas G. Youmans, George A. Hart
Schafer Corporation
321 Billerica Rd., Chelmsford, MA 01890

ABSTRACT

Direct-detection laser radars can measure the range and the intensity returns from a target, with or without clutter, for each part of the target resolved in angle by the optical system. Because the ladar's angular resolution is in micro-radians, there are generally at least a few angular pixels "on target." In addition, for narrow pulse ladar systems, there may be ten or so sequential intensity measurements in range per pixel as the laser pulse propagates down the target's surface. The output image is, therefore, potentially a three dimensional "cube" of intensity measurements and quantized in the range axis by the range-bin size or "voxel." This is known as "range resolved angle-angle-intensity" ladar, and one such system is being built by BMDO under the DITP effort.

Transforming this 3D-matrix image into the spatial-frequency domain using 3D-Fourier transforms, we have followed conventional 2D template-correlation techniques to perform target recognition and identification. Results of target image correlations using the "joint transform correlator," "the inverse filter," the "symmetric phase-only matched-filter," and the classical "matched filter" among others are presented. Also, projection of the 3D-matrix image onto the x-y, x-z, and y-z planes allows the use of conventional (2D) correlators, but their outputs must be combined. Simulated far-field test data using conical shaped targets are presented to study the 3D correlators, and the effects of laser speckle are discussed. Recent developments in negative-binomial driven shot-noise effects in range-resolved direct-detection ladar are outlined as well. We note that 3D template correlation may supplement or refine less computationally intensive algorithms such as total signal, range-extent, x-z, y-z, and x-y plane image centroid estimation, and image moments.

1.0 INTRODUCTION

There are many two dimensional image processing algorithms useful in automatic target recognition and identification that can be found in the literature. We summarize some of these in Section 3.0 as developed by the passive sensor community, but now we extrapolate them to three dimensions: elevation, azimuth, range, and intensity per voxel. Even with a single range measurement per elevation / azimuth pixel (current tactical ladars), the effects of laser speckle must be accurately modeled. Recent work has allowed the numerical evaluation of the speckle "M" parameter for arbitrary source region, illumination irradiance, and receiver aperture. These speckle effects are briefly summarized in Section 2.0. In addition, as the photons are detected by a photon-counting photo-multiplier tube, the detector's response and the electronic's bandwidth result in a classical "shot-noise" impulse-response summation process. This is also reviewed in Section 2.0 based on state of the art photomultiplier tube detector data.

The 3D template correlation results to date are described in Section 5.0. Simple diffuse cone, sphere, and cylinder numerical targets without clutter are used in this initial work and are described in Section 4.0.

2.0 SUMMARY OF LADAR SPECKLE AND SHOT-NOISE EFFECTS

In order to accurately simulate ladar target images for algorithm development, it is necessary to have the correct laser radar speckle and detector response models. In this section we review laser speckle theory, photon counting statistics, and the detector with electronics bandwidth and resulting shot-noise stochastic process effects. Round-trip turbulence modulation of the Poisson counting statistics are also mentioned, but no further analysis of endo-atmospheric ladar will be presented in this paper.

2.1 SPECKLE IRRADIANCE STATISTICS

When laser light is back-scattered from a rough target, constructive and destructive interference results in the well known "laser speckle" pattern distribution back at the receiving aperture. Goodman¹⁻⁴ has shown that the sum of a number of uncorrelated irradiances, collected by the finite size ladar receiving aperture, has a probability density function given by:

$$p_{\Sigma}(I) = \sum_{k=1}^M \langle I_k \rangle^{M-2} \exp(-I/\langle I_k \rangle) / \prod_{\substack{p=1 \\ p \neq k}}^M (\langle I_k \rangle - \langle I_p \rangle) \quad (1)$$

This can be approximated by a simpler gamma distribution given by

$$p_{\Sigma}(I) \equiv \frac{(M/\langle I \rangle)^M I^{M-1} \exp(-MI/\langle I \rangle)}{\Gamma(M)} \quad (M \geq 1) \quad (2)$$

The "M" parameter was shown by Goodman³ to be equal to the reciprocal normalized-variance-of-irradiance

$$\frac{1}{M} \equiv \frac{\sigma_{I_{rec}}^2}{\langle I \rangle^2} = \frac{1}{A_{rec}^2} \iint R_{A_{rec}}(\Delta x, \Delta y) |\mu_E(\Delta x, \Delta y, z)|^2 d\Delta x d\Delta y \quad (3)$$

where $R_{A_{rec}}$ is the "autocorrelation function" of the ladar receiving aperture, and μ_E is the "complex coherence factor" or "spatial coherence function"⁴ given by the inverse Fourier transform of the irradiance from the target source region (ξ, η) being measured:

$$\mu_E(\Delta x, \Delta y, z) \equiv \frac{\iint |E(\xi, \eta)|^2 \exp\left(\frac{j2\pi}{\lambda z} (\xi \Delta x + \eta \Delta y)\right) d\xi d\eta}{\iint |E(\xi, \eta)|^2 d\xi d\eta} \quad (4)$$

where $\Delta x = (x_1 - x_2)$ and $\Delta y = (y_1 - y_2)$ over the receiving aperture. The back-propagated pixel sensitive region must be at least $2.44 \lambda / D \times 2.44 \lambda / D$ in angular dimension, due to diffraction by the receiving aperture. The numerical evaluation of "M" for arbitrary source region irradiance (an illuminated single pixel range-bin on target) and arbitrary aperture geometry versus range z was described in a recent paper⁵.

2.2 PHOTON COUNTING STATISTICS

When counting individual photons, as when using photo-multiplier tubes, an "inhomogeneous" or "doubly stochastic" Poisson process^{3,4} results where the Poisson counting probability density function (pdf) is averaged over the statistics of the fluctuating received energy:

$$p_S(n) = \int_0^\infty \left[\frac{(\alpha E)^k}{k!} \exp(-\alpha E) \delta(n-k) \right] p_E(E) dE \quad (5)$$

Here, α is $\eta/h\nu$, the detector quantum efficiency divided by the photon energy, and n may equal 0, 1, 2, 3, etc. discrete events. The energy, E , is the received irradiance, I , multiplied by the receiver area and the integration or counting time, T . Averaging the photo-electron counts over the gamma distribution of equation (2), corresponding to M independent correlation cells with identical average intensities, the discrete "negative-binomial" distribution^{1,2,4} results:

$$p_S(n) = \sum_{k=0}^{\infty} \frac{\Gamma(k+M)}{k! \Gamma(M)} \left(1 + \frac{M}{N_S}\right)^{-k} \left(1 + \frac{N_S}{M}\right)^{-M} \delta(n-k) = \sum_{k=0}^{\infty} P_S(k) \delta(n-k) \quad (6)$$

The lower case letters indicate a "pdf," whereas the upper case letters represent the discrete probabilities of the pdf. The mean of " n " is denoted as N_S , where " S " denotes signal, as opposed to dark-counts (D) or background-counts (B). The variance of n is $\sigma_n^2 = N_S + N_S^2/M$. The pdf $p_S(n)$ becomes Poisson for $M \gg N_S$ and Bose-Einstein distributed for $M \ll N_S$.

We also point out that when converting the photon statistics to photo-electron statistics, a new negative-binomial distribution results⁶ having a mean count number which is reduced by the quantum efficiency of the photo-cathode surface or semiconductor absorption region ($\eta \times N_S$). The M parameter remains the same, however.

When a target voxel has a glint component, a constant intensity in time is observed, by definition of a glint. This is like looking at a very weak corner-cube-retroreflector. In equation (5) $p(E)$ would become a delta function, and the counting statistics are Poisson. If we assume the glint component is independent of the diffuse component, hence, no interference, then the photon counts are the sum of the two processes and the pdf is the convolution of a negative-binomial and a Poisson. These pdf's have been evaluated in the literature and will not be discussed here.

2.3 DETECTOR AND ELECTRONICS SHOT-NOISE EFFECTS

In reality, the photons returning from a target are spread over time as are the electron pulses produced by a PMT. These distributed electron pulses are amplified and filtered by the electronics prior to digitization and signal processing. The voltage pulse per photo-electron event pulse is known as the "impulse-response-function" of the electronics, $h(t)$. The impulse response is usually an exponential decay or triangular shape depending on the filter bandwidths and frequency roll-offs. The shot noise random process^{10,11} is defined as the sum of these voltage impulse responses:

$$v(t) = \sum_i h(t - t_i) \quad (7)$$

where $h(t)$ is the impulse response of the detector and the electronics, and the t_i are random points in time due to the negative-binomial process described in (6) and its Poisson or Bose-Einstein limits. For a fixed counting time, the number of t_i photo-electron events is " n " with pdf $p_S(n)$.

The probability density function of $v(t)$ is constructed following Papoulis¹⁰ as

$$p_v(v) = \sum_{n=0}^{\infty} P_S(n) g_n(v) \quad (8)$$

where $g_0(v)$ is defined to be a delta function, $g_1(v)$ is the voltage pdf of the impulse response function $h(t)$ (ordinarily denoted $p_h(v)$) and, for $n \geq 2$, $g_n(v)$ is the n^{th} -convolution of $g_1(v)$, i.e., $g_1 \otimes g_1 \otimes g_1 \dots \otimes g_1$ $n-1$ times. The " g_n " are the "conditional densities" of v , conditioned on the result that $n = 0, 1, 2, 3$ etc. photo-electron events has occurred at a given time. The probability density function of $h(t)$, denoted by $g_1(v)$,

can be geometrically determined from $h(t)$ which is in volts vs time. For a **triangular** impulse response function we find

$$g_1(v) = \begin{cases} \frac{1}{v_{\max} - v_{\min}} & \text{for } v_{\min} \leq v \leq v_{\max} \\ 0 & \text{otherwise} \end{cases} \quad (9)$$

which is a uniform pdf centered at $(v_{\max} + v_{\min})/2$.

Photo-multiplier tube detectors have a small variation in the peak of their single photo-electron event output electron pulses, exclusive of the baseline noise, known as the "pulse height distribution." We may model this by assuming that the impulse responses are triangles with varying height. The voltage probability density function is then given by equation (9) with varying v_{\max} . We make v_{\max} a Gaussian (Normal) random number with mean equal to "PV" peak volts and a variance equal to $c_1 \times PV$:

$$g'_1(v) = \begin{cases} \frac{1}{(PV + N(0, c_1 PV)) - v_{\min}} & \text{for } v_{\min} \leq v \leq v_{\max} \\ 0 & \text{otherwise} \end{cases} \quad (10)$$

"PV" is the mean peak voltage of 2.3 mV peak per photo-electron, and $c_1 = 5 \times 10^{-5}$ for a high performance Intevac²² photo-multiplier tube. Many Monte Carlo runs are made, and the average of the runs is used as g'_1 . The minimum voltage is zero since $h(t)$ is nonnegative. The set of g'_n conditional densities are then computed by multiple convolutions as above.

Since we also have additive Gaussian baseline noise, we must also convolve the g'_n conditional densities with a normal distribution with zero mean and baseline-noise standard deviation σ_n . Equation (8) for the lidar detector output then becomes

$$p_v(v) = \sum_{n=0}^{\infty} P_s(n) [g'_n(v) \otimes N(0, \sigma_n^2)] \quad (11)$$

per pixel range-bin.

Figures 1A and 1B show data²² for a 1 m diameter, 2 m long cone at a simulated 141 km distance. An Intevac intensified vacuum photo-diode with avalanche-diode gain detector was used. The dashed line in Figure 1B is an analytical gamma pdf (based on equation (2)) that may be used to generate continuous random voltage samples for a pixel range-bin output given N_s and M for that voxel. Scaling the gamma pdf of equation (2) by $N_s^{0.83}$ and $M^{0.7}$ using $N_v \equiv N_s^{0.83}$ and $M_v \equiv M^{0.7}$:

$$p_v(v) \equiv \frac{(M_v / (N_v \times PV))^{M_v} v^{M_v-1} \exp(M_v v / (N_v \times PV))}{\Gamma(M_v)} \quad (12)$$

gives a good fit²² to the shot-noise voltage pdf for one or more photo-electron events. Zero photo-electron events (sampling of the baseline noise) will, of course, be thresholded out. Equation (12) reflects the degradation of the gamma irradiance distribution by the Poisson photon-detection process -- a reduced effective mean and a smaller effective M . This distribution can be used for quickly generating speckled target realizations during Monte Carlo runs for algorithm development. It is effectively a smoothed negative-binomial driven shot-noise pdf based on the Intevac PMT characteristics.

2.4 ROUND-TRIP TURBULENCE EFFECTS (ENDO-ATMOSPHERIC SCENARIOS)

Round-trip passage lidar scintillation from **resolved** targets has been well characterized in the literature by Holmes and Gudimetla¹²⁻¹⁵. They found that a "two-parameter K distribution" irradiance distribution fits the data and theory of round-trip propagation effects well:

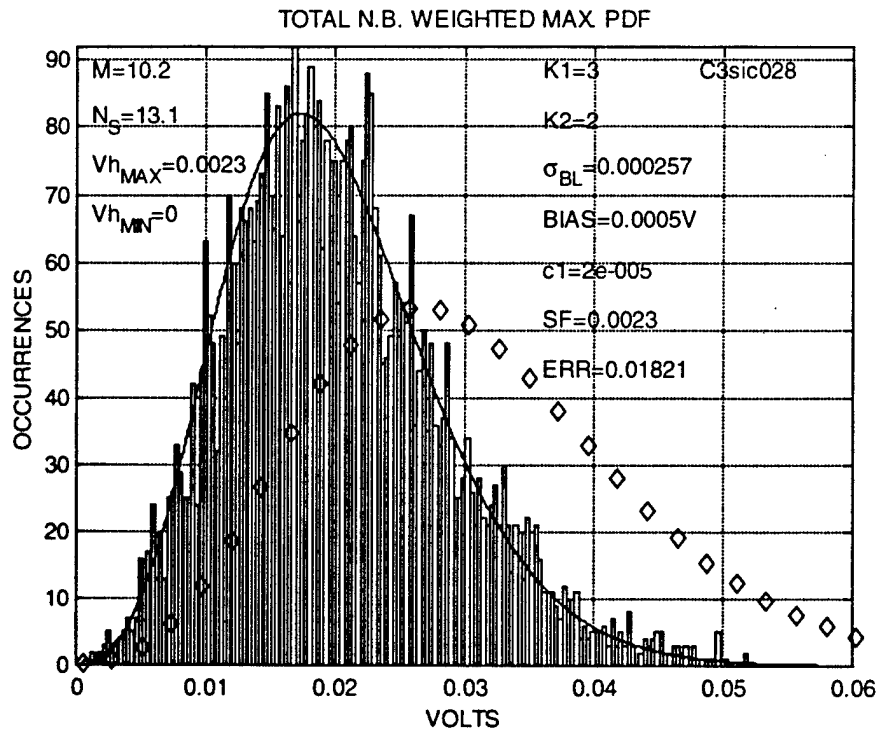


Figure 1A. Histogram data fit²² (solid line) to range-bin #6 of a 2 m long cone at 141 km.

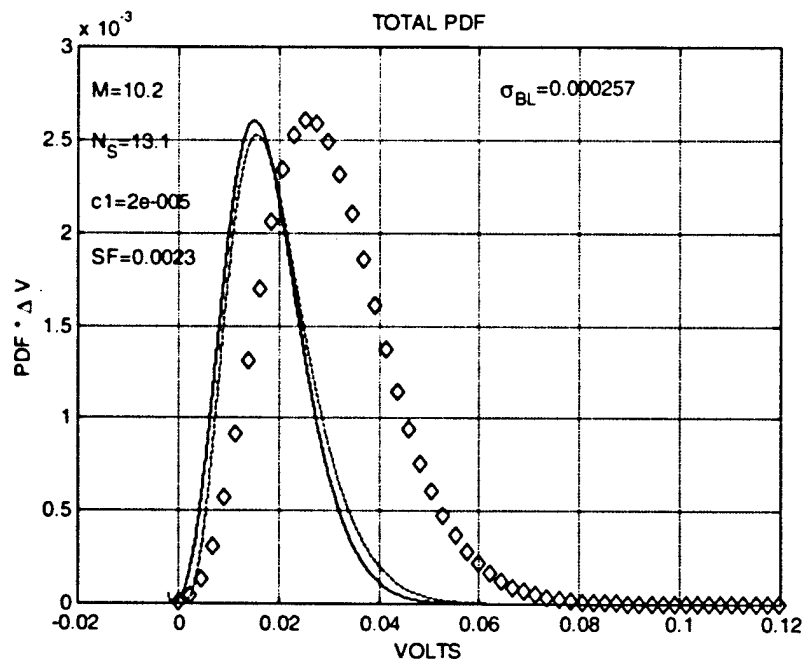


Figure 1B. Probability density function determined by least-squares error data fit using equation (11), solid line. Dashed line is simple pdf fit given by equation (12) for fast Monte Carlo realizations. Diamonds are negative-binomial discrete event probabilities in the absence of random impulse-response summation (shot-noise)²².

$$p_{I_n}(I_n) = \frac{(M_l M_t)^{(M_l + M_t)/2}}{\Gamma(M_l) \Gamma(M_t)} 2 I_n^{(M_l + M_t)/2 - 1} K_{|M_l - M_t|} (2(M_l M_t I_n)^{1/2}) \quad (13)$$

where K is the modified Bessel function of the second kind, I_n is the normalized intensity ($I / \langle I \rangle$), and M_l is the number of uncorrelated laser modes and M_t is the "turbulence M parameter." These are related to the normalized-intensity-variance by

$$\sigma_{I_n}^2 = \left(1 + \frac{1}{M_l} \right) \left(1 + \frac{1}{M_t} \right) - 1 \quad (14)$$

The aperture-averaged normalized-intensity-variance due to turbulence is approximated by

$$\sigma_{I_n}^2 = \exp(\gamma 4 \sigma_x^2) - 1 \quad (18)$$

which is reduced by aperture averaging via the factor γ , the "aperture-averaging factor." Complicated analysis¹²⁻¹⁵ can calculate the aperture averaged normalized intensity variance, but it is possible to make a simple curve fit to data, and the aperture averaging factors

$$\gamma \approx \frac{0.6}{1 + 100 \sigma_x^4} \quad \text{RESOLVED}, \quad \gamma \approx \frac{12}{1 + 250 \sigma_x^4} \quad \text{UNRESOLVED} \quad (19)$$

appear to give a good simple fit to the data and theory. The Rytov variance or the **nonfluctuating point-source, point-receiver, one-way** propagation "log-amplitude variance" is defined as

$$\sigma_x^2(R) = 0.56 k^{7/6} \int_0^R dz C_n^2(z) (z/R)^{5/6} (R-z)^{5/6} \quad (20)$$

where $C_n^2(z)$ is the refractive index structure coefficient. The path integrals over $C_n^2(z)$ can be numerically integrated for the scenarios of interest.

Similar analysis has been applied to **unresolved** targets in references 16 through 18. Using the larger experimental aperture averaging factor in equation (19), the irradiance pdf of equation (13) can be applied for **unresolved** targets within the atmosphere¹⁸. The Poisson counting distribution in equation (5) must be averaged over equation (13) to include round-trip turbulence effects on photon counting. This has not been analytically evaluated to our knowledge¹⁹, and endo-atmospheric lidar will not be discussed here.

3.0 REVIEW OF TEMPLATE CORRELATION MATCHING

There are many two dimensional image (elevation, azimuth and intensity) correlation filters in the literature^{20,21}. We summarize them here and how they may be extended to 3D direct-detection lidar images. The correlation process is done in the "spatial-frequency" domain, taking advantage of the fast discrete Fourier transform, denoted FFT. The correlation peaks and their energies (volumes) are independent of the location of the image in the focal plane because the FFT is a linear shift invariant operator. The effects of negative-binomial lidar speckle or shot-noise on correlation filtering, either 2D or 3D, have not yet been investigated, to our knowledge.

1) Classical Template Matching (Modified for 3D), Correlation over x,y, & z Simultaneously (TMF)

- 1) Invert a reference image through origin -- x, y, and z location values
- 2) Take 3DFFT
- 3) Store in computer
- 4) Take 3DFFT of each noisy lidar image
- 5) Multiply by reference images for that range
- 6) Take Inverse 3DFFT
- 7) Select max correlation peak or max sum (energy)

2) Template Matching w. Phase-only Filters (PoF)

- 1) Filter = $\exp(j \angle(3DFFT(\text{reference-image})))$
- 2) Follow steps from 1). Gives sharper correlation peak.

3) Binary Phase-only Filter (BPoF)

- 1) The phase-only filter of 2) is made binary by $H(f_x, f_y) = +1, \cos(\phi) \geq 0; -1$ otherwise
- 2) Follow steps from 1)

4) Symmetric (Normalized) Phase-only Matched Filter (SPoF)

- 1) Filter = $\exp(j \angle(3DFFT(\text{reference-image}))) / \text{magnitude}(3DFFT(\text{input-image}))$
- 2) Same steps as 1)

5) Quad-phase-only Filter (QPoF)

- 1) Let $F_{ref} = 3DFFT(\text{reference-image})$
- 2) Then, $F_{qpof} = \text{sgn}(\text{Real}(F_{ref})) + i \text{sgn}(-\text{Imag}(F_{ref}))$
- 3) Works better when the reference object has both even and odd components

6) Joint Transform Correlator (JTC)

- 1) Add noisy ladar 3D image to reference image (The images may be appended.)
- 2) Take 3DFFT
- 3) Take magnitude squared (PSD)
- 4) Take inverse 3DFFT
- 5) Select correlation peak or max sum (energy)

7) Binary Joint Transform Correlator (BJTC)

- 1) Add noisy ladar 3D image to reference image
- 2) Take 3DFFT
- 3) Take magnitude squared
- 4) Select threshold value and $PSD = 1 > \text{threshold}, = -1 < \text{threshold}$
- 5) Take inverse 3DFFT
- 6) Select correlation peak or max sum (energy)

8) Joint Transform Correlation with Phase-encoded Reference (JTCPR)

- 1) Reference image is multiplied by an inverse 3DFFT {pseudo-random phasors}
- 2) Take 3DFFT of sum
- 3) Take magnitude squared and multiply by pseudo-random phase mask from 1)
- 4) Take inverse 3DFFT
- 5) Select correlation peak or max sum (energy)

9) Inverse Filter (Optimum for Zero Signal-Independent Additive Gaussian Noise, No Speckle)

- 1) Invert reference image through origin -- x, y, and z location values
- 2) Take 3DFFT
- 3) Store in computer
- 4) Take 3DFFT of each noisy ladar image
- 5) Divide by stored filter for that range, element by element
- 6) Take Inverse 3DFFT
- 7) Select max correlation peak or max sum (energy)

10) Inverse Filter, Binarized Input

- 1) The input image and reference image are binarized (0 or 1) by thresholding
- 2) Proceed as in filter 9)

11) Fourier Descriptor Differencing

- 1) The reference images' x and y components are combined to form a complex number, $x + jy$, for each z slice
- 2) A 1D FFT is taken in each z plane
- 3) Translation independence is obtained by ignoring the DC component at the origin for each z
- 4) The magnitude of each Fourier component is taken to eliminate rotation effects
- 5) Size effects are eliminated by dividing the magnitudes by that of element (1) at each z level
- 6) The Fourier descriptors are compared to the same from each ladar measurement via steps 1) to 5), in a least squares difference sense, as the ladar data are taken

A 3D Fourier transform of a 3D cone image to the spatial-frequency domain is difficult to visualize. The real part of a $16 \times 16 \times 16$ 3DFFT of a 30° azimuth, 0° elevation reference cone image is shown in Figure 2, gray scale coded. The elements are both positive and negative and are displayed in 4×4 z-slices, side by side, as indicated. The imaginary part is roughly 90° out of phase (in 3D) with the real part and is not reproduced here. Following the steps of the classical template matching filter in 1) above, the speckled ladar image is 3DFFTed and multiplied element by element by the stored reference template. The inverse 3DFFT results in a typical correlation output as shown in Figure 3. Figure 3 corresponds to a 2m long, 1m dia. cone at 100 km distance and a total mean photo-electron count per pulse of 400. This is a large signal, typical of the DITP pulse energies and aperture at this range.

3.1 COMBINING REFERENCE IMAGE SETS

Reference image sets of a target at many different aspect angles may be combined to form a more complete reference matrix. Some of these filters from the literature are the "equal correlation peak," the "minimum average correlation energy," the "maximum average correlation height," the "minimum noise and correlation energy," and the "hybrid composite" filter. The extension of these composite matrix filters to three dimensional images has not yet been examined, to our knowledge.

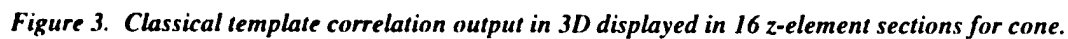
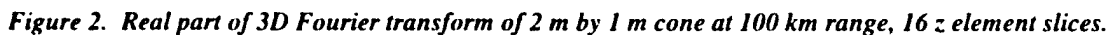
4.0 TARGET GENERATION

Cone, cylinder, and sphere targets are easily generated by forming x, y, z surface points as a function of the azimuthal angle around the target axis of symmetry, z, and the z-axis height. (The z-axis is also the ladar optical axis.) In this way only 100 or 200 points are needed to describe a target's surface. Each point is then rotated in azimuth (around x) and then in approximate elevation (around z) by a coordinate transform. Each surface point is then assigned a cosine of the angle-of-incidence w.r.t. the laser radar optical axis, z. Using two interpolation routines, the cosines of the angles of incidence and the surface-point z-values are interpolated onto x-y plane elements, 7×7 per detector pixel and in 20 cm range-bins. The cosines of the angle-of-incidence values are then summed (49 points) into each x, y detector pixel range-bin to form a 3D image. Figure 4A shows an example 2 m long, 1 m diameter bi-cone rotated 30° in azimuth and another 30° rotation in (approximate) elevation. Figure 4B shows the 7×7 elements per detector pixel, prior to sorting into the individual pixel range-bins, as determined by the right-side figure in 4B which are the corresponding (over sampled) z values.

In this study each detector pixel is defined to be a square $2.44 \lambda / D_{\text{receiver}}$ or $5.3 \mu\text{m}$ wide at 532 nm wavelength and a 25 cm aperture. Consequently, in Figure 4C the image is two or three detector pixels across the cone base for a 1 m diameter cone at 100 km range. With this large angular size pixel, convolution with the telescope point-spread function would have a very small effect on the focal plane irradiance distribution as observed by each of these detector pixels. Each detector pixel range-bin output voltage is generated, including target speckle, following equation (12) in Section 2.0. The lower montage in Figure 4C shows a strong-signal, $N_s = 400$ photo-electrons (total) realization which is typical of a 100 km range conical target for the DITP ladar.

5.0 CORRELATION RESULTS TO DATE

The target ranges of interest are from about 50 km to 400 km. The targets of interest are spheres, cones, and cylinders of various sizes. The cones and cone-cylinders may be at aspect angles of from -45° to $+45^\circ$ in elevation and azimuth combinations. This constitutes a very large number of possible ladar



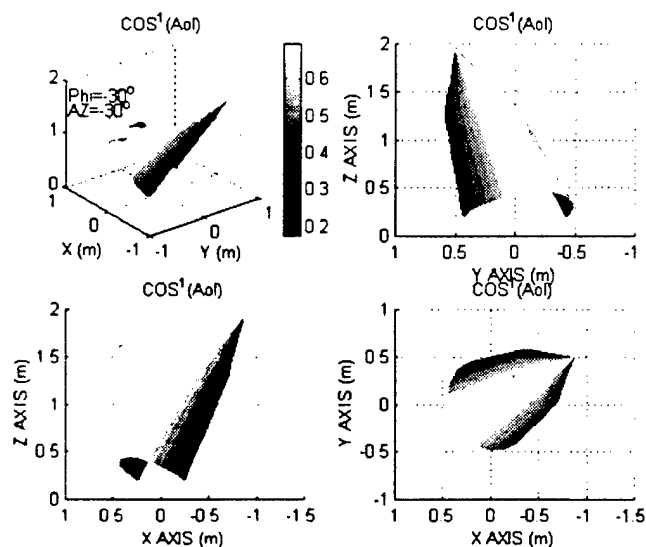


Figure 4A. Bi-cone example at 30° azimuth and 30° elevation. The cosine of the angle of incidence of each element is gray scale coded for projection onto the x-y plane for interpolation at each z level of 20 cm each.

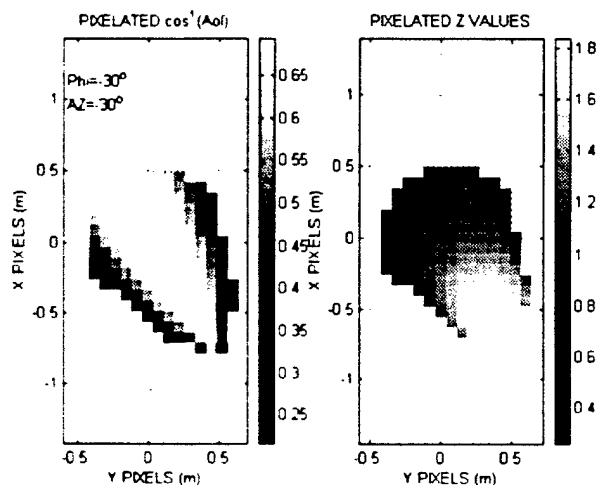


Figure 4B. Interpolated bi-cone cross-section at 7^2 elements per detector pixel at a target range of 100 km. Corresponding z-axis values (gray scaled) are indicated on the right side for partitioning into the range-bins.

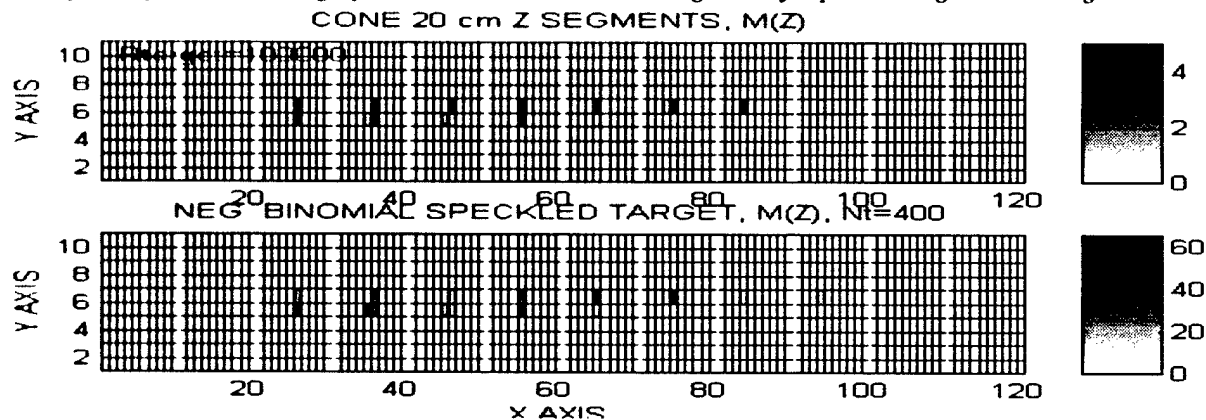


Figure 4C. Example bi-cone normalized cross-sections per detector pixel in z-axis 20 cm segments, left to right. Lower montage is one speckle realization in millivolts, following equation (12) applied to each pixel range-bin.

measurements. We point out here that, having acquired an object, the ladar very accurately determines the range to the object via time-of-flight. Thus, we would know exactly which reference template range-set to use, thereby greatly reducing the number of reference templates. At this point in our research we have examined the performance of filters 1) Classical Template Matching Filter (CTMF), 2) Phase-only Filter (PoF), 3) Binary Phase-only Filter (BPoF), 4) Symmetric Phase-only Filter (SPoF), 6) Joint Transform Correlator (JTC), and 9) Inverse Filter. Since we normalize the 3DFT of the reference image and the 3DFT of the ladar signal image as it comes in to compare correlation voltage outputs, the PoF below is really the SPoF.

5.1 INVERSE FILTER STUDIES

The inverse filter (number (9)) is the optimum filter for no signal-independent additive noise and no target surface speckle (signal-dependent noise). A thumb-tack or delta function correlation peak results when the correct template is selected. However, when ladar speckle and shot-noise effects are included, the small magnitude spatial-frequency domain components of the reference template are no longer divided into the same small magnitude elements from the ladar data (speckled) image. The inverse-filter therefore blows up to large unrealistic values at certain locations in the correlation output. At this point in the 3D filter study, we eliminate the inverse-filter from consideration. It may be possible to apodize or constrain this filter, or it may be possible to combine the inverse-filter with other filters for more robust correlation outputs. This concept will be investigated in the future.

5.2 SIGNAL STRENGTH VS SPECKLE MONTE CARLO STUDIES

We first examine the effects of negative-binomial speckle and shot-noise on the 3D correlators assuming we have selected the correct reference image template. We take a 2 m long, 1 m diameter cone at 100 km range and 30° aspect angle in azimuth and examine the fluctuation of the correlation peaks relative to the mean peak value for decreasing total photo-electron counts. We also look at the "width" of the 3D correlation peak by finding the second largest correlation value which is in an adjacent z-axis range-bin for this target. If this value were 0.5, then the full-width at half maximum would be approximately two z elements. In Table I are the results of 51 Monte Carlo runs for each level of mean

Table I. Correlation Peak Fluctuations and Second (adjacent) Maximum Magnitude (=Width) vs N_s

Range	N_s	Az.	El.	CTMF		PoF		BpoF		JTC	
				$\sigma/\langle v \rangle$	Width	$\sigma/\langle v \rangle$	Width	$\sigma/\langle v \rangle$	Width	$\sigma/\langle v \rangle$	Width
100k	400	30°	0°	.080	.74	.098	.58	.106	.69	.033	.66
	200			.083	.76	.121	.60	.122	.70	.038	.64
	100			.070	.77	.109	.61	.124	.73	.034	.65
	50			.093	.75	.130	.57	.114	.68	.040	.64
	25			.091	.75	.131	.56	.138	.67	.034	.63
	12			.101	.78	.124	.58	.120	.71	.035	.60
	6			.139	.75	.150	.56	.151	.74	.028	.55
	3			.285	.78	.237	.67	.221	.79	.022	.49
200k	50	30°	30°	.078	.74	.096	.55	.093	.66	.047	.65
	12			.087	.71	.094	.49	.102	.70	.050	.61
	3			.193	.74	.223	.61	.193	.80	.052	.50

* Includes peak from reference image.

total photo-electrons, N_s , for filters number 1), 2), 3), and 6). Each 3D detector image output is corrupted by 250 μV rms of additive Gaussian baseline noise and thresholded at 750 μV following the data fits of Section 2.3 and Figure 1A. The first row, where $N_s = 400$, corresponds to Figure 3 above. We see that

speckle and shot-noise do not seriously further degrade the peak fluctuations until the mean total count (N_s) is less than 12 photo-electrons or about **1 p.e. per pixel-range-bin**. The normalized standard deviation of the Joint-Transform-Correlator (JTC) is the smallest, due to the addition of the reference and measured images, followed by the Classical Template Matched Filter (CTMF), the Phase-only-Filter (PoF), and Binary-Phase-only-Filter (BPoF). The correlation-peak 3D-width of the **PoF is the narrowest**, followed by the JTC, BPoF, and CTMF. We note that a correlation filter output "peak to mean ratio," an often used statistic, is not relevant here due to these target speckle fluctuations.

5.3 LARGE SIGNAL, TARGET ASPECT ANGLE SPECKLE STUDY

Next, we take the nominal 2 m long by 1 m diameter cone target and a typical strong-signal return of $N_s = 400$ photo-electrons at 100- km range and examine the variation in correlation peak and peak width as a function of aspect angle. At this nominal strong signal level, all output fluctuations are caused by speckle and shot-noise. In Table II we see that the PoF again produces the narrowest 3D peak width

Table II. Peak Fluctuations and Second (adjacent) Maximum Magnitude (\approx Width) vs Aspect Angle

Range	N_s	Az.	El.	CTMF		PoF		BPoF		JTC*	
				$\sigma/\langle v \rangle$	Width	$\sigma/\langle v \rangle$	Width	$\sigma/\langle v \rangle$	Width	$\sigma/\langle v \rangle$ *	Width*
100k	400	30°	0°	.080	.74	.098	.58	.106	.69	.033	.66
		30°	15°	.083	.74	.096	.55	.111	.73	.038	.66
		30°	30°	.093	.77	.100	.56	.113	.74	.044	.68
		15°	0°	.083	.87	.132	.69	.131	.78	.060	.80
		15°	15°	.080	.85	.143	.64	.142	.76	.082	.77
		15°	30°	.082	.84	.129	.63	.129	.72	.072	.76

*Includes correlation peak from reference image.

followed by the BPoF, JTC, and CTMF widths respectively. The JTC has a somewhat smaller normalized peak standard deviation than the CTMF, which is smaller than those of the PoF and BPoF correlators. We also see that the JTC, PoF, and BPoF peak standard deviation increases when the cone is at 15° aspect angle, presumably due to the reduced x and y image extent.

5.4 JOINT TRANSFORM CORRELATOR REFERENCE-IMAGE PEAK

The JTC filter creates a correlation peak due to the reference image. This is added to the correlation peak from the image data. Consequently, the JTC normalized standard deviations and widths found in Tables I and II are misleading -- the variation due to speckle relative to the image data peak is much larger. We have attempted to remove the reference image correlation peak following 2D approaches^{23,24} but found them not to work in 3D application using the spatial-frequency domain calculations. We are currently investigating the removal of this reference image produced correlation peak. Otherwise, we note that from Tables I and II the **CTMF has the least sensitivity to ladar speckle** and that the **PoF has the narrowest correlation peak**.

5.5 IMAGE DISPLACEMENT EFFECTS

The Fourier transform is a linear shift invariant operator. The correlation peaks and their energies (the volume sum) should remain constant as the data image moves in x, y, and z across the detector focal plane and the range-bins. This is shown to be true for **integer** pixel translations of multiples of 0.2 m in z and/or 5.2 μ r x target range = 0.52 m in x or y for this study. However, as the image translates **between** integer pixel centers, the correlation peak spreads to the adjacent 4 or 6 nearest neighbors. This is shown in Table III:

Table III. Image Displacement Effects on Correlation Peaks.

R	N _s	Az.	El.	$\Delta x, \Delta y, \Delta z$	CMTF		PoF		JTC*	
					Peak (loc.)	E	Peak (loc.)	E	Peak (loc.)*	E*
100k	320	30°	30°	0, 0, 0 (m)	1.000 (8,8,8)	1.43	1.000 (8,8,8)	1.92	1.000 (9,9,9)	5.73
				0, .52, 0	0.995 (8,9,8)	1.44	0.992 (8,9,8)	2.05	0.991 (9,9,9)	5.76
				-.52, 0, 0	0.989 (7,8,8)	1.41	0.996 (7,8,8)	1.90	0.986 (9,9,9)	5.75
				-.52, .52, 0	0.991 (7,9,8)	1.42	0.996 (7,9,8)	1.96	0.869 (9,9,9)	5.70
				0, 0, .2	0.999 (8,8,9)	1.43	1.000 (8,8,9)	1.92	1.130 (9,9,9)	5.73
				0, 0, .1	0.903 (8,8,8)	1.47	0.803 (8,8,8)	2.37	1.056 (9,9,9)	5.87
					0.919 (8,8,9)		0.783 (8,8,9)			
				0, .26, 0	0.741 (8,8,8)	1.51	0.631 (8,9,8)	3.28	1.023 (9,9,9)	6.04
					0.725 (8,8,7)		0.549 (8,8,7)			
					0.666 (8,9,9)					
				-.26, 0, 0	0.787 (7,8,9)	1.40	0.631 (7,8,9)	2.94	0.972 (9,9,9)	5.58
					0.713 (8,8,7)		0.545 (8,8,8)			
				-.26, .26, 0	0.611 (8,8,6)	1.30	0.496 (8,8,6)	3.37	0.926 (9,9,9)	5.21
					0.570 (8,8,7)		0.557 (7,9,9)			
					0.638 (8,9,9)					
				-.26, .26, .1	0.725 (8,8,7)	1.50	0.545 (8,8,7)	3.62	1.009 (9,9,9)	6.02
					0.723 (7,8,10)		0.545 (7,9,10)			

* Includes correlation peak from reference image.

Table III considers the 2m long, 1m diameter cone rotated 30° in azimuth and 30° in elevation. The reference image is perfectly centered in the focal plane and the data image is translated as indicated. We see that the energies of the CMTF and JTC are relatively insensitive to data image translations w.r.t. the fixed reference image. The peak of the JTC is again insensitive to data image movement (including the reference image peak), and that the CMTF has about a 30% variation throughout one x, y, z pixel translation. The PoF has about a 50% variation in correlation peak value throughout one pixel translation, and the filter energy also varies by about 50%.

5.6 CORRELATION OF CONE VS SPHERES STUDY

We next use the cone at 30° elevation and 30° azimuth as the reference image and spatial-frequency domain template and correlate this with spheres of radii of 0.75, 1, and 2 m translated across a pixel. The results shown in Table IV can be compared to those of Table III, and we see that the correlation peaks are about 1/2 to 1/3 of the cone-cone correlation peaks. The filter energies are also comparable due to a broadening of the correlation peaks. Since these reduced peaks are about 6 σ to 7 σ below the speckle fluctuation of the correct cone-cone peak, good discrimination of cones from spheres

Table IV. Correlation Peaks and Energies of Spheres vs Cone at 30° Az and 30° Elevation.

				CMTF		PoF		JTC*	
R	N _s	Sphere Dia. & Δx, Δy, Δz		Peak (loc.)	E	Peak (loc.)	E	Peak (loc.)	E*
100k	320	1 m	0, 0, 0 (m)	0.594 (8,8,8)	1.20	0.492 (8,8,8)	4.40	0.981 (9,9,9)	4.84
		2 m	0, 0, 0	0.375 (8,8,11)	1.51	0.434 (8,8,11)	4.71	1.111 (9,9,9)	6.05
		0.75 m	0, 0, 0	0.530 (8,8,9)	1.38	0.451 (8,8,9)	4.32	1.065 (9,9,9)	5.53
		1 m	0, .52, 0	0.369 (8,9,10)	1.49	0.451 (8,9,10)	4.61	0.972 (9,9,9)	5.97
		1 m	0, .26, 0	0.375 (8,8,8)	1.57	0.455 (8,9,11)	4.47	1.051 (9,9,9)	6.30
		1 m	-.26, .26, 0	0.389 (8,8,8)	1.64	0.455 (7,9,11)	4.38	0.955 (9,9,9)	6.57
		1 m	-.26, .26, .1	0.372 (7,9,9)	.601	0.525 (7,9,9)	3.40	0.801 (9,9,9)	2.88
		1 m	-.26, .26, .2	0.407 (8,8,7)	.614	0.455 (8,8,7)	3.46	0.796 (9,9,9)	2.93

* Includes correlation peak from reference image.

can be made. This capability should apply out to 200 km since $N_s \approx 40$ at 200 km which is > 1 pe per voxel. Also, we see that the JTC again adds the correlation peak from the sphere, thus the sphere-cone JTC peaks are unacceptably large under the present filter implementation.

5.7 CONE ASPECT ANGLE SENSITIVITY

We again use the 2m long, 1m diameter cone at 30° elevation, 30° azimuth and 100 km range as the reference image with its spatial-frequency domain template and correlate this with identical cones at various aspect angles. In Table V we see that going from an aspect angle of 30° to 15° causes a $>20\%$ reduction in correlation peak size. Changes in the elevation angle at the same aspect angle result in only

Table V. Cone Image Rotation Effects on Correlation Peak w.r.t. Cone at 30° Az, 30° El.

Table 7: Cone Image Rotation Effects on Correlation Peak Width, Cone at 30° Az, 30° El.												
R	N _s	Image		CMTF		PoF			JTC*			
		Az.	El.	Peak	(loc.)	E	Peak	(loc.)	E	Peak	(loc.)	E
100k	320	30°	30°	1.000	(8,8,8)	1.43	1.000	(8,8,8)	1.92	1.000	(9,9,9)	6.11
		30°	15°	0.998	(8,8,8)	1.53	0.914	(8,8,8)	2.69	1.042	(9,9,9)	6.68
		30°	0°	0.961	(8,8,8)	1.66	0.824	(8,8,8)	3.95	1.106	(9,9,9)	6.12
		30°	-15°	0.726	(8,8,8)	1.53	0.570	(8,8,8)	4.75	1.056	(9,9,9)	5.70
		30°	-30°	0.590	(8,8,8)	1.43	0.520	(8,8,8)	4.89	1.046	(9,9,9)	5.73
		15°	30°	0.745	(8,8,8)	1.65	0.590	(8,8,8)	3.92	1.014	(9,9,9)	6.62
		15°	15°	0.779	(8,8,8)	1.71	0.615	(8,8,8)	4.08	1.306	(9,9,9)	6.90
		15°	0°	0.840	(8,8,8)	1.81	0.664	(8,8,8)	4.55	1.370	(9,9,9)	7.35
		15°	-15°	0.764	(8,8,8)	1.71	0.643	(8,8,8)	4.70	1.306	(9,9,9)	6.90
		15°	-30°	0.671	(8,8,8)	1.65	0.135	(8,8,8)	4.90	1.292	(9,9,9)	6.62

*Includes correlation peak from reference image.

a few percent decrease in the correlation peak at this 30° reference image angle. When the aspect (azimuth) angle is decreased to 15° , a 25% - 40% decrease in filter peak is observed. Since this is 3σ below the correct cone-cone peak, reasonably robust discrimination of a difference of 15° in aspect is possible out to ≥ 200 km. Due to the spread in the correlation peaks and the increase in side peaks, the energies of the three filters increases.

5.8 RANGE-BIN OUTPUT CONCATINATION WITH 2D FILTERING

In Figure 4C above we see that it is possible to arrange the detector outputs, 10×10 pixels in this study, into a "montage plot" where the range-bin outputs are placed side by side, from left to right. This obviously constitutes a **2D matrix** which can be processed following the 2D template matching filters from the literature without modification. For a maximum target length of 2 m, the image matrix would become 10×110 elements or less depending on aspect angle. We note that all measurement information is contained within this 2D matrix, and the ladar data image will always be within ± 0.5 range-bin pixels of the reference image. This may then be zero padded to $16 \times 128 = 2048$ elements vs the $16 \times 16 \times 16 = 4096$ elements for 3D processing. One template correlation would therefore require about 300 k FLOPs which is less than one half of the 650 k FLOPs required for a single 3D correlation. Consequently, we have terminated 3D Monte Carlo studies temporarily to investigate this concept and its sensitivity to negative-binomial speckle driven shot-noise.

6.0 SUMMARY AND CURRENT WORK

In this initial study we are introducing the concept of three-dimensional spatial-frequency domain correlation filtering for target recognition and identification. This follows an extrapolation of current two-dimensional filter algorithms. The use of the spatial-frequency domain is important because the correlation peaks and energies are independent of the image location in the focal plane for integer x , y , and z voxel displacements. The correct ladar speckle and shot-noise effects are complicated and detector dependent, and these are summarized in Section 2.0. The effects of round-trip turbulence on endo-atmospheric ladar operation are also complicated and have not yet been fully solved, as also discussed in Section 2.0.

This exo-atmospheric study with partially resolved cones and spheres and with no clutter or dark counts but with Gaussian base-line noise has shown that the 3D Phase-only-Filter (PoF) produces the narrowest 3D correlation peaks of the filters studied. Small fluctuations of 8% to 10% in the correlation filter peaks for all the filters due to speckle have been demonstrated. Robust separation of spheres from cones has been demonstrated out to >200 km. Cone vs cone aspect angle determination is not nearly as robust, due to the geometries involved, and needs to be further investigated. The 3D JTC and 3D Inverse filters need to be modified to be useful. About 1 mean photo-electron per voxel produces strong correlation peaks. We are now implementing target range-slicing and 2D image formation by concatenation to implement 2D correlation filters as discussed in Section 5.8. We also note that 3D template correlations may supplement or refine less computationally intensive algorithms such as total signal, range-extent, x - z , y - z , and x - y plane image centroid estimation, and image moments.

7.0 ACKNOWLEDGEMENTS

This work was partially sponsored under BMDO/NRL contract N00014-97-D-2014 supporting the Discriminating Interceptor Technology Program. The authors would like to thank Dr. Frank Hanson, executing agent; LCDR James Buckley, program manager; and Dr. Walter Dyer, technical advisor, for their support and guidance. The authors would also like to thank Tom Driscoll and Paul Titterton of EOO, Inc., Guy Beaghtler of Fibertek, Inc., and Verle Aebi of Intevac, Inc. for useful technical discussions concerning the DITP ladar system and breadboard ladar and target experimental test results.

8.0 REFERENCES

1. Goodman, J., "Some Effects of Target-Induced Scintillation on Optical Radar Performance," Proc. IEEE, Vol. 53, No. 11, Nov. 1965.
2. Goodman, J., "Comparative Performance of Optical-Radar Detection Techniques," IEEE Trans. AES, Vol. AES-2, No. 5, Sept. 1966.
3. Goodman, J., *Laser Speckle and Related Phenomena*, J.C. Dainty Ed., Springer-Verlag, 1975, Second Edition, 1984.
4. Saleh, B., *Photoelectron Statistics*, Springer-Verlag, 1978.
5. Youmans, D., Hart, G., "Numerical evaluation of the "M" parameter for direct detection ladar," SPIE Proc. Vol. 3380, April 1998.
6. Teich, M., B. Saleh, "Effects of random deletion and additive noise on bunched and anti-bunched photon counting statistics," Opt. Lett, Vol. 7, No. 9, Aug. 1982.
7. Papoulis, *Probability, Random Variables, and Stochastic Processes*, McGraw-Hill, 1965, p. 127.
8. Papoulis, p. 37.
9. Papoulis, p. 193.
10. Papoulis, p. 560.

11. Pratt, W. K., *Laser Communication Systems*, John Wiley, 1969, p.260.
12. Lee, M., F. Holmes, R. Kerr, "Statistics of speckle propagation through the turbulent atmosphere," J. Opt. Soc. Am. 66, Nov. 1976.
13. Holmes, F., M. Lee, R. Kerr, "Effect of the log-amplitude covariance function on the statistics of speckle propagation through the turbulent atmosphere," J. Opt. Soc. Am. 70, April 1980.
14. Gudimetla, R., F. Holmes, R. Elliott, "Two-point joint-density function of the intensity for a laser-generated speckle field after propagation through the turbulent atmosphere," J. Opt. Soc. Am. A 7, June 1990.
15. Gudimetla, R., Holmes, J. Opt. Soc. Am. 72, Sept. 1982.
16. McIntyre, C., Kerr, Lee, Churnside, "Enhanced variance of irradiance from target glint," Appl. Opt. 18, 1 Oct. 1979.
17. McIntyre, C., Lee, Churnside, "Statistics of irradiance scattered from a diffuse target containing multiple glints," J. Opt. Soc. Am. 70, Sept. 1980.
18. Youmans, D., R. Gudimetla, "Round-trip turbulence scintillation effects on laser radar: Monte Carlo simulation results for unresolved targets," SPIE Proc. Vol. 3065, *Laser Radar Technology and Applications II*, April 1997.
19. Diamant, P., M. Teich, "Multiply stochastic representations for K distributions and their Poisson transforms," J. Opt. Soc. Am. A, Vol. 6, Jan. 1989.
20. Duda, R., Hart, P., *Pattern Classification and Scene Analysis*, John Wiley and Sons, 1973, Chapter 8.
21. Gonzalez, R., Woods, R., *Digital Image Processing*, Addison-Wesley, 1992, Chapter 9.
22. Driscoll, T., et al., "Comparison of Theory and Experiments in the Effects of Speckle on NMD/TMD Target Recognition with Direct-Detection LADAR," Proc. IRIS Active Systems, Feb. 1999.
23. Takanori, N., "Phase-encoded joint transform correlator to reduce the influence of extraneous signals," Appl. Opt., Vol. 37, No. 17, 10 June 1998.
24. Li, C., et al., "Nonzero-order joint transform correlator," Opt. Eng., Vol. 37, No. 1, Jan. 1998.

Appendix K

COMPARISON OF THEORY AND EXPERIMENTS IN THE EFFECTS OF SPECKLE ON NMD/TMD TARGET RECOGNITION WITH DIRECT DETECTION LADAR

February 1999

Thomas Driscoll
EEO, Inc.

269 N. Mathilda Ave., Sunnyvale, CA 94086

Guy Beaghtler
Fibertek, Inc.

510 Herndon Pkwy., Herndon, VA 22070

George Hart and Douglas Youmans
Schafer Corporation
321 Billerica Rd., Chelmsford, MA 01824

Frank Hanson
SPAWARSYSCEN
53490 Dow St., San Diego, CA 92152

ABSTRACT

A series of experiments were conducted to simulate speckle effects encountered in NMD/TMD target detection, recognition, and identification using direct detection ladar at 532 nm wavelength. Targets in these scenarios are generally in the optical far-field to near-field transition region (partially resolved), and analysis and laboratory simulations are complicated. The primary experiment used a full size conical (NMD) target resolved in range with 20 cm resolution and rotated to several aspect angles. Several supporting and calibration experiments were implemented using greatly attenuated 1.0 ns and picosecond pulsed lasers, CW light emitting diodes, as well as small annular mask and circular mask source region targets to simulate cone range-bin source regions at distance. The detectors employed were intensified vacuum photo-diodes (IPD) and microchannel plate photomultipliers (MCP). Good agreement with speckle theory and shot noise stochastic process theory was observed in the tests, and the results are discussed. The importance of the detector and electronics impulse-response-function and bandwidth must be taken into consideration in ladar algorithm performance and will be emphasized in this paper. The incorporation of ladar negative-binomial driven shot-noise is a straightforward extension of current (Poisson driven) theory.

1.0 INTRODUCTION

To achieve a required range resolution of 20 cm, a direct detection ladar transmits a 1.0 to 1.3 ns laser pulse toward the target. As the E-field propagates down the surface of the target, backscattered light returns to the ladar receiving aperture and is collected. Due to constructive and destructive interference, "laser speckle" effects are observed. The finite sized collecting aperture produces some "speckle averaging" thereby smoothing the irradiance fluctuations that would be seen by a point aperture. This smoothing is characterized by the "M" parameter as described in Section 3.1. For a photon-counting detector, such as a photomultiplier tube at 532 nm, the Poisson counting statistics must be

averaged over the irradiance fluctuation statistics. This results in the negative-binomial distribution, in the absence of round-trip atmospheric turbulence (exo-atmospheric scenario), as discussed in Section 3.2. The individual photo-electrons are amplified by the photomultiplier tube to form an electron pulse which is then converted by a preamplifier to a voltage waveform called the "impulse-response-function." The impulse-response-functions add up randomly in time, depending on the photon arrival rate, and the superposition of these voltage impulse-responses is known as "shot noise." A shot-noise process is observed by a particular pixel range-bin and this signal, along with all the other pixel range-bin signals, is used for automatic target detection, recognition, and identification algorithms. Bandwidth and data transfer rate limitations often require that the impulse-response-functions are made temporally wide (lower bandwidth) than the individual photo-electron event pulses from the photo-multiplier tube. In the DITP lidar, lower bandwidth data transfer rates are accomplished by thresholding electronics for each pixel range-bin signal.

2.0 OVERVIEW OF THE DITP LADAR CONCEPT AND HARDWARE

The BMDO Discriminating Interceptor Technology Program (DITP) is developing¹⁻⁶ sensor systems to provide enhanced seeker and guidance capability against postulated advanced TMD/NMD threats. These seeker systems include multicolor infrared imaging detectors, laser radars, tracking and discrimination software, and a fusion processor. The laser radar is required to provide high-resolution imagery and track data for discrimination of threat objects from decoys and debris.

The transmitter is based on a proven 100 Hz diode-pumped Nd:YAG compact laser design. The 1.06 μm laser pulse is frequency doubled to provide a ≈ 1.3 nsec pulse at 532 nm, which can be efficiently coupled to a 25cm telescope. The DITP laser will produce 0.25 J at 100 Hz. The laser radar receiver includes a multi-pixel detector, each pixel of which has a range resolution of ≈ 20 cm, and the receiver thus provides simultaneously both range- and angle-resolved imagery. The 3-D imagery is used to provide discrimination of threat objects from decoys and debris. The laser radar provides data which are either unresolved (resolved in depth only), angle only, or complete angle-angle-range imagery with amplitude resolution. The use of single-photon detection extends the useful discrimination ranges to 450 km. The laser oscillator, frequency-doubler and a prototype receiver were tested in 1997, together with four discrimination algorithms in tests against full scale targets at the Army Missile Optical Range (AMOR). In that series of tests no target surface speckle modulation was simulated. More recent testing in 1998 against full size conical NMD targets have measured speckle effects for correctly degrading the target recognition/identification algorithms under consideration.

3.0 SUMMARY OF SPECKLE STATISTICS THEORY

We summarize here the irradiance (W/m^2) fluctuations produced by laser speckle, the resulting photon and photo-electron counting statistics, and some relevant random variable theory necessary for fitting the laser radar data.

3.1 Irradiance Statistics

When laser light is back-scattered from a rough target, constructive and destructive interference results in the well known "laser speckle" pattern distribution back at the receiving aperture. Goodman^{7,9}

has shown that the sum of a number of uncorrelated irradiances, collected by the finite size ladar receiving aperture, has a probability density function given by

$$p_{\Sigma}(I) = \sum_{k=1}^M \langle I_k \rangle^{M-2} \exp(-I/\langle I_k \rangle) / \prod_{\substack{p=1 \\ p \neq k}}^M (\langle I_k \rangle - \langle I_p \rangle) \quad (1)$$

This can be approximated by a simpler gamma distribution given by

$$p_{\Sigma}(I) \equiv \frac{(M/\langle I \rangle)^M I^{M-1} \exp(-MI/\langle I \rangle)}{\Gamma(M)} \quad (M \geq 1) \quad (2)$$

The "M" parameter was shown by Goodman⁹ to be equal to the reciprocal normalized-variance-of-irradiance

$$\frac{1}{M} \equiv \frac{\sigma_{I_{rec}}^2}{\langle I \rangle^2} = \frac{1}{A_{rec}^2} \iint R_{A_{rec}}(\Delta x, \Delta y) |\mu_E(\Delta x, \Delta y, z)|^2 d\Delta x d\Delta y \quad (3)$$

where $R_{A_{rec}}$ is the "autocorrelation function" of the ladar receiving aperture, and μ_E is the "complex coherence factor" or "spatial coherence function"¹⁰ given by the inverse Fourier transform of the irradiance from the target source region (ξ, η) being measured:

$$\mu_E(\Delta x, \Delta y, z) \equiv \frac{\iint |E(\xi, \eta)|^2 \exp\left(\frac{j2\pi}{\lambda z} (\xi \Delta x + \eta \Delta y)\right) d\xi d\eta}{\iint |E(\xi, \eta)|^2 d\xi d\eta} \quad (4)$$

where $\Delta x = (x_1 - x_2)$ and $\Delta y = (y_1 - y_2)$ over the receiving aperture. The numerical evaluation of "M" for arbitrary source region irradiance (an illuminated single pixel range-bin on target) and arbitrary aperture geometry versus range z was described in a recent paper¹¹.

3.2 Photon Counting Statistics

When counting individual photons, as when using photomultiplier tubes, an "inhomogeneous" or "doubly stochastic" Poisson process^{9,10} results where the Poisson counting probability density function (pdf) is averaged over the statistics of the fluctuating received energy:

$$p_S(n) = \int_0^{\infty} \left[\frac{(\alpha E)^n}{n!} \exp(-\alpha E) \delta(n-k) \right] p_E(E) dE \quad (5)$$

Here, α is $\eta/h\nu$, the detector quantum efficiency divided by the photon energy, and n may equal 0, 1, 2, 3, etc. discrete events. The energy, E , is the received irradiance, I , multiplied by the receiver area and the integration or counting time, T . Averaging the photo-electron counts over the gamma distribution of equation (2), corresponding to M independent correlation cells with identical average intensities, the discrete "negative-binomial" distribution^{7,8,10} results:

$$p_S(n) = \sum_{k=0}^{\infty} \frac{\Gamma(k+M)}{k! \Gamma(M)} \left(1 + \frac{M}{N_S}\right)^{-M} \left(1 + \frac{N_S}{M}\right)^{-M} \delta(n-k) = \sum_{k=0}^{\infty} P_S(k) \delta(n-k) \quad (6)$$

The lower case letters indicate a "pdf," where as the upper case letters represent the discrete probabilities of the pdf. The mean of "n" is denoted as N_S , where "S" denotes signal, as opposed to dark-counts (D) or background-counts (B).

We also point out that when converting the photon statistics to photo-electron statistics, a new negative-binomial distribution results¹² having a mean count number which is reduced by the quantum

efficiency of the photo-cathode surface or semiconductor absorption region ($\eta \times N_s$), yet the M parameter remains the same.

3.2.1 Addition of a Glint Component

When a target voxel has a glint component, a constant intensity in time is observed, by definition of a glint. This is like looking at a very weak corner-cube-retroreflector. In equation (5) $p(E)$ would be a delta function, and the counting statistics are Poisson. If we assume the glint component is independent of the diffuse component, hence, no interference, then the photon counts are the sum of the two processes and the pdf is the convolution of a negative-binomial and a Poisson. Goodman⁷ has evaluated the convolution and found

$$P_{s,g}(k) = \left(\frac{M}{M + N_s} \right)^M \frac{\exp(-N_g)}{\Gamma(M)} \sum_{j=0}^{\infty} \frac{\Gamma(k + M - j)}{j!(k - j)!} (N_g)^j \left(\frac{N_s}{M + N_s} \right)^{k-j} \quad (7)$$

where we denote the mean glint photon count by N_g . Analytically expressed, this probability can be found in Saleh¹⁰

$$P_{s,g}(k) = \frac{(N_s/M)^k}{(1 + N_s/M)^{k+M}} \exp\left(\frac{-N_g}{1 + N_s/M}\right) L_k^{M-1}\left(\frac{-N_g M/N_s}{1 + N_s/M}\right) \quad (8)$$

where L is the Laguerre polynomial. Looking at equations (7) and (8) it is obvious that it is easier to compute $p_{s,g}(k)$ by numerically convolving the negative-binomial and Poisson distributions. Small glint components were added to the negative-binomial distributions in order to better fit the opal glass and styrofoam cone histogram data discussed below. In no case did the addition of a glint component improve the fit to the data, indicating that both targets were optically rough, as expected. Interference between the glint component and the diffuse component of a target return is known as the "autodyne" effect.

3.3 Converting to Voltage Probability Density Functions and Histogram Fitting

An ideal photomultiplier tube produces a voltage pulse for each photo-electron produced by the photo-cathode surface. In the simplest model a new random variable is created given by

$$v_{PMT} = SF \times n \quad (9)$$

where SF is a scale factor ranging from 2.05 mV to 2.3 mV/photo-electron for the Intevac IPD and 5.5 to 5.6 mV/photo-electron for the Hamamatsu MCP. The resulting pdf of " v " is given by¹³

$$p_s(v) = \frac{1}{SF} \sum_{k=0}^{\infty} \frac{\Gamma(k + M)}{k! \Gamma(M)} \left(1 + \frac{M}{N_s}\right)^{-k} \left(1 + \frac{N_s}{M}\right)^{-M} \delta\left(\frac{v}{SF} - k\right) \quad (10)$$

which is just equation (6) divided by SF at discrete voltage points. To fit any voltage pdf to a histogram of ladar return data, we must multiply the pdf by dv per histogram bin and by the total number of data points used in constructing the histogram:

$$N_{\text{per bin}} = (\text{Total no. of data points}) \times p_s(v) \times \frac{V_{\text{max}} - V_{\text{min}}}{\text{No. of bins}} \quad (11)$$

We see that this leaves only two parameters to adjust, M and N_s , in order to fit a particular set of histogram data as described below.

3.3.1 Maximum of "K" Samples of a Random Variable

When the detector output voltage is sampled, it is stored digitally during a finite time window size and the **maximum voltage within the time window** stored, simulating the threshold-crossing signal processing used in the DITP lidar. In this manner a large number of target returns can be analyzed and conveniently displayed in a histogram. When the maximum voltage within the window is selected, a maximum of a number of independent samples of a random voltage is recorded. For example, when no photo-electron event occurs, we sample the Gaussian baseline noise a number of times, selecting the maximum value. The pdf of the maximum of a number of samples of a random voltage is easily analyzed following Papoulis.^{15,16} Let

$$Z = \text{MAX}(V_1, V_2, V_3, \dots, V_K) \quad (12)$$

Then the pdf of Z is given by

$$p_Z(z) = p_{V_1}(z)F_{V_2}(z) \dots F_{V_K}(z) + p_{V_2}(z)F_{V_1}(z) \dots F_{V_K}(z) + \dots + p_{V_K}(z)F_{V_1}(z) \dots F_{V_{K-1}}(z) \quad (13)$$

where F denotes the "cumulative distribution function" for that random variable. If the random voltages are identically distributed, this reduces to

$$p_Z(z|K) = K p_V(z) F_V(z)^{K-1} \quad (14)$$

As an example, for the maximum of K samples of a Gaussian RV, such as the zero mean Gaussian baseline noise in the absence of a photo-electron event, this would become

$$p_Z(z|K) = \frac{K \exp(-z^2/2\sigma_n^2)}{\sqrt{2\pi}\sigma_n} \left[\frac{1}{2} + \text{erf}\left(\frac{z}{\sigma_n}\right) \right]^{K-1} \quad (15)$$

This pdf is seen just above zero volts in the histogram data below (**Figure 2**) representing multiple samples of the Gaussian baseline noise in a window when no photo-electrons are detected. The same pdf could be applied to the peaks of single or multiple photo-electron event pulses, which are approximately Gaussian distributed in maxima, when a number (K) of these are observed in one time window measurement.

3.3.2 (Simple Model) Negative-Binomial Weighted Pulse Height Distribution Data Fit

The DITP intensified vacuum photo-diode (IPD) with impact-ionization and avalanche-diode gain and Hamamatsu detectors under test are imperfect devices having fluctuating gain. The fluctuating peak gain is usually called the "pulse height distribution." For one photo-electron produced, there is a pulse height distribution centered at 1 x SF volts. For a two photo-electron event, there is another pulse-height-distribution centered at 2 x SF, and so forth. (See **Section 4.0** below) The individual pulse-height-distributions may be approximately modeled as Gaussian voltage pdf's each, and the output voltage is a continuous random variable, not discrete. Because the negative-binomial discrete events are mutually exclusive, i.e., only 0, or 1, or 2, or 3, etc. events may occur, we may use the "theorem on total probability" from Papoulis¹⁴ to determine the device output-voltage pdf:

$$p_{PMT}(v) = \sum_{n=0}^{\infty} P_S(n) p_{phd}(v|n) \quad (16)$$

This is obviously the weighted sum of the individual pulse-height-distribution pdf's using the negative-binomial event probabilities from equation (6) as the weights. (This approach may not be applied to signal plus dark-counts or background-counts which are not mutually exclusive.) In reality, the creation times of the photo-electron events and their electron pulses are not simultaneous, and they do not add perfectly. The temporal distribution of the photo-electron events and the resulting summation of their separated individual impulse-response-functions are analyzed by "shot-noise" stochastic process theory

as discussed in Section 5 below. Equation (16) is incorrect for photons which are not constrained in arrival time.

4.0 PHOTON-COUNTING WITH AN INTENSIFIED VACUUM PHOTO-DIODE: PULSE HEIGHT DISTRIBUTION TESTS

In a carefully designed experiment, Eckhardt Lorentz at the Max Planck Institute measured the pulse height distribution of an Intevac, Inc. intensified vacuum photo-diode with impact ionization and avalanche diode gain. Pico second laser pulses, greatly attenuated, illuminated the detector. Single photo-electron, two photo-electron, three photo-electron, etc. peak voltage events were measured as shown in **Figure 1**. When no photo-electron events occurred, samples of the baseline noise were measured as indicated near zero volts. The probabilities of these discrete events are Poisson distributed since a laser source with nearly constant pulse energies was used. **Figure 1** shows the analytical fit to the Max Planck data using a negative-binomial pdf with a large M of 100 which is very nearly Poisson (equation (5) with $p(E)$ a delta function). In these data the bandwidth of the laser pulse is much higher than the bandwidth of the detector and the electronics, and the photon arrival times are precisely controlled to have nearly perfect temporal alignment and, therefore, perfect summation in the output peak voltages.

A similar experiment at much lower counting rates was made at EOO, Inc. with a 1.0 ns FWHM pulsed frequency-doubled Nd:YAG laser and a 6.5 ns observation window. The maximum of the windowed voltage points (13 at 0.5 ns / sample and 26 for 0.25 ns / sample) was stored for each pulse, and a histogram constructed from repeated laser shots. The results are shown in **Figure 2** for a 4 GS/s rate:

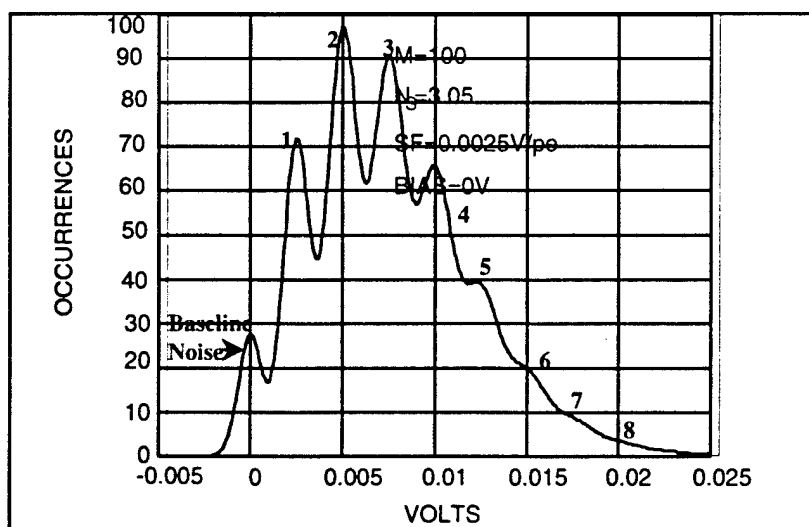
1) When no photo-electron event occurs, samples of the baseline noise are made for 6.5 ns. Of the 13 samples of noise, some will be correlated due to the electronics bandwidth. If we assume that a maximum of 8 or 9 independent samples of the Gaussian noise is taken, then equations (12) through (15) apply for the 0 pe event voltage pdf. The dark current noise (no laser pulses) was measured to have a standard deviation of 257 μ V and a very small bias which we may neglect. Equation (15) scaled by equation (11) gives an excellent fit to the baseline noise histogram peak.

2) When a single photo-electron is present, a ≈ 2.3 mV peak occurs added to the Gaussian baseline noise. The variance of the IPD & amplifier peak height (shown in **Figure 1**) is much smaller than the baseline noise variance, therefore we observe the Gaussian peak at 2.3 mV, as seen in **Figure 2**, with a standard deviation of 257 μ V due to the baseline noise.

5.0 SHOT NOISE THEORY: THE INCLUSION OF ELECTRONIC IMPULSE RESPONSE AND RANDOM PHOTO-ELECTRON CREATION TIMES

In reality the photons returning from an extended target are spread over time as are the electron pulses produced by a PMT. These distributed electron pulses are amplified and filtered by the electronics prior to digitization and signal processing. The voltage pulse per photo-electron event pulse is known as the "impulse-response-function" of the electronics, $h(t)$. The impulse response is usually an exponential decay or triangular shape depending on the filter bandwidths and frequency roll-offs. The shot noise random process¹⁷⁻¹⁹ is defined as the sum of these voltage impulse responses :

$$v(t) = \sum_i h(t - t_i) \quad (17)$$



$$\sigma_{VPD}^2 = c_1 n_{pe} SF + \sigma_n^2$$

$c_1 = 5 \times 10^{-5}$ $SF \equiv 2.5 \text{ mV / pe}$ $\sigma_n = 0.64 \text{ mV (Baseline Noise)}$

$$p_{VPD}(v) = \sum_{n_{pe}=0}^{\infty} P_i(n_{pe}) N(n_{pe} SF, \sigma_{VPD}^2)$$

$$P_i(n_{pe}) = \frac{\Gamma(n_{pe} + M)}{n_{pe}! \Gamma(M)} \left(1 + \frac{M}{N_i}\right)^{-n_{pe}} \left(1 + \frac{N_i}{M}\right)^{-M} N_i \equiv \langle n_{pe} \rangle$$

Figure 1. Intevac IPD pulse-height-distribution data fit.

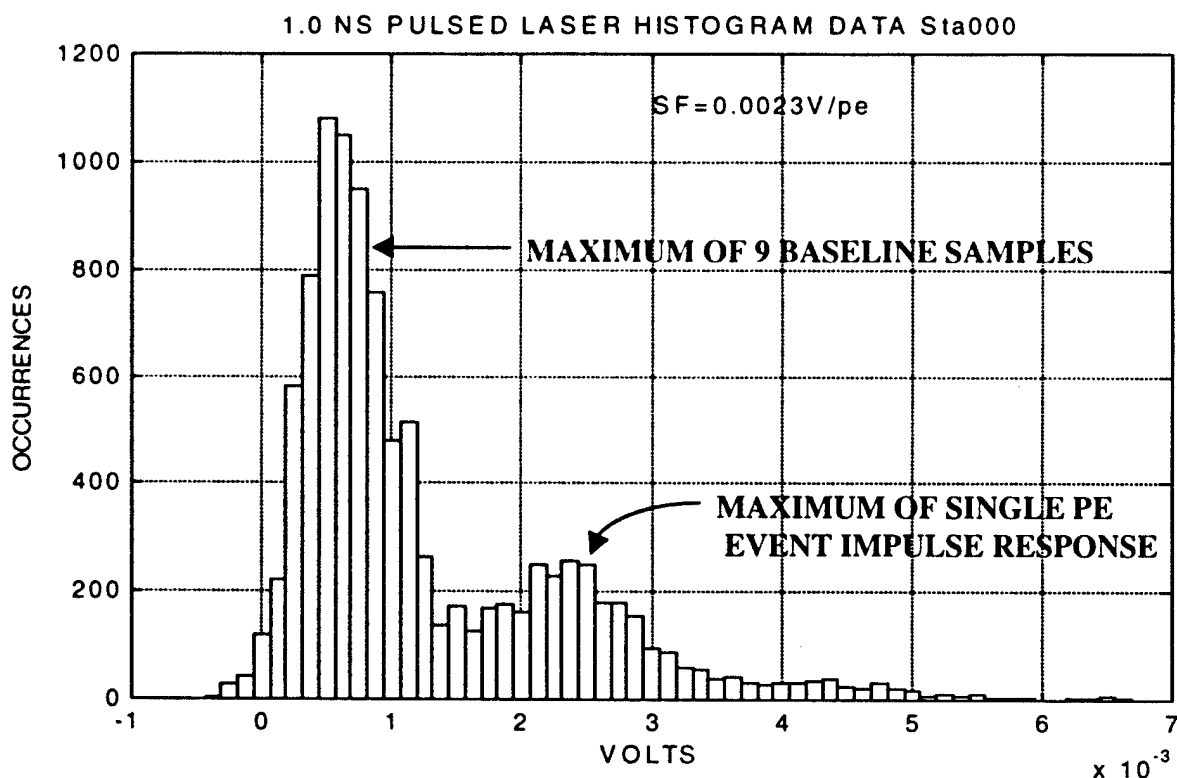


Figure 2. Fibertek/EOO 1.0 ns laser, 6.5 ns time window pulse-height-distribution data.

where $h(t)$ is the impulse response of the detector and the electronics, and the t_i are random points in time due to the negative-binomial process described in (6) and its Poisson or Bose-Einstein limits. The autocorrelation of $v(t)$ is found in the literature to be given by

$$R_{vv}(\tau) = \lambda^2 \left[\int_{-\infty}^{\infty} h(t) dt \right]^2 + \lambda \int_{-\infty}^{\infty} h(\alpha) h(\tau + \alpha) d\alpha = E\{v(t)\}^2 + \lambda R_{hh}(\tau) \quad (18)$$

The power spectral density of $v(t)$ is given by

$$S_{vv}(f) = \lambda^2 H(0) \delta(f) + \lambda |H(f)|^2 = E\{v\}^2 \delta(f) + \lambda |H(f)|^2 \quad (19)$$

where $H(f)$ is the frequency response of the filter with impulse response $h(t)$, and λ is the rate parameter for the process. In addition, in the literature we find "Campbell's theorem" for shot noise:

$$E\{v(t)\} = \lambda \int_{-\infty}^{\infty} h(t) dt \quad E\{v^2(t)\} = \lambda^2 \left[\int_{-\infty}^{\infty} h(t) dt \right]^2 + \lambda \int_{-\infty}^{\infty} h^2(t) dt \quad (20)$$

The probability density function of $v(t)$ is constructed by¹⁷

$$p_v(v) = \sum_{n=0}^{\infty} P_s(n) g_n(v) \quad (21)$$

where $g_0(v)$ is defined to be a delta function, $g_1(v)$ is the voltage pdf of the impulse response function $h(t)$ (ordinarily denoted $p_h(v)$) and, for $n \geq 2$, $g_n(v)$ is the $(n-1)^{\text{th}}$ convolution of $g_1(v)$, i.e., $g_1 \otimes g_1 \otimes g_1 \dots \otimes g_1$ $(n-1)$ times. The g_n are the "conditional densities" of v , conditioned on the result that $n=1, 2, 3$ etc. photo-electron events has occurred at the sample time. The probability density function of $h(t)$, denoted by $g_1(v)$, can be geometrically determined from $h(t)$. For a triangular shaped impulse response function we find

$$g_1(v) = \begin{cases} \frac{1}{v_{\max} - v_{\min}} & \text{for } v_{\min} \leq v \leq v_{\max} \\ 0 & \text{otherwise} \end{cases} \quad (22)$$

which is a uniform pdf centered at $(v_{\max} + v_{\min})/2$. We note that a time window, determined by a digital storage oscilloscope, may be set close to the peak (v_{\max}) of a fixed-in-time impulse response such that v_{\min} is only slightly smaller than v_{\max} . (See Figure 4 below.) In this situation equation (22) reduces to a delta function, and equation (21) reduces to equation (16) above.

5.1 Incorporating the Pulse-Height-Distribution into the Conditional Densities

As shown in Section 4.0 above, the IPD and MCP detectors have a small variation in the peak of their single photo-electron event output electron pulses, exclusive of the baseline noise. We may model this by assuming that the impulse responses are triangles, as in Figure 4, with varying height. The voltage probability density function is then given by equation (22) with varying v_{\max} . We make v_{\max} a Gaussian (Normal) random number with mean peak voltage equal to "PV" and a variance equal to $c_1 \times \text{PV}$ (See Figure 1.):

$$g'_1(v) = \begin{cases} \frac{1}{(PV + N(0, c_1 PV)) - v_{\min}} & \text{for } v_{\min} \leq v \leq v_{\max} \\ 0 & \text{otherwise} \end{cases} \quad (23)$$

Many Monte Carlo runs are made, and the average of the runs is used as g'_1 . The minimum voltage is zero for a nonnegative $h(t)$. The set of g'_n are then computed by multiple convolutions.

Since we also have additive Gaussian baseline noise, we must also convolve the conditional densities, g'_n , with a normal distribution with zero mean and baseline noise standard deviation σ_n , and equation (21) for our experiment becomes

$$p_V(v) = \sum_{n=0}^{\infty} P_S(n) [g'_n(v) \otimes N(0, \sigma_n^2)] \quad (24)$$

To determine the pdf of the **maximum** within a measurement time window of this shot-noise process, we may then **numerically** apply (14) as

$$p_{V_{\max}}(v) = K [g'_n(v) \otimes N(0, \sigma_n^2)] (F_{g'_n \otimes N}(v))^{K-1} \quad (25)$$

and the total pdf becomes

$$p_V(v) = \sum_{n=0}^{\infty} P_S(n) p_{V_{\max}}(v) \quad (26)$$

This equation can be fitted to the histogram data following the scaling given in equation (11) above.

6.0 CW LIGHT EMITTING DIODE SHOT-NOISE THEORY EXPERIMENT (NO SPECKLE, POISSON STATISTICS)

Using a greatly attenuated CW LED source and the IPD detector we have observed the train of pulses from the detector/amplifier on top of the baseline noise as shown in **Figure 3A and 3B**. As the arrival rate increases, the voltage pulses start to superimpose and pile up (equation (17)). The data of **Figures 3A and B** has had its linear slope removed (detrended) and a bias added to bring the center of the Gaussian baseline noise histogram back up to zero volts where it would be with no photo-electron pulses. A histogram of the **peaks** of this output voltage indicates about a 2.05 mV peak for the single photo-electron impulse response. (In these data the Intevac tube gain was set slightly lower than for the pulsed laser tests in Section 4.0 and **Figure 2**.) We note that these data would correspond to the returns from a long flat or cylindrical target with no speckle (Poisson statistics).

6.1 Impulse Response Model

To evaluate equations (18) to (20) we examine the voltage output waveform of **Figure 3B** looking for clean single photo-electron events. We form a simple triangle model for $h(t)$ as shown in **Figure 4A**. The peak of $h(t)$ is taken from the maximum of the single photo-electron event histogram as 2.05 mV. We then compute the autocorrelation and power spectrum of $h(t)$ as well as the sums $\sum h(t) dt$ and $\sum h^2(t) dt$ to evaluate (18), (19), and (20) as indicated in **Figure 4A, 4B, and 4C**.

6.2 Data Autocorrelation-Function Results

We compute the autocorrelation of the data of **Figure 3A and 3B** as shown in **Figure 5**. The DC bias of 0.2 mV numerically applied to recenter the baseline noise produces the noisy baseline triangle autocorrelation. The peak at zero lag is given by $(0.2 \text{ mV})^2$ times the number of data points of 20,000 as indicated. This is the first term on the right side of equation (18). Subtracting this DC value from the peak of the data autocorrelation and dividing by $R_{hh}(0)$ we estimate the rate parameter, λ , as 710 in 10 μ s or 7.1×10^7 per second.

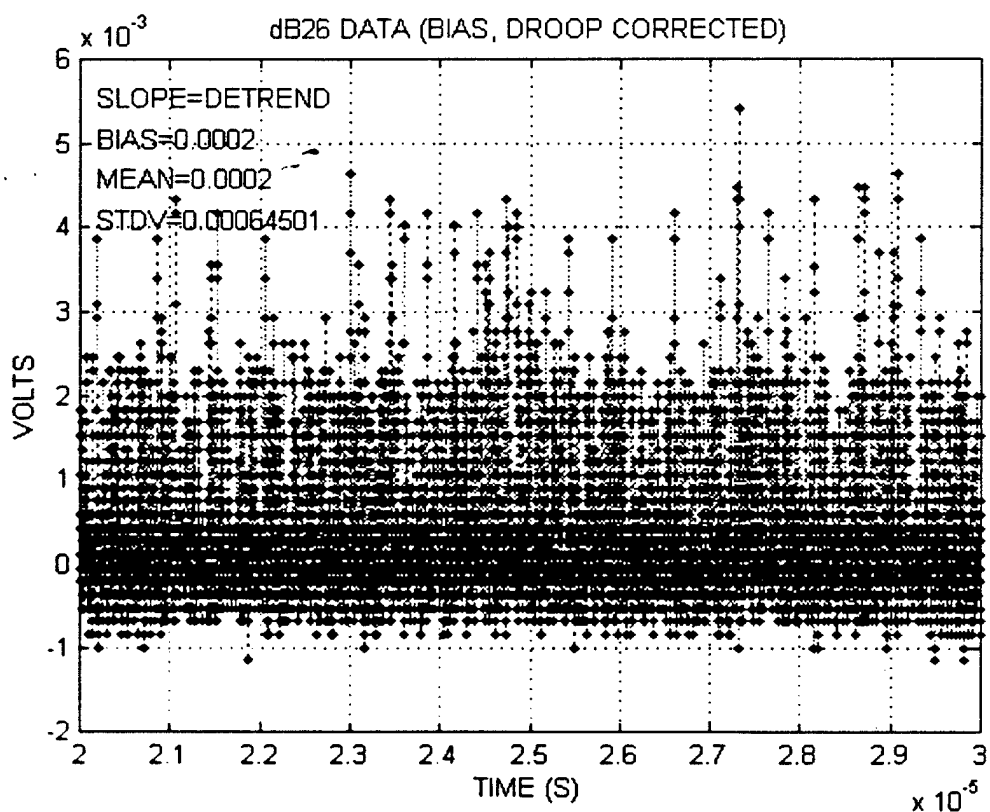


Figure 3A. CW LED individual impulse response events.

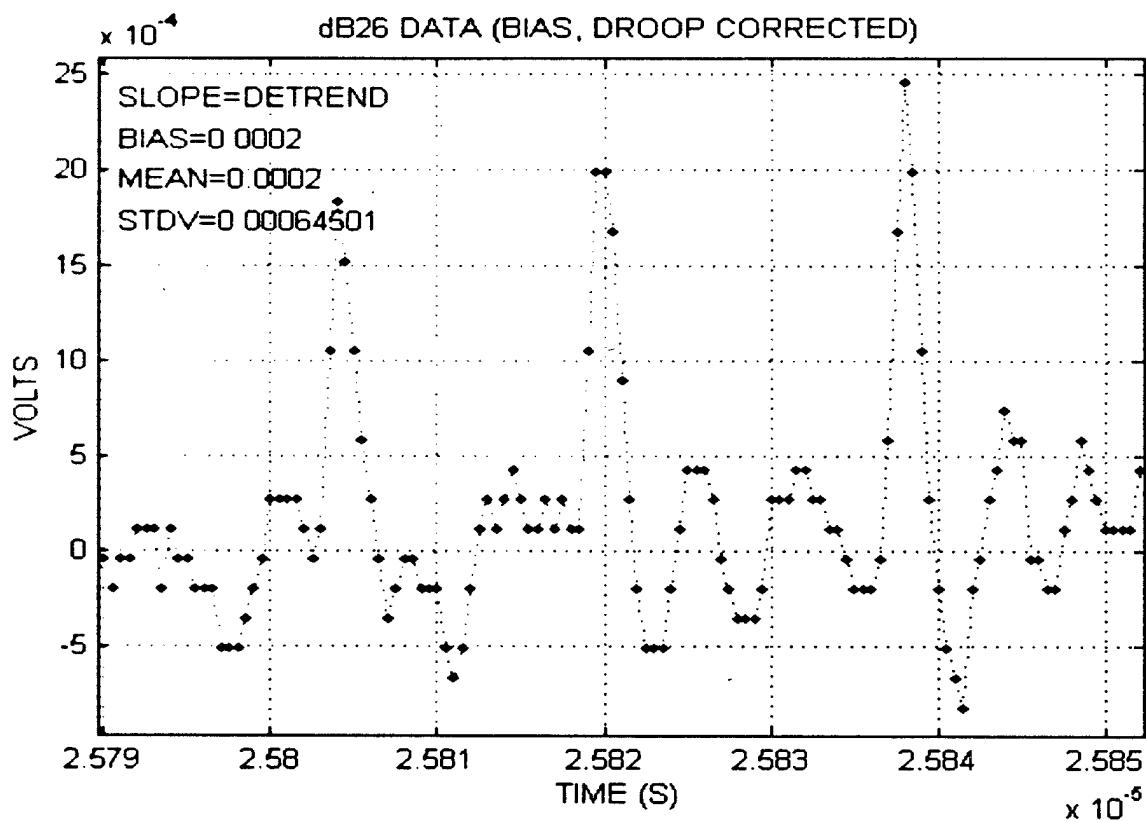


Figure 3B. Expanded scale, 2 GS/s sampling rate.

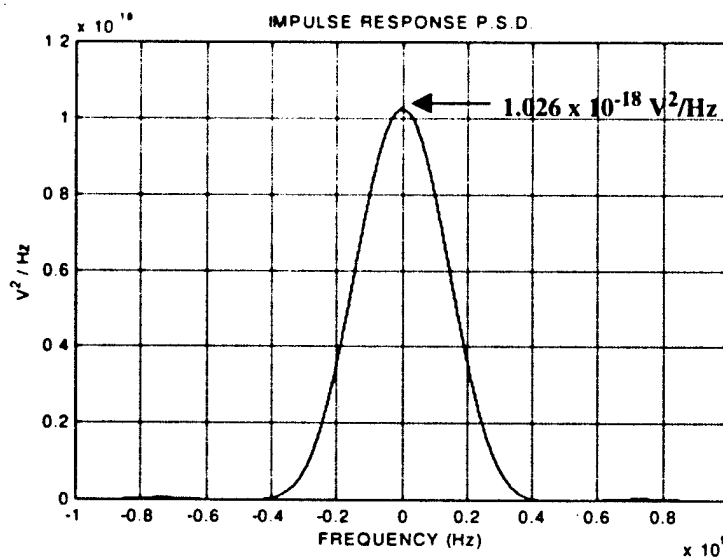
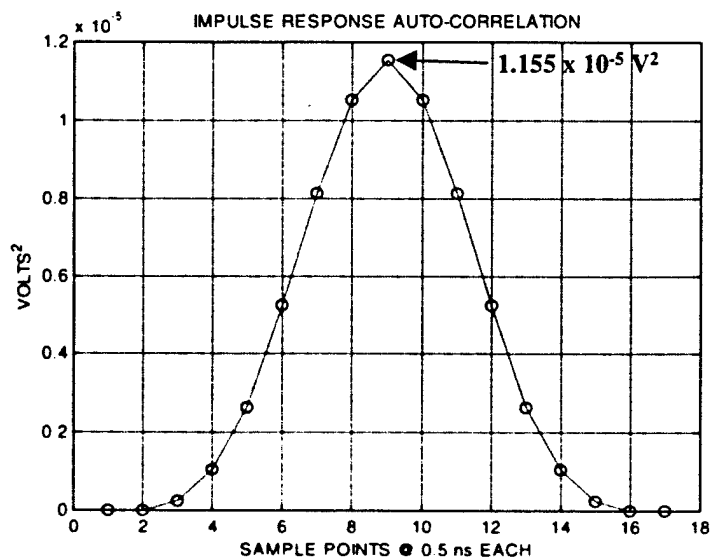
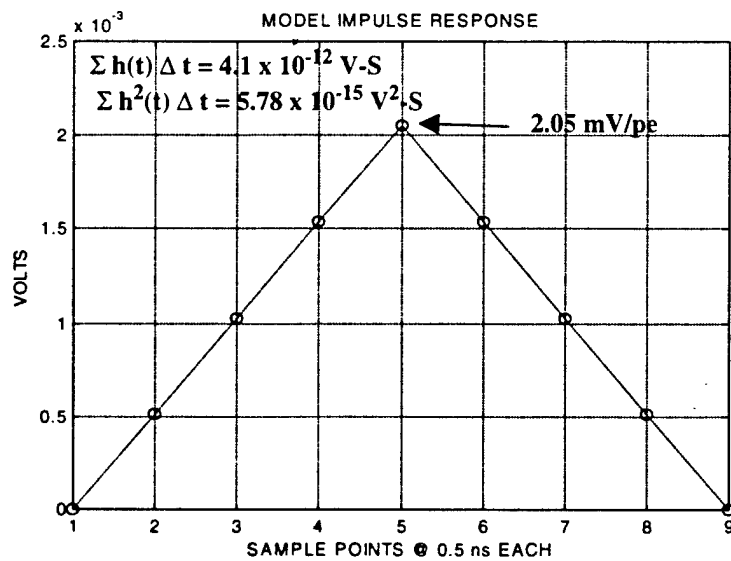


Figure 4. Impulse response model, auto-correlation, and power spectrum.

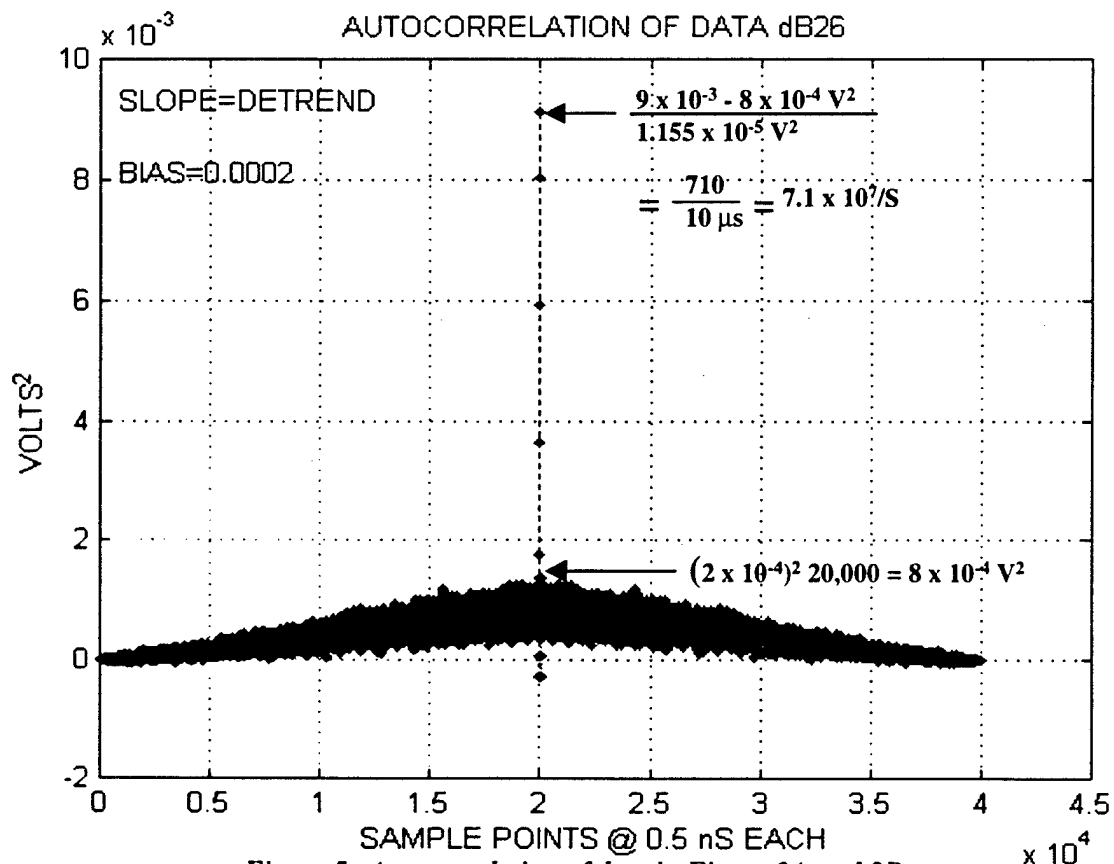


Figure 5. Autocorrelation of data in Figure 3A and 3B.

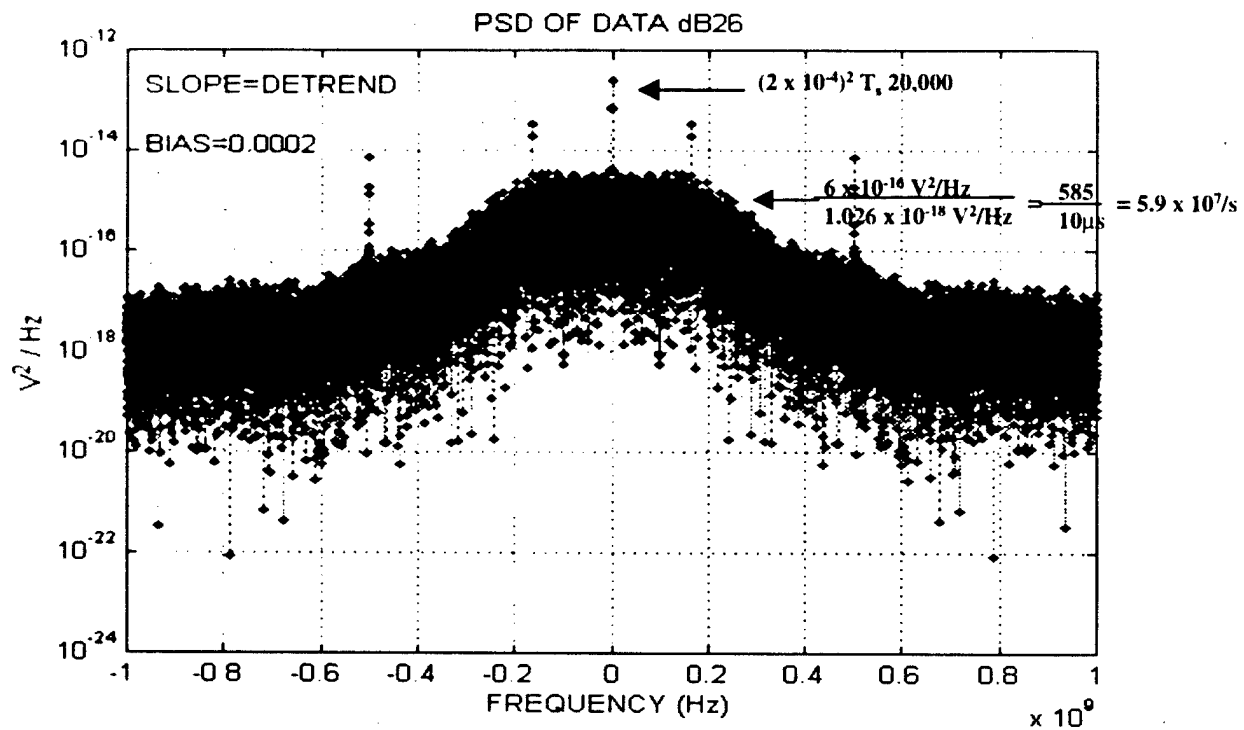


Figure 6. Power spectrum of data in Figure 3A and 3B.

6.3 Data Power-Spectral-Density Results

We next compute the power spectral density of the LED data using the periodogram spectral estimator²⁰ as shown in **Figure 6**. The DC component at 0 Hz is seen to be equal to $(0.2 \text{ mV})^2 \times T_s \times 20,000$ sample points following spectral theory²⁰ with T_s the sampling time of 0.5 ns. The mean spectral density of the signal plus noise surrounding the 0 Hz delta function is about $6 \times 10^{-16} \text{ V}^2/\text{Hz}$. From equation (19) second term on the right, we divide this value by the peak of the impulse response PSD to estimate λ and find 585 per 10 μs or 5.85×10^7 per second.

6.4 Results of Campbell's Theorem Applied to the Data

Since we have applied a bias to the CW LED data to reset the baseline noise to 0 volts after detrending the data, the first equation for the mean of the shot noise process is no longer valid as a statistic. From the second equation in (20) we see that the variance in the shot noise signal data is

$$E\{v^2(t)\} - E\{v(t)\}^2 = \sigma_v^2 = \lambda \int_{-\infty}^{\infty} h^2(t) dt \quad (27)$$

In **Figure 3A** the variance of the data is computed as $(645 \mu\text{V})^2$ and subtracting off the known variance of the baseline Gaussian noise of $(257 \mu\text{V})^2$ we find

$$\sigma_v^2 = (592 \mu\text{V})^2 = \lambda \sum h^2(t) dt = \lambda 5.78 \times 10^{-15} \text{ V}^2 - s \quad (28)$$

and the rate parameter is estimated to be 5.97×10^7 in good agreement with the other three estimates. We note that Campbell's variance in equation (25) is independent of the mean and of the detrending of the data and is, therefore, a robust estimator of λ .

Performing the same three calculations for the other three neutral density filter tests we find the following results:

Table I. Estimation of the Rate Parameter, λ (photo-electrons / s)

Neutral Density	Peak Counting Estimate	Power Spectrum Estimate	Autocorrelation Estimate	Campbell's Var. Estimate
ND 2.6	5.66×10^7	5.85×10^7	7.01×10^7	5.97×10^7
ND 2.3	1.01×10^8	9.75×10^7	1.24×10^8	1.11×10^8
ND 2.0	1.88×10^8	1.95×10^8	2.34×10^8	2.21×10^8
ND 1.6	4.63×10^8	5.85×10^8	6.23×10^8	6.00×10^8

We note that as the rate parameter increases and pulse pile-up becomes more significant, the peak counting algorithm begins to miss more and more impulse responses. The application of shot-noise theory in Section 5 fits the experimental data well. Again, these data are equivalent to the signal from a long flat or cylindrical target with no speckle (Poisson statistics, $M \gg N_s$).

7.0 SIMULATED FAR-FIELD STYROFOAM CONE TESTS

A two meter long, one meter diameter cone made of styrofoam was illuminated as shown in **Figure 7**. A pinhole located before the last focusing lens creates a virtual pinhole located in front of the first collecting lens. The magnification of the first two lenses is 3.58, thus, a pinhole of 100 μm results in a virtual pinhole size of $100 \mu\text{m} / 3.58 = 28 \mu\text{m}$. The virtual pinhole aperture is 15.8 m in front of the cone tip, and, as seen by the target, this represents a 25 cm diameter receiver at 141 km range effective angular aperture.

The signal is digitized at 4 GS/s by a LeCroy LC574A digital oscilloscope. Measurement cursors bracketed the detected photo-electron pulse shot-noise, and this window was set at 1.25 ns. Since the detector response is faster than the window duration, it is possible to occasionally see a voltage pulse at the leading edge of the window as well as at the trailing edge. This event would be stored as a single pe event instead of two pe's, therefore, a 200 MHz bandpass filter was used to lengthen the impulse response (see **Figure 4A**) so the individual amplitudes would add and be recorded as a 2 pe event.

The M values for the cone range-bins may be evaluated using discrete 2D-Fourier transform techniques to solve equations (3) and (4) above, as discussed in reference 16. In addition, μ_E may be analytically evaluated²¹ by applying Fraunhofer diffraction theory to a uniformly illuminated annular source region and setting the E-field (as opposed to the intensity required in (4)) as unity:

$$\mu_E(r) = \frac{\lambda z}{\pi r (\rho_2^2 - \rho_1^2)} \left[\rho_2 J_1 \left(\frac{2\pi \rho_2 r}{\lambda z} \right) - \rho_1 J_1 \left(\frac{2\pi \rho_1 r}{\lambda z} \right) \right] \quad (29)$$

where the inner and outer radii are ρ_1 and ρ_2 , respectively. M must then be numerically evaluated by

$$M = \frac{1}{8} \left[\int_0^1 \rho a(\rho) |\mu_E(\rho D_{rec})|^2 d\rho \right]^{-1} \quad (30)$$

where

$$a(\rho) = \frac{2}{\pi} \left[\cos^{-1}(\rho) - \rho(1 - \rho^2) \right] \quad (31)$$

is the autocorrelation function of a circular aperture. Both computations give identical results.

7.1 Comparison of Data with Theory

The impulse-response-function of **Figure 4** is used to construct g_1 with $v_{min} = 0$ and $v_{max} = 2.3$ mV, slightly higher gain than the LED data. g_1 is modified by using the pulse-height-distribution pdf, defined in **Figure 1**, for the IPD following Section 5.1. The set of conditional densities is then created by multiple convolutions following Section 5. These conditional densities are then convolved with the baseline noise since the noise sample is added to the measurement given that the discrete photo-electron event occurred. The cone data were taken using the maximum function in a range-bin window period of 1.25 ns. Consequently, the maximum of K samples pdf must be applied as given in equation (25) above. Finally, these conditional densities are weighted by the negative-binomial distribution as in equation (26) above. A least squared error fit between the scaled pdf and the histogram data is made as illustrated in **Figures 8A and 8B**, and the minimum error M and N_s are computed, as these are the only two variables allowed, given the assumptions described. The theoretical M values for each cone range-bin and the data fits are given in Table II. Theory and experiment for determining M appear to be in good agreement. In range-bin #1 there can be no impulse-response-functions prior to the tip of the cone, and, therefore, there are no $h(t)$ tails to superimpose from in front of range-bin #1. We make the approximation that the cone

Short Range Cone Test

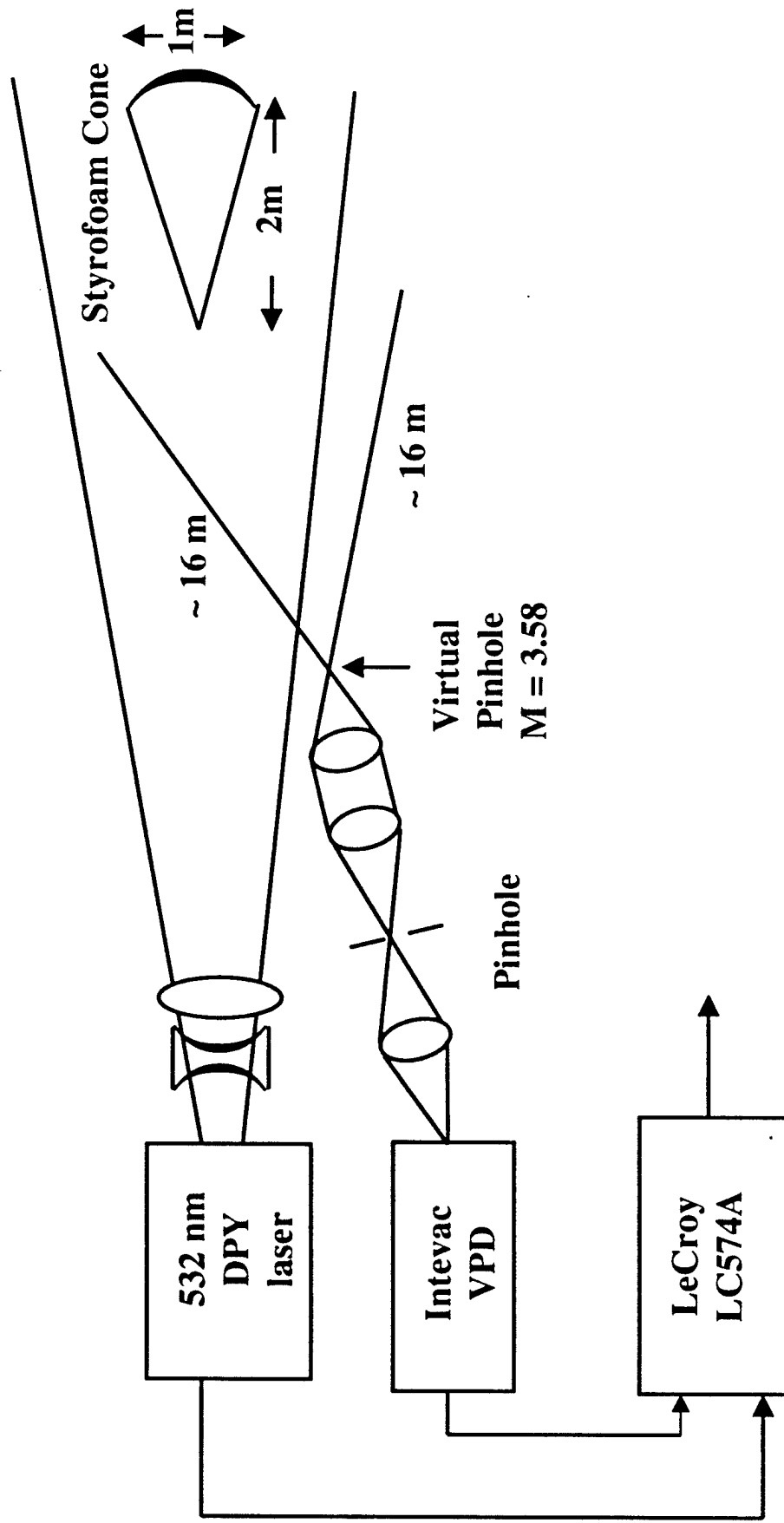


Figure 7. Simulated 141 km range full scale target test.

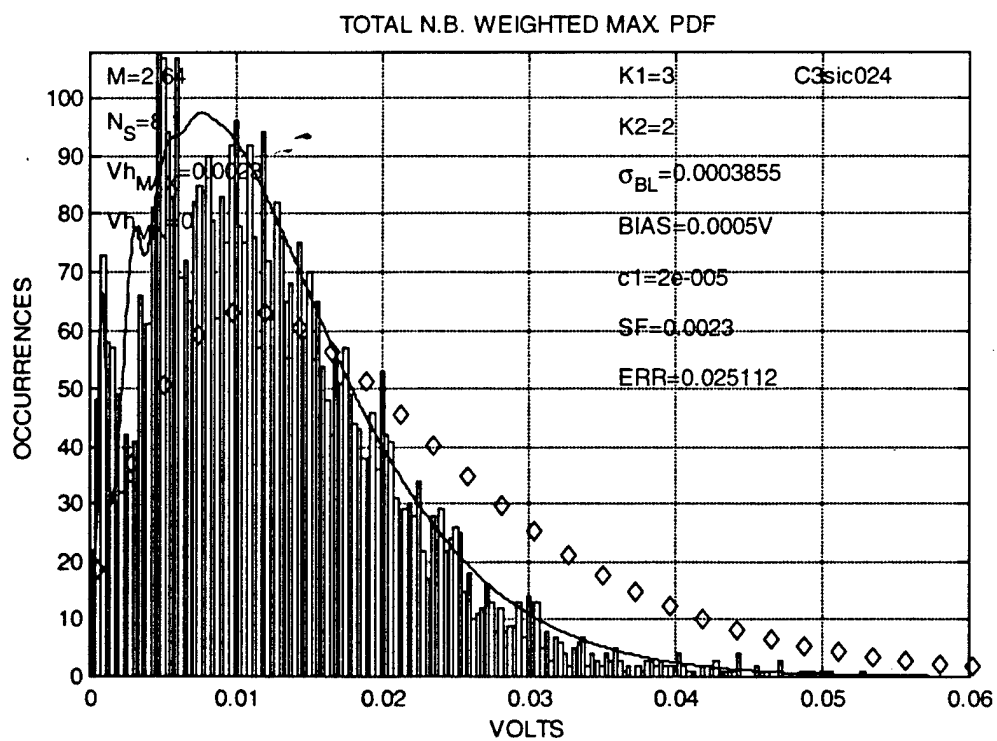


Figure 8A. Numerical fit to cone range-bin number 2. Diamonds are negative-binomial.

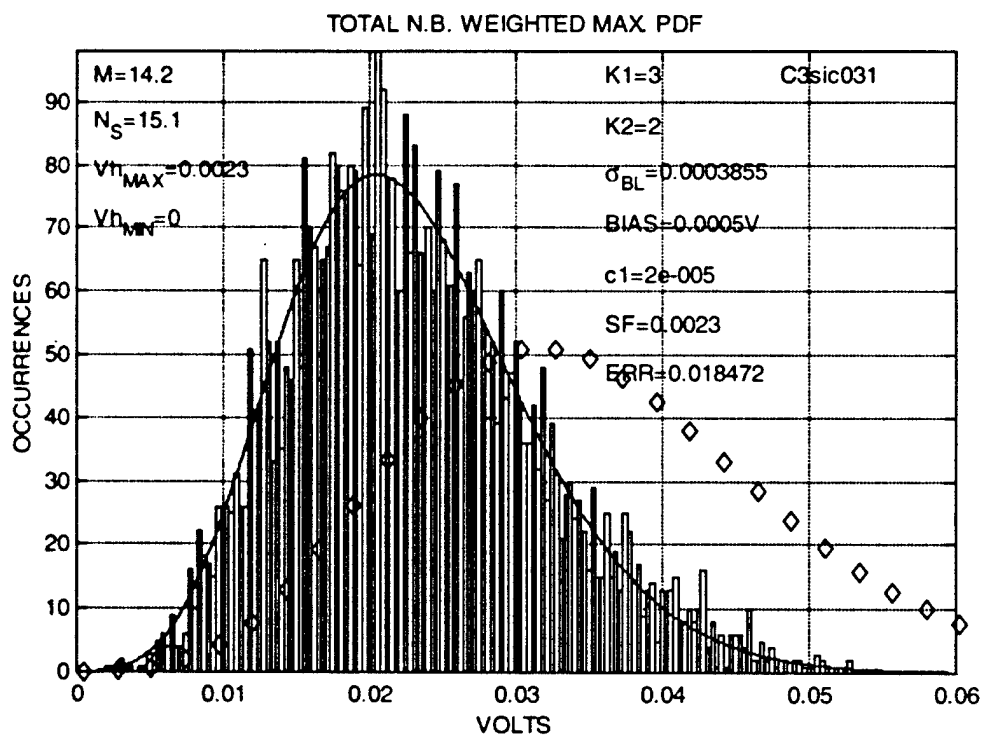


Figure 8B. Numerical fit to cone range-bin number 9. Diamonds are negative-binomial.

tip is 3 cm (15% of one 20 cm range-bin) behind the start of the range-bin and compute the minimum error M and N_s .

Table II. Cone Range Bin "M" Parameter Theory and Data

141 km Range Bin #	Theoretical M (2 polarization)	Least Sq Error Fit for M value	Least Sq Error Fit for N_s	M With Range Bin Smearing	Chirped Pulse
1	2.12	1.8*	5.4	3.5	TBD
2	2.62	2.64	10.6	6	TBD
3	3.78	6.5	12.6	8.5	TBD
4	5.44	7.8	13.6	13	TBD
5	7.42	7.9	15.6	17	TBD
6	9.04	9.9	17.0	21	TBD
7	10.68	10.3	17.9	25	TBD
8	12.04	13.2	18.7	29	TBD
9	13.78	14.2	19.2	32	TBD
10	15.38	12.2	18.7	31	TBD

The data in **Figures 8A and 8B** can be well fit by an analytical gamma pdf (based on equation (2)) that may be used to generate continuous random voltage samples for a pixel range-bin outputs given N_s and M for that range-bin. Scaling the gamma pdf by $N_s^{0.83}$ and $M^{0.7}$ using $N_v \equiv N_s^{0.83}$ and $M_v \equiv M^{0.7}$:

$$p_v(v) \equiv \frac{(M_v / (N_v \times PV))^{M_v} v^{M_v-1} \exp(-M_v v / (N_v \times PV))}{\Gamma(M_v)} \quad (32)$$

was found to give a good fit to the shot-noise voltage pdf (prior to selecting the maximum voltage within the window) for one or more photo-electron events. The zero photo-electron events or the sampling the baseline noise will, of course, be thresholded out. Equation (32) reflects the degradation of the gamma irradiance distribution by the Poisson photon detection process – a reduced effective mean and a smaller effective M. This distribution can be used for quickly generating speckled target realizations during Monte Carlo runs for algorithm development.

The propagation of a Gaussian temporal shaped pulse over a conical-segment pixel range-bin has been theoretically investigated by Hanson following suitable modifications of equations (29) and (30). This results in a spatial range-bin smearing of the return E-field and increases the expected M parameter as shown in column 5 of Table II. This effect is under investigation. The effects of "pulse chirp" where the laser intra-pulse frequency-chirp magnitude approaches or exceeds the reciprocal pulsewidth (1.3 ns) are also being investigated.

8.0 OPAL GLASS DIFFUSER PLATE WITH MASK TESTS

As shown in **Figure 9** a Fibertek 1.0 ns pulsed laser illuminates an opal glass diffuser plate at 17m distance through the rear surface. In front of the diffuser plate is placed one of a set of small circular or annular masks simulating a disk source or the range-bins of a cone at 0° aspect angle. A four mm diameter pupil simulates a receiving aperture at 141 km range so that the correct M values are produced. A polarizer and neutral density filters follow the aperture to select a single polarization and control the mean number of photons per 1 ns laser pulse to 4 to 10 pe's per pulse. A Hamamatsu 4110U micro-channel plate detector with only one pixel illuminated was use to measure the speckle irradiance.

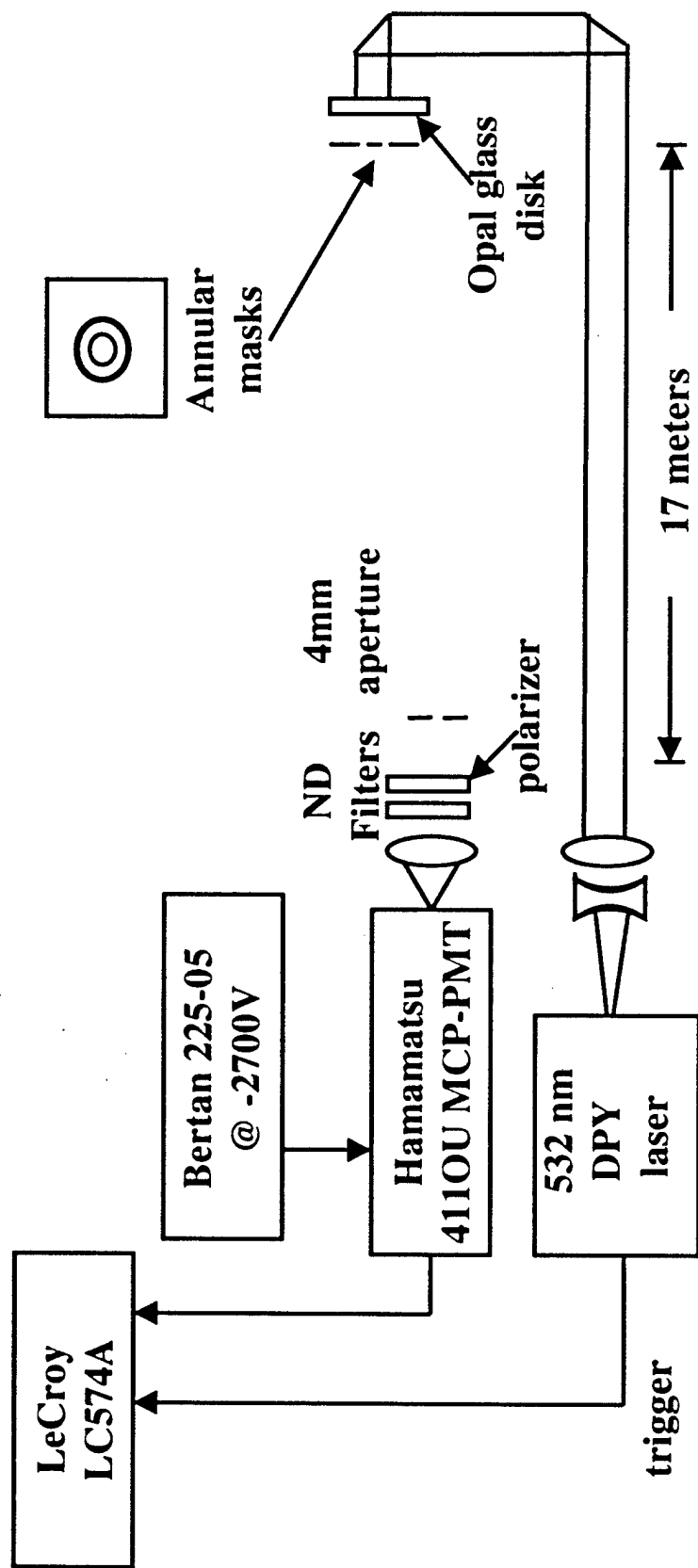


Figure 9. Diffuse plate with annular masks experiment.

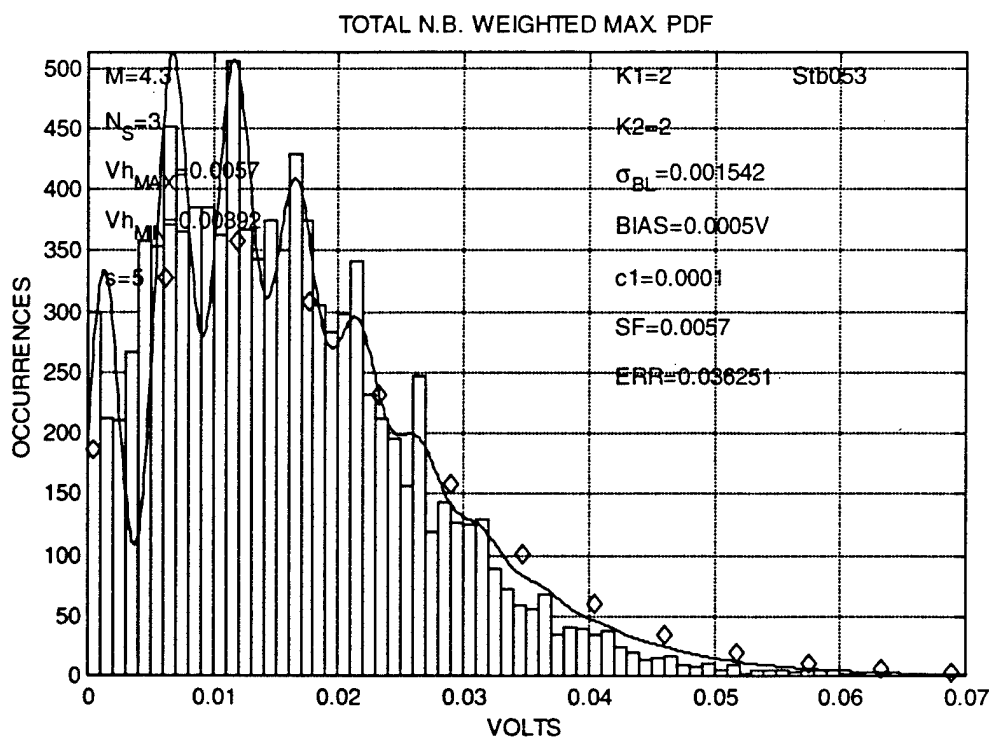


Figure 10A. Numerical data fit to circular mask with Hamamatsu MCP.

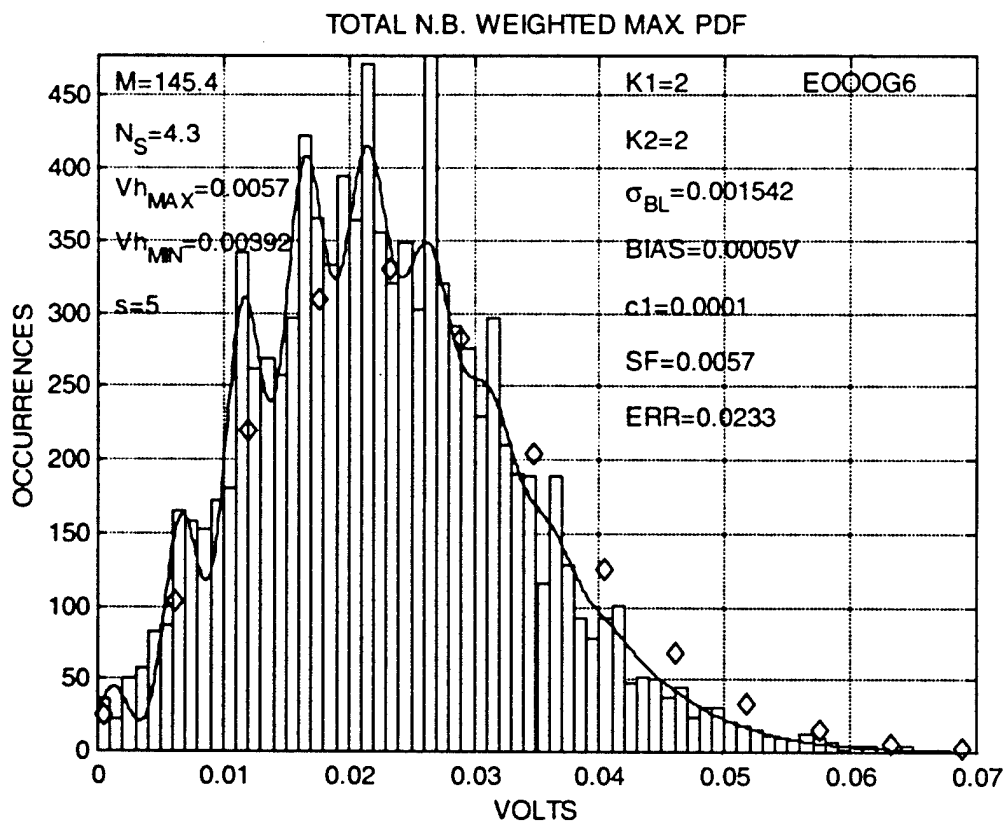


Figure 10B. Numerical fit to annular mask data corresponding to cone range-bin #6.

The opal glass diffuser is rotated to produce a new speckle realization with each laser pulse while the data are being recorded and histogrammed by a LeCroy LC574A digital storage oscilloscope.

8.1 Comparison of Data with Theory

The conditional densities, g_n , are constructed as in Section 7, but we assume a 5.6 mV peak impulse response triangle for the higher gain Hamamatsu MCP tube. The photo-electron creation times within the observation window are controlled by the width of the 1.0 ns laser pulse. This is a different stochastic process from the cone experiment in Section 7. To model this effect we assume that v_{min} is $0.7 \times v_{max}$ corresponding to a triangular impulse-response-function near the center of the observation window. This "effective" $h(t)$ would be the only waveform possible when sampled within the 1.25 ns window. The pulse-height-distribution pdf variance for the Hamamatsu MCP was found to be about twice as large ($c_1 = 1 \times 10^{-4}$) as for the Intevac IPD tube. This is, however, considerably superior to the conservative data sheet specification. Also from the Hamamatsu 4110U data sheets, "gain saturation" had to be included. This was modeled as a linear decrease of $0.5 \text{ mV} \times (n_{pe}-1)$ for n_{pe} events. This simple saturation model allowed the peaks of the shot-noise pdf to align with the peaks of the histogram as seen in Figures 10A and 10B.

Good agreement with theory was found for the three circular masks as seen in Table III. For the three equal area annular range-bin masks, however, M was found to be larger than the theoretical M , approaching Poisson statistics in value:

Table III. Opal Glass Diffuser Plate Theoretical M and Data Fit

127 km Range-Bin #	Annulus Theoretical M (1 polarization)	Least Sq Error Data Fit	Disk Theoretical M (1 polarization)	Least Sq Error Data Fit
3	2.34	4.3	2.1	2.5
6	5.32	Poisson (M large)	3.2	4.1
9	8.33	Poisson (M large)	4.3	4.9

One possibility is that the diffuser plate did not produce random phasors across the mask and the laser mode propagates through the diffuser without enough phase perturbation to create speckle, i.e., an attenuated laser mode results, producing the observed Poisson statistics. The increase in M as we go from a disk source region to an equal area annular region is in good agreement with theory, however.

9.0 SUMMARY AND CONCLUSION

A series of experiments were conducted to simulate speckle effects encountered in NMD/TMD target detection, recognition, and identification using direct detection lidar at 532 nm wavelength. The primary experiment used a full size conical (NMD) target resolved in range with 20 cm resolution and rotated to several aspect angles. Several additional supporting and calibration experiments were implemented using greatly attenuated 1.0 ns and pico-second pulsed lasers, CW light emitting diodes, as well as small annular and circular mask source region targets to simulate cone range-bin source regions at distance. The detectors employed were intensified vacuum photodiodes and microchannel plate photomultipliers. Good agreement with speckle theory and shot-noise stochastic process theory was demonstrated in these tests. The importance of the detector and electronics impulse-response-function and bandwidth must be taken into consideration when

simulating ladar automatic target recognition algorithm performance. The incorporation of ladar negative-binomial driven shot-noise is a straightforward extension of current (Poisson driven) shot-noise theory.

Current research involves the determination of the optimum bandwidth and the impulse response shape of the preamplifiers. Approximately a 500 MHz bandwidth with a 1.3 ns basewidth triangular impulse response function appears near optimum at this time. Laboratory brassboard tests and system ground testing are scheduled for the summer of 1999.

10.0 ACKNOWLEDGEMENTS

This work was sponsored under BMDO contract 84-92-C008. The authors would like to thank LCDR. James Buckley, program manager, and Dr. Walter Dyer, technical advisor, for their support and guidance. Also, we would like to thank Erhard Schimitischek, former executing agent, for his initial efforts in this BMDO program along with Alan Hays and Nikolay Ter-Gabrielyan of Fibertek for their support of the short pulsed laser during the experiments.

11.0 REFERENCES

1. Dyer, W., "Missile Seeker Technology at the Ballistic Missile Defense Organization," Proc. AIAA Missile Sciences Conf., Dec. 1996.
2. Burnham, R., et al, "Short Pulse 3D Imaging Ladar for Advanced Target Discrimination," Proc. IRIS Active Systems, Vol. 1, 1997.
3. Leslie, D., et al, "Direct Detection Laser Radar Angle/Angle/Range-Imaging Target Identification Capabilities," Proc. IRIS Active Systems, Vol. 1, 1997.
4. Dyer, W., "Review of the Ballistic Missile Defense Organization's Advanced Sensor and Seeker Technology Programs," Proc. IRIS Active Systems, Vol., 1997.
5. Hart, G., et al, "Solid-state Laser Radar for DITP - New Discrimination Algorithms and Test Results with AMOR Targets," Proc. IRIS Active Systems Conf. March 1998.
6. Hart, G., et al., "New Discrimination Algorithms and Test Results Using a Solid-state 3D Imaging Laser Radar," Proc. 7th AIAA/BMDO Technology Readiness Conf., Aug. 1998.
7. Goodman, J., "Some Effects of Target-Induced Scintillation on Optical Radar Performance," Proc. IEEE, Vol. 53, No. 11, Nov. 1965.
8. Goodman, J., "Comparative Performance of Optical-Radar Detection Techniques," IEEE Trans. AES, Vol. AES-2, No. 5, Sept. 1966.
9. Goodman, J., *Laser Speckle and Related Phenomena*, J.C. Dainty Ed., Springer-Verlag, 1975, Second Edition, 1984.
10. Saleh, B., *Photoelectron Statistics*, Springer-Verlag, 1978.
11. Youmans, D., Hart, G., "Numerical evaluation of the "M" parameter for direct detection ladar," SPIE Proc. Vol. 3380, April 1998.
12. Teich, M., B. Saleh, "Effects of random deletion and additive noise on bunched and anti-bunched photon counting statistics," Opt. Lett, Vol. 7, No. 9, Aug. 1982.
13. Papoulis, *Probability, Random Variables, and Stochastic Processes*, McGraw-Hill, 1965, p. 127.
14. Papoulis, p. 37.
15. Papoulis, p. 193.

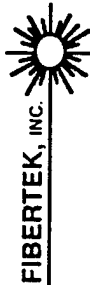
16. Youmans, D., Flukiger, D., "Linear FM chirp pulse compression ladar receiver-operating-characteristic: maximum of M Rayleighs statistics," SPIE Proc. Vol. 3065, *Laser Radar Technology and Applications II*, April 1997.
17. Papoulis, p. 560.
18. Pratt, W. K., *Laser Communication Systems*, John Wiley, 1969, p.260.
19. Lowen, S.B., Teich. M., "Power-Law Shot Noise," IEEE Trans. Info. Theo., Vol. 36, Nov. 1990.
20. Fante, R., *Signal Analysis and Estimation*, John Wiley, 1988.
21. Born, M., E. Wolf, *Principles of Optics*, Pergamon Press, 1970, p. 416.

Appendix L



Speckle Test Results

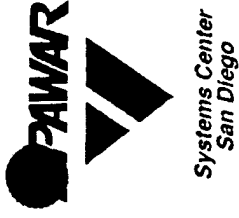
George Hart - Schafer





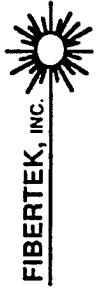
Speckle Test Results

- Data collected was exhaustively analyzed statistically revealing many parameters and phenomena which affect results
- M values observed were at least as large as those calculated by Youmans method
- Independent calculation technique by Hanson is in exact agreement with Youmans method
- Although impact on M value for target base annulus is large, effect on total target or individual voxel intensity measurement accuracy is actually quite small



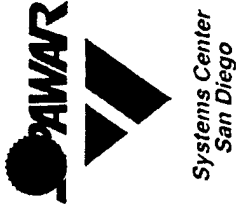
If your experiment needs statistics,
you ought to have done a better experiment.

Lord Rutherford





Phenomena Affecting Speckle Results (Histogram of Observed Peak Heights)



- Pulse stacking
- Detector saturation
- A/D converter impulse response
- Pre-amplifier bandwidth
- Gaussian baseline noise (3σ events)
- Pulse height distribution of detector response
- LSB of oscilloscope
- Baseline droop during long (> 10 ns) windows
- Temporal addition of speckle lobes from pulse length





Types of Speckle Tests Conducted



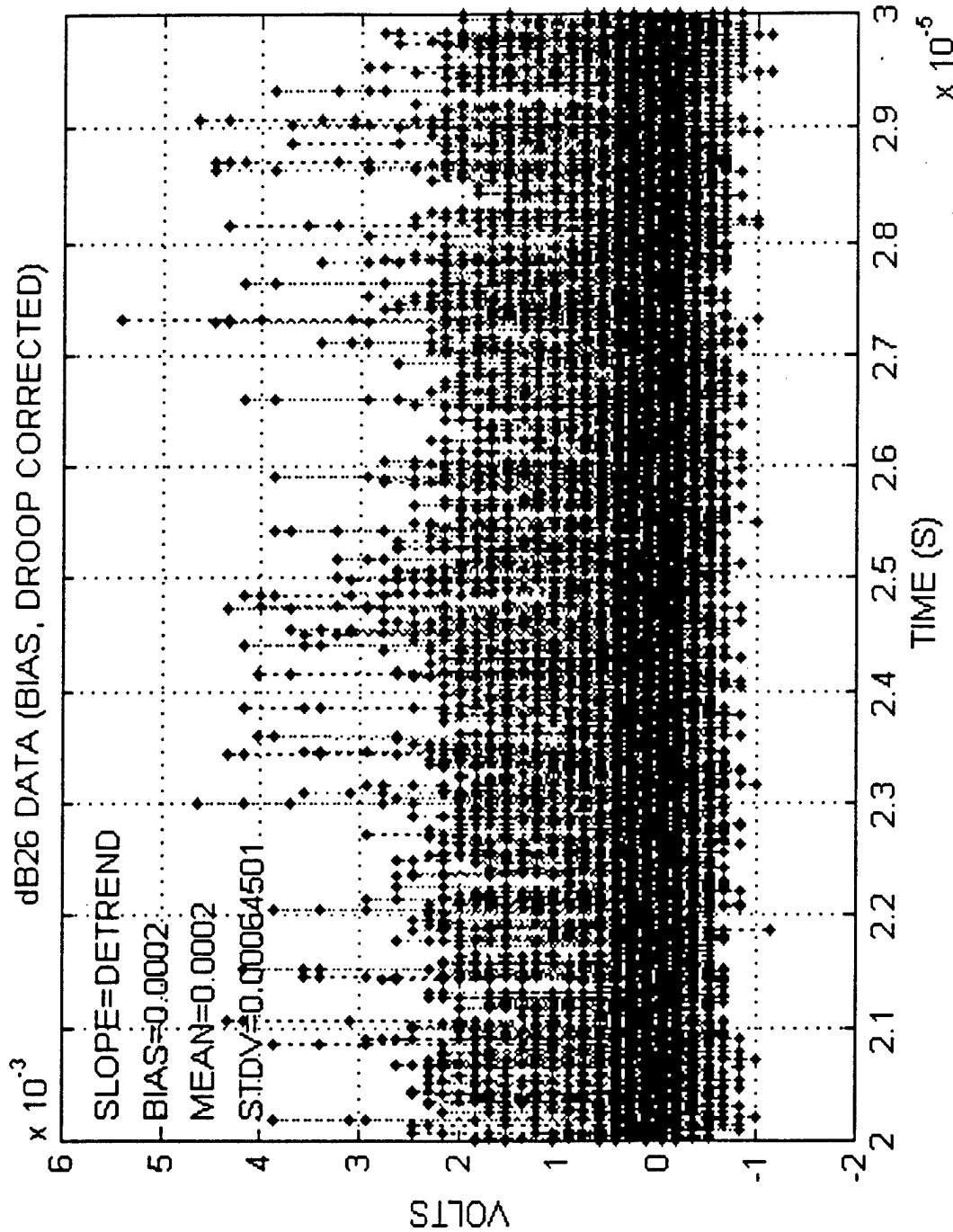
Systems Center
San Diego

- No light in 100 ns and 20 μ s windows
Used to characterize baseline Gaussian noise
- ND filter attenuated LED input in 100 ns and 20 μ s windows
Used to determine mv/PE, pulse stacking, noise droop, etc.
- ND filter attenuated Fibertek oscillator viewed in 6.25 ns window
Used to examine isolated signal peaks
- Opal glass annulus measurements with attenuated LED
Used to verify M value calculation for ideal ring shapes
- Full cone measurements at several aspect angles
Used to verify M value calculation and examine temporal effects



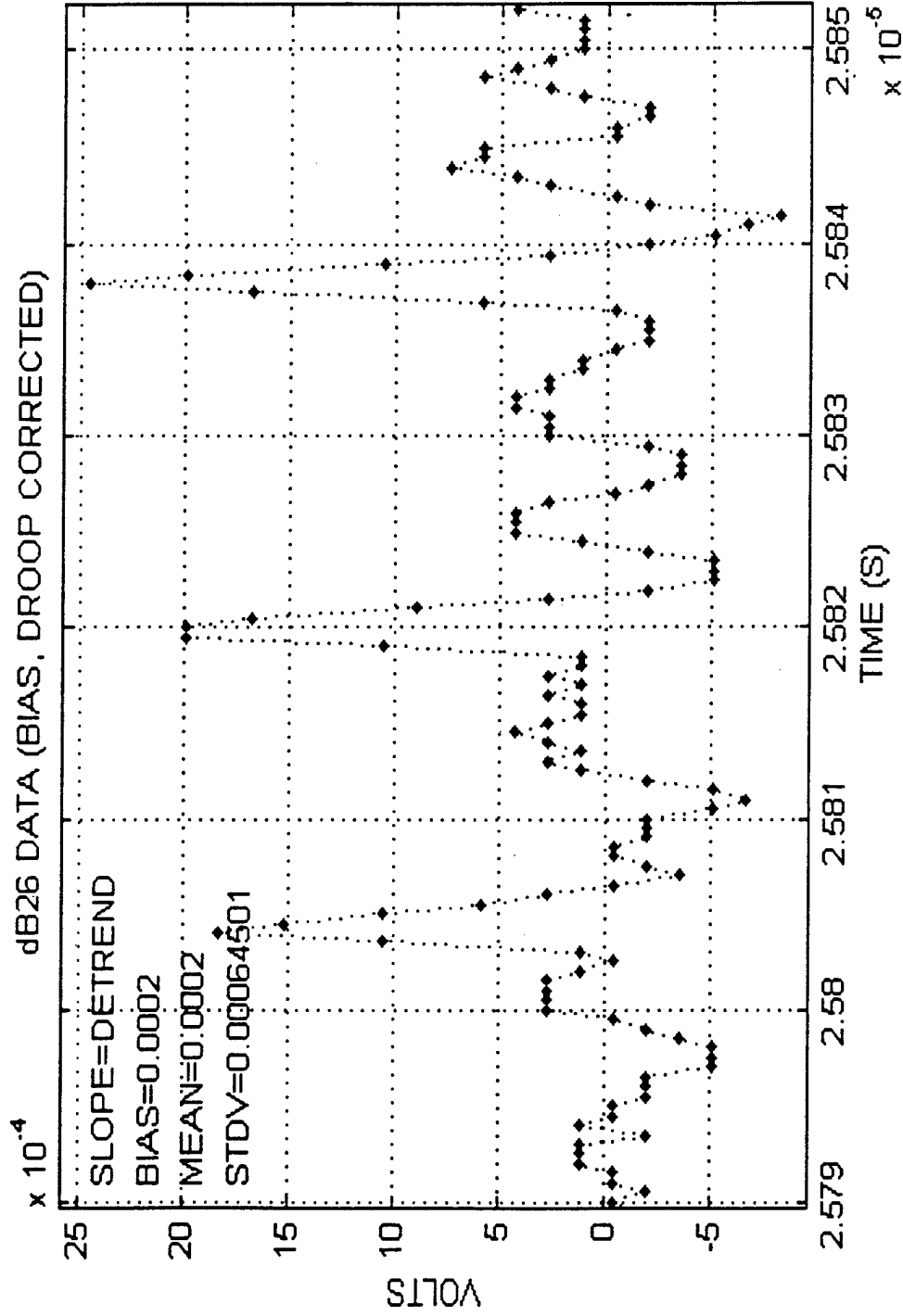


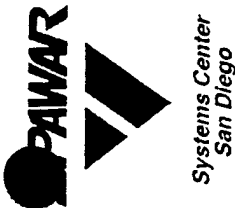
ND2.6 CW LED Data



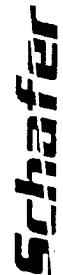
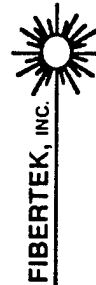
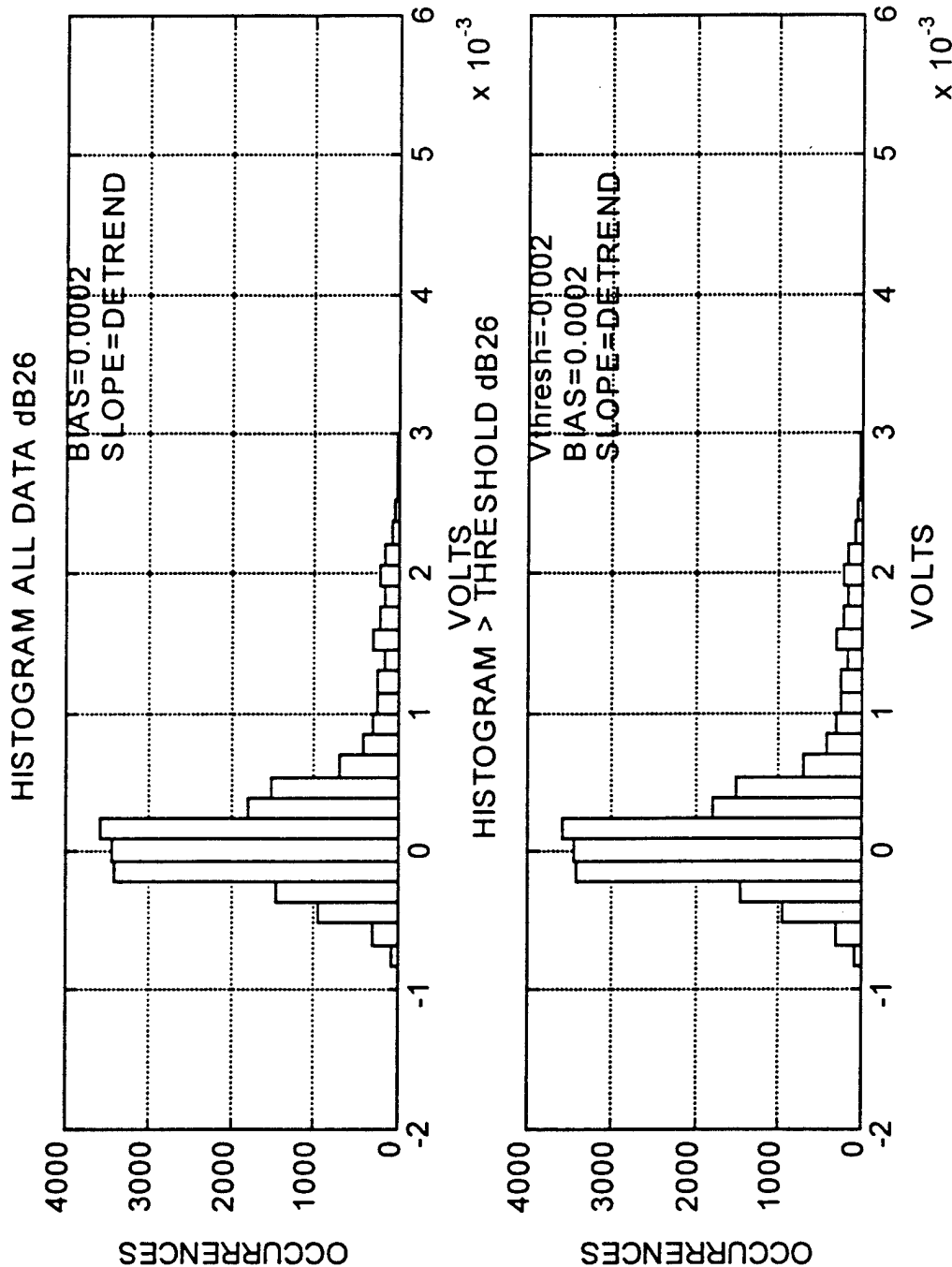


Expanded ND2.6 CW LED Data





ND2.6 CW LED Histogram

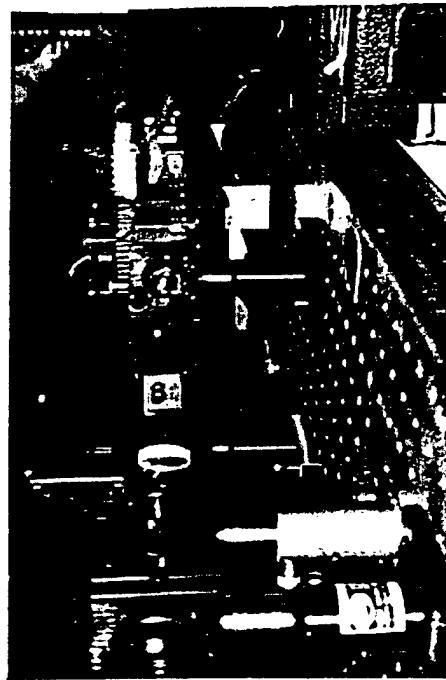




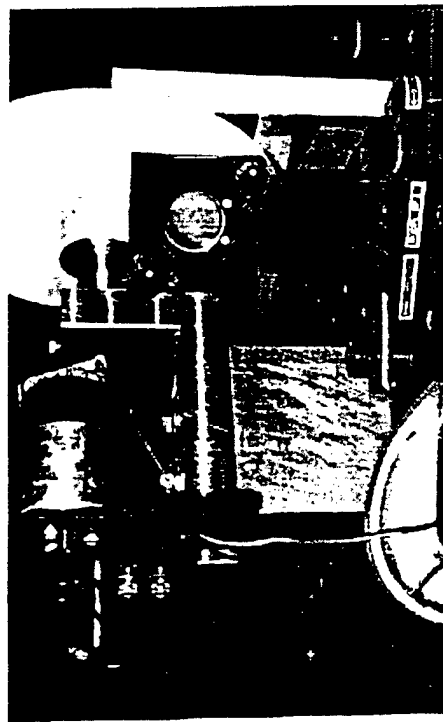
Systems Center
San Diego

Annular Target Test Hardware

Fibertek
Laser



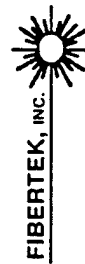
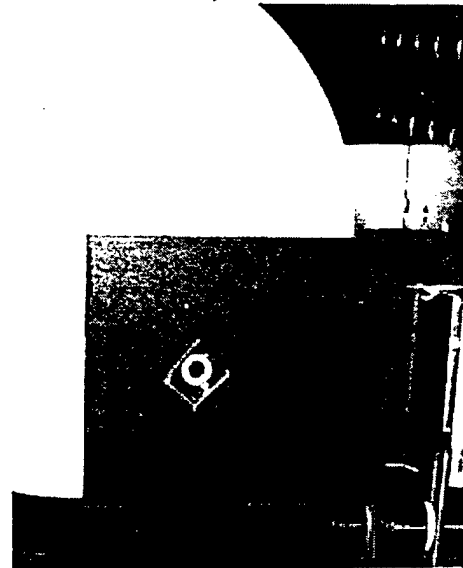
Rotating
Opal Glass
Disk



Rotating
Opal Glass
Disk

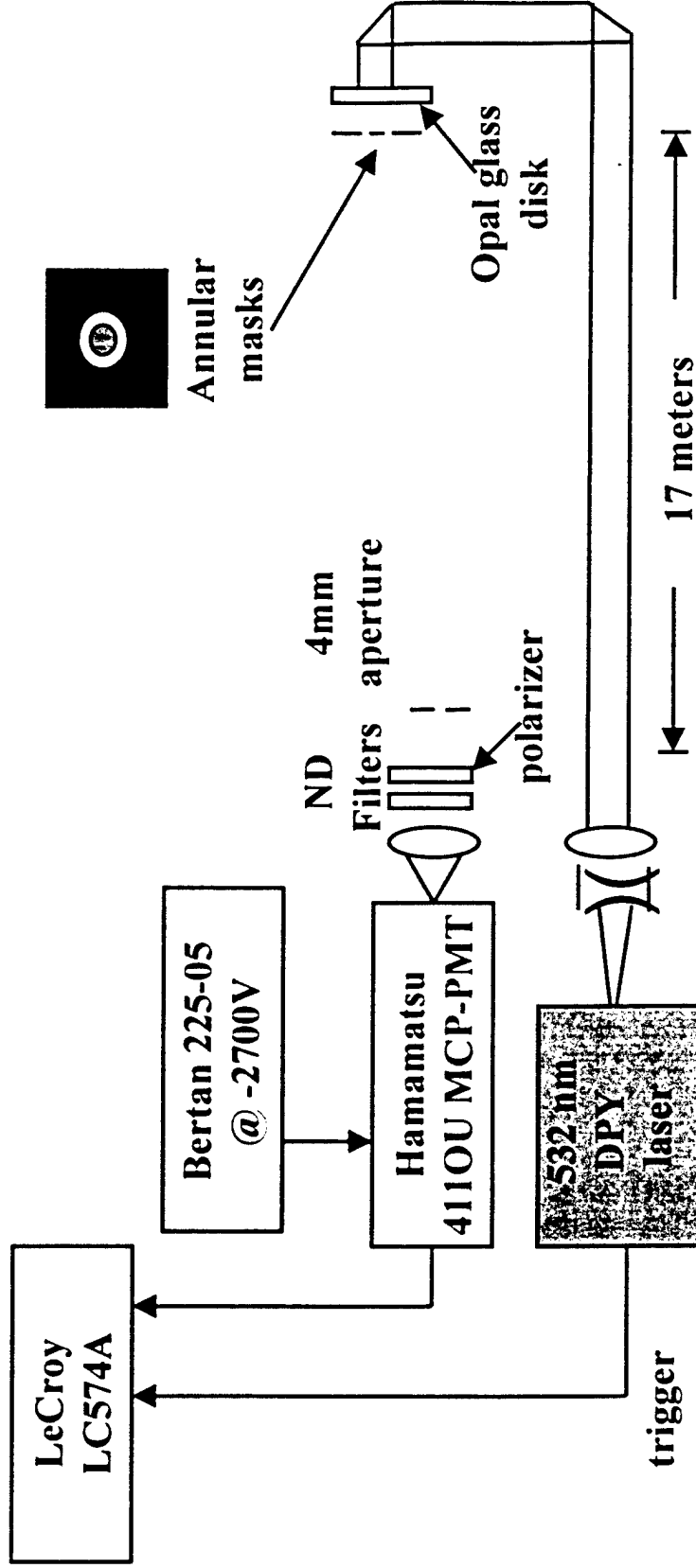


Illuminated
Annular
Mask



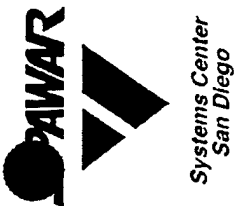


Opal Glass Diffuser w/ Masks Test

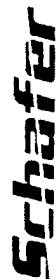
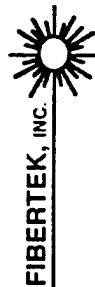
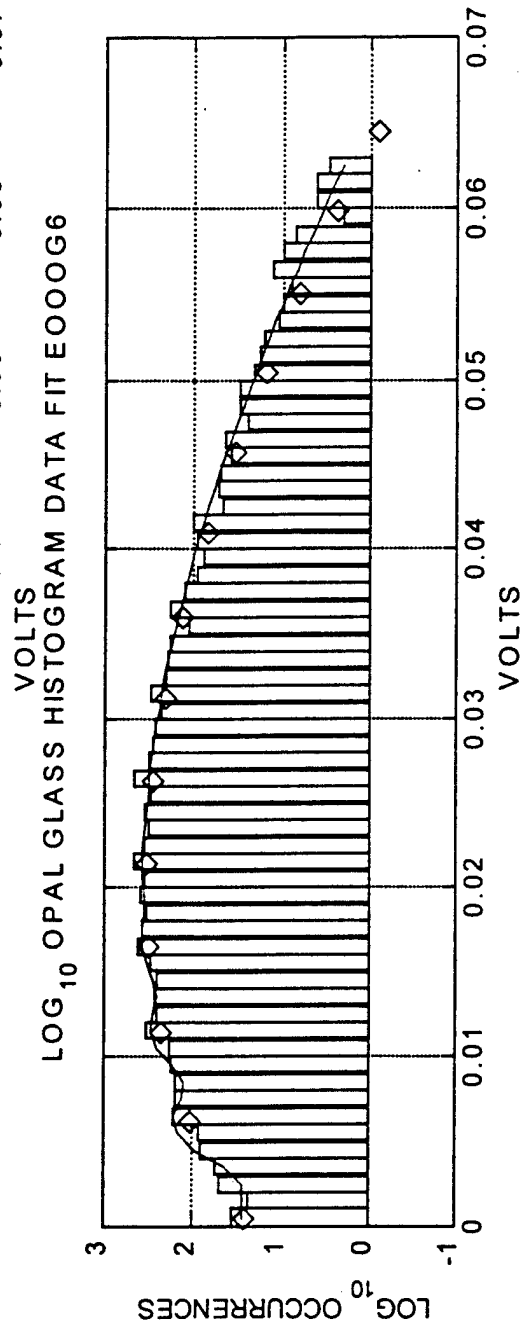
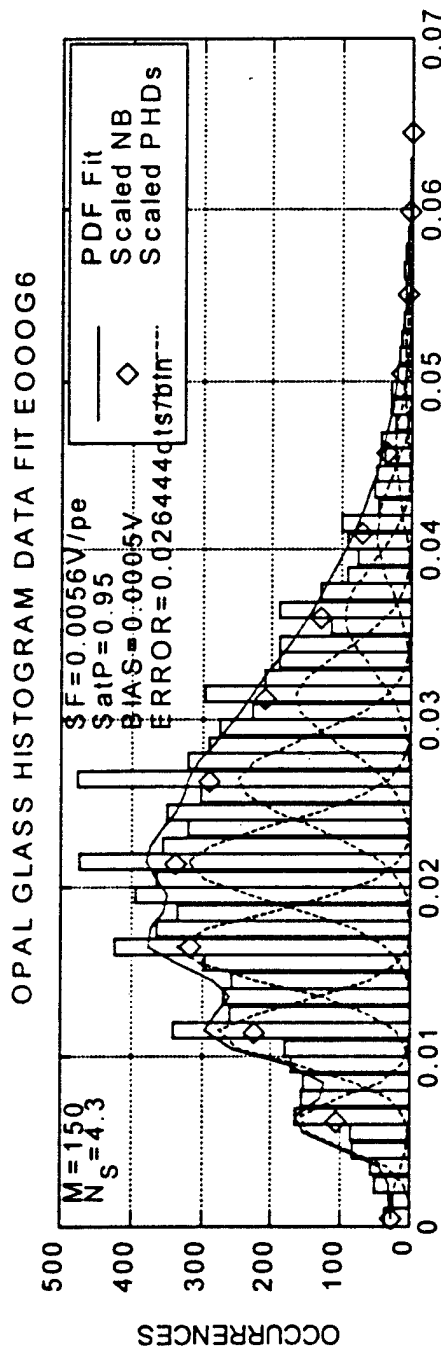


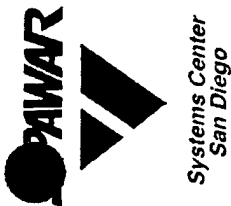
Test Goal: Validate "Exact" M-parameter theory by measuring probability density function from annular targets at various illumination levels



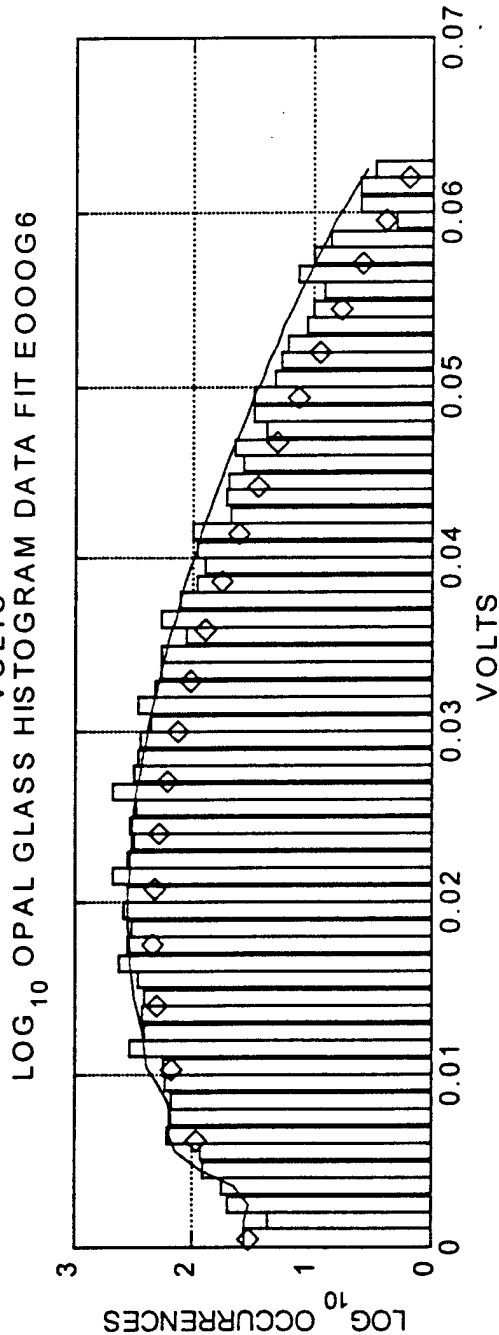
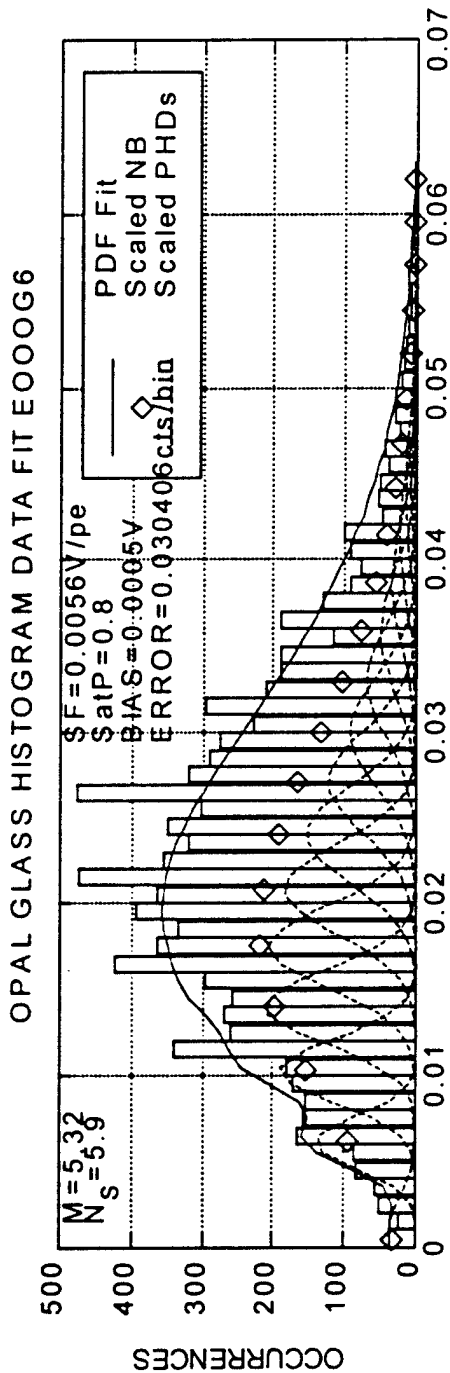


Opal Glass RB#6, Histogram Fit





Opal Glass RB#6, Histogram Fit





Summary Opal Glass with Masks Data



Systems Center
San Diego

Opal Glass Diffuser Plate Theoretical M and Data Fit

127 km Range Bin #	Theoretical M (1 polarization)	Saturation Parameter $n^{0.95}$ Data Fit	Saturation Parameter $n^{0.8}$ Data Fit
3	2.34	4	2.34
6	5.32	Poisson (M large)	5.32
9	8.33	Poisson (M large)	8.33

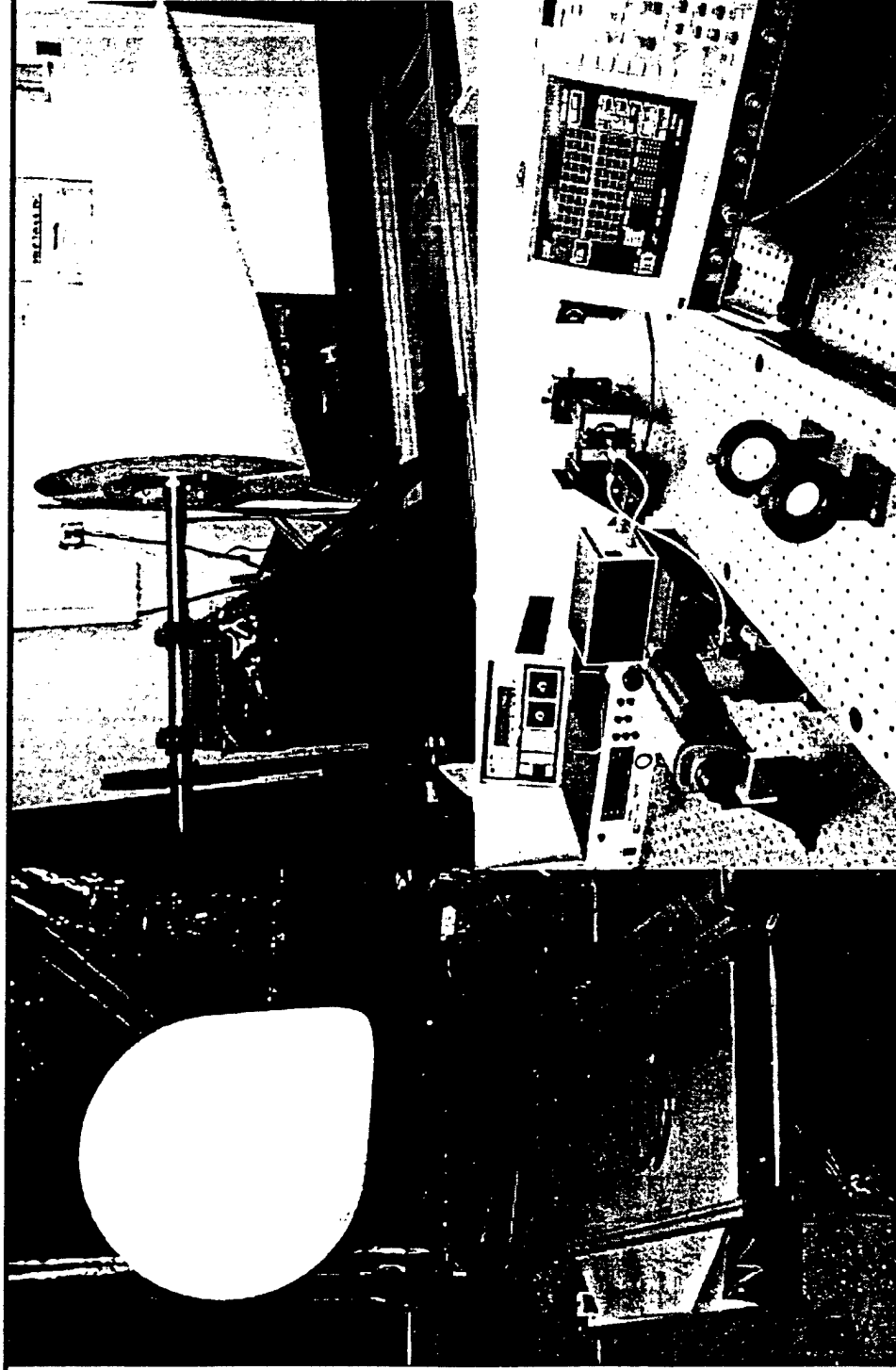




Full-size Cone Test Hardware



Systems Center
San Diego



Cone
Target
on
Rotating
Mount

Polystyrene
Cone on
Rotating
Mount

Receiver
Optics &
Lecroy
'scope



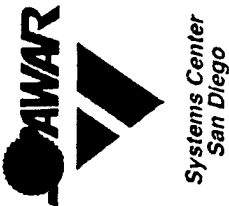
FIBERTEK, INC.



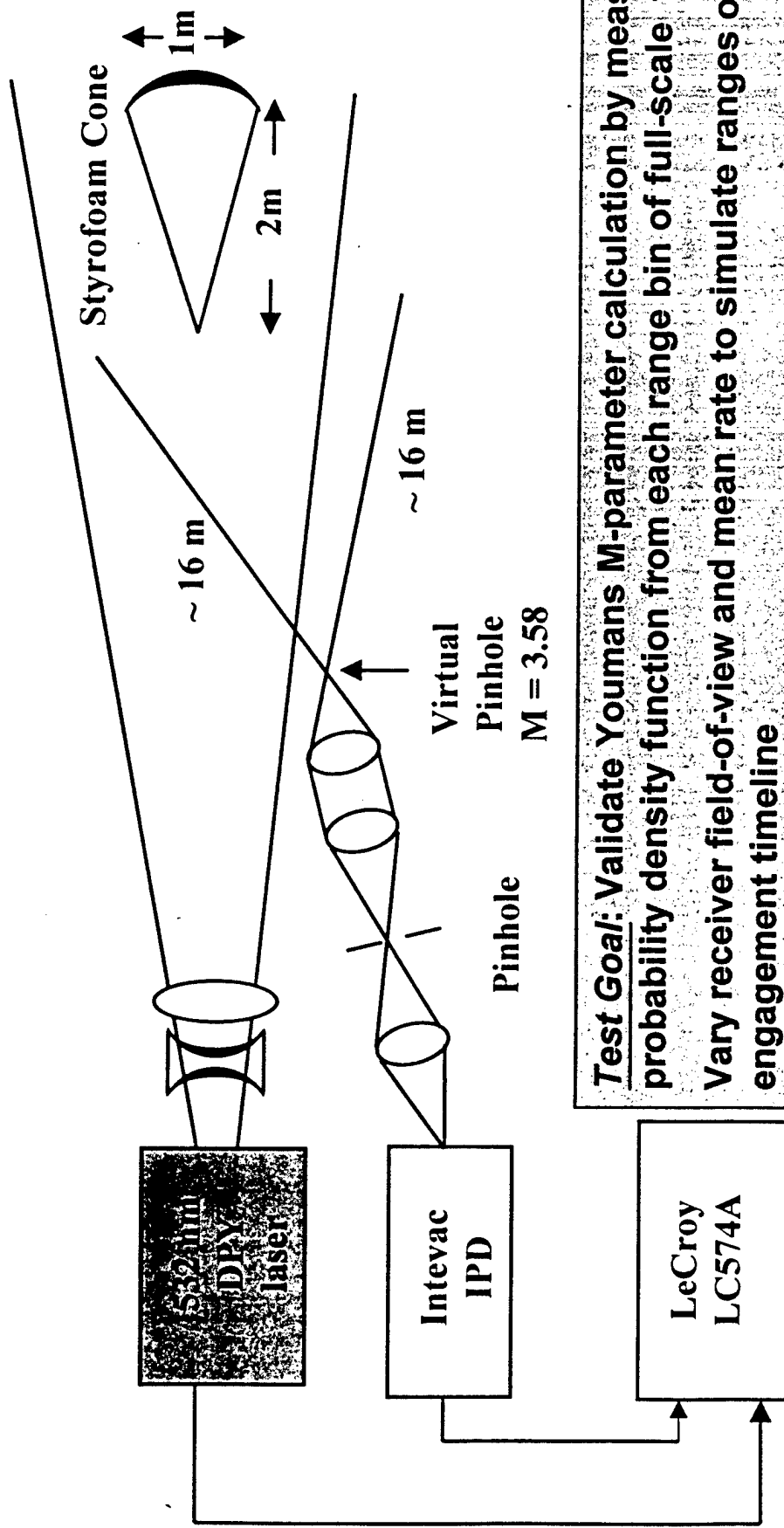
ThermoTrex Corporation

Schafer

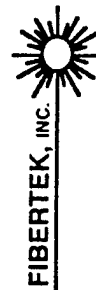
vac



Short Range Cone Test



trigger

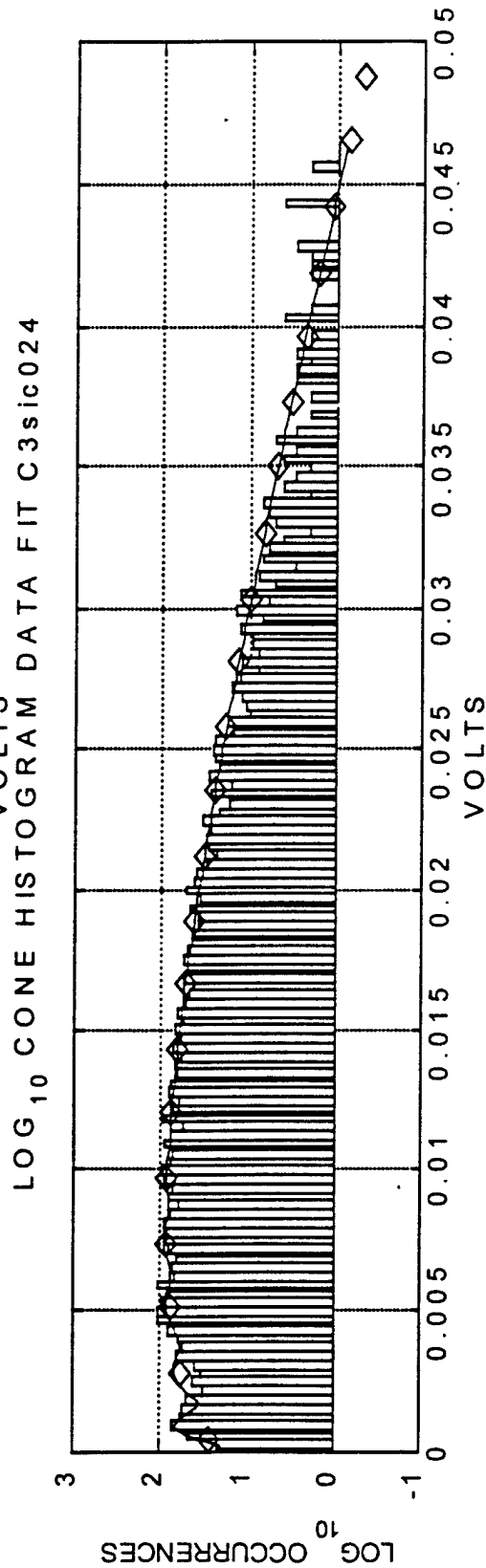
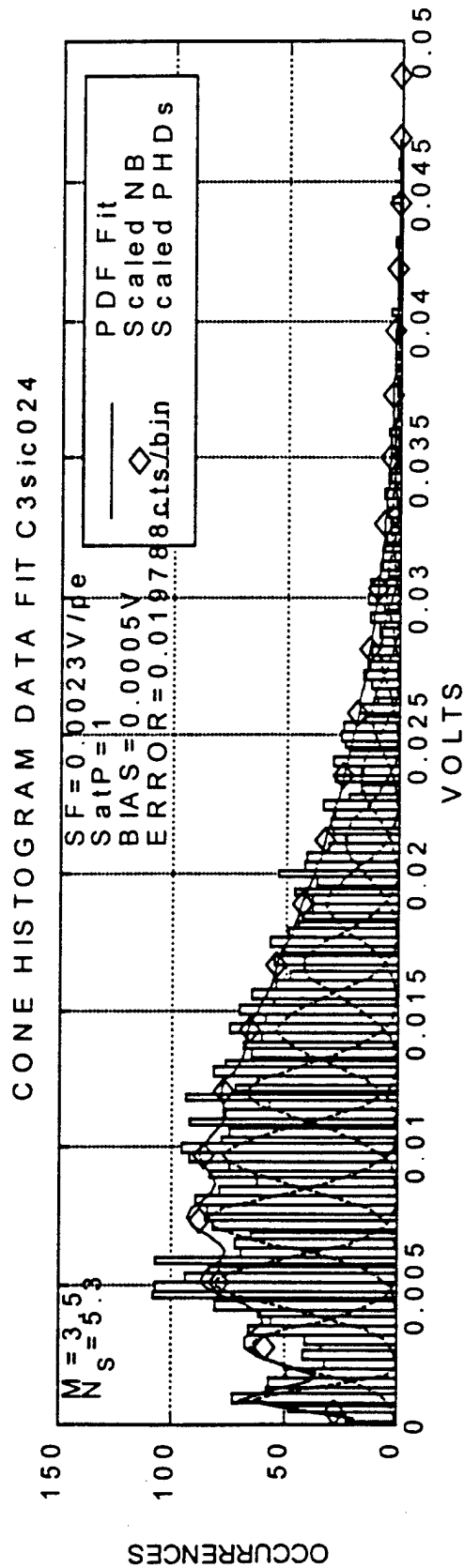


Test Goal: Validate Youmans M-parameter calculation by measuring probability density function from each range bin of full-scale target
Vary receiver field-of-view and mean rate to simulate ranges on DITP engagement timeline



Systems Center
San Diego

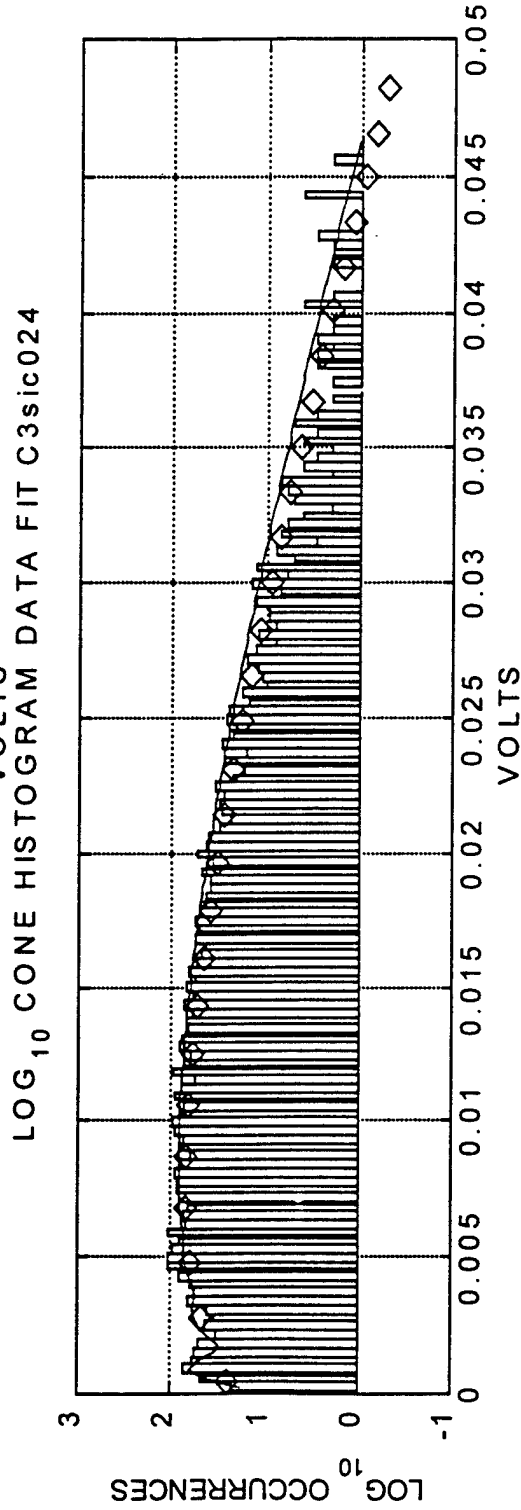
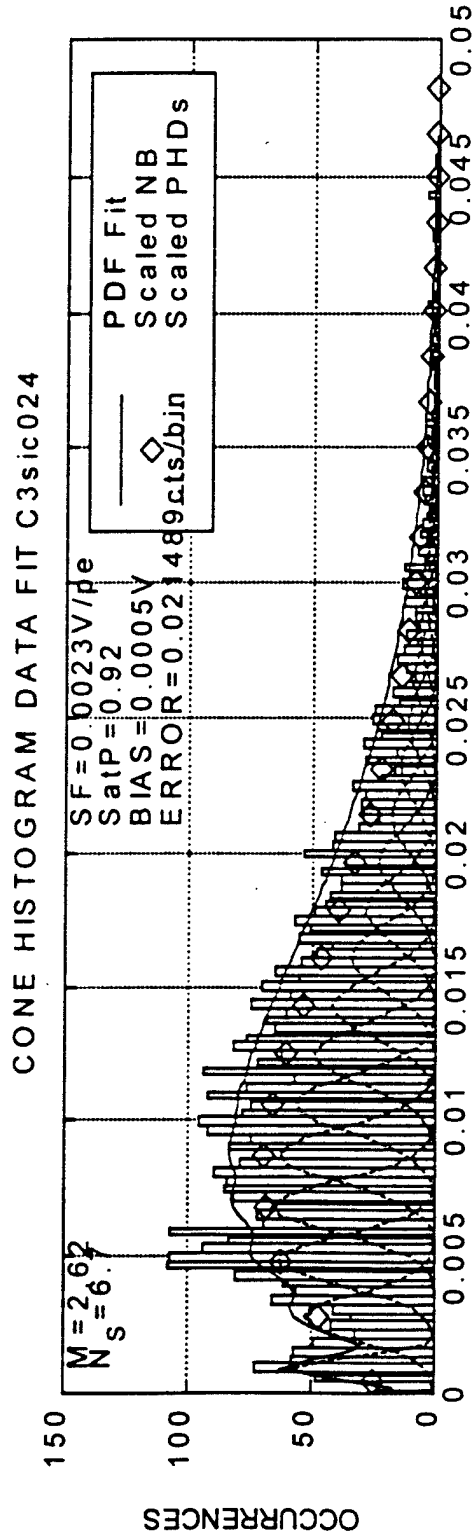
Cone RB#2, Histogram Fit





Systems Center
San Diego

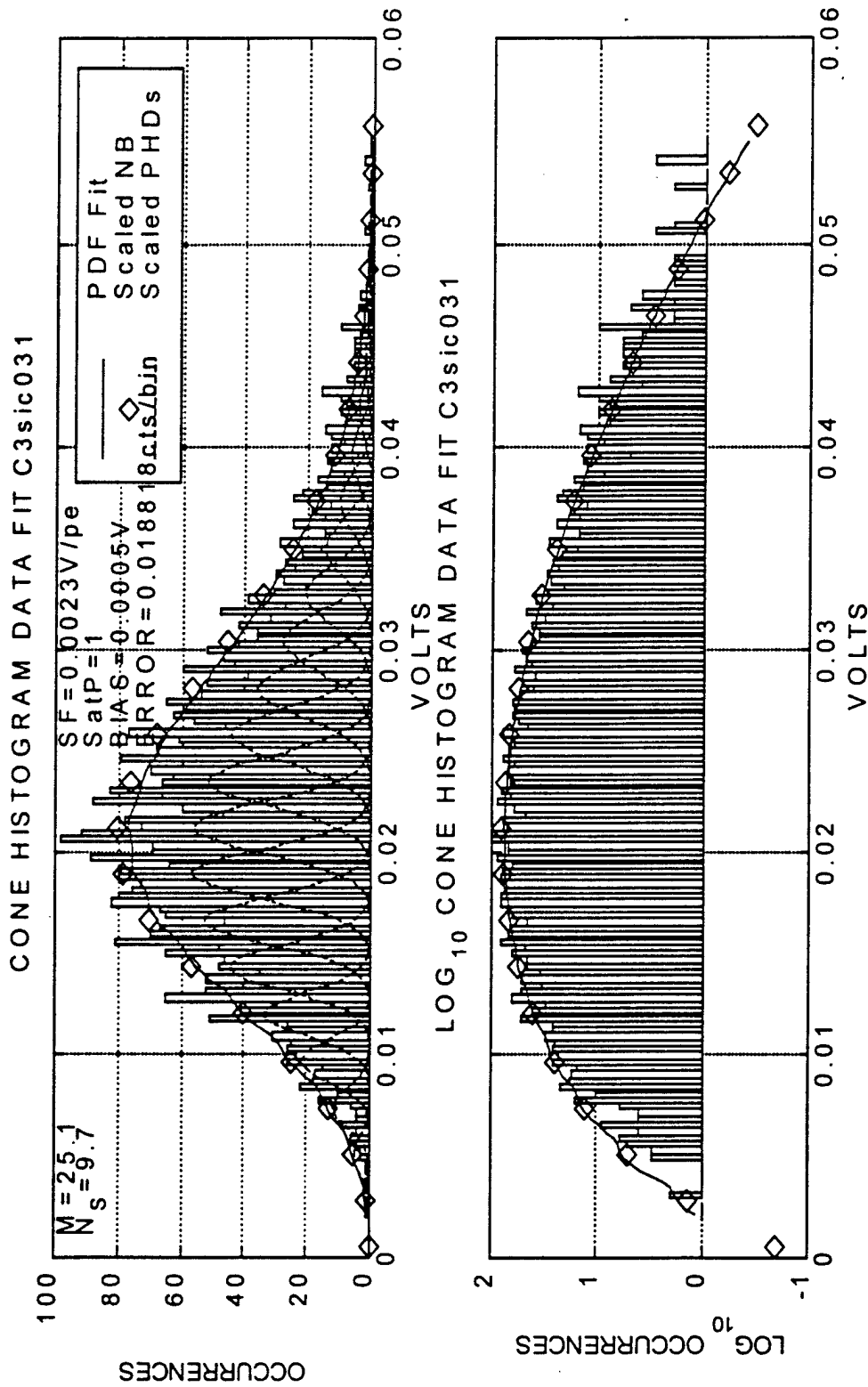
Cone RB#2, Histogram Fit





Systems Center
San Diego

Cone RB#9, Histogram Fit

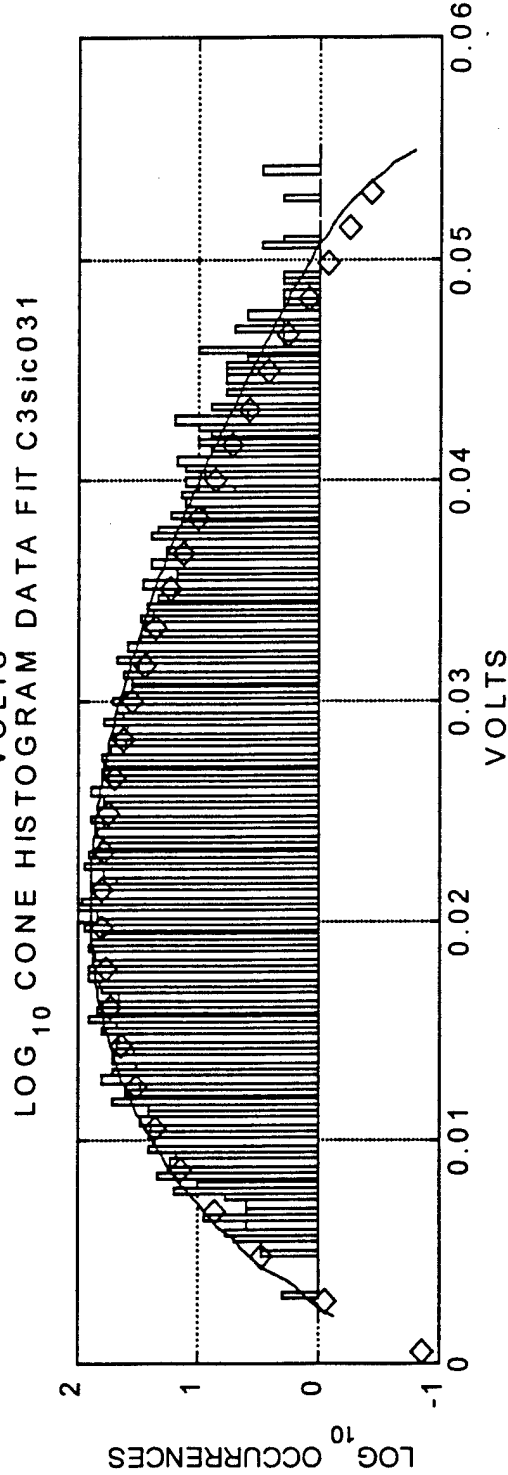
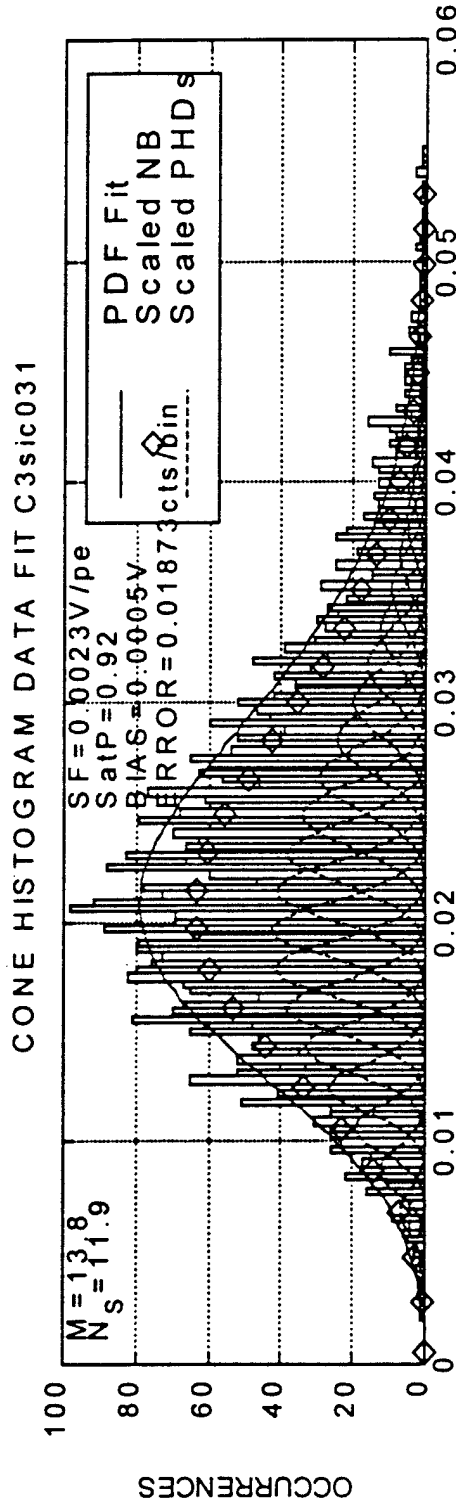


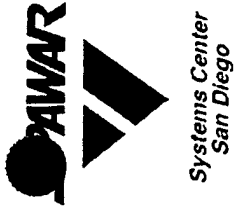
Schafer

PAWAR



Cone RB#9, Histogram Fit

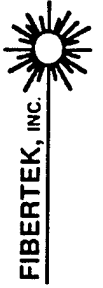




Summary Cone Range-Bin Data

Cone Range Bin M Parameter Theory and Data

141 km Range Bin #	Theoretical M (2 polarization)	Least Sq Error Fit (No Sat.)	$n^{0.92}$ Saturation Parameter Fit	M With Range Bin Smearing	Chirped Pulse
1	2.12	1.0	1.4	2.4	TBD
2	2.62	3.5	2.62	3.8	TBD
3	3.78	9.9	3.78	4.2	TBD
4	5.44	12.1	5.44	6	TBD
5	7.42	11.4	7.42	8.2	TBD
6	9.04	15.2	9.04	11	TBD
7	10.68	16.1	10.68	13.8	TBD
8	12.04	23.4	12.04	16	TBD
9	13.78	25.1	13.78	18	TBD
10	15.38	---	---	20	TBD





Impact of M Value on Timeline

- Even at small aspect angles when cone range bins are ring-like, “enhanced” M values have small impact on discrimination timeline
- At large ranges, number of photoelectrons is so small that Poisson term in variance dominates, M is unimportant
- At small ranges, at least 10 shots are needed for threshold crossing determination of intensity, so benefit of larger M value is never realized



Impact of M Values on Timeline 0 Degree Aspect 8% Reflectivity

Systems Center
San Diego

Range (km)	365	300	260	210	180	150	120
N_s	1.6	3.5	6.3	14.7	27.2	56.4	137.5

$\sigma = \text{sqrt}(N_s)$ Poisson	1.26	1.87	2.51	3.83	5.21	7.50	11.73
σ/N_s	.79	.53	.40	.26	.19	.13	.08

Shots for 10%
Relative Accuracy

63	29	16	7	4	2	1
----	----	----	---	---	---	---

M_{calc}	22	28	32	41	49	60	78
$\sigma = \text{sqrt}(N_s + N_s^2/M)$	1.31	1.98	2.75	4.48	6.57	10.69	20.25
σ/N_s	.82	.57	.44	.31	.24	.19	.15

Shots for 10%
Relative Accuracy

67	32	19	9	6	4	2
----	----	----	---	---	---	---

M_{Yura}	11	13	14	15	16	20	24
$\sigma = \text{sqrt}(N_s + N_s^2/M)$	1.35	2.11	3.02	5.40	8.57	14.68	30.41
σ/N_s	.85	.60	.48	.37	.32	.26	.22

Shots for 10%
Relative Accuracy

72	36	23	13	10	7	5
----	----	----	----	----	---	---





Systems Center
San Diego

Impact of M Values on Timeline 0 Degree Aspect 16% Reflectivity

Range (km)	365	300	260	210	180	150	120
N _s	3.2	7.0	12.6	29.4	54.4	112.8	275.0

$\sigma = \sqrt{N_s}$ Poisson	1.79	2.65	3.55	5.42	7.37	10.60	16.59
σ/N_s	.56	.38	.28	.18	.13	.09	.06

Shots for 10%

Relative Accuracy

36	15	8	3	2	1	1
----	----	---	---	---	---	---

M _{calc}	22	28	32	41	49	60	78
$\sigma = \sqrt{N_s + N_s^2/M}$	1.91	2.96	4.19	7.10	10.71	18.02	35.28
σ/N_s	.60	.42	.33	.24	.20	.16	.13

Shots for 10%

Relative Accuracy

36	18	11	6	4	3	2
----	----	----	---	---	---	---

M _{Yura}	11	13	14	15	16	20	24
$\sigma = \sqrt{N_s + N_s^2/M}$	2.03	3.28	4.89	9.32	15.47	27.37	58.53
σ/N_s	.64	.47	.39	.32	.28	.24	.21

Shots for 10%

Relative Accuracy

40	22	15	10	8	6	5
----	----	----	----	---	---	---



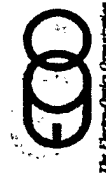
Appendix M



Systems Center
San Diego

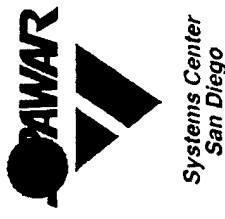
LADAR System Analysis

George Hart - Schafer

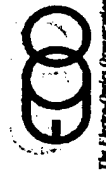




LADAR System Analysis

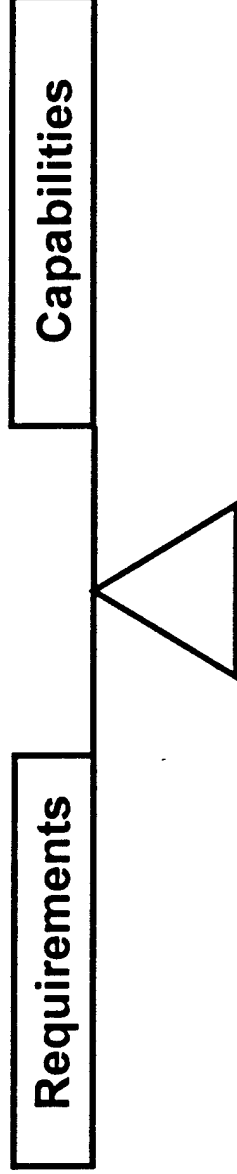


- OPS WG derived LADAR pointing accuracy requirements necessitated redefining LADAR acquisition conops
- Effect on acquisition of reduced signal from scaled target examined
- M-O-I methods for coping with wavefront error explored
- New wavefront error tolerant orientation angle algorithm developed
- Amount of jitter produced by registration process determined
- Impact of jitter on M-O-I target orientation angles assessed





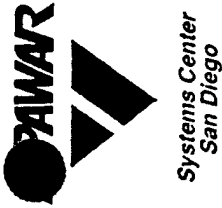
Balance Must Be Achieved



Paths to imbalance

- Imposing excessively conservative or unrealizable requirements
- Failing to rethink conops for each subsystem to enhance capability
- Ignoring LCDR Buckley re: need for 90% solution in Flight Demo 1





What we have here,
is failure to co-operate





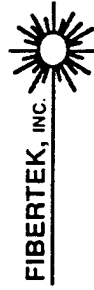
True Teamwork Essential for Test Effort



Systems Center
San Diego

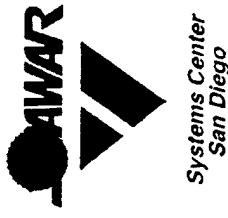
Problem Areas

- Lack of flexibility/adaptivity in responding to evolving requirements
- Dogged attachment to solutions in search of a problem
- Lobbyist-like advocacy of particular test approaches
- Refusal to carefully consider inputs from subsystem experts
- Adversarial attitude with presumption of incompetence or malfeasance
- Failure to trim down participants to manageable and effective team



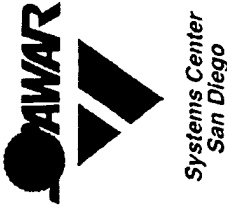


LADAR System Analysis



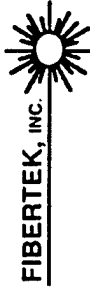
- OPS WG derived LADAR pointing accuracy requirements necessitated redefining LADAR acquisition CONOPS
- Effect on acquisition of reduced signal from scaled target examined





Revised LADAR Acquisition CONOPS

- Previous LADAR acquisition CONOPS required acquisition on first attempt
- OPS WG derived LADAR pointing requirements [10ur bias (worst case) plus 5ur track error, 5 ur control error, 5 ur jitter] made this problematic
- Revised CONOPS permits multiple acquisition attempts over x km until success achieved (x= 20-100, depends on scenario)
- Acquisition can be made in DITP test flight with > 99% probability by 350 km. Ample timeline exists for this approach
- LADAR can begin attempts as soon as thermal battery permits, to enhance passive track with LADAR data ASAP





Derived requirements summary

Dictated by beam transmission requirements for Ladar acquisition and intensity modulation discrimination

- 5 μ rad residual Jitter, 1 σ , 1 axis rms
on laser beam in target space
- 26 μ rad $1/e^2$ point, beam profile in target space
- <2% fluctuation in transmitted beam power

Dictated by Ladar FOV, laser profile, acquisition time, and test scenario

- 10 μ rad (worst case) static optical system handover error
[7 μ rad PSS to Ladar and 7 μ rad Ladar Tx to Rx boresight error]
- 5 μ rad (1 σ each axis) centroiding and tracking handover error
- 5 μ rad (1 σ each axis) OPS control residual handover error

Dictated by spatial resolution and discrimination algorithm requirements

- Telescope primary aperture 25 cm
- $\lambda/14$ wavefront error over narrow FOV
- $\lambda/8.3$ wavefront error over full FOV
- Telescope FOV $2^\circ \times 1.6^\circ$
- $\lambda/14$ wavefront error for Ladar receiver optics

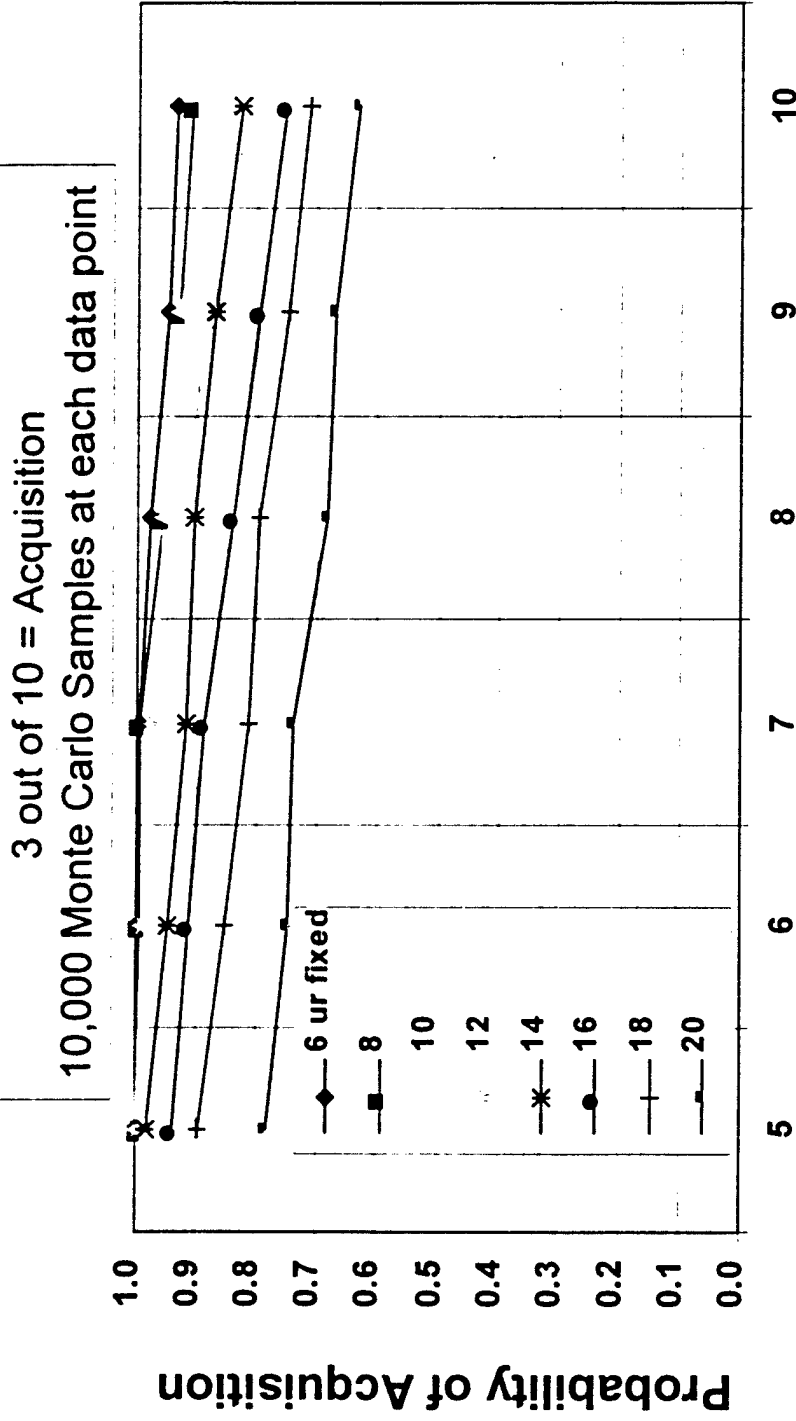




Acquisition for 8% 2x1m target Attempts made at 450, 425, 400 km



Systems Center
San Diego

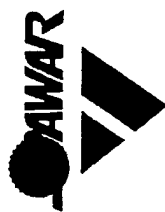


Size of Tracking Error and Control Error Individually (urad)

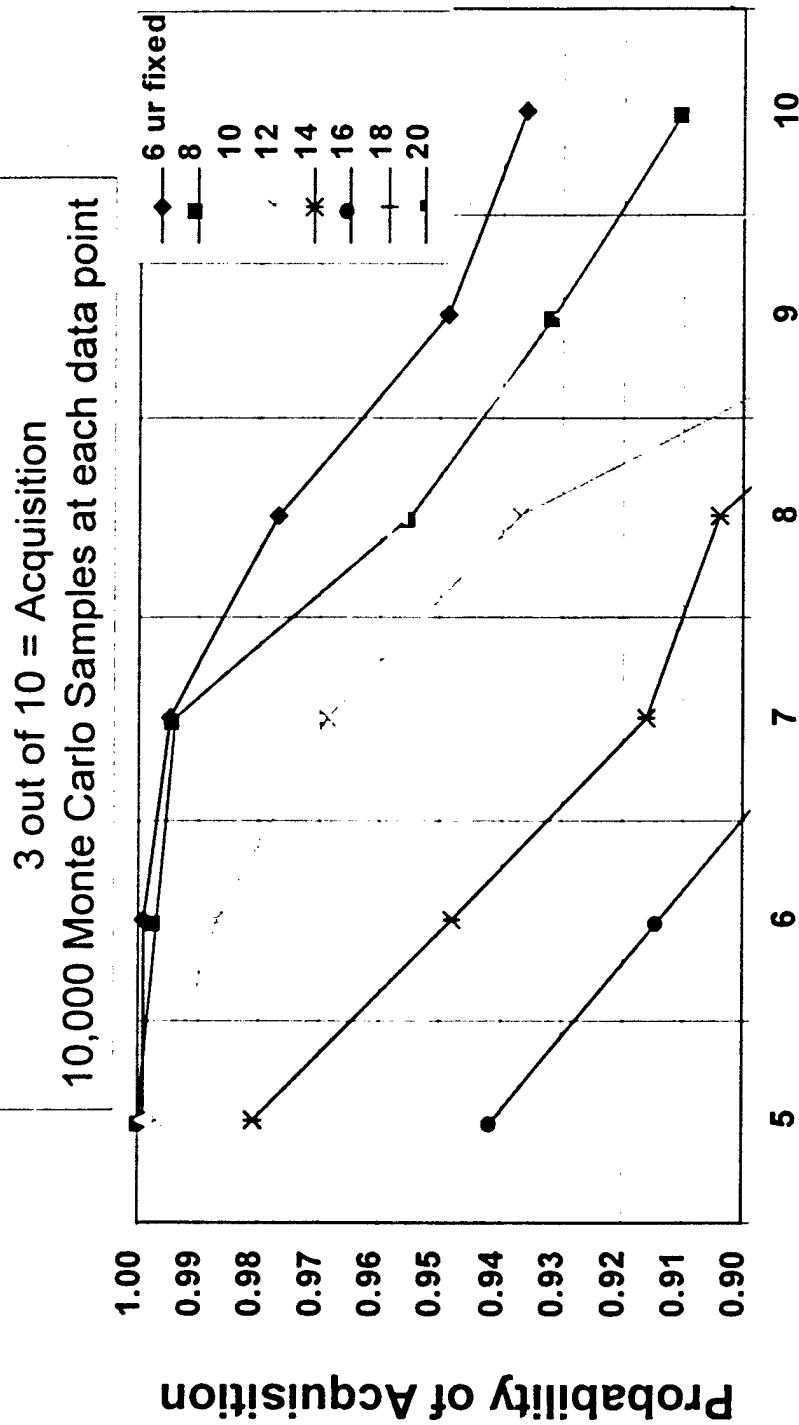




Acquisition for 8% 2x1m target Attempts made at 450, 425, 400 km

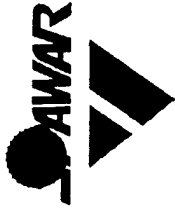


Systems Center
San Diego



Size of Tracking Error and Control Error Individually (urad)

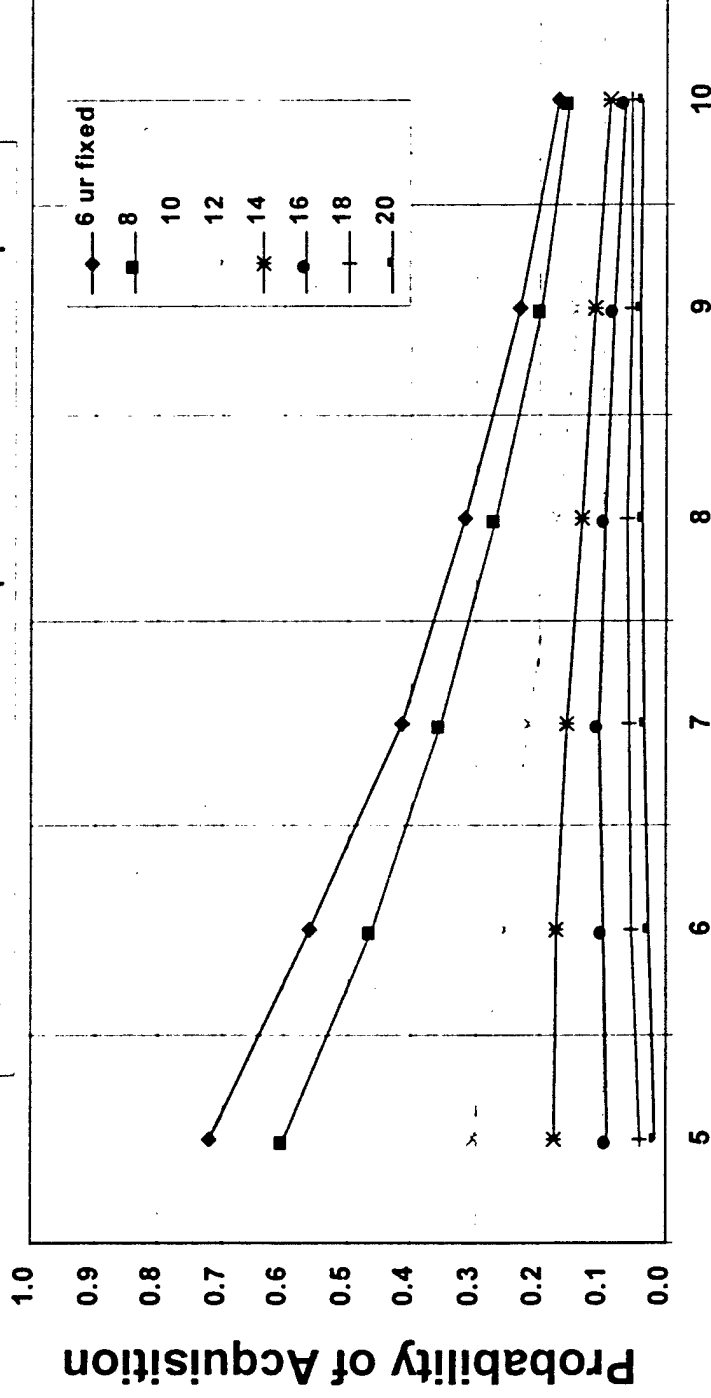




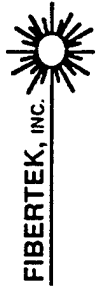
Acquisition for 8% 2x0.4m target Attempts made at 400, 375, 350 km

Systems Center
San Diego

3 out of 10 = Acquisition
10,000 Monte Carlo Samples at each data point

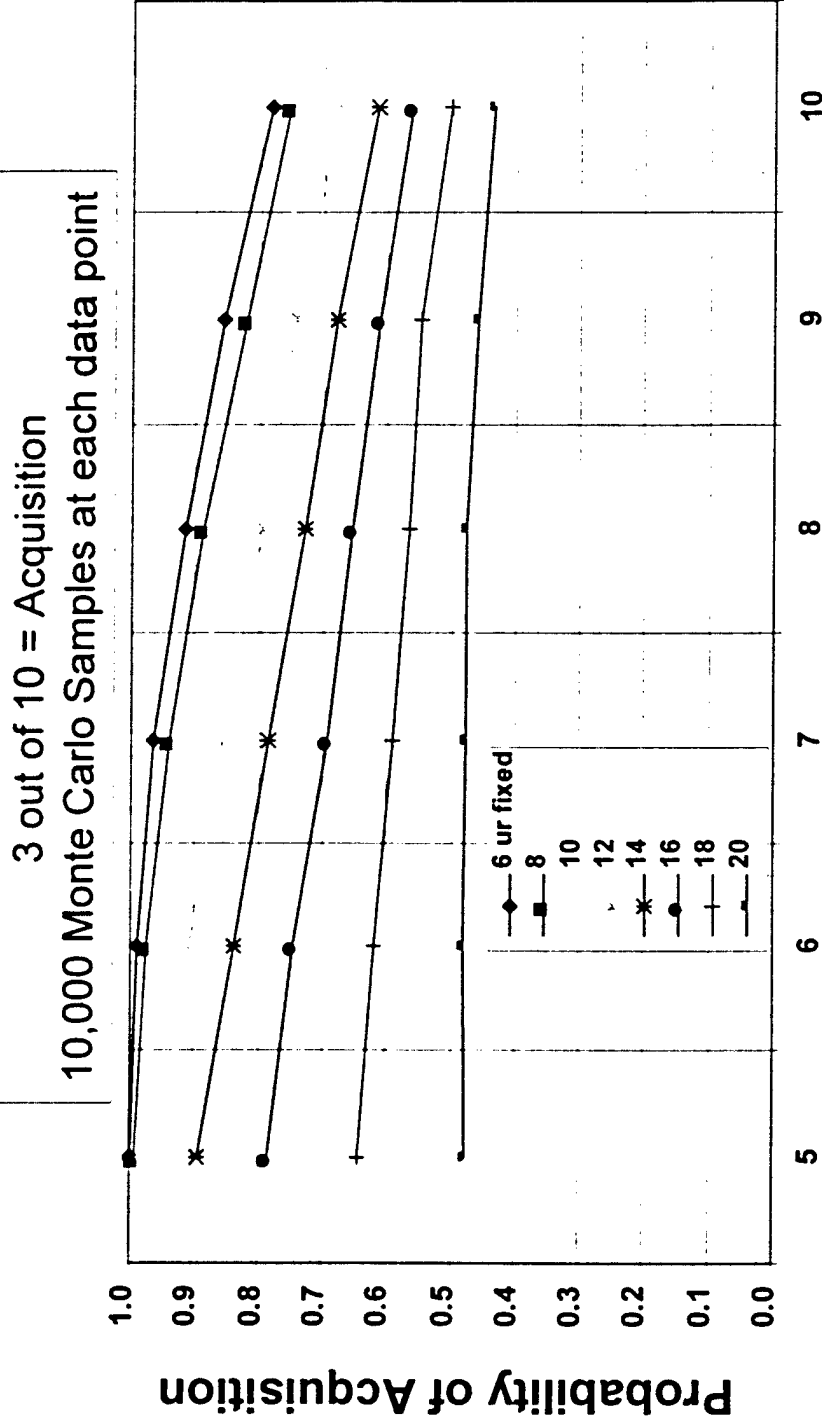
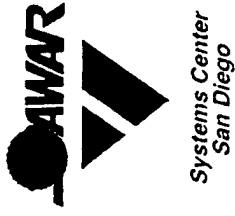


Size of Tracking Error and Control Error Individually (urad)





Acquisition for 16% 2x0.4m target Attempts made at 400, 375, 350 km

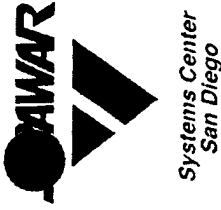


Size of Tracking Error and Control Error Individually (urad)

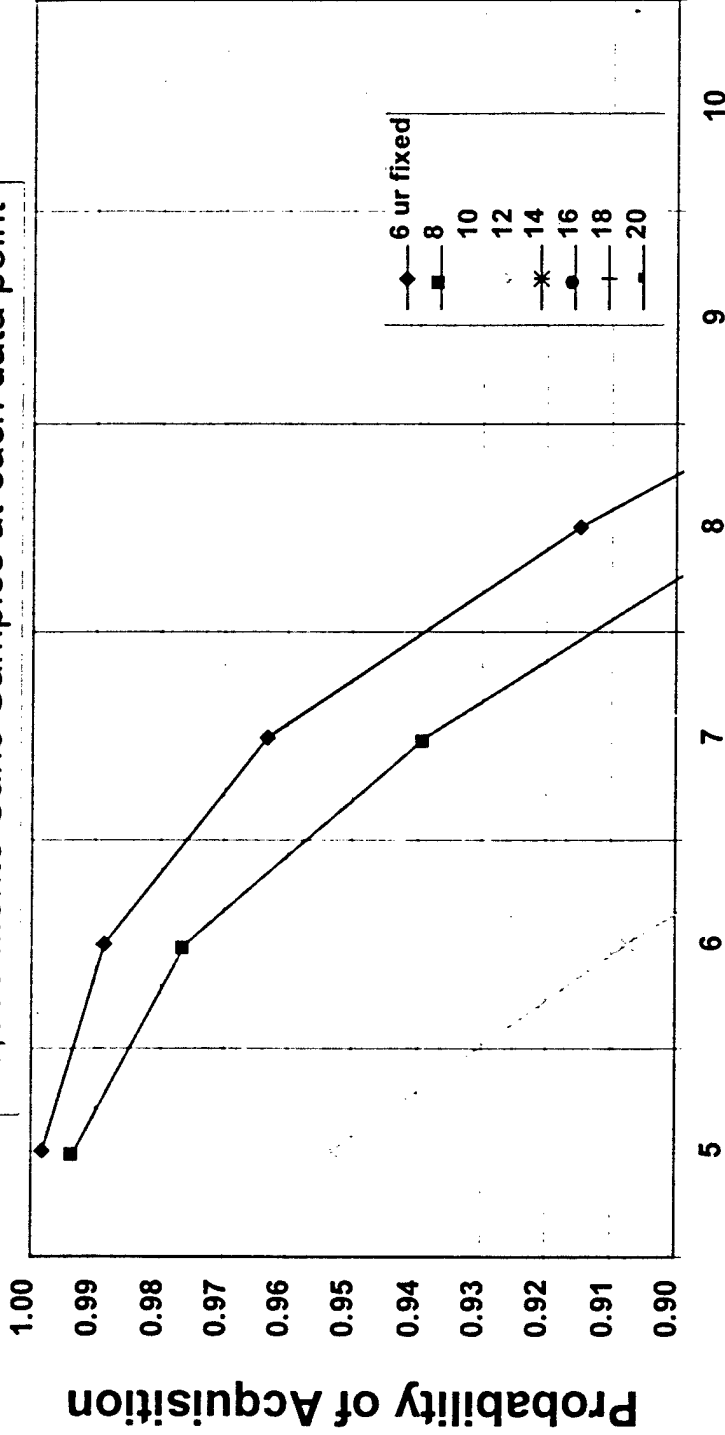




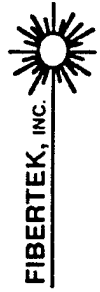
Acquisition for 16% 2x0.4m target Attempts made at 400, 375, 350 km



3 out of 10 = Acquisition
10,000 Monte Carlo Samples at each data point



Size of Tracking Error and Control Error Individually (urad)



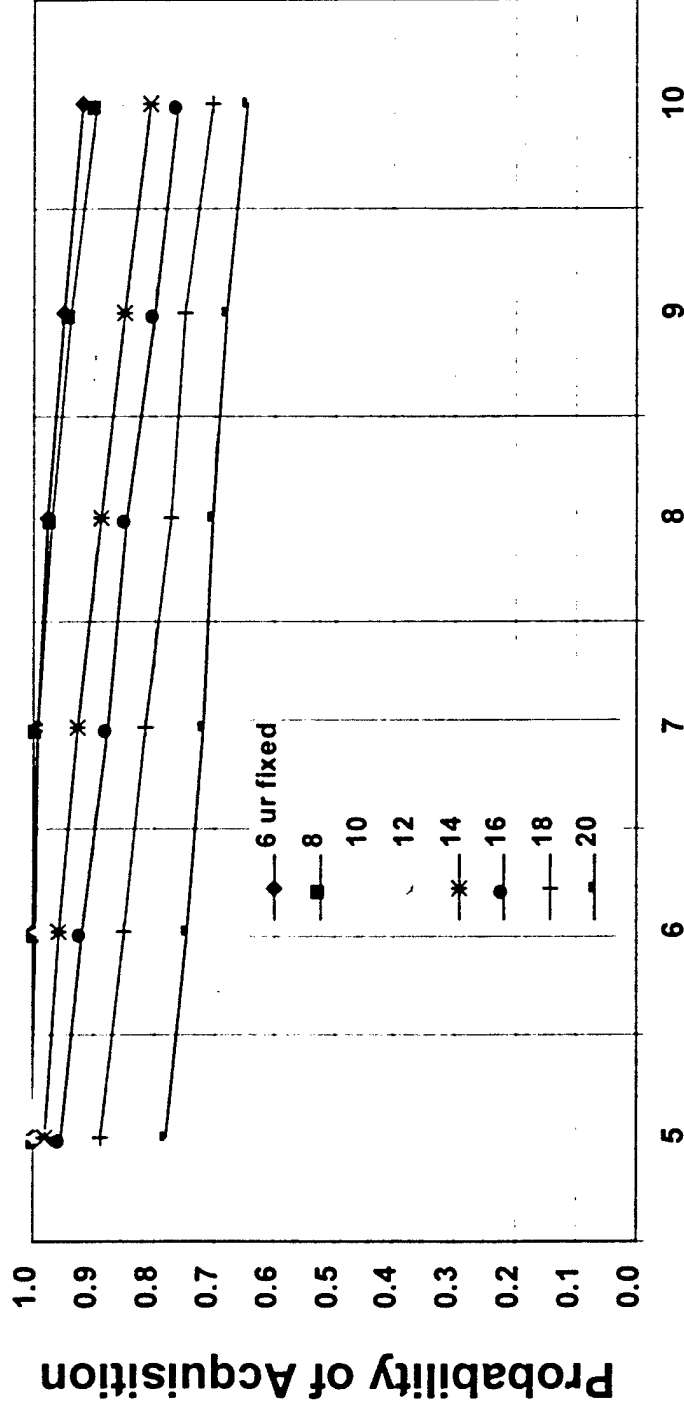


Acquisition for 24% 2x0.4m target Attempts made at 400, 375, 350 km



Systems Center
San Diego

3 out of 10 = Acquisition
10,000 Monte Carlo Samples at each data point



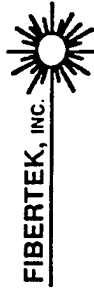
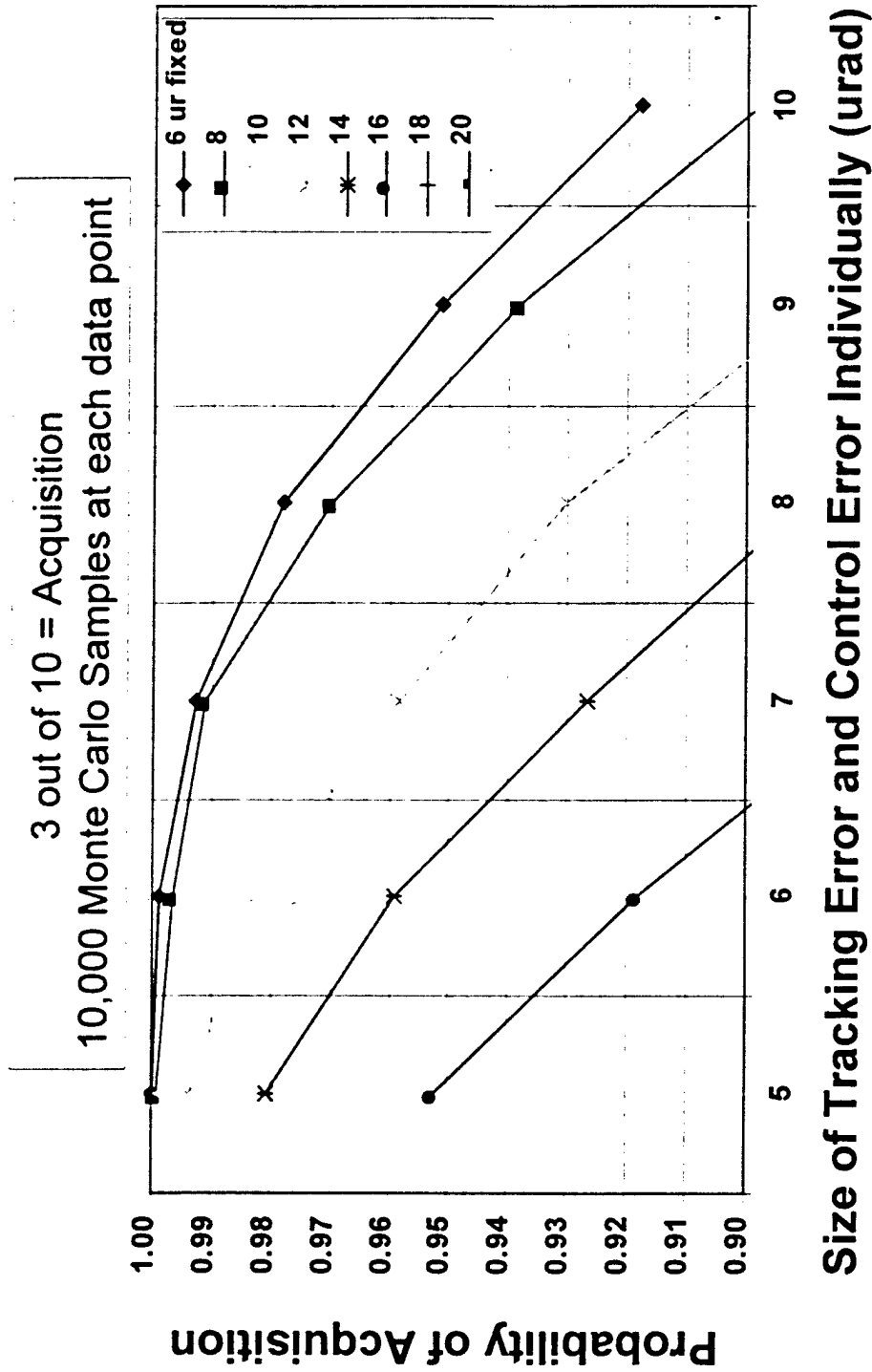
Size of Tracking Error and Control Error Individually (urad)





Systems Center
San Diego

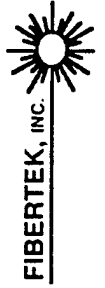
Acquisition for 24% 2x0.4m target Attempts made at 400, 375, 350 km

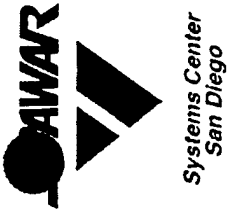




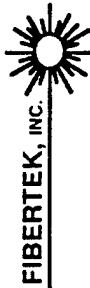
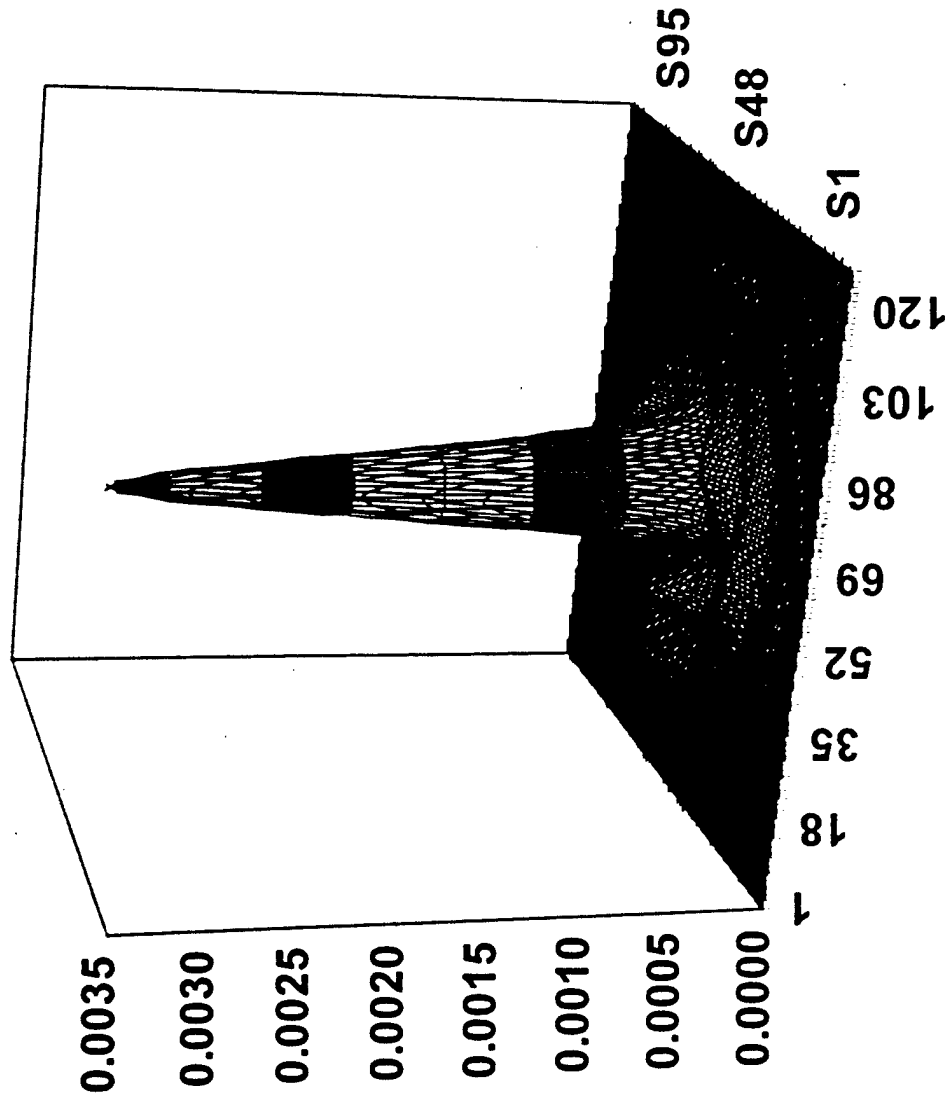
LADAR System Analysis

- M-O-I methods for coping with wavefront error explored
- New wavefront error tolerant orientation angle algorithm developed





0.1 λ rms Point Spread Function



FIBERTEK, INC.



The Electro-Optics Organization



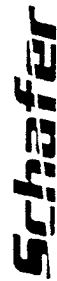
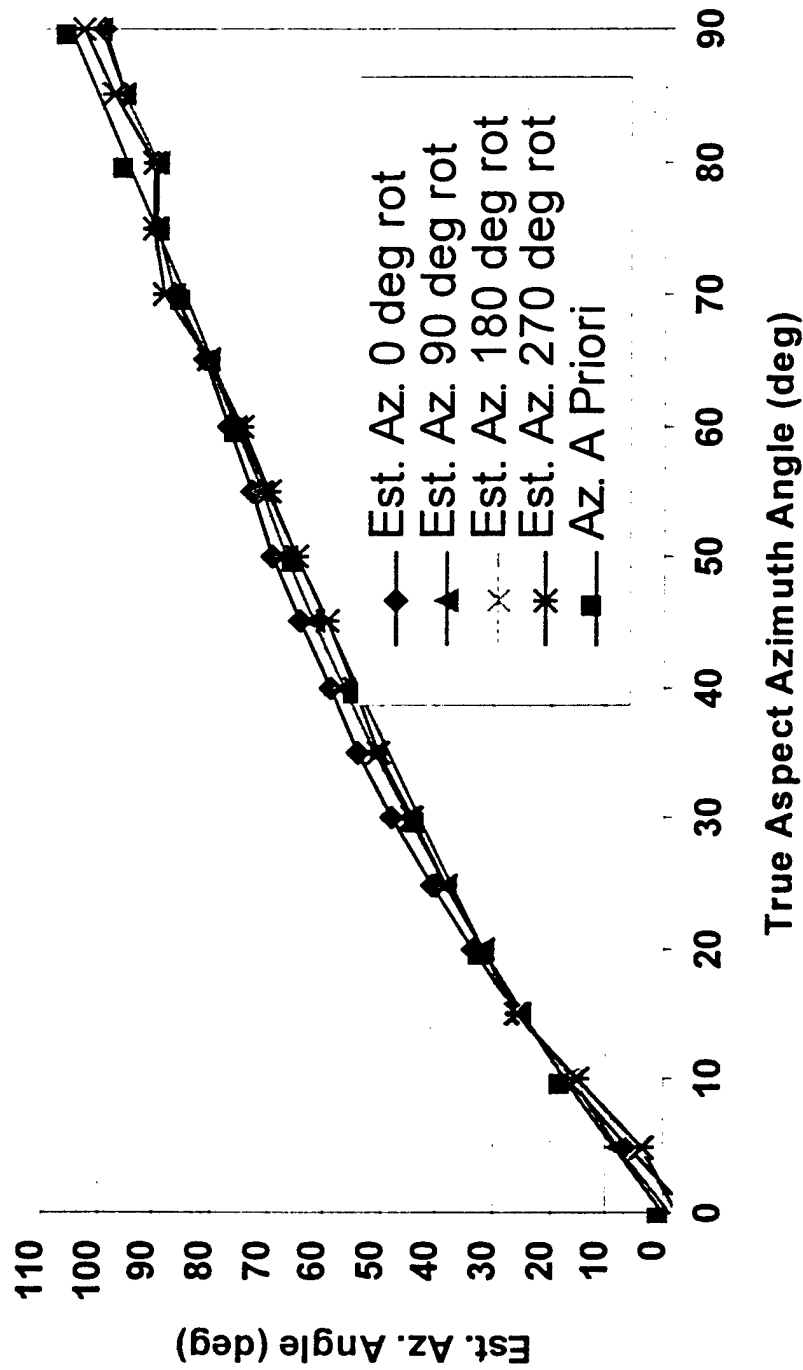
Thermo-Trex Corporation

Schafer

Malcev



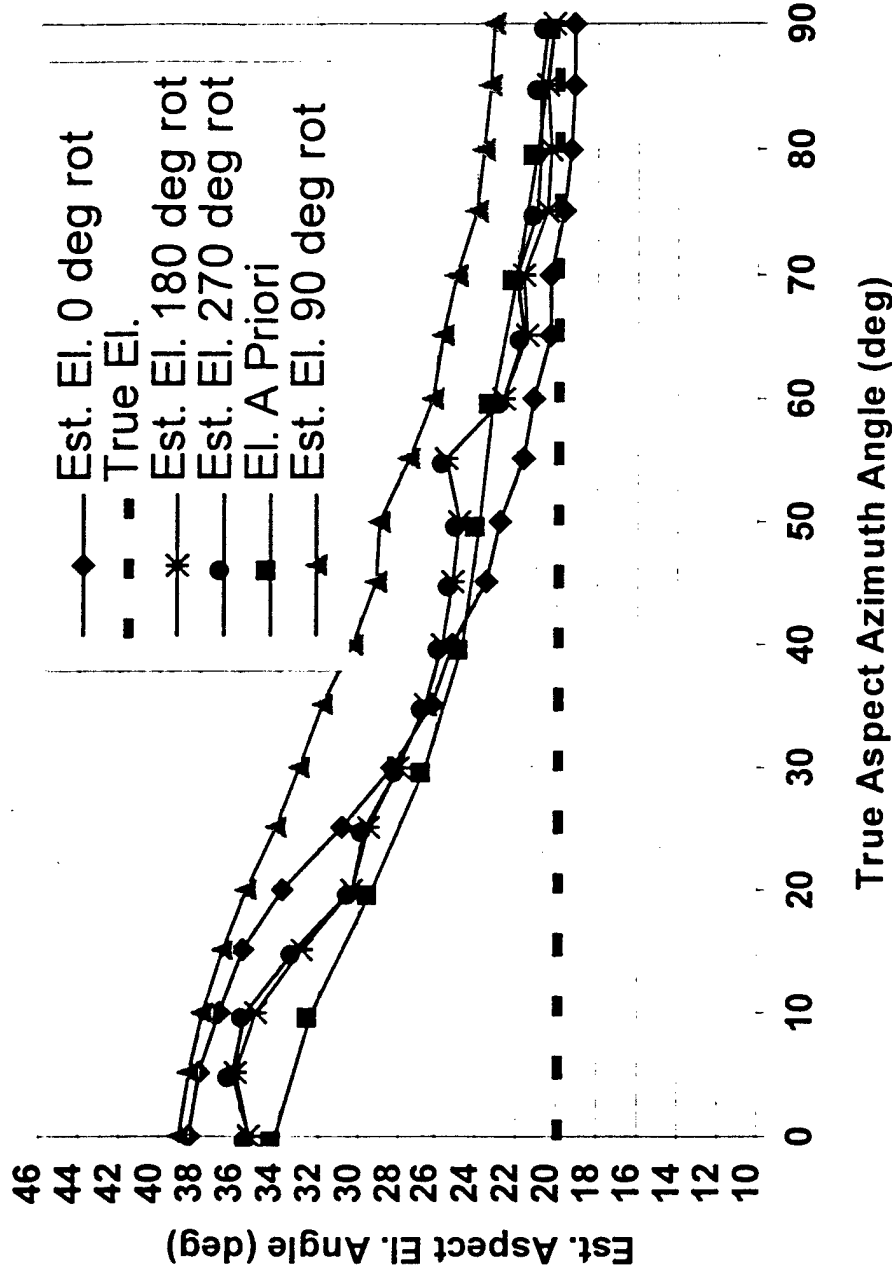
Aspect Azimuth Angle Estimates 160 km 0.05λ rms Threshold = 0.01 2x1m Cone





Systems Center
San Diego

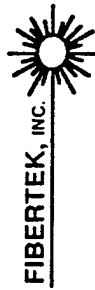
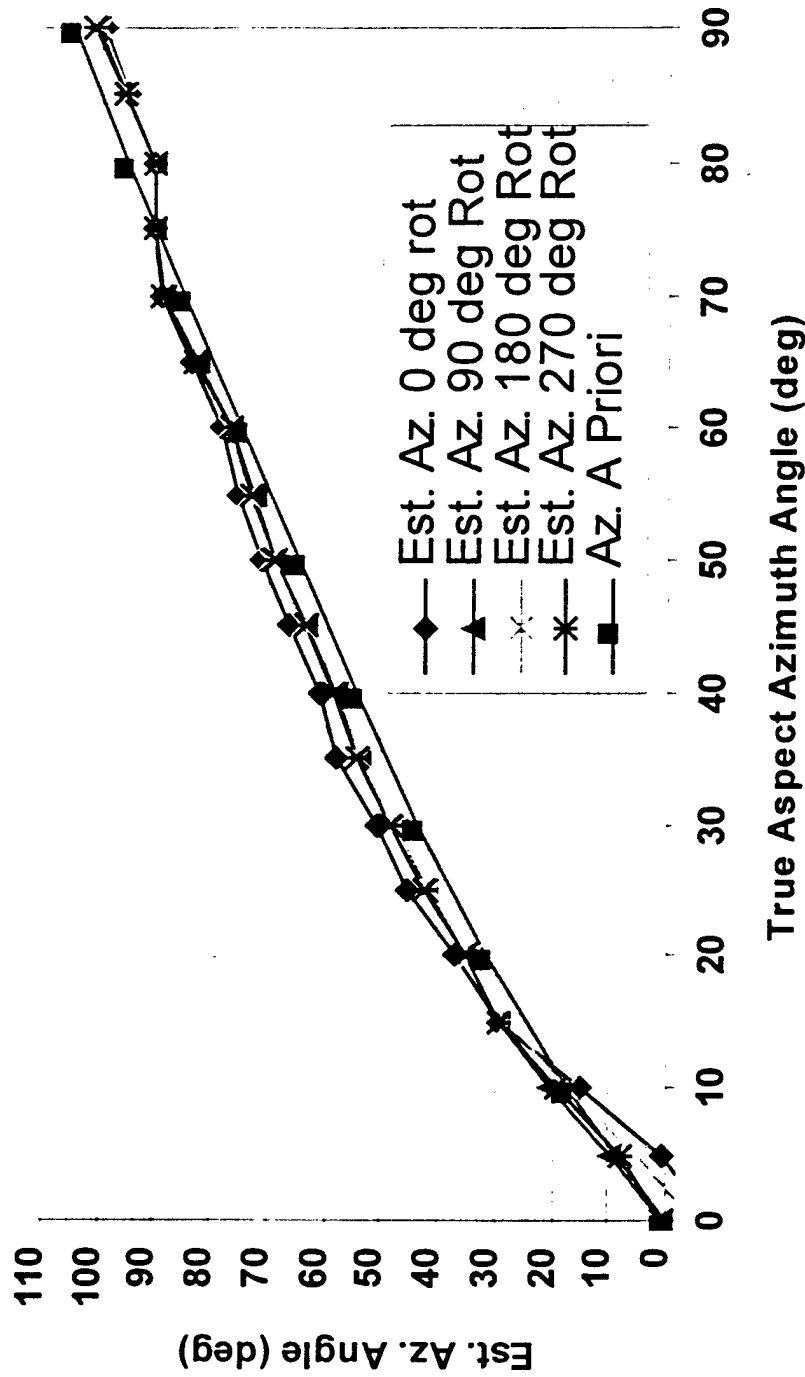
Aspect Azimuth Angle Estimates 160 km 0.05λ rms Threshold = 0.01 2x1m Cone

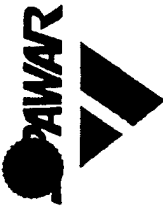




Aspect Azimuth Angle Estimates 160 km 0.20λ rms Threshold = 0.01 2x1m Cone

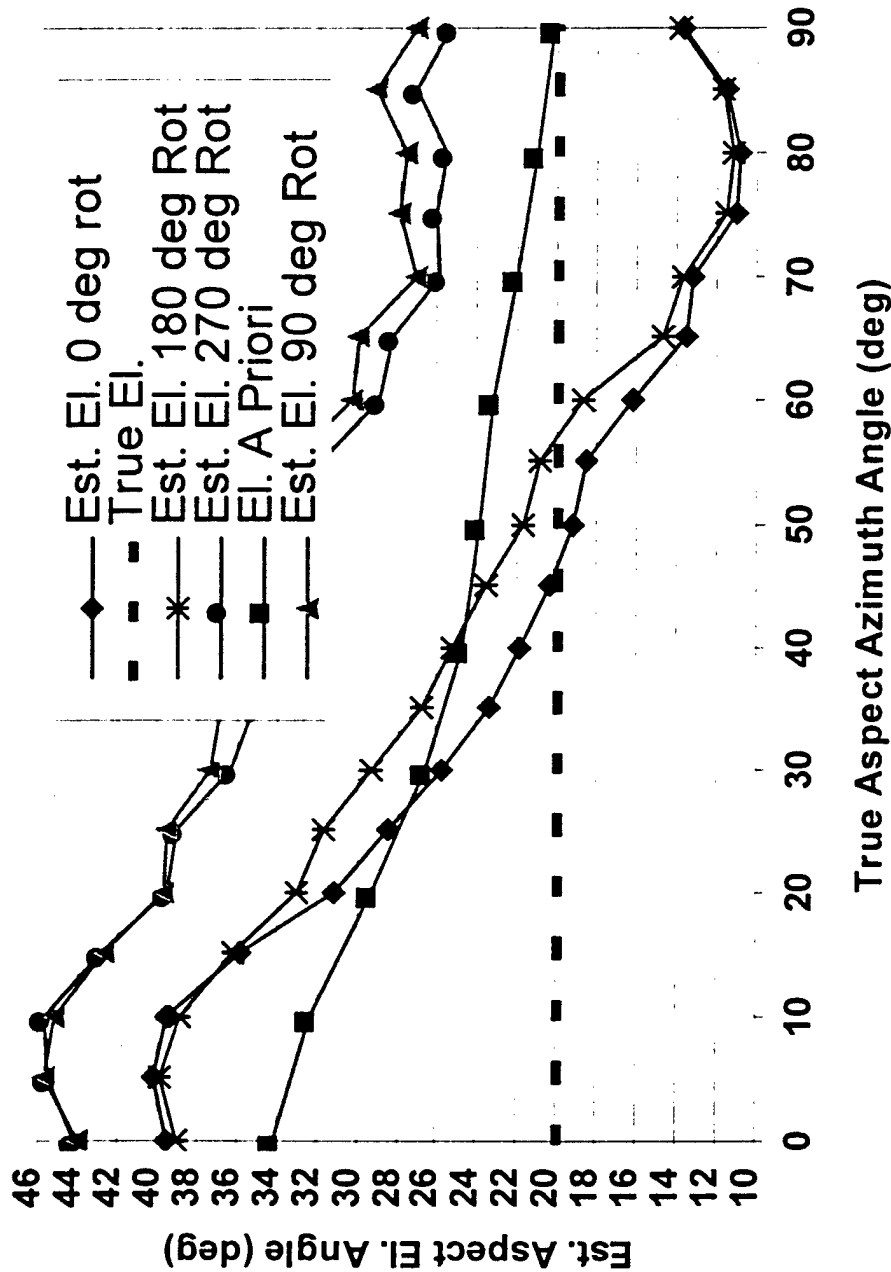
Systems Center
San Diego





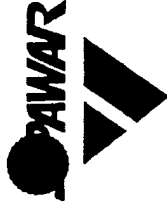
Systems Center
San Diego

Aspect Azimuth Angle Estimates 160 km 0.20λ rms Threshold = 0.01 2x1m Cone





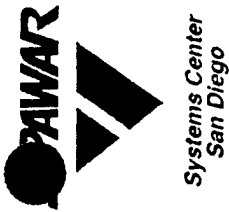
Solution Found For Wavefront Error Impact on LADAR Discrimination



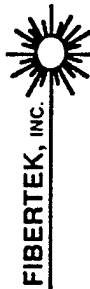
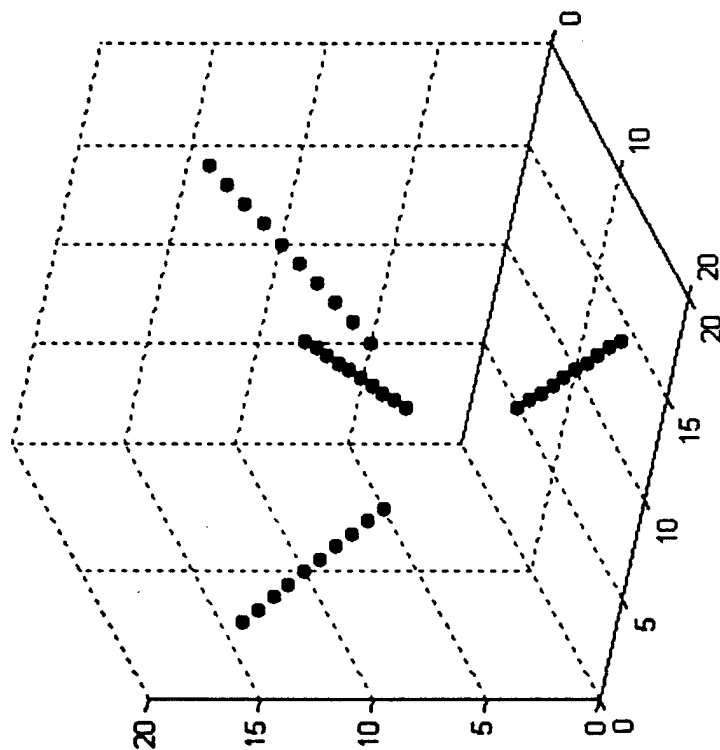
Systems Center
San Diego

- Non-circularly symmetric wavefront error served to greatly complicate utilization of M-O-I algorithm for target body orientation determination
- Using first rather than second moment of intensity provides effective means of coping with wavefront error
- First moment (intensity center of gravity in each range bin) is very simple to calculate and diagnose in the event of poor performance
- Maximum wavefront error tolerable before new algorithm fails is currently being investigated





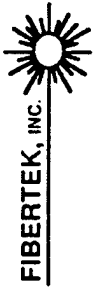
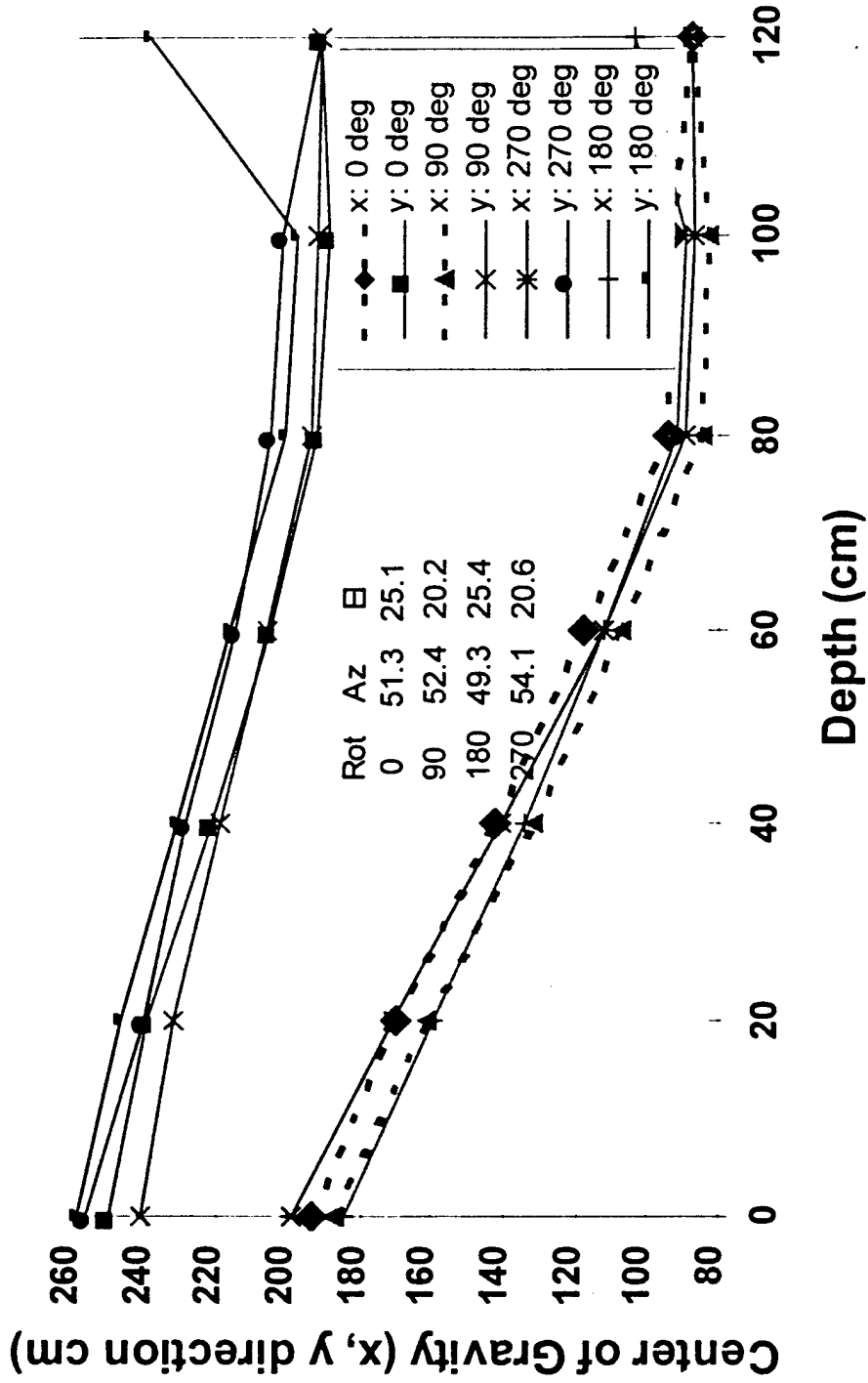
Centerline of Cone Body





Systems Center
San Diego

Image Projection on xz(Az),yz(EI) Planes 45 deg Az 20 deg EI 0.20λ rms



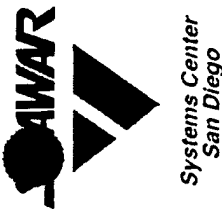
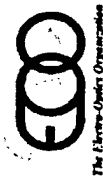
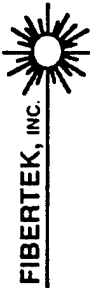
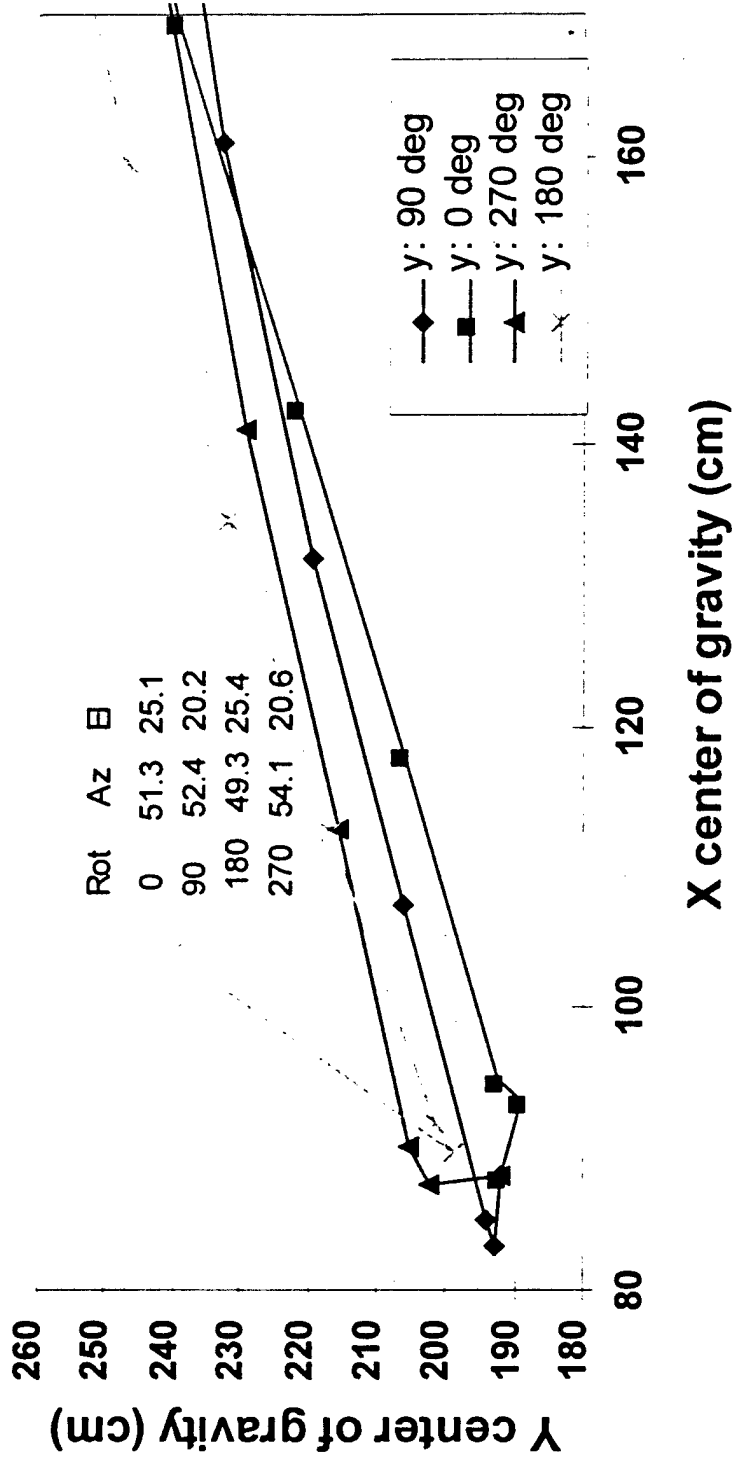
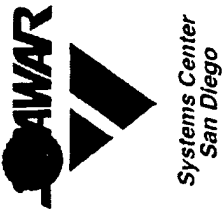


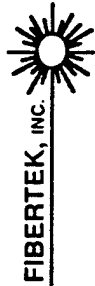
Image Projection on xy(EI) Plane 45 deg Az 20 deg El 0.20λ rms





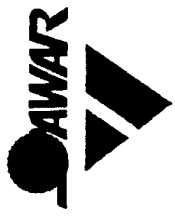
LADAR System Analysis

- Amount of jitter produced by registration process determined





Accuracy of Shot-to-Shot Registration Quantified



Systems Center
San Diego

- For proper accumulation of threshold crossings in an individual voxel to determine intensity, each shot in a group of 10-25 shots must be aligned or registered within that voxel
- Even without jitter, speckle causes voxels to swing between zero and multiple photoelectrons, shot to shot, causing apparent motion of the image center of gravity
- Monte Carlo simulation indicates registration will localize returns within x and y dimensions of pixel. Some spillover between adjacent range bins may occur.
- Effect on discrimination algorithm performance is being assessed, but should be slight

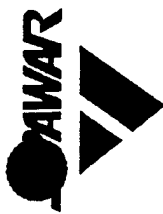


Schafer

vac



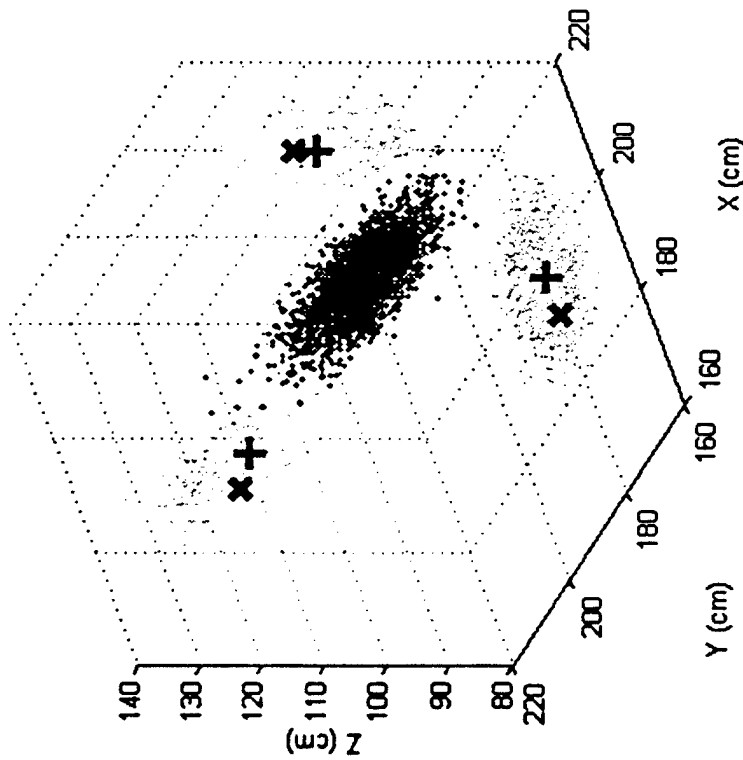
Shot to Shot Registration With "Binary" Voxel Weighting Displays Aliasing



Systems Center
San Diego

2500 Shots; Speckle Included

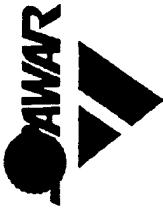
DTP Centroids: 2500 shots; X,Y,Z Means: 197.5408, 179.8924, 109.1336 (Nom: 191.1672, 180, 112.7448)



Range: 160 km
Azimuth: 30 deg
Elevation: 0 deg

X: Nominal Centroid
+: Average Centroid



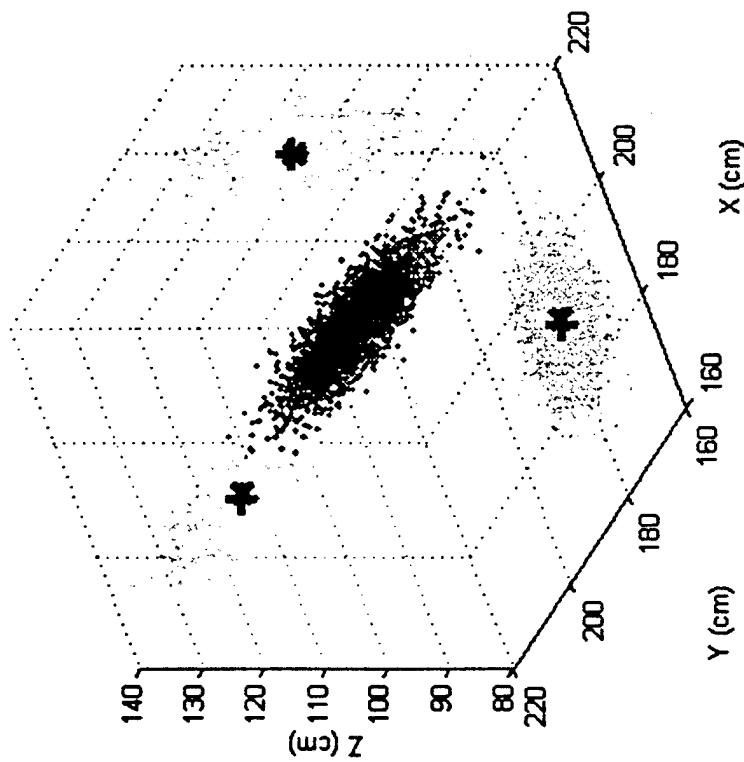


Systems Center
San Diego

Registration With Threshold Based Weighting Is Preferable

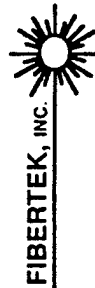
2500 Shots; Speckle Included

DITP Centroids: 2500 shots, X,Y,Z Means: 190.1726, 179.9694, 113.2377 (Nom: 191.1672, 180, 112.7448)



Range: 160 km
Azimuth: 30 deg
Elevation: 0 deg

X: Nominal Centroid
+: Average Centroid

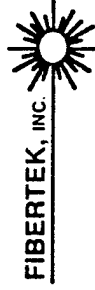




LADAR System Analysis

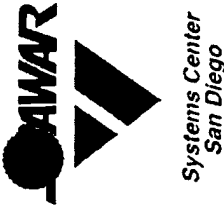


- Impact of x-y jitter on M-O-I target orientation angles assessed



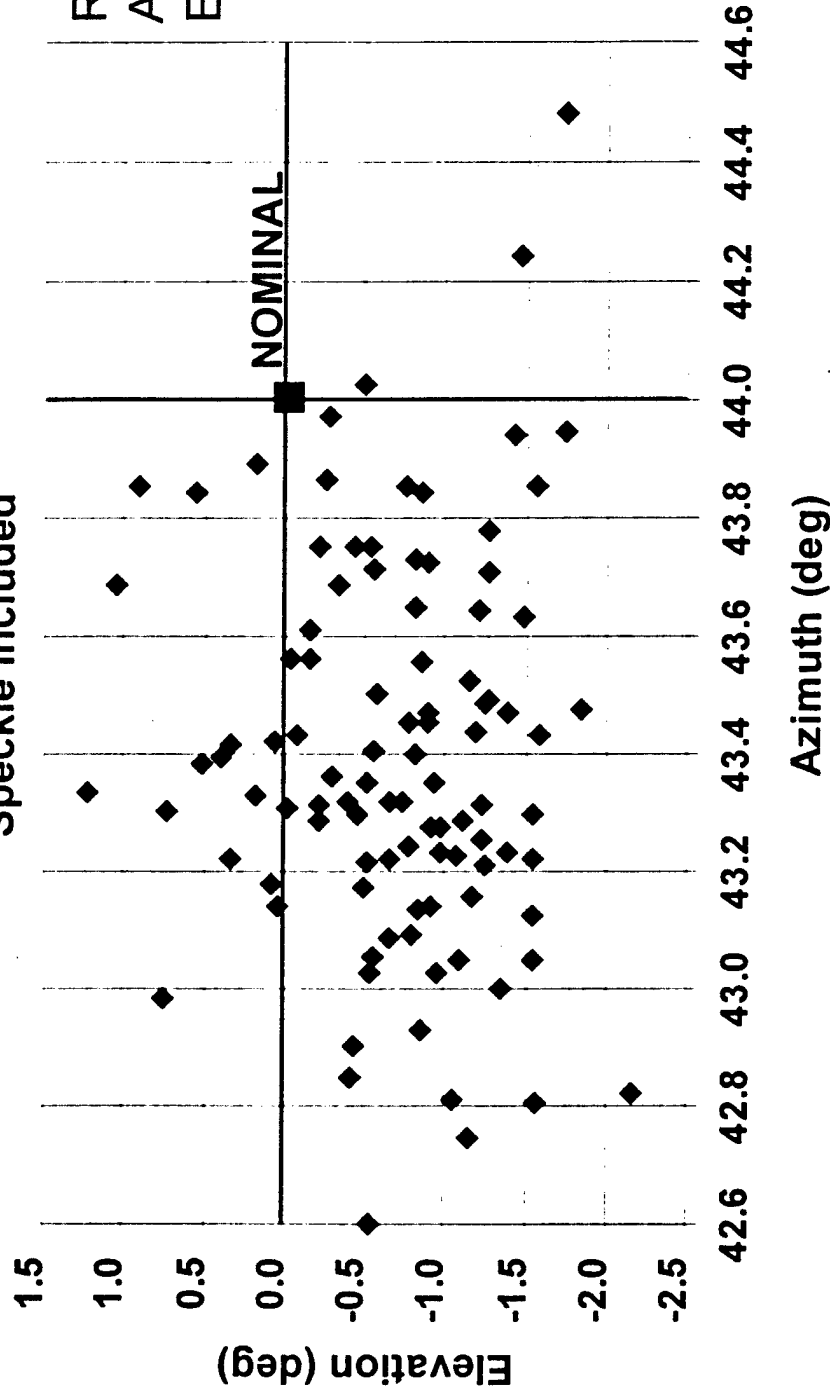


Jitter Has Minimal Effect on M-O-I Estimates of RV Orientation



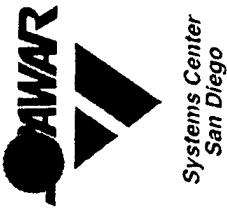
Jitter Standard Deviation = 1 ur

190 groups of 25 shots
Jitter Standard Deviation = 1 ur
Speckle Included

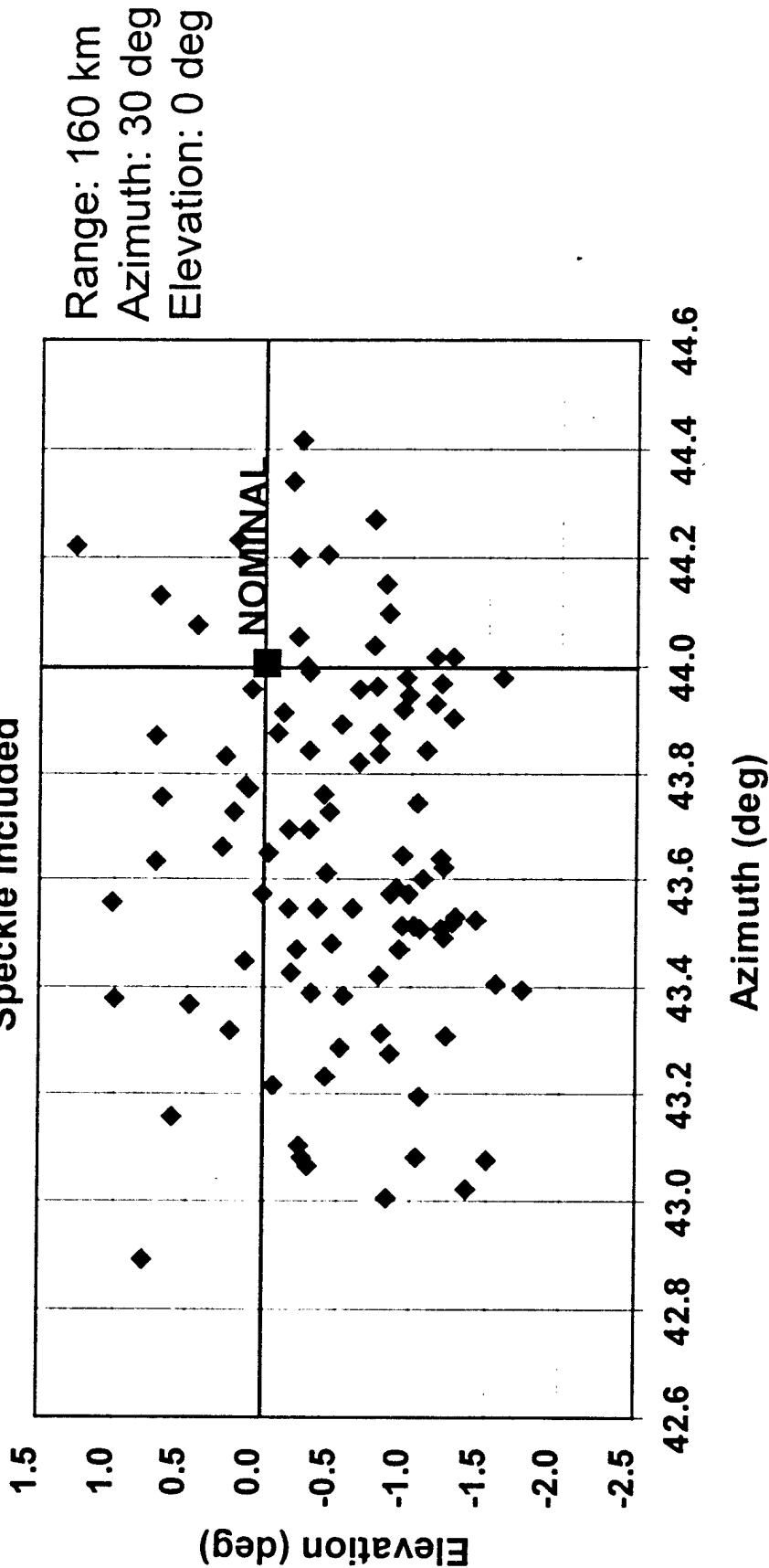




Jitter Has Minimal Effect on M-O-I Estimates of RV Orientation



Jitter Standard Deviation = 5 ur
100 groups of 25 shots
Speckle Included



Appendix N

NAVAL RESEARCH LABORATORY NAVAL CENTER FOR SPACE TECHNOLOGY

DITP System Specification

NCST-S-DT001

Approved By: _____ Date: _____
C Merk, TBI Project Manager

Draft Input To NRL

DISTRIBUTION STATEMENT C: Distribution authorized to U.S. Government agencies and their contractors; Administrative or Operational Use. Other requests for this document shall be referred to Mr. C. Merk, Code 8222, Naval Research Laboratory, 4555 Overlook Avenue, S.W., Washington, D.C. 20375-5000.

4555 Overlook Avenue, S.W.
Washington, D.C. 20375-5000

Table of Contents

1.	INTRODUCTION.....	9
1.1	Scope.....	10
1.2	Definitions	10
1.3	DITP System Description	10
1.3.1.1	DITP Flight Target System (FTS)	10
1.3.1.2	DITP Flight System (FS)	11
1.3.1.3	DITP Launch Vehicle System	11
1.3.1.4	Test Range	11
2.	APPLICABLE DOCUMENTS.....	12
2.1	Government Documents	12
2.2	Non-Government Documents	12
2.3	Codes and Standards	12
2.4	Program Documents	12
3.	REQUIREMENTS.....	13
3.1	System Definition	13
3.1.1	DITP Overview	13
3.1.1.1	Technology Development.....	13
3.1.1.1.1	Technology Development Objectives	13
3.1.1.2	Technology Demonstration.....	13
3.1.1.2.1	Technology Demonstration Objectives	13
3.1.2	DITP Demonstration Scenarios	14
3.1.2.1	DITP Demonstration Goals	14
3.1.2.2	Demonstration Scenario Constraints	15
3.1.2.2.1	Closing Velocity.....	15
3.1.2.2.2	Exoatmospheric Observation Altitude	15
3.1.2.2.3	Solar Exclusion Angle.....	15
3.1.2.2.4	Lunar Exclusion Angle.....	Error! Bookmark not defined.
3.1.2.2.5	Earth Exclusion Angle.....	15
3.1.2.2.6	Other Exclusion Angles.....	15
3.1.2.2.7	Flight Scenarios.....	Error! Bookmark not defined.
3.1.2.2.7.1	Angle Between Seeker Line of Sight and Target Coning Axis	16
3.1.2.2.7.2	Collision Avoidance.....	16
3.1.2.2.7.3	Vehicle(s) Recovery.....	16
3.1.2.2.8	Position Determination.....	16
3.1.2.2.8.1	Flight System Position Determination.....	16
3.1.2.2.8.2	Target System Position Determination.....	16
3.1.3	System States and Modes	16
3.1.3.1	Dormant State	17
3.1.3.2	Operational State Modes.....	18
3.1.3.2.1	Operational State - Flight Demonstration Modes	18
3.1.3.3	Operational State - Second Flight Demonstration	20
3.1.3.4	Operational State - Ground Demonstration Modes	20
3.1.4	System Configuration	22
3.1.4.1	Flight Target System.....	22
3.1.4.1.1	Target Object Sets	22
3.1.4.1.2	Minimum Set.....	22
3.1.4.1.3	Enriched Target Set	23
3.1.4.1.4	Target Bus/Dispenser	23
3.1.4.1.5	Supporting Subsystems	23
3.1.4.1.6	Ground Support Equipment (GSE)	24
3.1.4.2	DITP Flight System (FS).....	24

3.1.4.2.1	Seeker Subsystems	24
3.1.4.2.2	Bus Subsystems	24
3.1.4.2.3	Supporting Subsystems	25
3.1.4.2.4	Ground Support Equipment (GSE)	25
3.1.4.3	Launch Vehicle System	25
3.1.4.4	Test Range	25
3.1.4.4.1	Test Range Facilities	25
3.1.4.4.2	Test Range Instrumentation	26
3.1.4.4.3	DITP-Unique Instrumentation	26
3.1.4.4.4	Ground Support Equipment	26
3.1.5	Interface Requirements	26
3.1.5.1	DITP Interfaces With Non-DITP Sites and Organizations	26
3.1.5.2	Internal Interfaces	26
3.2	System Characteristics	26
3.2.1	Design Lifetime	26
3.2.1.1	Dormant State Lifetime	26
3.2.1.2	Operating Lifetime	27
3.2.2	Physical Requirements	27
3.2.2.1	Target System Requirements	27
3.2.2.2	Flight System Requirements	27
3.2.2.2.1	Probability of Target Designation	27
3.2.2.2.2	Acquisition Ranges	27
3.2.2.2.2.1	Passive Sensor Acquisition Range – Flight Demonstration	27
3.2.2.2.2.2	LADAR Acquisition Range – Flight Demonstration	27
3.2.2.2.3	Optics Field of View (FOV) and Field of Regard (FOR)	27
3.2.2.2.3.1	Telescope Field of View (FOV)	27
3.2.2.2.3.2	Passive Sensor Field of Regard (FOR)	27
3.2.2.2.3.3	Passive Sensor Field of View	27
3.2.2.2.3.4	LADAR Field of Regard	27
3.2.2.2.3.5	LADAR Field of View	27
3.2.2.2.4	Pointing Accuracy	27
3.2.2.2.4.1	Passive Sensor Angular Pointing Accuracy	27
3.2.2.2.4.2	LADAR Tracking Precision	28
3.2.2.2.4.3	Pointing and Tracking Handover Error Budget	28
3.2.2.2.4.3.1	Optical System Handover Error	28
3.2.2.2.4.3.2	Centroiding and Tracking Handover Error	28
3.2.2.2.4.3.3	Control Residual	28
3.2.2.2.4.4	Seeker Boresight Pointing Accuracy	28
3.2.2.2.5	Passive Sensor Instantaneous Field Of View	28
3.2.2.2.6	LADAR Range Resolution	28
3.2.2.2.7	LADAR Instantaneous Field of View	28
3.2.2.2.8	Pointing - Number of Targets	28
3.2.2.2.9	Seeker Jitter Budget	28
3.2.2.2.9.1	IOS Jitter	28
3.2.2.2.9.2	Passive Sensor Jitter	28
3.2.2.2.9.3	LADAR Jitter (Transmitter)	28
3.2.2.2.9.3.1	Laser Jitter	28
3.2.2.2.10	FS Bus Inertial Pointing Accuracy	28
3.2.2.2.11	FS Bus Angular Acceleration	28
3.2.2.2.12	Seeker Maximum Aperture	29
3.2.2.2.13	FS Mass Properties	29
3.2.2.2.13.1	Seeker Subsystems Mass	29
3.2.2.2.13.2	FTS and FS Centrs of Mass	29
3.2.2.2.14	FTS and FS Volume	29
3.2.2.2.15	FS Electrical Power	29
3.2.2.2.16	FS Thermal Management	29
3.2.2.2.16.1	FS Thermal Environment Stability	29
3.2.2.2.16.2	Subsystems Thermal Management	29

3.2.2.2.16.3	FS Thermal Management.....	29
3.2.2.2.17	FS Bus Communications	29
3.2.2.2.18	FS Data Processing.....	29
3.2.2.2.18.1	Seeker Subsystems Data Availability	29
3.2.2.2.18.2	FS Bus Flight Data Recording	30
3.2.2.3	Launch Vehicle System Requirements.....	30
3.2.2.4	Test Range Requirements	30
3.2.2.4.1.1	Communications Uplink	30
3.2.2.4.1.2	Communications Downlink	30
3.2.2.4.1.3	Test Range Data Storage.....	30
3.2.2.4.1.4	Test Range Communication Protocol	30
3.2.3	Environmental Conditions	30
3.2.4	Design and Construction.....	30
3.2.4.1	Parts, Materials, and Processes.....	30
3.2.4.2	Failure Reporting and Corrective Action System.....	32
3.2.4.3	Part Stress Derating	32
3.2.4.4	Soldering and Other Processes	32
3.2.4.5	Electrostatic Discharge Sensitive Parts	32
3.2.5	Electromagnetic Environment	32
3.2.5.1	Electromagnetic Compatibility (EMC)	32
3.2.5.2	Corona and Triboelectric Suppression.....	33
3.2.5.3	Bonding.....	33
3.2.5.4	Lightning Protection and Grounding	33
3.2.5.4.1	Lightning Protection	33
3.2.5.4.2	Premature Launch or Detonation	33
3.2.5.4.3	No Launch in Presence of Lightning.....	33
3.2.6	electromagnetic interference.....	33
3.2.7	Workmanship.....	33
3.2.7.1	Interchangeability	33
3.2.7.2	Nameplate and Product Marking	34
3.2.8	Safety	34
3.2.8.1	Safety From Emissions	34
3.2.8.2	Critical Safety Hazards	34
3.2.8.3	Personnel Safety	34
3.2.8.4	Test Range Safety	34
3.2.8.5	LADAR Safety.....	34
3.2.9	Nuclear Control.....	34
3.2.10	System Security	34
3.3	Computer Resources	35
3.4	Standards of Manufacture	35
3.4.1	Contamination Control and Cleanliness	35
3.4.1.1	Protection From Contamination	35
3.4.1.2	Contamination Control Guidelines	35
3.4.2	Connectors	35
3.4.3	Positive Locking Devices	35
3.5	Documentation.....	35
3.5.1	Specifications.....	36
3.5.2	Drawings	36
3.5.3	Software Support Documentation.....	36
3.5.4	Test Plans and Procedures	36
3.5.5	Structural Analysis Plan	36
3.6	Logistics.....	36
3.6.1	Support Concept	36
3.6.1.1	Support Facilities.....	36
3.6.1.2	Hardware Support	37
3.6.1.3	Computer Software Support	37
3.6.1.4	Personnel and Training	37

3.6.2	Maintenance Concept	37
3.7	Quality Factors.....	37
3.7.1	Survivability/Hardness	37
3.7.2	Hazardous Material.....	37
3.7.3	Other Quality Factors.....	37
3.7.3.1	Guidelines for Packaging and Shipping	37
3.7.4	Precedence and Criticality of Requirements	37
4.	QUALIFICATION REQUIREMENTS.....	38
4.1	Verification Methods	38
4.1.1	Analysis	38
4.1.2	Demonstration.....	39
4.1.3	Inspection.....	39
4.1.4	Test.....	39
4.1.4.1	Assembly Level Tests	39
4.1.4.2	Assembly Feasibility Test.....	39
4.1.4.3	Assembly Design Verification Tests (DVT)	39
4.1.4.4	Assembly Qualification Tests.....	39
4.1.4.5	Assembly Acceptance Tests	39
4.1.4.6	Subsystem Acceptance Test.....	40
4.1.4.7	System Level Test.....	40
5.	NOTES.....	40
5.1	DRD Cross Reference.....	40
5.2	Table of Acronyms	41
5.3	Glossary	44
6.	APPENDIX A - REQUIREMENTS VERIFICATION MATRIX	47

List of Figures

<i>Figure 1-1 DITP Configuration Items</i>	12
<i>Figure 3.1-1 DITP Ground Demonstration Mode Transitions</i>	Error! Bookmark not defined.
<i>Figure 3 1-2 DITP Flight Demonstration Mode Transitions</i>	21
<i>Figure 3 1-4 DITP System in Launch Configuration</i>	24

List of Tables

<i>Table 3.1-1 DITP Demonstration Specific Goals</i>	14
<i>Table 3.1.5-1 Target Set for First DITP Flight Demonstration</i>	22
<i>Table 3.1.5-2 Enriched Target Set for Second DITP Flight Demonstration</i>	23

Index of TBD/TBR

<i>(TBD) resolve PSS acquisition range</i>	14
<i>(TBD) resolve solar and lunar exclusion angle uncertainties</i>	15
<i>(TBD) Need figure</i>	16
<i>(TBD) Resolve position accuracies for FS and FTS</i>	16
<i>(TBD) need batteries, ordnance storage and T&H discussion from Chris</i>	17
<i>(TBD) resolve question of when FTS despin occurs (launch mode or Initialize mode?</i>	18
<i>(TBD) paragraph needs review</i>	19
<i>(TBD) Suggest adding this paragraph to Flight Demo Section also, per suggestion by FP&A (i.e., Don Fronterhouse)</i>	19
<i>(TBD) Also suggest adding this paragraph to Flight Demo Section, per request from FP&A (i.e., Don Fronterhouse)</i>	21
<i>(TBD) Need launch packaging figure</i>	24
<i>(TBD) Need descriptions of Test Range items.</i>	25
<i>(TBD) Need TRD #</i>	27
<i>(TBD) Need to resolve prob of target designation</i>	27
<i>(TBD) Need to resolve PSS acquisition range</i>	27
<i>(TBD) Need top down definition of pointing accuracy</i>	27
<i>(TBD) Need top down allocation of jitter</i>	28
<i>(TBD) need final review of thermal mgmt section</i>	29
<i>(TBD) Need discussion of LV requirements</i>	30
<i>(TBD) Need final review by J. Chapman</i>	30
<i>(TBD) Need reference from Jack</i>	31
<i>(TBD) Need to resolve where EMC req reside—here or in ERD?</i>	32
<i>(TBD) Need to resolve where EMC req reside—here or in ERD?</i>	33

<i>(TBD) Suggestion to add "satellite predictive avoidance" for outgoing LADAR pulses per W. Von Worley (note: Hess had Space Command waiver for ASTP)</i>	34
<i>(TBD) Need updated Spec Tree</i>	38
<i>(TBD) Need review and additional definitions</i>	44

1. INTRODUCTION

This System Specification describes the Naval Research Laboratory's (NRL) system requirements for the conduct and implementation of a Discriminating Interceptor Technology Program (DTHP), under the aegis of the Ballistic Missile Defense Organization (BMDO) Advanced Technology Director (TOS). DTHP is being implemented with the prime objective of supporting both Theater Missile Defense (TMD) and National Missile Defense (NMD) interceptor seeker upgrade needs. DTHP is developing advanced technology sensors and a sensor fusion processor. It will demonstrate, for the first time, data fusion from miniaturized, collocated, dissimilar sensors on an interceptor platform. During ground and flight demonstrations, DTHP will demonstrate interceptor-based discrimination against simulated threats. DTHP includes Executive Agents (EA) identified by the BMDO TOS to provide government furnished equipment (GFE) as well as technical expertise to support the successful completion of the overall program goals. BMDO TOS, NRL, EA, and contract support representatives will be called upon to participate in the overall program management.

The EAs will develop the following advanced seeker technology subsystems:

- Passive Sensor Subsystem (PSS). Air Force Research Laboratory/VSSS (Kirtland) (AFRL/VSSS (Kirtland));
- Laser Radar Subsystem (LADAR). U. S. Army Space and Missile Defense Command/TC/SR (Huntsville) (USASMDC/TC/SR (Huntsville));
- Fusion Processor and Algorithms Subsystem (FP&A). Air Force Research Laboratory/IFEA (Rome) (AFRL/IFEA Rome)).

Passive Sensor Subsystem (PSS) - The PSS is a multi-color infrared (IR) sensor. It consists of a 256x256 pixel medium wavelength IR (MWIR) and long wavelength IR (LWIR) HgCdTe focal plane array with read-out integrated circuit and a malleable signal processor (MSP) for signal conditioning, integer signal processor, sensor controller, steering mirror, and interface to the fusion processor via Myrinet crossbar network.

Laser Radar Subsystem (LADAR) - The LADAR subsystem is a short pulse, direct detection Angle-Angle-Range (AAR) imaging LADAR. It consists of a frequency-doubled Nd:YAG laser transmitter, a multi-pixel intensified photo diode (IPD) receiver with a 10x10 pixel focal plane array, steering mirror, robust discrimination algorithms, a thermal battery, a LADAR control MSP and associated optics.

Fusion Processor & Algorithms (FP&A) Subsystem - The FP&A is a gigaflop-capable floating point processor consisting of wafer-scale signal processors (WSSP) communicating through a crossbar Myrinet to the sensor. The majority of computer processing and signal processing for the seeker technology subsystems are performed by the FP&A. The algorithms consist of most of the software/firmware required to provide acquisition, tracking, and discrimination of target clusters.

1.1 Scope

This System Specification identifies the mission and technical requirements for the Discriminating Interceptor Technology Program (DITP) flight demonstration system, allocates requirements to functional areas, specifies design constraints, and specifies the interfaces between and among the functional areas.

1.2 Definitions

For the purpose of the DITP, the following terms apply. The NRI was selected by the BMDO IOS to be the "Test Bed Integrator" (TBI) for DITP. The TBI is responsible for overall mission success and system integration. "Subsystems" are defined as each of the complete packages the EAs and the NRI will deliver as GFE to include the PSS, LADAR, FP&A, and Integrated Optics Subsystem (IOS). "Seeker" is defined as the integrated PSS, LADAR, FP&A, and IOS. "Bus" will describe the integration of the subsystems provided by the TBI needed to allow the seeker to function in exoatmospheric flight (structure, mechanism, thermal control, (e. g., guidance/navigation/control, RF communications, command/telemetry/data handling). "Flight System" describes the integrated seeker, bus, and supporting subsystems (launch vehicle supplied components above the boost motor). "Launch Vehicle" is a sounding rocket or missile (boost motor and below). The "Launch System" describes the flight system integrated with the launch vehicle. Test Range describes the facilities and equipment required to conduct system flight demonstrations.

1.3 DITP System Description

The block diagram of Figure 1.3-1 identifies the DITP configuration hierarchy. Following is a summary of the items in the figure. More detailed descriptions of the configuration items shown in the figure are contained in Paragraph 3.1.5.

Prior to developing the flight subsystems, the EAs will develop advanced technology components which will undergo partial integration at a brassboard level (nominally 10 kg per subsystem). These will be integrated as appropriate with elements of other subsystems and the elements of IOS to perform ground testing using both simulated scenarios and targets of opportunities. The purpose of the tests is to validate performance parameters of key components (laser, detector arrays, processors) to verify key subsystem interfaces and to obtain data to check proposed timelines.

Subsequent development will lead to flight hardware (each flight verion subsystem to be designed for a nominal five kg mass) for each subsystem (PSS, LADAR, and FP&A). This flight hardware will be integrated and tested with the IOS, in various configurations, in preparation for formal ground demonstrations against approved target scenarios. After successful ground testing, the flight hardware will be integrated to and checked out with the Flight System Bus, integrated to and checked out with a launch vehicle. Upon successful checkout, an exoatmospheric flight demonstration will be performed against representative TMD and NMD targets in FY01. A second flight demonstration will be performed in FY02. The goal of the technology demonstration is fusion and processing of passive and active seeker sensors combined with the ability to discriminate against multiple, combined targets.

1.3.1.1 DITP Flight Target System (FTS)

The Flight Target System (FTS) is comprised of the Target Objects that will be used during the flight demonstration, a Bus/Dispenser that supports the objects through launch and initialization for deployment and dispersal, Supporting Subsystems that provide interfaces with the launch vehicle and deployment functions, and Ground Support Equipment necessary for pre-launch checkout.

1.3.1.2 DITP Flight System (FS)

The Flight System (FS) is comprised of the Seeker Subsystems, Bus Subsystems, Supporting Subsystems, and Ground Support Equipment.

1.3.1.3 DITP Launch Vehicle System

The Launch Vehicle System is comprised of a Flight System launch vehicle and a Flight Target System launch vehicle. The baseline launch vehicle is the Black Brant 9 (BB9) built by Bristol Aerospace. The BB9 consists of a first stage Terrier Mark 70 motor and a Black Brant 5 second stage. The Terrier first stage will be a DOD surplus motor. The Black Brant 5 second stage will be acquired from Bristol Aerospace. The various subsystems (i.e. attitude control, propulsion, telemetry) will be acquired as separate modules and will be in concert with the bus needs. The launch range will be White Sands Missile Range (WSMR) in New Mexico with the Pacific Missile Range Facility (PMRF) in Kauai, Hawaii as a back up.

1.3.1.4 Test Range

The Test Range includes the test range facilities, test range instrumentation, DITP-specific instrumentation, and GSE necessary to perform the flight demonstrations.

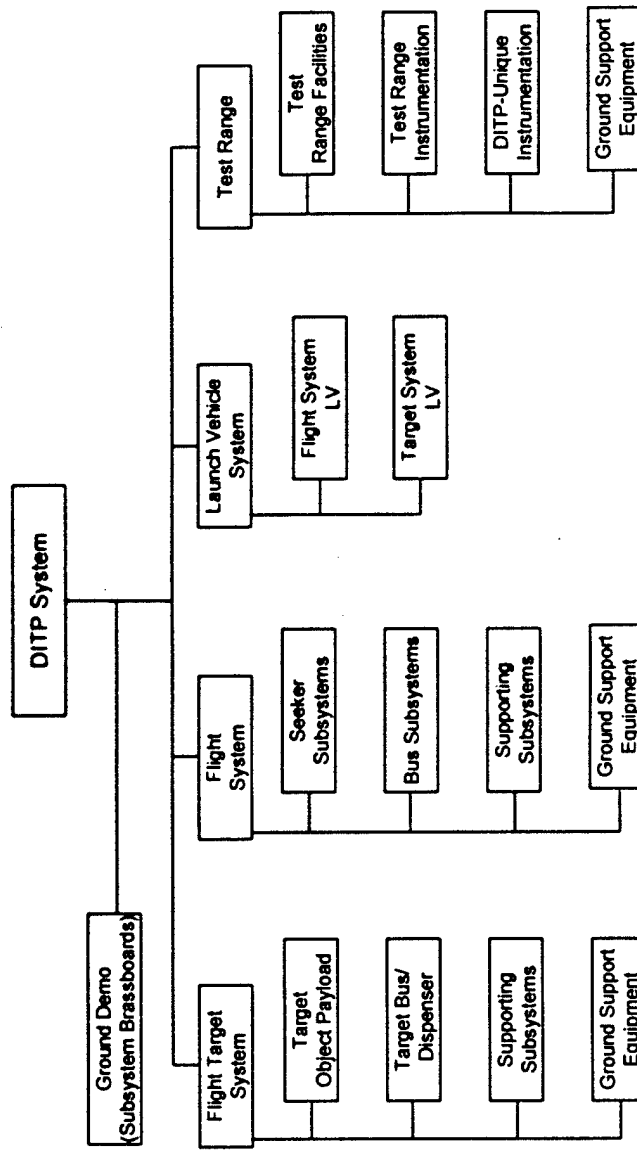


Figure 1.3-1 DITP Configuration Items

2. APPLICABLE DOCUMENTS

The following documents of the exact issue shown form a part of this specification to the extent specified herein. If no date for a document is specified, the date of this specification shall be used. In the event of a conflict between the documents referenced herein and the contents of this specification, the contents of this specification shall be considered a superseding requirement.

2.1 Government Documents

1. Program Plan for the Discriminating Interceptor Technology Program (DITP), BMDO, 25 February 1998
2. DITP Technology Program Goals Document (TPGD), BMDO, 26 February 1998
3. Discriminating Interceptor Technology Program Demonstration Requirements Document (DRD), BMDO, 29 September 1998 (Draft)
4. Passive Sensor Program Description Document, AFRL/VSSS (Kirtland), current version
5. LADAR Program Description Document, USASMDC/TC/SR (Huntsville), current version

2.2 Non-Government Documents

1. ANSI Z136.1-1993 American National Standard for the Safe Use of Lasers

2.3 Codes and Standards

Various documents (e. g., MIL-STD-XXX) are identified throughout this specification. Identified standards are to be used as indicated in the text for designing and testing DITP configuration items.

2.4 Program Documents

1. DITP Environmental Requirements Document, NCST-D-DT004
2. DITP System Test Plan, NCST-TP-DT001
3. DITP Targets Requirements Document, NCST-D-D006 (*TBD*)

3. REQUIREMENTS

DITP functional requirements and external interfaces are defined in the following paragraphs. A Requirements Verification Matrix (RVM) is included as Appendix A.

Classified requirements are denoted by X**. Requirements not yet defined are denoted as "to be defined" (TBD). Requirements not yet finalized are denoted as "to be resolved" (TBR).

3.1 System Definition

3.1.1 DITP OVERVIEW

The DITP will first develop technologies which can be incorporated into advanced interceptor seekers and second will demonstrate the performance and technical maturity of the technologies. This will be accomplished by choosing a subset of the developed technologies to be used in an integrated demonstration.

3.1.1.1 Technology Development

3.1.1.1.1 TECHNOLOGY DEVELOPMENT OBJECTIVES

The objective of DITP is to develop advanced technologies which will enhance and enable current and future interceptor seeker systems. Specifically, these advanced technologies will be developed to demonstrate capabilities that are traceable to interceptor performance against advanced missile threats as described in the TPGD and DRD.

Under DITP, seeker sensor (active and passive) and data fusion processing technologies will be developed. These technologies will be applicable to select BMDO, NMD, and TMD missions with emphasis placed on NMD. These technologies will focus on exoatmospheric applications.

3.1.1.2 Technology Demonstration

3.1.1.2.1 TECHNOLOGY DEMONSTRATION OBJECTIVES

The DITP will perform a series of tests at both subsystem and system levels, which, when combined with the appropriate analyses will demonstrate that the technology development objectives are met. The DITP will perform its test series culminating in exoatmospheric flight demonstrations to validate the performance and technical maturity of the chosen seeker and sensor fusion data processing technologies developed in the program. Major objectives are to demonstrate:

- passive sensor acquisition of predefined target objects
- passive sensor track of acquired target objects
- perform discrimination and bulk filtering
- handover of filtered objects to allow LADAR tracking of acquired target objects

- capability to discriminate, in real time, targets in the presence of countermeasures and decoys (including CSO) by enhancing discrimination through fusion of data
- capability to designate, in real time, targets in the presence of countermeasures and decoys
- capability to execute the seeker demonstration from a single in-flight-target update or target object map handover

3.1.2 DITP DEMONSTRATION SCENARIOS

3.1.2.1 DITP Demonstration Goals

The DITP ground tests and flight test scenarios shall be such that the data obtained show that DITP performance can be traced to the specific goals identified in the DITP Demonstration Requirements Document (DRD). These goals were derived from the threat scenarios in the DITP Technology Program Goals Document (TPGD). The first three columns of Table 3-1-1 summarize these DRD/TPGD technology goals. The fourth column of the table shows the corresponding requirements that have been derived for the DITP demonstration. Differences that occur are due to constraints imposed by a combination of launch range capabilities and budget.

Table 3.1-1 DITP Demonstration Specific Goals

(TBD) resolve PSS acquisition range

Goal	Value	Note	DITP Demonstration Goal
Passive IR Acquisition Range	1,200 km (scaleable)	Sensitivity, resolution, and aperture scaleable to 1,200 km or potential MDAP scenarios	400 km TBR
Passive IR Tracking Accuracy (σ_{az}) (circular error, one σ , perpendicular to LOS)	< 25 μ rad	Closely spaced object (CSO) resolution, tracking accuracy necessary for laser handover; Scenario refinement	< 5 μ rad, 1 axis, 1 σ
LADAR Acquisition Range	350 km (scaleable)	Power-aperture, target LADAR cross section scaleable to demonstrate acquisition by 350 km	350 km
LADAR Tracking Accuracy	< 20 μ rad	Precision tracking for CSO resolution	\leq 5 μ rad
Range Resolution	< 20 cm	CSO range resolution, discrimination	20 cm
Subtarget (Spatial Feature)	< 20 cm	CSO resolution, discrimination	< 52 μ rad

Resolution			$\leq 5 \mu\text{rad}, > 200 \text{ km}$ $\leq 25 \mu\text{rad}, < 200 \text{ km}$
Probability of Target Designation (P_d)	> 0.995	Discrimination requirement with real-time sensor data fusion, to be evaluated in combination with post-processing to simulate multiple tests	Obtain data for MDAP to analyze as appropriate

3.1.2.2 Demonstration Scenario Constraints

The DRD goals in Table 3.1-1 translate into a set of scenarios which are constrained by sensor capabilities and test constraints. Variations in these performance parameters are possible, however further analyses will need to be identified or applied to reduce the risk which these changes may incur in using the demonstration data to verify technology applicability.

3.1.2.2.1 CLOSING VELOCITY

The relative closing velocity between the seeker and target set shall be at least 2 km/sec to within a separation range of 80 km between the Flight System and Target Objects.

3.1.2.2.2 EXOATMOSPHERIC OBSERVATION ALTITUDE

The flight test demonstration observation altitude shall be at least 100 km.

3.1.2.2.3 SOLAR AND LUNAR EXCLUSION ANGLES

Flight Demonstration, Ground Demonstration, and testing scenarios shall be selected such that Seeker and Bus subsystems will not suffer damage from solar and lunar radiation.

(TBD) resolve solar and lunar exclusion angle uncertainties

3.1.2.2.4 EARTH EXCLUSION ANGLE

During FDLight emonstration, the angle from the Seeker to the target set shall be at least 90 degrees above Earth nadir. This is to be representative of or scaleable to the proposed NMD missions.

3.1.2.2.5 OTHER EXCLUSION ANGLES

Flight Demonstration, Ground Demonstration, and testing scenarios shall be selected such that Seeker and Bus subsystems will not suffer damage from radiation emanating from planets, stars, and orbital debris.

3.1.2.2.6 ANGLE BETWEEN SEEKER LINE OF SIGHT AND TARGET CONING AXIS

Figure 3.1.2-1

(TBD) Need figure

3.1.2.2.7 COLLISION AVOIDANCE

Flight scenarios shall be such as to ensure a probability of collision less than 10^{-6} between the Flight and Target Systems or between either of these systems and land, sea, and air vessels and Earth-orbiting objects.

3.1.2.2.8 VEHICLE(S) RECOVERY

Flight scenarios shall be such to ensure that Flight Syssem hardware can be recovered as required.

3.1.2.2.9 POSITION DETERMINATION

(TBD) Resolve position accuracies for FS and FTS

3.1.2.2.9.1 Flight System Position Determination

The FS shall be capable of determining its absolute position to (*TBR*) meters (1 sigma). The FS shall be capable of determining its relative position and velocity through out the flight to (*TBR*) meters 1 sigma.

3.1.2.2.9.2 Flight Target System Position Determination

The intrumented target shall be capable of determining its absolute position to (*TBR*) meters (1 sigma). The intrumented target shall be capable of determining its relative position through out the flight to (*TBR*) meters (1 sigma).

3.1.3 SYSTEM STATES AND MODES

The DITP system has two states, Dormant and Operational. The Operational State includes both Ground Demonstration, and Flight Demonstration. The system may exist in several distinct modes in either of these states. The system transitions between modes in response to specific decisions/commands as shown in Figures 3.1-1 (Ground Demonstration) and Figure 3.1-2 (Flight Demonstration). The sequence of mode transitions shall be accomplished during the times allocated for the flight scenario as identified in the System Test Plan, (NCST-TP-DT001).

3.1.3.1 Dormant State

The Dormant State encompasses all conditions when no electrical power is being applied. It includes the modes of Storage, Transportation and Handling (T&H), Integration and Checkout (I&C/O), and post-demonstration retirement/refurbish. DITP hardware shall be capable of meeting operational requirements after encountering the Dormant State environmental conditions described in the DITP Environmental Requirements Document, NCST-D-DT004.

Storage Mode

In this mode, system configuration items are in storage. This includes storage before transport to operational site(s) and, if applicable, storage after recovery and retirement.

(TBD) need batteries, ordnance storage and T&H discussion from Chris

Transportation and Handling (T&H) Mode

In this mode the system is either assembled or disassembled and packaged to enable transportation by highway, rail, air, or sea.

Integration and Checkout (I&C/O) Mode

In this mode, the Test Range subsystems are assembled into their operational configuration and are checked out to certify readiness to support the flight demonstration pre-launch and flight operations.

Also in this mode, the Flight Target, Flight, and Launch Vehicle Systems are completely assembled into their integrated launch configuration and checked out before entering the Operational State. The objective here is to ensure that the system hardware has been assembled into its correct configuration before transitioning to the Pre-Launch Mode. After completion of the I&C/O activities, the Flight Target, Flight, and Launch Vehicle Systems are ready for the start of their respective pre-launch activities.

Refurbish Mode

In this mode, hardware recovered after completion of a flight demonstration is refurbished and made ready for transition back to the Flight Demonstration State.

Retirement/Disposal Mode

In this mode, the system has completed all demonstrations and system hardware will be returned to the Storage Mode, returned to the cognizant E.A., or retired.

3.1.3.2 Operational State Modes

3.1.3.2.1 OPERATIONAL STATE - FLIGHT DEMONSTRATION MODES

The objective of the Flight Demonstration is to demonstrate functionality and performance of flight version Seeker subsystem designs at exo-atmospheric altitudes against representative TMD and NMD targets that are also at exo-atmospheric altitudes. The Operational State Modes for Flight Demonstration address both the Flight System and the Target System. Flight Demonstration comprises all system modes from pre-launch through recovery of flight hardware.

Pre-Launch Mode

The first activity in the Pre-Launch Mode is to perform all necessary functional and performance testing of the Test Range hardware and software needed to support all Operational State modes for the Target, Flight, and Launch Vehicle Systems.

In this mode, the Target and Flight Systems have been mated to their respective launch vehicles and they are ready to undergo functional and performance testing necessary to certify launch readiness. The Flight Target System, Flight System, and Launch Vehicles undergo diagnostic testing, calibration, and all activities are performed that are necessary to allow transition to the Launch and Ascent Mode.

Launch and Ascent Mode

In this mode, all umbilicals are removed from the Flight Target System, Flight Target Launch Vehicle, Flight System, and Flight System Launch Vehicle. The Flight Target System and Flight System are deployed into their respective Flight Demonstration trajectories in accordance with the demonstration flight scenario.

The Test Range tracks the launch trajectories and monitors the launch vehicles. For the Flight Target System, this mode ends with the separation of the Bus/Dispenser from the FTS launch vehicle. For the Flight System, this mode ends with despin and separation of the FS from the FS launch vehicle.

(TBD) resolve question of when FTS despin occurs (launch mode or Initialize mode?)

Initialize Mode

For the Flight Target System (FTS), the Bus/Dispenser and if applicable, the Target Objects are powered up as required for in-flight operation. The FTS Bus/Dispenser is deployed (*TBR*) and begins operation. The Bus/Dispenser is commanded to initialize and separate the Target Object Payload from the Bus/Dispenser. Essential target initialization data are transmitted to the Test Range.

For the Flight System, this mode is comprised of those functions required to ready the Seeker subsystems to perform the in-flight demonstration scenario and for the Bus subsystems to provide flight support functions. For example, in this mode the Bus points the sensor aperture at the target cluster location, PSS thermal control is provided, and the FP&A may perform diagnostics/BIT. The optics telescope is uncapped. Essential initialization data are stored and transmitted to the Test Range. Examples of Bus subsystem functions performed in this mode include control and distribution of electrical power, verifying and establishing telemetry capability with the Test Range, stabilizing and controlling Bus attitude, and commanding the system to enter the Acquisition and Tracking Mode.

Acquisition and Tracking Mode

In this mode, the Target Objects are coasting in their flight trajectory. Target Object tracking is initiated and target state vectors are computed and maintained by the Test Range. If applicable, Target Object data are transmitted to the ground.

For the Flight System, the PSS searches within its field of regard (FOR) for the target cluster. The FP&A correlates and verifies the PSS data to establish acquisition of the target cluster and identifies discrete objects. The FP&A computes and maintains target tracks. The LADAR is powered up.

During this mode, the Bus subsystems continue operate as necessary to support the Seeker subsystems and perform the flight demonstration. Seeker and Bus subsystem data are stored and transmitted to the Test Range.

Discrimination and Designation Mode

(TBD) paragraph needs review

In this mode, Target Object track vector states have been established, targets resolved and discriminated, and potential threat objects are identified. The FP&A fuses track data from the PSS to classify targets and commands the LADAR when a classified target is within the LADAR acquisition range. The FP&A fuses the data from both sensors to designate the highest probability target. Seeker data are stored by the Bus CT&DH Subsystem and transmitted to the Test Range.

During this mode, the Bus subsystems continue operate as necessary to support the Seeker subsystems and perform the flight demonstration. Seeker and Bus subsystem data are stored and transmitted to the Test Range.

End Game Homing Mode

In this mode, the primary objective is to collect pertinent target imagedata on the designated target only for subsequent post-test analysis to assess the potential system improvement in applying synergistic active/passive aimpoint selection techniques, as compared to existing passive only algorithm solutions. Target signature data for region of interest are extracted from both the passive IR sensors and the Ladar as commanded by the FP&A; then the data are transmitted down to a groundstation and also recorded into the on-board recorder.

(TBD) Suggest adding this paragraph to Flight Demo Section also, per suggestion by FP&A (i.e., Don Fronterhouse)

Post-Engagement Mode

In this mode, the Seeker subsystems are safed and electrical power from the Bus is turned off. Bus subsystems are reinitialized and commanded as necessary to accomplish controlled re-entry.

Re-Entry and Recovery Mode

In this mode, the Supporting Subsystems and, as applicable, Bus subsystems are operated to perform re-entry and safe landing of the FS. Flight System hardware is recovered as after landing and flight data are obtained from the flight data recorder. Recovered hardware is prepared for shipment to be either refurbished for subsequent flight demonstration or returned to the cognizant EA.

3.1.3.3 Operational State – Second Flight Demonstration

The modes associated with the second flight demonstration are identical to the modes for the first flight demonstration.

3.1.3.4 Operational State - Ground Demonstration Modes

For the Ground Demonstration, the applicable modes are Initialize, Acquisition and Tracking, Discrimination and Designation, and End Game Homing. Other modes identified for the Flight Demonstration are not applicable to the Ground Demonstration. Note that the functions that are performed during Ground Demonstration may be a subset of the functions performed during Flight Demonstration.

Initialize Mode

For the Ground Demonstration, this mode is comprised of those activities required to ready the Seeker subsystems for testing (e. g., applying electrical power, checking interfaces).

Acquisition and Tracking Mode

For Ground Demonstration, this mode is functionally similar to the corresponding Flight Demonstration mode although not all mode functions and activities may be implemented.

Discrimination and Designation Mode

For Ground Demonstration, this mode is functionally similar to the corresponding Flight Demonstration mode although not all mode functions and activities may be implemented.

End Game Homing Mode

In this mode, the primary objective is to collect pertinent target imagedata on the designated target only for subsequent post-test analysis to assess the potential system improvement in applying synergistic active/passive aimpoint selection techniques, as compared to existing passive only algorithm solutions. Target signature data for region of interests are extracted from both the passive IR sensors and the Ladar as commanded by the FP&A; then the data are transmitted down to a groundstation and also recorded into the on-board recorder.

(TBD) Also suggest adding this paragraph to Flight Demo Section, per request from FP&A (i.e., Don Fronterhouse)

Dormant State			Operational State - Flight Demonstration				
STORE/ RETIRE	Decision to deliver to site						
Command Storage/ Retire	T&H	Accept Delivery					
	Command transport	I&C/O	Command Power On				
		Abort Launch	PRE- LAUNCH	Command Launch			
				LAUNCH & ASCENT	Command Initialize		Command Abort and Recovery
					INITIALIZE	Command Acquire	Command Abort and Recovery
						ACQUISITION & TRACKING	Command Abort and Recovery
							Command Abort and Recovery
						DISCRIM- INATION & DESIGNATION	Automatic Command Abort and Recovery
							Automatic
						POST- ENGAGEMENT	Automatic
	Command transport						PS RECOVERY

Figure 3.1-2 DITP Flight Demonstration Modes and Transition Paths

3.1.4 SYSTEM CONFIGURATION

The block diagram shown previously in Figure 1.3-1 identified the configuration item breakdown for the DITP. This paragraph contains descriptions of the subsystems that comprise each of the DITP systems.

3.1.4.1 Flight Target System

The Flight Target System (FTS) is comprised of the Target Object Payload, Target Bus/Dispenser, FTS Supporting Subsystems, and FTS Ground Support Equipment.

3.1.4.1.1 TARGET OBJECT SETS

The target object sets will have traceability to both NMD and TMD missions. The first flight demonstration will provide a target set which allows discrimination and designation performance to be assessed. The second flight mission will provide a target set which challenges the DITP seeker in that the target set will be populated with enough targets in the cluster that the discrimination timeline for potential operational systems can be assessed. The Ground Demonstration target set will be more stressing and will be representative of the threat description in the TPGD.

3.1.4.1.2 MINIMUM SET

For the first flight demonstration, a minimum essential target set is defined as presented in Table 3.1.4-1. A primary objective of this flight is to perform a live demonstration of interceptor seeker functionality, such as acquisition and cueing of the Ladar, and performing post-flight analysis and verification of system performance capability. In particular, the goal to quantify performance of the Ladar/IR discriminations by measuring target dynamic features on an otherwise thermally matched target set, represented by two rigid lightweight replicas (RLR) with one having a light weight instrumentation system package and being designated as the primary surrogate RV. A motivating factor in selecting the target set is to maintain a minimal target procurement and integration costs; e.g., procure target as is off-the-shelf, if possible, and not adding extra mass or changing mass moment to passively control target dynamics. The proposed set will allow discrimination to occur based on typical discrimination characteristics such as shape, thermal properties, and dynamics.

Table 3.1.4-1 Target Set for First DITP Flight Demonstration

Object Ident.	Shape	Class	Quantity
RLR w/LWIS	Cone	C2/C3	1
RLR	Cone	C2/C3	1
Inflatable Cone	Cone	C2	1
CLB (ref.)	Sphere	C1	1
Canister, etc.	misc.	C1	1+
		TOTAL :	5+ obj.

3.1.4.1.3 ENRICHED TARGET SET

For the second flight demonstration, the enriched target set summarized in Table 3.1.4-2 will be deployed. This set will have a greater number of objects making it nearly equal to an advanced threat cluster that a next-generation interceptor may typically encounter. Again, a primary RV is substituted by an instrumented RLR to reduce the procurement/integration cost. Several conical objects are added to provide a live demonstration of the system functionality by testing a capability of automated decision logic designed in the fusion algorithms which generates commands for the dynamic sensor operations and target scheduling. This Flight will also demonstrate system and subsystem performance limits in a real time, during an in-flight space environment and will further challenge the discrimination timelines.

Table 3.1.4-2 Enriched Target Set for Second DITP Flight Demonstration

Object Ident.	Shape	Class	Quantity
RLR w/LWIS	Cone	C2/C3	1
RLR	Cone	C2/C3	1
Dixie Cups	Cone	C2	2
Inflatable Cone	Cone	C2	1
CLB (ref.)	Sphere	C1	1
CMB	Sphere	C1	2
MBC	Spheres	C1	Set of 5
Canisters, etc.	misc.	C1	5+
		TOTAL	18+ obj.

3.1.4.1.4 TARGET BUS/DISPENSER

The Target Bus/Dispenser is comprised of the hardware necessary to support the targets during launch and to spin up and deploy the target objects. The DITP target bus provides load carrying capability from the target payload to the launch vehicle. The target bus is the physical enclosure, support and attachment of all of the DITP target components and associated subsystems. The target bus consists of the following: primary cylindrical skin structures, fairing that can be jettisoned, electronics deck structures, access ports and panels, thermal blanketing, and interface to all launch vehicle specific subsystems.

3.1.4.1.5 SUPPORTING SUBSYSTEMS

The supporting subsystems include those subsystems of the launch vehicle that interface the launch vehicle to the Flight Target System (e. g., C-Band Radar Transponder, Thrust Termination Subsystem, Flight Termination Subsystem, and Ignitor Assembly).

3.1.4.1.6 GROUND SUPPORT EQUIPMENT (GSE)

The Flight Target System GSE is comprised of equipment required for testing, calibrating, handling, transporting, storing, and protecting DITP Flight Target System hardware during all activities prior to launch. This GSE shall include the equipment necessary to perform Pre-launch Mode calibration, alignment, and test activities, including collection and on-site analysis of pre-launch data. Where practical, the same instrumentation used for development and integration tests shall be used as GSE.. When different instrumentation is used as GSE, a metrology report shall be provided to ensure consistency of test results using the different instrumentation equipment. This GSE will be used as applicable for Flight Target and Launch Vehicle Systems integration at the Test Range for specific launch support operations. All supplier-furnished GSE shall be returned to the Supplier after the completion of post-launch testing.

3.1.4.2 DITP Flight System (FS)

The Flight System (FS) is comprised of the Seeker Subsystems, Bus Subsystems, Supporting Subsystems, and Ground Support Equipment. Figure 3.1.4-1 illustrates a concept for packaging the Flight System on a launch vehicle. These four subsystems are briefly described in the following paragraphs.

Figure 3.1.4-1

(TBD) Need launch packaging figure

Figure 3.1-4 DITP Flight System in Launch Configuration

3.1.4.2.1 SEEKER SUBSYSTEMS

The Seeker is comprised of the three advanced seeker technology subsystems identified previously in Section 1.4 (PSS, LADAR, FP&A) plus the Integrated Optics Subsystem (IOS). The IOS is an integrated optical train, which includes a telescope, fast steering mirror, dichroic beam steering mirror, IMU, and beam splitter.

3.1.4.2.2 BUS SUBSYSTEMS

The Bus is comprised of the subsystems necessary to support FS Seeker operations and to provide interfaces with the FS Launch Vehicle and Test Range. Bus subsystems include:

- Structure and Mechanisms (S&M)
- Command, Telemetry, and Data Handling (CT&DH)
- Guidance, Navigation, and Control (GN&C)
- Thermal Management (TM)
- RF Subsystem (RFS)
- Electrical Power (EPS)

3.1.4.2.3 SUPPORTING SUBSYSTEMS

The supporting subsystems include those subsystems of the launch vehicle that interface the launch vehicle to the flight system (e. g., Recovery Subsystem, C-Band Radar Transponder, Thrust Termination Subsystem, Flight Termination Subsystem, and igniter assembly).

3.1.4.2.4 GROUND SUPPORT EQUIPMENT (GSE)

The Flight System GSE is comprised of equipment required for testing, calibrating, handling, transporting, storing, and protecting DITP Flight System hardware during all activities prior to launch. This GSE includes the equipment necessary to perform Pre-Launch Mode calibration, alignment, and test activities, including collection and on-site analysis of pre-launch data.

Where practical, the same instrumentation used for development and integration tests shall be used as GSE. When different instrumentation is used as GSE, a metrology report shall be provided to ensure consistency of test results using the different instrumentation equipment. This GSE will be used as applicable for Flight Target and Launch Vehicle Systems integration at the Test Range for specific launch support operations. All supplier-furnished GSE shall be returned to the Supplier after the completion of post-launch testing.

3.1.4.3 Launch Vehicle System

The baseline launch vehicle selected for the Flight System and the Target System is the Black Brant 9 (BB9) built by Bristol Aerospace. The BB9 consists of a first stage Terrier Mark 70 motor and a Black Brant 5 second stage. The various subsystems (i.e. attitude control, propulsion, telemetry) will be acquired as separate modules and will be in concert with the bus needs.

3.1.4.4 Test Range

The test range will be White Sands Missile Range (WSMR) in New Mexico with the Pacific Missile Range Facility (PMRF) in Kauai, Hawaii as a back up.

(TBD) Need descriptions of Test Range items.

3.1.4.4.1 TEST RANGE FACILITIES

The Test Range Facilities are comprised of the hardware and software necessary to conduct the DITP flight demonstrations and to support personnel involved in the I&C/O and Operational Modes. The TBI will be responsible for providing interfaces to test range facilities and equipment such as displays and workstations. Equipment interfaces will be provided as needed by the EAs to allow them to verify that their subsystems are performing properly during a demonstration. The Test Range will provide telemetry capability for commanding the FS, for acquiring flight and range data, and, if necessary, for communicating between the Target System and Flight System launch sites. Commanding capability may include functions such as initialization, initial IFTU, resets, and calibration. The Test Range will also include computer resources necessary to process and store data acquired via telemetry during a flight demonstration. In addition, the Test Range will include displays needed to support conduct of the demonstrations, for example, real-time flight diagnostics.

3.1.4.4.2 TEST RANGE INSTRUMENTATION

3.1.4.4.3 DITP-UNIQUE INSTRUMENTATION

3.1.4.4.4 GROUND SUPPORT EQUIPMENT

The Test Range GSE is comprised of equipment required for testing, calibrating, handling, transporting, storing, and protecting Test Range hardware to perform Flight Demonstration I&C/O, pre-launch, and flight activities.

3.1.5 INTERFACE REQUIREMENTS

Interfaces include both physical interfaces and signal interfaces. Physical interfaces include mechanical and electrical connectivity such as physical locations and types of connections. Signal interfaces describe the content and nature of information transferred via electrical connections. Signal interfaces may exist between configuration items even though no physical interface exists.

3.1.5.1 DITP Interfaces With Non-DITP Sites and Organizations

Mechanical, electrical, and signal interfaces, if required, between the DITP system and sites and organizations not identified in Figure 1.3-1 will be identified and described in the DITP System Test Plan, NCST-TP-DT001.

3.1.5.2 Internal Interfaces

Mechanical, electrical, optical, and signal interfaces between DITP configuration items shall be documented by interface control documents (ICD). Examples of DITP-internal interfaces that must be defined include, but are not limited to:

- Launch System To Flight System Interfaces
- Launch System To Target System Interface
- Launch System to Test Range
- FS Bus/IOS To PSS Interfaces
- FS Bus/IOS To LADAR Interfaces
- FS Bus/IOS To FP&A Interfaces
- PSS to IOS Interfaces
- LADAR to IOS Interfaces

3.2 System Characteristics

3.2.1 DESIGN LIFETIME

3.2.1.1 Dormant State Lifetime

Flight Target System and Flight System hardware shall be designed for a Dormant State nominal lifetime of three years. This lifetime is comprised of the accumulated time DITP hardware may be in the Storage, T&H, and I&C/O Modes, including time associated with recovery and reuse.

3.2.1.2 Operating Lifetime

As a goal, DITP hardware shall be designed to allow operating for the cumulative time and number on/off cycles the hardware will be in a powered up configuration, that is, the time required to support all ground testing and Ground and Flight Demonstrations.

3.2.2 PHYSICAL REQUIREMENTS

3.2.2.1 Target System Requirements

Target Object physical characteristics shall be traceable to the TMD and NMD target characteristics identified in the DRD. Specific target characteristics are specified in the DITP Targets Requirements Document, NCST-S-xxxx. (TBD)

(TBD) Need TRD #

3.2.2.2 Flight System Requirements

3.2.2.2.1 PROBABILITY OF TARGET DESIGNATION

Data shall be acquired to show that the probability of target designation for a single encounter shall be ≥ 0.95 . (TBD)

(TBD) Need to resolve prob of target designation

3.2.2.2.2 ACQUISITION RANGES

3.2.2.2.2.1 Passive Sensor Acquisition Range – Flight Demonstration

The range for initiating passive sensor acquisition shall be at least 400 (TBD) for the target set described in Paragraph 3.1.5.1.

(TBD) Need to resolve PSS acquisition range

3.2.2.2.2.2 LADAR Acquisition Range – Flight Demonstration

The LADAR shall be capable of demonstrating acquisition range of at least 350 km.

3.2.2.2.3 OPTICS FIELD OF VIEW (FOV) AND FIELD OF REGARD (FOR)

3.2.2.2.3.1 Telescope Field of View (FOV)

The telescope FOV shall be at least 1.2 x 1.6 degrees. (TBR)

3.2.2.2.3.2 Passive Sensor Field of Regard (FOR)

The passive sensor FOR shall be the telescope FOV.

3.2.2.2.3.3 Passive Sensor Field of View

The passive sensor FOV shall be 0.6 (azimuth) x 0.6 degrees (elevation).

3.2.2.2.3.4 LADAR Field of Regard

The LADAR field of regard shall be the PSS FOV.

3.2.2.2.3.5 LADAR Field of View

The LADAR FOV shall be greater than or equal to 52 μ rad without use of electronic zoom.

3.2.2.2.4 POINTING ACCURACY

(TBD) Need top down definition of pointing accuracy

3.2.2.2.4.1 Passive Sensor Angular Pointing Accuracy

The passive sensor angular pointing accuracy (1 σ) shall be less than 5 μ rad.

3.2.2.2.4.2 LADAR Tracking Precision

The LADAR tracking precision shall be less than 2 or 5 μrad (*TBR*).

3.2.2.2.4.3 Pointing and Tracking Handover Error Budget

3.2.2.2.4.3.1 Optical System Handover Error

The static boresight alignment error shall be no greater than 10 μrad (worst case).

3.2.2.2.4.3.2 Centroiding and Tracking Handover Error

The PSS centroiding and tracking handover error shall be no greater than 5 μrad (1σ) per axis.

3.2.2.2.4.3.3 Control Residual

The FSM/BSM beam pointing error shall be no greater than 5 μrad (1σ) per axis.

3.2.2.2.4.4 Seeker Boresight Pointing Accuracy

The passive sensor boresight bias pointing accuracy shall be no greater than 10 μrad per axis (1σ).

3.2.2.2.5 PASSIVE SENSOR INSTANTANEOUS FIELD OF VIEW

The passive sensor instantaneous field of view shall be no greater than 50 μrad .

3.2.2.2.6 LADAR RANGE RESOLUTION

The LADAR range resolution shall be 20 cm.

3.2.2.2.7 LADAR INSTANTANEOUS FIELD OF VIEW

The LADAR shall provide a capability for two values of instantaneous field of view. These values shall be equal to 5.2 μrad for the normal mode and equal to 2.6 μrad for the zoom mode.

3.2.2.2.8 POINTING - NUMBER OF TARGETS

The LADAR/BSM shall demonstrate capability of pointing at a minimum of 10 objects per second during the Discrimination and Designation Mode.

3.2.2.2.9 SEEKER JITTER BUDGET

(TBD) Need top down allocation of jitter

3.2.2.2.9.1 IOS Jitter

The IOS jitter, defined as the jitter of the received LADAR beam on the active focal plane array, shall be less than 4.2 μrad (1σ) per axis (*TBR*).

3.2.2.2.9.2 Passive Sensor Jitter

The passive sensor jitter component shall be less than TBD μrad .

3.2.2.2.9.3 LADAR Jitter (Transmitter)

The residual jitter of the transmitted LADAR beam in target space shall no greater than 5 μrad (1σ) per axis (*TBR*)

3.2.2.2.9.3.1 Laser Jitter

The laser jitter, in target space, shall be no greater than 5 μrad (1σ) per axis.

3.2.2.2.10 FS BUS INERTIAL POINTING ACCURACY

The FS Bus inertial error at initial acquisition shall be no greater than 0.35 degrees per axis (3σ).

3.2.2.2.11 FS BUS ANGULAR ACCELERATION

The FS Bus shall be capable of angular accelerations of at least 1.8 deg/sec^2 .

3.2.2.2.12 SEEKER MAXIMUM APERTURE

The seeker aperture shall be no greater than 25 cm.

3.2.2.2.13 FS MASS PROPERTIES

Total mass of the FS should not exceed the BB9 payload capability .

3.2.2.2.13.1 Seeker Subsystems Mass

The mass of the Flight Demonstration seeker subsystems shall not exceed the following values:

PSS – 5 kg

LADAR – 5 kg

FP&A – 5 kg

3.2.2.2.13.2 FTS and FS Centsr of Mass

The FTS and FS center of mass shall be consistent with the launch payload envelopes specified for the FTS Launch Vehicle and FS Launch Vehicles respectively and Flight Demonstration scenarios described in the System Test Plan, NCST-TP-DT001.

3.2.2.2.14 FTS AND FS VOLUME

The FTS and FS volumes shall be consistent with the allowable launch payload envelope specified for the Black Brant 9 launch vehicle.

3.2.2.2.15 FS ELECTRICAL POWER

Electrical power required by Flight System Seeker and Bus subsystems (exclusive of self-contained batteries as applicable) shall be provided by the Bus Electrical Power Subsystem.

3.2.2.2.16 FS THERMAL MANAGEMENT

The TBI shall be responsible for thermal management and control during the Pre-Launch and Recovery Modes to maintain subsystem non-operating temperatures within the values specified in the Environmental Requirements Document, NCST-D-DT004 (*TBD*).

(TBD) need final review of thermal mgmt section

3.2.2.2.16.1 FS Thermal Environment Stability

The TBI shall provide a stable thermal environment with predominantly adiabatic interfaces. Thermal control shall be primarily a function of component and local structure mass.

3.2.2.2.16.2 Subsystems Thermal Management

Seeker and Bus subsystems' thermal management shall be integral to each subsystem's design with the exception that accommodating 20 W heat rejection for the PSS Cryocooler will be the responsibility of the TBI.

3.2.2.2.16.3 FS Thermal Management

3.2.2.2.17 FS BUS COMMUNICATIONS

The FS Bus shall provide downlink and uplink communications with the Test Range to receive commands and transmit flight demonstration data.

3.2.2.2.18 FS DATA PROCESSING

3.2.2.2.18.1 Seeker Subsystems Data Availability

FS Seeker subsystems shall be designed to provide for output of data to enable assessment of each subsystem's performance.

3.2.2.2.18.2 FS Bus Flight Data Recording

If adequate data can not be transmitted to the Range System, flight data recording shall be provided that is capable of recording all performance and status data during the flight demonstration, starting with the Initialization Mode and continuing until start of the Recovery Mode.

3.2.2.3 Launch Vehicle System Requirements **(TBD) Need discussion of LV requirements**

3.2.2.4 Test Range Requirements

3.2.2.4.1.1 Communications Uplink

Communications capability shall be provided to uplink commands and data to the Flight System, Flight Target System, and Launch Vehicle Systems as required to support flight demonstration scenarios.

3.2.2.4.1.2 Communications Downlink

The Test Range shall provide communications to receive transmitted data from the Flight System, Target System, and Launch Vehicles.

3.2.2.4.1.3 Test Range Data Storage

Test Range computer(s) shall have the capability to store data on accessible media (e. g., fixed hard drive, CD-ROM, removable disk) to support mission planning, operations, and assessment applications, and data transmitted from the flight system and target system.

3.2.2.4.1.4 Test Range Communication Protocol

Test Range computers shall communicate with each other using a common protocol.

3.2.3 ENVIRONMENTAL CONDITIONS

The DITP system must be capable of meeting its performance requirements after exposure to the Dormant State and Operational State natural and induced environmental conditions described in the Environmental Requirements Document, NCST-D-DT004.

3.2.4 DESIGN AND CONSTRUCTION

The following subparagraphs describe the general requirements for design and construction that are applicable to the DITP Flight System and its subsystems.

3.2.4.1 Parts, Materials, and Processes

(TBD) Need final review by J. Chapman

Parts, materials, and processes (PMP) selection and control procedures shall emphasize quality and reliability to meet the Dormant and Operational States lifetime requirements, including all environmental degradation effects. The materials employed in the design shall be selected to assure acceptable reliability and performance in the specified environment within the volume and weight constraints. The selection of parts, materials and processes shall minimize the variety of parts, related tools, and test equipment required in fabrication, installation, and maintenance. No identical parts, such as electrical connectors, fittings, etc., shall be used where inadvertent interchange of items or interconnections could cause a malfunction.

a. **EEE Parts:** Electronic parts shall be designed or selected for high-reliability and lifetime consistent with storage, test, launch, exo-atmospheric flight, and. As applicable, for re-entry and recovery. Electronic parts and materials that have been permanently installed in an assembly and which are then removed from an assembly for any reason shall not be used in any item of demonstration hardware unless authorized by the TBI. A formal Electrical, Electronic, and Electromagnetic (EEE) Parts Program is not required. The Supplier's parts program shall ensure that the results of receiving inspection, parts tests, material review boards and parts problems reported from testing are documented and periodically reviewed.

b. **Materials:** Materials shall be selected for low out-gassing characteristics. The DITP Flight System and its subsystems shall use only materials exhibiting Total Mass Loss (TML) of 1.0% or less and Volatile Condensable Material (VCM) values of 0.1% or less per NASA Reference Publication 1124 (NRP-1124). Any materials that fail to meet these criteria shall be identified to the TBI. All usage of silicone shall be identified to the TBI.

c. **Metallic Materials:** Metallic materials shall be corrosion resistant by nature or shall be corrosion inhibited by means of protective coatings. Materials using the guidelines of MIL-HDBK-5G shall be selected. Any materials that fail to meet these criteria shall be identified to the TBI. Base metals intended for inter-metallic contact that form galvanic couples shall be plated with those metals that reduce the potential difference or shall be suitably insulated by a non-conducting finish. Electrical bonding methods shall include provisions for corrosion protection of mating surfaces. Use of dissimilar metals shall be avoided. Magnesium alloys shall not be used for electrical bonding or grounding.

d. **Magnetic Materials:** The use of magnetic materials should be avoided whenever possible. Magnetic materials shall be used only if necessary for equipment operation. The materials used should minimize permanently induced and transient magnetic fields. Use of magnetic materials shall be reported to the TBI.

e. **Protective Coatings and Finishes:** Protective methods and materials for cleaning, surface treatment, and applications of finishes and protective coatings shall conform to MIL-F-7179 and MIL-STD-1568 (or equivalent). Neither cadmium nor zinc coatings shall be used.

f. **Materials Flammability and Compatibility:** All materials shall meet the flammability and compatibility requirements of *TBD*. All nonmetallic materials shall meet the flammability requirements of NHB-8060.1C for control of flammability and hazardous fluid compatibility.

(TBD) Need reference from Jack

g. **Prohibited Materials:** The following materials shall not be used unless approved by the TBI: Teflon insulation subject to "cold-flow"; Nylon, polycarbonates, polyvinylchloride (PVC); silicone grease with zinc oxide filler; cadmium; zinc; and non-fused tin-electroplated parts.

h. **Pressurized vessels used in launch system** shall meet the guidelines of MIL-STD-1522, Standard General Requirements for Safe Design and Operation of Pressurized Missile and Space Systems. Containers that will be pressurized in the presence of personnel shall comply with ANSI/ASME B31.3, Code for Chemical Plant and Refinery Piping and ASME B&PV Code, Section VIII, Division I or Division II Pressure Vessels, as applicable.

3.2.4.2 Failure Reporting and Corrective Action System

A closed loop failure reporting and corrective action system (FRACAS) for reporting, analysis, and corrective action shall be in effect for failures occurring during the acceptance testing phases. The FRACAS shall determine whether failures are caused by design deficiencies, human error, defective parts, infant mortality, test equipment, environmental exposure, or software.

3.2.4.3 Part Stress Derating

The application of all EEE parts in the design shall be derated such that the applied stresses do not exceed the derating criteria guidelines contained in the manufacturer's data sheets.

3.2.4.4 Soldering and Other Processes

Soldering and other processes shall be consistent with the requirements of MIL-STD-1547A, Paragraph 4.4.4, Processes and Controls (or equivalent). Soldering and other processes shall be specified in Supplier-approved process specifications that employ the guidelines of MIL-STD-1546, Paragraph 5.1, Parts, Materials, and Processes Control Program Planning (or equivalent). Other special processes (e.g., adhesive bonding, plating, etc.) shall be according to the Supplier's approved process specifications. Printed Circuit Boards (PCBs) used in the fabrication of the equipment shall conform to the requirements of IPC-D-275, Standard for PCB Design and Assembly; IPC-FC-250, Performance Specification for Single and Double-Sided Flexible Printed Boards; IPC-FC-250A-86, Specification for Single and Double-Sided Flexible Wiring; and IPC-A-600D, Acceptability of Printed Wiring Boards (or their equivalents).

3.2.4.5 Electrostatic Discharge Sensitive Parts

All electrical components utilizing electrostatic discharge sensitive parts shall provide adequate protection to preclude part failure resulting from handling, shipment, or storage situation, according to guidelines of MIL-STD-1686A (or equivalent).

3.2.5 ELECTROMAGNETIC ENVIRONMENT

(TBD) Need to resolve where EMC req reside— here or in ERD?

The DITP Flight System and its subsystems shall be designed and constructed such that each item is compatible with itself and with its known test, launch, and exo-atmospheric operational environments.

3.2.5.1 Electromagnetic Compatibility (EMC)

The designs of the DITP Flight System and its subsystems shall meet the requirements for generated emissions and susceptibility levels and conform to the external and self-induced environments likely to be encountered during performance testing, launch, and on-orbit operational environments. The DITP Flight System shall not be susceptible to, nor shall it radiate emission levels greater than those specified in MIL-STD-461, Electromagnetic Emissions and Susceptibility Requirements for Control of Electromagnetic Emissions (or equivalent). The DITP Flight System shall be designed to operate without malfunction, undesirable response, or deviation from specified performance tolerances when subjected to these electromagnetic environments. Compliance shall be proven using the procedures of MIL-STD-462, Electromagnetic Interference Characteristics, Measure of, and an EMI test plan. Testing will be accomplished at either the subassembly level or at the system (integrated bus and seeker) level.

3.2.5.2 Corona and Triboelectric Suppression

The DITP Flight System shall be designed to minimize the occurrence of corona discharge in all normal operating environments. All conducting items subject to triboelectric (frictional) or any other charging mechanisms shall have a mechanically secure electrical connection to the structure. The resistance of such a connection shall be less than one ohm.

3.2.5.3 Bonding

Equipment containing electrical circuits that may generate radio frequencies (RF) or circuits that are susceptible to RF shall be so installed that there is a continuous, low-impedance path from the equipment enclosure to the structure. The metallic shells of all equipment electrical connectors shall be electrically bonded to the equipment case or the bulkhead mount with a DC resistance of less than 2.5 milliohms. Wire harness shields external to equipment, requiring grounding at the equipment, shall have provisions for grounding the shields to the equipment through the harness connector backshell, or for carrying single point grounded shields through the connector pins.

3.2.5.4 Lightning Protection and Grounding

3.2.5.4.1 LIGHTNING PROTECTION

The Test Range shall provide lightning protection with grounding based on the guidelines of NFPA 780 and MIL-HDBK-419.

3.2.5.4.2 PREMATURE LAUNCH OR DETONATION

When in the Pre-Launch Mode, the Flight Target and Flight Systems shall be safe from a premature launch or detonation of explosive devices after exposure to a cloud-to-ground direct strike.

3.2.5.4.3 NO LAUNCH IN PRESENCE OF LIGHTNING

Launch of the DITP Flight and Target Systems shall not be allowed in the presence of lightning at either launch site.

3.2.6 ELECTROMAGNETIC INTERFERENCE

The DITP design shall use Mil-Std-461 and Mil-Hdbk-419 as guidance for control of electromagnetic interference generation and susceptibility. Applicable emission and susceptibility constraints are identified in the ERD, (TBD).

3.2.7 (TBD) NEED TO RESOLVE WHERE EMC REQ RESIDE—HERE OR IN ERD?WORKMANSHIP

Equipment shall be manufactured, processed, tested, and handled such that finished items are of sufficient quality to ensure reliable operation, safety, and service life in the Ground and Flight Demonstration environments. All parts and assemblies shall be designed, constructed, and finished in a quality manner intended to produce defect-free equipment. Particular attention shall be given to critical operations (e.g., adhesives, soldering, plating, painting, riveting, machine screw assembly, welding, brazing, deburring, cleaning, and marking of parts and assemblies). The items shall be free of defects that would interfere with Ground and Flight Demonstration use (e.g., excessive scratches, nicks, burrs, loose material, fluxes, contamination, and corrosion).

3.2.7.1 Interchangeability

Assemblies, components, and parts having identical part numbers shall be interchangeable. The TBI shall be notified of interchanges.

3.2.7.2 Nameplate and Product Marking

DITP Flight, Target, and Launch Vehicle Systems and Test Range components and/or equipment that are interchangeable shall be identified by part number and serial number.

3.2.8 SAFETY

The DITP shall use MIL-STD-882 as a guideline to identify specific hazards and to determine the necessary design and operational safety requirements for hazard identification and mitigation.

3.2.8.1 Safety From Emissions

The DITP System shall not present uncontrollable health hazards associated with electrical discharge, ionizing or non-ionizing radiation, noise, or other emissions.

3.2.8.2 Critical Safety Hazards

The Flight, Target, and Launch Vehicle Systems and Test Range shall be designed such that no single failure or single operator error can result in a critical hazard.

3.2.8.3 Personnel Safety

DITP GSE shall be capable of being safely stored, handled, transported, installed, and checked out at all times prior to launch, according to procedures agreed to between the TBI and the Supplier. No health hazards shall exist when DITP Flight, Target, and Launch Vehicle Systems and Test Range Equipment are removed, maintained, installed, or in storage.

3.2.8.4 Test Range Safety

The DITP Flight, Target, and Launch Vehicle Systems shall comply with the applicable range safety regulations of the selected Test Range.

3.2.8.5 LADAR Safety

The DITP LADAR Subsystem shall comply with the application regulations of OSHA, the NRL, and the selected launch range for hazardous operations in the presence of LASER optical emissions. The current release of ANSI Z136.1 shall be used as a guideline to determine eye and skin hazard levels of the LADAR, including residual reflections. Compliance with the applicable industrial health and safety requirements is mandatory.

(TBD) Suggestion to add "satellite predictive avoidance" for outgoing LADAR pulses per W. Von Worley (note: Hess had Space Command waiver for ASTP)

3.2.9 NUCLEAR CONTROL

Materials containing natural or man-made radioisotopes (in any quantity, including trace amounts) shall not be used in any DITP hardware, unless formal approval is received from the TBI.

3.2.10 SYSTEM SECURITY

System security requirements shall be as specified by the applicable DITP Security Classification Guide.

3.3 Computer Resources

Computer resources include all hardware and software required to develop, test, implement, operate, and evaluate Flight, Target, and Launch Vehicle Systems and the Range. Examples of hardware resources include computers/workstations, peripheral devices, and networks. Examples of software resources include analysis applications, simulations, operational codes, and test codes.

Capability to upload software changes and to provide memory verification capabilities via ground test ports during pre-launch operations.

3.4 Standards of Manufacture

General manufacturing requirements for the DITP Target, Flight, and Launch Vehicle Systems and their subsystems shall be according to established practices for exo-atmospheric experiment equipment. General manufacturing requirements for Test Range equipment shall be according to established practices for test range equipment

3.4.1 CONTAMINATION CONTROL AND CLEANLINESS

Cleanliness requirements for Ground and Flight Demonstration hardware:

3.4.1.1 Protection From Contamination

Hardware shall be protected from unacceptable contamination during fabrication, integration, testing, storage, handling, transportation, and at the launch base.

3.4.1.2 Contamination Control Guidelines

Contamination control guidelines shall be established by the TBI. These guidelines will address a cost-effective contamination control approach, including the methods for control during development, testing, and Ground and Flight Demonstration activities.

3.4.2 CONNECTORS

Connector keying or equivalent means shall be used to prevent mismatching. Connectors and connections shall have durable stripes, arrows or other indications to show the positions of alignment pins or equivalent devices to prevent improper connection.

3.4.3 POSITIVE LOCKING DEVICES

Screw-type hardware on the DITP Flight System shall employ positive locking.

As a goal, lockwashers will not be used.

3.5 Documentation

Documentation shall be prepared according to the Supplier's established practices. The documents shall meet the intent of TBI's methods and practices for control of DITP hardware. The results of trade studies, analyses, and development efforts shall be documented to support critical design decisions and milestone technical reviews during the course of the system development. The TBI shall define its configuration management practices in a Configuration Management Plan. Delivery of documents electronically, rather than in hard copy, will be the preferred media.

3.5.1 SPECIFICATIONS

This DITP System Specification shall be provided and maintained by the TBI. Subsystem specifications shall be provided by the cognizant EA for the , the Passive Sensor Subsystem (PSS), and the Fusion Processor; LADAR Subsystem, and Algorithm (FP&A) Subsystem. These documents shall be subject to the respective EA change control procedures. Any changes to subsystem specifications shall be reported to the TBI. Any changes to the System Specification shall be reported to the respective EAs. and every proposed engineering change should consider the effect of that change on these documents so that compatibility is maintained. Delivery of documents electronically, rather than in hard copy, will be the preferred media.

3.5.2 DRAWINGS

Specifications and hardware shall be supported by drawings according to the tailored guidelines of MIL-T-31000 and DOD-D-1000B (or equivalent). The final system documentation should be such that subsequent demonstration hardware items can be produced or procured that are essentially equivalent to those initially tested or delivered.

3.5.3 SOFTWARE SUPPORT DOCUMENTATION

Software documentation shall be provided to include the following as a minimum:

A Software Product Specification (SPS) for each Computer Software Configuration Item (CSCI) as well as a Test Plan for each of the CSCIs. The SPS shall include the requirements for that particular CSCI, a general description of the software and its interfaces, and the actual source code.

3.5.4 TEST PLANS AND PROCEDURES

System and subsystem test plans shall be provided that identify what tests will be performed, the overall objectives of tests, and the chronological sequence of tests. Test procedures will be provided for planned tests. Procedures will identify all information required to conduct a test, including documentation of test results. Test plans and procedures will be documented to the level that allows testing of the system by DITP engineering and scientific personnel. Delivery of documents electronically, rather than in hard copy, will be the preferred media.

3.5.5 STRUCTURAL ANALYSIS PLAN

A structural analysis plan shall be provided using guidelines provided by the TBI. Positive margins shall be demonstrated. Delivery of documents electronically, rather than in hard copy, will be the preferred media.

3.6 Logistics

3.6.1 SUPPORT CONCEPT

Logistics planning shall include identification and procurement of long-lead and critical spares, repair parts, support facilities and equipment, training of personnel, and maintenance support at the test and launch sites, consistent with system testing and demonstrations. No scheduled or preventive maintenance shall be required to meet the system requirements specified herein.

3.6.1.1 Support Facilities

Support facilities will be provided as applicable during test and demonstrations by:

- a. BMDO's existing AMOR, KHILS, and ISTEf test and calibration facilities;
- b. NRL's integration and test facilities located in NRL's Building A-59, Payload Processing Facility.

- c. the Test Range.

3.6.1.2 Hardware Support

The DITP Target, Flight, and Launch Vehicle Systems' and Test Range integration and test planning, along with related calibration activities, shall maximize the use and minimize the modification of existing BMDO, NRL, WSMR and Supplier facilities and equipment.

3.6.1.3 Computer Software Support

Specific requirements for these areas of computer software support are defined in the Software Development Plan.

3.6.1.4 Personnel and Training

A concise, informal, and streamlined training program shall be planned and implemented to train the appropriate NRL and TBI support personnel for conducting tests, processing, and on-orbit operations defined herein.

3.6.2 MAINTENANCE CONCEPT

Formal maintenance shall not be required for the DITP Flight System. Repairs and replacements of hardware will be accomplished as necessary during conduct of tests and demonstrations using personnel intimately familiar with the specific hardware. Common laboratory equipment, coupled with developmental GSE shall be used to support hardware repairs and adjustments. Software maintenance shall be accomplished using the expertise of personnel who are intimately familiar with the existing code and computer hardware.

3.7 Quality Factors

3.7.1 SURVIVABILITY/HARDNESS

No survivability or hardness requirements shall be assigned to the DITP systems.

3.7.2 HAZARDOUS MATERIAL

All expendable materials used in packing, shipment, and storage shall not contribute to corrosion caused by rain or condensation leaching objectionable chemicals contained in the expendable material. Objectionable chemicals are lead, mercury, chloride, fluoride, sulfur, copper, and zinc. In order to assure that such corrosion does not occur, it is expected that the Seller/shipper shall select expendable materials which contain objectionable chemicals in trace concentrations only. Where any shipment contains hazardous materials, as defined in the regulations of the U.S. Department of Transportation, all packing lists, containers, and shipping documents shall be marked accordingly and in strict compliance with the rules and regulations governing the transportation of such materials.

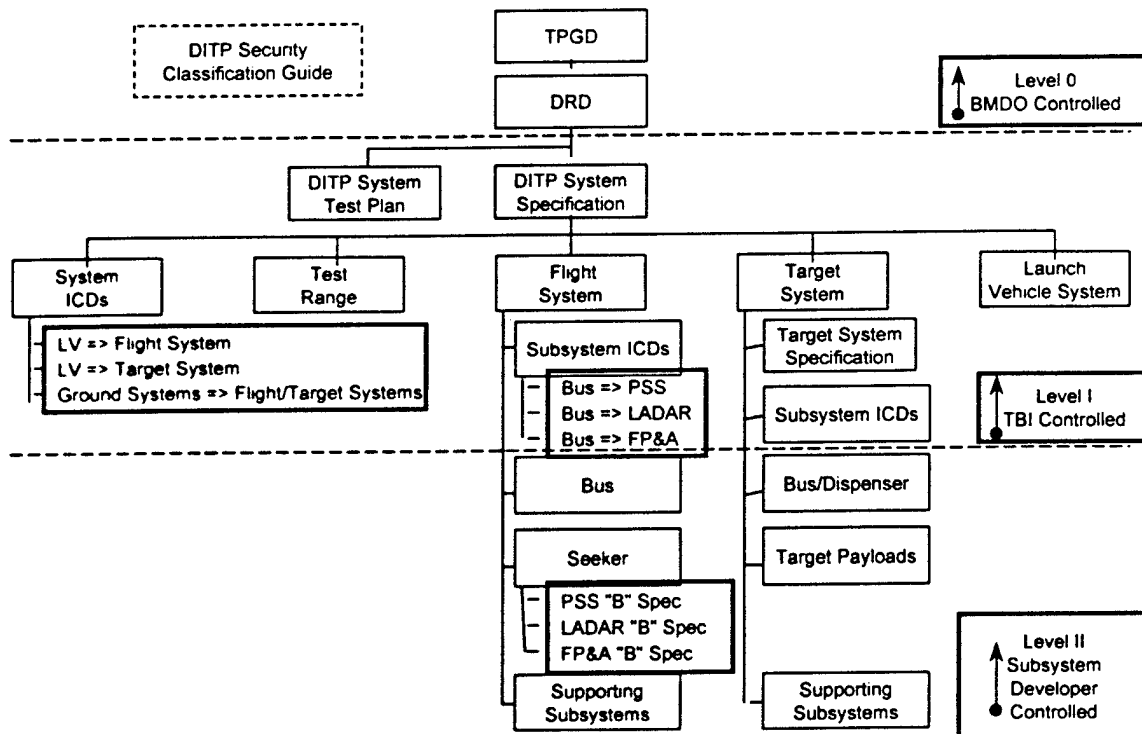
3.7.3 OTHER QUALITY FACTORS

3.7.3.1 Guidelines for Packaging and Shipping

The following shall be used as guidelines for packaging and storing DITP hardware. Specific packaging requirements developed to accommodate the environmental conditions specified for storage and T&H in the ERD shall be defined in subsystem and lower level specifications. Each shipment shall contain a detailed packing list.

3.7.4 PRECEDENCE AND CRITICALITY OF REQUIREMENTS

The order of precedence for the DITP System program is defined in the DITP System Specification Tree shown in Figure 3.7-1.



(TBD) Need updated Spec Tree

Figure 3.7-1 DITP Specification Tree

4. QUALIFICATION REQUIREMENTS

Responsibilities and recommended approaches for verifying Section 3.0 requirements are identified in the Requirements Verification Matrix, Appendix A. The RVM identifies the organization(s) responsible for verifying each requirement. Inspections, demonstration, testing, and analysis shall be performed to verify compliance with the requirements. Following are definitions of each of these four verification methods.

4.1 Verification Methods

4.1.1 ANALYSIS

Analysis is the processing of accumulated data obtained from other qualification methods. Examples are reduction, interpolation or extrapolation of test results. The selected techniques may include similarity, systems engineering computations, statistics and qualitative analysis, computer and hardware simulations, and analog modeling.

Analytical techniques may be used in lieu of tests for such things as reliability assessment, life, storage, failure analysis, safety, interchangeability and other performance requirements which cannot readily be tested.

Another analysis verification is similarity, the process of assessing (by review of prior test data or hardware configuration and applications) that the article is similar or identical in design and manufacturing process to another article that has previously been qualified to equivalent or more stringent specifications.

4.1.2 DEMONSTRATION

Demonstration is observation of operation of the system or system element that relies upon observation of its functional operation without resorting to use of instrumentation, special test equipment, or subsequent analysis.

4.1.3 INSPECTION

Inspection is the visual examination of system/system element components and documentation. It may be used instead of or in conjunction with testing to verify features such as design, construction, workmanship, dimensions and physical condition.

4.1.4 TEST

Verification by test consists of operating the system with real or simulated inputs, recording data during the test, analyzing the data, and comparing the results to the specification requirements to determine compliance. Following are brief descriptions of tests which may be performed.

4.1.4.1 Assembly Level Tests

Before subsystem testing, assembly level tests shall be performed to verify compliance with assembly development/acceptance specifications.. These assembly level tests are categorized as follows.

4.1.4.2 Assembly Feasibility Test

These are tests of critical components of the assemblies which are conducted prior to detail design to reduce technical risk to the project by acquiring data necessary for the design or to verify that minimum critical requirements can be attained. The assembly provider defines these tests.

4.1.4.3 Assembly Design Verification Tests (DVT)

These are tests conducted that validate the design by testing sub-scale hardware and obtaining test results that can be scaled to full-scale hardware..

4.1.4.4 Assembly Qualification Tests

These are defined primarily as manufacturing compliance tests. These may include, but are not limited to:

1. Radiography examination, as required
2. Dye penetrant or magnetic particle examinations, as required
3. Hydrostatic proof tests
4. Gas leak checks
5. Cable continuity checks

4.1.4.5 Assembly Acceptance Tests

Assembly-level compliance with specifications that require verification by means of test shall be performed.

4.1.4.6 Subsystem Acceptance Test

These are tests that are conducted prior to system integration that are intended to demonstrate compliance with subsystem specification Section 3 requirements.

4.1.4.7 System Level Test

System Level tests are conducted to verify compliance with Section 3.0 requirements of this specification. The RVM provides the guidelines for system requirements verification. The detailed description of system tests is contained in the System Test Plan, NCST-TP-DT001.

5. NOTES

5.1 DRD Cross Reference

Table 5.1-1 shows the traceability from the DRD to paragraphs of this system specification.

Table 5.1-1 DRD to System Specification Cross-Reference

DRD Paragraph	System Spec Paragraph
1.0 INTRODUCTION	1.0 INTRODUCTION
2.0 REFERENCE DOCUMENTS	2.0 APPLICABLE DOCUMENTS
3.0 DEMONSTRATION DESCRIPTIONS	1.3 DITP System Description
3.1 Acceptance Testing	4.1.5 Test Levels (details contained in System Test Plan, NCST-TP-DT001)
	4.1.5.2 Subsystem Acceptance Test (details contained in System Test Plan, NCST-TP-DT001)
3.2 Integrated System-Level Demonstrations (Fused-Sensor Suite)	4.1.5.3 System Test (details contained in System Test Plan, NCST-TP-DT001)
3.2.1 Laboratory/Field Tests	4.1.5.3 System Test (details contained in System Test Plan, NCST-TP-DT001)
3.2.3 Flight Demonstrations	4.1.5.3 System Test (details contained in System Test Plan, NCST-TP-DT001)
3.2.3.1 Flight Test Requirements/Constraints	3.1.2.2 Demonstration Scenario Constraints
3.2.3.1.1 Trajectory	3.1.2.2.1 through 3.1.2.2.8
3.2.3.1.2 Target Set	3.2.2.1 Flight Target System Requirements
3.2.3.1.3 Fused-Sensor System	3.2.2.2 Flight System Requirements
3.3 Environments	3.2.3 Environmental Conditions (Refer to Environmental Condition Document, NCST-D-DT004)
4.0 Demonstration Requirements	3.1.1 DITP Overview
4.1 Major Objectives	3.1.1.1.1 Technology Development Objectives 3.1.1.2.1 Technology Demonstration Objectives

DRD Paragraph	System Spec Paragraph
4.2 Primary Objectives	3.1.1.1.1 Technology Development Objectives 3.1.1.2.1 Technology Demonstration Objectives
4.3 Secondary Objectives	3.1.1.1.1 Technology Development Objectives 3.1.1.2.1 Technology Demonstration Objectives
4.4 Specific Goals	3.1.2.1 DITP Demonstration Goals
4.5 Major Objectives Evaluation Methodology	see System Test Plan (
5.0 Detailed Test Plan	see System Test Plan

5.2 Table of Acronyms

Acronym	Definition
AAR	Angle-Angle-Range
AFRL	Air Force Research Laboratory
AMOR	Army Missile Optical Range
ANSI	American National Standards Institute
az	Azimuth
BB9	Black Brant IX
BIT	Built-In-Test
BMDO	Ballistic Missile Defense Office
C1	Capability level One (NMD Threshold Capability)
C2	Capability level Two (NMD Intermediate Capability)
C3	Capability level Three (NMD Objective Capability)
CLB	Canisterized Large Balloon
cm	centimeter
CMB	Canisterized Medium Balloon
CSO	Closely Spaced Objects
CT&DH	Command, Telemetry and Data Handling
deg	degree
DITP	Discriminating Interceptor Technology Program
DOD	Department of Defense
DRD	Demonstration Requirements Document
DTI	Design-To Threat

Acronym	Definition
DVT	Design Verification Test
EA	Executing Agent
EEE	Electrical, Electronic, and Electromagnetic
el	Elevation
EMIC	Electromagnetic Interference Compatibility
EPS	Electrical Power Subsystem
ERD	Environmental Requirements Document
FAB	Fabricate
FCA	Flight Cryostat Assembly
FAB	Fabricate
FOR	Field Of Regard
FOV	Field of View
FPA	Focal Plane Array
FP&A	Fusion Processing and Algorithms
FS	Flight System
FTS	Flight Target System
FY00, FY01	Fiscal Year 2000, Fiscal Year 2001 etc.
GFE	Government Furnished Equipment
giga	prefix = 1×10^9
GN&C	Guidance, Navigation, and Control
GSE	Ground Support Equipment
HgCdTe	Mercury-Cadmium-Telluride
ICD	Interface Control Document
I&C/O	Integration and Checkout
IFTU	In-Flight Target Update
IOS	Integrated Optics Subsystem
IPD	Intensified Photo Diode
IR	InfraRed
ISTEF	Innovative, Science and Technology Experimentation Facility
IX	Roman number 9
kg	kilogram

Acronym	Definition
km	kilometer
KHILS	Kinetic kill vehicle Hardware-In-the-Loop Simulator
LADAR	Laser Radar
LOS	Line Of Sight
LRCS	Laser Radar Cross Section
LV	Launch Vehicle
LWIR	Long Wavelength InfraRed
LWIS	Light Weight Instrumentation System
m	meter
μrad	1 millionth of a radian
MBC	Multi-Balloon Canister
MDAP	Major Defense Acquisition Program
MSP	Malleable Signal Processors
MWIR	Medium Wavelength InfraRed
NA	Not Available, Not Applicable
Nd YAG	Neodymium Yttrium Aluminum Garnet
NMD	National Missile Defense
NRL	Naval Research Laboratory
IOS	Integrated Optical Subsystem
OPS	Optics, Pointing and Stabilization
PMRF	Pacific Missile Range Facility
PMRF	Pacific Missile Range Facility
PSS	Passive Sensor Subsystem
RCS	Reaction Control Subsystem
REFURB	Refurbish
RF	Radio Frequency
RFS	Radio Frequency Subsystem
RLR	Rigid Light Replica
RV	Reentry Vehicle
RVM	Requirements Verification Matrix
S&M	Structure and mechanisms

Acronym	Definition
sec	second
σ	Sigma, symbol for standard deviation
STP	System Test Plan
TBD	To be Determined or Defined
TBI	Test Bed Integrator (aka Charlie Merk)
TBR	To Be Resolved
T&H	Transportation and Handling
THAAD	Theater High Altitude Area Defense
TM	Thermal Management
TOS	Advanced Technology Directorate (BMDO)
3-D	Three dimensional
TMD	Theater Missile Defense
TOM	Target Object Map
TPGD	Technology Program Goals Document
WSMR	White Sands Missile Range
WSSP	Wafer-scale Signal Processor

5.3 Glossary

(TBD) Need review and additional definitions

Term	Definition
Demonstration	Demonstration is a process which relies upon observation of functional operation without resorting to use of instrumentation, special test equipment, or subsequent analysis.
Designation	Identify positively the threat object and calculate intercept vectors
Discrimination	To sense and identify the number of objects in the scenario and separate the threat from the countermeasures, decoys and other debris.
Field of Regard	
Field of View	
Filtered Objects	Objects which have been interrogated by some of the

[illegible]

Term	Definition

6. APPENDIX A - REQUIREMENTS VERIFICATION MATRIX

This appendix contains the DITP Requirements Verification Matrix. It establishes the means by which the validated requirements of this specification are to be verified, using the definitions presented in Section 4.1.3. The symbols A, D, I and T denote analysis, demonstration, inspection and test, respectively. For example, TBI/A/D means that verification is the responsibility of the TBI and will involve a combination of analysis and demonstration. Likewise, PSS/I/T would mean that the PSS EA is responsible for verification using a combination of inspection and test.

DITP System Requirements Verification Matrix for Version Aspect 14 doc

	DITP System Specification Paragraph	Requirement	Definition	Subsystem Verification Approach	System Verification Approach	Verification Basis	Status	Requirement Validation Traceability
3	REQUIREMENTS							
3.1	System Definition					Accepted at SRDR		title only
3.1.1	DITP Overview							title only
3.1.1.1	Technology Development	Guidelines/ goals			TBI/I	-		flowdown from TPGD 1.3
3.1.1.1.1	Technology Development Objectives	-	Traceable to advanced missile threats in ~		TBI/O	-		flowdown from TPGD 1.3
3.1.1.2	Technology Demonstration	-						flowdown from TPGD 1.3
3.1.1.2.1	Technology Demonstration Objectives	-	Major objectives		TBI/O	completion of flight demos		flowdown from TPGD 1.3
3.1.2	DITP Demonstration Scenarios	-						flowdown from TPGD 2.0
3.1.2.1	DITP Demonstration Goals	-			TBI/O	-		flowdown from TPGD 2.0
3.1.2.2	Demonstration Scenario Constraints							
3.1.2.2.1	Closing Velocity	≥ 2 km/sec	Closing velocity at Ladar acquisition		TBI/A/D	-		derived from DRD 3.2.3.1.1
3.1.2.2.2	Exoatmospheric Observation Altitude	≥ 100 km	Altitude for sensor demo	PSS/A/T	TBI/O	-		flowdown from DRD 3.2.3.1.1
3.1.2.2.3			Demonstration scenarios shall not result in sensor damage caused by pointing too close to sun or moon	LADAR/A/T		completion of subsystem tests		flowdown from DRD 3.2.3.1.1
3.1.2.2.4	Solar Exclusion Angle		Demonstration scenarios shall not result in sensor damage caused by pointing too close to sun or moon	PSS/A/T		-		flowdown from DRD 3.2.3.1.1
3.1.2.2.5	Lunar Exclusion Angle	≥ 90 deg above Earth nadir	Minimum angle from sensor LOS to Earth	PSS/A/T		-		derived from DRD 3.2.3.1.1
3.1.2.2.6	Earth Exclusion Angle		Demonstration scenarios shall not result in sensor damage caused by pointing at radiation sources (e.g. planets, stars, Earth-orbiting objects)	PSS/A/T		-		derived from DRD 3.2.3.1.1
3.1.2.2.7	Other Exclusion Angles							
3.1.2.2.7.1	Flight Scenarios	≥ 15 deg & ≤ 35 deg			TBI/A/D			title only
3.1.2.2.7.2	Angle Between Seeker Line of Sight and Target Coning Axis	Probability of Collision $< 10^{-4}$	Collision of DITP hardware with other vehicles		TBI/A/D	completion of flight demos		derived by TDWG
3.1.2.2.7.3	Collision Avoidance	Recover FS hardware			TBI/A	-		derived from DRD 3.2.3.1.1
3.1.2.2.8	Vehicle(s) Recovery Position Determination				TBI/A/D	-		Derived by TDWG at SRDR
3.1.2.2.8.1	Flight System Position Determination	(TBD) m			TBI/A/D	-		flowdown from DRD 3.2.3.1.1
3.1.2.2.8.2	Target System Position Determination	(TBD) m			TBI/A/D	-		flowdown from DRD 3.2.3.1.1 to be derived by TDWG
3.1.3	System States and Modes	context		PSS/A LADAR/A FP&A/A	TBI/A/D	States and modes accepted at SRDR	closed	derived from TPGD & DRD by FWG/TBI

	DITP System Specification Paragraph	Requirement	Definition	Subsystem Verification Approach	System Verification Approach	Verification Basis	Status	Requirement Validation Traceability
3.1.3.1	Dormant State	-		PSS/A LADAR/A FP&A/A	TBI/A	-	closed	-
3.1.3.2	Operational State Modes	-		PSS/A LADAR/A FP&A/A	TBI/A	-	closed	-
3.1.3.2.1	Operational State - Flight Demonstration Modes	-		PSS/A LADAR/A FP&A/A	TBI/A	-	closed	-
3.1.3.2.2	Operational State - Second Flight Demonstration	-		PSS/A LADAR/A FP&A/A	TBI/A	-	closed	-
3.1.3.2.3	Operational State - Ground Demonstration Modes	-		PSS/A LADAR/A FP&A/A	TBI/A	-	closed	-
3.1.4	System Configuration	Context			TBI/I	Configuration to be accepted at PDR		descriptions only
3.1.4.1	Flight Target System	-			TBI/I	-		-
3.1.4.1.1	Target Object Sets	-			TBI/I	-		-
3.1.4.1.2	Minimum Set	1 scaled down, instrumented RV 1 simulated replica, at least 1 sample decoy			TBI/I	-		Derived by TDWG, Y. Kinashi, finalized for 16 Jan 1999 req. Review
3.1.4.1.3	Enriched Target Set	1 scaled down, instrumented RV 1 high fidelity replica, 3 to 5 additional balloons			TBI/I	-		Derived by TDWG, Y. Kinashi, finalized for 16 Jan 1999 req. Review
3.1.4.1.4	Target Bus/Dispenser	-			TBI/I	-		-
3.1.4.1.5	Supporting Subsystems	-			TBI/I	-		-
3.1.4.1.6	Ground Support Equipment (GSE)	-			TBI/I	-		-
3.1.4.2	DITP Flight System (FS)	-			TBI/I	-		-
3.1.4.2.1	Seeker Subsystems	-		PSS/A/I LADAR/A/I FP&A/A/I	TBI/I	-		-
3.1.4.2.2	Bus Subsystems	-			TBI/I	-		-
3.1.4.2.3	Supporting Subsystems	-			TBI/I	-		-
3.1.4.2.4	Ground Support Equipment (GSE)	-			TBI/I	-		description only
3.1.4.3	Launch Vehicle System	-			TBI/I	-		-
3.1.4.4	Test Range	-			TBI/I	-		-
3.1.4.4.1	Test Range Facilities	-						-
3.1.4.4.2	Test Range Instrumentation	-						-
3.1.4.4.3	DITP-Unique Instrumentation	-						-
3.1.4.4.4	Ground Support Equipment	-						-
3.1.5	Interface Requirements DITP Interfaces With Non-DITP Sites and Organizations	Mechanical, electrical, and signal interfaces Interfaces between DITP system and non-DITP systems		PSS/A/I LADAR/A/I FP&A/A/I	TBI/A/I/T/D TBI/A/I/T/D	-		defined by allocation of functions title only

	DITP System Specification Paragraph	Requirement	Definition	Subsystem Verification Approach	System Verification Approach	Verification Basis	Status	Requirement Validation Traceability
3.1.5.2	Internal Interfaces		Interfaces between DITP configuration items	PSS/A/VT LADAR/A/VT FP&A/VT	TBI/A/VT/D			title only
3.2	System Characteristics			LADAR/VT PSS/VT FP&A/VT	TBI/A/VT/D			nominal
3.2.1	Design Lifetime			LADAR/A PSS/A FP&A/A	TBI/A/VT TBI/A			Defined by TBI team at 6 Jan 1999 req. review
3.2.1.1	Dormant State Lifetime	3 yrs		LADAR/A/D PSS/A/D FP&A/A/D	TBI/A/D			Defined by TBI team at 18 Jan 1999 req. review
3.2.1.2	Operating Lifetime	context		LADAR/A/D PSS/A/D FP&A/A/D	TBI/A/D			derived from DRD 3.2.3.1.2
3.2.2	Physical Requirements			LADAR/A/D PSS/A/D FP&A/A/D	TBI/A/D			flowdown from DRD 3.2.3.1.2
3.2.2.1	Target System Requirements			LADAR/A/D PSS/A/D	TBI/A/D			title only
3.2.2.1.1	Ground Demonstration Target Objects	TBD		LADAR/A/VT	TBI/A/VT			derived from DRD 3.2.3.1.2
3.2.2.1.2	Target Object Temperature	TBD		PSS/A/VT	TBI/A/VT			derived from DRD 3.2.3.1.2
3.2.2.1.3	LADAR Cross Section	0.95 ± TBD		LADAR/A/VT	TBI/A/VT			title only
3.2.2.1.4	LWIR Emissivity	TBD		LADAR/A/VT	TBI/A/VT			derived by TDWG
3.2.2.1.5	Target Object LADAR Reflectivity	< 20 deg			TBI/A/VT			-
3.2.2.1.6	Target Object Coning Angle	1.5 to 2.5 m/sec			TBI/A/VT			-
3.2.2.1.7	Target Objects Dispersion Velocity			LADAR/A/D PSS/A/D				-
3.2.2.1.8	Flight Demonstration Target Objects	300 ± TBD deg			TBI/A/VT			-
3.2.2.1.9	Target Object Temperature	K			TBI/A/VT			title only
3.2.2.1.10	RLR Target Object Dimensions	length 1.4 m base diameter 0.4 m half-cone angle 7 deg			TBI/A/VT			derived by OPS WG (SRDR)
3.2.2.1.11	LWIR Emissivity	0.95 ± TBD		PSS/A/VT	TBI/A/VT			title only
3.2.2.1.12	Target Object LADAR Reflectivity	0.6, 16 %		LADAR/A/VT	TBI/A/VT			title only
3.2.2.1.13	Target Object Coning Angle	20 deg			TBI/A/VT			derived - optical path analysis
3.2.2.1.14	Target Objects Dispersion Velocity				TBI/A/VT			
3.2.2.1.15	Flight System Requirements				TBI/A/VT			
3.2.2.1.16	Probability of Target Designation	0.95			TBI/A/VT			two position zoom
3.2.2.1.17	Acquisition Ranges				TBI/A/VT			
3.2.2.1.18	Passive Sensor Acquisition Range - Flight Demonstration	> 400 km (TBD)		PSS/A/VT	TBI/A/VT			Requirement to be finalized by TDWG and PSS EA
3.2.2.1.19	LADAR Acquisition Range - Flight Demonstration	350 km		LADAR/A/VT	TBI/A/VT			Flowdown from DRD 4.4
3.2.2.2	Optics Field of View (FOV) and Field of Regard (FOR)							
3.2.2.2.1	Telescope Field of View (FOV)	1.6 x 2.0 deg			TBI/A/VT			Derived by OPS WG
3.2.2.2.2	Passive Sensor Field of Regard (FOR)	1.6 x 2.0 deg		PSS/A/VT	TBI/A/VT			

	DITP System Specification Paragraph	Requirement	Definition	Subsystem Verification Approach	System Verification Approach	Verification Basis	Status	Requirement Validation Traceability
3.2.2.2.3.3	Passive Sensor Field of View	0.6 x 0.6 deg		PSS/IAT	TBI/A/D			
3.2.2.2.3.4	LADAR Field of Regard	> PSS FOV		LADAR/IAT	TBI/A/D			
3.2.2.2.3.5	LADAR Field of View	> 52 mrad	without zooming	LADAR/IAT	TBI/A/D			per axis, 3 σ
3.2.2.2.4	Pointing Accuracy				TBI/A/T/D			per axis, 3 σ
3.2.2.2.4.1	Passive Sensor Angular Pointing Accuracy	< 5 μ rad		PSS/IAT	TBI/A/D			flowdown from DRD 3.2.3.1.3
3.2.2.2.4.2	LADAR Tracking Precision	< 5 μ rad		LADAR/IAT	TBI/A/D			
3.2.2.2.4.3	Pointing and Tracking Handover Error Budget			FP&A/IAT				PSS, LADAR, & FP&A derived from selected launch vehicle
3.2.2.2.4.3.1	Optical System Handover Error	< 10 μ rad	worst case TBR		TBI/A/T			
3.2.2.2.4.3.2	Centroiding and Tracking Handover Error	< 5 μ rad	1 σ , per axis		TBI/A/T/D			
3.2.2.2.4.3.3	Control Residual	< 5 μ rad	1 σ , per axis		TBI/A/T/D			TBI functional analysis
3.2.2.2.4.4	Seeker Boresight Pointing Accuracy	< 10 μ rad	1 σ , per axis	PSS/IAT	TBI/A/D			
3.2.2.2.5	Passive Sensor Instantaneous Field Of View	< 50 μ rad		LADAR/IAT	TBI/A/D			
3.2.2.2.6	LADAR Range Resolution	< 20 cm		LADAR/IAT	TBI/A/D			
3.2.2.2.7	LADAR Instantaneous Field of View	< 2.6 μ rad < 5.2 μ rad < 10 objects per sec		LADAR/IAT	TBI/A/D			
3.2.2.2.8	Pointing - Number of Targets			FP&A/IAT	TBI/A/D			
3.2.2.2.9	Seeker Jitter Budget				TBI/A/D			
3.2.2.2.9.1	IOS Jitter	< 4.2 μ rad	1 σ , per axis	PSS/IAT	TBI/A/D			derived from DRD 3.2.3.1.3
3.2.2.2.9.2	Passive Sensor Jitter	TBD			TBI/A/D			
3.2.2.2.9.3	LADAR Jitter (Transmitter)	< 5 μ rad		LADAR/IAT	TBI/A/D			
3.2.2.2.9.3.1	Laser Jitter	< 5 μ rad		LADAR/IAT	TBI/A/D			
3.2.2.2.10	FS Bus Inertial Pointing Accuracy	< 0.2 deg			TBI/A/D			
3.2.2.2.11	FS Bus Angular Acceleration	< 0.15 deg per sec ²			TBI/A/D			
3.2.2.2.12	Seeker Maximum Aperture	25 cm	defined by launch system capability		TBI/I			derived from DRD 3.2.3.1.3
3.2.2.2.13	FS Mass Properties	TBD		FP&A/I PSS/IAT LADAR/IAT	TBI/IAT			
3.2.2.2.13.1	Seeker Subsystems Mass	< 5kg each	defined by launch system capability		TBI/IAT			
3.2.2.2.13.2	FTS and FS Center of Mass		defined by launch system capability		TBI/IAT			
3.2.2.2.14	FTS and FS Volume				TBI/IAT			
3.2.2.2.15	FS Electrical Power	context			TBI/IAT			
3.2.2.2.16	FS Thermal Management				TBI/IAT			
3.2.2.2.16.1	FS Thermal Environment Stability							
3.2.2.2.16.2	Subsystems Thermal Management							
3.2.2.2.16.3	FS Thermal Management							
3.2.2.2.17	FS Bus Communications				TBI/IAT			
3.2.2.2.18	FS Data Processing				TBI/IAT			
3.2.2.2.18.1	Seeker Subsystems Data Availability			FP&A/IAT PSS/IAT LADAR/IAT				derived by TBI based on DRD demonstration objectives
3.2.2.2.18.2	FS Bus Flight Data Recording				TBI/A/D			
3.2.2.3	Launch Vehicle System Requirements	TBD			TBI/A/D			
3.2.2.4	Test Range Requirements				TBI/A/D			

	DITP System Specification Paragraph	Requirement	Definition	Subsystem Verification Approach	System Verification Approach	Verification Basis	Status	Requirement Validation Traceability
3.2.2.4.1.1	Communications Uplink	TBD						
3.2.2.4.1.2	Communications Downlink				TBI/A/D			-
3.2.2.4.1.3	Test Range Data Storage				TBI/A/D			-
3.2.2.4.1.4	Test Range Communication Protocol				TBI/A/D			flowdown from DRD, TBI analysis
3.2.3					TBI/A/D/T			
	Environmental Conditions	guidelines only	See DRD for environment constraints and conditions	FP&AI PSS/I LADAR/I/T				-
3.2.4				FP&AI PSS/I LADAR/I	TBI/I			-
	Design and Construction	-		FP&AI PSS/I LADAR/I	TBI/I			-
3.2.4.1				FP&AI PSS/I LADAR/I	TBI/I			-
3.2.4.2	Parts, Materials, and Processes	-		FP&AI PSS/I LADAR/I	TBI/I			-
3.2.4.3	Failure Reporting and Corrective Action System			FP&AI PSS/I LADAR/I	TBI/I			-
3.2.4.4	Part Stress Derating	guidelines only		FP&AI PSS/I LADAR/I	TBI/I			-
3.2.4.5	Soldering and Other Processes	-		FP&AI PSS/I LADAR/I	TBI/I			flowdown from DRD 3.3.1.7
3.2.5	Electrostatic Discharge Sensitive Parts	-		FP&AI PSS/I LADAR/I	TBI/I			
3.2.5.1	Electromagnetic Environment	per MIL-STD-461B		FP&AI PSS/I LADAR/I	TBI/A/T			per NFPA 780 and MIL-HDBK-419
3.2.5.2	Electromagnetic Compatibility (EMC)			FP&AI PSS/I LADAR/I/T	TBI/A/T			
3.2.5.3	Corona and Triboelectric Suppression	guidelines only		FP&AI PSS/I LADAR/I/T	TBI/A/T			TBI analysis
3.2.5.4	Bonding	-		FP&AI PSS/I LADAR/I/T	TBI/A/T			
	Lightning Protection and Grounding	guidelines only		FP&AI PSS/I LADAR/I/T	TBI/A/T			
3.2.5.4.1	Lightning Protection							
3.2.5.4.2	Premature Launch or Detonation							
3.2.5.4.3	No Launch in Presence of Lightning							
3.2.6	electromagnetic interference							
3.2.7	Workmanship			FP&AI PSS/I LADAR/I	TBI/I			
3.2.7.1	Interchangeability	guidelines only		FP&AI PSS/I LADAR/I	TBI/I			
3.2.7.2	Nameplate and Product Marking			FP&AI PSS/I LADAR/I	TBI/I			per MIL-STD-882C
3.2.8	Safety	single (TBR)		FP&AI PSS/I LADAR/I	TBI/I			flowdown from DRD 3.2.3.1.1
3.2.8.1	Safety From Emissions	comply		FP&AI PSS/I LADAR/I	TBI/I			TBI analysis
3.2.8.2	Critical Safety Hazards			FP&AI PSS/I LADAR/I	TBI/I/A			per ANSI Z136.1 & OSHA
3.2.8.3	Personnel Safety	comply		LADAR/I/A	TBI/A			

	DITP System Specification Paragraph	Requirement	Definition	Subsystem Verification Approach	System Verification Approach	Verification Basis	Status	Requirement Validation Traceability
3.2.8.4	Test Range Safety	TBD		FP&AI PSS/I LADAR/I	TB/I			per ANSI/ASME B31.3 & ASME B&PV Code
3.2.8.5	LADAR Safety	comply		FP&AI PSS/I LADAR/I	TB/I			per OSHA req
3.2.10	System Security			FP&AI PSS/I LADAR/I	TB/I			TBI analysis
3.3	Computer Resources			FP&AI LADAR/I	TB/I			per STP
3.4	Standards of Manufacture	comply		FP&AI PSS/I LADAR/I	TB/I			
3.4.1	Contamination Control and Cleanliness			FP&AI PSS/I LADAR/I	TB/I			
3.4.1.1	Protection From Contamination							
3.4.1.2	Contamination Control Guidelines							
3.4.2	Connectors			FP&AI PSS/I LADAR/I	TB/I			
3.4.3	Positive Locking Devices			FP&AI PSS/I LADAR/I	TB/I			
3.5	Documentation			FP&AI PSS/I LADAR/I	TB/I			
3.5.1	Specifications			FP&AI PSS/I LADAR/I	TB/I			
3.5.2	Drawings			FP&AI PSS/I LADAR/I	TB/I			
3.5.3	Software Support Documentation			FP&AI PSS/I LADAR/I	TB/I			
3.5.4	Test Plans and Procedures			FP&AI PSS/I LADAR/I	TB/I			
3.5.5	Structural Analysis Plan			FP&AI PSS/I LADAR/I	TB/I			
3.6	Logistics			FP&AI PSS/I LADAR/I	TB/I			
3.6.1	Support Concept			FP&AI PSS/I LADAR/I	TB/I			
3.6.1.1	Support Facilities			FP&AI PSS/I LADAR/I	TB/I			
3.6.1.2	Hardware Support			FP&AI PSS/I LADAR/I	TB/I			
3.6.1.3	Computer Software Support			FP&AI PSS/I LADAR/I	TB/I			
3.6.1.4	Personnel and Training			FP&AI PSS/I LADAR/I	TB/I			
3.6.2	Maintenance Concept			FP&AI PSS/I LADAR/I	TB/I			
3.7	Quality Factors			FP&AI PSS/I LADAR/I	TB/I			
3.7.1	Survivability/Hardness	scalable		FP&AI PSS/I LADAR/I	TB/I			
3.7.2	Hazardous Material			FP&AI PSS/I LADAR/I	TB/I			flowdown from TPGD
3.7.3	Other Quality Factors			FP&AI PSS/I LADAR/I	TB/I			flowdown from DRD TBD
3.7.3.1	Guidelines for Packaging and Shipping			FP&AI PSS/I LADAR/I	TB/I			

	DITP System Specification Paragraph	Requirement	Definition	Subsystem Verification Approach	System Verification Approach	Verification Basis	Status	Requirement Validation Traceability
3.7.4	Precedence and Criticality of Requirements	comply with DITP Spec Tree		FP&AT PSSM LADAR	TBI			TBI analysis

Appendix O

NAVAL RESEARCH LABORATORY NAVAL CENTER FOR SPACE TECHNOLOGY

DITP System Test Plan NCST-TP-DT001

Approved By: _____ Date: _____
C. Merk, TBI Project Manager

Draft Input To NRL

DISTRIBUTION STATEMENT C: Distribution authorized to U.S. Government agencies and their contractors; Administrative or Operational Use. Other requests for this document shall be referred to Mr. C. Merk, Code 8222, Naval Research Laboratory, 4555 Overlook Avenue, S.W., Washington, D.C. 20375-5000.

**4555 Overlook Avenue, S.W.
Washington, D.C. 20375-5000**

1	INTRODUCTION.....	5
1.1	Background.....	5
1.2	Scope.....	6
1.3	Definitions.....	7
1.4	DITP System Description.....	7
1.4.1	Target System.....	8
1.4.1.1	Target Payload Objects.....	9
1.4.1.1.1	Minimum Set.....	9
1.4.1.1.2	Enriched Target Set.....	9
1.4.1.2	Target Bus/Dispenser Payload.....	10
1.4.1.3	Target Bus - Mechanical.....	Error! Bookmark not defined.
1.4.1.4	Target System Supporting Subsystems.....	11
1.4.1.5	Target System GSE.....	12
1.4.2	Flight System.....	12
1.4.2.1	Seeker Subsystems.....	12
1.4.2.1.1	Passive Sensor Subsystem (PSS).....	12
1.4.2.1.2	Laser Radar Subsystem (LADAR) Subsystem.....	16
1.4.2.1.3	Fusion Processor & Algorithms (FP&A) Subsystem.....	19
1.4.2.1.4	Integrated Optics Subsystem.....	19
1.4.2.2	Bus Subsystems.....	19
1.4.2.2.1	Bus Mechanical.....	19
1.4.2.2.2	Bus Electrical Subsystems.....	20
1.4.2.2.3	EPS Description.....	20
1.4.2.2.4	CT&DH Subsystem Description.....	20
1.4.2.2.5	GN&C Subsystem Description.....	21
1.4.2.2.6	RFS Description.....	21
1.4.2.2.7	supporting system description.....	21
1.4.3	Launch System.....	21
1.4.4	Ground Systems Description.....	22
1.5	Scope of Tests.....	22
1.5.1	Subsystem and Assembly Testing.....	23
1.5.2	System Testing.....	24
2	DOCUMENTS.....	25
3	SUBSYSTEM DEVELOPMENT & TEST.....	25
3.1	Target System Subsystem Testing.....	25
3.1.1	Introduction.....	25
3.1.2	Target Object Payload Testing.....	25
3.1.3	Target Bus/Dispenser Testing.....	26
3.1.4	Target System Supporting Subsystems Testing.....	26
3.1.5	Target System Ground Support Equipment Testing.....	26
3.1.6	Target System Analyses – Reflectivity; Traceability; etc.....	26
3.1.7	Integrated Target System Tests (Non WSMR Tests).....	26
3.1.7.1	Integrated Target System Mechanical Tests (Non WSMR Tests).....	26
3.2	Flight System subsystems Testing.....	26
3.2.1	Seeker Subsystem Tests and Analyses Joe.....	26
3.2.1.1	PSS Tests and Analyses.....	26
3.2.1.2	LADAR Subsystem Tests and Analyses.....	27
3.2.1.2.1	Assembly Tests.....	Error! Bookmark not defined.
3.2.1.2.1.1	Ladar Testbed Component Integration.....	28
3.2.1.2.1.2	Ladar Testbed Receiver Component Tests III.....	28

3.2.1.2.1.3.....	Ladar CSO Performance Test.....	29
3.2.1.2.1.4.....	Brassboard Ladar Acceptance Test.....	30
3.2.1.2.1.5.....	Ladar Performance Test at ISTE F.....	30
3.2.1.2.1.6.....	Flight System #1 Ladar Acceptance Test.....	31
3.2.1.3	FP&A Subsystem Testing and Analyses	32
3.2.1.4	IOS Testing and Analyses Amy + Others.....	32
3.2.1.5	Seeker Subsystem Integration Tests George H./Yas	36
3.2.1.5.1	Seeker Integration Tests.....	36
3.2.1.5.1.1.....	10 Kg brassboard units (AMOR/KHILS) George/Yas	36
3.2.1.5.1.2.....	5 Kg flight units (AMOR/KHILS) George/Yas	36
3.2.2	Bus Subsystems Testing Joe.....	36
3.2.2.1	Bus Mechanical Tests Joe.....	36
3.2.2.1.1	Mechanical Testing Chris.....	Error! Bookmark not defined.
3.2.2.2	Electrical Subsystems Testing Tim.....	36
3.2.2.2.1	EPS.....	36
3.2.2.2.2	CT&DH.....	36
3.2.2.2.3	GN&C.....	36
3.2.2.2.4	RFS	36
3.2.2.2.5	Supporting Subsystems (radar beacon).....	36
3.2.2.3	Bus Subsystem Analyses Chris/Tim.....	36
3.2.2.4	Integrated Subsystem Tests Jack	36
3.2.2.5	Supporting Subsystems Tests Jack	36
3.2.2.6	Ground Support Equipment Tests Jack.....	36
3.2.2.7	Flight System Analyses Other than Bus/Seeker	36
3.2.2.8	Integrated Flight System Tests (pre WSMR).....	36
3.3	Launch vehicle Subsystem Testing and Analyses	36
3.3.1	Launch Vehicle Subsystems Testing	36
3.3.1.1	Flight System LV.....	36
3.3.1.2	Target System LV	37
3.3.2	Launch Vehicle System Analyses	37
3.3.2.1	Mass Properties Analysis.....	37
3.3.2.2	Orbit/Trajectory Analysis	37
3.3.2.3	Water Recovery/Salt Water Ingress Analysis.....	37
3.3.2.4	Structure Analysis.....	37
3.3.2.5	Thermal Analysis.....	37
3.3.3	Integrated Launch Vehicle Tests.....	37
3.3.4	Interface Tests with other systems.....	38
3.3.4.1	Vibe.....	38
3.3.4.2	Thermal.....	38
3.3.4.3	Electrical/Mechanical C/O at the Range.....	38
3.3.4.4	Visual Inspection at the Range	38
3.4	Ground System subsystem testing and analysis.....	38
3.4.1	Subsystem Tests Jack	38
3.4.1.1	Launch Range Facilities Jack.....	38
3.4.1.2	Launch Range Instrumentation Jack.....	38
3.4.1.3	DITP Unique Instrumentation Tim.....	38
3.4.1.4	Ground Support Equipment Jack.....	38
4	SYSTEM TESTING AND ANALYSES.....	38
4.1	10 Kg System Level Functionality Tests [WSMR/ISTEF] George.....	38
4.2	5 Kg System Level Performance Tests [Risk Reduction AMOR/KHILS].....	38
4.3	5 Kg System Level Functionality Tests [ISTEF/WSMR] George.....	38
4.4	Flight System/Launch Vehicle/Ground System Checkout Tests (WSMR) Joe.....	38

4.5	Target System/Launch Vehicle/Ground System Checkout Tests (WSMR)	38
5	FLIGHT DEMONSTRATION.....	38
6	ROLES AND RESPONSIBILITIES.....	38
6.1	Support Engineering	38
6.1.1	Safety	38
6.1.1.1	Range Safety	39
6.1.1.2	Fault Tolerance	39
6.1.1.3	Laser Radar Safety	39
6.1.1.4	Pressurized Containers Safety	39
6.1.2	Reliability and Maintainability	39
6.1.3	Quality Assurance	39
6.1.3.1	Contamination Control	39
6.1.3.2	Configuration and Data Management	39
6.2	Test Responsibilities	39
6.3	Test Documentation	40

1 INTRODUCTION

The Ballistic Missile Defense Organization (BMDO) is developing technologies and systems to defend the United States, its forces and its allies against ballistic missile attack. Advanced sensor and processing technologies are critical areas being pursued by BMDO to support these objectives. The Discrimination Interceptor Technology Program's (DITP) primary objective is to develop technologies and demonstrated capabilities which support both Theater Missile Defense (TMD) and National Missile Defense (NMD) interceptor seeker upgrade capabilities needed for negating advanced threats. Under DITP, BMDO will develop advanced sensors and a sensor fusion processor. It will demonstrate data fusion from miniaturized, collocated, dissimilar sensors and during scheduled test flights, will demonstrate interceptor-based discrimination capability for interception against simulated threats.

1.1 BACKGROUND

DITP is a result of BMDO's need for advanced technologies to enhance and enable current and future interceptor seeker systems. The charter of the Technical Operations (TO) Deputate is to "support research on more advanced ballistic missile defense technologies to improve performance of components of both TMD and NMD systems, and provide advanced capabilities such as Boost Phase Intercept (BPI)." In light of this charter, TO conducted an FY93 survey of technologies needed for advanced and future BMD systems. The survey, based on Operational Requirements Documents (ORDs), the System Threat Analysis Report (STAR), and the Architecture Integration Study (AIS), identified several core technology needs. Midcourse discriminating interceptor seekers, BPI sensors, and cruise missile acquisition sensors were recognized as requiring component improvements. The fusion of data from dissimilar sensors on a single platform, was viewed as an area in which modest investment could significantly enhance existing seeker performance and produce high payoffs.

Based on an exhaustive advanced sensor technology review during FY94, weighing technology deficiencies against existing research efforts, several advanced component technologies were selected for development. These technologies included: passive simultaneous multi-color infrared (IR) sensors, long-range laser radars (LADAR), and multispectral discrimination algorithms.

This led to a technology development program, the Advanced Sensor Technology Program (ASTP) which was initiated to investigate advanced technologies in the areas of IR focal plane arrays (FPAs), LADAR technologies and multi-sensor tracking and discrimination algorithms. DITP seeks to capitalize on ASTP's advancements and focus selected technologies to answer the advanced interceptor issues developed in the DITP Technology Program Goals Document (TPGD). Target data from these advanced sensors will be synergistically fused to demonstrate enhanced target acquisition, selection, and hit-to-kill aimpoint performance for the multispectral domain.

The aim then of DITP is to choose a technology from each of the potential technologies for the two color passive sensor, the Laser Radar and the Fusion Processor and Algorithms and integrate them to do a series of ground and flight demonstrations. These will demonstrate advanced detection and discrimination technology to be used against the advanced threats described in the TPGD. In accordance with the guidance of the Director, BMDO, the TO Deputate has involved the three US military services in DITP to take advantage of expertise and advancements in seeker technology. Motivations for this partnership include the need to decrease technology development time and build upon existing research programs.

The DITP system is thus being developed under the direction of four government entities. The Naval Research Laboratory (NRL) serves as the Test Bed Integrator and is responsible for integrating and testing, the DITP technologies to demonstrate system level objectives. This culminates in a flight demonstration which is also NRL's responsibility.

DITP includes Executive Agents (EA) identified by the BMDO TOS to provide government furnished equipment (GFE) as well as technical expertise to support the successful completion of the overall program goals. BMDO/TOS, NRL, EA, and contract support representatives will be called upon to participate in the overall program management. The EAs will develop the following advanced seeker technology subsystems:

- Passive Sensor Subsystem (PSS), Air Force Research Laboratory/VSSS (Kirtland) (AFRL/VSSS (Kirtland));
- Laser Radar Subsystem (LADAR), U. S. Army Space and Missile Defense Command/TC/SR (Huntsville) (USASMD/TC/SR (Huntsville));
- Fusion Processor and Algorithms Subsystem (FP&A), Air Force Research Laboratory/IFSB (Rome) (AFRL/IFSB (Rome)).

Based on this, the top level goal for the DITP System is to demonstrate the performance and technical maturity of the EA-provided sensor technologies through a series of ground tests and demonstrations which verify sensor performance and validate their acceptability to perform a flight test demonstration. These culminate in a flight test demonstration which serves to show that the sensors can function and perform in a seeker configuration and environment. Specifically, these tests must demonstrate the DITP system can perform the following:

- The Acquisition of Predefined Target Objects Using the Passive Sensor Subsystem (PSS)
- The Track of Acquired Target Objects Using the PSS
- The Handover of Filtered Objects From the PSS to the Laser Radar (LADAR)
- The Ability to Execute Discrimination After a Single In-Flight Target Update (IFTU)

In addition, during the tests enough data must be obtained to demonstrate that an advanced seeker based on DITP technologies has the capability to discriminate and designate in real time the target in the presence of realistic countermeasures and decoys and to demonstrate that aimpoint selection is possible.

1.2 SCOPE

This System Test Plan (STP) describes the Naval Research Laboratory's (NRL) approach for the conduct and implementation of Discriminating Interceptor Technology Program (DITP) testing under the aegis of the Ballistic Missile Defense Organization (BMDO) Advanced Technology Director (TOS). This STP identifies the approach for all DITP Test & Evaluation activities, with an emphasis on integrated Seeker ground demonstration and flight demonstration. Verification of the DITP requirements occurs by one or more of four verification methods. They are: 1) verification by inspection (I), 2) verification by analysis (A), 3) verification by demonstration (D), and 4) verification by test (T). A matrix of DITP requirements versus method(s) of verification is included in Appendix B of the DITP System Specification (A-Spec).

The purpose of the STP is to provide a top-level description of the activities which will verify the DITP system's capability against the requirements defined and allocated by the Requirements Verification Matrix in the DITP System Specification. Completion of the test and verification procedures identified here will provide the data to enable assessment of the DITP system's traceability to the demonstration goals and objectives identified in the DRD and TPGD. This

STP emphasizes verification by testing and is supplemented by individual test plans and procedures for assembly, and subsystem tests. The detailed test plans will include:

- Test description/ definition of test concepts
- Objectives/requirements to be satisfied
- Resources required for test
- Prerequisite tests
- Test configuration
- Methods, elements, sequence and responsibilities
- Test reports

1.3 DEFINITIONS

For the purpose of the DITP, the following terms apply. The NRL was selected by the BMDO TOS to be the "Test Bed Integrator" (TBI) for DITP. The TBI is responsible for overall mission success and system integration. "Subsystems" are defined as each of the complete packages the EAs and the NRL will deliver as GFE to include the PSS, LADAR, FP&A, and Integrated Optics Subsystem (IOS). "Seeker" is defined as the integrated PSS, LADAR, FP&A, and IOS. "Bus" will describe the integration of the subsystems provided by the TBI needed to allow the Seeker to function in exoatmospheric flight (e. g., structure, , thermal management, guidance, navigation, and control, communications, flight termination). "Flight System" describes the integrated Seeker, Bus, and supporting subsystems (launch vehicle supplied components above the boost motor). "Launch Vehicle" is a sounding rocket or missile (boost motor and below). The "Launch System" describes the flight system integrated with the launch vehicle.

1.4 DITP SYSTEM DESCRIPTION

The DITP Flight System will consist of the subsystems shown in Figure 1.4-1. While all subsystems will be tested prior to flight demonstration, the DITP performance-driven requirements will be tested primarily for the Seeker subsystems.

After integration of brass-board level (i. e., 10 kg class) advanced technologies (PSS, LADAR, and FP&A) with elements of the IOS, the Seeker system, in various configurations, will be tested on the ground in preparation for the formal ground demonstration proof of concept. Subsequent development will lead to 5 kg flight capable advanced technologies (PSS, LADAR, and FP&A) which will be integrated and tested with the IOS, in various configurations, in preparation for formal ground demonstrations against approved target scenarios. After successful ground demonstrations, the integrated flight hardware will be matched to a sub-orbital launch vehicle for two separate flight demonstrations against (TBD) targets, in FY01 and FY02. The goal of the technology demonstration is fusion and processing of passive and active Seeker sensors combined with the ability to discriminate against multiple, combined targets. Figure 1.4-1 shows the hardware configuration items that comprise the DITP system.

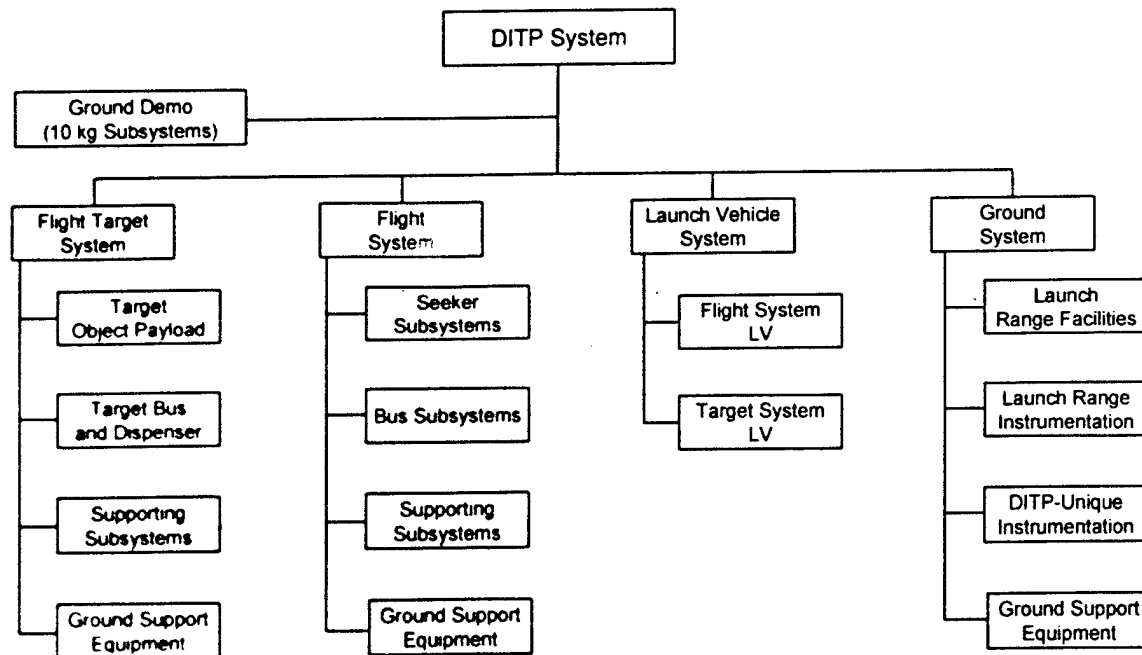


Figure 1.4-1 DITP System Hierachy

1.4.1 Target System

The Target System consists of the following:

- Target Object Payload
- Target Bus/Dispenser
- Target System Supporting Subsystems
- Target System Ground Support Equipment

Since the program objective is to demonstrate the capabilities required to support both TMD and NMD interceptor seeker upgrades needed to negate advanced threats, the target system employed for this technology demonstration shall be traceable to these advanced threats. The traceability to both the NMD Design-To Threat (DTT) and the Mid- and Far-term TMD threats as defined in the Capstone STAR is addressed in a separate Target Requirements Document (TRD). The key criterion for selection of the target system is to choose the target objects that best represent critical features and parameters of the defined threats. These features are that both RVs and sophisticated decoys are not only very closely matched in their surface material properties and thermal characteristics, but they are also the same size and shapes. In addition, they are precisely deployed to form closely spaced objects (CSO) that will be difficult to resolve. The sophisticated decoys are designed to closely approximate dynamic motions of the RVs, however there are physical limits to how close the decoys can be built to replicate the RV characteristics. Thus, dynamics discrimination is a prime motivation for the DITP technology and therefore must be a selection criterion for the target system used in DITP for tests and demonstrations.

As defined in the TRD, two threat scenarios from the GPALS Threats, heretofore referred to as Scenario A and Scenario B, capture all of the threat characteristics described above. Hence they were selected for test and evaluation of DITP fusion algorithms in an end-to-end system simulation, called FPSIM, by the Air Force Research Lab., Rome Research Site. A representative TMD far-term Scenario, based on a North Korean Campaign, was also defined.

For the ground test experiments, the two advanced NMD Design-To Threats, Scenarios A and B, will be simulated in an integrated hardware in-the-loop (HWIL) tests to characterize the system performance and to demonstrate the capability of the DITP seeker technology. For the two flight test demonstrations, target sets will be selected to satisfy the flight objectives while exhibiting a clear traceability to the Design-To Threats.

1.4.1.1 Target Payload Objects

Target payload sets will be provided for each of the two planned exoatmospheric flights. Each Target Payload will consist of an instrumented rigid light replica (RLR) as a surrogate primary reentry vehicle (RV), additional non-instrumented RLRs to replicate sophisticated penoids, "Dixie Cups" as additional conical decoys and traffic balloons (large and small). Along with the payload bus dispenser, additional associated objects and reference balloon are typically in close proximity of the targets. Following are detailed descriptions of both Target Object Payloads.

1.4.1.1.1 MINIMUM TARGET OBJECTS SET

For the first flight, a minimum essential target set is defined as presented in Table 1.4.1-1. A primary objective of this flight is to perform a live demonstration of interceptor seeker functionality, such as acquisition and cueing of the Ladar, and performing post-flight analysis and verification of system performance capability. In particular, the goal to quantify performance of the Ladar/IR discriminations by measuring target dynamic features on an otherwise thermally matched target set, represented by two rigid lightweight replicas (RLR) with one having a light weight instrumentation system package and being designated as the primary surrogate RV. A motivating factor in selecting the target set is to maintain a minimal target procurement and integration costs; e.g., procure target as is off-the-shelf, if possible, and not adding extra mass or changing mass moment to passively control target dynamics. The proposed set will allow discrimination to occur based on typical discrimination characteristics such as shape, thermal properties, and dynamics.

Table 1.4.1-1 Minimum Target Objects Set for DITP Flight Demonstration

Object Ident.	Shape	Class	Quantity
RLR w/LWIS	Cone	C2/C3	1
RLR	Cone	C2/C3	1
Inflatable Cone	Cone	C2	1
CLB (ref.)	Sphere	C1	1
Canister, etc.	misc.	C1	1+
		TOTAL	5+ obj.
		:	

1.4.1.1.2 ENRICHED TARGET SET

For the second flight, scheduled one year later, the enriched target set summarized in Table 1.4-2 will be deployed. This set will have a greater number of objects making it nearly equal to an

advanced threat cluster that a next-generation interceptor may typically encounter. Again, a primary RV is substituted by an instrumented RLR to reduce the procurement/integration cost. Several conical objects are added to provide a live demonstration of the system functionality by testing a capability of automated decision logic designed in the fusion algorithms which generates commands for the dynamic sensor operations and target scheduling. This Flight will also demonstrate system and subsystem performance limits in a real time, during an in-flight space environment and will further challenge the discrimination timelines.

Table 1.4-2. Proposed Enriched Target Set for DITP Flight Demonstration

Object Ident.	Shape	Class	Quantity
RLR w/LWIS	Cone	C2/C3	1
RLR	Cone	C2/C3	1
Dixie Cups	Cone	C2	2
Inflatable Cone	Cone	C2	1
CLB (ref.)	Sphere	C1	1
CMB	Sphere	C1	2
MBC	Spheres	C1	Set of 5
Canisters, etc.	misc.	C1	5+
		TOTAL :	18+ obj.

1.4.1.2 Target Bus/Dispenser

The target objects will be deployed from a bus dispenser, which is designed to spin-up and dispense the target objects at a velocity between 0.5 to 2.5 m/sec. The bus dispensing vehicle may be attached to the final upper stage rocket to maintain the large mass moment ratio in order to deploy the targets with minimal dispersion.

The combined target set will be integrated in a single stacked payload bus package, as shown in Figure 1.4-1. This is similar to the GBI-IFT target payload bus package. The objective of the single stacked payload is to conform to the envelope of a narrow sounding rocket launch vehicle without enlarging the fairing cover. The only difference in the configuration will be that the DITP bus will eject the inflatable objects off the top as compare to along the side as shown in the figure. This ejection option may be necessary to minimize the total target dispersion to maintain the targets within the telescope field-of-view (FOV) throughout the demonstration scenario.

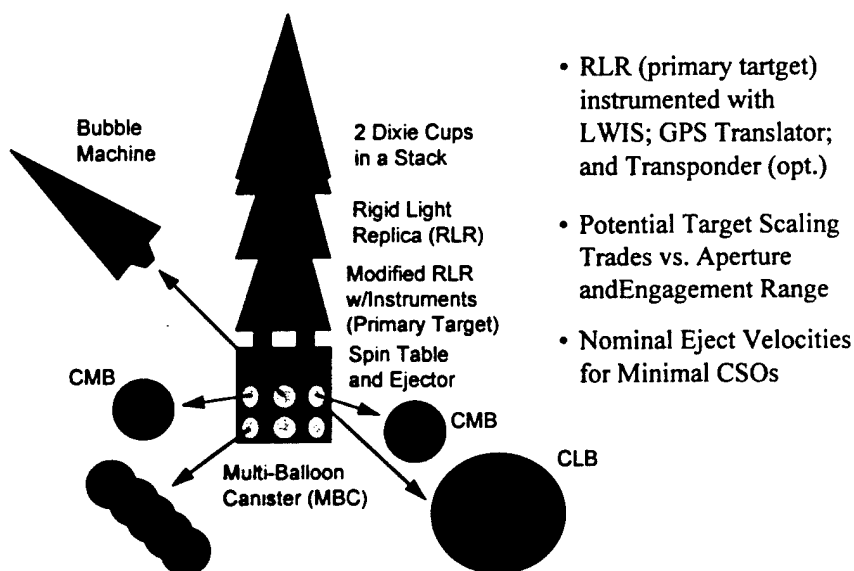


Figure 1.4-1. A Potential DITP Flight Demo Target Payload

Because of the limited envelope of the launch vehicle, due to a limited base diameter (~40 cm), the target dimensions for rigid objects will be required to be scaled down along with possibly mission engagement, geometry and timelines. Potential scaling of the target size and surface material properties are provided in Table 1.4.1-3.

Table 1.4.1-3. Potential Target Size Scaling Options for the Flight Demos

Target Parameters	Nominal	Scaled	Comments/Issues
Length (m)	1.75	1.4	<i>Closer Range for Imaging</i>
Base Diameter (m)	1	0.4	<i>Launch Envelope Limit</i>
Half-Cone Angle (deg)	8.9	~7	Maintain Close Angle
IR Emissivity	0.9	~0.95	MWIR/LWIR Sensitivity
Ladar Reflectivity	0.1	~0.15	Acquisition Range
Temperature (K)	< 280	> 300	MWIR Sensitivity
Eject. Velocity (m/s)	1.5	1.5-2.5	<i>No CSO Requirement</i>
Viewing Aspect (deg)	20 -120	~30	Length Measure vs. Sensitivity
Coning Angles (deg)	<< 20	< 20	<i>Primary Target < Decoys</i>

The bus provides load carrying capability from the DITP target deploying payload to the launch vehicle. The target bus is the physical enclosure, support and attachment of all of the DITP target components and associated subsystems. The target bus consists of the following: primary cylindrical skin structures, fairing that can be jettisoned, electronics deck structures, access ports and panels, thermal blanketing, and interface to all launch vehicle specific subsystems.

1.4.1.3 Target System Supporting Subsystems

The supporting subsystems include those subsystems of the launch vehicle that interface the launch vehicle to the Flight Target System (e. g., Recovery Subsystem, C-Band Radar

Transponder, Thrust Termination Subsystem, Flight Termination Subsystem, and Ignitor Assembly.

1.4.1.4 Target System GSE

GSE is comprised of equipment required to support Target System integration and checkout.

1.4.2 Flight System

As shown previously in Figure 1.4-1, the flight system is comprised of the Seeker subsystems, Bus subsystems, Supporting Subsystems, and Ground Support Equipment.

1.4.2.1 Seeker Subsystems

The Seeker Subsystems are:

- Passive Sensor
- Laser Radar
- FP&A
- IOS

The Flight Demonstration subsystems will meet the size and weight requirements for DITP.

1.4.2.1.1 PASSIVE SENSOR SUBSYSTEM (PSS)

The DITP PSS is designed to provide BMDO with an interim, advanced, multi-band detector for long-range infrared sensing of ballistic missile targets during trajectory mid-course. The PSS operates in conjunction with the Fusion Processor and Algorithms (FP&A) subsystem to: 1) receive an off-board, in-flight-target-update (IFTU), 2) detect, resolve and track multiple targets, 3) perform limited (IR-only) discrimination, and 4) handover command data to cue the LADAR subsystem.

As shown by Figure 1.4.2-1, the PSS consists of three primary assemblies: 1) focal plane array (FPA) containing a detector and read-out integrated circuit (ROIC), 2) a cryogenic cooler, and 3) sensor adaption layer/control processor.

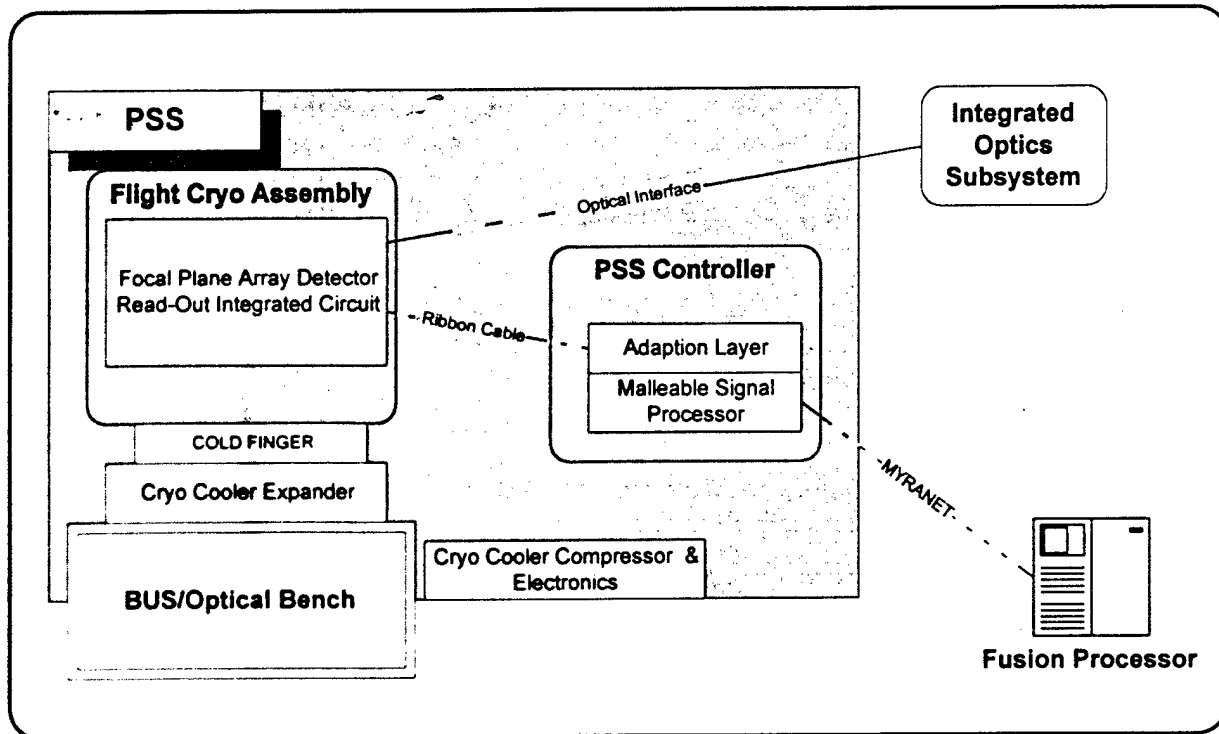


Figure 1.4.1-1 PSS Major Components

PSS functions provided by the primary assemblies are shown below in Figure 1.4.2-2. Figure 1.4.1-3 shows the functional flow between assemblies. Following these figures are descriptions of each assembly.

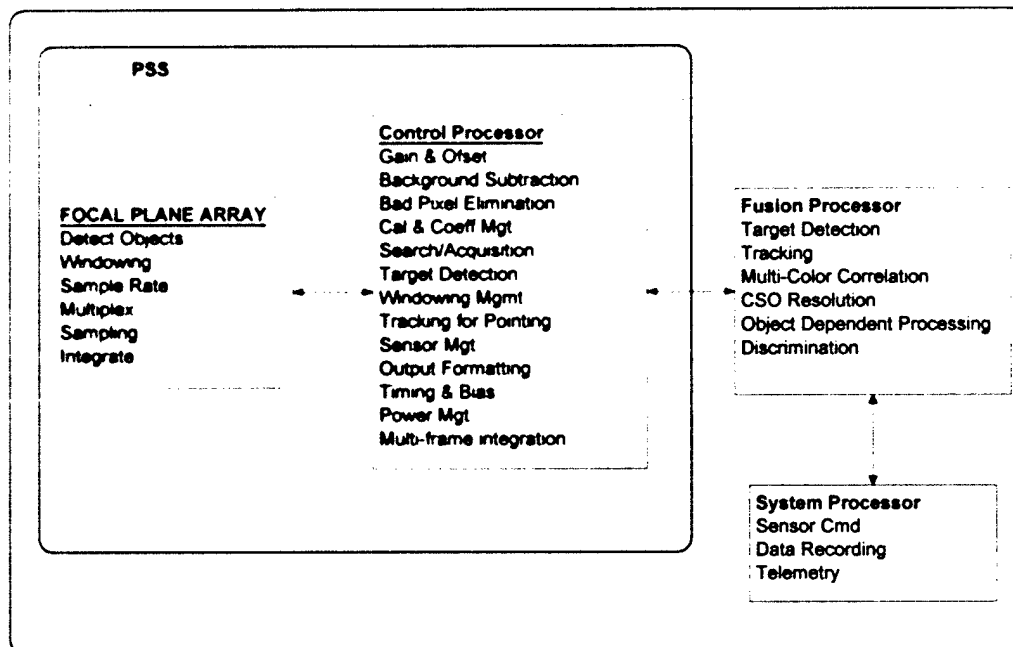
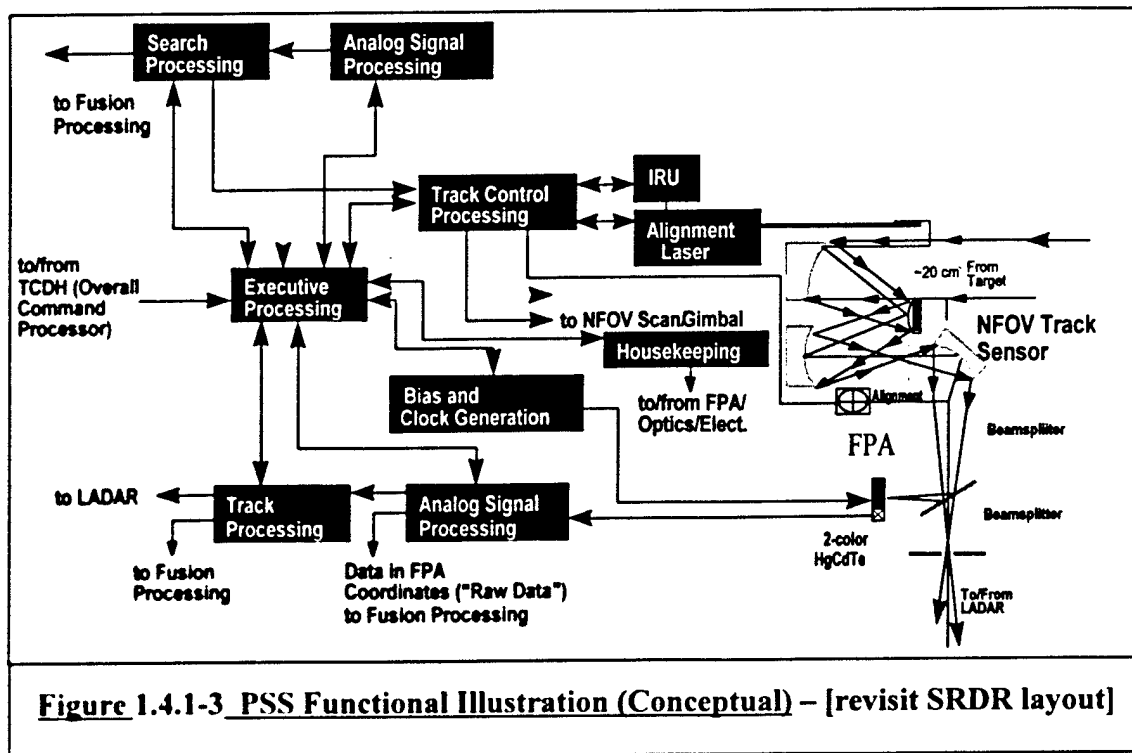


Figure 1.4.2-2 Major Functions of PSS Assemblies



1.4.2.1.1 Focal Plane Array

The FPA detector is a multi-band mercury cadmium telluride (HgCdTe, also referred to as MCT) array of 256 x 256 pixels. Objects are imaged using both mid-wave infrared (MWIR, 3-5 μ m) and long-wave infrared (LWIR, 8-10 μ m) detectors co-located within the same cell. This configuration provides:

- Simultaneous detection and integration,
- Operating temperature greater an TBD K,
- Minimum spectral and spatial crosstalk,
- High fill factor, high quantum efficiency, background limited infrared performance (BLIP) sensitivity,
- Unit cell size at 50 microns,
- Compatibility with 256 x 256 staring IRFPA and larger (traceability to operational systems),
- ROIC customized for high and low background applications with windowing, and
- Variable gain in each band.

FPA ROIC multiplexes and pre-processes the data at a programmable frame-rate up to 120 Hz.

1.4.2.1.1.2 Flight Cryogenic Assembly

The PSS flight cryogenic assembly (FCA) consists of a vacuum vessel that houses the FPA (detector and electronics). Using an externally mounted cryogenic cooler (to isolate vibration) and a cold finger able to remove a heat load of TBD W, the FCA temperature is maintained at approximately 60 K, 10⁻⁶ torr, 1% relative humidity. This minimizes background noise to the FPA and permits FPA sensitivity required to detect NMD

targets at long range. Imaging optics are mounted external to the vacuum vessel and focus collimated light from the IOS (telescope and mirrors) to the FPA detector.

1.4.2.1.1.3 PSS Controller

The major components of the PSS Controller are the malleable signal processor (MSP) and FPA sensor adaption segment. The MSP is a reconfigurable processor developed using a real-time embedded processor, which is the interface with the FP&A via myranet crossbar. Though primarily intended for data mapping and routing, the MSP reconfigurable core is capable of potentially performing several billion operations per second for simple time-intensive operations such as gain and offset correction, gamma circumvention, background removal, and similar operations.

The sensor adaption segments provide FPA specific bias-generation and signal conditioning between a particular sensor and the MSP. The MSP expects to receive and generate CMOS-compatible digital interface levels. By implementing a barebones interface from the room-temperature/cryogenic transition of a complex imaging sensor, the adaption segments provides the small degree of normalization required to permit the MSP to control and acquire data from sensors. Furthermore, the adaption segments provide a "plug-and-play" recognition interface which allows the MSP to initialize into the correct set of "personalities" for a particular sensor. In this manner a true form of plug-and-play is realized, permitting the rapid interchange of sensors.

Utility Controller "Plug-in". Recognizing that operational systems require more than complex imaging sensor data interfaces for true field demonstration, a simple but highly functional low power controller will be used in PSS for low-level data interchange. The controller does not replace, but supplements, the PSS interfaces. It can support 32 analog inputs, 8 analog outputs, six serial ports, and 32 bi-directional I/O per unit.

The primary software for the PSS relies on the existence of an adequate real-time operating system (RTOS). Diverse requirements lend themselves to modularization and distribution across an array of processors. Functions to be accomplished within software include:

- Those in signal processing of individual sensors not completed by other, lower level processing agents (such as the on-and near-focal plane processors and neuromorphically equipped detectors).
- Interface coordination.
- Control commands for a fast steering mirror (FSM) assembly.
- Interpretation of IMU data.
- FPA thermal sensing and control.
- Advanced sensor conditioning for primary data fusion (external to PSS).
- Command interface.
- System status monitoring.

1.4.2.1.1.4 PSS Performance Goals

PSS performance goals are provided in Table 1.4.2-1. Subsystem bench and hardware-in-the-loop tests will be performed to assess the ability of the PSS to meet these goals.

Table 1.4.2-1 PSS Performance Goals

PSS Performance Parameter	Performance Goal
Quantum Efficiency	>77%
Specific Detectivity (D^* peak)	$4.5 \times 10^{11} \text{ cm Hz}^{1/2} \text{ W}^{-1}$
Spectral Response (MW)	3 – 5 μm
(LW)	8 – 10 μm

PSS Performance Parameter		Performance Goal
Uncompensated Non-Uniformity	(MW)	<6%
	(LW)	<10%
Post Correction Non-Uniformity	(MW)	TBD
	(LW)	TBD
Max % of Bad Pixels	(MW)	<1%
	(LW)	<3%
Maximum Frame Rate		120 Hz
Operating Temperature		60 °K - TBR
Noise Equivalent Power		
Background	(LW)	$5 \times 10^{13} \text{ ph cm}^{-2} \text{ sec}^{-1}$
	(MW)	

1.4.2.1.2 LASER RADAR SUBSYSTEM (LADAR) SUBSYSTEM

The LADAR subsystem is a short pulse, direct detection Angle-Angle-Range (AAR) imaging LADAR. It consists of a frequency-doubled Nd:YAG laser transmitter, a multi-pixel IPD receiver with a 10x10 pixel focal plane array, time slicing electronics, steering mirror, a thermal battery, a laser radar interfaced with a MSP, and associated optics. Table 1.4.2-2 summarizes key performance parameters of the LADAR.

Table 1.4.2-2 Summary of the LADAR Performance Parameters

Component	Key Parameters
Short-Pulse Direct Detection 3-D Imaging LADAR	<ul style="list-style-type: none"> • 20 cm range resolution • 2.5 μrad cross range (Rayleigh) resolution • discrimination capability out to 350 km
Diode-Pumped Solid-State Laser Transmitter	<ul style="list-style-type: none"> • 25 W • 532 nm • 1.3 ns pulse width • 250 mJ • 100 pps repetition rate • 7 x 7 mm beam, super Gaussian distribution • < 7 mm μrad beam quality
Multipixel Receiver	<ul style="list-style-type: none"> • 10x10 pixel detector array, 1GHz bandwidth • 40 bin range slicer with 5 thresholds, 1.3 ns minimum bin width
Other	<ul style="list-style-type: none"> • Malleable Signal Processor (MSP) Controller with MSP/Fusion Processor software • Thermal Battery for Lasing Power • Phase-Change Cooling with approximately 60-90 seconds of run time
Size, Mass and Power	<ul style="list-style-type: none"> • ~ 10 Kg (for Brassboard system) • 5,600 cc Volume (for flight system) • 5.2 Kg (for flight system) • ~ 156 Watts of DITP Flight System Prime Power

The LADAR is broken up into 6 functional parts, Transmitter, Receiver, MSP, Beam Steering Mirror, supporting electronics and Optics. Figure 1.4.2-4 shows a schematic diagram of the LADAR subsystem. Required interfaces to the Flight System Bus and IOS are also shown.

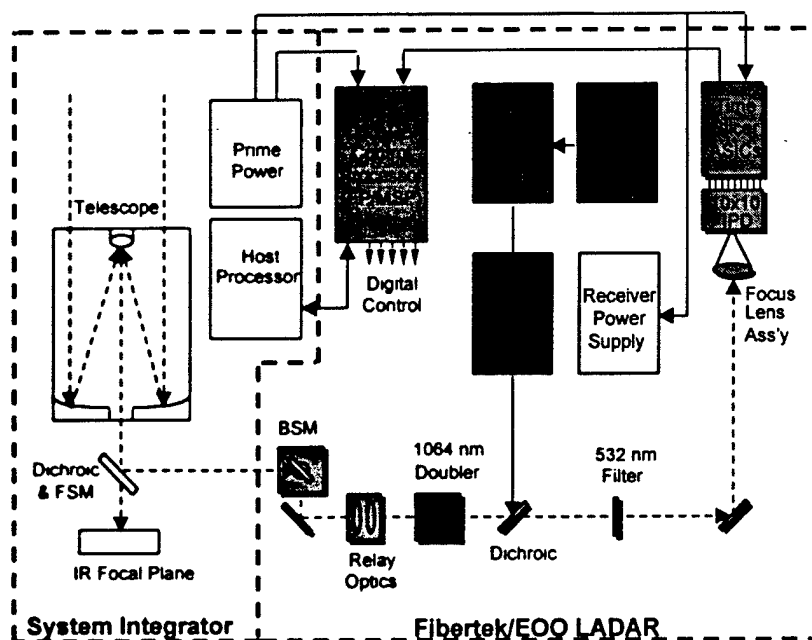


Figure 1.4.2-4 LADAR Subsystem Schematic

The transmitter is made up of a diode pumped Nd:YAG laser and includes a thermal battery for powering the diodes. The system also has a Doubler for generating 532 nm laser signal. The receiver comes in two versions: the first is a ten kg brass board design to support ground demonstrations. This design has two detectors, a 10x10 PMT and a quad IPD, integrated in a parallel configuration. The Quad IPD detector is used for long-range discrimination and the 10x10 PMT is used short-range discrimination.

The second LADAR version, a five kg design for the flight demonstration, uses just a single 10x10 imaging IPD. Both versions of the receiver system also contain time slicing electronics for recording the range data of the target. These data are then transferred to the MSP. The associated optics contain the relay lenses which adjust the transmitted and received signals to match the telescope. The optics also contain a dichroic beam splitter for separating the transmitted and received signals, and a 532 nm filter for blocking residual transmitted signal and spurious noise. The supporting electronics contain the power conditioning for the detector, time slicer, MSP and Doubler, along with the control signals for the beam steering mirror.

The compact, short-pulse laser transmitter design includes a single-mode Nd:YAG passively Q-switched oscillator, followed by two stages of amplification. After amplification, the pulse is frequency doubled in KTP resulting in a 0.532 μm , ~1.3 nsec pulse. Figure 1.4.2-5 below shows an oscilloscope trace of the pulse energy at 0.532 μm and 100 Hz.

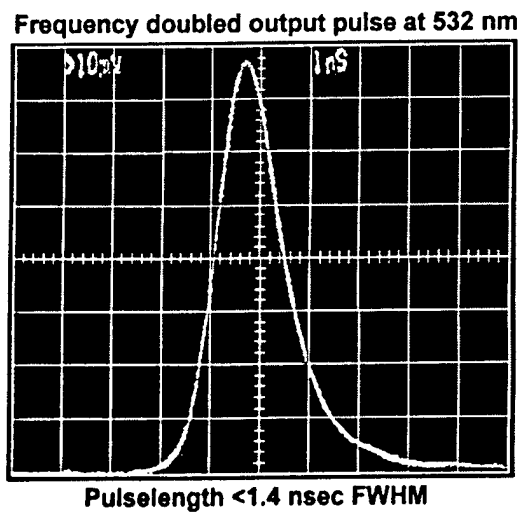


Figure 1.4.2-5 0.532 μm output pulse recorded using high speed PIN photodiode and 1 GHz oscilloscope

The laser radar will be cooled using phase change material and will be powered by an internal thermal battery. The full laser radar system, including the thermal battery and phase change cooling modules has an estimated mass and volume of 5 kg / 5 liter respectively and is shown below in Figure 1.4.2-6.

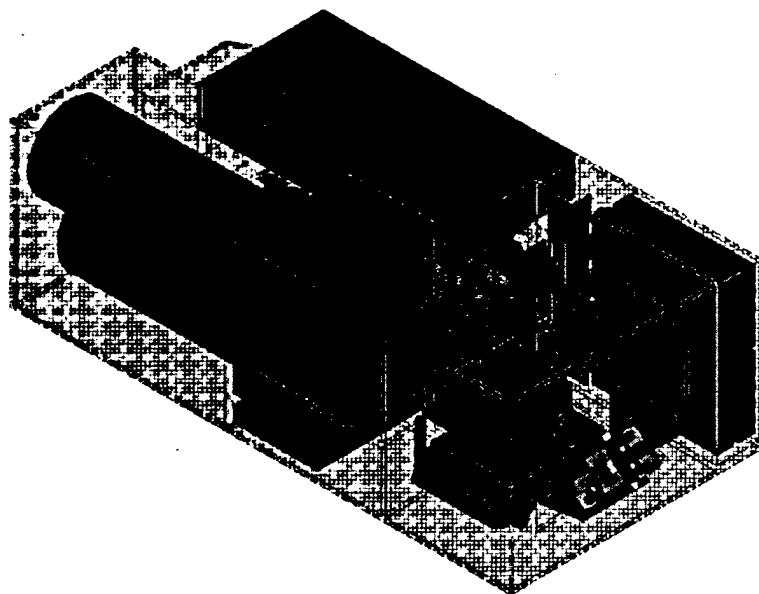


Figure 1.4.2-6 Solid Geometry Model of the Flight Demonstration LADAR Subsystem

1.4.2.1.3 FUSION PROCESSOR & ALGORITHMS (FP&A) SUBSYSTEM

The FP&A is a gigaflop-capable floating point processor consisting of wafer-scale signal processors (WSSP) communicating through a crossbar Myrinet to the sensor. The majority of computer processing and signal processing for the Seeker technology subsystems are performed by the FP&A. The algorithms consist of most of the software/firmware required to provide acquisition, tracking, and discrimination of target clusters.

The fusion processor consists of TBD MCM layers each containing X processing elements, X Mbits of SRAM, and X Mbits of DRAM. The processing elements on an MCM are connected via a 64 bit local bus running at 50 MHz. MCMs are connected to a configuration of X eight port Myrinet switches via a custom Myrinet interface chip the PCIF ??????

1.4.2.1.4 INTEGRATED OPTICS SUBSYSTEM

The IOS, shown schematically in Figure 1.4.2-7, is an optica/mechanical bench structure that includes:

- a mechanical bench structure for mounting the PSS and LADAR
- an afocal telescope
- a dichroic beam splitter
- a fast steering mirror
- an IMU used in the GN&C subsystem

Figure 1.4.2-7 IOS Schematic

The IOS telescope has a primary aperture of 15 inches (25 cm)??? with a field of view of 2.0 by 1.6 degrees. The wavefront error is specified to 0.12 waves RMS at 0.532 micrometer wavelength. The IOS receiver boresight alignment between the PSS and LADAR subsystems is 7 microradians. The telescope optical efficiency equates to 90% transmissivity at 0.532 micrometers and 0.79% at MWIR and LWIR.

1.4.2.2 Bus Subsystems

1.4.2.2.1 BUS MECHANICAL

The DITP Bus is the backbone of the DITP flight system, providing the physical enclosure, support, and attachment for the IOS and Bus subsystems. The Bus consists of the following:

- primary cylindrical skin structures
- sensor bench support structures

- electronics deck structures
- access ports and panels
- sensor door mechanism
- thermal blanketing and temperature control
- interfaces to all DITP subsystems
- interfaces to the launch vehicle

The Bus provides subsystems' thermal and vibration isolation as required and also supports a controlled temperature environment prior to launch.

1.4.2.2.2 BUS ELECTRICAL SUBSYSTEMS

- Electrical subsystems include:
- Electrical Power Subsystem (EPS)
- Command, Telemetry, & Data Handling (CT&DH)
- Guidance, Navigation and Control (GN&C)
- RF Subsystem (RFS)
- Supporting Subsystems (radar beacon)

1.4.2.2.2.1 EPS Description

The electrical power subsystem provides power and conditioning to Bus and Seeker subsystems as required (some Seeker subsystems include integral power and conditioning). Power is provided by (N) TBD power Busses with separate batteries (e. g., FS power Bus, Sparcs power Bus, Seeker and Data handling Bus). All Busses are tied to a single point ground. The power budget for the various Busses is shown in the chart below.

Power budget chart (TBD)

The EPS includes modules that provide conditioning for Seeker and Bus subsystems as required. Some Seeker subsystems include power and conditioning)that require additional power conditioning (e. g., LADAR, PSS, FP&A).

1.4.2.2.2.2 CT&DH Subsystem Description

The command telemetry and data handling subsystem provides all Bus commanding and data collection for the flight vehicle and Seeker. The CT&DH subsystem consists of:

- Myrinet interface to payload for commanding and data collection
- 1pps time ref and frequency ref to data recorder GPS receiver
- solid state data recorder (if required)
- Computer for test and Ethernet interface PCM/encoder

The CT&DH system collects data from each of the Seeker subsystems. Data is received from the Seeker over the Myrinet interface. Data from each of the subsystems is either sent on to the WFF93 TBD for downlink or to the SSDR based on the priority flag (timdebu) in the packet. The proposed downlink rates for the Seeker are included in table TBD.

Table xxx TBD

The CT&DH system is the global time and frequency source for the Seeker. It will provide a frequency reference and a 1pps pulse via a GPS receiver for clock phase locking and time synchronization. The CT&DH system functions as the front end to the Seeker and the Bus for executing commands such as the following:

- packets to be routed onto the Myrinet
- power on commands=20
- system level reset
- force battery start (fusion processor is primary source for battery start timing)
- system initialization

The CT&DH system collects status from all the Bus components in the form of analog measurements, RPI's ??? TBD, digital status. This data is collected both for system test and for post-demonstration analysis.

1.4.2.2.3 GN&C Subsystem Description

The GN&C subsystem is defined by Bus pointing and mirror pointing functions. Bus pointing is controlled via an off the shelf ACS such as the SPARCS system. This off the shelf system provides attitude control to within TBDdegrees absolute and TBDdegrees relative. Bus pointing commands are sent to the ACS from the CT&DH system via a TBDinterface. The source of the pointing updates may be the FP&A (via Myrinet), the ground (via the uplink), or a timed command.

The mirror pointing function of the GN&C provides mirror pointing /jitter removal. If there is a need to remove jitter from the Bus this will be accomplished by reading an IMU and or ADS and subtracting this off what is sent to the mirror. The source of pointing is the FP&A. The FP&A passes LOS updates up to 100 Hz over the Myrinet to the control loop for mirror pointing.

1.4.2.2.4 RF Subsystem Description

The RFS system is off the shelf.

1.4.2.3 Supporting Subsystems Description (Dave Cofelt)

The supporting subsystems interface the launch vehicle to the flight system and provide capabilities for recovery of FS hardware (e. g., Recovery Subsystem, C-Band Radar Transponder, Thrust Termination Subsystem, Flight Termination Subsystem, and igniter assembly).

1.4.2.4 GSE Description

1.4.3 Launch System

The launch vehicle identified for the Seeker and the Target Set is the Black Brant 9 (BB9) built by Bristol Aerospace. The BB9 consists of a first stage Terrier Mark 70 motor and a Black Brant 5 second stage. The Terrier first stage will be a DOD surplus motor. The Black Brant 5 second stage will be acquired from Bristol Aerospace. The various subsystems (i.e. attitude control, propulsion, telemetry) will be acquired as separate modules and will be in concert with the bus needs. The launch range will be White Sands Missile Range (WSMR) in New Mexico with the Pacific Missile Range Facility (PMRF) in Kauai, Hawaii as a back up.

1.4.4 Ground Systems Description

The Ground System (GS) for support of the will include the hardware and software necessary to conduct the flight demonstrations. The TBI will be responsible for providing interfaces to test range facilities and equipment such as displays and workstations. The EAs will be responsible for providing equipment needed to verify that their subsystems are performing properly during a demonstration. The GS will provide telemetry capability for commanding the FS, for acquiring flight and rangedata, and, if necessary, for communicating between the Target System and Flight System launch sites. Commanding capability may include functions such as initialization, initial IFTU, resets, and calibration.

The GS will also include computer resources necessary to process and store data acquired via telemetry during a flight demonstration. In addition, the GS will include displays needed to support conduct of the demonstrations, for example, real-time flight diagnostics.

1.5 SCOPE OF TESTS

During the entire DITP program a series of tests will be performed which will validate both performance and functional requirements. The requirements were developed in the DITP System Specification and were flowed down to the subsystems. Verification of the requirements was then allocated, as appropriate, to both system and subsystem levels. The test and evaluation program is designed to verify that the requirements are met and that the DITP system can meet the program goals stated in the system specification. Table 1.5-1 summarizes

Table 1.5-1 Representative Test and Demonstration Phases TBD

representative tests which will be performed during the various phases of the program. Each test phase will demonstrate compliance to a subset of the program goals/requirements that are specified in the DITP documents.¹ No single test phase or segment is expected to demonstrate compliance with all goals/requirements and the composite results of all subsystem testing, Seeker integration, and flight system demonstration shall be traceable to each individual objective requirements.

Figure 1.5-2 depicts the overall test logic from assembly-level tests to subsystem-level tests to system integration tests to the Ground Demonstration, then another series of tests culminating with the Flight Demonstration. Figure 1.5-3 shows the corresponding program schedule for the DITP to provide a context for the test plan described herein.

Insert fig. 1.5-2 here TBDget from R. Horrocks

¹ DITP Technology Program Goals Document, Final Draft, 5 September 1996
DITP Demonstration Requirements Document, 26 February 1998
DITP Technology Determination Plan, 3 December 1997
DITP System Specification - Draft, 1 December 1998

Figure 1 DITP Test Logic Flow

Insert fig. 1.5-3 here TBD

Figure 1.5-3 DITP Program Schedule

Based on the objectives of the DITP demonstration the objectives of the test and evaluation program are to:

- Demonstrate Passive Sensor acquisition (5-kg Class) of simulated NMD and/or TMD targets/objects after initial cue
- Demonstrate Passive Sensor track of simulated targets/objects and perform bulk filtering
- Demonstrate handover of filtered objects from Passive Sensor tracks to LADAR tracks (5-kg Class)
- Demonstrate capability of the Fused-Sensor to discriminate and designate, in real-time, simulated targets in the presence of countermeasures and decoys, with single in-flight target update (IFTU)

Additional goals of the test and evaluation program are to:

- Collect Passive-IR Intensity Fluctuation Measurements
- Estimate Object Temperatures Based on Simultaneous Multi-Color IR Irradiance Measurements and Quantify Object Thermal Characteristics (i.e., Cooling and Heating)
- Quantify the LADAR's 3-D Angle-Angle-Range (AAR) Performance
- Quantify Active-Passive Sensor Capability to Resolve Closely-Spaced Objects (CSO) in Angle and Range
- Characterize Target and Object Dynamic Motion (i.e., Precession-Rate, and Tumble)

And finally, where feasible the program will provide data to:

- Post-Process Data for Further Algorithm Development and Refinement
- Obtain Target Phenomenology Data
- Validate Sensor Models and Engagement Simulations
- Establish Handover and Correlation Methodologies; Establish Accuracies
- Investigate Aimpoint Selection Capability
- Perform Post-Engagement Analysis
 - Investigate Discrimination and Kill-Assessment Performance of the Fused-Sensor Suite
 - Demonstrate BMC³ Concept of Operations for Autonomous Interceptor

1.5.1 Subsystem and Assembly Testing

This phase of the DITP program consists of the design, fabrication, integration and functional testing of the subsystems and their assemblies and components. These tests will be performed under the auspices of the executing agencies but will be supported by the TBI as necessary. Test results will be provided to the TBI to assess any system impacts.

These tests will be performed at the developers' locations (component and assembly) while subsystem tests will occur at subsystem integrator sites. The PSS will be integrated at the Air

Force Research Laboratory (Kirtland). The Fusion Processor & Algorithms Subsystem will be integrated at the Air Force Research Laboratory (Rome). The Laser Radar Subsystem will be integrated at Fibertek Corporation. The IOS and Bus will be integrated at the Naval Research Laboratory. Two subsystems will be provided for the PSS, FP&A and Ladar. First, 10 kg brassboard versions will be built for testing in FY99/00. These tests will be performed to collect data which will be used to verify that the subsystems can meet their requirements and that performance is traceable to the DITP DRD. They will also be collecting data to demonstrate that the brassboards meet all the functional requirements for system level experiments and verifications. This is consistent with a build-a-little/test-a-little approach useful for technology demonstration programs. Results of the brassboard tests will be used to validate that the second subsystem versions (5 kg flight designs) will meet both the performance requirements of the system specification including obtaining data which will be used to demonstrate traceability to the DRD and the level of maturity for the flight demonstration.

In addition to the development test the subsystems will undergo integration tests. These tests will be performed under various levels of integration and will be performed at both development locations and at test ranges. Candidate test ranges include KHILS, AMOR, ISTEf and WSMR. Tests will be performed to verify functionality and subsystem interfaces as well as to get performance data. When developed, the flight subsystems will undergo a similar level of developmental and integration tests in FY00/01.

Similarly the Bus subsystems, the IOS, launch vehicles, and ground systems will undergo a series of assembly and subsystem tests first at the developers and ultimately at NRL before system integration. The purpose of these tests will be to verify functionality, interface constraints, performance and control. Both mechanical and electrical (signal and power) subsystems will be tested.

1.5.2 System Testing

System level testing will be performed at test facilities and ranges and will be used to verify system level requirements. These tests will piggyback on subsystem integration tests when feasible. The purpose of these tests are to demonstrate system functionality and performance, and to verify system level interfaces. Candidate test ranges include KHILS, ISTEf and WSMR. These tests will also serve as risk reduction tests for the flight demonstration, and will obtain data to both validate system level performance and provide traceability to DRD requirements. System level testing will occur with both the brassboard and flight systems. These tests will occur in FY00/01.

Another level of system testing will be checkout of the flight demonstration systems. Checkouts will occur at both the NRL integration facility and the test range (WSMR or PMTR). These will culminate in the flight demonstrations which will occur in FY01/02/03.

At present, the plan is to recover the Bus with the Seeker system from the first test flight demonstration, refurbish the equipment, and then perform a second test flight demonstration. Following the refurbishment, additional system level ground tests are probable. These will be assessed as part of the post-flight demonstration evaluations.

The system level ground tests will be performed using targets of opportunity at ISTEf or WSMR. These will include rocket, munitions, or missile launches that can provide targets to collect data. Ground testing will also be performed using simulated scenes (KHILS) which provide physically realistic scenes for optical sensors. Where possible realism will be enhanced through either injection of real data signals or incorporation of enhanced simulators.

The first flight test demonstration will use a minimum target set to demonstrate functionality and discrimination performance based on target thermal characteristics, shape and dynamics. Data

will be obtained and used to assess target discrimination and designation capability for TPGD target sets but no intercept will occur. Future flight test demonstrations will use enriched target sets which will stress the discrimination timelines.

2 DOCUMENTS

The following documents of the exact issue shown serve as guidelines for this STP.

Number	Title	Tailoring Guidelines	Internet URL	Para Reference
NCST-S-DT001	DITP System Specification	—	—	
NCST-S-DT002	DITP Mission Assurance Plan			
NCST-D-DT004	DITP Environmental Requirements Document (ERD)	—	—	—
NCST-D-DT005	DITP Contamination Control Plan	—	—	
NCST-TP-DT001	DITP System Level Test Plan	—	—	

Number	Title	Tailoring Guidelines	Internet URL	Para Reference
MIL-STD-1246	Product Cleanliness Levels and Contamination Control Program	—	—	
MIL-STD-1541A	Electromagnetic Compatibility Requirements for Space Systems	—	—	
MIL-STD-461C	Requirements for the Control of Electromagnetic Interference Emissions and Susceptibility	—	—	—
MIL-HDBK-5G(2)	Metallic Materials and Elements for Aerospace Vehicle Structures	—	—	—

3 SUBSYSTEM DEVELOPMENT & TEST

3.1 TARGET SYSTEM SUBSYSTEMS TESTING

3.1.1 Introduction

The Target System is described in Section 1.4. Target System subsystem tests will first focus on acquiring data to characterize the target objects (e. g., surface emissivity and reflectivity, thermal, dynamics). Tests will also assure that Target System interfaces conform and that the Target System will perform as expected.

3.1.2 Target Object Payload Testing

Need to test targets to determine characteristics: reflectance, emissivity, MOI, mass, c.m., etc. Tests will be conducted primarily at AMOR.

3.1.3 Target Bus/Dispenser Testing**3.1.4 Target System Supporting Subsystems Testing****3.1.5 Target System Ground Support Equipment Testing****3.1.6 Target System Analyses**

(– Reflectivity; Traceability; etc. To be supplied, later)

3.1.7 Integrated Target System Tests (Non WSMR Tests)

(To be supplied, later will focus on the following primary DITP seeker functions:)

- CSO Resolution
- Tracking /Cueing
- Discrimination based primarily on Target Dynamics (coning, precession, nutation), against otherwise thermally matched conical objects that are nearly indistinguishable in size and shapes
- Designation with high probability and confidence

3.1.7.1 Integrated Target System Mechanical Tests (Non WSMR Tests)

The target flight system will be tested in accordance to the specification in the Environmental Requirements Document (ERD, NCST-D-DT004). Mechanical systems testing shall include, but not be limited to, random vibration, pyro-shock, static loads, and thermal verification.

3.2 FLIGHT SYSTEM SUBSYSTEMS TESTING

The Flight System is described in Section 1.4. Flight System tests will first focus on characterizing the functionality and performance of individual Seeker and Bus subsystems, including assurance that interfaces conform and that the integrated Flight System will perform as expected.

Joe

3.2.1 Seeker Subsystems Tests and Analyses

Joe

3.2.1.1 PSS Tests and Analyses

The section describes performance acceptance tests and documentation, to be performed in conduction with TBI representatives prior to delivery to the TBI, at Phillips Lab AFRL focal plane test laboratory and contractor facilities, on components of the DITP Passive Sensor Subsystem (PSS). Components to be tested include the cryocooler drive electronics, cryocooler compressor, flight cryostat assembly (FCA), infrared focal plane array, external imaging optics, PSS malleable signal processor (MSP), and the PSS fast steering mirror (FSM)/MSP combination. Compliance with mechanical interface requirements described in the PSS interface control document (ICD xxxxxx) will be demonstrated by the traceability of all parts to the drawings referenced therein. That document also is the source for all performance levels described herein. Reference to those numbers in this document indicates the verification of that parameter as a formal part of the PSS-TBI acceptance test procedure.

The cryocooler compressor shall be shown to dissipate < TBD watts when operating at the input power required to achieve the IRFPA operating temperature, TBD K, at an ambient temperature of 30C. The cryocooler compressor shall be shown to induce vibrations less than those described in the PSS ICD. The cryocooler drive electronics shall be shown to dissipate less than TBD watts, when operating the cryocooler compressor at the input power required to achieve the focal plane operating temperature, at an ambient temperature of 30C.

The FCA shall be shown to dissipate less than TBD watts with the focal plane operating at the required temperature and the cryocooler on at an ambient temperature of 30C. The FCA shall be shown to induce vibrations less than those described in the PSS ICD. The FCA shall be shown to achieve a temperature at the IRFPA of TBD Kelvin, with a cool down time from 30C of < TBD minutes. The IRFPA temperature shall be shown to be stable to $\pm 0. \text{TBD K}$ at this temperature, over a time period of TBD minutes. The IRFPA shall be shown to have 3 axis mechanical stability, with the cryocooler operating, in compliance with the PSS ICD. The FCA shall be demonstrated to have F# TBD cold shielding, with an efficiency > TBD %. The FCA window shall be shown to have transmission and emissivity characteristics in compliance with the PSS ICD.

The PSS imaging optics (IO) shall be shown to have a TBD cm diameter clear input aperture and an image plane location in compliance with the PSS ICD. They shall be shown to have an Airy disc with a diameter (first dark ring) of < TBD, over the full TBD1 x TBD2 cm image plane. The PSS IO will be shown to have transmission > TBD% from TBD to TBD microns. The PSS IO will be shown to contribute < TBD1 and TBD2 photons/cm²-sec background flux in spectral bands 1 and 2 respectively, at the IRFPA.

The PSS MSP shall be shown to be capable of receiving a software upload from the fusion processor (FP), and resetting the clock and bias generation patterns in < TBD sec. The PSS MSP shall be shown to generate clock and bias levels in compliance with the PSS ICD. The PSS MSP A/D converter shall be shown to have a conversion rate of TBD MHz with TBD bit accuracy over an input range from TBD1 to TBD2 volts. The PSS MSP will be shown to dissipate < TBD watts when operating the IRFPA.

All PSS IRFPA performance parameters are to be achieved in the FCA at an operating temperature of TBD Kelvin driven by the MSP electronics. The spectral bands of the PSS IRFPA shall be shown to be TBD1-TBD2 (Band 1) and TBD3-TBD4 (Band 2) microns at the TBD% response points for start and cutoffs. The focal plane shall be shown to operate at a 100 Hz frame rate, with an integration time of >3 msec. The output voltage ranges for band 1 and band 2 respectively shall be shown to be TBD1 to TBD2 and TBD3 to TBD4, for flux levels corresponding to starvation and saturation. The IRFPA shall be shown to have a dynamic range of TBD dB. The IRFPA will be shown to have a mean NEP (NEQ) of <TBD1 (TBD1a) and TBD2(TBD2a) watts, (photons/cm²-sec) for band 1 and band 2 respectively. The IRFPA shall be shown to have an operability of > TBD % for both bands. A pixel shall be deemed to be inoperable if its NEP is >TBD time the mean. There shall be < TBD clusters of >2 inoperable pixels in the central TBD1 x TBD2 pixels. There shall be < TBD clusters of >2 inoperable pixels in the entire array. The IRFPA shall be shown to have post-correction nonuniformity of < TBD over the flux range from TBD1 to TBD2, following gain and offset correction.

The PSS/FSM/MSP shall be shown to generate the required FSM control voltages with the required slew rates. The PSS/FSM/MSP shall be shown to have a TBD dB bandwidth. The FSM shall be shown to achieve slew rates of > TBD rad/sec (add FSM settle time) over an angular range of \pm rad. The PSS/MSP/FSM control loop shall be shown to achieve a jitter of < TBD μ rad (each axis, 3 σ) note that this is conditioned on optical bench jitter - specify power spectrum.. The PSS MSP shall be shown to provide 100 Hz frame rate TBD bit data to the fusion processor (FP) with a latency of less than TBD μ sec. The PSS/FP tracker shall be shown to achieve a track accuracy of better than TBD μ rad (each axis, 3 σ).

3.2.1.2 LADAR Subsystem Tests and Analyses

The LADAR subsystem tests are broken up into two sets. The first is the testing of subsystem assemblies and components. The second is the testing of the overall subsystem.

3.2.1.2.1 LADAR TESTBED COMPONENT INTEGRATION

Objective:	Verify Testbed Ladar component communication performance and integration.
Test Date(s) and Location:	TBD
Performing Organization:	Fibertek, Inc.
Cooperating or Supporting Agencies:	None
Subsystem to be Tested:	Testbed laser, testbed receiver components including quad IPD with electron optics, new Hamamatsu PMT, new analog and digital ASIC chips, CPLD interface to PC and/or MSP if available. Integration of laser and receiver components and interfaces.
Narrative Test Description:	The Testbed laser and 24 channel receiver components will be integrated together and tested to verify interfaces. The receiver CPLD will provide the interface of the receiver electronics to the laser, a PC and/or MSP if available. Supporting test equipment includes a short pulse green laser oscillator, GHz digital oscilloscope, flat plate target.
Data to be Collected:	Ladar component interface verification between receiver, laser and PC and/or MSP if available, and flat plate target data.
Pass Fail Criteria:	Pass if interfaces between laser, receiver and PC and/or MSP are demonstrated.
Expected Report Date (draft and final):	A test report will be provided to the Ladar EA 15 days after the test (draft) and 30 days following the test (final).

3.2.1.2.2 LADAR TESTBED RECEIVER COMPONENT TESTS III

Test Objective:	Verify complete Testbed receiver performance.
Test Date(s) and Location:	TBD
Performing Organization:	TBD.
Cooperating or Supporting Agencies:	None
Subsystem to be Tested:	Testbed receiver components including 76 channel IPD with electron optics, analog and digital ASIC chips, CPLD interface to PC/MSP.
Narrative Test Description:	A seventy six channel preamp board will be connected to a 76 channel IPD. The signals will be sent into time slicer circuit boards containing analog and digital ASIC chips. A CPLD will provide the interface of the receiver electronics to the PC and MSP. Supporting test equipment includes a short pulse green laser oscillator, GHz digital oscilloscope, EOO flat plate and cone targets.

Data to be Collected:	Total Detector Quantum Efficiency (DQE) including Collection Efficiency (CE) and Quantum Efficiency (QE), IPD detector nonuniformity (pixel-to-pixel and inside each pixel, dark count, electronic crosstalk, fill factor of 76 channel IPD, receiver electronics linearity, receiver electronics bandwidth, flat plate and cone target data.
Pass/Fail Criteria:	Pass if IPD Total Detector Quantum Efficiency (DQE) including Collection Efficiency (CE) and Quantum Efficiency (QE) >35% for all detectors in the array, receiver electronics linear TBD (error bar) over range of 1 to 200 pe's, receiver bandwidth compatible with 20 cm range resolution, interfaces between receiver and PC/MSP demonstrated.
Expected Report Date (draft and final):	A test report will be provided to the Ladar EA 15 days after the test (draft) and 30 days following the test (final).

3.2.1.2.3 LADAR CSO PERFORMANCE TEST.

(this test may not be necessary. Or this test could be done with the entire system using simulated data already collected at AMOR. Ask Ken if still necessary).

Test Objective:	Verify Testbed Ladar performance with CSO targets.
Test Date(s) and Location:	TBD
Performing Organization:	TBD
Cooperating or Supporting Agencies:	AMOR/Ground Test Facility
Subsystem to be Tested:	Testbed Ladar.
Narrative Test Description:	The Testbed Ladar will be tested against CSO targets (at least two targets in the LADAR FOV and depth range) with speckle at simulated ranges of 100-400 km. Supporting test equipment includes a GHz digital oscilloscope, flat plate, sphere and cone targets, target range including target mounts at AMOR/Ground Test Facility. Add jitter to the receive path both in angle and range (time delay) to test image to image registration and to test the image extraction algorithms. Both a diffuse disk and a cone will be measured simultaneously and the range separation between the two objects reduced until they are not discernable as two objects.
Data to be Collected:	Ladar voxel data will be taken for various single and CSO target sets. Data will be recorded for "playback" into FPSIM and KHILS tests. Ladar voxel data from 1 to 200 pe range.
Pass/Fail Criteria:	Pass if Ladar can distinguish CSO targets separated by 1 meter in depth and/or < 1-2 angle pixels.
Expected Report Date (draft and final):	A test report will be provided to the Ladar EA 15 days after the test (draft) and 30 days following the test (final).

3.2.1.2.4 BRASSBOARD LADAR ACCEPTANCE TEST

Test Objective:	Verify Brassboard Ladar performance prior to delivery to NRL.
Test Date(s) and Location:	TBD
Performing Organization:	TBD
Cooperating or Supporting Agencies:	NRL/USASMDC
Subsystem to be Tested:	Brassboard Ladar
Narrative Test Description:	The Integrated Brassboard Ladar will be tested to verify performance and interfaces. Supporting test equipment includes a MSP board, GHz digital oscilloscope, optical power meter, beam analyzer, flat plate target and moving full scale conical target enough to displace the target by a minimum of 1 and 2 range bins (0.2 m bin width) per interpulse interval.
Data to be Collected:	Ladar interface verification with MSP and NRL interfaces; laser energy @ 0.532 μ m and 100 pps, pulse width and beam quality; receiver sensitivity Define in detail., range resolution and flat plate target data. Collect range, velocity, and truth data on moving full scale conical target at 1-200 pe levels.
Pass/Fail Criteria:	Pass if LADAR interfaces with TBI (yet to be determined) are within specification; laser energy >250 mJ/pulse @ 100 pps and 0.532 μ m, pulse width <1.3 ns (FWHM), beam quality/divergence <12.5 mm-mrad Discuss test, receiver photon counts with DQE >35% in all pixels, electronic crosstalk and fill factor, velocity resolution = 40 cm/sec, Image quality TBD, range resolution <20 cm on conical targets and at low signal levels, 1 to 200 detected photoelectrons.
Expected Report Date (draft and final)	A test report will be provided to the Ladar EA 15 days after the test (draft) and 30 days following the test (final).

3.2.1.2.5 LADAR PERFORMANCE TEST AT ISTEf

Test Objective:	Verify Testbed LADAR performance with passive sensor handover in an outdoor range.
Test Date(s) and Location:	TBD
Performing Organization:	Fibertek, Inc., EOO Inc.
Cooperating or Supporting Agencies:	ISTEF
Subsystem to be Tested:	Testbed Ladar, TBD

Narrative Test Description:	The Testbed LADAR will be integrated with a surrogate passive sensor into a tracking telescope and mount at ISTEf. Targets of opportunity (ground targets, airplanes?, launches from the Cape and LEOSATs) will be used to demonstrate passive sensor handover to the Ladar, Ladar acquisition and tracking, Ladar range, range-rate and target images. Supporting test equipment includes a GHz digital oscilloscope, flat plate, sphere and cone targets, target range at ISTEf plus other range assets. BB or 5-kg? This test is meaningless unless the DITP beam steering is used. Tracking software (FP&A) also required. Optics and passive sensor choice is critical.
Data to be Collected:	Ladar voxel data at 1 to 200 pe level will be taken for various target sets. [Questionable: Data will be recorded for "playback" into FPSIM and KHILS tests.] Collect data on range, velocity data, etc.
Pass/Fail Criteria:	Pass if Ladar can acquire targets based on passive sensor handover, after correct optical signal attenuation to simulate long range target case, determine absolute target range to 1 meter, range resolution of 20 cm, and velocity resolution of 40 cm/sec, provide track signals to optical tracking mount, determine target size and classify target shape.
Expected Report Date (draft and final):	A test report will be provided to the LADAR EA 15 days after the test (draft) and 30 days following the test (final).

3.2.1.2.6 FLIGHT SYSTEM #1 LADAR ACCEPTANCE TEST

Test Objective:	Verify Flight 1 LADAR performance prior to delivery to NRL.
Test Date(s) and Location:	TBD
Performing Organization:	Fibertek, Inc. and EOO Inc.
Cooperating or Supporting Agencies:	USASMD, NRL
Subsystem to be Tested:	Flight System #1 LADAR .
Narrative Test Description:	The Integrated Flight 1 Ladar will be tested to verify performance and interfaces. Demonstration of the LADAR operation with thermal battery and phase change cooling. Supporting test equipment includes a MSP board, GHz digital oscilloscope, optical power meter, 2-D beam analyzer, flat plate target and moving full scale conical target. Received signals at the 1-200 pe levels.
Data to be Collected:	Ladar interface verification with MSP and NRL interfaces, size < 5 liters, mass < 5 kg; laser energy at 0.532 μ m, pulse width, pulse repetition rate and beam quality Define Test, receiver sensitivity Define, FPA detection uniformity, total DQE (QExCE)]>35% on pixels, dark count <1 pe/sec/pixel for each detector, for simulated

	optical background (including in-band target solar scattered radiation) expected in flight: resulting background noise count (limited by narrowband spectral filter) <1 pe/sec/pixel for each detector, electronic crosstalk and fill factor, range resolution, flat plate target data and range/velocity data on moving full scale conical target at the 1 to 200 pe signal level. Ladar/MSP functional testing. BSM and optics required.
Pass/Fail Criteria:	Pass if Ladar interfaces with TBI (yet to be determined) are within specification, size < 5 liters, mass < 5 kg, power requirements from vehicle bus <135W, laser energy >250 mJ/pulse @ 0.532 μ m and 100 pps, pulse width <1.3 ns (FWHM), beam quality/divergence <7 mm-mrad Define measurement, receiver photon counts with DQE >35% in all pixels, electronic crosstalk and fill factor., range resolution <20 cm. Operation of 60 to 90 seconds for thermal battery and PCM cooling.
Expected Report Date (draft and final):	A test report will be provided to the Ladar EA 15 days after the test (draft) and 30 days following the test (final).

3.2.1.3 FP&A Subsystem Testing and Analyses

The FP&A will be tested by providing stimulus in the form of simulated data that would be generated by the Bus and sensors during a flight scenario. The FPSIM results will be leveraged as a "known good" for comparison. The FPA's response to suboptimal stimulus will be evaluated (e. g., for poor quality IFTU). Extensive EA involvement will be required for definition of these tests and subsequent evaluation of test results. Extensive effort by the TBI will be required to determine that the stimulus provided to the FP&A is an accurate representation of what would be seen during flight and that the response of the simulated Bus subsystems is representative. Examples of suboptimal inputs to the FP&A include:

- inaccurate IFTU
- poor position updates
- poor ACS updates
- failure of Bus to respond to FP&A pointing command
- failure of mirror to point where commanded
- ground updates and resets at unplanned times during the acquisition sequence

3.2.1.4 IOS Testing and Analyses

Amy + Others

3.2.1.4.1 IOS TELESCOPE TESTING

Test Objective:	Verify telescope optical performance
Test Date(s) and Location:	TBD
Performing Organization:	TBI

Cooperating or Supporting Agencies:	PSS, LADAR
Subsystem to be Tested:	IOS
Narrative Test Description:	<ol style="list-style-type: none"> 1. Verify telescope boresight alignment 2. Measure wavefront error over telescope field of view 3. Determine telescope optical efficiency for PSS and LADAR 4. Determine stability of optical performance over TVAC 5. Shock and vibration testing to determine effects on optical performance and stability 6. Determine whether or not in-flight calibration is needed for PSS and LADAR boresight alignment
Data to be Collected:	TBD
Pass/Fail Criteria:	TBD
Expected Report Date (draft and final):	A test report will be provided to the TBI Manager 15 days after the test (draft) and 30 days following the test (final).

3.2.1.4.2 IOS BEAM PATH ALIGNMENT TEST

Test Objective:	Verify alignment of PSS/LADAR/FSM/BSM Dichroic beamsplitter with IOS
Test Date(s) and Location:	TBD
Performing Organization:	TBI
Cooperating or Supporting Agencies:	PSS, LADAR
Subsystem to be Tested:	IOS
Narrative Test Description:	<ol style="list-style-type: none"> 1. Install all components for alignment 2. Assume prior checkout of all assemblies including CT&DH 3. Power on PSS and LADAR receivers for boresight alignment with telescope 4. Provide collimator/Point source for "far field" alignment <ul style="list-style-type: none"> ▪ Planar blackbody source from PSS ▪ LED for LADAR (if LADAR operating conditions require) ▪ Integrating sphere for radiometrics
Data to be Collected:	TBD
Pass/Fail Criteria:	TBD
Expected Report Date (draft and final):	A test report will be provided to the TBI Manager 15 days after the test (draft) and 30 days following the test (final).

3.2.1.4.3 IOS SHOCK AND VIBRATION TEST

Test Objective:	Verify alignment stability over shock and vibration environment
Test Date(s) and Location:	TBD
Performing Organization:	TBI
Cooperating or Supporting Agencies:	PSS, LADAR
Subsystem to be Tested:	IOS
Narrative Test Description:	1. 2.
Data to be Collected:	TBD
Pass/Fail Criteria:	TBD
Expected Report Date (draft and final):	A test report will be provided to the TBI Manager 15 days after the test (draft) and 30 days following the test (final).

3.2.1.4.4 THERMAL VACUUM TEST

Test Objective:	Verify optical performance, alignment stability, and steering mirror performance over thermal environment
Test Date(s) and Location:	TBD
Performing Organization:	TBI
Cooperating or Supporting Agencies:	PSS, LADAR, FP&A
Subsystem to be Tested:	IOS
Narrative Test Description:	1. 2.
Data to be Collected:	TBD
Pass/Fail Criteria:	TBD
Expected Report Date (draft and final):	A test report will be provided to the TBI Manager 15 days after the test (draft) and 30 days following the test (final).

3.2.1.4.5 BSM/FSM TEST

Test Objective:	Verify steering mirrors operation and performance
Test Date(s) and Location:	TBD
Performing Organization:	TBI
Cooperating or Supporting Agencies:	PSS, LADAR, FP&A
Subsystem to be Tested:	IOS
Narrative Test Description:	<ol style="list-style-type: none"> 1. Calibrate steering mirrors absolute position over expected operating temperature 2. Measure and calibrate repeatability of mirrors absolute position in turn on stage 3. Measure optical transmission at LADAR wavelength 4. Verify FSM and BSM slew rate and settling performance
Data to be Collected:	TBD
Pass/Fail Criteria:	TBD
Expected Report Date (draft and final):	A test report will be provided to the TBI Manager 15 days after the test (draft) and 30 days following the test (final).

3.2.1.4.6 SYSTEM JITTER TEST

Test Objective:	Verify system jitter budget
Test Date(s) and Location:	TBD
Performing Organization:	TBI
Cooperating or Supporting Agencies:	PSS, LADAR
Subsystem to be Tested:	IOS
Narrative Test Description:	<ol style="list-style-type: none"> 1. Requires GN&C IMU and controls to characterize effect of bus vibration reduction control in FSM 2.
Data to be Collected:	TBD
Pass/Fail Criteria:	TBD
Expected Report Date (draft and final):	A test report will be provided to the TBI Manager 15 days after the test (draft) and 30 days following the test (final).

3.2.1.5 Seeker Subsystem Integration Tests George H./Yas**3.2.1.5.1 SEEKER INTEGRATION TESTS****3.2.1.5.1.1 10 Kg brassboard units (AMOR/KHILS)** George/Yas**3.2.1.5.1.2 5 Kg flight units (AMOR/KHILS)** George/Yas**3.2.2 Bus Subsystems Testing** Joe**3.2.2.1 Bus Mechanical Tests**

The FS Bus will be tested to verify compliance with the Environmental Requirements Document (ERD, NCST-D-DT004). Mechanical systems testing shall include, but not be limited to, random vibration, pyro-shock, static loads, and thermal verification.

3.2.2.2 Bus Electrical Subsystems Testing Tim**3.2.2.2.1 EPS****3.2.2.2.2 CT&DH****3.2.2.2.3 GN&C****3.2.2.2.4 RFS****3.2.2.2.5 SUPPORTING SUBSYSTEMS (RADAR BEACON)****3.2.2.3 Bus Subsystems Analyses** Chris/Tim**3.2.2.4 Bus Subsystems Integration Tests** Jack**3.2.3 FS Supporting Subsystems Tests** Jack**3.2.4 FS Ground Support Equipment Tests** Jack**3.2.5 Flight System Analyses Other than Bus/Seeker****3.2.6 Integrated Flight System Tests (pre WSMR)****3.3 LAUNCH VEHICLE SYSTEM TESTING AND ANALYSES****Introduction****3.3.1 Launch Vehicle Subsystems Testing****3.3.1.1 Flight System LV**

- BB5 Motor Testing at Bristol Proof Pressure test of motor case Propellant performance test

- BB5 Motor Testing at the Range
 - Tap Test
 - Alcohol rub on Exit Cone
 - Visual Inspection
- Recovery System Testing Vibe Electrical and Mechanical functionality
- Ignitor Housing Testing Vibe Electrical and Mechanical functionality
- Terrier Mark 70 Testing after refurbishment

3.3.1.2 Target System LV

- BB5 Motor Testing at Bristol
 - Proof Pressure test of motor case
 - Propellant performance test
- BB5 Motor Testing at the Range
 - Tap Test
 - Alcohol rub on Exit Cone
 - Visual Inspection
- Recovery System Testing
 - Vibe
 - Electrical and Mechanical functionals
- Ignitor Housing Testing
 - Vibe
 - Electrical and Mechanical functionals
- Terrier Mark 70 Testing after refurbishment

3.3.2 Launch Vehicle System Analyses

3.3.2.1 Mass Properties Analysis

A system level mass properties report will be provided the launch vehicle for dynamic analyses needed for launch success.

3.3.2.2 Orbit/Trajectory Analysis

3.3.2.3 Water Recovery/Salt Water Ingress Analysis

3.3.2.4 Structure Analysis

3.3.2.5 Thermal Analysis

3.3.3 Integrated Launch Vehicle Tests

Launch system testing will include final spin balance testing for launch system stability, about the spin axis, in accordance with range and vehicle requirements. Mass, as necessary, will be added appropriately to the spin balance ring located at the forward portion of the launch system.

3.3.4 Interface Tests with other systems**3.3.4.1 Vibe****3.3.4.2 Thermal****3.3.4.3 Electrical/Mechanical C/O at the Range****3.3.4.4 Visual Inspection at the Range****3.4 GROUND SYSTEM SUBSYSTEM TESTING AND ANALYSIS****Introduction****3.4.1 Subsystem Tests****Jack****3.4.1.1 Launch Range Facilities** Jack**3.4.1.2 Launch Range Instrumentation** Jack**3.4.1.3 DITP Unique Instrumentation** Tim**3.4.1.4 Ground Support Equipment** Jack**4 SYSTEM TESTING AND ANALYSES****4.1 10 KG SYSTEM LEVEL FUNCTIONALITY TESTS [WSMR/ISTEF] GEORGE****4.2 5 KG SYSTEM LEVEL PERFORMANCE TESTS [RISK REDUCTION AMOR/KHILS]****4.3 5 KG SYSTEM LEVEL FUNCTIONALITY TESTS [ISTEF/WSMR] GEORGE****4.4 FLIGHT SYSTEM/LAUNCH VEHICLE/GROUND SYSTEM CHECKOUT TESTS (WSMR) Joe****4.5 TARGET SYSTEM/LAUNCH VEHICLE/GROUND SYSTEM CHECKOUT TESTS (WSMR)****5 FLIGHT DEMONSTRATION****6 ROLES AND RESPONSIBILITIES****6.1 SUPPORT ENGINEERING****6.1.1 Safety**

DITP testing shall comply with OSHA safety requirements. Test procedures will be designed to ensure maximum personnel safety and to minimize the probability of accidents. Safety hazards to both nearby population and the environment will be taken into consideration. The system will be compliant with existing health and safety standards using MIL-STD-882C as a guide to identify specific hazards and determine the necessary design/operational safety requirements for hazard control.

6.1.1.1 Range Safety

During any mode other than the Recovery Mode, the probability of impact of the flight vehicle or target vehicle with land, sea/air vessels, and satellites shall be no greater than 10^{-6} .

6.1.1.2 Fault Tolerance

Test procedures shall be designed to prevent personnel injury, with emphasis on prevention of life threatening injury.

6.1.1.3 Laser Radar Safety

DITP LADAR operation shall comply with OSHA, test, and range safety requirements. ANSI Z136.1 shall be used as a guide in determining eye and skin hazard level of the LADAR, including residual reflections. Compliance with applicable industrial health and safety requirements is mandatory.

6.1.1.4 Pressurized Containers Safety

Containers that will be pressurized in the presence of personnel shall comply with ANSI/ASME B31.3 Code for Chemical Plant and Refinery Piping and ASME B&PV Code, Section VIII, Division I or Division II Pressure Vessels.

6.1.2 Reliability and Maintainability

6.1.3 Quality Assurance

6.1.3.1 Contamination Control

DITP contamination environments (e. g., blowing sand and dust, rain, fungus) are described in the Environmental Requirements Document (ERD, NCST-D-DT004). Testing should be planned and scheduled to minimize adverse effects of potential contamination sources.

No material containing asbestos shall be utilized during testing.

6.1.3.2 Configuration and Data Management

DITP configuration and data management is being managed and controlled by the TBI. The most recent approved version of this STP and associated test procedures, along with all other controlled documentation is available at via the DITP home page, <http://www.px1.com>. Actions and decisions will be carried out and documented in accordance with the configuration management approach described in the DITP Project Management Plan, NCST-D-DT001. Configuration controlled documents maintained via this web site will include, but not be limited to:

1. DRD
2. TPGD
3. System Specification
4. Program Management Plan
5. System Test Plan
6. System Test Reports
7. TBI Action Item List
8. DITP Templates and Forms - Templates and forms for capturing and reporting DITP information
9. Master Schedule
10. Presentations and Reviews
11. Configuration Control List - History of CCB-approved changes to Baseline Architecture

6.2 TEST RESPONSIBILITIES

The primary goals of test data acquisition and analysis are:

- Ensure early access to all data by all stakeholders
- Ensure independence for credible assessment
- Minimize duplicate effort and resources

The TBI Manager and EAs are responsible for assessing the ramifications of discrepancies that occur during integrated subsystems tests. Corrective action is prescribed, reviewed, and approved under direction of the TBI Manager.

EAs are responsible for assessing the ramifications of discrepancies that occur during individual subsystem and assembly tests. All discrepancy data will be reviewed for completeness and approved by the TBI manager before release outside the DITP.

Table 6-1 outlines the process steps for test data acquisition and analysis and it also allocates testing responsibilities between the TBI and the government. The government community includes the different organizations that will be involved in the overall test and verification process (e. g., EAs, KHILS, WSMR, AMOR, ISTEf).

Table 6-1 Data Acquisition and Review Steps and Responsibilities

Process Step	DITP	Government Community
Data requirements definition	TBI identifies required data from System Specification and ICDs	EAs support review process and request additions as part of the review process of each test requirements document
Modeling	TBI maintains and tunes DITP system models (and utilizes government system models depending on model's delivery schedule and capability)	EAs build and tune government model(s).
Data collection	TBI conducts system tests and collects internal data TBI supports process for Seeker subsystem tests conducted by EA	EAs conduct assembly and subsystem tests and collect internal data ISTEF, KHILS, AMOR, and WSMR collect external data.
Data reduction and verification	TBI reduces and verifies internal data from system tests TBI merges internal and external data	EAs reduce and verify internal data for their subsystem/assembly tests EAs merge internal and external data for their subsystem and assembly tests Government facility reduces and verifies external data
Data management	TBI manages and maintains all raw and technical data	EAs and government facilities archive all raw and technical data
Test series evaluation	TBI evaluates the success of system tests and Ground and Flight Demonstrations TBI supports evaluation of EA-conducted subsystem/assembly tests	EAs evaluate (via analysis) the success of subsystem/assembly tests EAs support evaluation of integration tests and Ground and Flight Demonstrations
Test and demonstration data validation	TBI builds a data base of validated test and demonstration data.	EAs and ranges support validation process
DITP evaluation	TBI provides performance estimates for the DITP against the TPGD/DRD objectives, utilizing NRL system models or government models	EAs provide independent evaluation of system

6.3 TEST DOCUMENTATION

Test procedure guidelines will be prepared for each test. Each test procedure will include, as a minimum, the following:

1. Test description/ definition of test concepts (e. g., test location, test participants)

2. Objectives/requirements to be satisfied
3. Resources required for test
4. Prerequisite tests
5. Test configuration (e. g., required test hardware and software, test configuration drawings and schematics)
6. Methods, elements, sequence and responsibilities (step-by-step test procedure)
7. Test reports

Appendix A shows an example of the recommended format for a test procedure.

Appendix A Example Test Procedure

1. TEST DESCRIPTION/DEFINITION

Test Title: Data Reduction Test

Item	Entry
Date test was performed	
Location where tested	

Test Participants:

Discipline	Presence	Participant
HW Design Lead	On-call	
Test Conductor	Mandatory	
SW Design Lead	Mandatory	
Simulator Design Lead	Optional	
Facility Support	Mandatory	
TBI & Subsystems Representatives	Optional	

2. OBJECTIVES/REQUIREMENTS TO BE SATISFIED

This test is designed to verify ~

3. PREREQUISITE TESTS

The test conductor shall certify that the following prerequisite tests have been successfully performed.

Prerequisite Test	Date Test Completed	Test Report

4. RESOURCES REQUIRED**4.1 Guiding Documentation**

Verify that the following guiding documentation is available. Enter the version (or release date) for each required document in the following table.

Drawing/Document	Number

4.2 DITP Hardware or Software To Be Tested

DITP Item Being Tested	Version

4.3 Test Equipment

Verify that the following test equipment is available. Enter equipment version identification in the following table.

Test Equipment Item	Version

4.4 Required Test Software

Verify that the required test software is available. Enter the test software descriptive information in the following table.

Software	Version	Checksum	Created Date
Applications			
Databases			

5. TEST CONFIGURATION

Verify that DITP and test equipment hardware identified in 4.1 through 4.4 are configured in accordance with the guiding documents and drawings identified in 4.1.

6. TEST PROCEDURE

This section should contain the step-by-step instructions for conducting the test. Completion of each step should be noted.

All results and any discrepancies found during this test should be documented as follows.

Test Comments/Discrepancies

Step No.	Requirement/Objective	Comment/Discrepancy

7. TEST REPORT

A test report should be prepared for each test. A filled in copy of the test procedure described here can serve as the test report.

Appendix P



Systems Center
San Diego

Innovative Science & Technology Experimentation Facility (ISTEF)

DITP Support

Feb 1999

Dr. John Stryjewski
Nichols Research Corporation



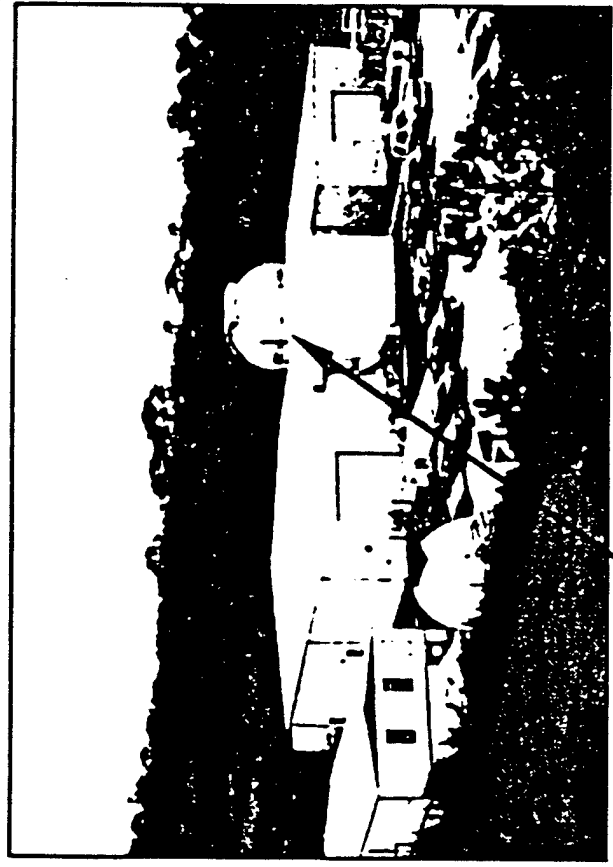
ISTEF



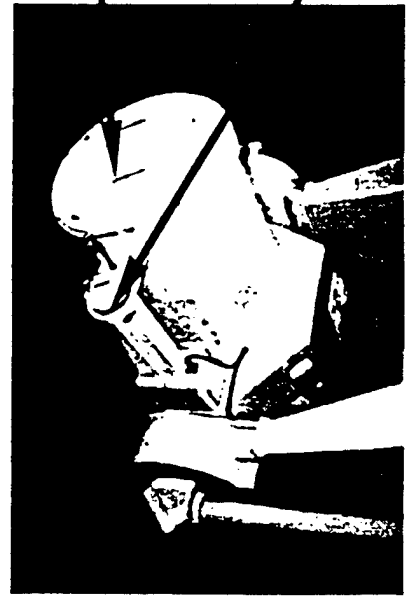
ISTEF Site Location



Systems Center
San Diego

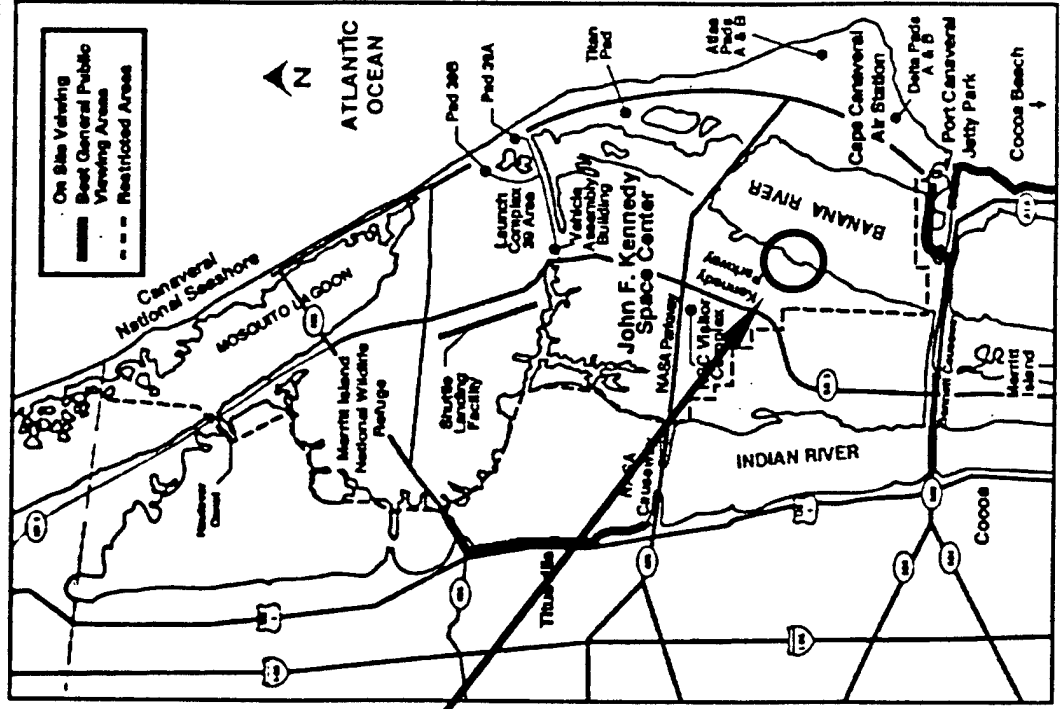


GRAZ Mount (Dome)



0.5 meter Receiver
Aperture

2" Coude Path





Innovative Science and Technology Experimentation Facility



Systems Center
San Diego

- **ISTEF is a BMDO/TORI Asset:**
- **The ISTEf is Government owned and managed, and contractor operated and maintained (Nichols Research Corporation)**
- **The ISTEf conducts research on, develops, tests and evaluates new electro-optical sensor technologies**
- **The ISTEf collects and analyzes both metric and signature data on BMDO threat targets and surrogates**



ISTEF

ISTEF Points of Contact



Systems Center
San Diego

- **Program Manager: Mike Lovern**

SPAWARSYSCEN San Diego D853

Attn: Michael Lovern

53490 Dow Street

San Diego, CA 92152-5742

(619) 553-3724

- **ISTEF/NRC Site Manager: Mac Monroe (NRC)**
- **Principle Investigator, Passive Sensor Experiments: Al Tietjen (NRC)**
- **Principle Investigator, Active Sensor Experiments: John Stryjewski (NRC)**

BMDO/ISTEF

Bldg. TRM-037

Kennedy Space Center, FL 32899

(407) 853-5285

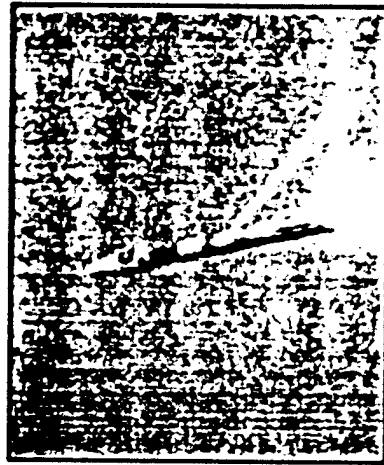


ISTEF

Optical Target Characterization at ISTEF



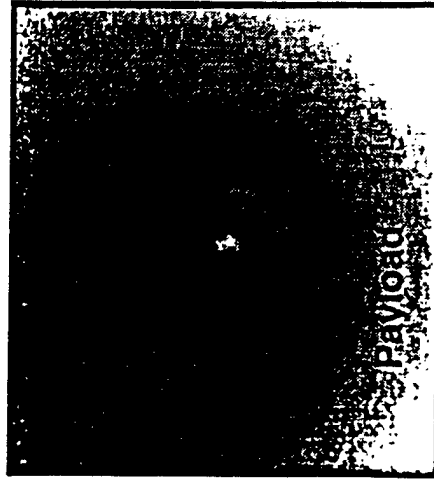
Systems Center
San Diego



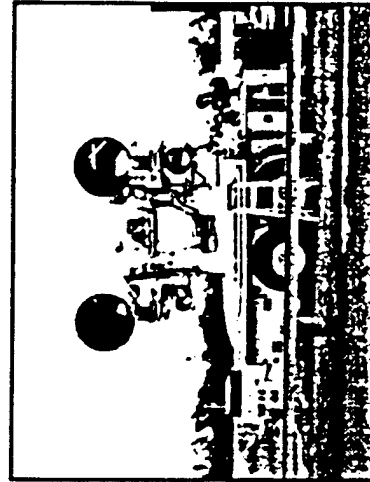
Laser signatures of
rockets and Plumes

Applying state-of-the-art active and passive optical sources, sensors and techniques to develop and demonstrate innovative scientific concepts relating to BMDO missions:

- d)
 - Booster typing
 - Tracking
 - Target discrimination
 - Aimpoint selection
 - Kill assessment



DUNDEE Narrow field of view
(NFOV) MWIR reentry image;
altitude = 114 km & range = 118 km

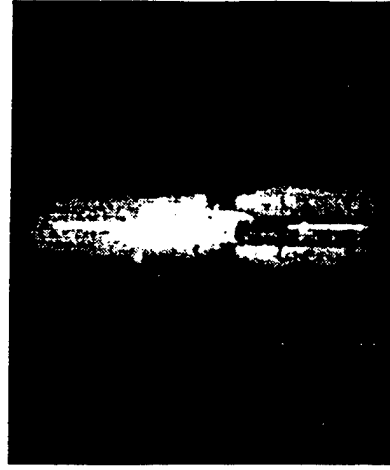


KTM at WFF during Red
Tigress III

Supporting Research in:

- Passive UV† - LWIR§ imaging/tracking
- Active plume / hardbody signatures
- Laser radar / active imaging
- Sensor data fusion

† UV: Ultraviolet
§ LWIR: Long Wavelength InfraRed
‡ MWIR: Mid-Wavelength InfraRed



Laser illuminated imagery of Titan
Cassini (Oct 97)



ISTEF

ISTEF Mobile Mounts and Some Typical Configurations



Systems Center
San Diego

- **KTM:**

- (2) - 24" UV - LWIR NFOV Telescopes
- 12" UV - NIR NFOV Telescope
- 7" Vis - NIR MFOV Telescope
- 3" Vis WFOV Telescope

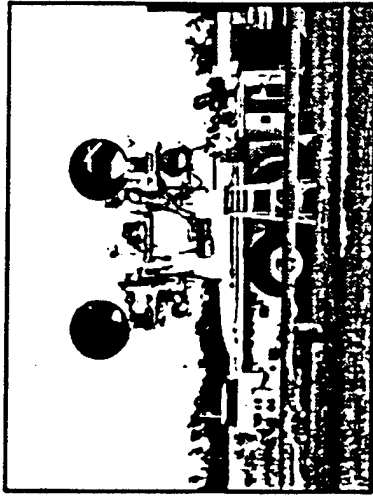
- **NRL:**

- 30" UV - LWIR NFOV Telescope
- 12" UV - NIR NFOV Telescope
- 10" UV - NIR MFOV Telescope
- 7" Vis - NIR MFOV Telescope
- 3" Vis WFOV Telescope

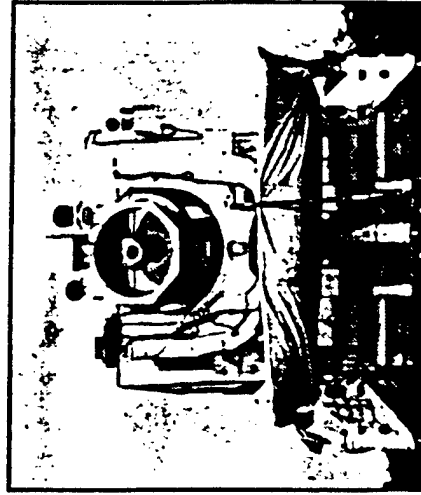
- **STRIPS:**

- (2) - 12.5" UV - LWIR NFOV Telescope
- 10" UV - NIR MFOV Telescope
- 7" Vis - NIR MFOV Telescope
- 3" Vis WFOV Telescope

KTM



STRIPS

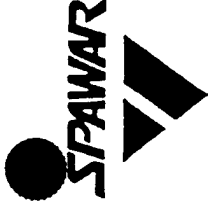


NRL



ISTEF

ISTEF Support of Other Programs



Systems Center
San Diego

- **BMDO Programs:**

- Navy LEAP FTV-3 and FTV-4
- Australian ATM's Track Fusion Experiment
- Sensor Fusion Experiment (laser)
- Red Tigress III
- DUNDEE Australian trials (laser)

- **Other Programs:**

- CASSINI (laser)
- Titan and Delta launch support
- NASA shuttle launch constraints (laser)
- Aerospace Corp. ozone experiments (RISO) support



ISTEF

ISTEF Support to DITP



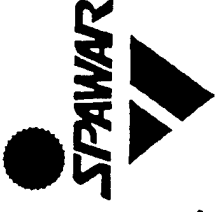
*Systems Center
San Diego*

- **Easy access to a surrogate target complex**
 - spent Delta strap-on boosters can provide a nice surrogate target.
- **Surrogate DITP components**
 - ISTEf Can provide surrogate LWIR, MWIR, optics and laser components to aid in system testing
- **True system integration testing**
 - DITP sub-systems can control ISTEf tracking mount pointing or ISTEf fast steering mirror to "close the loop" for hand-over and discrimination algorithm closed-loop testing
- **Ground truth**
 - ISTEf sensors can provide metric and radiometric ground truth for DITP testing at Cape Canaveral or elsewhere
- **Logistics and manpower support**
 - ISTEf can provide manpower and coordinate laser safety and other issues with with test ranges.



ISTEF

Surrogate Components



*Systems Center
San Diego*

- **LWIR**
 - ISTEf has calibrated MgCdTe and QWIP LWIR sensors
- **MWIR**
 - ISTEf has several Amber InSb 3-5 micron cameras (also calibrated)
- **Laser**
 - ISTEf has a 10Hz 0.5J Nd:YAG(fixed site) and a 30Hz 0.15J Nd:YAG (transportable). We also have calibrated APD and Pin diode receivers
- **Optics**
 - ISTEf has many all reflecting optics available, from 4in up to 30in at a variety of focal lengths (20in to 400in)



ISTEF



Surrogate targets at Cape Canaveral



Systems Center
San Diego

	Titan IV-B	Delta II		Atlas IIAS	
Number of Boosters	2	6	3	2	2
Separation TALO Time (seconds)	132	67	133	92	126
Elevation Angle (degrees)	37	40	28	40	35
Range at Separation (km)	102	28	117	30	68
Angular Extent at Separation (microradians)	340	460	110	300	130

- Many opportunities in one year (>10)
- Target ranges and angular extents can be adjusted by using ISTEFT transportable tracking mounts at other viewing sites

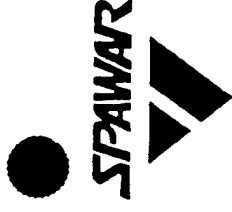
NOTE: Ranges are referenced to the ISTEFT Site



ISTEF

Suggested Testing

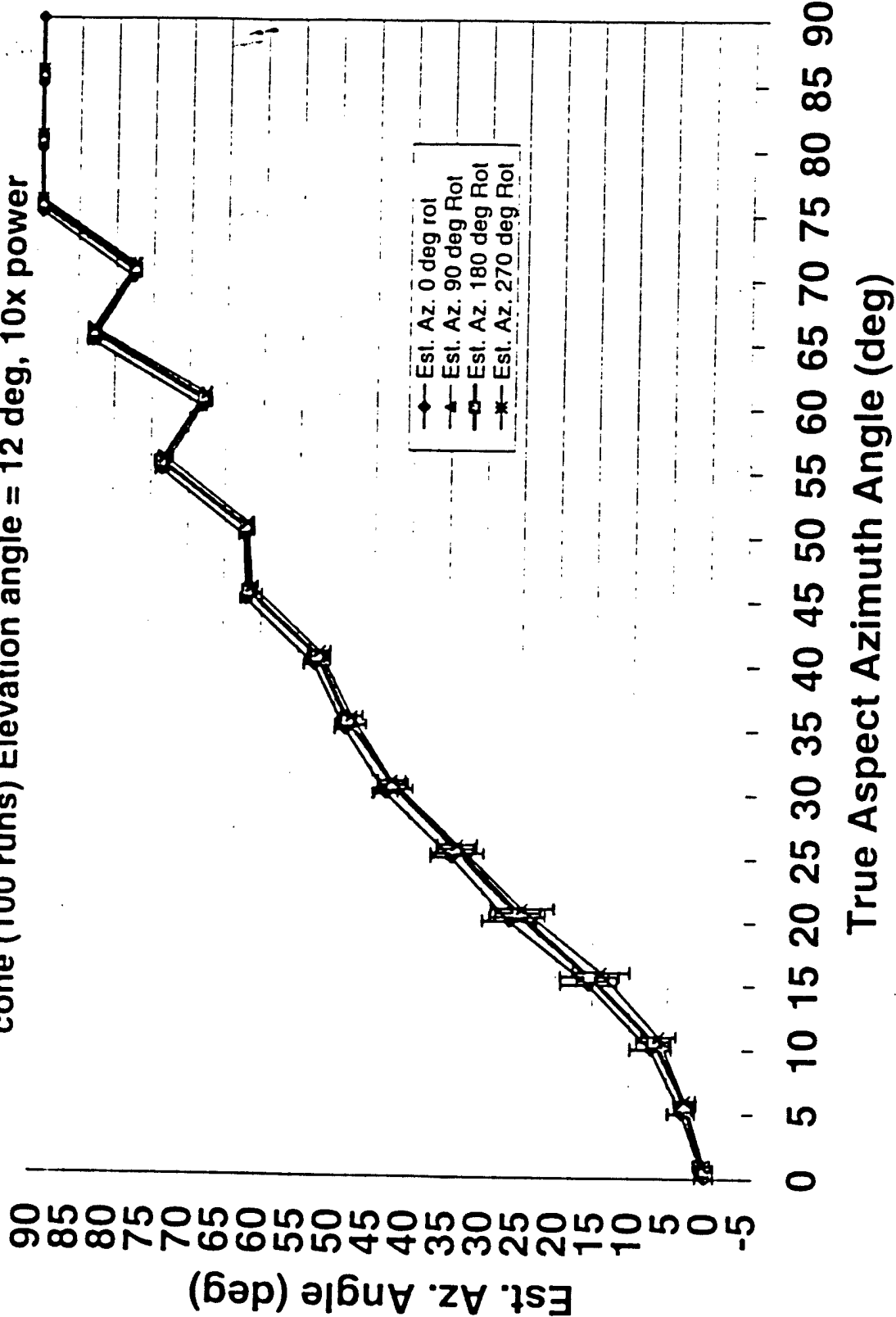
- Phase one
 - Use all ISTEf assets (LWIR,MWIR,laser) to validate Delta boosters as a surrogate target complex for DITP
 - Provide "real" data to DITP for algorithm testing
- Phase two
 - Use the DITP components (eg. ladar) with ISTEf assets to accomplish system level testing in the near term
 - Allow DITP hand-over algorithms to point laser on ISTEf mount
 - Goal is an end-to-end closed loop test of passive-active hand over and pointing
 - ISTEf to provide calibrated metric and radiometric ground truth for LWIR, MWIR and laser
- Phase three
 - Full up test of brass board testing (maybe using ISTEf optics)
 - Use ISTEf transportable mount to provide captive HW in the loop system
 - Start out at ISTEf and proof test this setup and then move to WSMR or PMRF to observe BMDO launches
 - ISTEf to provide calibrated metric and radiometric ground truth for LWIR, MWIR and laser



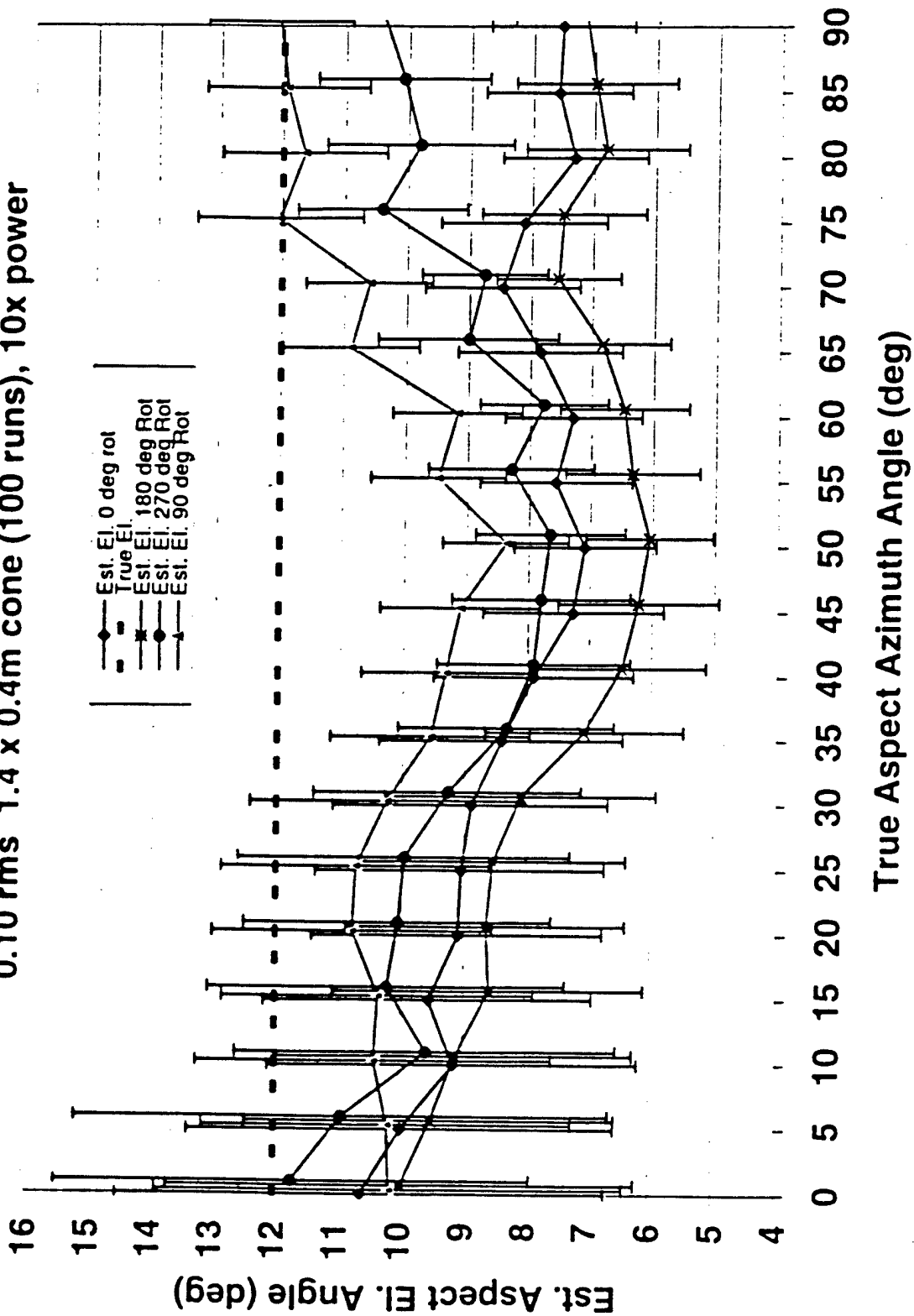
Systems Center
San Diego

Appendix Q

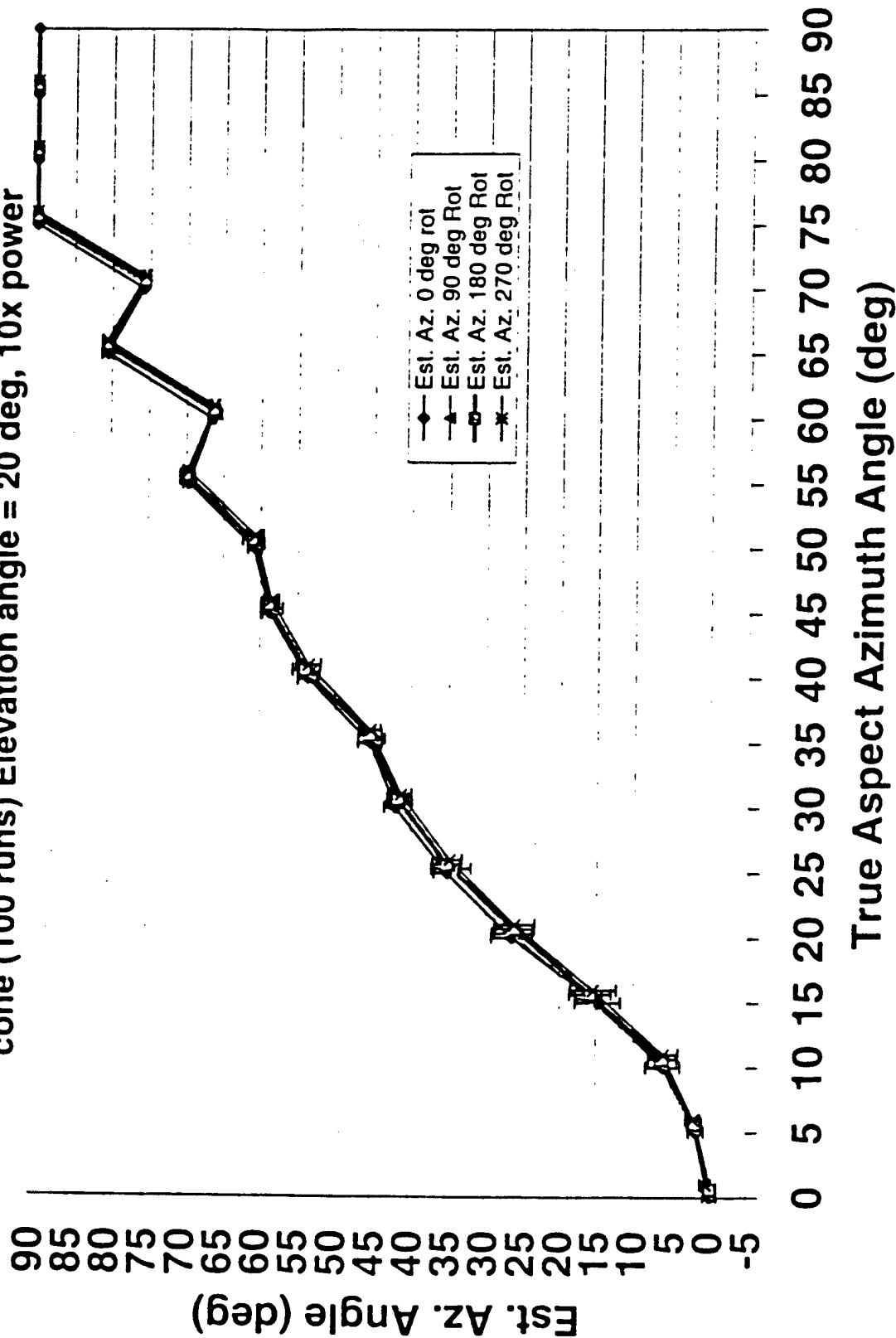
Aspect Azimuth Angle Estimates($I^{2.5}$) 160 km 0.10 rms 1.4 x 0.4m
cone (100 runs) Elevation angle = 12 deg, 10x power



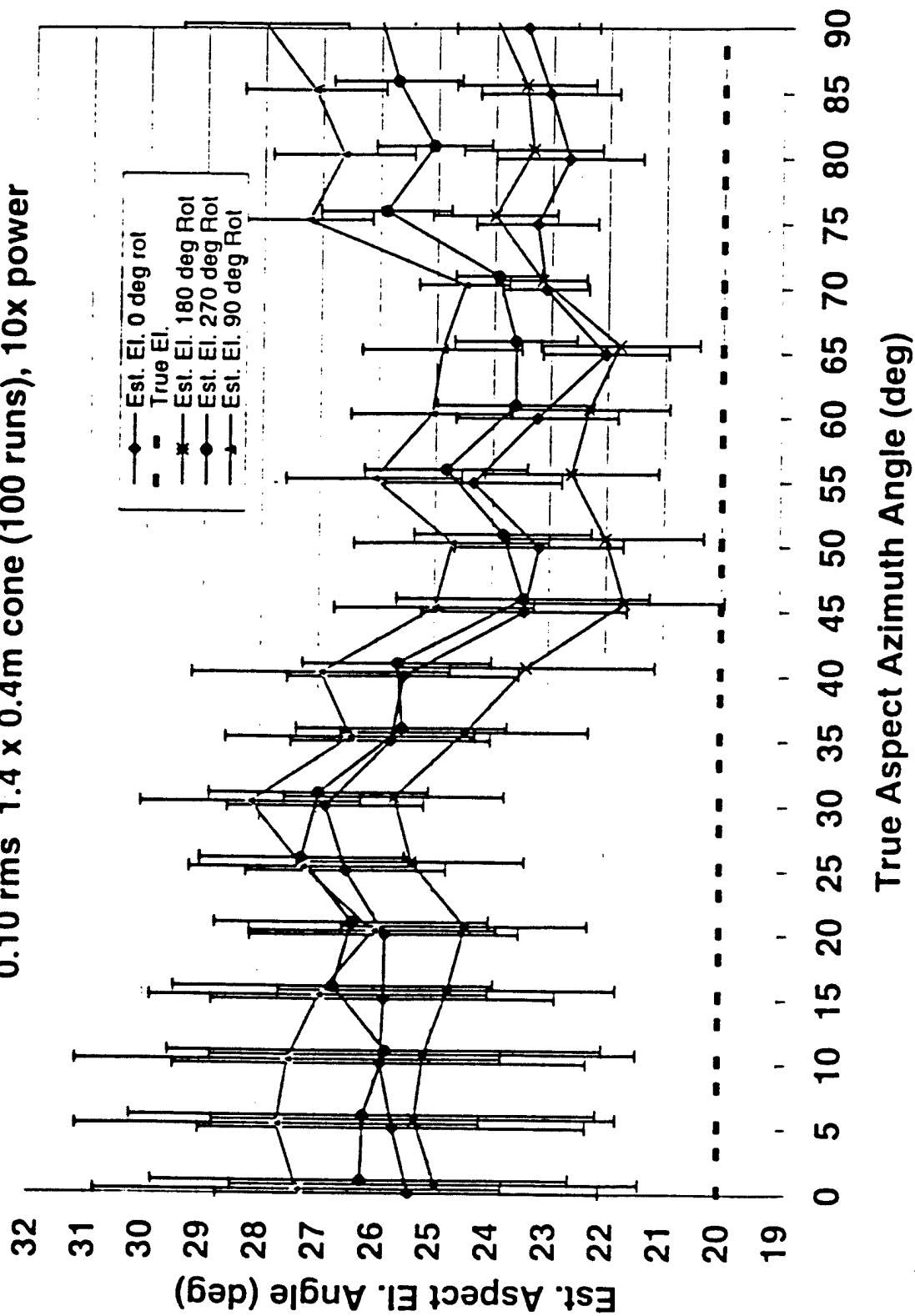
Aspect Elevation Angle Estimates($1^{2.5}$) 160 km
 0.10 rms 1.4 x 0.4m cone (100 runs), 10x power



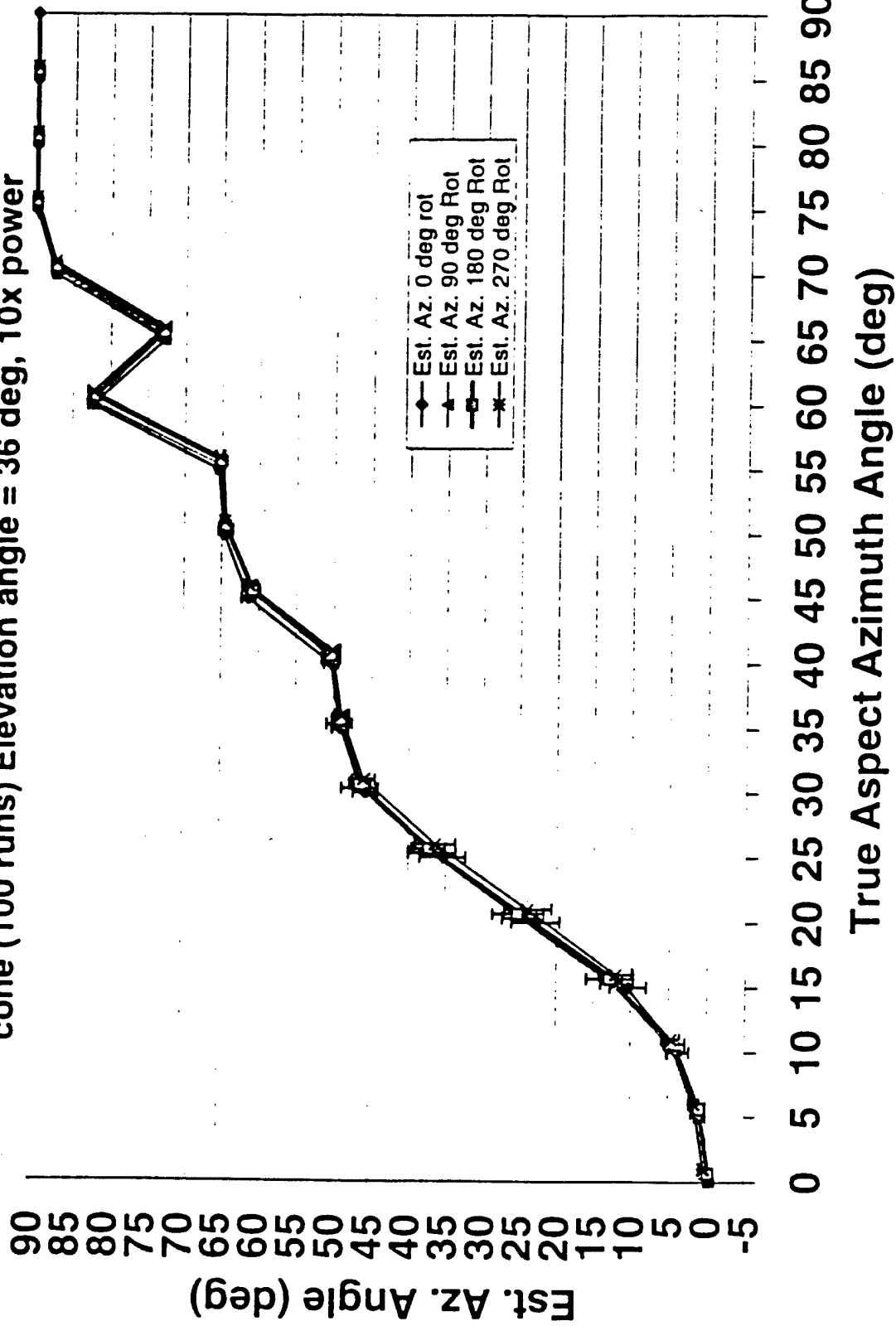
Aspect Azimuth Angle Estimates($I^{2.5}$) 160 km 0.10 rms 1.4 x 0.4m
cone (100 runs) Elevation angle = 20 deg, 10x power



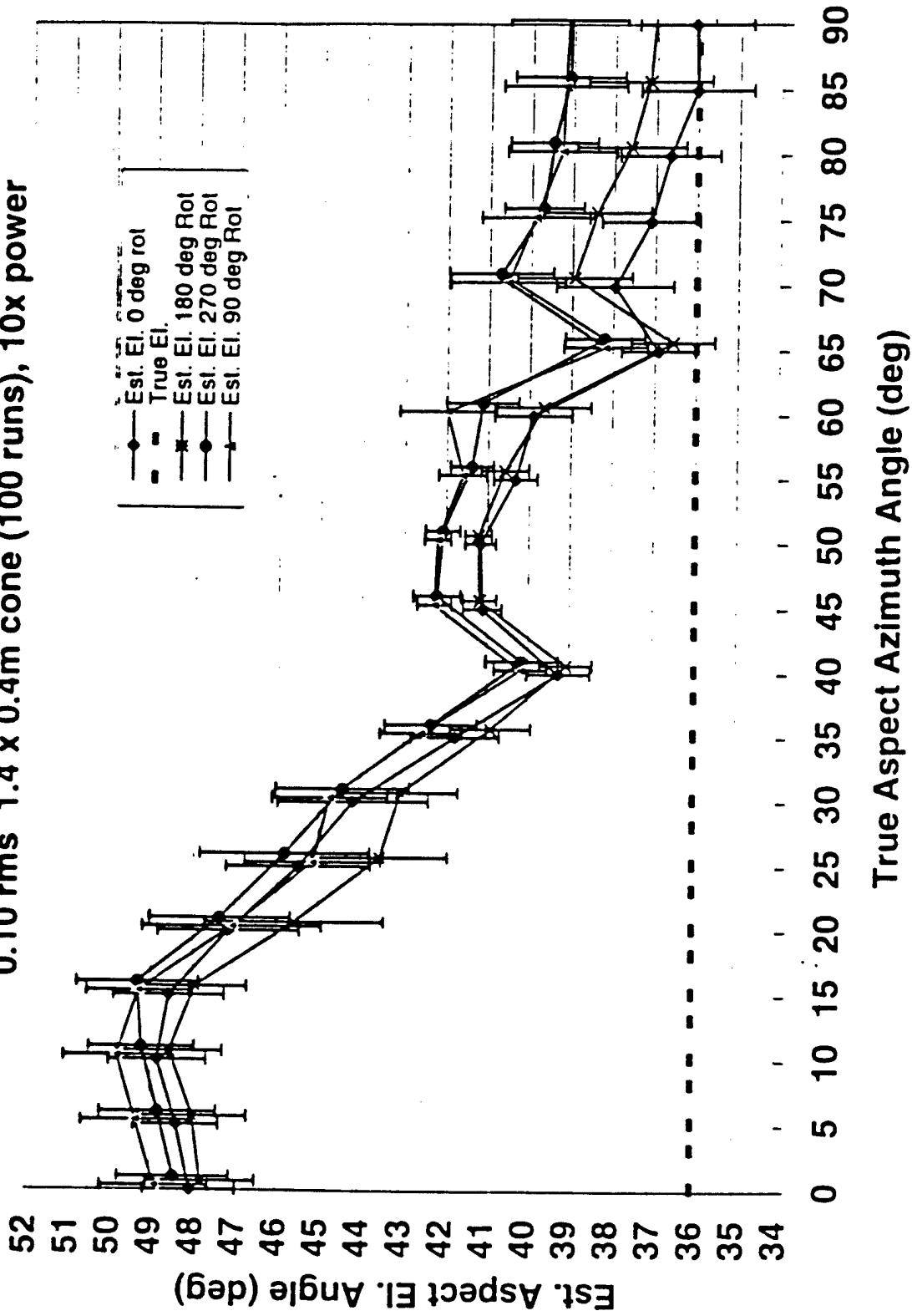
Aspect Elevation Angle Estimates ($I^{2.5}$) 160 km 0.10 rms 1.4 x 0.4m cone (100 runs), 10x power

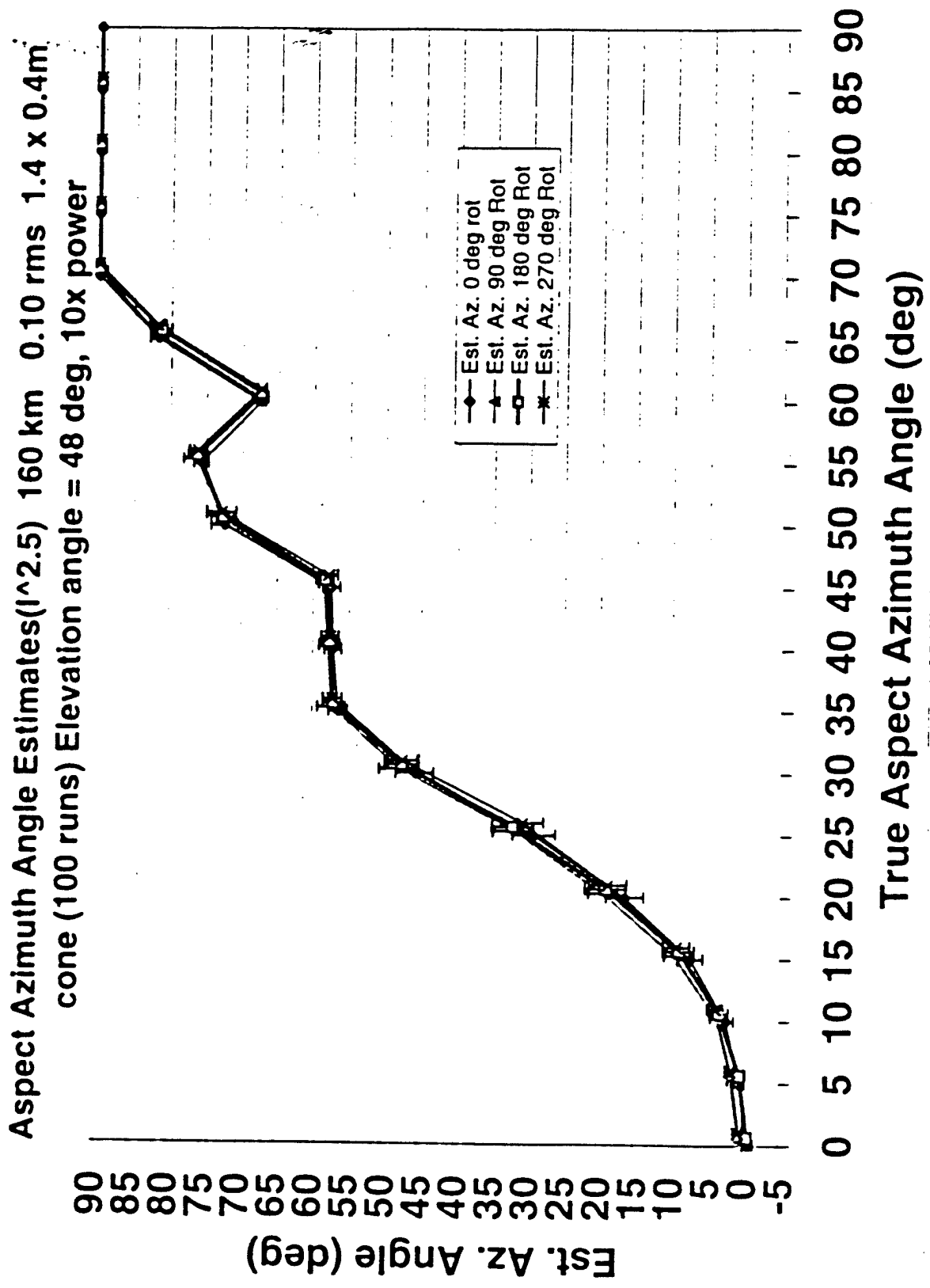


Aspect Azimuth Angle Estimates($I^{2.5}$) 160 km 0.10 rms 1.4 x 0.4m
cone (100 runs) Elevation angle = 36 deg, 10x power

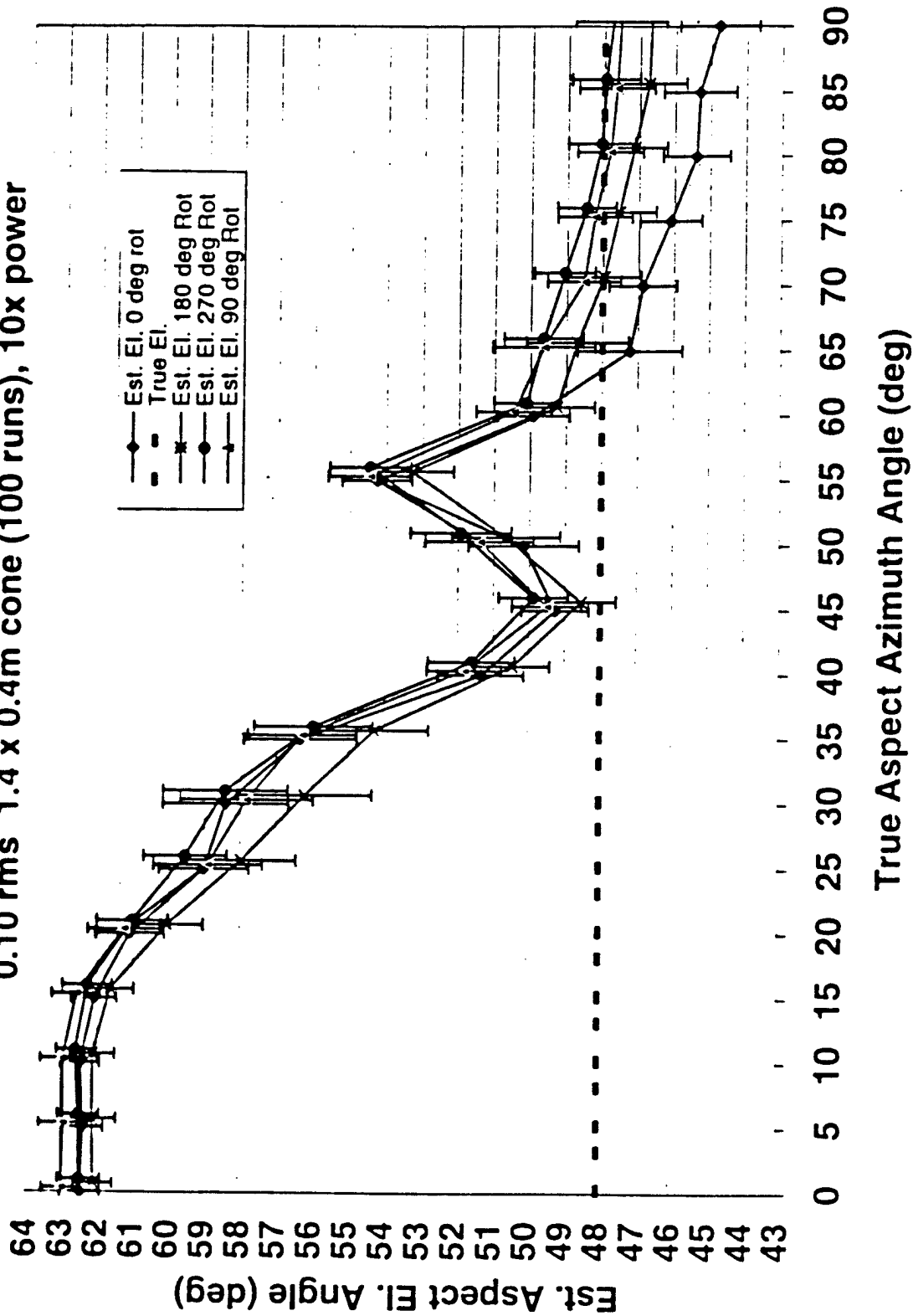


Aspect Elevation Angle Estimates($10^2.5$) 160 km 0.10 rms 1.4 x 0.4m cone (100 runs), 10x power

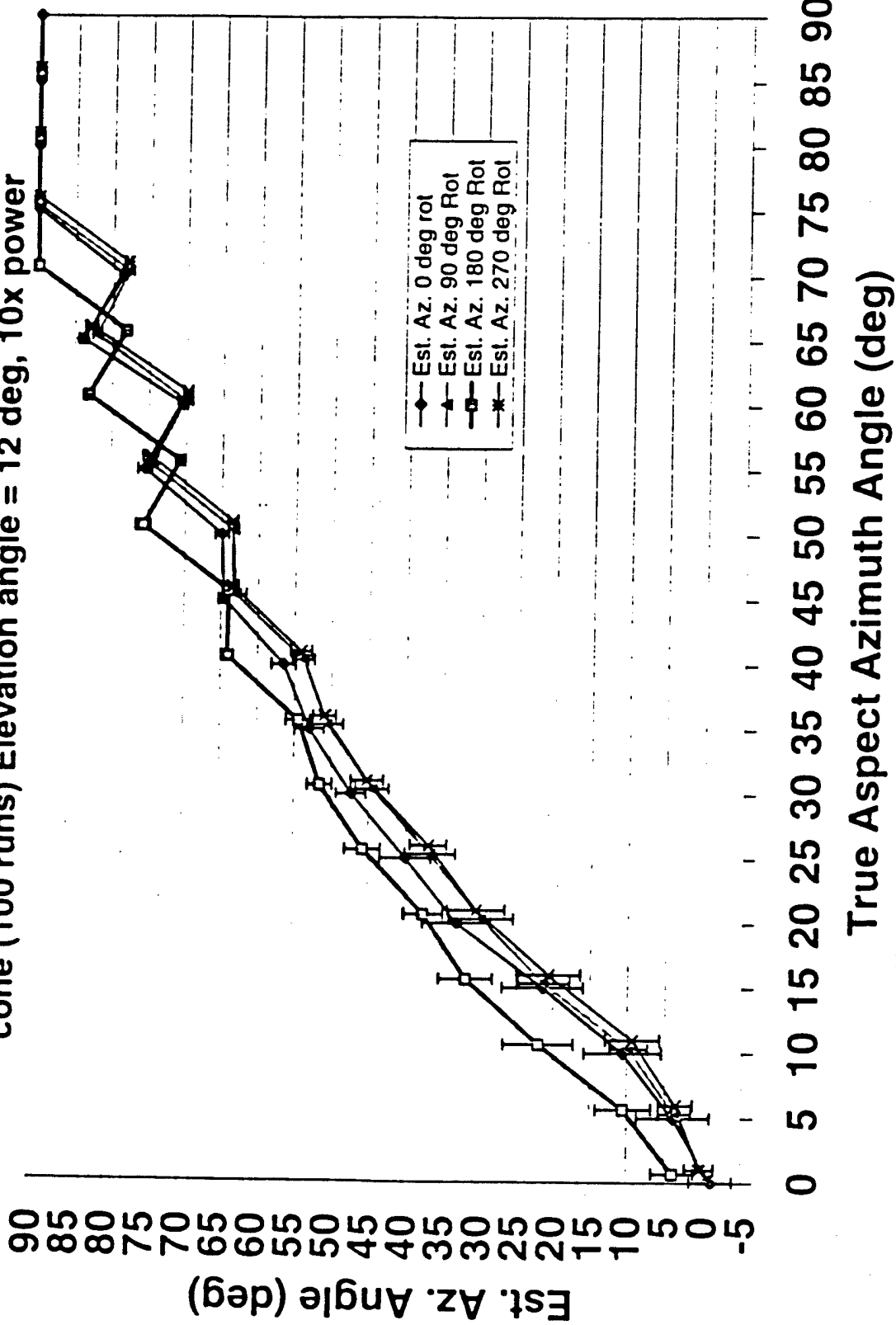




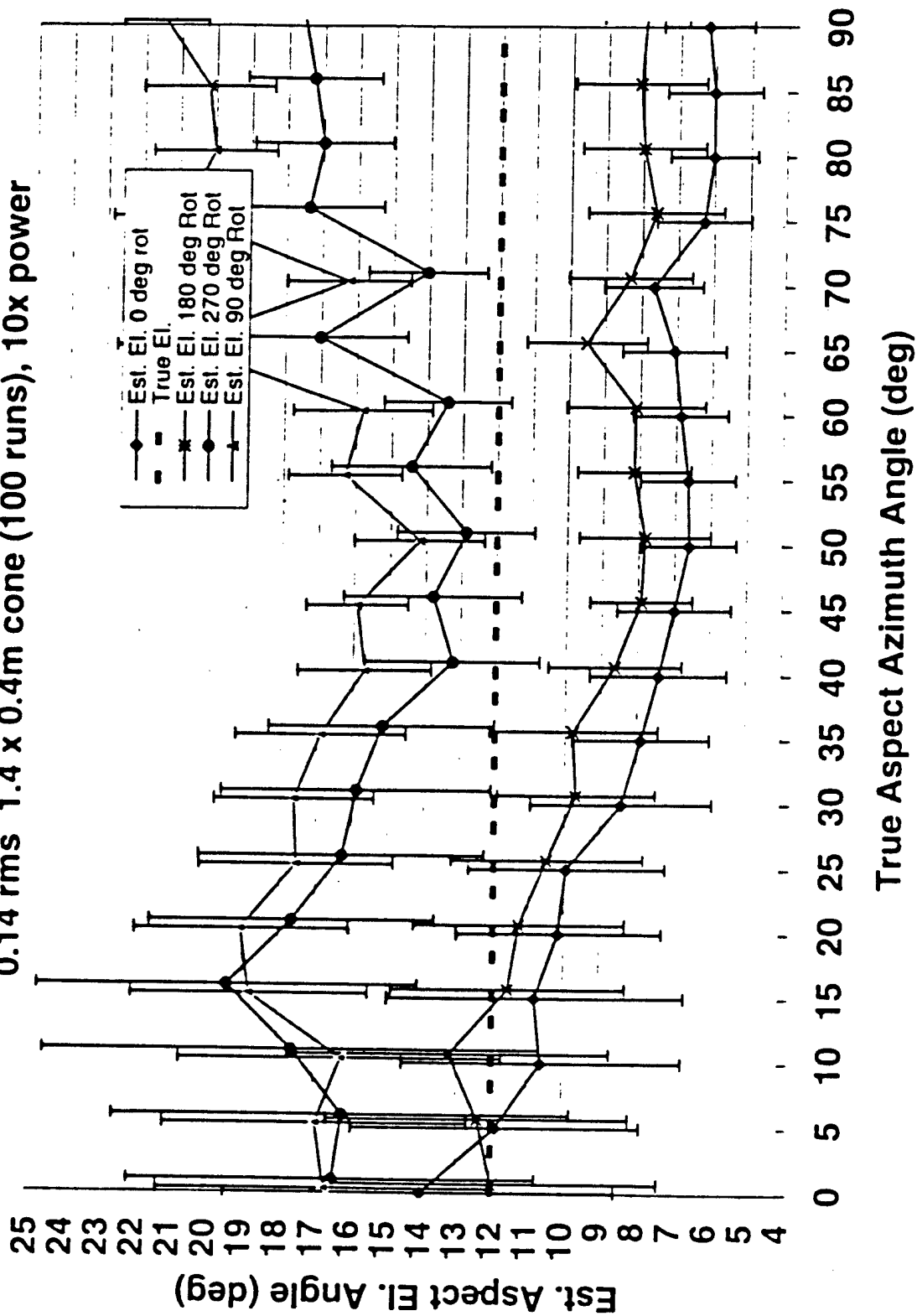
Aspect Elevation Angle Estimates($1^{\wedge}2.5$) 160 km
0.10 rms 1.4 x 0.4m cone (100 runs), 10x power

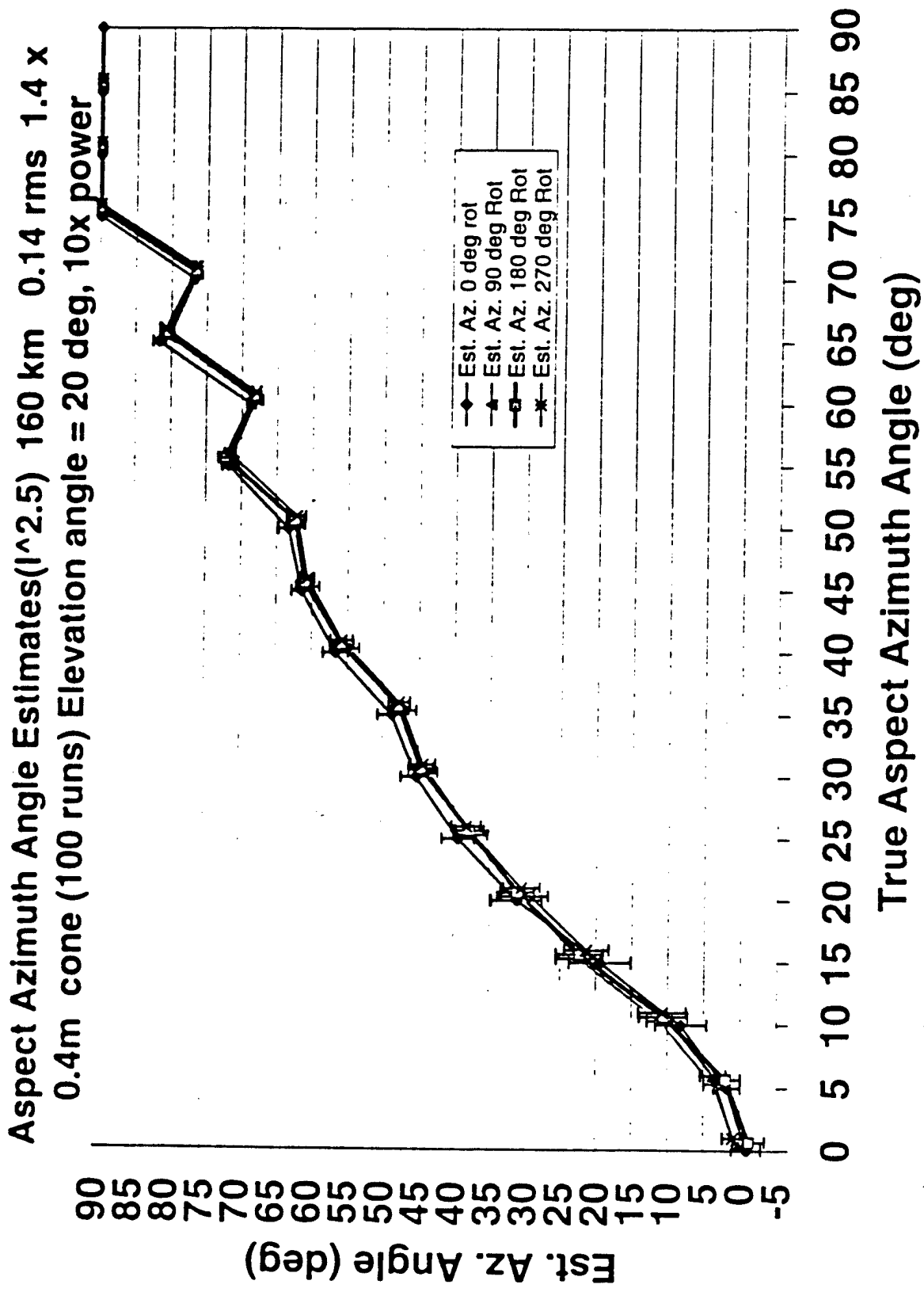


Aspect Azimuth Angle Estimates($I^2.5$) 160 km 0.14 rms 1.4 x 0.4m
 cone (100 runs) Elevation angle = 12 deg, 10x power

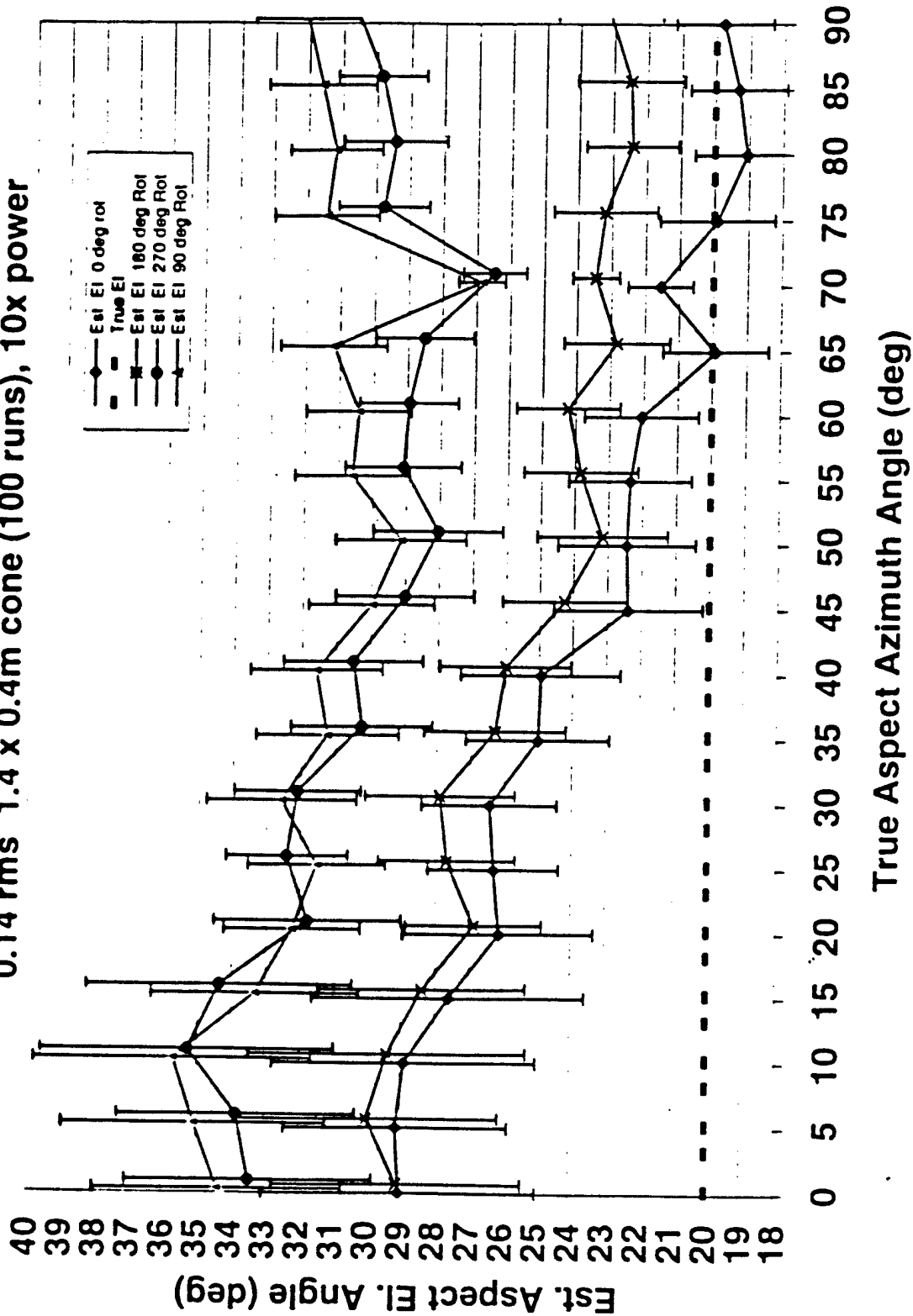


Aspect Elevation Angle Estimates($I^{2.5}$) 160 km 0.14 rms 1.4 x 0.4m cone (100 runs), 10x power

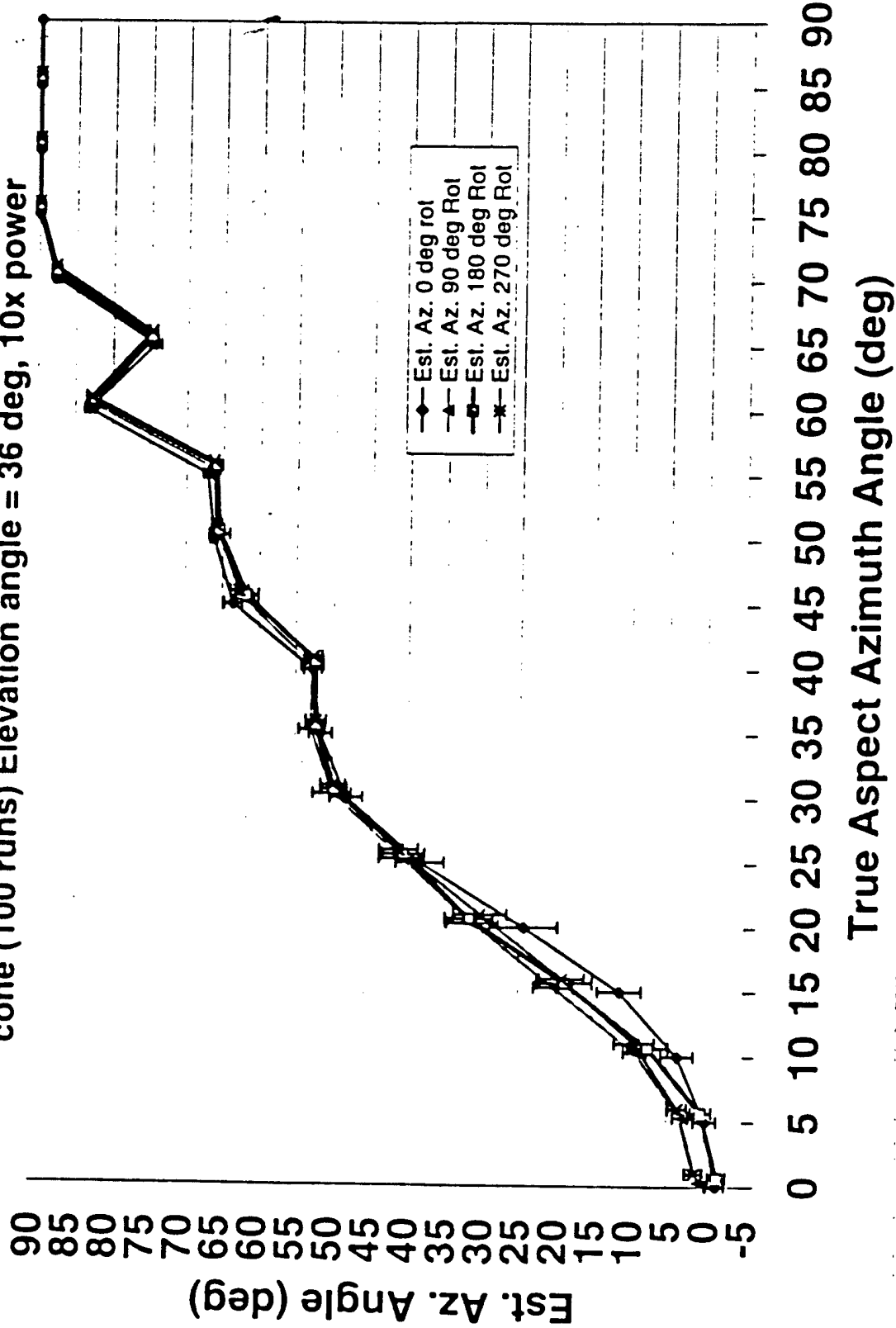




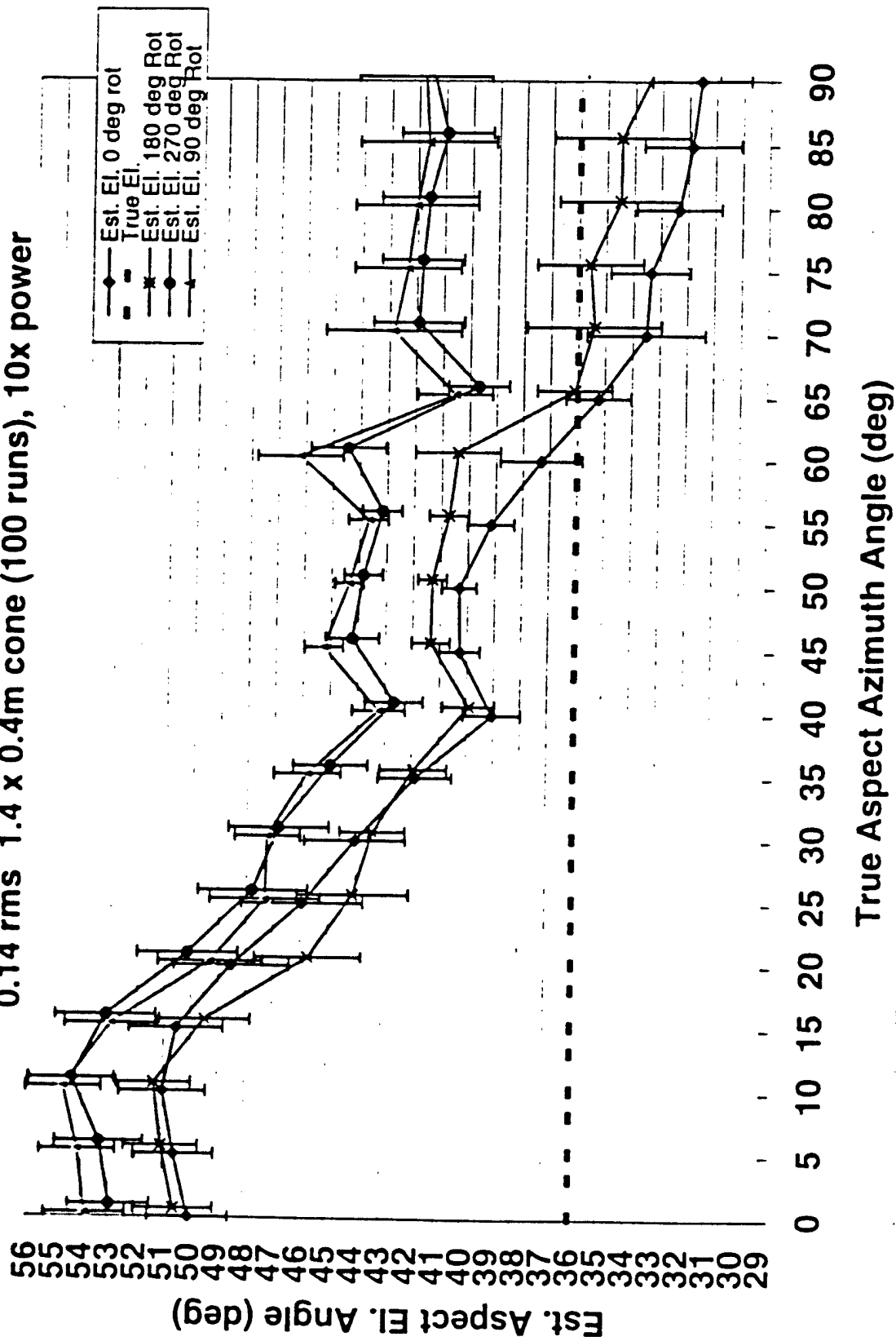
Aspect Elevation Angle Estimates($l^{2.5}$) 160 km 0.14 rms 1.4 x 0.4m cone (100 runs), 10x power



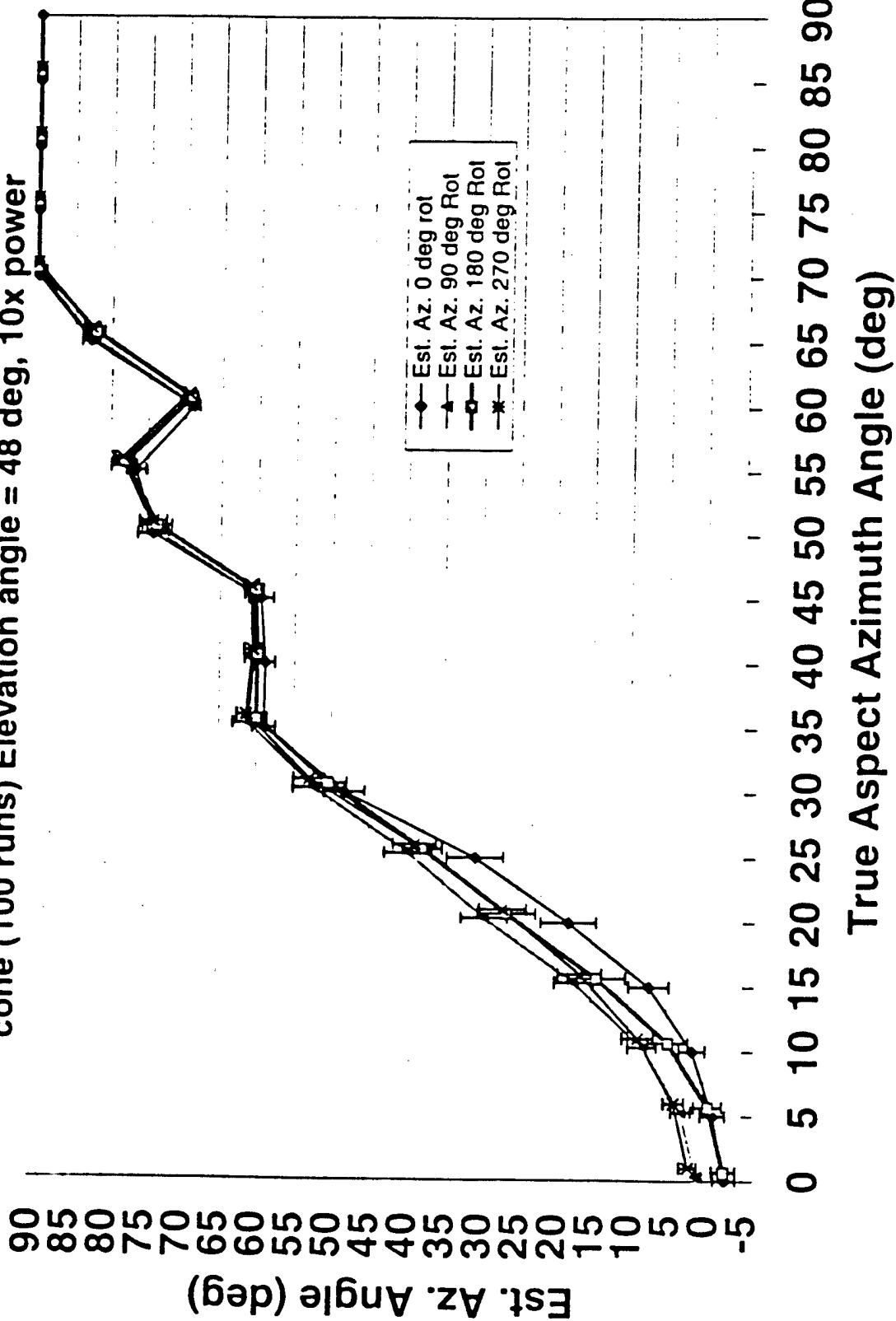
Aspect Azimuth Angle Estimates($I^{2.5}$) 160 km 0.14 rms 1.4 x 0.4m
cone (100 runs) Elevation angle = 36 deg, 10x power



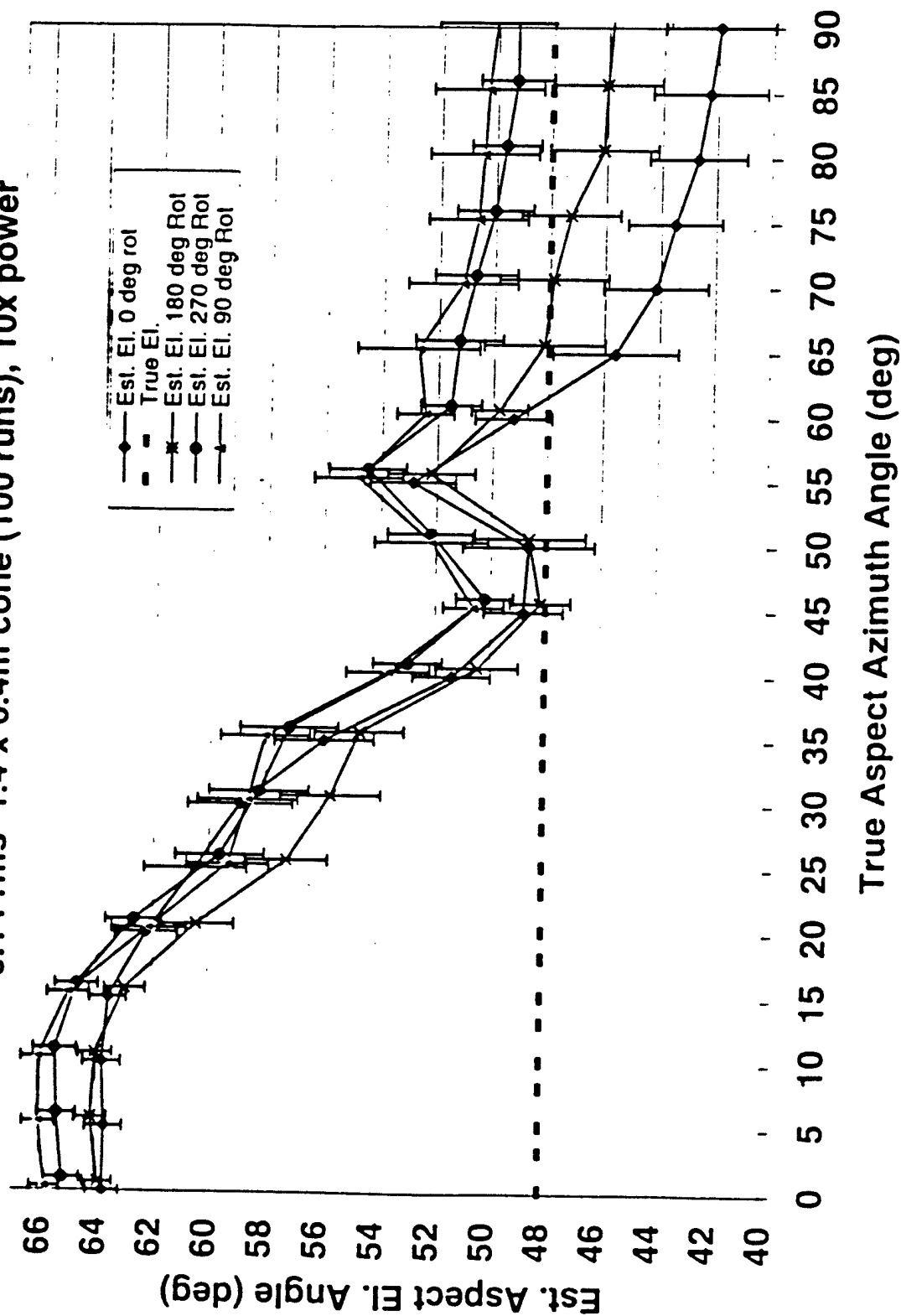
Aspect Elevation Angle Estimates($I^2.5$) 160 km
 0.14 rms 1.4 x 0.4m cone (100 runs), 10x power

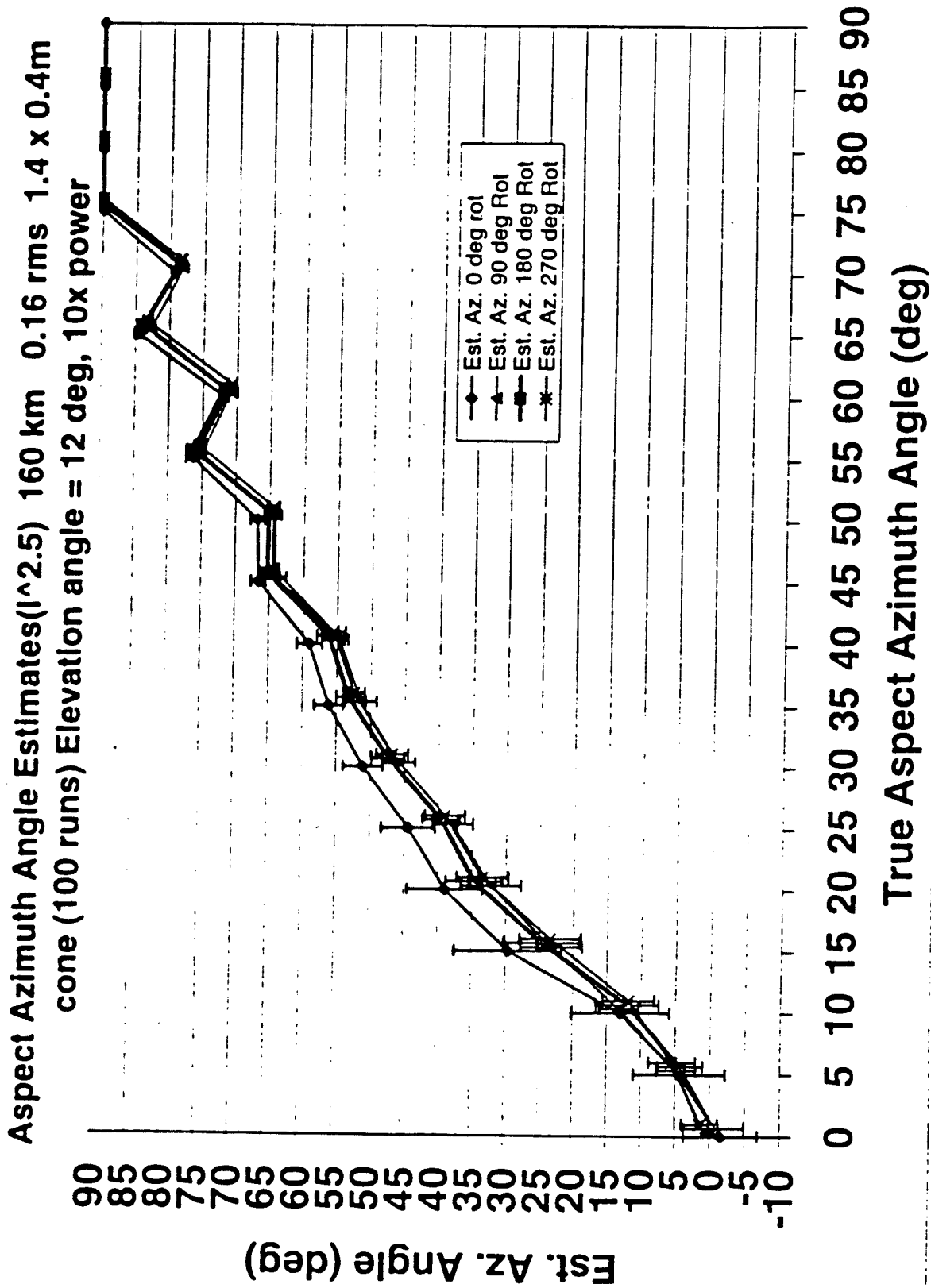


Aspect Azimuth Angle Estimates ($l^{2.5}$) 160 km 0.14 rms 1.4 x 0.4m
cone (100 runs) Elevation angle = 48 deg, 10x power

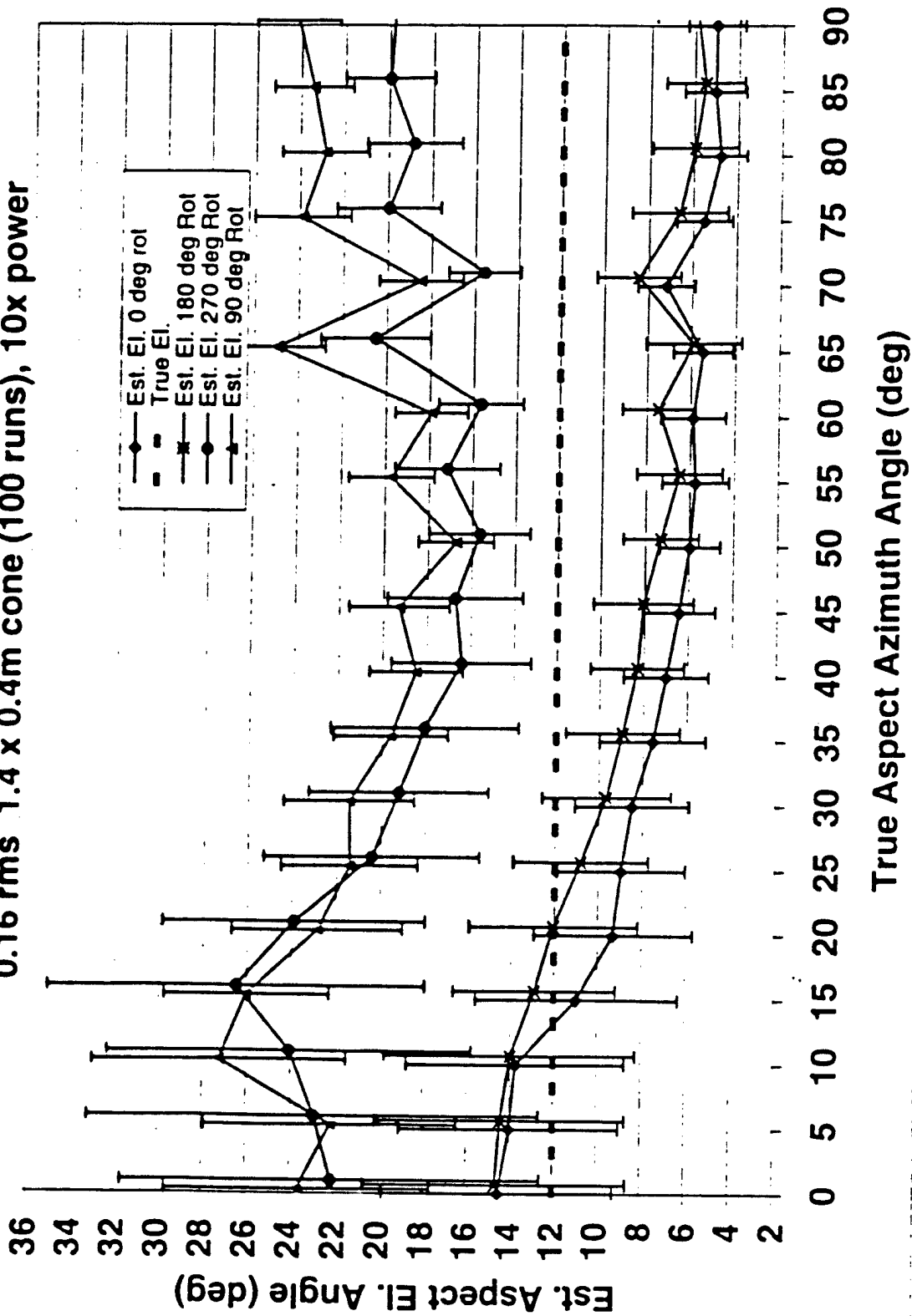


Aspect Elevation Angle Estimates($I^{2.5}$) 160 km 0.14 rms 1.4 x 0.4m cone (100 runs), 10x power

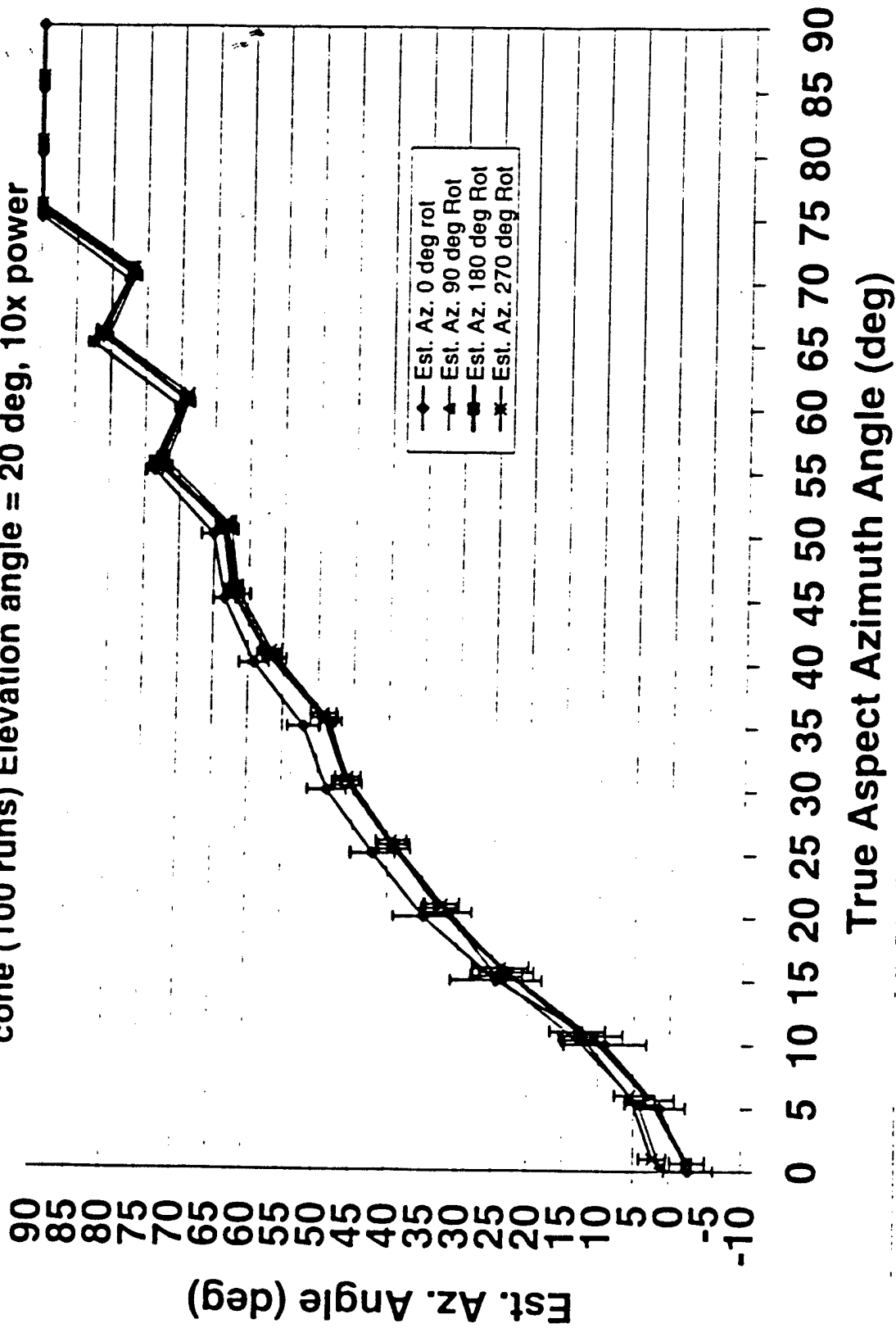




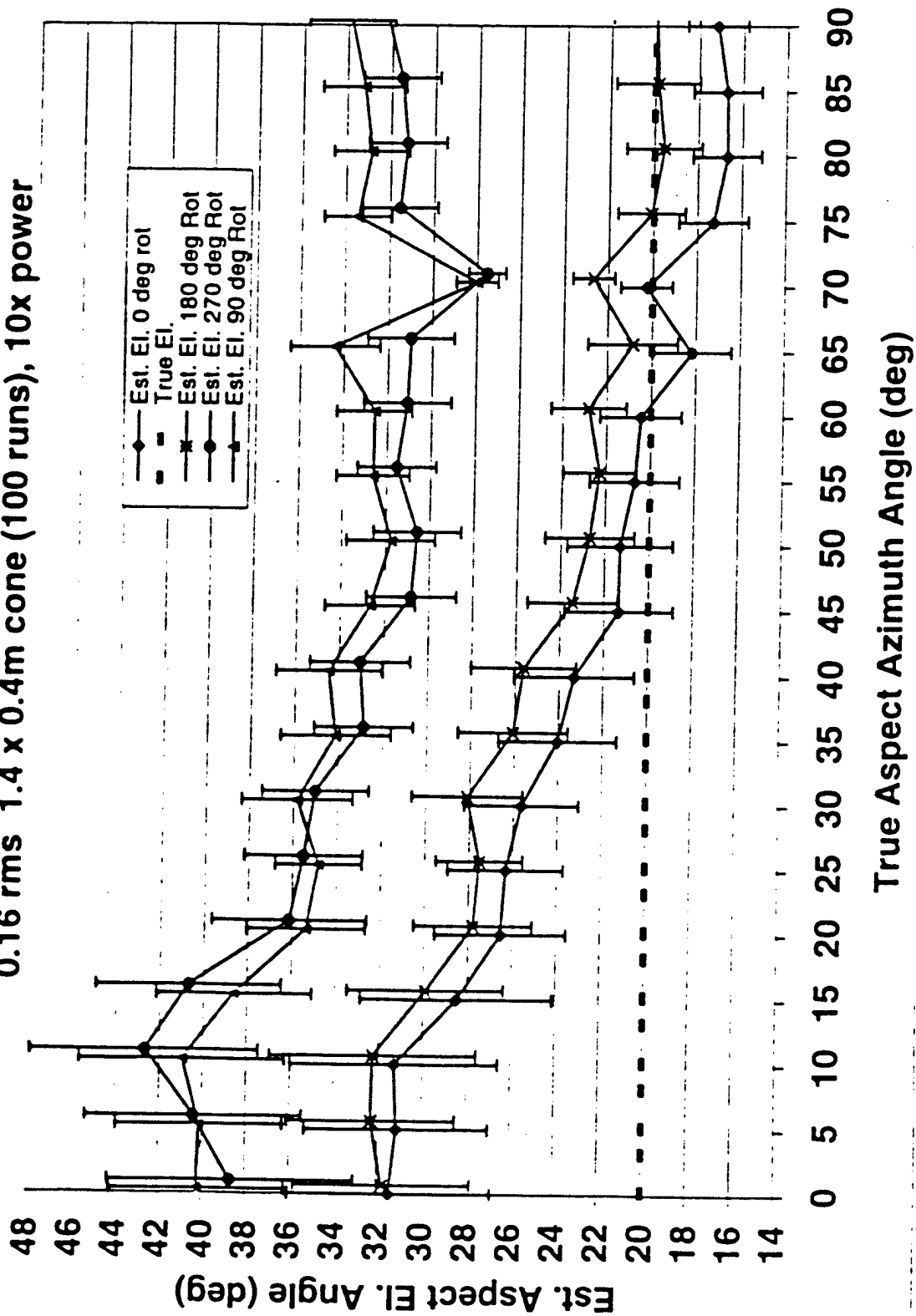
Aspect Elevation Angle Estimates(1[^]2.5) 160 km
0.16 rms 1.4 x 0.4m cone (100 runs), 10x power

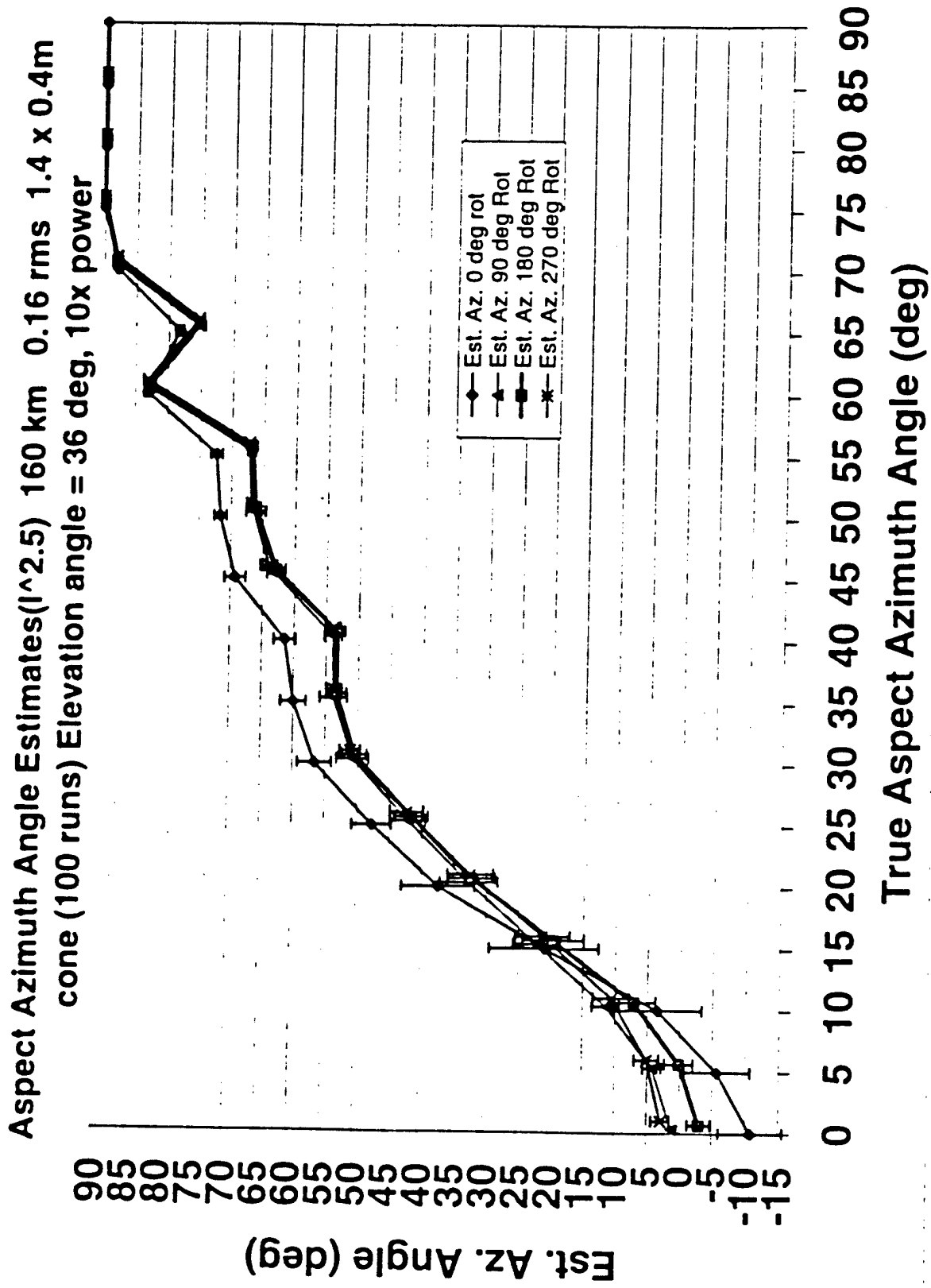


Aspect Azimuth Angle Estimates($1^{2.5}$) 160 km 0.16 rms 1.4 x 0.4m
 cone (100 runs) Elevation angle = 20 deg, 10x power

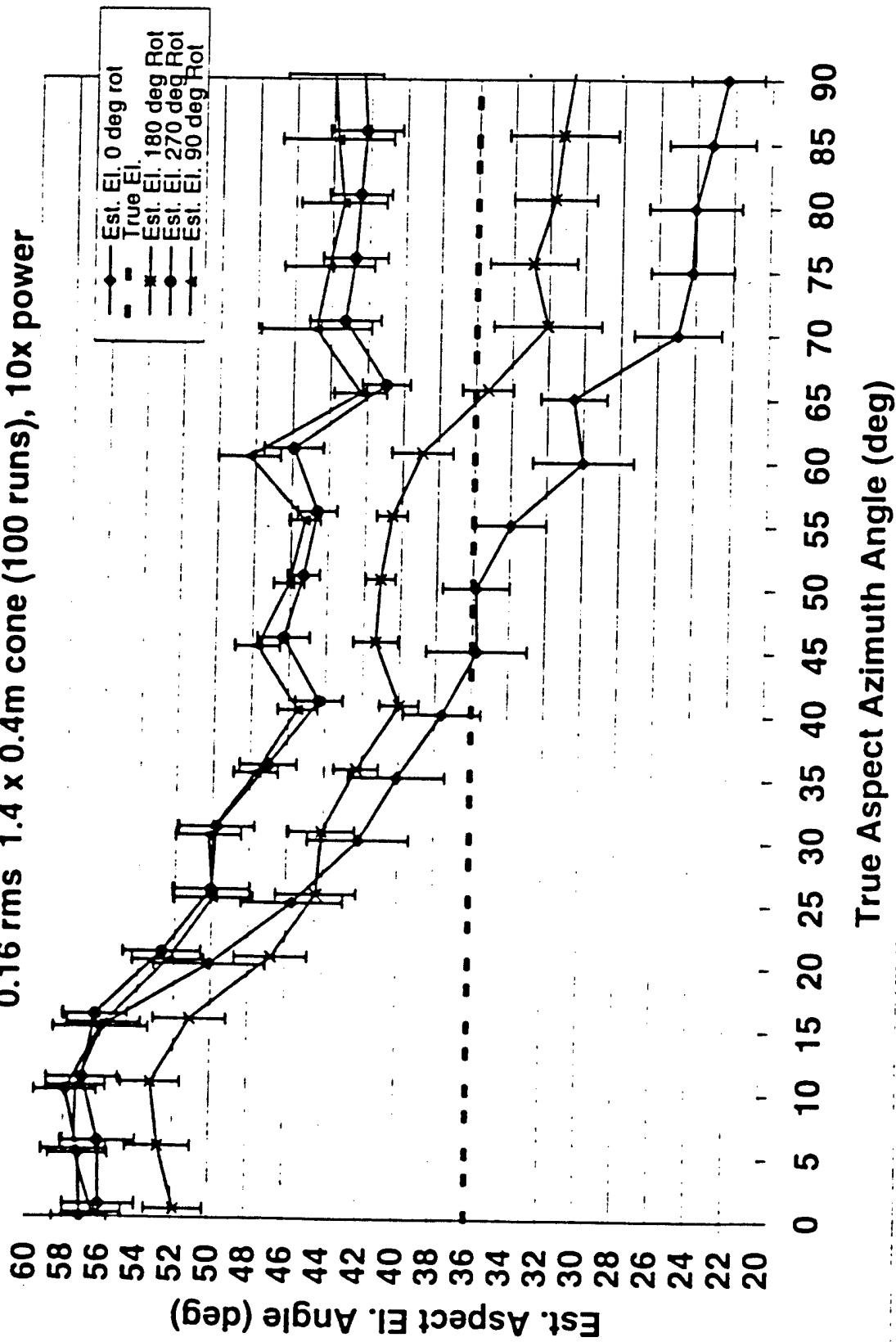


Aspect Elevation Angle Estimates($1^{2.5}$) 160 km
0.16 rms 1.4 x 0.4m cone (100 runs), 10x power

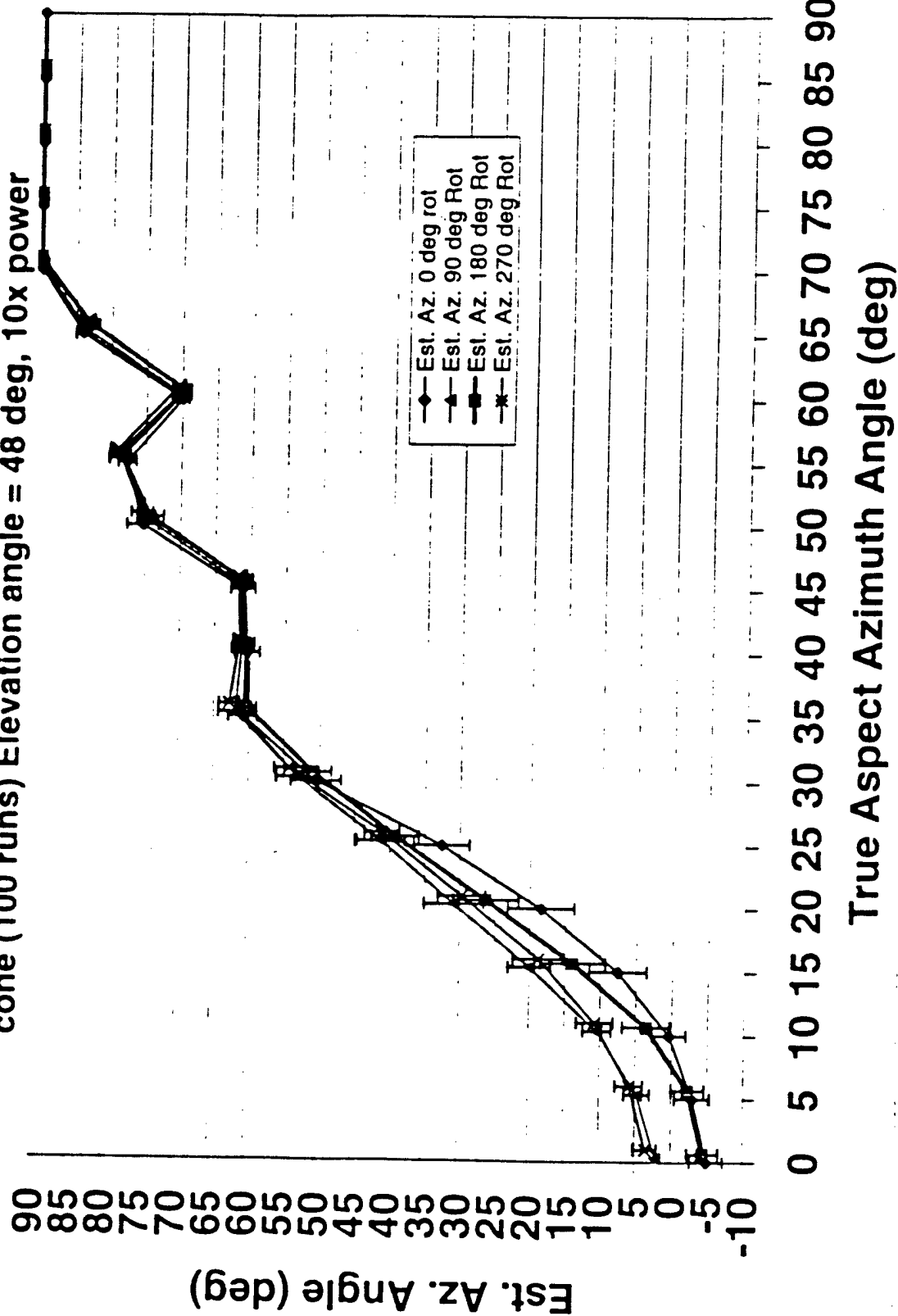




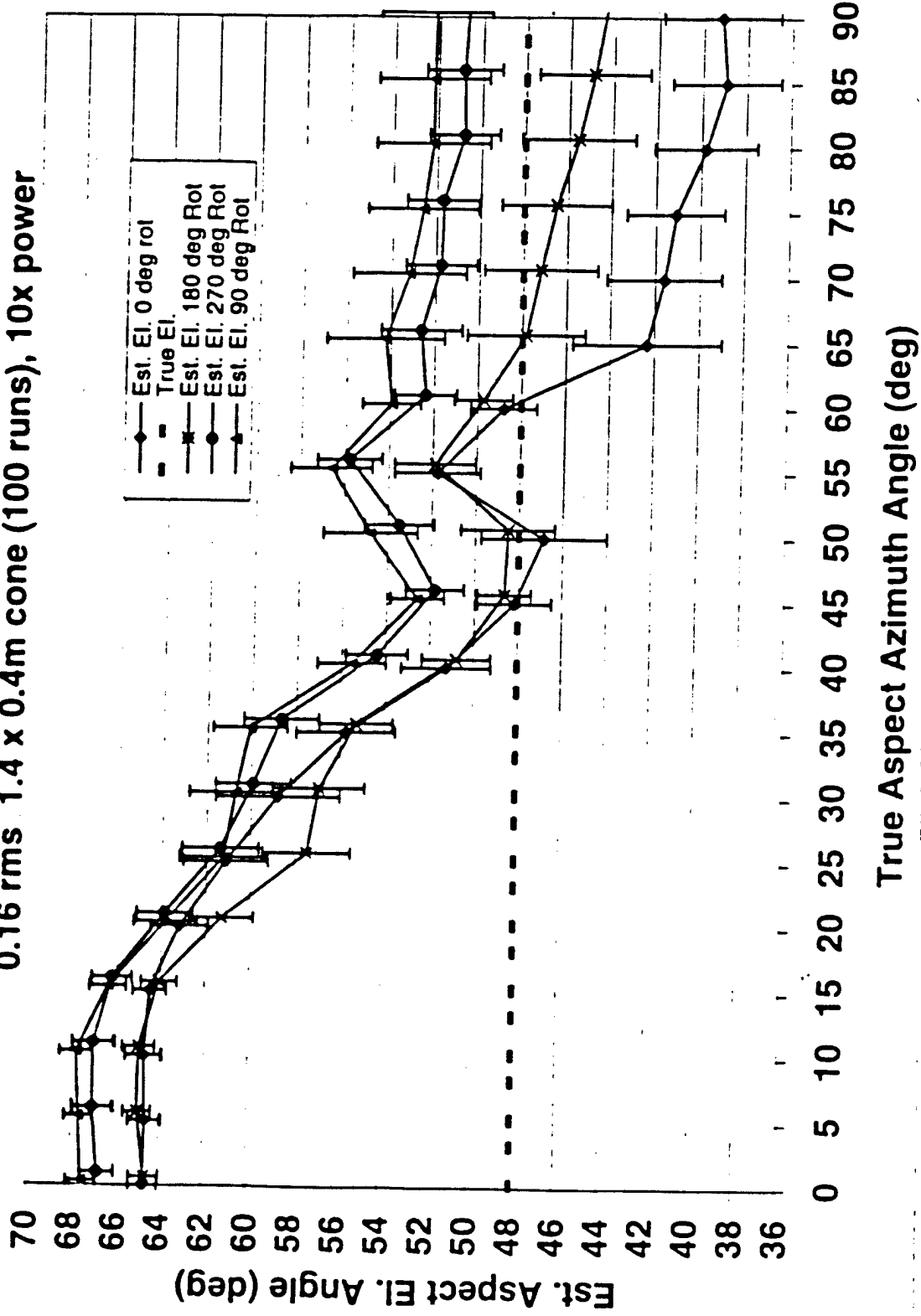
Aspect Elevation Angle Estimates($1^{2.5}$) 160 km
0.16 rms 1.4 x 0.4m cone (100 runs), 10x power



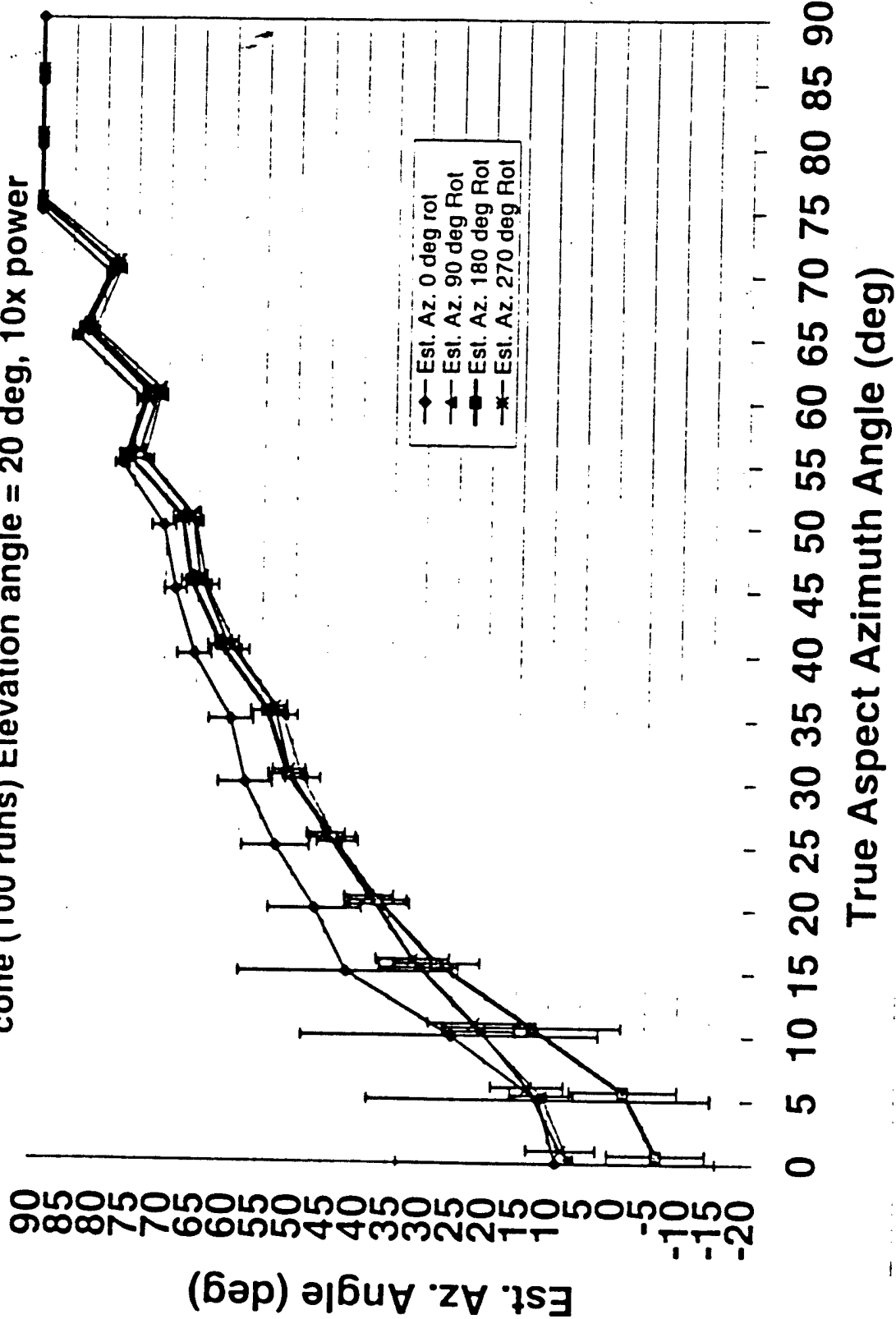
Aspect Azimuth Angle Estimates($l^{2.5}$) 160 km 0.16 rms 1.4 x 0.4m
 cone (100 runs) Elevation angle = 48 deg, 10x power



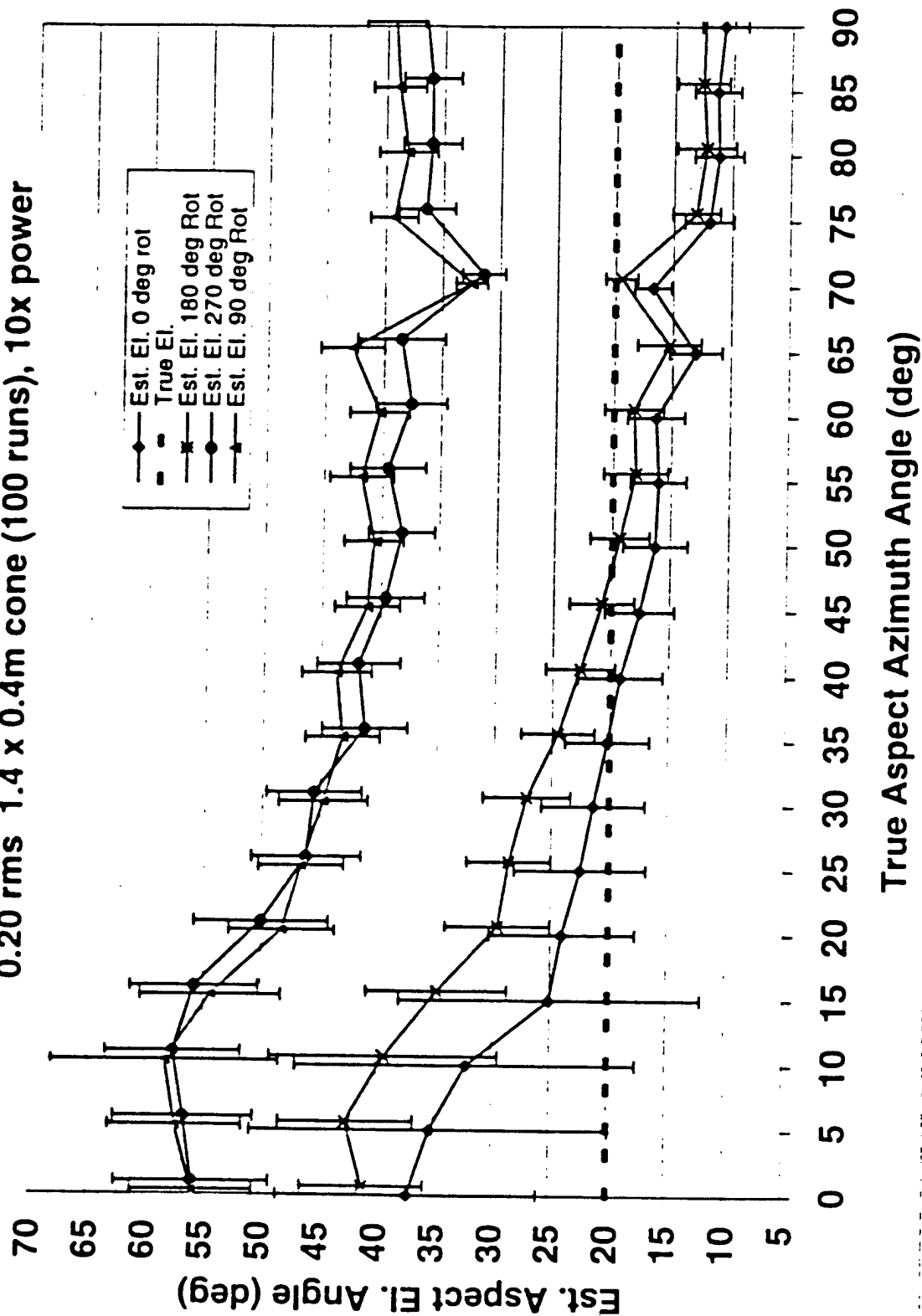
Aspect Elevation Angle Estimates($\sqrt{2.5}$) 160 km
 0.16 rms 1.4 x 0.4m cone (100 runs), 10x power

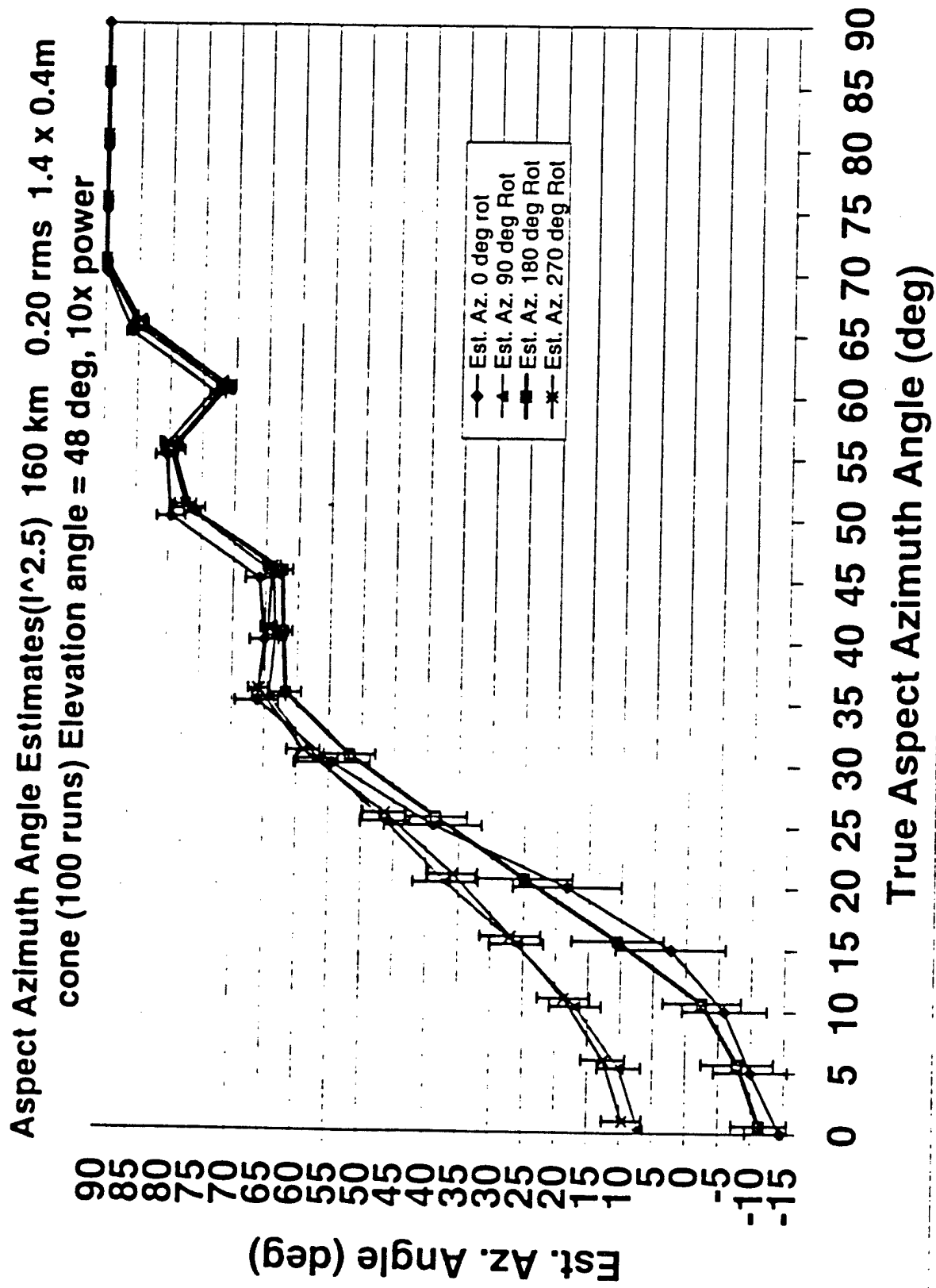


Aspect Azimuth Angle Estimates($1^{\wedge}2.5$) 160 km 0.20 rms 1.4 x 0.4m
cone (100 runs) Elevation angle = 20 deg, 10x power

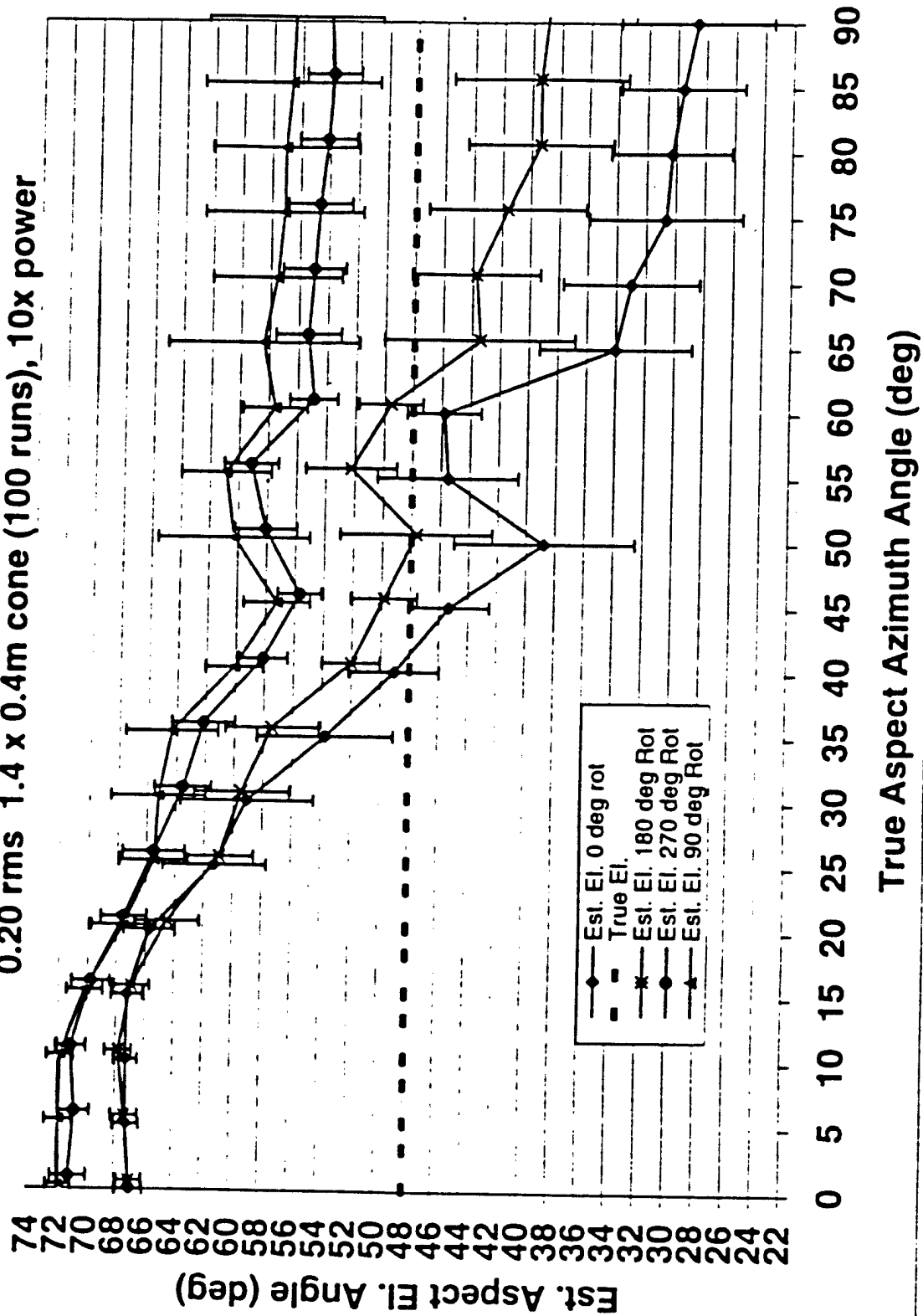


Aspect Elevation Angle Estimates ($I^{2.5}$) 160 km
0.20 rms 1.4 x 0.4m cone (100 runs), 10x power





Aspect Elevation Angle Estimates($I^{2.5}$) 160 km
0.20 rms 1.4 x 0.4m cone (100 runs), 10x power



Appendix R

DITP OPS Working Group: Requirements Summary and Analysis

Robert K. Tyson, February 1999

Test Operation timeline assumptions that affect requirements

Time	Range to Target	Operation	Requirement / comments
L-370		Target deploy	
L+0		Seeker launch	
L+68	470 km	Seeker separation	
L+78		In-flight cal complete	FSM to align source to PSS, (7 μ r); BSM to align source to ladar FP, fixed align laser to focal plane
		Slew to tgt cluster	Tgt & flight sys. uncertainty, pointing error, rss to 0.23°(4 mrad)
		Center on tgt cluster	5 μ r error, open loop, 20 ms settle Maintain 5 μ r 1- σ stability over test
		Handover to ladar	5 μ r track error, 5 μ r BSM posit. error, & 10 μ r static boresight error, 5 μ r jitter
L+103 - L+128	400-350 km	Ladar acquire	3 visits, 10 shots each, look ahead 13 μ r in <530 μ s.
		Center on ladar	by open loop bias of BSM
L+128 - L+208	350-200 km	Ladar intensity measurements	Strehl at least 0.6 over 350-200km
L+208- L+258	200-100 km	Ladar AAR imaging	Center image by open loop bias of BSM, 4.2 μ r, 1 σ error
L+272		Re-entry	
		Recover	

Angles are specified in the body of this report in payload--target (output) space, except where otherwise noted.

1.0 Requirements derived for the operation of the PSS

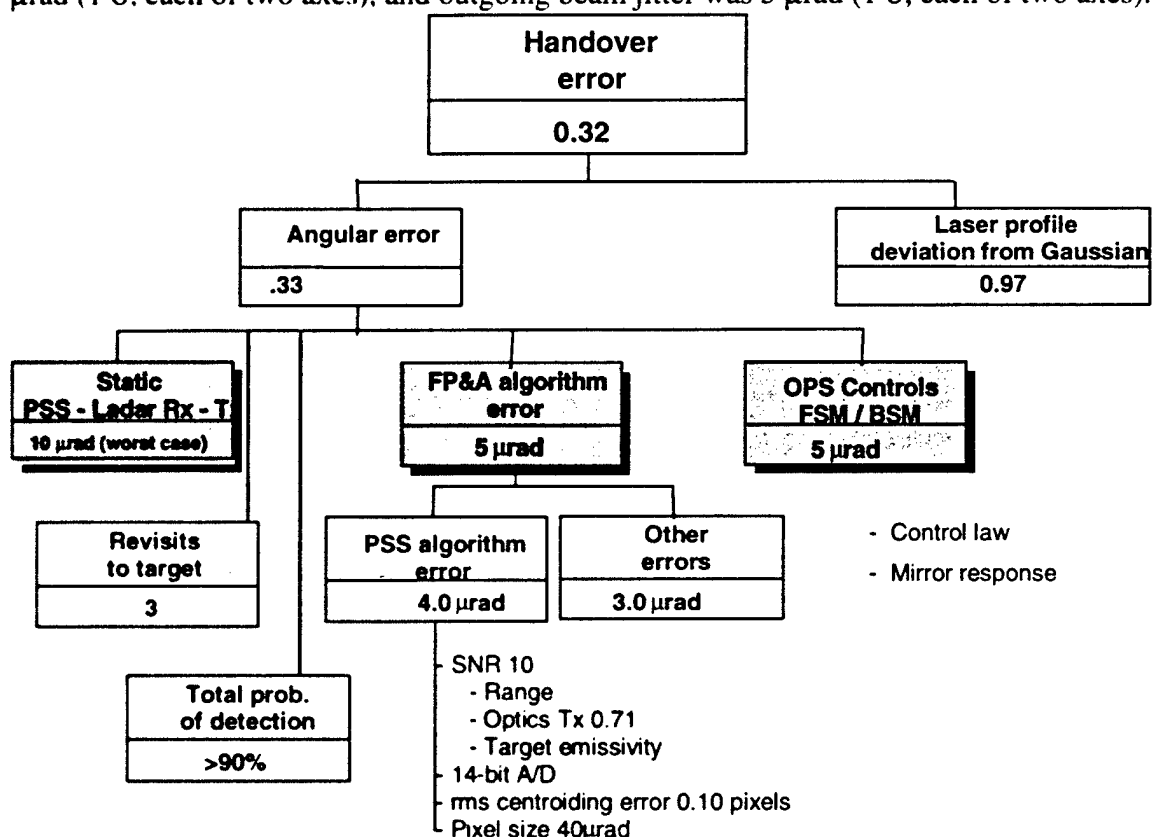
1.1 Centroiding and tracking error for handover to ladar acquisition is $5\text{ }\mu\text{rad}$ ($1\text{ }\sigma$, 1- each axis). This implies that the PSS angular tracking error is less than $5\text{ }\mu\text{rad}$ ($1\text{ }\sigma$)

Justification:

The ladar must have a greater than 98% probability of acquiring the target before 350 km range.

Analysis:

Monte Carlo analysis showed that the 98% detection probability was reached with $5\text{ }\mu\text{rad}$ error if the post-calibration boresight error between the ladar and the PSS was held to less than $10\text{ }\mu\text{rad}$, and the integrated control error for the BSM pointing the laser beam was $5\text{ }\mu\text{rad}$ ($1\text{ }\sigma$, each of two axes), and outgoing beam jitter was $5\text{ }\mu\text{rad}$ ($1\text{ }\sigma$, each of two axes).



1.3 Residual jitter of the outgoing laser and incoming light on the ladar focal plane and on the PSS focal plane will be less than $5.0\text{ }\mu\text{rad}$, $1\text{ }\sigma$, each axis.

Justification:

The laser must be nearly centered on the target so that the central portion, the brightest intensity, is reflected off the target.

Analysis:

The ladar Strehl ratio budget allows for a reduction in intensity of 0.92 contributed by the laser jitter. A nominally 52 μrad beam (full width at $1/e^2$ value at the target plane) will exhibit reduced intensity by 10-12% with 5 μrad rms jitter and boresight errors between 5 and 10 μrad .

1.4 The fast(fine) steering mirror (FSM) will be >4.4 cm clear aperture.

Justification:

The mirror must be sized so that the ladar can be pointed off-axis within the field of view.

Analysis:

The IOS optical aperture is 25 cm diameter. Assuming a telescope magnification of 8, no beam walk, and a maximum angle of incidence of 45 degrees, the mirror size is $(25 / 8) \times 2 \cos(45^\circ)$

1.5 The stroke (throw) of the FSM will be maximum 5.1° .

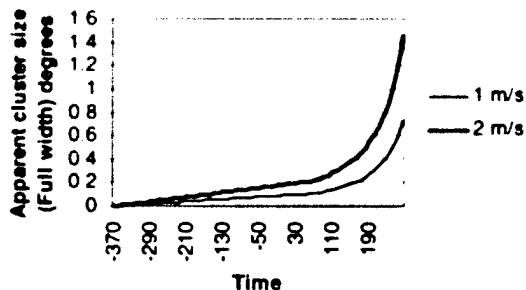
Justification:

The throw of the FSM must be able to point the PSS FOV into any region of the field-of-regard (FOR).

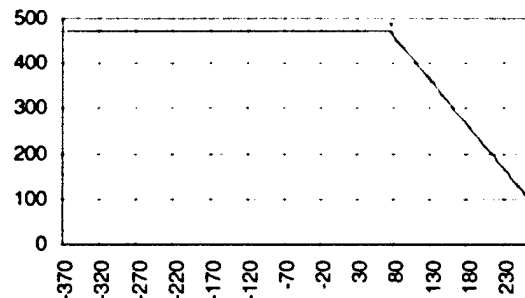
Analysis:

The worst case target cluster size (with 2 m/s target dispersion) is 1.5° . The FOV of the PSS is 0.6° . With a magnification 8 telescope and a mirror angle vs. optical beam angle conversion of $\sqrt{2}$, the stroke (in mirror-space) becomes $(1.5 - 0.6) \times 8 / 1.414 = 5.1^\circ$.

Cluster size vs. time



Range to Target vs. time



1.6 The FSM will be able slew to a point in the FOR and settle to less than 5 μ rad error within 20 ms.

Justification:

The throw of the FSM must be able to point the PSS FOV into any region of the field-of-regard (FOR) and maintain stability.

Analysis:

This retargeting maneuver of the PSS within the FOV for repointing the ladar should minimize wasted laser pulses but be balanced to unrealistic mirror motion requirements. This slew and settle requirement allows for only one wasted ladar pulse (which occurs in 10 ms intervals). This requirement does not account for additional wasted shots of BSM slew and settle delay.

1.7 Optical efficiency for the PSS optical train shall be better than 0.5.

Justification:

The targets must be detectable on the MWIR and LWIR focal planes at maximum range.

Analysis:

Analysis assumes that the MWIR and LWIR optical efficiencies for the PSS optical path elements are equal to or better than:

PSS TMA 0.74; Window 0.98; Fold flat 0.98

Analysis assumes that the MWIR and LWIR optical efficiencies for the common optical path elements are equal to or better than:

Telescope 0.79

FSM 0.95

Beamsplitter/ dichroic 0.95

Obscuration 1.00

The product of these efficiencies is 0.50

1.8 The total pointing error slewing the bus, shall be less than 0.23° (4 mrad).

Justification:

Errors in ground and flight systems limit the overall accuracy of the system pointing to achieve cluster acquisition. They limit the minimum field-of-regard of the system.

Analysis:

Target cluster uncertainty from radar or GPS handover is 1.0 km.

Flight system position uncertainty from radar or GPS handover 0.1 km.

Initial acquisition pointing error is 0.2° (3.5 mrad)

At 500 km range, the values root-sum-square to

$$[(1/500 \text{ rad})^2 + (0.1/500 \text{ rad})^2 + (.0035 \text{ rad})^2] = .004 \text{ radians}$$

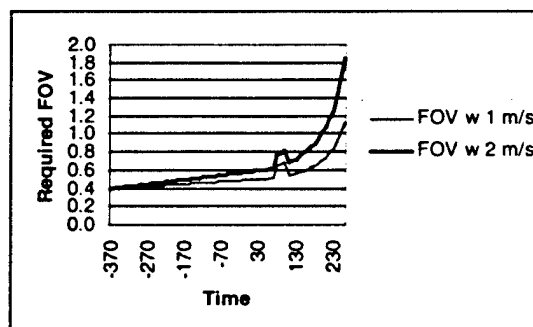
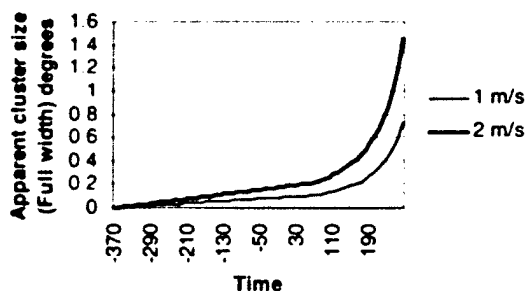
1.9 The field-of-regard of the telescope shall be between 1.1° and 1.9° .

Justification:

The field-of-regard (FOR) or telescope FOV, must be large enough to encompass any target within a target cluster at any point in the operation from a range of 470 km to 100 km.

Analysis:

The FOR can be calculated by adding the cluster size (the two outermost, most separated targets) and the bus pointing error, assumed to be $\pm 0.2^{\circ}$. During passive acquisition, in the range from 470km to 400 km, the error in target location and the error in system position location are also added. It is assumed that the scenario can be designed such that a non-symmetrical FOV can be accommodated with *a priori* information about the target cluster. The requirement allows for uncertainty in the target separation rate. A maximum of 2 m/s is accommodated.



2.0 Requirements derived for the operation of the LADAR

Acquisition requirements

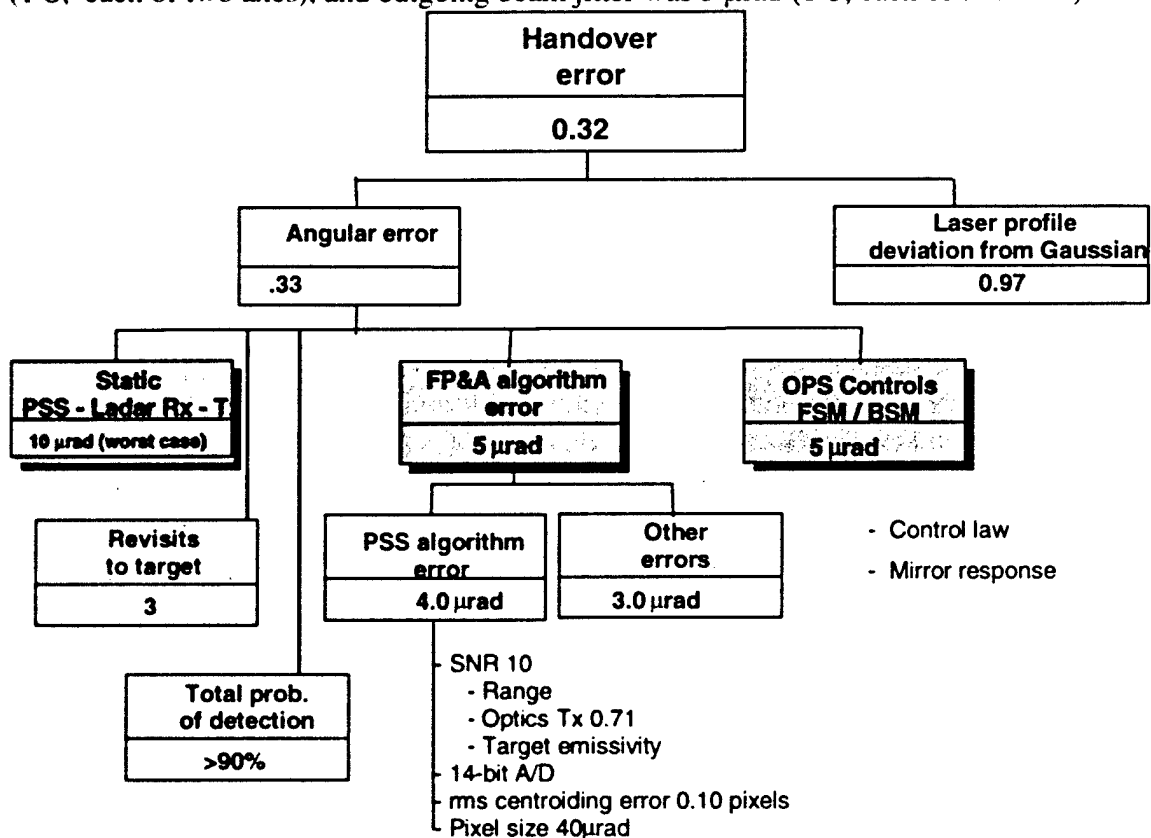
2.1 Positioning error for open loop movement of the ladar LOS during handover from the PSS for ladar acquisition is $5\text{ }\mu\text{rad}$ ($1\text{ }\sigma$, 1-each axis)

Justification:

The ladar must have a greater than 98% probability of acquiring the target before 350 km range.

Analysis:

Monte Carlo analysis showed that the 98% detection probability was reached with $5\text{ }\mu\text{rad}$ positioning error if the post-calibration boresight error between the ladar and the PSS was held to less than $10\text{ }\mu\text{rad}$, and the centroiding and tracking error for the PSS was $5\text{ }\mu\text{rad}$ ($1\text{ }\sigma$, each of two axes), and outgoing beam jitter was $5\text{ }\mu\text{rad}$ ($1\text{ }\sigma$, each of two axes).



2.2 The beam steering mirror (BSM) will be 4.4 cm clear aperture.

Justification:

The mirror must be sized so that the ladar can be pointed anywhere within the field of view.

Analysis:

The IOS optical aperture is 25 cm diameter. Assuming a telescope magnification of 8, no beam walk, and a maximum angle of incidence of 45 degrees, the mirror size is $(25 / 8) \times 2 \cos(45^\circ)$

2.3 The stroke (throw) of the BSM will be maximum 4.8 °.

Justification:

The throw of the BSM must be able to point the ladar into any region of the PSS field-of-view (FOV).

Analysis:

The FOV of the PSS is 0.6° . With a magnification 8 telescope and a mirror angle vs. optical beam angle conversion of $\sqrt{2}$, the throw (in mirror-space) becomes $(0.6) \times 8 / 1.414 = 7.4^\circ$.

2.4 The BSM will be able to slew open-loop to a point in the FOV and settle to less than 5 μrad error within 15-20 ms.

Justification:

The throw of the BSM must be able to point the ladar into any region of the field-of-regard (FOV) and maintain stability.

Analysis:

This retargeting maneuver should minimize wasted laser pulses but be balanced to unrealistic mirror motion requirements. This slew and settle requirement allows for only one wasted ladar pulse (which occurs in 10 ms intervals).

2.5 Optical efficiency for the ladar transmitter optical train shall be better than 0.83.

Justification:

Sufficient laser energy must reach the target.

Analysis:

Analysis assumes that the optical efficiencies for the transmitter optical path elements exhibit negligible losses.

Transmitter optics efficiency 1.0

Analysis assumes that the 532 nm optical efficiencies for the common optical path elements are equal to or better than:

Telescope	0.90
FSM	0.995
BSM	0.995
Beamsplitter/ dichroic	0.96
Relay optics	0.98
Fold flat	0.995

The product of these efficiencies is 0.83

2.6 Optical efficiency for the ladar receiver optical train shall be better than 0.62.

Justification:

Sufficient diffuse or specular reflected laser energy must reach the ladar focal plane.

Analysis:

Analysis assumes that the 532 nm optical efficiencies for the receiver optical path elements are equal to or better than:

Doubler	0.97
Doubler dichroic	0.995
Filter	0.80
Fold flat	0.995
Focus assembly	0.98
Obscuration	1.0

The product of these efficiencies is 0.75.

Analysis assumes that the 532 nm optical efficiencies for the common optical path elements are equal to or better than:

Telescope	0.90
FSM	0.995
BSM	0.995
Beamsplitter/ dichroic	0.96
Relay optics	0.98
Fold flat	0.995

The product of these efficiencies is 0.83.

The total product of the efficiencies is 0.63.

2.7 The BSM must be able to slew and settle for ladar point ahead up to $13\text{ }\mu\text{rad}$ in less than $530\text{ }\mu\text{s}$.

Justification:

The ladar must point the transmitted beam ahead of the moving target and slew the ladar LOS to receive the pulse return.

Analysis:

The maximum angular lead angle is v/c where v is the velocity of the target perpendicular to the line-of-sight and c is the speed of light. The point ahead mirror angle, in target space is $2 v/c$. For $v=2\text{ km/s}$, the point ahead angle is $13\mu\text{rad}$. The BSM must slew and settle open-loop so that the received pulse is stable within $5\text{ }\mu\text{rad}$ on the focal plane while the mirror is on the moving (tracking) platform. The slew and settle should be faster than the round trip time of the pulse. ($80\text{ km range minimum} / c = 530\text{ }\mu\text{s}$.)

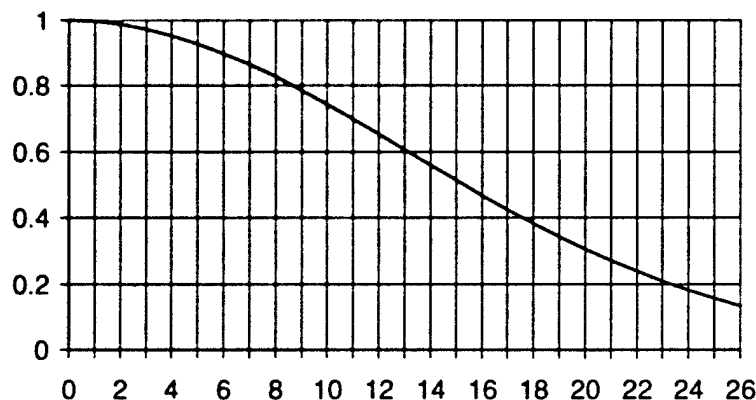
2.8 The relay optics in the ladar shall be sufficient to provide a nearly-Gaussian intensity distribution of the laser in the target plane with a full angle beam divergence (twice the beam waist) of $52\text{ }\mu\text{rad}$.

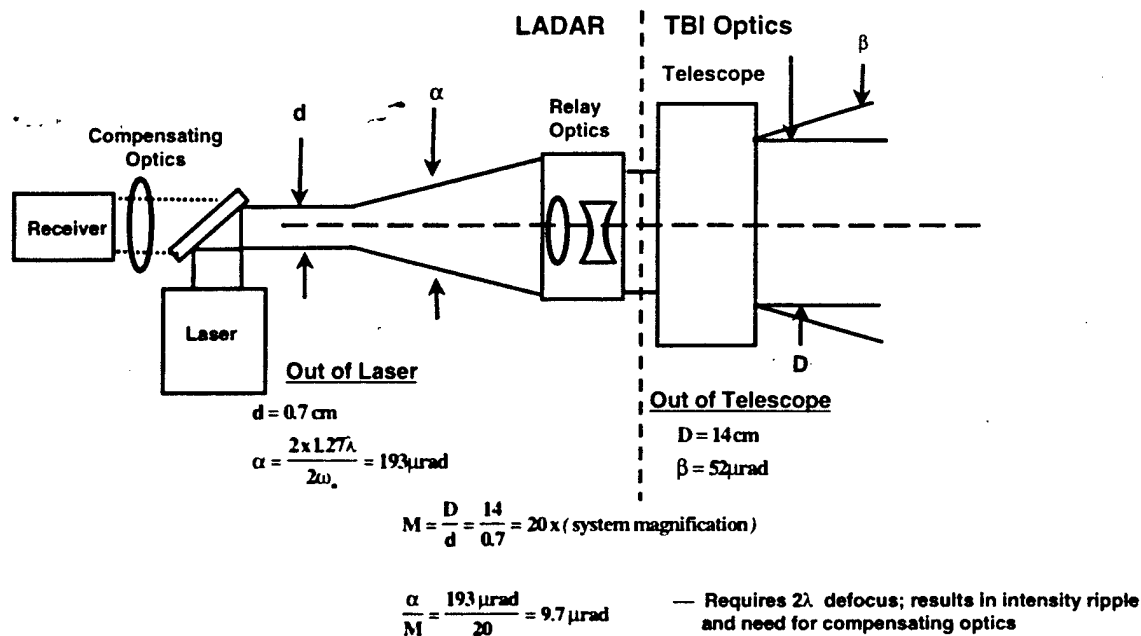
Justification:

There must be sufficient energy deposited on the target for acquisition at long range and imaging at short range.

Analysis:

Assumptions used in the jitter and Strehl ratio analyses are that the target plane beam pattern is near-Gaussian. To achieve this, a 532 nm beam leaving the telescope aperture with a diameter of 14 cm will need to be defocused by about 2 waves to reach $52\text{ }\mu\text{rad}$ full width at $1/e^2$ value.





- Relay Optics must bring divergence from $9.7 \rightarrow 52 \mu\text{rad}$ (output space)
- Return path (Receiver) must compensate for focus addition

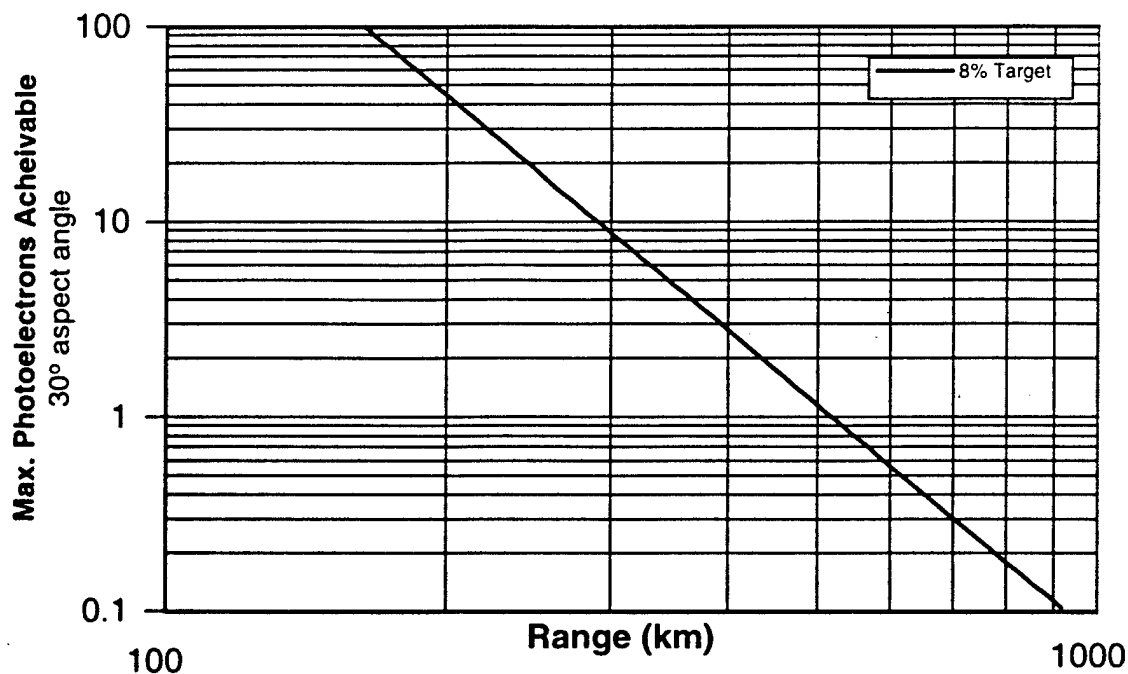
2.9 The optical losses for ladar acquisition must not reduce the Strehl ratio to less than 0.25.

Justification:

Sufficient power must be transmitted, reflected, and received from the target to indicate ladar acquisition.

Analysis:

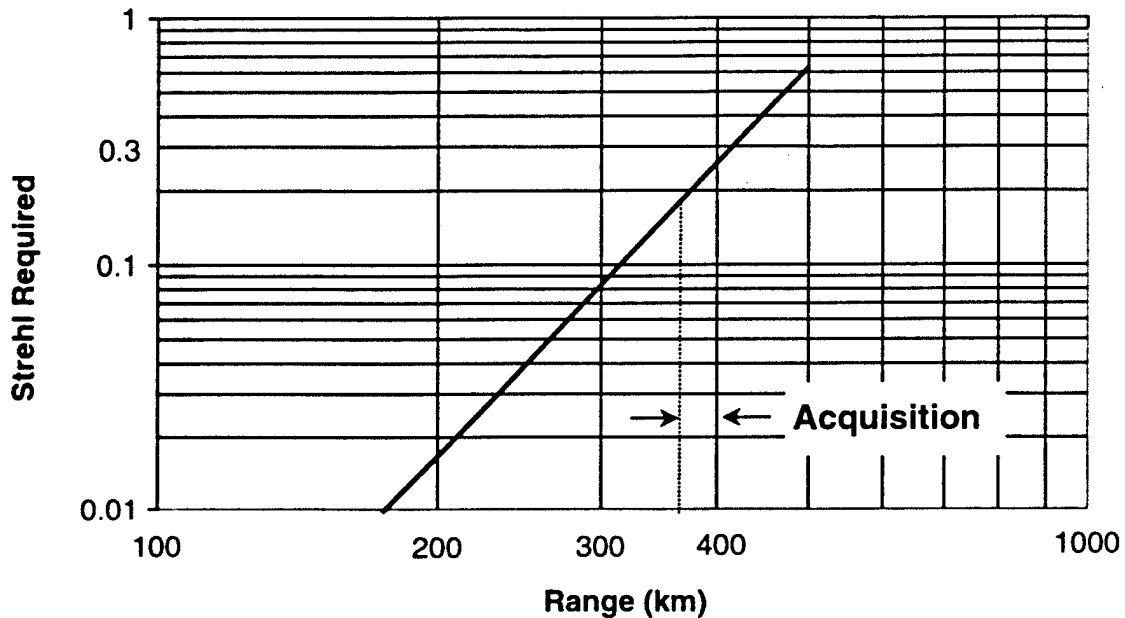
From a radiometric calculation, including modeling of the ladar detector focal plane and assumptions for the peak laser power, the relationship of maximum received photoelectrons versus target range is given by the figure.



(Assumes Transmitter Optical Efficiency .86 and Receiver Optical Efficiency .66)

This assumes a 30° aspect angle for an operational (not a test) target with 8% reflectivity in the visible band. Note that the photoelectrons available at 400 km is 2.8. Noting the next chart, analysis indicates that 90% probability of detection is available during **3 stages of acquisition** (reducing the range bin resolution each time), **visiting each target 3 times** at ranges of 400, 375, and 350 km, with **3 detected hits out of 10 shots** at each range with a detected mean photoelectron count of 0.7. This allows a Strehl ratio of 0.25 which includes all errors including handover offset, jitter, and static power losses. The previous losses assumed, and incorporated in this chart, were transmitter optical efficiency of 0.86 and receiver optical efficiency of 0.66.

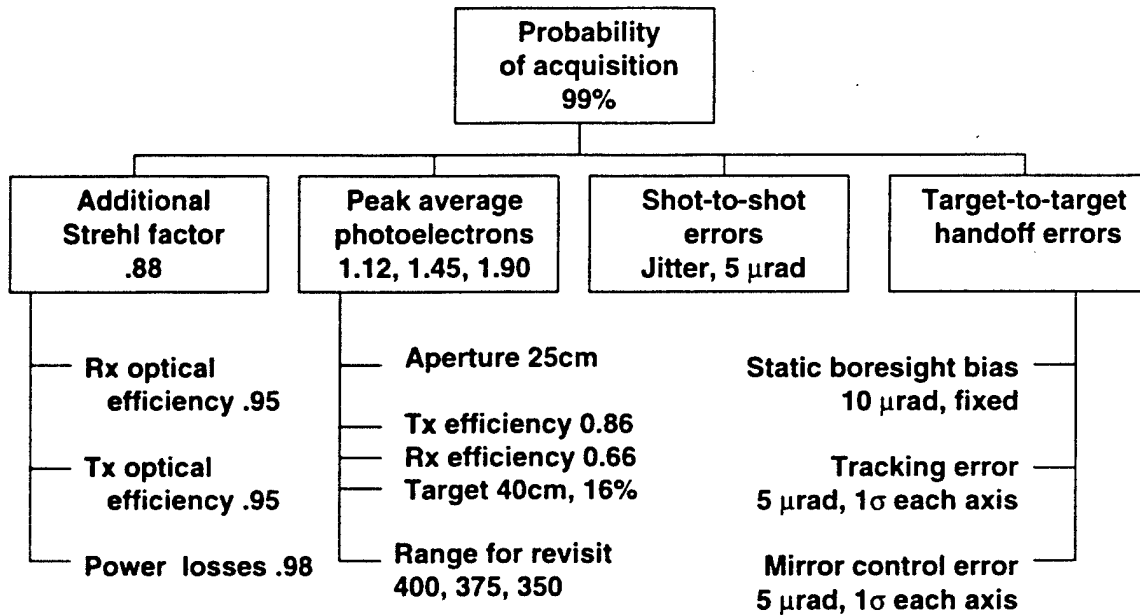
With the 0.7 mean photoelectrons as the goal, analysis shows the available Strehl ratio as a function of range. We proceed with the assumption that a Strehl ratio of at least 0.25 is required for acquisition. at 350 km.



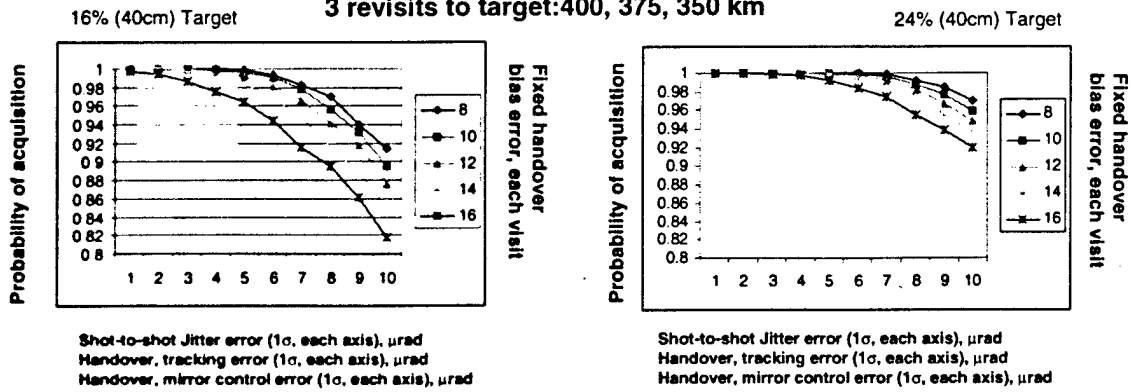
Assumes $\sigma_{jit}(5 \mu\text{rad jit, } 2 \mu\text{rad bias after centering})=0.06$

The 0.25 Strehl ratio can be achieved with an allocation like that shown in the figure. Static errors affect the placement of the laser beam on the target and the optical efficiency not accounted for in the previous 2.8 photoelectron calculations.; dynamic errors reflect motion of the beam in the target plane and power fluctuations. Receiver errors are primarily the budget for the optical efficiency not accounted for in the previous 2.8 photoelectron calculations. These two optical efficiency budgets are a safety margin for the design, however, in the next section, it will be shown that the Strehl ratio for intensity modulation measurement function is more stressing and will be the driving requirement.

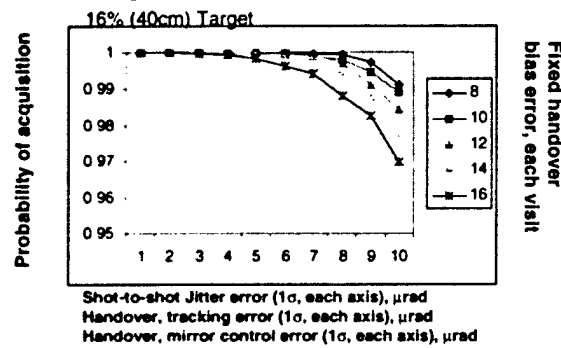
With various target and test scenarios under consideration, other analysis indicates that an acquisition strategy, whereby the ladar is allowed to revisit a target for up to 3 times after handover, while the 16%-reflectivity target is closing range from 400 to 350 km, will provide a near 99% acquisition probability with static errors, algorithm errors, and controls errors as specified in the figure. The analysis assumes a 5 μ rad shot-to-shot jitter.



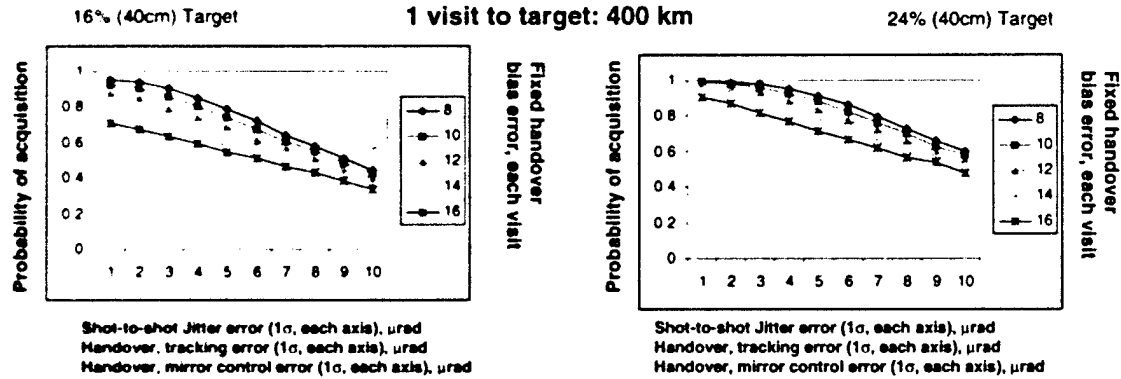
Acquisition probability 3 revisits to target: 400, 375, 350 km



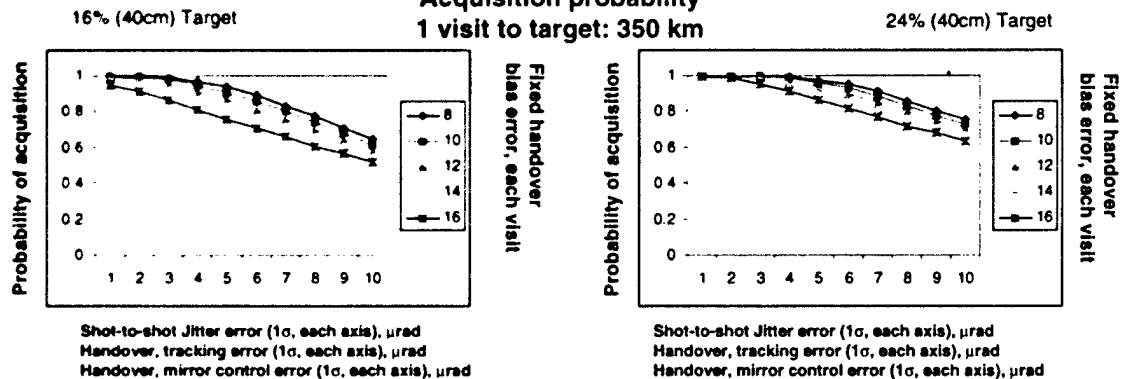
Acquisition probability 6 revisits to target: 400, 390, 380, 370, 360, 350 km



Acquisition probability 1 visit to target: 400 km



Acquisition probability 1 visit to target: 350 km



2.10 The ladar shall provide a 532 nm notch filter to reject solar background.

Justification:

Solar radiation reduces the detector signal-to-noise ratio.

Analysis:

Value TBD based upon test scenario conditions.

Intensity modulation requirements

2.11 The optical losses for ladar intensity modulation must not reduce the Strehl ratio to less than 0.60.

Justification:

The ladar revisits various targets during the operation to determine the coning angle from modulation of the received intensity. The intensity of the laser transmission must remain constant from visit to visit, which can occur over a period of seconds, and the mean photoelectron count must be high enough for intensity modulation. The accuracy of the modulation measurement must be 10% to distinguish the difference between 12° and 4° coning. It must be 7% to distinguish the difference between 8° and 4° coning.

Analysis:

The measure of intensity modulation error is σ_I . The ratio σ_I / I must be small so that the difference between coning angles can be resolved. It requires sufficient photon return, which is dependent upon range, total number of pulses, and the speckle M-factor. Aberrations, transmission losses, and boresight error, reduce the total intensity and alter the σ_I / I ratio.

$$\sigma_I = \sqrt{\frac{SI}{n}}$$

where S = Strehl due to boresight, transmission, other losses

$$\sigma_u = \sqrt{\frac{S^2 I^2}{nM}}$$

I = mean photoelectron count

n = # of pulses

M = Speckle factor

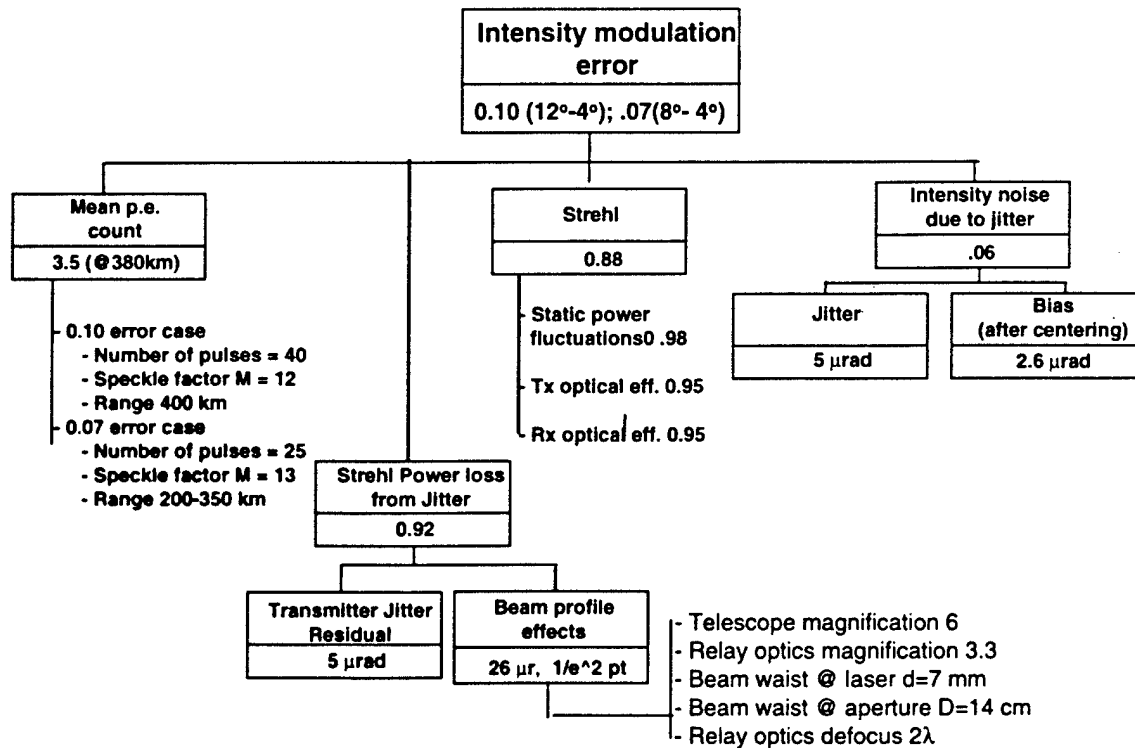
$$\sigma_j = \frac{SI \delta_{jit}}{\sqrt{n}}$$

δ_{jit} = intensity noise due to jitter

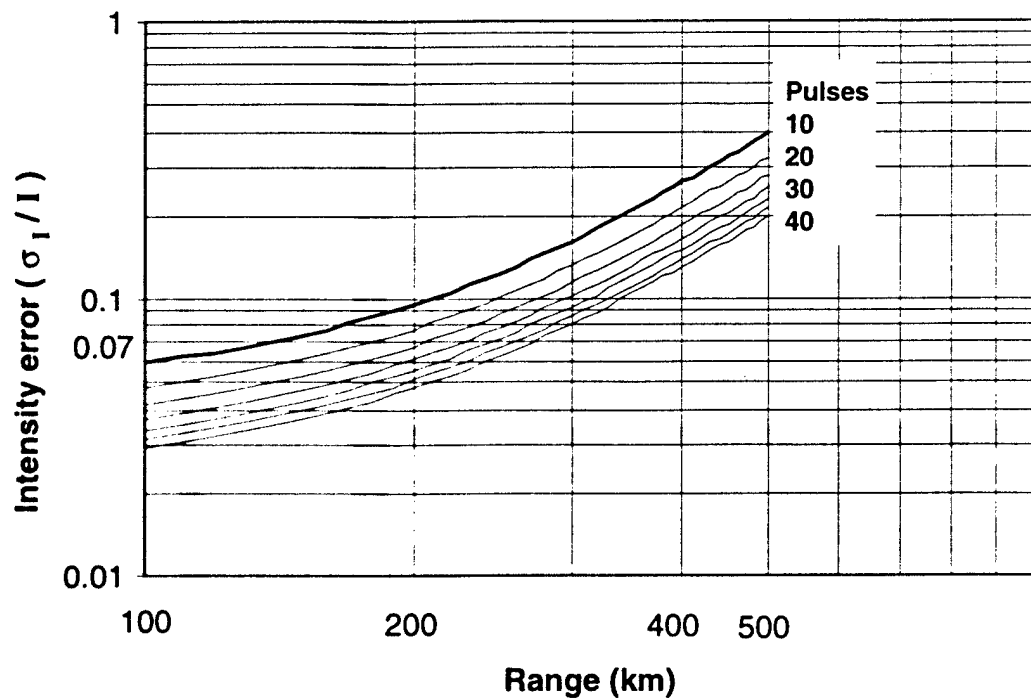
$$\sigma_I = \sqrt{\sigma_u^2 + \sigma_j^2}$$

$$\left(\frac{\sigma_I}{I} \right) = \frac{\sigma_I}{SI} = \frac{\sqrt{SI + \frac{S^2 I^2}{M} + S^2 I^2 \delta_{jit}^2}}{\sqrt{n} SI}$$

Analysis determined that a Strehl ratio of 0.6 was required to keep the modulation noise low enough so that discrimination was possible. (Note: for acquisition, a Strehl ratio of 0.88 was required that did not include the effects of jitter.) This is based upon calculations at a maximum intensity modulation measurement range of 350 km, after ladar acquisition. The Strehl ratio was allocated to jitter, optical efficiency, power fluctuations, and bias.



Range can be traded against intensity modulation error by varying the number of pulses used to interrogate the target on each visit. The intensity modulation measurement error is affected by three factors: constant intensity losses which reduce the Strehl ratio, slow drift intensity variations which affect the mean intensity on target from one point in the modulation cycle to another, and fast shot-to-shot intensity variation which appears as a modulation and can be misinterpreted as coning variation.



2.12 The ladar shall maintain less than 2 μ rad bias error on the ladar focal plane after acquisition and target centering.

Justification:

A region of constant intensity should be placed on the target. Each shot on a target should not be in a different part of the laser spot distribution.

Analysis:

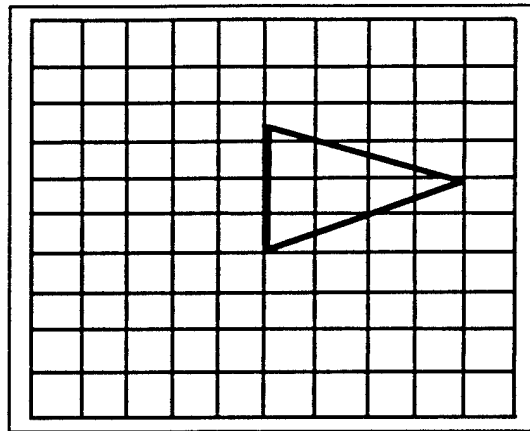
The BSM will be used to center the unresolved spots on the focal plane so as to keep the laser spot pointed at the same point relative to the target. The discrimination algorithms of the angle-angle-range (AAR) imaging assume constant and controlled placement of the target image on the focal plane. 2 μ rad is approximately $\frac{1}{2}$ pixel.

Angle-angle-range imaging requirements

2.13 Residual jitter on the ladar focal plane will be less than $4.2\ \mu\text{rad}$ after target centering and placement on the focal plane.

Justification:

The resolved image of a cone on a 10×10 focal plane has the appearance of the figure. Because the large end of the cone contains important information regarding the coning angle and attitude, it must not "walk off" the edge of the focal plane.



Analysis:

At shortest ranges, each pixel of the focal plane is $2.5\ \mu\text{rad}$. Five pixels from the center to the edge are $12.5\ \mu\text{rad}$. The requirement assumes the $12.5\ \mu\text{rad}$ is $3\ \sigma$ probability, thus a $4.2\ \mu\text{rad}$, $1\ \sigma$ requirement is set.

2.14 Ladar tracking accuracy will be less than $2.0\ \mu\text{rad}$.

Justification:

Subpixel accuracy is needed to maintain the target image in a known position on the focal plane.

Analysis:

$\frac{1}{2}$ pixel centroiding accuracy is needed to maintain pixel placement on the focal plane.

2.15 The ladar receiving aperture should be no less than 25 cm diameter with an obscuration not to exceed 12% of the aperture area.

Justification:

High spatial resolution is required for AAR imaging.

Analysis:

Resolution should be better than about $3.0\ \mu\text{rad}$ in the ladar focal plane. The ratio $\lambda/D = 2.1\ \mu\text{rad}$ for a 25 cm aperture. The blur to $3.0\ \mu\text{rad}$ is allocated to the $\lambda/10$ wavefront error within the ladar receiver field.

2.16 The total wavefront error for the receiver optics, including the common path optics, shall be less than 0.14 waves.

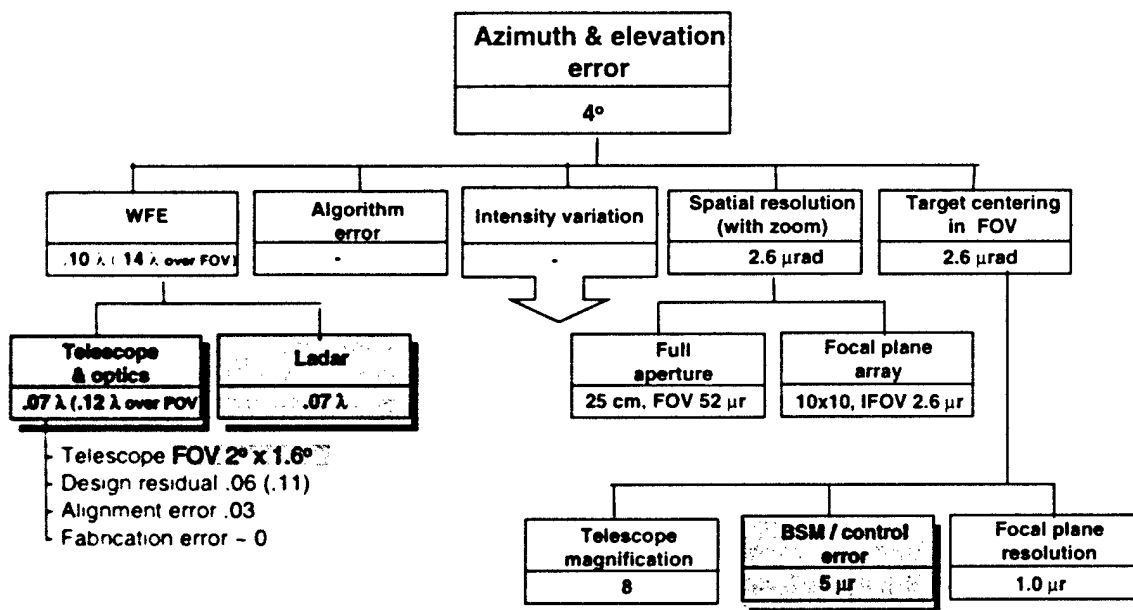
Justification:

The discrimination algorithms of the ladar require a constant or predictable point spread function so that blurring does not mask the discrimination information.

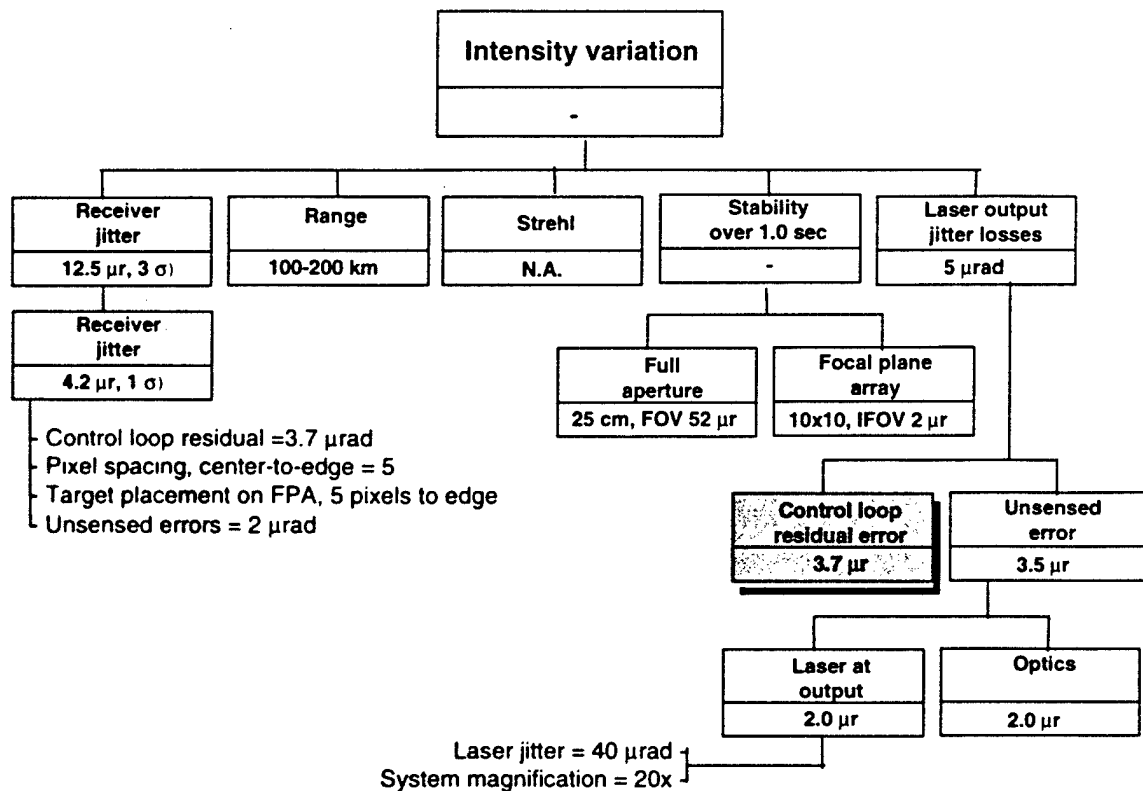
Analysis:

Monte Carlo simulation of ladar discrimination algorithms indicate successful discrimination of the coning angle within 4° when the rms wavefront error is less than 0.14 waves. The form of the wavefront aberration derives from a set of Zernike aberration polynomials typical of a flight qualified three mirror telescope supplied by SSG.

Allocating the wavefront error as 0.12 waves for the telescope and 0.07 waves for the remainder of the ladar receiver optics provides a root-sum-square total wavefront error of 0.14 waves.



The intensity variation has minimal effect on the AAR imaging function and algorithm results.



2.17 The relay optics in the ladar shall be compensated in the receiver path to maintain the receiver path wavefront error at 0.07 waves.

Justification:

The addition of wavefront error to provide the necessary beam divergence must be compensated.

Analysis:

Increasing beam divergence in the optical transmitter path, either in the 532 nm region or in the 1.06 micron region, would be more than allowed by the total wavefront error budget. Compensating optics, such as complementary mirror must be introduced into the ladar receiver beam path.

3.0 Requirements for the Optical Bench

3.1 The optical bench assembly shall fit within the payload envelope of 15" (38 cm).

Justification:

Analysis:

3.2 The optical bench assembly, with all supported subsystems, shall weigh not more than 130 lbs.

Justification:

Analysis:

3.3 The optical bench assembly, with all supported subsystems, shall have a natural frequency greater than 100 Hz.

Justification:

Analysis:

3.4 The optical bench assembly will support the following subsystems and assemblies: afocal telescope, FSM, dichroic beamsplitter, BSM, ladar subsystem, flight cryostat assembly, PSS imaging optics, and IMU.

Justification:

Analysis:

The bench may support the alignment device, as specified in the preliminary design, and a vacuum cell for ground-based testing of the laser at full power.

4.0 Requirements for the Telescope

4.1 The telescope shall have a field-of-view of $1.6^{\circ} \times 2^{\circ}$.

Justification:

Analysis:

SSG FOR vs. on-axis trade

SSG on axis vs off axis trade

4.2 The telescope shall have an optical efficiency at $0.532 \mu\text{m}$ of 0.90, in the band 3-5 μm of 0.79, and in the band 8-12 μm of 0.79, or better.

Justification:

Analysis:

4.3 The telescope shall impart a wavefront error of no more than 0.12 waves rms ($\lambda=0.532 \mu\text{m}$).

Justification:

Analysis:

SSG cost vs wavefront trade

4.4 The telescope shall have a primary mirror aperture diameter of 25 cm.

Justification:

The aperture should be large enough to collect sufficient photons for ladar acquisition and it should also be large enough so that the resolution in the ladar imaging focal plane exhibits sufficient information for AAR discrimination.

Analysis:

Analysis of the ladar with specified laser power requirements indicates that a 25 cm aperture is sufficient for ladar acquisition prior to the target reaching 350 km range. The diffraction-limited resolution (FWHM of point spread function) of a 25cm telescope at $0.532 \mu\text{m}$ is 2 μrad which is roughly 1 pixel in the high resolution imaging configuration.

SSG aperture size vs envelope trade

4.5 The telescope shall have a magnification of between 6 and 10.

Justification:

Analysis:

4.6 The telescope shall have beam path obscurations not to exceed 12% of the clear aperture area.

Justification:

Analysis:

4.7 The telescope shall fit within the payload envelope of >15" (38cm) and be attachable to the optical bench assembly.

Justification:

Analysis:

4.8 The telescope shall not have a design where the energy density at the internal focus results in air breakdown during a ground test of the laser at full power.

Justification:

Ionization of the air during testing will cause damage to the optical system and surrounding electromechanical system.

Analysis:

A vacuum cell can be used for ground testing.

5.0 Requirements for the optical assembly

5.1 The total optical efficiency for the optics common to both the PSS and the ladar at 0.532 μm shall exceed 0.85. The total optical efficiency for the optics common to both the PSS and the ladar in the IR bands shall exceed 0.71.

Justification:

Sufficient energy must pass through the optical train and reach the PSS and ladar focal planes.

Analysis:

The optical efficiencies for the elements are assumed to be:

Telescope assembly, 0.90 (0.532 μm) and 0.79 (IR).

Beamsplitter dichroic, 0.96 (0.532 μm) and 0.95 (IR).

FSM, 0.995 (0.532 μm) and 0.95 (IR).

5.2 The total optical wavefront error imparted by the optics common to both the PSS and the ladar shall not exceed 0.12 waves rms. ($\lambda = 0.532 \mu\text{m}$) The total optical wavefront error imparted by the optics common to both the PSS and the ladar shall not exceed 1.0 waves rms. ($\lambda = 5 \mu\text{m}$).

Justification:

Spatial blurring of the optical signal must be kept to a minimum so it does not mask the information regarding target position or shape.

Analysis:

5.3 The optical system design should provide a plane in the optical train near a pupil.

Justification:

A pupil position or a conjugate is the only place where beam steering mirrors can be placed that do not force large beam walk and oversized optics on the other elements of a wide field-of-view system.

Analysis:

SSG strawman design and beamwalk analysis.

5.4 The optical system design should provide a dichroic beamsplitter for separating the incoming PSS path and the ladar path with transmission of greater than 0.96 at 0.532 μm and a transmission greater than 0.95 at MWIR and LWIR bands.

Justification:

No detectors are common to the MWIR, LWIR, and the 0.532 μm wavelengths.

Analysis:

The beamsplitter, nominally a dichroic, must split the IR incoming energy from the outgoing high energy ladar pulse and incoming ladar return. To avoid beamsplitter energy absorption and subsequent optical distortion, the high power 0.532 μm pulse will be reflected off a coated surface while the IR return will be transmitted through it. The ladar pulse is assumed to be 250 mJ, 1.3 ns width with a 100 pulses-per-second repetition rate (25W average power, 190 MW peak pulsed power). The beamsplitter should have a reflectivity of greater than 0.96 at 0.532 μm and a transmissivity greater than 0.95 at MWIR and LWIR bands.

5.5 The beam steering mirror (BSM) shall allow for open-loop pointing of the outgoing ladar and point ahead correction for the return pulse.

Justification:

The tracking function and optical pointing function of the beam train is provided by the PSS and the FSM. Within the FOV of the PSS, the target will appear. The FP&A will direct the controls of the BSM to steer the outgoing ladar pulse toward the target with the point ahead bias.

Analysis:

6.0 Requirements for the IOS integrated controls assembly

6.1

Justification:

Analysis:

6.2

Justification:

Analysis:

6.3

Justification:

Analysis:

7.0 Interface Requirements

7.1 PSS to ladar static boresight alignment after calibration shall be $<10 \mu\text{rad}$

Justification:

The errors associated with pointing the laser after PSS handover must be low enough so that ladar acquisition can occur with at least 90% probability outside 350 km range.

Analysis:

7.2 The system must be capable of being tested in ambient conditions, 1.0 atmosphere dry air, 1 g.

Justification:

Ground testing of an integrated system is required.

Analysis

7.3 The system must be capable of being tested and operated in flight conditions, vacuum, $<.01 \text{ g}$.

Justification:

Flight test conditions.

Analysis

Appendix S

DITP OPS Working Group:

Preliminary Report on the optical system dichroic beamsplitter

Jose Presilla, February 1999

This report discusses whether it is possible to design a Beam Splitter able to reflect a high power visible laser beam ($\lambda = 0.532 \mu\text{m}$, $E = 250 \text{ mJ/pulse}$, $\tau = 1.3 \times 10^{-9} \text{ s}$, $n = 100 \text{ pulses/s}$), and to transmit in the infrared ($8 - 12 \mu\text{m}$).

Preliminary background

Beam splitters (B/S) divide a beam of light into two components. They are available in two configurations: The simplest one, called the slab beam splitter, is made of a plane parallel substrate with a beam splitting coating, exposed to the air, on one side, and an anti-reflection (AR) coating on the other. The cube beam splitter is designed to be more rugged, by avoiding exposure to the environment, which is accomplished by immersing the coating in a medium with an index of refraction close to that of the substrate.

Each type of beam splitters has its advantages: In the slab beam splitter the angle of incidence can easily be varied and this type of design is relatively inexpensive when compared with a cube type. The cube configuration – a symmetric system – is designed to function at a nominal angle. This can be advantageous in optical systems where equal path lengths are required in both beams, to minimize aberrations or other differences between the two beams, which is especially true when the beams are recombined in a second pass through the beam splitter. In the cube beam splitter, the coating is protected against the environment by the bonding cement, and up to four surfaces may require an AR coating in this design.

The coating used in beam splitters can be either a dielectric stack or a metal layer. Most metal films can be used as beam splitter coating, though some have specific properties that are better than others. Dielectric stacks are preferred in high power laser systems/applications because dielectric layers absorb very little energy.

Beam splitters are generally polarizers, and therefore, need to be used with care in an optical system. Multiple polarizing beam splitters in a system with no other polarizers can lead to difficulties when the polarizing components are not explicitly identified.

(i) Slab Beam Splitter

Because the surfaces and coatings of these beam splitters are usually oriented such that the light is incident at non-normal angles, polarization parameters of the optical system need to be considered. The unequal reflectances, that are usually obtained, can cause difficulties when a laser beam with randomly polarized output is directed at such a device. This is because the beam splitter would convert the fluctuations in the plane of polarization into intensity noise.

Studies of the angular performance of slab beam splitters are informative because they may frequently be used at variable angles of incidence.

(ii) Cube Beam Splitters

Cube beam splitters are inherently rugged as the coatings are not exposed to the environment. These beam splitters are designed to function at a nominal angle of incidence, and are ideal for optical systems that require equal path lengths in both beams. The symmetry of the cube ensures that there can be no problem with orientation of the incident light with respect to the beam splitter. The performance of this type of beam splitter is very similar to that of the slab design. Most of the comments that were made about the slab beam splitter are also pertinent to the cube version. The same effects, as for the slab B/S, can be observed at high angles of incidence, and the polarization effects are similar.

(iii) Dichroic and Trichroic Filters

Dichroic and trichroic filters separate wavelength bands, transmitting certain wavelengths while reflecting others. Although this can be accomplished with edge filters, color splitters are frequently used at non-normal angles of incidence. Because they are used at angles where polarization can be severe, a primary consideration should be the state of polarization of the incident light beam. If the light is mostly polarized in one plane, then the designing process can at times be simplified over what may be necessary if the incident light's polarization state has to be assumed to be random or unpolarized. During the lay-out of an optical system, it is useful to keep in mind the difficulties polarization may cause so as to avoid a situation in which the desired filter cannot be built.

The most extensive use of dichroic filters is in the separation of infrared radiation from visible light so that the reflected beam is *cold*; this is the origin of the term *cold mirror* (ex. projector lamps, medical or dental reflector lamps).

Cold Mirror Design

On the basis of the requirements stated above, i.e. separation of visible and infrared beams, the cold mirror is the most appropriate design for this application.

In designing such B/S the first choice made was to find a substrate material with the highest possible transmittance in the 8–12 μm region. The materials investigated were

$\text{Al}_2\text{O}_3(\text{c})$, $\text{Si}(\text{c})$, SiO_2 and $\text{ZnSe}(\text{c})$. The transmittance for $\text{Al}_2\text{O}_3(\text{c})$ and $\text{SiO}_2(\text{a})$ are less than 0.1 ppm all along the 8–12 μm region, while the transmittance for $\text{Si}(\text{c})$ and $\text{ZnSe}(\text{c})$ average 30% and 68% along the same range, see Figures 1-2. Thus $\text{ZnSe}(\text{c})$, with the overall largest transmittance of the two, was selected for this task. A thickness of 4.905 mm was chosen for this substrate. The thicknesses used for the $\text{Al}_2\text{O}_3(\text{c})$, $\text{Si}(\text{c})$, and $\text{SiO}_2(\text{a})$ substrates were 5.031, 5.080, and 5.009 mm.

A case for a $\text{ZnSe}(\text{c})$ substrate with a thickness of 9.810 mm (twice the one above) was also investigated. The transmittance (not shown) is also about 68% from 8–11 μm and decreases slowly to about 65% from there on.

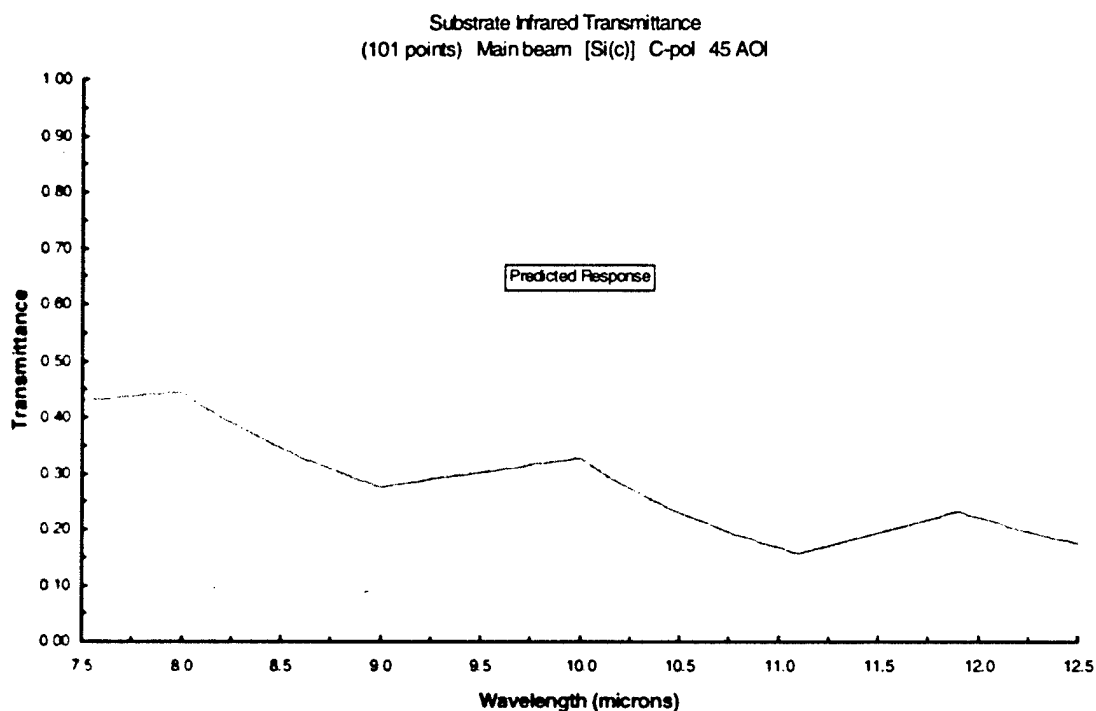


Figure 1. Silicon substrate infrared transmittance.

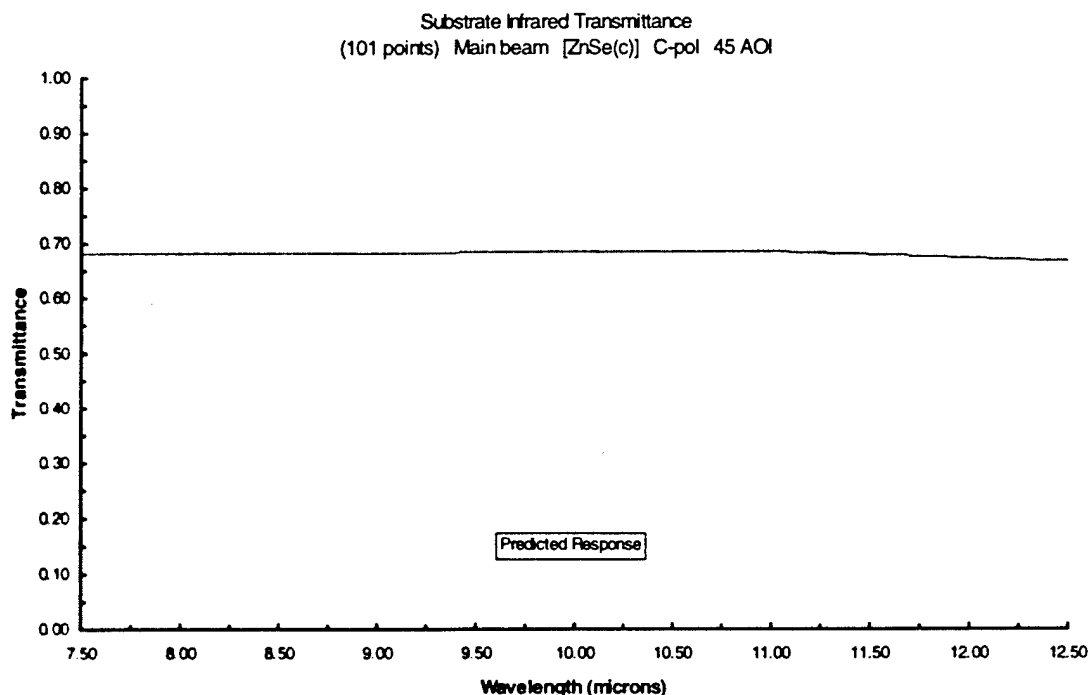


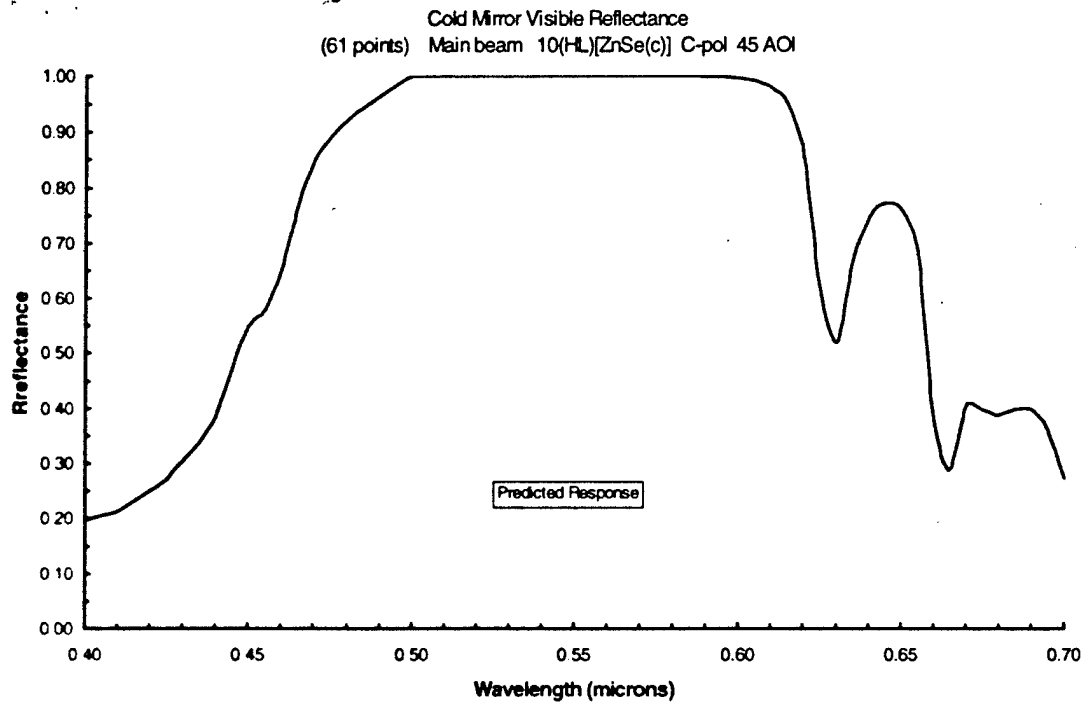
Figure 2. ZnSe(c) substrate infrared transmittance.

After selecting the most transmissive IR substrate, the next step consisted in creating a coating design capable of maximizing the reflectance of the $0.532\text{ }\mu\text{m}$ band. This was accomplished with a ten ZnSe/ThF₄ layer pair (LP) stack, designed to have QWOT at $0.532\text{ }\mu\text{m}$ and 45° AOI. The cold mirror's (10 LP plus substrate) $0.4 - 0.7\text{ }\mu\text{m}$ reflectance (R_s) is shown in Figure 3. The R_s values in the $0.50 - 0.60\text{ }\mu\text{m}$ plateau are as follows: $R_s \geq 99.98\%$ between $0.50 - 0.555\text{ }\mu\text{m}$, with $R_s = 99.989\%$ at $0.532\text{ }\mu\text{m}$; $99.90\% \leq R_s \leq 99.98\%$ between $0.56 - 0.58\text{ }\mu\text{m}$; and $R_s = 99.4\%$ at $0.60\text{ }\mu\text{m}$, dropping below 99% from there on. For completeness, the cold mirror's IR reflectance is shown in Figure 4.

The other parameter defining the design criterion is the transmittance in the $8 - 12\text{ }\mu\text{m}$ region. This, of course, is now influenced by and dependent on the properties of the front coating design. The resulting cold mirror transmittance all along the $8 - 12\text{ }\mu\text{m}$ region of interest (shown in Figure 5) is well over 75% . For completeness, the cold mirror visible transmittance is shown in Figures 6.

The cold mirror's front film and substrate visible and IR absorptance are shown in Figures 7-10.

Figure 3. Cold mirror visible reflectance.



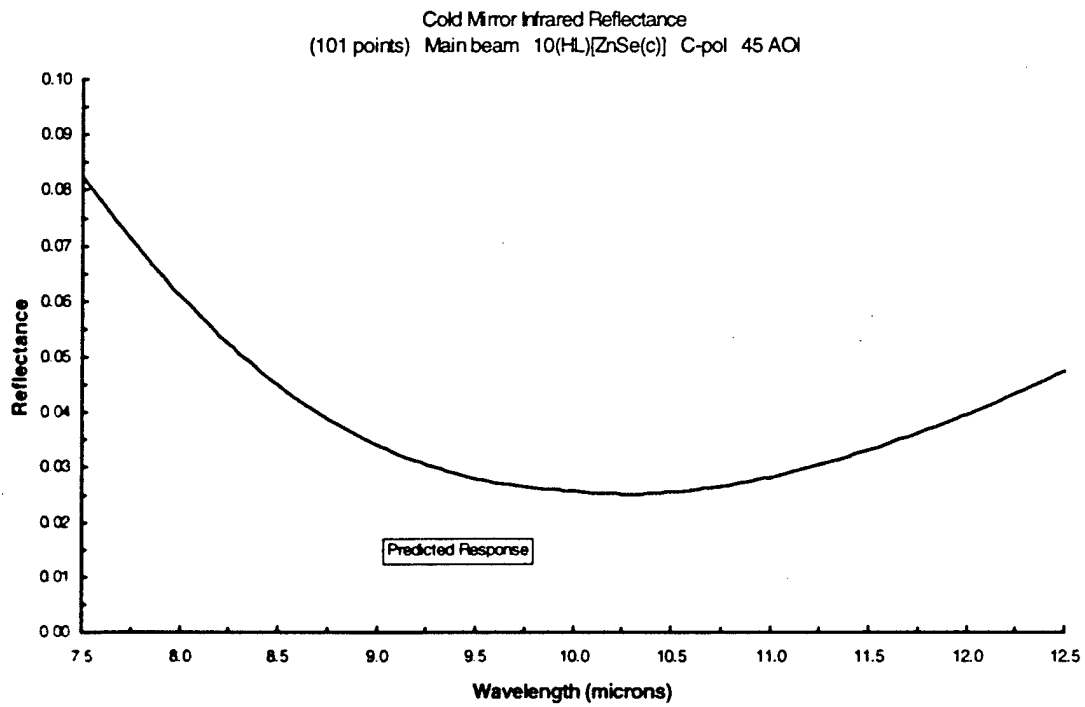
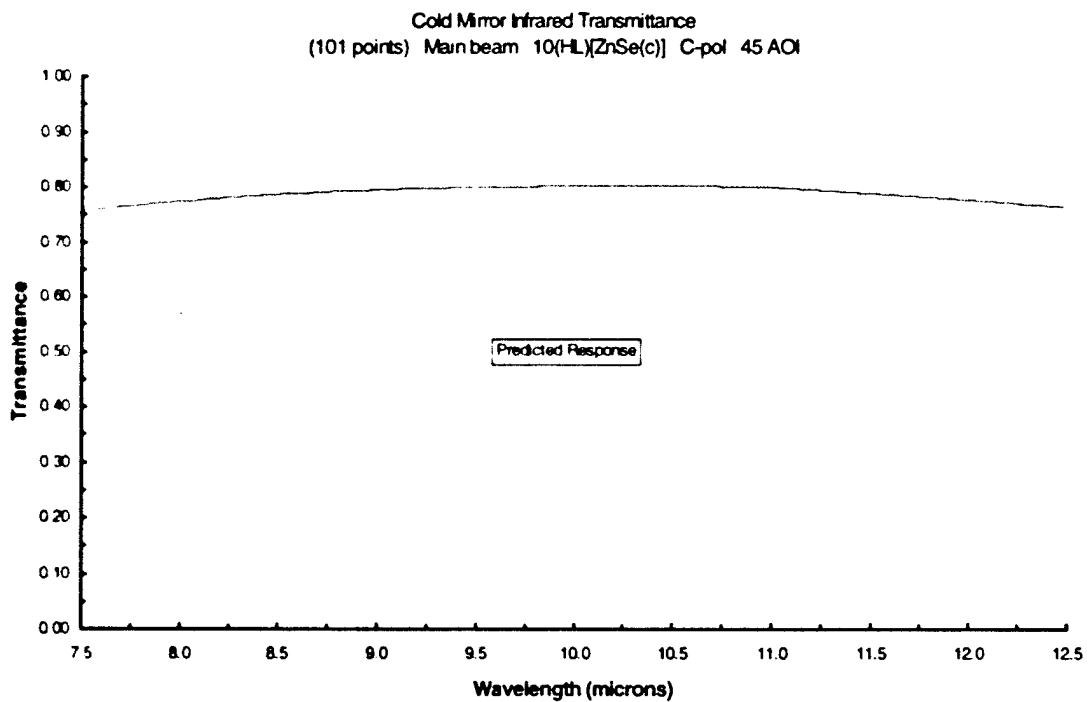
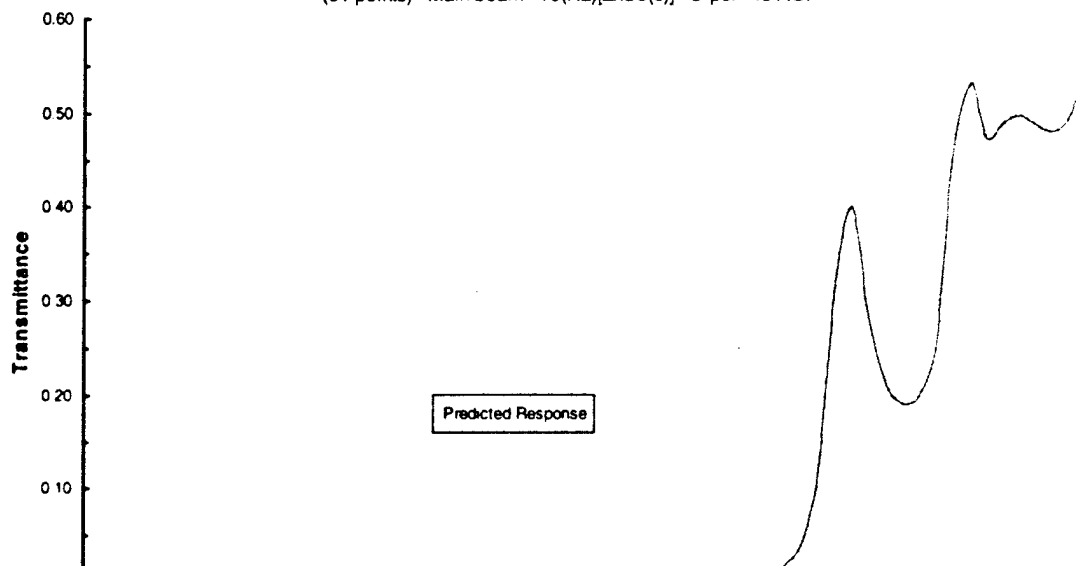


Figure 4. Cold mirror IR reflectance.

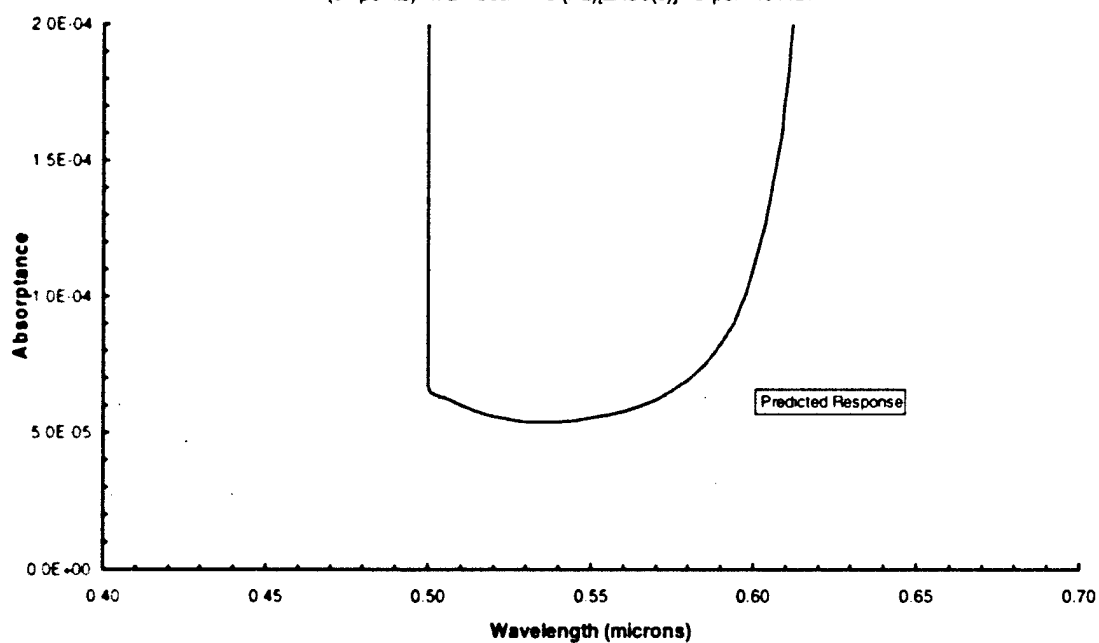
Figure 5. Cold mirror IR transmittance.



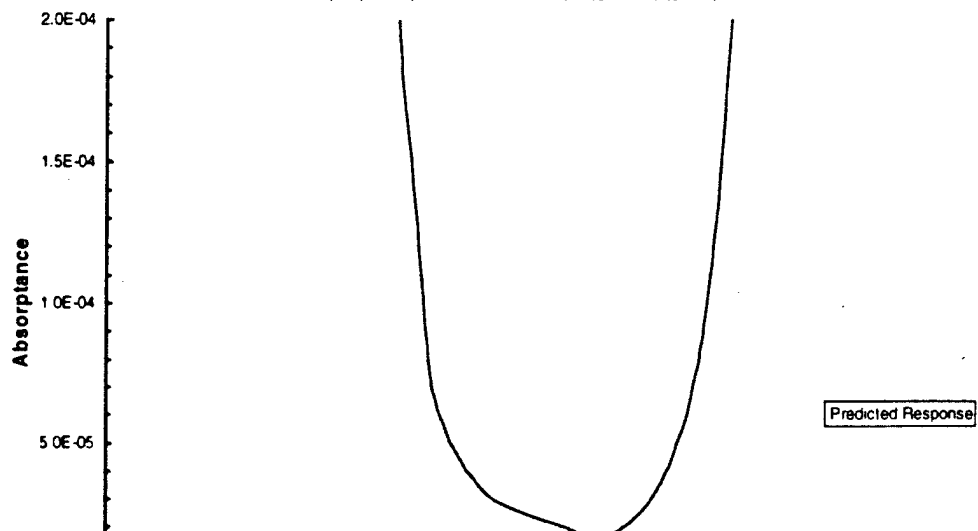
Cold Mirror Visible Transmittance
(61 points) Main beam 10(HL)[ZnSe(c)] C-pol 45 AOI



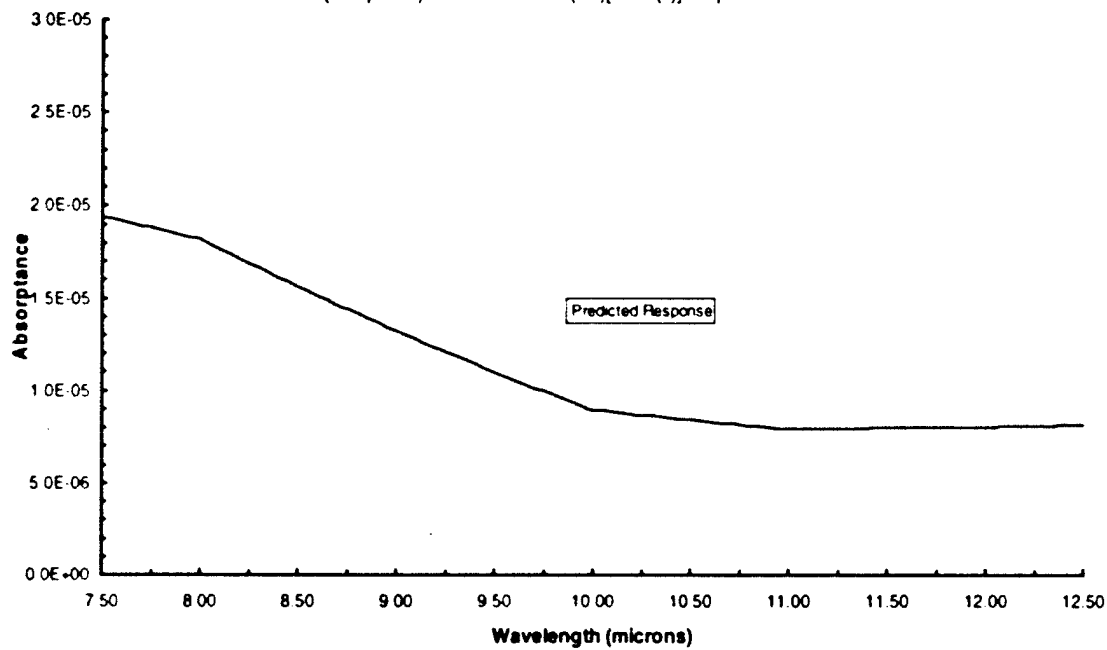
Cold Mirror Visible Front Film Absorptance
(61 points) Main beam 10 (HL)[ZnSe(c)] C-pol 45 AOI

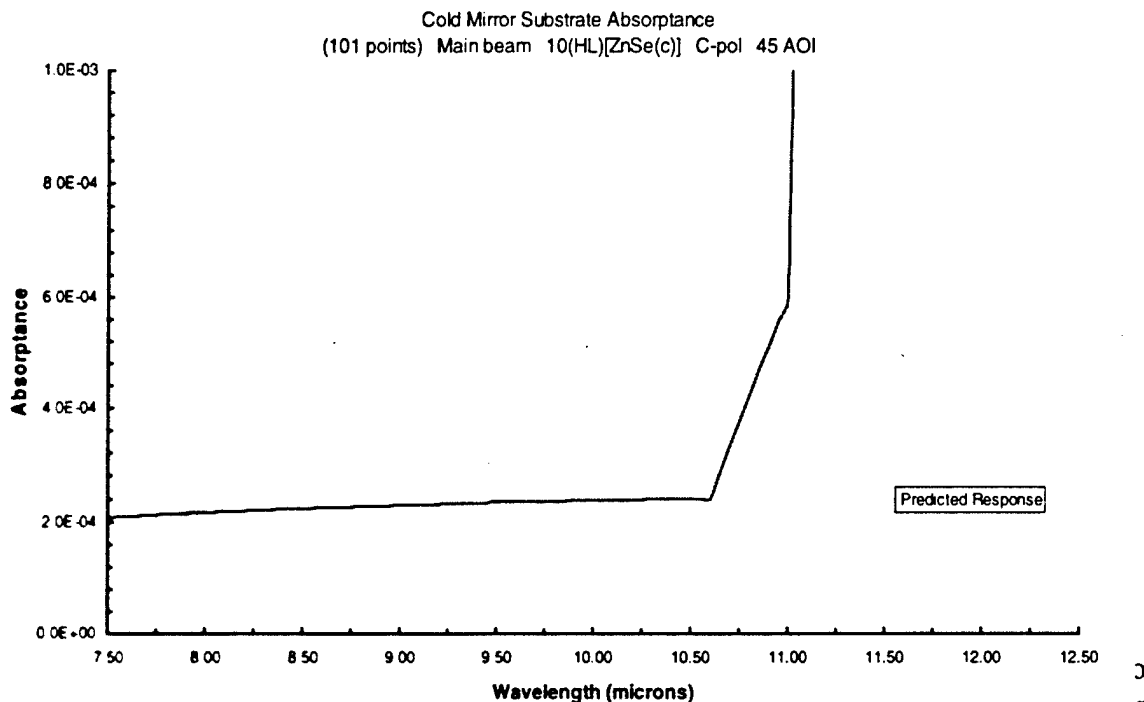


Cold Mirror Substrate Absorptance
(61 points) Main beam 10 (HL)[ZnSe(c)] C-pol 45 AOI



Cold Mirror Infrared Front Film Absorptance
(101 points) Main beam 10 (HL)[ZnSe(c)] C-pol 45 AOI





density, for the nominal 2 cm diameter beam at the $1/e^2$ points, 61.2 Mega-Watts/cm². A very important question to answer is whether the planned materials for the cold mirror will be able to tolerate such incident intensities.

Laser damage threshold measurements on single-silicon crystal substrates coated with 13 LP of ZnSe/ThF₄ conducted by Mr. Remesh Shori at U.C.L.A. for the BMDO DE/SETA Support Contract in 1997 [see pages 3-26(8) of Task 79 Final Report], suggest that the answer may be affirmative. In these tests, one of the samples tested, having a surface roughness of 2.2 Å, was able to survive several 15 – 20 minute duration tests with incident intensities of between 977 – 1036 Mega-Watts/cm², while a second sample, with a larger surface roughness, damaged at this intensity within the first 1– 5 pulses. Since the coating materials in the witness samples tested are identical to the ones planned in the cold mirror (the substrate materials are different though, Si(c) instead of ZnSe), this suggest that it might be possible that the cold mirror will be able to survive the planned power levels, with the proviso that similar surface roughness are employed. It is however recommended that witness samples of the planned configuration be fabricated and damage tested.

Even though, the cold mirror's front film and substrate absorptance values for the 0.532 μm band are below 60 ppm and 30 ppm respectively, see Figures 7 and 8, we ought to mention that near 0.5 μm the k-values for ZnSe and ThF₄ in our data base have not been experimentally verified/contrasted, and therefore the absorptance values near that wavelength could be as much as an order of magnitude higher from the ones depicted in these figures. Nevertheless, we believe that the absorptance would still remain sufficiently low to allow this application (depending on the laser damage threshold). The cold mirror's front film IR absorptance stays under 19 ppm throughout the 8 – 12 μm region (see Figure 9), while the cold mirror's substrate absorptance is less than 250 ppm

from 8 – 10.5 μm , and raises rapidly thereafter (see Figure 10). Figure 10 shows significant slope discontinuities in this region due to the small number of data points used in the calculations (100 data points on a 5 μm span is equivalent to sampling a data point each 0.05 μm). These discontinuities also apply, in some measure, to Figures 7 and 8 (despite the fact that the sampling rate now is 10 times higher) but here, they also may be due to an incomplete (insufficient) material data base for this region. Although IR-power levels were not specified, in the future they will have to be defined to determine if the cold mirror material's properties are compatible with them.

Even though the angle of incidence, polarization, visible-reflectance and IR-transmission performance requirements for this application were loosely defined, the cold mirror design described above, with 10 ZnSe/ThF₄ layer pairs on a ZnSe(c) substrate, is an excellent starting design prototype. In conclusion, design of this beam splitter seems to be feasible, but witness samples need to be fabricated and damage tested. When the performance specifications will be more clearly delineated, this design will be tailored more closely in order to meet the particular requirements. The final design will include an anti-reflection coating on the back surface.

Appendix T

Issues on DITP ladar concept of operation

Robert K. Tyson, February 1999

I studied three different issues using a Monte Carlo analysis of DITP ladar. The first issue addressed how the acquisition probability would change if the far-field laser spot at the target plane was not Gaussian shaped, but flat along the field with reduced peak intensity. The second issue addressed detection probability during acquisition considering that each laser pulse is a unique jitter realization. The third issue addressed the intensity modulation error induced by laser jitter with a Gaussian or a flat spot.

1. Acquisition probability

Comparison of Gaussian spot or flat spot

The analysis was as follows: The target was assumed to be a 40cm diameter cone x 1.4 m long. All cases analyzed assumed that the mean aspect angle is 30°. The total probability of acquisition was determined by assessing the probability of acquiring at each shot and looking at success criteria. A successful acquisition is defined as one where there are 3 "hits" out of 10 "shots" from (at least) one range between 400km and 350km. There are 3 visits to the target, 400km, 375km, and 350 km. For statistical accuracy, we used 10,000 Monte Carlo test cases for each data point.

The beam axis has a fixed boresight error offset (10 or 16 μ rad) from the center of the target at each range. The handover error is composed of a value Q with contributors from the centroiding/tracking error of the PSS, and the beam pointing error of the BSM/ladar. The value Q is a 1 σ error, in each of two orthogonal axes, for each of the two contributors, at each range. An additional pointing error arises due to jitter which is assumed to be different at each shot (not each range). For this analysis, we assume that the residual jitter, a 1 σ error, in each of two orthogonal axes, is also value Q . Note: these fixed and variable handover values and jitter residuals can be traded against one another. Handover values are changed at each range; jitter values are changed with each shot, or pulse.

For this analysis, we also assume that we can "flatten" the far field laser spot on the target. With appropriate optics, not yet defined, we assume that we can create a spot with a broad supergaussian-like intensity profile, with reduced peak intensity. Peak intensities of 25% and 50% of a pure Gaussian spot are analyzed.

The results are embodied in Fig. 1-1 and 1-2. Acquisition success is plotted against the value Q (remembering that Q is the value for three independent error sources, each with two axes).

In Fig. 1-1, a 16% reflectivity target is assumed. The two lower lines (flat intensity 25% peak compared to Gaussian) show that for a flat spot, even with as low as 10 μ rad fixed boresight error, barely 85% acquisition success is achieved. When 16 μ rad fixed error is applied, the 50% intensity/ flat beam can achieve better than 95% success with $Q=6$ μ rad or less. The Gaussian beam requires 5 μ rad or less to achieve 95% success. When the fixed boresight error is held to 10 μ rad, the top two lines on Fig. 1-1, the difference between a Gaussian spot and a flat spot with 50% reduced peak intensity is small. To achieve 95% success, the value Q should be kept less than 8 μ rad for all error sources. The baseline case, that which we have assumed for OPS Working Group requirements analysis, assumed a Gaussian beam, 10 μ rad fixed boresight error, and $Q < 5$ μ rad. Greater than 99% probability of successful acquisition is achieved.

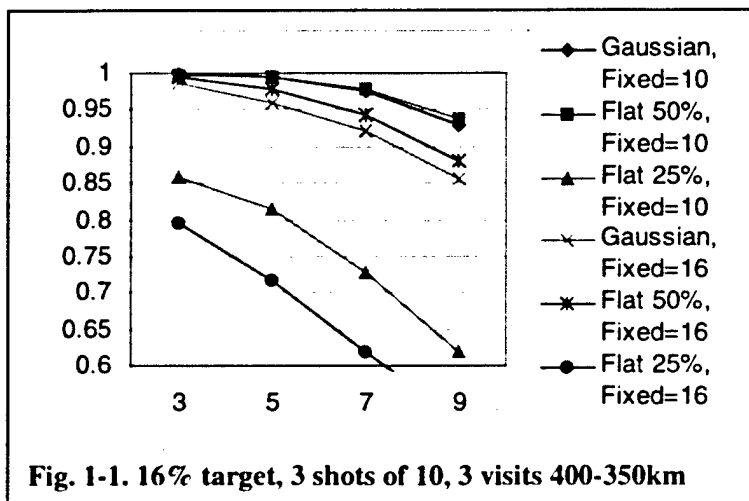


Fig. 1-1. 16% target, 3 shots of 10, 3 visits 400-350km

In Fig. 1-2, a 24% reflectivity target is assumed. The two lower lines (25% flat spot) show that with 10 μ rad fixed boresight error, only 98% acquisition success is achieved with as little as $Q=3$ μ rad. When 16 μ rad fixed error is applied, the 50% intensity/ flat beam can achieve better than 95% success with $Q=9$ μ rad or less. The Gaussian beam requires 8 μ rad or less to achieve 95% success. When the fixed boresight error is held to 10 μ rad, the top two lines on Fig. 1-2, to achieve 98% success, the value Q should be kept less than 7 μ rad for all error sources.

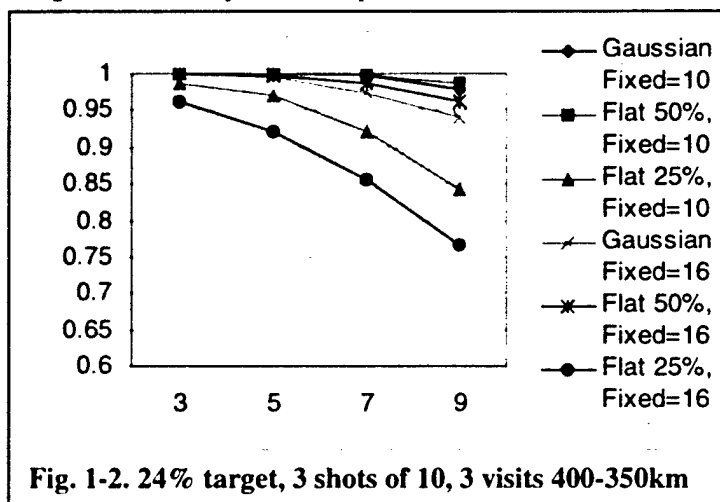


Fig. 1-2. 24% target, 3 shots of 10, 3 visits 400-350km

2. Acquisition probability

Probability of hits due to range, target, boresight bias, jitter, and number of shots

To analyze some effects of statistics on the target acquisition scheme, I looked at how target acquisition takes place by a Monte Carlo analysis. The variables were: Target Range & Target Reflectivity (which convert to average photoelectrons received from the peak of the Gaussian laser spot) and Boresight Offset & Jitter (which determine the position off-peak for the target illumination).

The system Strehl ratio was set at 0.8 to account for losses other than the assumed optical transmission losses. All values are scaled from the value: peak of 2.8 photoelectrons at 400 km with an 8% target and no offset and jitter. Reinterating, the target was assumed to be a 40cm diameter cone x 1.4 m long with a mean aspect angle of 30°.

What is calculated is the probability of the n^{th} hit to occur at the j^{th} shot when m shots are tried. Values from n, j , or $m=1$ to 25 were calculated. for 16% and 24% targets, the ranges 400km and 350km, and 0, 5, 10, 15 μrad fixed boresight error, and 0,5, 10 μrad jitter. The boresight error includes fixed offset, random centroiding/tracking, and random mirror positioning error.

This analysis produced 48 permutations of targets, ranges, boresight, and jitter, and 625 n - j combinations for each permutation. Probability values for each permutation were compiled in table form. A few of the more representative data sets is presented below.

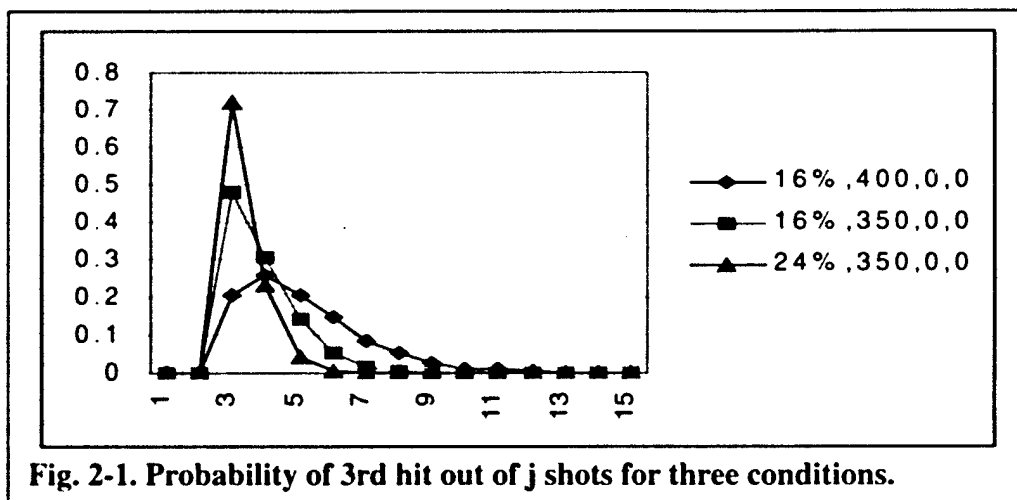


Fig. 2-1. Probability of 3rd hit out of j shots for three conditions.

No boresight error or jitter

Fig. 2-1 shows how the received photoelectron count, affected by reflectivity and range, greatly affects the probability of detection. The upper curve, (triangle symbol, 24% reflectivity, 350km range, no handover error, and no jitter), indicates that the third successful detection (a "hit") occurs 72% of the time on the third shot. The third hit is

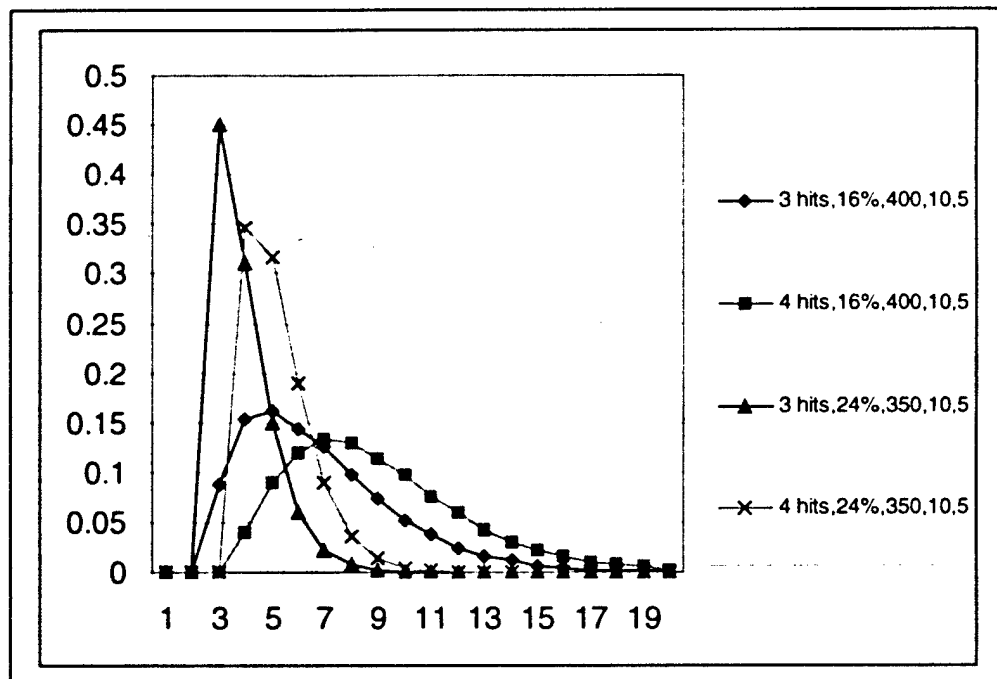
detected on the fourth shot 23% of the time; and the third hit is detected on the fifth shot 4% of the time. Thus, in 5 shots, 3 hits are detected 99% of the time. By 7 shots, 3 hits are always detected. For the middle curve, (square symbol, 16% reflectivity, 350km range, no handover error, and no jitter), indicates that the third hit occurs 48% of the time on the third shot. The third hit is detected on the fourth shot 31% of the time; and the third hit is detected on the fifth shot 14% of the time. Thus, in 5 shots, 3 hits are detected 93% of the time. By 9 shots, 3 hits are almost always detected.

For the lower curve, (diamond symbol, 16% reflectivity, 400km range, no handover error, and no jitter), the third hit occurs on the third shot only 21% of the time. It takes 5 shots, to get the third hit 66% of the time. It takes 10 shots to get the third hit over 99% of the time.

With boresight error and jitter

When boresight errors and jitter are included in the analysis, the probabilities differ. We consider two extreme cases for acquisition: a 16% target at 400km and a 24% target at 350km. All cases assume **10 μ rad fixed boresight bias and 5 μ rad jitter**. We compare how many shots are needed for either 3 detections (hits) or 4 detections.

From Fig. 2-2, we can follow the 3 hits/16% curve. The third hit is reached on the third shot only 9% of the time. It takes 11 shots to get 3 hits 95% of the time. It takes 15 shots to get 3 hits 99% of the time.



If a successful acquisition is defined as getting 4 hits, for the 16% target, 400 km case, it takes 15 shots to get 4 hits 95% of the time. It takes 18 shots to get 4 hits 99% of the

time. In 10 shots, 4 hits are achieved 72% of the time. In 11 shots, 4 hits are achieved 80% of the time.

For the brighter return (24% target, 350 km), results are considerably improved. 3 hits are achieved in 5 shots 91% of the time. By 7 shots, 3 hits are achieved virtually 100% of the time. For the 4-hit criterion, 95% of the time, 4 hits are achieved in 7 shots. 99% of the time, 4 hits are achieved in 9 shots.

3. Modulation error due to jitter

Comparison of Gaussian spot or flat spot

It is necessary to have a steady and predictable ladar beam on the target in the range between acquisition (350km) and the beginning of resolved AAR imaging (200km). The response of the coning algorithm depends upon a steady intensity on the target, altered only by range differences. We studied the effect of handover error on the jitter-induced modulation error of the signal returning from the target.

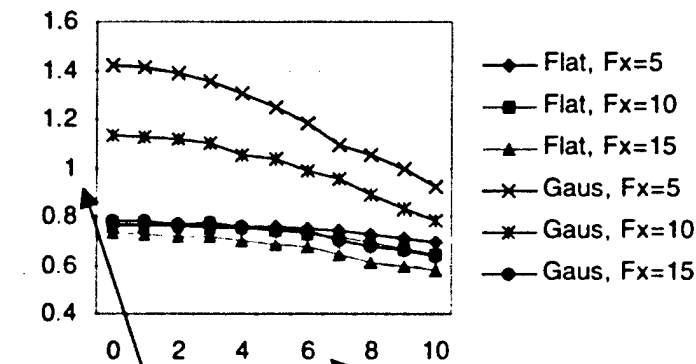
The analysis was similar to that from Sec. 1. The target was assumed to be a 40cm diameter cone. For each range, the boresight bias was held constant. For statistical accuracy, we used 10,000 Monte Carlo test cases for each data point. We analyzed numerous target reflectivities and ranges, but only the two extremes, 24% target at 200km and the 16% target at 350km, are shown here.

For this analysis, we also assume that we can "flatten" the far field laser spot on the target. For this analysis we used a smooth far field spot with an intensity peak of 50% of the Gaussian equivalent. We assume that the optical system Strehl ratio is 0.8 which accounts for fixed power losses of the laser and optics transmittivities.

Fig. 3-1 shows plots of the average photoelectron count at each jitter value, for boresight errors of 5, 10, and 15 μ rad. The top of Fig. 3-1 shows the average p.e. count for the 16% target at 350 km. The bottom plot is for 24% target at 200 km. The 14X increase in p.e. count between the two graphs is due to 1.5X for the difference in reflectivity and 9.4X for the difference

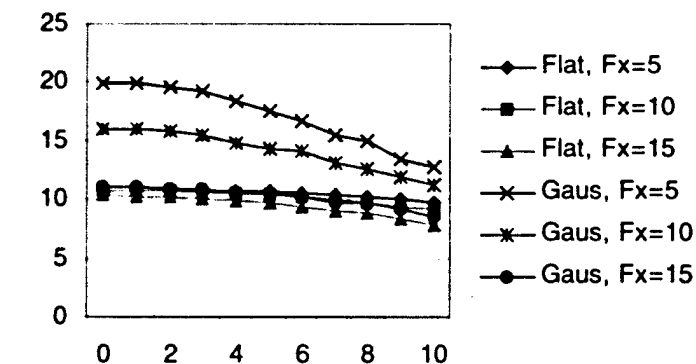
Fig. 3-1

16% target 350 km



Avg. photoelectrons Jitter (μ rad)

24% target 200 km



in range. The top two lines are for a Gaussian spot. The target return is higher because the peak is higher for the Gaussian (vs. the flat spot). The lines representing Gaussian spots show much more sensitivity to jitter error represented by the horizontal axis. When the spot has a flat intensity profile, there is little sensitivity to handover error and jitter. When the fixed error is large, 15 μ rad, and the target is near the edge of the spot, large handover errors or jitter reduce the overall photoelectron count.

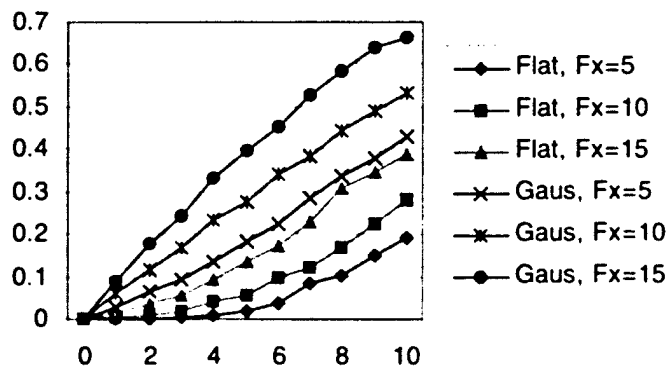
The modulation noise (error) due to jitter, for single pulse intensity measurements, is shown in Fig. 3-2. The error is calculated in the following way. At each range, the fixed boresight error is assigned. The "fixed" value includes both fixed boresight errors and random handover errors as they were defined in Sec. 1. This process isolates the jitter contribution. 10,000 samples are taken at each range. The jitter angle realization is changed for each sample, maintaining the proper standard deviation for the jitter angle. The standard deviation of the *received intensity* is compared to the average p.e. count. The modulation noise to jitter ratio is plotted in the vertical axis of Fig. 3-2.

The modulation error increases strongly with increasing jitter. For the Gaussian spot, the modulation noise increases with jitter at a faster rate than that of a flat spot because the slope of the spot is larger and variations along the spot profile are seen as intensity noise.

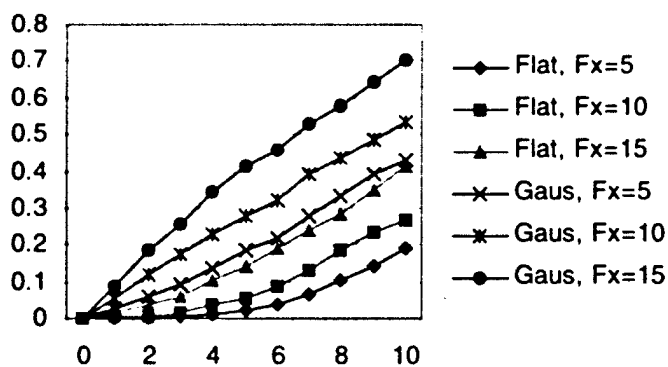
It is necessary that intensity modulation noise be kept to a small value so that coning angle algorithms perform correctly. For example, to detect the difference between 12° coning and 4° coning, the modulation noise ratio should be below 0.1. To detect the difference between 8° coning and 4° coning,

Fig. 3-2

Modulation noise 16% target, 350 km



Modulation noise 24% target, 200 km



the modulation noise ratio should be below 0.07. Because there are also other sources of modulation noise, such as laser intensity nonuniformity and target reflectivity variation, the noise from jitter should be below these total allowed values.

From this analysis, observing Fig. 3-2, we see that, **for single pulse intensity measurements**, for the 16% or the 24% targets, the preferred spot profile should be flat, rather than Gaussian. (There is little sensitivity to the target reflectivity.) With a flat profile, and fixed boresight bias error of 10 μ rad, a modulation noise less than 0.1 is possible with jitter less than 6 μ rad. With a fixed error of 15 μ rad, a modulation noise less than 0.1 is possible with jitter less than 4 μ rad.

If the spot is Gaussian in the target plane, with a fixed error of 10 μ rad, a modulation noise less than 0.1 is possible with jitter less than 1.5 μ rad (which is physically unrealistic).

To achieve a modulation noise less than 0.07, even less jitter is tolerated. For a flat profile, and 15 μ rad fixed error, a modulation noise less than 0.07 is possible with jitter less than 3.5 μ rad. For a Gaussian profile, and 15 μ rad fixed error, a modulation noise less than 0.07 is possible with jitter less than about 0.8 μ rad.

Further analysis indicates that this jitter-induced noise can be reduced significantly with multiple-pulse integration. Using the same Monte Carlo techniques as the single-pulse case, we find *that intensity modulation noise error is reduced by the square root of the number of pulses in the integration*. Thus, for a Gaussian spot, we can achieve less than 10% modulation noise (on the 16% target, 350 km, Fig. 3-2) by holding the fixed error to 10 μ rad and the jitter to 5 μ rad, and integrating 9 pulses rather than making the measurements with a single pulse. This can be further reduced for a Gaussian spot at the closer (200km) range and higher reflectivity target. We can achieve less than 7% modulation noise by holding the fixed error to 10 μ rad and the jitter to 5 μ rad, and integrating 16 pulses.